Cranfield University

MAUD SERAFFON

PERFORMANCES OF AIR PLASMA SPRAYED THERMAL BARRIER COATINGS FOR INDUSTRIAL GAS TURBINES

School of Applied Sciences
Centre for Energy and Resource Technology
Cranfield University, Cranfield, Bedfordshire MK43 0AL

PhD Thesis
Cranfield University

School of Applied Sciences
Academic year 2012

MAUD SERAFFON

PERFORMANCES OF AIR PLASMA SPRAYED THERMAL BARRIER COATINGS FOR INDUSTRIAL GAS TURBINES

Supervisors: Pr. John Nicholls and Dr. Nigel Simms

This thesis is submitted in fulfilment of the requirements for the degree of Doctor of Philosophy

ACKNOWLEDGMENTS

I would like to thank the people who have assisted me throughout the 3 years and a half of my PhD. studies at Cranfield University, and without whom this work would not have been possible.

Firstly I would like to express my deepest gratitude to my academic supervisors, Dr. Nigel Simms and Prof. John Nicholls for their advice, discussions and support during the entire PhD. Even if very busy, they were always available and enthusiastic to encourage me, answer questions and tackle endless corrections. I am also very grateful to them for allowing me to present this work in UK and US renowned conferences and meetings.

This work was supported by industrial partners (Alstom Power Ltd., Doosan Babcock, E.ON, National Physical Laboratory, Praxair Surface Technologies Ltd, QinetiQ, Rolls-Royce plc, RWE npower, Siemens Industrial Turbomachinery Ltd. and Tata Steel) and universities (Loughborough, Bristol and Nottingham University) as part of the Supergen PLE project. Dave Rickerby from Rolls-Royce always gave his honest opinions, helpful suggestions and practical knowledge on gas turbines and thermal barrier coatings. The visit to Tilbury coal power plant organised by RWE was also a very enjoyable and educational experience. From Loughborough University, Prof. Rachel Thompson allowed me to use the facilities, where I was supervised by Dr.Geoff West. Dr. Mudith Karuaratne's expertise enabled me to understand better certain aspects of elemental diffusion. From Bristol University, were I spent memorable week-ends, I would like to acknowledge the wonderful Dong Liu with whom it was a pleasure to work. Her supervisor Prof. Peter Flewitt advice was very constructive. I would like to thank other PhD students and staff from the Supergen project, especially Alexandros Skouras, Sabrina Yan, Troy Liu, Mikolaj Lukaszewicz and Tomasz Dudziak for making the meetings seem shorter.

Many people from the staff at Cranfield contributed to this work, by technical advices and sharing their experience: Dr. Joy Sumner and her attention to details taught me to perfect my writing skills. Mr Tim Pryor always here to help with the high temperature facilities and especially those furnace dials I never managed to set up myself. Mr Andrew Dyers for his patience during the time I spent using the

metallographic facilities but above all for his help with the nano-indentor and the FIB. Mrs Christine Kempton and Mr. Matt Kershaw trained me on the SEM and the XRD. Mr Xian Wei Liu helped me with the SEM and TEM analysis. Mr Andrew Potter helped in the oxidation lab. Dr Jeff Rao's help and patience to sort out the endless problem with the stubborn CVCI and Leybold were inestimable. The technical knowledge of Andrew Stellard and Matthew Taunt were also priceless around the sputtering machines. I still blame Dr. Mark Craig and Tim Rose for the abominable achy legs, arms and abs after circuit training. There was way too much berpees. Sharing an office with Christine Chalk and Sandra Craig was a delight. A thought to Dr. Richard Wellman and his non-stop taunting about Pandas. I would also like to thank the adorable and helpful Sharon McGuire and Jessica Greenwood without whom the organisation of meetings and communication with the project partners would have been a struggle. I will miss the lively morning tea breaks with all of them.

My years at Cranfield would not have been the same without friends I met there, especially Marina, Grant, Julien, Julian, Yannick, Marc, Roy and Jean-Bernard. I still believe the Frenchies produced the best music this University will ever hear. My loving thought to Andy who went through all my mood swings and still stayed with me those past few years.

At last, I would like to thank my family; they were always here during good and difficult times.

ABSTRACT

Future industrial gas turbines will be required to operate at higher temperatures to increase operating efficiencies and will be subjected to more frequent thermal cycles. The temperatures that the substrates of components exposed in the harshest environments experience can be reduced using air-cooling systems coupled with ceramic thermal barrier coatings (TBCs); however, few studies have been carried out at the substrate temperatures encountered in industrial gas turbines (e.g. 900 – 1000 °C). Better understanding of their behaviour during service and, their various potential failure mechanisms, would allow more accurate prediction of TBC lifetimes and improve coatings.

The aim of this research, as a part of the Supergen Plant Life Extension (PLE) project, was (a) to investigate the influence of industrial gas turbine blade geometry on TBC system lifetimes, and (b) to extend knowledge on the effect of bond coat composition on the oxide growth at temperatures below 1000 °C.

The main results of this thesis, obtained using mass change and characterisation techniques, increase the understanding of the significant interactions between the different coating layers, samples' geometry, interdiffusion and failure mechanisms involved during oxidation. Curvature was found to affect the quality of manufacture and thus promoted premature failure at the convex features of modified aerofoil-shaped samples. In parallel new bond coat compositions, suitable for industrial gas turbines were suggested from the wide range investigated in oxidation exposures. The selective growth of protective Cr_2O_3 or Al_2O_3 oxides or other mixed oxides was observed and mapped in ternary diagrams. Furthermore two novel techniques were successfully used during this project. Pulsed flash thermography proved to be efficient in identifying areas of sub-surface TBC delamination non-destructively. Magnetron co-sputtering using 2 and 3 targets was found to be a flexible method to deposit thick coatings with a wide range of compositions.

CONTENTS

LIST OF FIGURES

LIST OF TABLES

ABBREVIATIONS

Chemical elements are abbreviated according to the periodic table (e.g. Fe for iron…)
81-BSYA-xx: Modified aerofoil-shaped samples code name
APS: Air Plasma Spray
BC: Bond Coat
CCGT: Combined Cycle Gas Turbine
CFD: Computational Fluid Dynamics
DC: Direct Current
EB-PVD: Electron Beam Physical Vapour Deposition
EDX: Energy Dispersive Spectrometry
ESEM: Environmental Scanning Electron Microscope
FIB: Focused Ion Beam
HVOF: High Velocity Oxy-Fuel
IGCC: Integrated Gasification Combined Cycle
InCF: Intrinsic Chemical Failure
LPPS: Low Pressure Plasma Spray
MICF: Mechanically Induced Chemical Failure
NDE: Non-destruction examination
NPL: National Physical Laboratory
OGCT: Open-Cycle Gas Turbine
PVD: Physical Vapour Deposition
RF: Radio Frequency
RR-xx: Rolls-Royce samples code name
SEM: Scanning Electron Microscope
SFEG: Field Emission Gun SEM
SRZ: Secondary Reaction Zone
TBC: Thermal Barrier Coating
TC: Top Coat
TCP phases: Topologycally Closed Pack phases
TEM: Transmission Electron Microscope
TGO: Thermally Grown Oxide
VPS: Vacuum Plasma Spray
XRD: X-Ray Diffraction
YSZ : Yttria Stabilized Zirconia

CHAPTER I - INTRODUCTION

1.1 Challenges of electricity generation

World energy consumption has been continually increasing over the past decades (Figure 1.1) and is expected to increase by 57 % from 2004 to 2030, in order to satisfy the demand by industrial, transportation, domestic and commercial service sectors. Thus, the consumption of fuels employed to provide energy is projected to increase as well, but by different degrees for the various fuels types (Figure 1.2) [1-3].

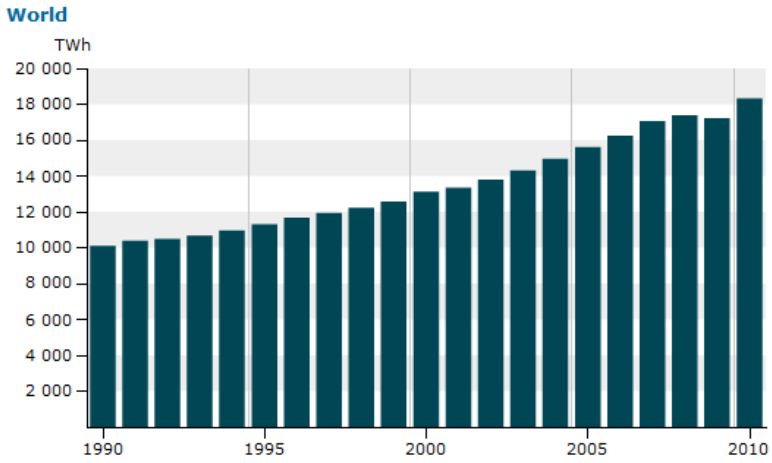

Figure 1.1 World energy consumption in TWh from 1990 to 2010 [2].

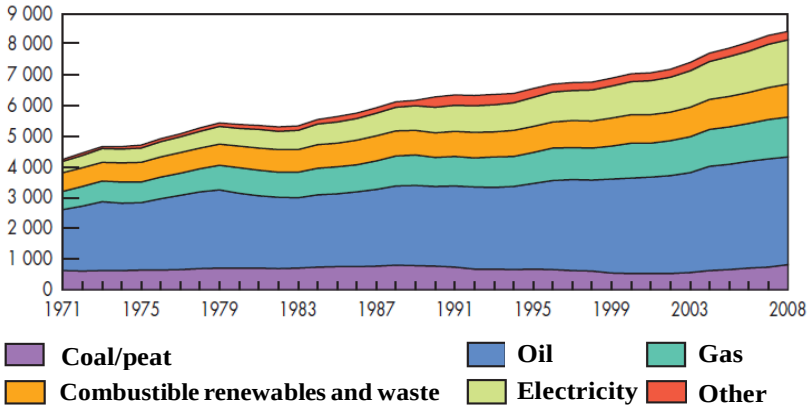

Figure 1.2 Evolution from 1971 to 2008 of world total final consumption by fuel (Mtoe) [3].

Europe, whose energy intensity (gross consumption divided by domestic product) dropped for six consecutive years (2003-2009), is facing great challenges, including regulations to reduce its impact on the climate change, its increasing import dependence and higher energy prices. EU energy import dependence is expected to reach 65 % by 2030. Reliance on imports of gas are projected to increase from 57 % to 84 % and of oil from 82 % to 93 % by 2030 (gas and oil are the main type of fuels used in Europe (Figure 1.3)) [4].

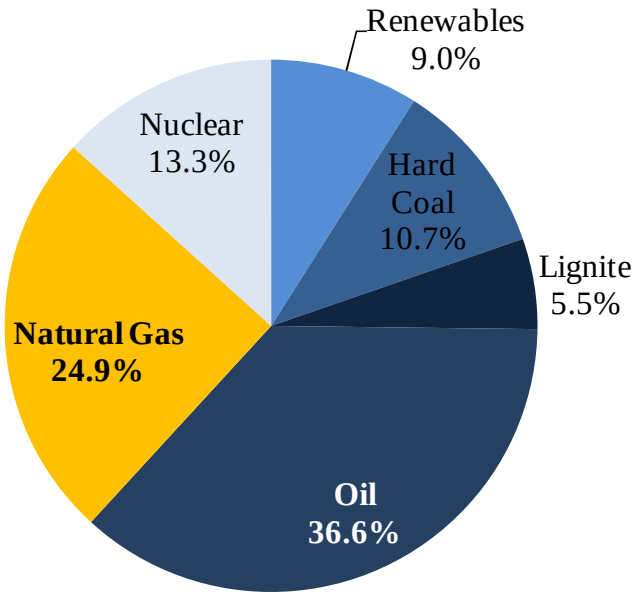

Figure 1.3 Europe gross inland consumption of resources in 2009 [5].

Combine Cycle Gas Turbines (CCGTs) are a suitable approach to the challenge of electricity generation because their cost is low (35-45 €/MWh compare to 40-50 €/MWh for coal (Integrated Gasification Combined Cycle)), they are highly efficient (50 % compared to 30 % for IGCC), and release fewer emissions (400 Kg CO_2 eq/MWh compared to 750 Kg CO_2 eq/MWh for IGCC) [4]. However, the price of gas supplies,

RAMO (reliability, availability, maintainability and operability) and the political risk accompanying the increasing need to import natural gas will dominate their ability to supply electricity profitably [4,6]. The solution to this issue is to increase the cyclic operation as well as the inlet temperature of the gas turbine and to use cheaper (and thus more corrosive) gases, while optimising engine materials [6].

1.2 What is a Gas Turbine?

The gas turbine, which has found increasing service in the past 40 years in the power industry, is a critical component within various combined cycle power plant [1,7,8]. It is composed of three main parts [7,9] (Figure 1.4). Firstly, the compressor pressurizes (pressure ratio of 1.05 to 1.3 per stage [7]) a working fluid (air or gas). Secondly, the compressed working fluid (up to ~ 30 bars) enters a combustion chamber where fuel is injected. All gas turbine combustors perform the same function which is to increase the temperature of the compressed gas (~800 to ~1430°C). Thirdly, the combustion products expand through multiple turbine blade rows, and the spinning shaft generates electricity and drives the air compressor. The first stage (combination of stator and rotor) experiences the most severe conditions [10]. Hot gases leave the gas turbine via the exhaust at temperatures around 600°C and a pressure of 1 bar [1].

The simplest gas-fired power station uses an open-cycle gas turbine (OGCT) that ideally operates according to the Brayton cycle (Figure 1.5(a)). However, in real life, the hot exhaust gases are vented to the atmosphere and most of the heat energy they contained is wasted causing their efficiency to rarely rise above 33% [1,11]. In order to improve that number, it is possible to combine two or more thermodynamic cycles. In a CCGT, the exhaust gases are reused to heat water to produce steam which drives a

steam turbine and electricity generator. In that case, the Rankine cycle (Figure 1.5(b)) of a steam turbine and Brayton cycle of a gas turbine are used simultaneously and the efficiency can be improved to 60-65 % [1,7,11].

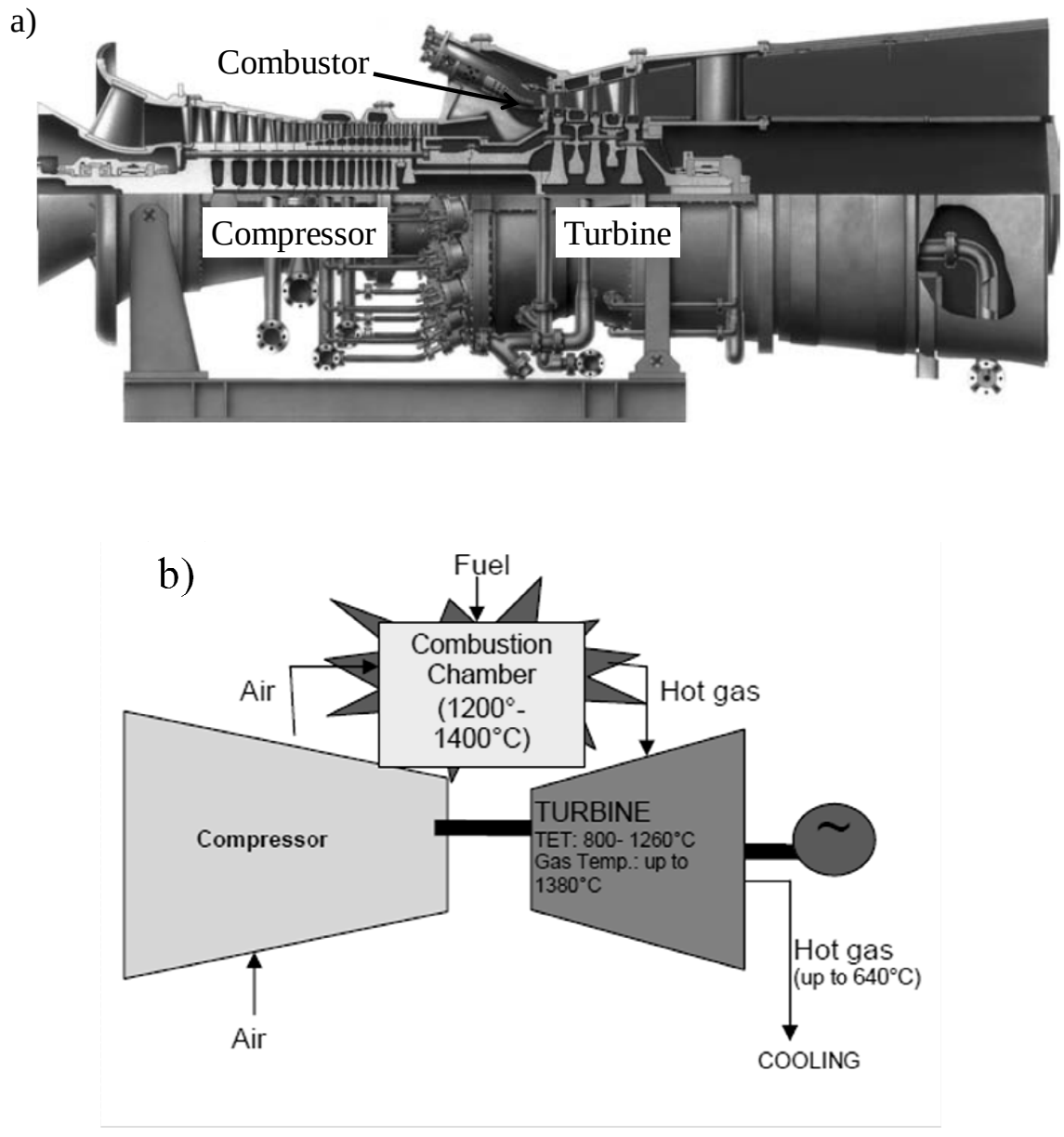

Figure 1.4 (a) A frame type gas turbine engine [7] (b) schematic of the main components of a gas turbine engine [1].

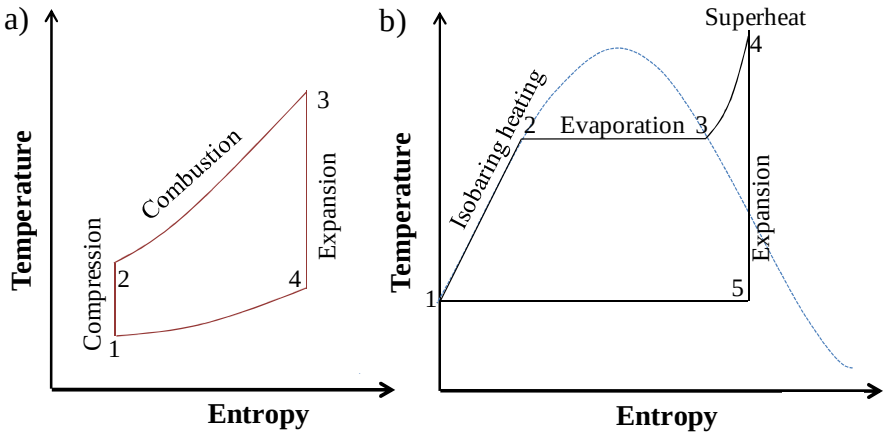

Figure 1.5 (a) Ideal Brayton cycle describing cycle of gas in a gas turbine and (b) Ideal Rankine cycle describing cycle of steam in a boiler [11].

1.3 How to improve gas turbine efficiency?

The efficiency (η) of a gas turbine is defined in terms of the maximum temperature (T_{max}) of the working fluid and the minimum temperature (T_{min}) at the end of the thermodynamic cycle.

$$\eta = \frac{(T_{max} - T_{min})}{T_{max}}$$

An improvement in efficiency requires either an increase in the maximum temperature or a decrease of the minimum, which can be done by four different approaches [10]:

- Improve the high temperature strength of the substrate alloy,
- Improve the cooling of the blades and vanes,
- Use **protective coatings** to improve the corrosion resistance and the strength of the blades,
- Use **thermal barrier coatings** (TBCs) to reduce the temperature of the substrate metal surface.

1.4 The project

To improve their efficiency, gas fired gas turbines will be subjected to more frequent thermal cycles in more corrosive environments. This is why, it is critical to perfect the TBCs protecting turbine parts and to understand failure behaviour.

Material issues focus on the assessment of the potential behaviour of coatings, as it is important to avoid expensive and unpredictable failure. Research also focuses on the production of improved coating meeting new life time requirements.

The Engineering and Physical Sciences Research Council (EPSRC) supports the SUPERGEN Consortium on “Conventional Power Plant Lifetime Extension”. This project including several industrial partners and four universities investigates increased efficiency and extending components lifetime in power plants. Cranfield University concentrates on the influence of oxidation and corrosion on components behaviour.

This PhD project will investigate the oxidative degradation mechanisms of air plasma sprayed (APS) TBCs coated CMSX4 and the effect of the components’ shape on its behaviour. Experimental data will be generated to improve existing models for the prediction of turbine components’ lives. In a second part, new coating compositions will be deposited by magnetron sputtering and oxidised in order to achieve a better knowledge of MCrAlYs behaviour under oxidation.

After this introduction, the second chapter of this thesis is a literature review covering current state of the art of TBC systems, oxidation mechanisms, understanding and modelling of the degradation modes, and current development in new type of high temperature protective coatings for industrial gas turbine environment.

The second chapter will describe in detail the aim and objectives of this thesis.

The results and discussion concerning the effect of curvature of the substrate on the behaviour and failure of APS/TBCs will be gathered in Part I. This section is divided into Chapter V, VI and VII. Chapter V describes the effect of the macro-geometry of the samples on the oxidation mechanisms within the APS/TBC and on the failure of the coating system. Chapter VI focuses on the effect of the micro-geometry of the interface between the ceramic and metallic bond coatings on failure mechanisms. Finally, Chapter VII is a general discussion of the two previous chapters.

Part II, made of Chapters VII, IX and X covers the work done on the study of new bond coating compositions for industrial gas turbine applications. Chapter VIII focuses on the behaviour of Ni-Cr-Al coatings at 900 and 950 °C while Chapter IX describes the behaviour of Co-Ni-Cr-Al ones at the same temperatures. The results are then discusses in Chapter X.

CHAPTER II - LITERATURE REVIEW

2.1 Thermal barrier coating systems

Commercial advanced TBC systems are typically four-layer structures (Figure 2.1) [12]. A ceramic top coat (TC) is used for thermal protection of components exposed to hot gases (e.g. turbine guide vanes and blades). Coupled with an active cooling system, they are known to lower the substrate temperature by about 100 to 150 °C [7,12-14]. Beneath the ceramic TC is deposited a metallic bond coat (BC). It enhances the adhesion of the TC and provides oxidation and/or corrosion protection. Under exposure to high temperature conditions, a protective alumina (Al_2O_3) layer (thermally grown oxide, TGO) is formed. Its structure and morphology is defined by the chemistry and microstructure of the BC. The BC must be sufficiently rich in Al to form a protective TGO scale of α-Al_2O_3. Underneath these three layers is the superalloy substrate [12]. The first TBC systems were designed in the 1950s for aircraft engine components. They were Al_2O_3 and ZrO_2 ceramics applied directly to the component surface by flame spraying. Important developments included new depositing technologies such as plasma spraying and electron beam – physical vapour deposition (EB-PVD), the introduction of a BC (usually MCrAlY overlay coatings) and a new ceramic TC made of Y_2O_3-stabilized ZrO_2 (YSZ) [12]. Up to the 1980s, TBCs were only used in low risk regions of the turbine section such as vane platforms since they still had poor surface finish, high heat transfer coefficient, low erosion resistance and poor mechanical compliance [13,14]. Because of the potential for TBCs to improve components life, they have been used in the early stages of power turbines for components, such as blades and vanes, that experience the highest gas temperatures (i.e.

the earliest stages of the combustion turbine). It has only been since the early 2000s that such coating systems have been used on highly stressed components within commercial gas turbines [15].

Section 2.1 introduces the four different layers of TBC systems, explaining their role, properties and conditions of use.

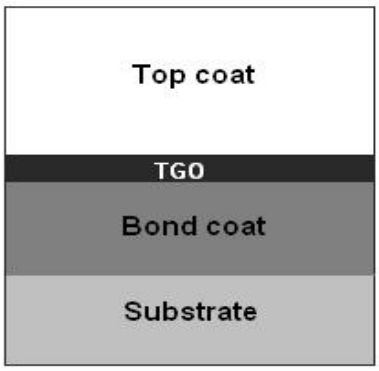

Figure 2.1 Schematic representation of a TBC system [12].

2.1.1 The superalloy substrate

In a gas turbine, the high pressure turbine blade operates under the most arduous conditions of temperature and stress compared to the other components. The stresses imposed on the blades are complex, being a mix between centrifugal stresses due to the high angular rotational speed; bending stresses caused by the high pressures involved; and high vibrations. The metal has to experience through thickness temperature gradients, rapid temperature transients and the hot gases surrounding the blade are highly oxidising and corrosive. The blades experience a complex thermal and mechanical history during a typical cycle operation, consisting of start-up, steady-state

operation, shut-down and emergency shut-down [16]. When temperatures exceed ~540 °C, steels and Ti alloys are no longer strong enough for this application [17,18]. Nickel based superalloys are the only materials possessing the properties required for turbines blades [9]. Their advantage comes from their austenitic face centred cubic (FCC) (the γ phase) structure which has the capability of maintaining good tensile, rupture and creep properties. Al, Ti and Nb are added to the alloy to help the formation of the FCC γ'-phase ($Ni_3(Al,Ti)$) which is the main strengthening phase. Its lattice is derived from the γ phase by ordering Al/Ti atoms on the cube corners and Ni atoms at the face centres [1,19]. Three main classes of those superalloys exist: Ni-base, NiFe-base (Inconels - Fe is substituted in part of Ni for cost purposes) and Co-base (less subject to hot corrosion) [20].

Grain shape and orientation affect greatly the mechanical and physical properties of any metal/alloy. The way alloys are processed can control the growth of the grain and therefore enhance the qualities of a chosen material. The evolution of the processing of turbine blades went from polycrystalline to directionally solidified gains and finally to single crystal directionally solidified. The later do not show grain boundaries (but still show a dendritic structure) and are endowed with ultra high strength [17].

2.1.2 The ceramic top coat

The material used for the ceramic TC must possess properties criteria in order to be a potential candidate for a TBC. It should be refractory, chemically inert, have a good wear resistance, good mechanical strength, thermal shock and erosion resistance, be phase stable, but most of all, it must possess a low thermal conductivity and have a thermal expansion coefficient similar to the nickel based superalloy substrate [14]. ZrO_2

is the best oxide fulfilling all the requirement but it needs to be alloyed with other oxides because of it polymorphisms [14].

The main function of the ceramic TC is to reduce the heat transfer to the metal substrate. It has a low thermal conductivity (~1 W/m² K) which is an order of magnitude below the one of Ni-based superalloys. YSZ has one of the lowest conductivities at elevated temperatures of all known ceramics [13,21,22].

Air plasma spray (APS) and electron beam physical vapour deposition (EB-PVD) are the two main techniques used to deposit TBCs. EB-PVD/TBCs are usually found in aeroengine turbine vanes and blades, while APS/TBCs are mainly used to protect larger components in stationary gas-turbine engines because their different properties are appropriate to the different conditions and requirements encountered in those fields [23]. Current industrial gas turbines for power generation application operate with temperatures going up to an average of 1430 °C, while jet engines use hotter firing temperatures that can reach 1550 °C. Coatings used for aeroengine applications undergo shorter thermal cycles at higher temperatures (around 950 ºC with peaks of up to 1100 °C) compared to those deposited on parts used in industrial gas turbines (800 to 900 ºC). Industrial gas turbines, in contrast to aeroengines, should be ramped slowly to their operating temperature and remain there for thousands of hours [24].

The EB-PVD coatings, as shown in Figure 2.2(a), consist of columnar grains with multiscale porosity. During their processing, the oxides are evaporated from ingots and the vapours directed onto preheated substrates. The columnar structure brings strain tolerance to the coating [12,13]. When tested for aeroengines conditions, it has been found that the EB-PVD TC systems also improve the adhesion to the bond coat, have a

better surface finish and erosion resistance [23]. The APS coatings as shown in Figure 2.2(b), consist of layers of splats. This can be explained by the different processing route in which a powder is fed into a plasma, heated (until molten) and sprayed onto the substrate. This produces a porous and microcraked coating. The cracks are necessary for an improved strain tolerance and the pores allow a reduction in the thermal conductivity of the coating as it increases the phonon and photon scattering. APS is a lower cost process compared to EB-PVD [12-14].

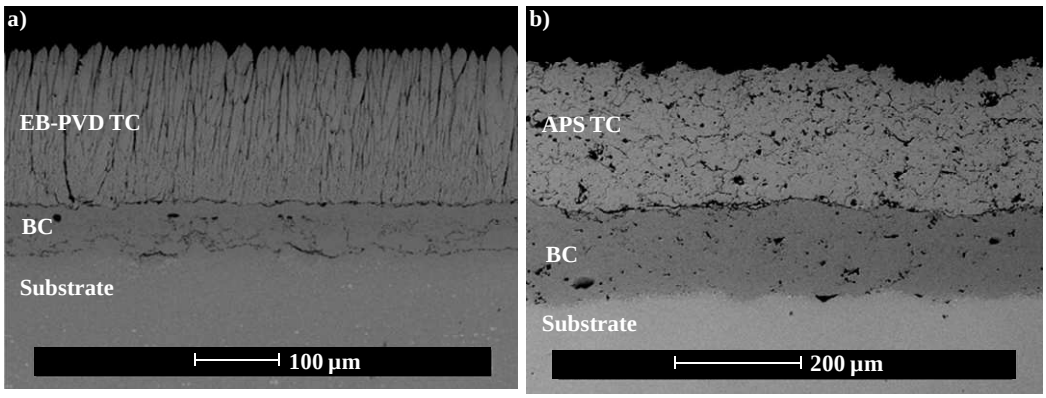

Figure 2.2 SEM images of (a) an as-deposited EB-PVD/TBC system [25] and (b) an as-deposited APS/TBC system.

The majority of TCs are ZrO_2 stabilized with 7-8 wt% of Y_2O_3. Above 1050°C and under equilibrium conditions, this amount of Y_2O_3 enters the ZrO_2 solid solution and stabilizes its tetragonal crystal structure. Then when cooling, the t-phase can transform to a blend of monoclinic and cubic YSZ. This transformation causes an unwanted cracking of the ceramic. For kinetic reasons and because of the rapid deposition rate of the TC, the YSZ exists in a metastable tetragonal-prime structure. This phase does not change when cooled down [14,23].

2.1.3 The bond coating

Evans et al. [21] affirm that the BC is the most crucial component of the TBC system as it influences the durability of the coating. Indeed, its chemistry and microstructure define the structure and morphology of the TGO created as it oxidises. Moreover, as the TC has high oxygen permeability, it means that the metallic BC has to be resistant to oxidation attack. As a consequence, the bond coat must be sufficiently rich in Al to form a protective TGO scale of α-Al_2O_3 [23].

BCs are of two categories. One is based on a diffusion coating, such as Pt aluminides. As it is not the main interest of this thesis, it will only be presented briefly. The components' surface is enriched by diffusion. The BC is fabricated by first the electroplating of a thin layer of Pt onto the superalloy and then, aluminizing by pack cementation (a relatively low cost process) or chemical vapour deposition. The microstructure of the coating as-processed consists typically of single-phase-β, with Pt in solution and this evolves into γ' phase at the β grain boundaries as Al diffuses when oxidised [21,26,27].

The other category consists of overlay MCrAlX systems, where M is Ni, Co or a combination of Ni and Co, and X is an active oxygen element such as Y, Si, Ta or Hf. The composition of this kind of BC influences the oxidation resistance, the corrosion resistance and the coating ductility. It is therefore important to select one that provides a good balance between those properties. The active oxygen element improves the oxide scale adhesion and decreases the oxidation rate [15,28]. It was observed that the addition of Y resulted in flat TGOs, promoted the fine columnar growth of Al_2O_3 and favoured the diffusion of oxygen anions over Al cations helping the formation of slow growing α-Al_2O_3 [29,30]. Methods to deposit MCrAlY coatings include EB-PVD, APS

and more recently, high velocity oxy-fuel spraying (HVOF) and low pressure plasma spraying (LPPS). All those processes bring advantages and disadvantages to the coating. Commercial EB-PVD, despite its high capital cost, allow the uniform deposition of a dense coating with good adhesion. APS has the advantage of being able to deposit a wide range of materials and generates homogeneous coatings with a fine equiaxed grained microstructure. Yet, the process requires complex robotic manipulation, reactive elements often oxidise if the spraying is conducted in air and the coating contains a porous structure. HVOF spraying has the inconvenience of a spraying process but on another hand has the advantage of lowering the powder temperature and increasing the kinetic energy of the particle impacting. The resulting coating is denser with less degradation of the powder during spraying. The BC strength is higher and the porosity reduced [15]. Also, HVOF plasma spraying deposits relatively smooth coating compared to other spraying techniques (e.g. LPPS or Shrouded Air Plasma Sprayed) [31].

The key property of a BC is to provide oxidation and corrosion resistance. Classic overlay coatings, with 18-22 wt% Cr and 8-12 wt% Al, are designed to perform better at temperatures above 900°C where oxidation is the dominant failure mode. Whereas CoCrAlYs are more efficient against type II corrosion (650-800°C), NiCrAlYs and NiCoCrAlYs perform better under highly oxidising conditions [15]. Figure 2.3 sums up the performances of the different types of coating systems [32].

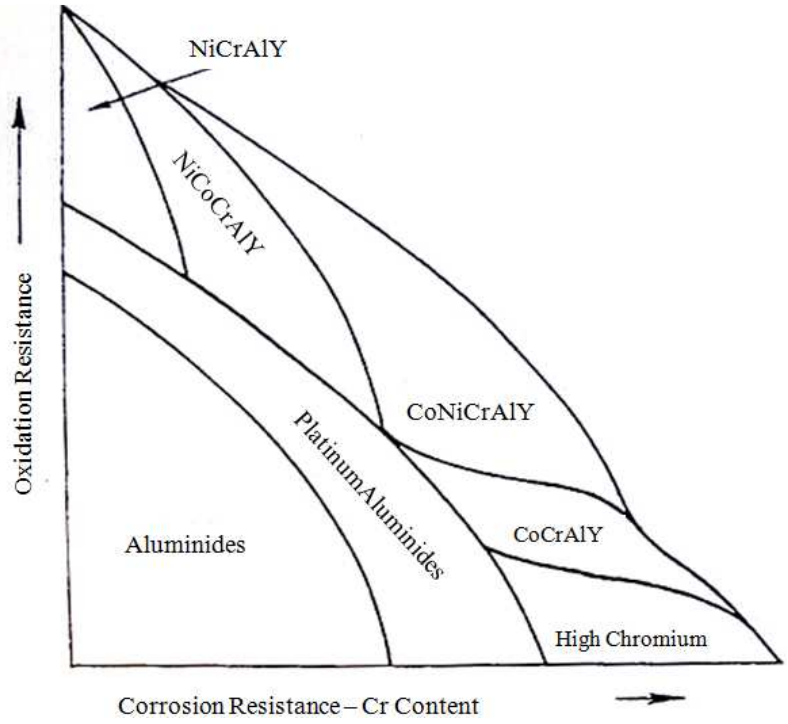

Figure 2.3 Relative oxidation and corrosion resistance of different high temperature coatings systems [32].

2.1.4 The thermally grown oxide

The TGO is a layer, consisting predominantly of Al_2O_3, which forms between the ceramic TC and the BC. It has a major influence on the TBC lifetime [21]. The presence of a α-Al_2O_2 layer is preferred because its growth rate is low, thanks to the highly stoichiometric structure of Al_2O_3 and its large bad gap which makes electronic conduction difficult [33], and its adherence is better [34]. Al_2O_3 at high temperatures transforms from an amorphous state through various transient polymorphs to the stable form, α-Al_2O_3 [35]. Its crystallography consists of hexagonally close-packed oxygen ions with two thirds of the octahedral interstices filled with trivalent cations [33]. While α-Al_2O_3 is the most favourable oxide to protect the system from oxidation, other less protective oxide forms can grow on the alloy, as it has been reported that mixed

$(Al,Cr)_2O_3$ oxides, spinels ($Ni(Cr,Al)_2O_4$) and nickel oxides (NiO), were also produced during oxidation, as shown in Figure 2.4 [36].

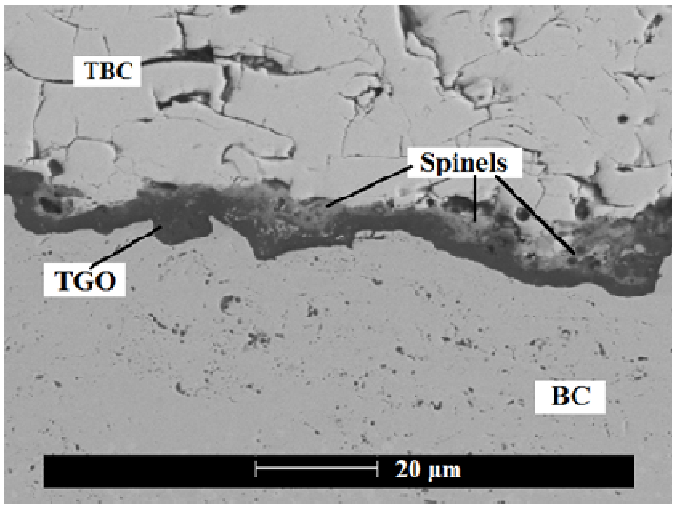

Figure 2.4 SEM image of spinels present in TGO.

Spinels are ionic compounds formed from strongly electropositive metal ions and strongly electronegative non-metal ions. The mechanisms of spinel formation depend on the nature of the spinel. Ni and Co aluminates (solid-state formation between (Ni,Co)O and Al_2O_3) are formed by an inverse cation diffusion. It is believed that chromites can be explained by vapour phase transport of Cr_2O_3 to the (Ni,Co)O [37,38].

2.2 Oxidation

Oxidation denotes the reaction between a metal and air or oxygen in the absence of water or an aqueous phase. High temperature will drive most metals to oxidation and may cause loss of material, failure of components in service, etc. Thus, for gas turbine application, it is a necessity to understand and to control the high temperature oxidation behaviour of a material.

2.2.1 Oxidation mechanisms

The total chemical reaction for the reaction of a truly clean metal (M) and oxygen gas (O_2) to form the oxide M_aO_b may be written as [12]:

$$aM + (b/2)O_2 = M_aO_b$$

In order to understand the oxide scale formation, it is necessary to consider that the oxidation process must take place by the migration of both ions and electrons. Either the anion or the cation exhibits variable valence on its sub-lattice: for example, giving rise to the formation of vacancies on the cation lattice together with electron holes. So, the diffusion of ions (or vacancies) is rate determining (Wagner theory, Figure 2.5).

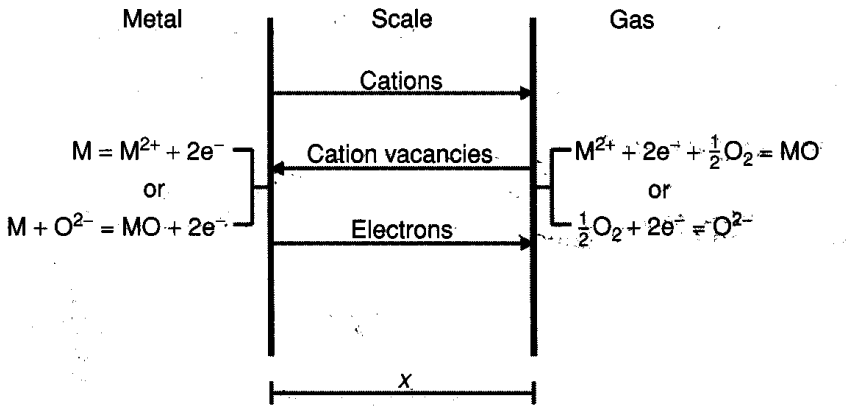

Figure 2.5 Simplified model for diffusion-controlled oxidation [12].

The simplest growth mechanism of an oxide on metal can be described as the combination of five steps [39]:

- The adsorption and dissociation of oxygen onto the surface of an existing oxide surface (external interface),
- The transfer of the adsorbed oxygen from the surface into the oxide lattice,

- The transport of the adsorbed oxygen through the oxide lattice,
- Reaction of the oxygen with the metal surface. Transfer of metal atoms into the oxide lattice which leads to the creation of vacancies in the metal lattice,
- Annihilation of cation vacancies through the climbing of interfacial dislocations at the oxide-metal interface.

The oxidation of an alloy must take into account many more parameters than for the oxidation of a metal alone. Different components in the alloy have different affinities for the oxygen and there are also different diffusion rates through the metal lattice(s) and the oxide(s). Moreover, the oxidation mechanisms can change during exposure, according to the establishment of different metal activity gradients (as a result of preferential consumption of one element) and gas pressure [40]. Reactants may travel through short-circuit paths such as dislocations or grain boundaries for example [41,42]. Rapid, short circuit, gaseous entry from the atmosphere is favoured by porous layers. When the layer is less porous, the oxide nearer the outer surface has a higher oxygen potential than the one at the inner surface, and can dissociate to provide gaseous supply to build oxide nearer the metal [43].

When an alloy is oxidised, the oxides produced may be completely miscible or partially miscible enabling, respectively, oxide solid solutions or multiphase scales [43]. For the Ni-Co alloys, NiO and CoO give a single solid solution of composition (Co,Ni)O. Certain Ni-Cr alloys form a double oxide layer which may give a complete surface layer of variable composition. If the reaction is incomplete, particles are incorporated into a matrix of NiO. If the Ni-Cr alloy is reasonably rich in Cr, an

external layer of Cr_2O_3 is formed [43]. Oxides formed on Ni-Al and Ni-Cr-Al systems are described in section 2.2.4.

2.2.2 Diffusion of elements between the different layers of a TBC system

MCrAlY coatings typically consist of a mixture of β-NiAl, γ'-Ni_3Al and γ-Ni phases, depending on the initial composition [44,45]. The β-NiAl, which acts as an Al reservoir for the formation of the TGO, depletes during oxidation and transforms gradually into a γ'-Ni_3Al phase (less Al-rich) and then into a γ-Ni solid solution. The differences in composition between the BC and the γ/γ'substrate (also rich in rare and heavy elements such as Co, Ta, Hf, W, Re and Mo), help the diffusion of elements at their interface. The interdiffusion zone between the BC and the substrate, also called the Secondary Reaction Zone (SRZ) has got a distinct microstructure. It can contain intermetallic topologically close packed (TCP) phases such as σ, μ and P phase [17,21,19,44,46]. It is believed that the precipitation of Ta in the substrate close to the interface is caused by the diffusion of Al from the BC to the superalloy [47].

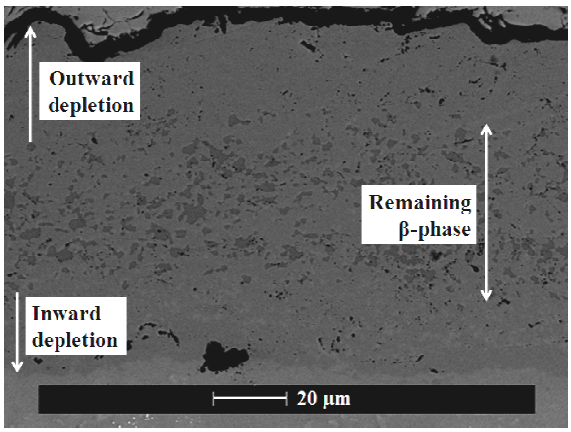

Figure 2.6 SEM image of the β-NiAl phase in the BC in a sample oxidised at 900°C for 4000h.

As a result of the Al diffusion, two β-phase depletion zones develop, one close to the substrate and the other next to the TGO (Figure 2.6), and after longer exposure time, the β-phase disappears completely [48].

The composition of the depletion zone does not vary with the test temperature and time; its Al content is around 4 wt% [49]. Rabiei and Evans [48] have oxidised Ni-based superalloy samples coated with a CoNiCrAlY BC and APS/TBC at 1100°C and observed their cross-sections after different exposure times. Using EMPA scans they found that the depleted zones coincide with reduced concentration of Al, reinforcing the idea that the β-phase is the Al reservoir and implying that diffusion of Al towards the substrate as well as towards the TC controls the microstructural evolution.

2.2.3 Growth of a TGO

Prior to oxidation, the TGO is a very thin layer the thickness of which does not exceed 0.5 µm. After exposure, its thickness can reach an average of 7 µm (depending on the type of coating and substrate). Wu et al. [50] have measured, TGO thicknesses reaching 12 µm just before spalling.

The growth of the TGO between the TC and BC can be divided into three stages: a transient stage, when all thermodynamically stable oxides can form; a steady-state stage, when the long-term most stable oxide phase (α-Al_2O_3) is established; and finally a breakaway stage, when protective oxides are no longer produced anymore resulting in the failure of the scale. The transient stage lasts from only seconds to days and is defined by rapid weight gain, whereas for the steady-state stage, the oxidation kinetics decrease to a near parabolic rate [51].

In the early stages of oxidation, the fast growing metastable oxides γ-Al_2O_3, δ-Al_2O_3 and θ- Al_2O_3 grow. Brumm and Grabke [52] observed that cubic γ-Al_2O_3 and δ-Al_2O_3 were the first forms of Al_2O_3. A few hours later (16 hours at 900 °C) those oxides transformed to the monoclinic θ-Al_2O_3. The first traces of hexagonal α-Al_2O_3 mixed with θ-Al_2O_3 were found after 135 hours of oxidation at 900 °C and after 60 hours at 950 °C. At higher temperatures, γ-Al_2O_3, δ-Al_2O_3 and θ-Al_2O_3 were more difficult to detect [52].

The TGO growth becomes more important to the long-term TBC stability during the steady-state oxidation stage, the duration of which depends on the alloy system, the oxidizing atmosphere and the temperature [23]. For industrial turbines, α-Al_2O_3 is the most stable oxide only at the highest operating temperatures, while α+θ Al_2O_3 or θ-Al_2O_3 co-exist at lower temperatures. In 1999, Grabke [53] developed a temperature-time transformation diagram for the high temperature oxidation of β-NiAl describing which phases form at given time and temperatures. Figure 2.7 illustrates the Al_2O_3 transformation.

During the formation of transient Al_2O_3, the outward transport of Al is preferred. These oxides exhibit special features during growth such as needle-, pyramid-, plate-like grains and whiskers. The transformation of the unstable Al_2O_3 into α-Al_2O_3 causes stresses which result in a ridge structure, as seen on Figure 2.8 [54,55].

Where growth is diffusion controlled, rather than interface controlled, the growth of the TGO is theorized to be in most cases parabolic until spalling occurs:

$$h^2 = 2k_p t + C \qquad (1)$$

where h is the thickness, t time, k_p the parabolic rate constant and C a constant depending on the system and oxidation conditions. The Al_2O_3 component of the TGO is

known to grow mostly by inward diffusion of anions along the TGO grain boundaries. However, an outward growth, sensitive to cations dissolved in the Al_2O_3, is also thought to contribute to the overall rate constant k_p [21,57,58].

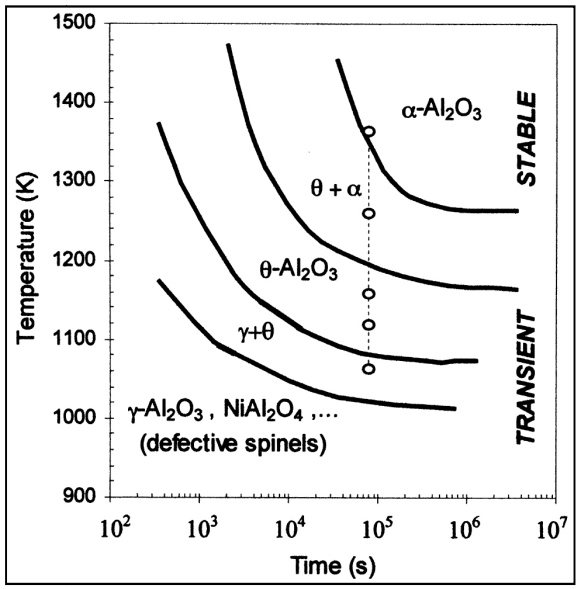

Figure 2.7 Schematic temperature-time transformation diagram for the high temperature oxidation of β-NiAl [53].

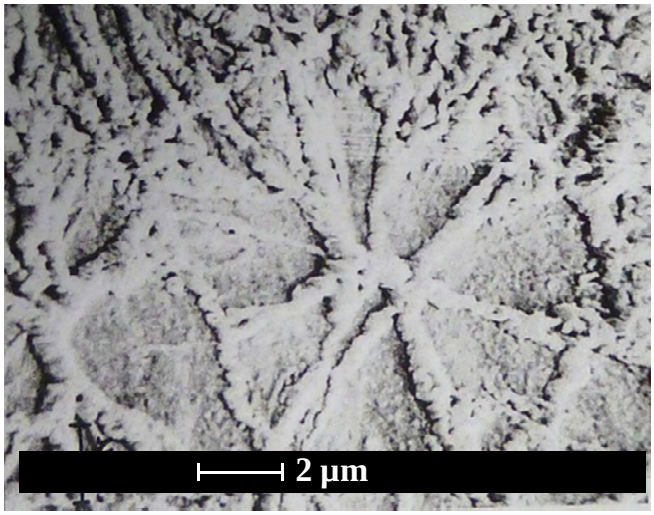

Figure 2.8 SEM image of the NiAl surface morphology after 100 hours at 1000 °C [56].

Niranatlumpong et al. [57], observed that for long exposure (up to 1000 hours at 1100 °C), the growth kinetics went from parabolic to sub-parabolic. This was associated with the depletion of Al from the BC and the formation of less protective oxides beneath the Al_2O_3 layer. The oxidation behaviour of the TGO varies as a function of the exposure temperature and the composition of the BC [40,59]. Kvernes and Kofstad [40] by oxidising a range of Ni-Cr-Al alloys at 800 °C – 1300 °C for 50 hours found that at lower temperatures (up to 900 °C), the oxidation kinetics tended to be linear and then became parabolic. Also the rate of reaction went through a maximum between 1000 and 1200 °C, reflecting a change in oxidation behaviour with temperature [40].

2.2.4 The effect of BC composition on the TGO growth

Variation in coating compositions provides different protective properties due to the nature of the oxides growing on them. The composition of the MCrAlY, as well as the exposure time and temperature, greatly influence the oxide layer(s) created. Ni-Cr-Al and Co-Cr-Al ternary systems undergoing oxidation above 1000 °C have been subjected to extensive studies since the original work of Talboom et al. [60] in 1970. However, this is not the case for oxidation at lower temperatures. Information on the oxidation performance of the Co-Ni-Cr-Al quaternary system is also difficult to find. Co is added to the NiCrAl system for its high corrosion resistance properties and high strength at high temperatures. It has a good high temperature resistance to softening as well as good wear resistance compared to Ni alone [61]. It reduces the solubility of aluminium in the Ni-Cr matrix, thus increasing the γ’ solvus temperature, which allows the maintenance of strength at higher temperatures [19].

When looking at the Ni-Al binary system at temperatures above 800 °C, only Al_2O_3 forms on β-NiAl. On γ'-Ni_3Al, an external layer of Ni-rich oxide, either NiO and/or $NiAl_2O_4$, grows above the Al_2O_3 layer. The addition of Cr to the Ni-Al system promotes Al_2O_3 formation by the "third element effect", i.e. Cr has the effect of increasing the Al activity so that protective Al_2O_3 scales are formed at lower Al concentrations. A possible mechanism to explain this phenomenon is that Cr_2O_3 initially develops, and reduces the entry of oxygen into the alloy, thus helping preferential oxidation of Al_2O_3, which requires less oxygen to form. It promotes the growth of a complete external layer of Al_2O_3 beneath the Cr_2O_3 layer rather than its precipitation as an internal oxide [43,52,62,63]. Brumm and Grabke [52] also proposed that a higher fraction of Cr accelerates the transition from transient θ-Al_2O_3 to stable α-Al_2O_3. This was confirmed by Klumpes et al. [56] as they found that Cr particles in θ-Al_2O_3 oxides acted as nuclei for this transformation. However, the amount of Cr did not influence the nodular morphology of the scale, indicating the outward growth of the θ-phase, and the ridged structure, associated with the α-phase [56]. As the "third element effect" reduces the Al concentration needed in the alloy to form an Al_2O_3 scale, it therefore helps avoid brittleness, a common issue in high Al concentration alloys [64]. In the early stages of oxidation (transient oxidation), NiCrAl alloys grow an outer layer of NiO and an inner layer consisting of mixed oxides ($Ni(Al,Cr)_2O_4$), Cr_2O_3 and θ-Al_2O_3, regardless of the temperature of exposure. However, the same alloy exposed for longer oxidation times and at higher temperatures forms a continuous α-Al_2O_3 layer, while at temperatures between 900 °C and 1000 °C, layers of NiO, Cr_2O_3 and Al_2O_3 are still present [40,59].

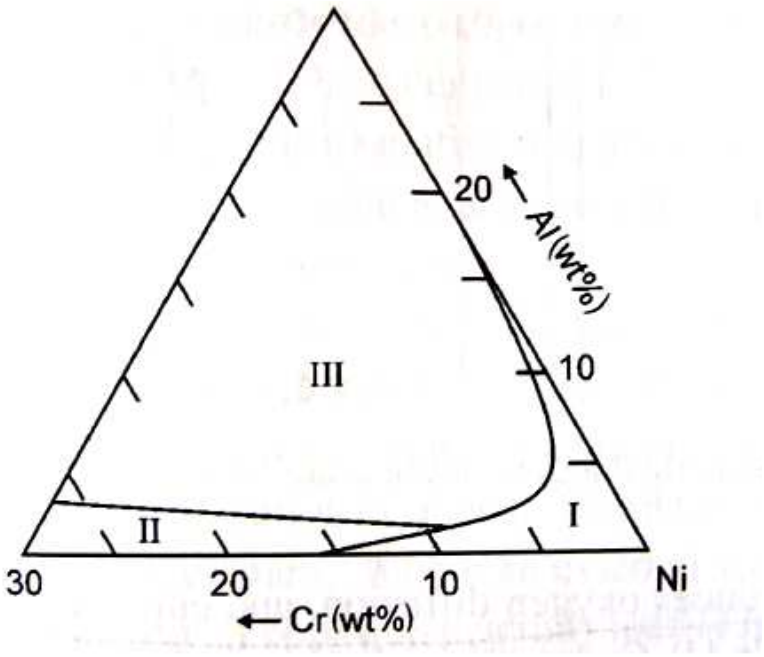

Figure 2.9 Compositional effects on the oxidation (over 1000 °C) of Ni-Cr-Al ternary alloys [40], cited in reference [12] and [63]. I) NiO + internal oxidation of Al and Cr ; II) Cr_2O_3 + internal oxidation of Al ; III) an Al_2O_3 external scale.

Over 1000 °C, the Ni-Cr-Al compositions that lead to the formation of α-Al_2O_3 scales have been well researched and documented, as summarized in Figure 2.9, an oxide predominance diagram. Three primary oxidation regions are observed, corresponding to: (I) a NiO external scale + Al_2O_3/Cr_2O_3 internal oxides; (II) a Cr_2O_3 external scale + Al_2O_3 internal oxides; and, (III) an Al_2O_3 external scale [12,65,66].

For temperatures below 1000 °C, only one Ni-Cr-Al ternary oxide predominance diagram exists. This is at 950 °C from the works of Nicholls et al. [63] who studied the behavior of a range of Ni-Cr-Al compositions (deposited by magnetron sputtering) using combinatorial techniques to create an isothermal oxidation map as a function of alloy composition (Figure 2.10). By comparing Figures 2.9 and 2.10, it can be seen that lower temperatures would appear to promote the formation of mixed oxides. The optimum oxidation resistance observed in this study was obtained for coatings

containing between 20 and 30 at% Al and above 13 at% Cr (values were converted from wt% to at% for the purpose of this thesis) [63]; i.e. at Al levels greater than the minimum observed to form an Al_2O_3 scale, which was found to be 15 at%.

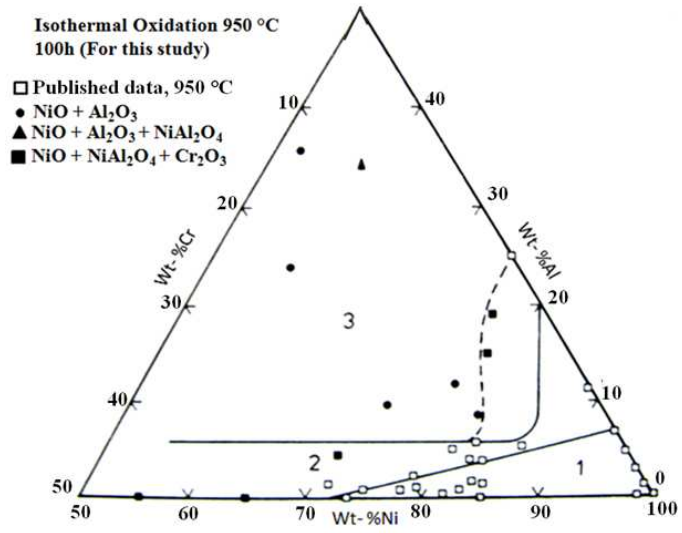

Figure 2.10 Oxide morphology map for ternary NiCrAl alloys at 950 °C [63].

2.3 Failure of a TBC system

The lifetime of a TBC system can be affected by a lot of factors depending on operating conditions. However, it is well understood that the BC oxidation stands as a crucial parameter for the coating's life. The time to failure depends on the oxidation temperature and on the thermal loading conditions. Trunova et al. [67] observed that pure thermal cycling caused spallation of the ceramic TC with cracks within the TBC itself, while isothermal exposure led to cracks propagating mainly in the TGO. The coating system failure was generally associated with the Al-depletion in the BC causing the formation of spinel/mixed oxides. However, failing of the coating prior to critical

depletion in most of the cases shows this phenomenon on its own does not explain the process [68].

Indeed, failures of APS/TBC systems under oxidation are complex processes involving several general phenomena [69]:

- thermal expansion mismatch stress,
- growth of a TGO at an undulating BC/TC interface,
- depletion of Al in the BC leading to the formation of spinels (more brittle oxides than Al_2O_3),
- sintering of the porous ceramic TC leading to a deterioration of strain tolerance and thermal resistivity,
- degradation of the metal/ceramic interface toughness,
- cracking, crack coalescence and delamination.

2.3.1 Depletion of the Al reservoir in a BC

Shillington and Clarke [70] suggested, amongst other researchers, that the Al depletion from the BC could lead to failure of the coating system. They associated depletion with a compositional change in the TGO from α-Al_2O_3 to a mixture of Cr_2O_3 and spinels. Their observation of failed sample surfaces, exposing BCs, revealed high concentrations of Cr compared to low amounts of Al, Co, Ni, Ti and Nb. A more accurate EDX analysis showed that the surface was mainly composed of Cr_2O_3 and a (Co,Ni)(Cr,Al) spinel phase. Less Al_2O_3 and ZrO_2 were present. It had been noticed that failure of the TC occurred during cooling, when the TGO had converted from a continuous Al_2O_3 layer to a scale of Cr_2O_3 and spinels. The delamination, driven by increasing stresses from the rough shape of the coating, suggested that the fracture

resistance of the interface of spinels/mixed oxide with the TC was lower than the one of an Al_2O_3/TC interface.

The formation of a spinel/mixed oxide layer is linked to the Al-depletion occurring during the oxidation of the coating. Indeed, as the Al activity in the BC decreases, those Cr phases can form more easily [70]. For the Ni-rich phases to form, the oxygen must be higher than the one favouring the growth of the Al_2O_3 layer [71]. Their location between the Al_2O_3 and the TC are caused by the cracking of the Al_2O_3 layer during cooling. The Al_2O_3 layer cracks because of its high curvature and expansion mismatch [70]. On re-heating, those cracks provide a direct transport path through the layer for oxygen to react with the BC. A high oxygen partial pressure is maintained at the interface. If the BC is locally depleted in Al, other oxides can form. This leads to further cracking of the Al_2O_3 scale, enhancing the formation of Cr_2O_3 and spinels. This phenomenon is found more for coatings undergoing cyclic oxidation, as they are more subject to cooling and reheating cycles [70]. Renusch et al. [72] developed a model confirming the effect of the Al depletion on the system's lifetime; predicting that TC systems with larger Al reservoirs had longer lifetimes. They assumed that lifetime was limited by the BC properties, such as: temperature dependent oxidation kinetics, the BC thickness, the Al content and the inter-diffusion of Al into the substrate. Their model took into account the substrate acting as a part of the Al reservoir, assuming that the Al could come from the γ'-Ni_3Al phase. Evans et al. [73,74], suggested that the BC, especially the sprayed ones, contained regions diffusionally isolated from the bulk of the coating as a result of the formation of Al_2O_3 layers at splat boundaries. Such regions would experience different Al depletion and the overall reservoir consumption would be enhanced.

The failure caused by severe depletion of Al from the BC can divided in two categories: (a) intrinsic chemical failure (InCF) where the formation of Al_2O_3 is replaced by Cr mixed oxides or Ni-based spinels; (b) mechanically induced chemical failure (MICF) where the Al_2O_3 layer cracks and then cannot heal [73,74]. Eschler et al. [75] assumed that those two types of failure, when leading to spallation, have different mechanisms with different temperature dependences. InCF is based on BC properties while MICF depends mostly on the TC properties. Evans et al. [73], while studying diffusion cells in MCrAlY BCs, produced the hypothesis that MICF happened before InCF if the Al_2O_3 layer cracked. If the integrity of the Al_2O_3 layer was maintained, MICF could not be initiated and the system lifetime would depend on InCF. Evans et al. [73] also wrote that chemical failure would trigger at different times along the sample because of different diffusion cells (deposition splats) sizes in the BC. However, subsequent study of LPPS coatings showed that the presence of diffusion cells depended on the type of spraying deposition used [76]. No splat boundaries were found within the BC after oxidation but only “bead-like” lines of internal oxidation having no influence on the diffusion of Al to the TGO [76].

The growth of the less protective spinels/mixed oxides instead Al_2O_3 is frequently reported [36,48,51,59,68,70,77-81] and is detrimental for the integrity of the coating for several reasons. First, their porosity is much higher than the Al_2O_3 layer [48,79,81] providing an easy path for the oxygen to reach the BC and enhance the oxidation kinetics [69,81]. Also, a higher growth rate of these spinel/mixed oxides could be due to the high amount of Cr promoting diffusion [49,77]. Secondly the high volume increases that accompany the growth of the spinel/mixed oxides result in the build-up of stress between the TC and the BC [36,59,80], and this finally leads to the initiation of

cracks, followed by crack propagation and the delamination of the TC [36,50,78,79]. However, it has also been reported that spinels/mixed oxides had no effect on the adhesion of the ceramic TC [51] and the crack pattern [48], showing that the influence of these oxides on the lifetime of the TBC systems still needs to be understood.

2.3.2 Roughness and uneven growth of the TGO

The TC/BC interface roughness can be caused before oxidation purposefully by the deposition process (to improve adherence) and during oxidation (by the deformation of the layer due to stress formation and relaxation).

Previous research has shown that the TC/BC interface roughness influences the depletion of Al. Taylor et al. [74] believed that depletion happened at a higher rate in BC asperities promoting the formation of less protective oxides (Figure 2.11). Their fast growth led to larger out-of-plane stresses between the asperities and added to the stresses generated by the growth of the TGO. The uneven surface profile of the BC caused an upward displacement of the TC and as a consequence, the TC experiences a range of strains to maintain continuity.

Taylor et al. [74] proposed a model to explain the rapid depletion of Al and the formation of less-protective oxides around BC peaks. They assumed that “the Al concentration was determined by the balance between the flux of Al entering the oxide layer and that arriving at the asperity from the bulk of the coating” and that the high surface to volume ratio in BC peaks accelerated Al depletion resulting in a gradient of Al concentration. Their model predicted the bulk of the BC asperity would only contain 1 at% of Al [74].

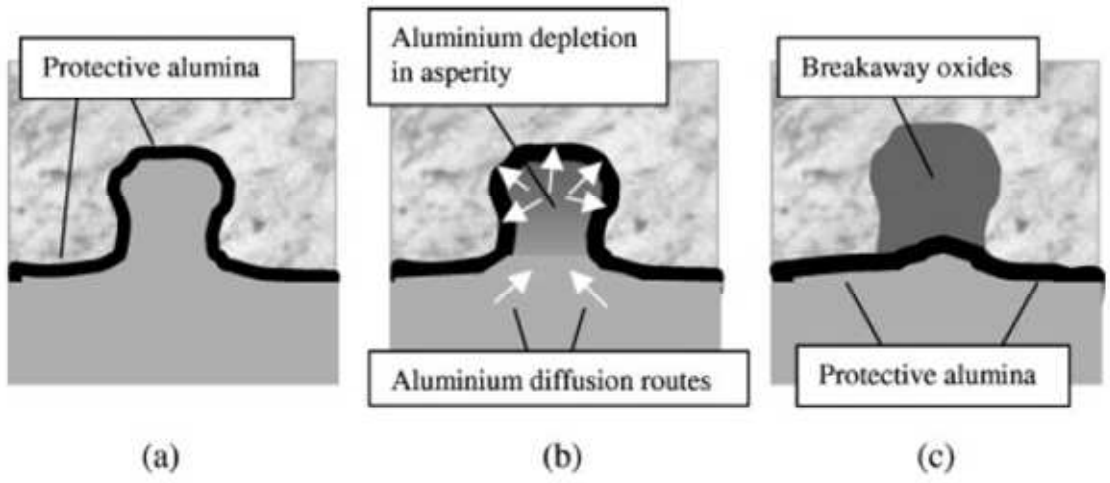

Figure 2.11 Schematic diagram describing the model proposed by [74]. (a) Sufficient Al present in asperity to grow Al2O3, (b) rapid depletion and restricted replenishment reducing Al levels in asperity, (c) remaining BC oxidise rapidly and form non protective oxide. Rehealing occurs at the base of asperity where Al levels are high enough.

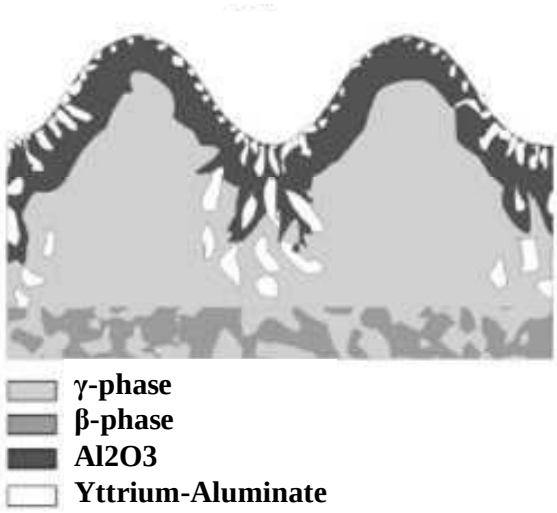

Figure 2.12 Schematic of alumina scale formation and Y-Al precipitation [82].

On the effect of roughness, Naumenko et al. [68] found that it was causing the inhomogeneous growth of the TGO. Convex surface areas were showing a thin Al_2O_3 scale accompanied by the formation of spinels/mixed oxides. On the other hand,

concave surface areas were growing thicker Al_2O_3 containing Y-rich pegs and few if any spinels/mixed oxides. They explained these uneven TGO thicknesses by the high fraction of Y-Al oxides in concave areas enhancing the scale growth rate (Figure 2.12) [68,82].

Uneven growth of the TGO was also observed and modelled by Che et al. [83] who stated that the TGO was thicker at "peaks" (convex areas) than at "valleys" (concave areas) of the undulations. They did not, however, differentiate the Al_2O_3 from spinels/mixed oxides in their measurements which means that they are not contradicting Naumenko et al. [68]. Another reason for local accumulation of the TGO can be the cracking and rehealing of the oxide layer during oxidation (Figure 2.13) [84], happening generally during thermal cyclic oxidation at temperatures above 1000 °C. After cracking of the first TGO layer, oxygen penetrates through the cracks in the delaminated TGO layer and reacts with the fresh BC, and this easy ingress of oxygen accelerates the BC oxidation, thus reforming a TGO [68,69,84].

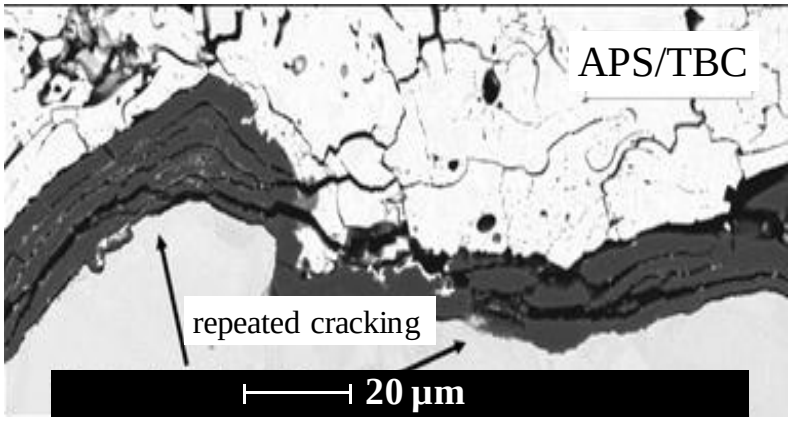

Figure 2.13 SEM image of repeated TGO-cracking/re-growth during cyclic oxidation at 1050 °C in an APS/TBC system with NiCoCrAlY/BC [68].

2.3.3 Evolution of stresses in a TBC system

The amount of stress generated during oxidation in a metal system is so considerable that it is common to observe that metal surfaces do not stay flat but instead wrinkle (or buckle) because of the presence of large compressive stresses in the oxide scale [85]. The understanding of the generation of stresses and their evolution in the complex four layered TBC system is challenging but necessary to forecast and delay TBC failure.

There are two main sources of stress during the oxidation of the TBC system. The most important of them are the thermal expansion misfit upon cooling (Table 3.1) and the strains caused by the TGO growth [21,86]. The stress caused by the thermal expansion misfit depends on the rate at which the system cools down. The slower the sample is cooled, the more time there is for creep relaxation to happen [87].

Material	Thermal expansion coefficient (C^{-1} ppm)
TGO	8-9
BC	13-16
TC	11-13

Table 3.1 Thermal expansion coefficients of the different layers of a TBC system [21].

2.3.3.1 Stresses in the TGO and BC

The strains involved during the TGO growth represent the overall volume increase when the alloy is converted into Al_2O_3 and other oxides. Formation of new TGO at the BC interface produces normal thickening strains with a corresponding rigid body displacement, meaning that lateral strains are induced on the grain boundaries

normal to the interface [86]. Those strains induce compression, which when large enough suppress internal TGO formation. Eventually, the growth stresses reduce because of the creep strength of the TGO [86]. Relaxation can also happen in the BC through metal deformation and the proportion of those two simultaneous stress-relaxation processes in the BC and in the TGO are determined by the stress values in both layers, which will change depending on the oxide-metal thickness ratio [86]. The displacement of the TGO, called "buckling" (Figure 2.14), increases the roughness of the TC/BC layer and induces tensile stresses normal to the interface, especially on crests (convex areas) and valleys (concave areas) of the wrinkling, which in the end can cause delamination [85].

The oxidation temperature also affects greatly the amount of stress developing in the oxide scale. Above 950 °C, creep in the metal limits the stresses in the oxide while at lower temperatures, elastic thermal-stress behaviour is maintained [84].

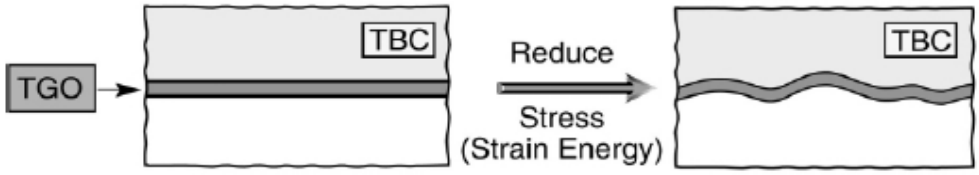

Figure 2.14 Sketch illustrating the attempt of the compressed TGO to lengthen in order to reduce stress [21].

2.3.3.2 Stresses in the ceramic

Ceramic spallation is known to be caused by the cyclic thermal stresses resulting from the differential thermal expansion between the ceramic and metal [21,60,88-94]. The evolution of residual stresses in the ceramic TC greatly affects the lifetime of the

APS/TBC system. Residual tensile stresses tend to induce coating failure normal to the TC/BC interface (vertical cracking through thickness), while compressive residual stresses can provide a driving force for buckling when the in-plane stresses exceed a critical value [95]. Thermal expansion misfit induces compression stresses reaching 3 to 4 GPa. Non-planarity of the rough plasma-spayed coating causes those stresses to redistribute. Shear stresses exist at inclined sections [34]. This local TC/BC interface geometry (roughness) has been found to greatly influence the nature and evolution of stresses in the ceramic as well as in the TGO. Protrusions of ZrO_2 into the BC are preferred sites for damage initiation (Figure 2.15), as the sintering effects at high temperature in such a small volume fixed by the geometry of the BC will produce localized tensile stresses. In the same time, the thermal shrinking of the substrate during cooling determines the strains in the axial direction. Hoop stresses are created by the displacement of the layer system in the radial direction [90].

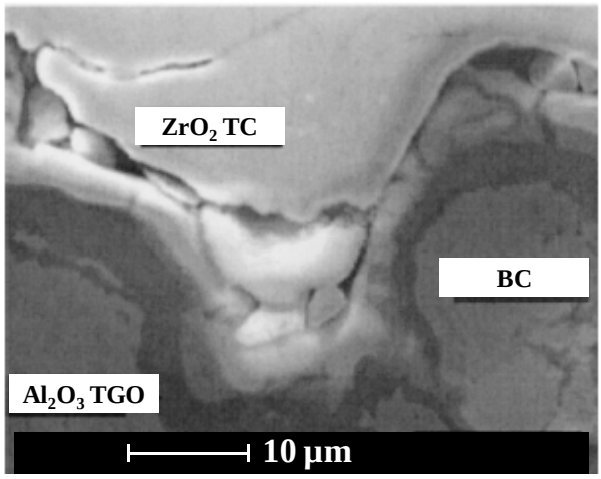

Figure 2.15 SEM image of damage introduced by thermal cycling at TC/BC interface [91].

The coefficient of thermal expansion of the BC is larger than that of the TC. Therefore, the BC induces tensile stresses in “peak regions” (convex areas) of the layer

and compressive ones in “valleys” (concave areas) (Figure 2.16). However, the TGO has the opposite effect and causes tensile stresses in the “valleys” and compressive ones in the “peaks” because of its smaller coefficient of thermal expansion. It determines the stresses occurring in the system during the cooling phase of a thermal load [89,90,96]. These tensile out-of-plane stresses on the “peaks” of the rough surface, lead to crack initiation at the TGO/BC interface. The resistance of the interface to delamination depends on the toughness of the interface, the TGO-thickness and the radius of the curvature [68]. Heating stresses tend to counteract compressive residual cooling stresses near the TC/BC interface. Cooling stresses are usually more compressive near the interface and get more tensile towards the surface (in the case of isothermal oxidation) [92,93].

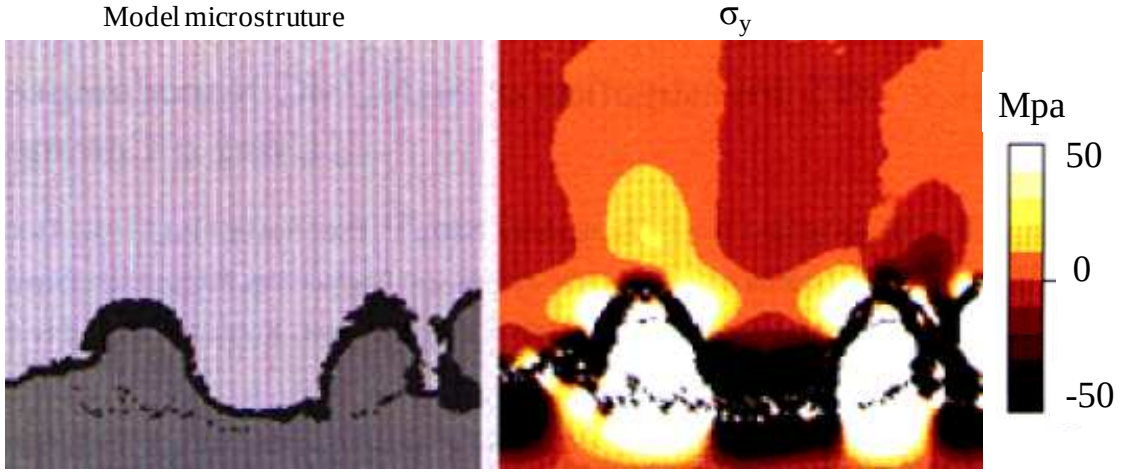

Figure 2.16 Model microstructures and the calculated residual stress (sy) for the TBC system [91].

Also at temperatures over a 1000 °C, the properties of the initially tetragonal ceramic, gradually evolve because of sintering and changes in microstructure into the monoclinic phase (more precisely during cooling). This mechanism is controlled by the

grain size and the chemical composition (amount of Y_2O_3) of the tetragonal phase. In APS systems, more monoclinic phase develops at the bottom of the ceramic TC. The monoclinic phase is not the preferred form for the YSZ as it is responsible for a toughening of the ceramic [94].

Oxidation also causes the microcracks and pores of the APS ceramic to close. The reduction of porosity increases the value of the Young modulus resulting in a ceramic less tolerant to strain and more subject to cracking [97].

2.3.4 Initiation and propagation of cracks

The zones of the coating that experience normal tensile stresses are the most important from a life predicting viewpoint, because those stresses are responsible for nucleating and propagating cracks. For example, radial cracks form in the TC as the TGO thickens but, the creep ductility of the TGO prevents the TC cracks from penetrating the TGO, even with appreciable hoop tension, as it redistributes concentrated stresses at the front of the radial crack in the TC. This phenomenon is helped by the compressive stresses at the TGO/BC interface. Cracks forming during thermal exposure should be thus confined to the TC [48]. However, during cooling, the "peaks" lead to the generation of tensile stresses in the TGO, which in turn lead to crack initiation at the TGO/BC interface. Cracks propagate along the interface following the rough profile, and when they propagate towards a "valley", the out-of-plane tensile stresses decrease and in-plane shear stresses increase. At some point, a critical shear stress is reached and fracture of the Al_2O_3 scale happens, after which the crack, initially confined to the TGO/BC interface, penetrates the oxide layer [68]. Figure 2.17 represents schematically the crack growth process. The oxidation temperature

influences the rate of crack propagation. It also depends on the microstructure of the TGO and the TC. Porosity in the TC is known to reduce its elastic modulus and thus decrease the driving force for crack propagation [94]. Echsler et al. [98] reported that for APS/TBC systems undergoing isothermal oxidation, a temperature of 1050°C or higher was needed to produce failure within an exposure time of 5000 hours. Tests were carried out at 950, 1000, 1050 and 1100 °C. The damage observed in samples' cross-sections prior to final failure was represented by micro-cracks in the vicinity of the TGO. Those cracks were oriented parallel to the BC/TGO/TC interface and seemed to start in the TGO or at the TGO/BC interface (Type C). When the samples underwent longer exposure, longest cracks were spotted within the TGO (Type B) and these penetrated into the ceramic TC (Type D). Figure 2.18 shows the different types of cracks identified by Echsler et al. [98]. Trunova et al. [67] also noticed that some cracks initiated at the TC/TGO interface after only 100 hours of isothermal exposure. After longer time cracks were found within the TGO as well as at the TGO/BC interface. Further exposure of the samples led to crack coalescence and formation of macroscopic cracks in the TGO. It was found that when reaching 50% of the total coating life, cracks penetrated into the ceramic TC, leading to delamination crack propagation through the TGO and the TC [67]. TC spallation is not a sudden fracture but rather the result of continuous damage evolution.

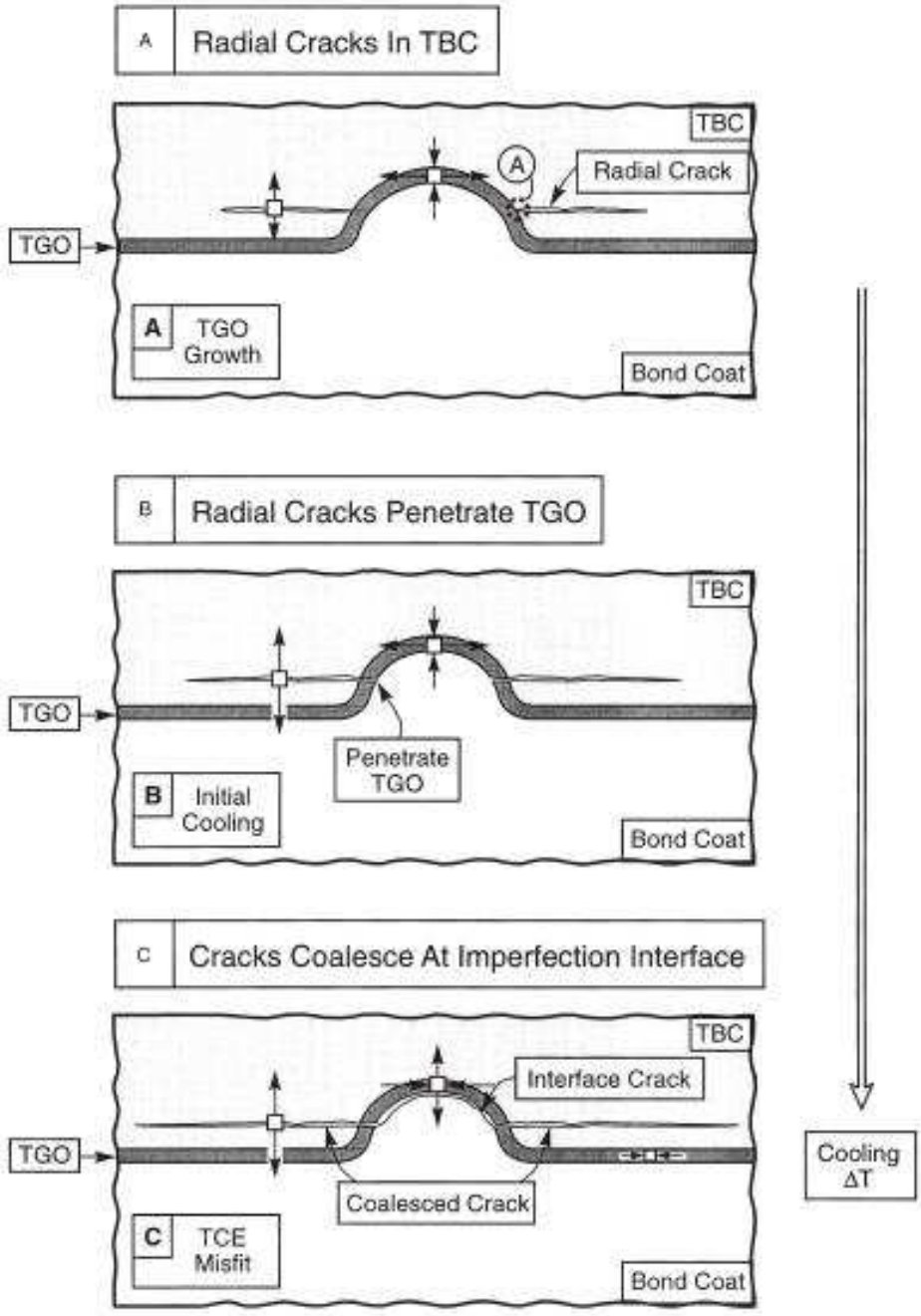

Figure 2.17 Cracking sequence suggested by the stresses due to growth and thermal misfit [21].

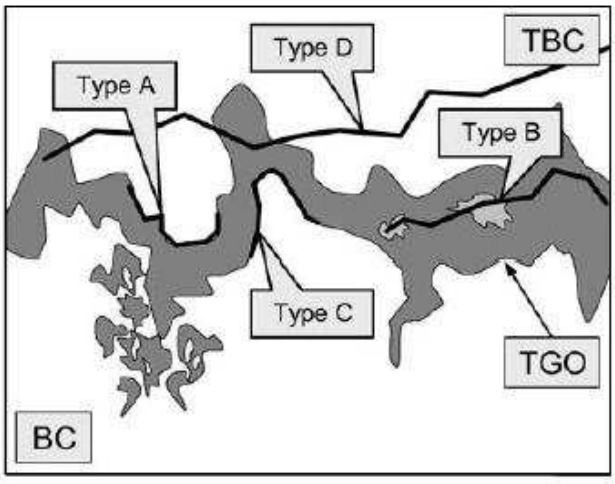

Figure 2.18 Schematic illustration defining various types of cracks in the TGO and its vicinity in an APS/TBC [98].

2.3.5 Effect of blade curvature on the failure of the TBC systems

Over the past few years, the effect of blade geometry on the lifetime of TBC coating systems has aroused curiosity. It is well known that during service in a gas turbine, the blade features are exposed at different temperatures causing temperature gradients around different geometries (as well as through the walls). The hottest regions exposed are the leading edge of the blade and the trailing edge (Figure 2.19) (from a maximum of 1100 °C to 600 °C in the centre of the aerofoil, in the case of a use in aeroengines), causing the oxidation extent to be more or less aggressive at different location of the blade [1,18,99].

Several researchers have observed the spallation of TBC system from service blades reaching the end of their lifetime. Sjöström and Brodin [100] explained that three sorts of spallation happen around a blade: (i) spallation on convex surfaces; (ii) spallation on flat surfaces; and (iii) spallation at sharp edges (Figure 2.19). Sohn et al. [101] observed that failures were localized near the tip of blades on both the pressure

and suction surfaces of ex-serviced high pressure turbine blades coated with EB-PVD/TBC. Compressive residual stresses increased in concave and flat regions after testing the blades, while those in the convex region remained unchanged. To investigate the samples' geometry influence on the microstructure of the layers present in a TBC, Altuncu et al. [102] tested disc-shaped and square-shaped substrates coated with APS/TBC under aeroengine conditions. They found that spallation was concentrated at the edges of the samples. Disc-shaped samples' failure appeared as chipping in the TC while failure in square-shaped samples occurred at the TC/TGO and TGO/BC interfaces [102]. DeMasi [103] also thought that the component geometry was an important life variable. He stated that normal stresses were introduced in the coating of a curved surface by the tangential compressive stresses present resulting in ceramic spallation. Koomparkping et al. [104], observed spallation of the ceramic TC in the leading and trailing edge as well, and also noticed that spinels/mixed oxides were present more at those two convex locations.

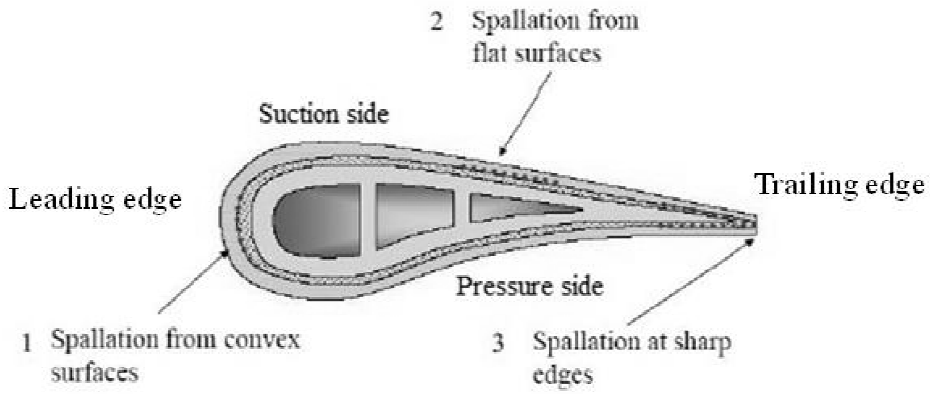

Figure 2.19 Basic failure mechanisms of a TBC; example: turbine blade [100].

Observations of different aspects of the effect of geometry on coating lifetime can be easily found in the literature. However, a holistic mechanism has not been identified to include the stress and microstructural behaviour of the different layers of the coatings at different curvatures, to explain the way the TBC systems fail around blades.

2.4 Prediction of TBC systems lifetime through modelling

The ability to predict the lifetime of TBC is a high priority for industrial gas turbine manufacturers and users, and a lot of research has been carried out with the aim of modelling the behaviour of coatings and creating predictive models for their failure. Those models generally require data to be acquired from material systems exposed to "similar" conditions to real components in operating plant, and then cover different aspects of the failure processes such as: environmental degradation, mechanical factors, synergistic effects and component end-of life criteria [6,105]. However models are usually "simplified" to deal with only one aspect of the coating failure mechanism. For the effect of oxidation different models concentrate on the stress distribution in the different layers and how this affects the initiation and propagation of cracks [105-107]. Other models predict the depletion of elements using diffusion calculations [72,108,109] and some relate the end of a component's lifetime to a critical oxide scale thickness [1,110-115]. It is believed that different TBC systems (APS≠EB-PVD and MCrAlY ≠ Pt-Aluminides) behave differently; making prediction models very specific of the system that was studied in the first place. This section presents examples of modelling methods used in research (different TBC systems).

2.4.1 Models based on stress distribution

This research does not focus on the stress distributions in the TBC system so such modelling is only described briefly. Using the finite element and starting with an undamaged TBC system, calculations allow the stress states and deformation inside the individual layers to be predicted. The superposition of several kinds of strains leads to prediction of the mechanical failure of the TBC and the TGO (Figure 2.20). These failures result from the external loading during the operation of the component, from temperature changes (as a result of the different thermal expansion coefficients of the different materials) and from the formation of the TGO. When the total strain exceeds a critical value, strain relief mechanisms occur in the ceramic layer [106,107].

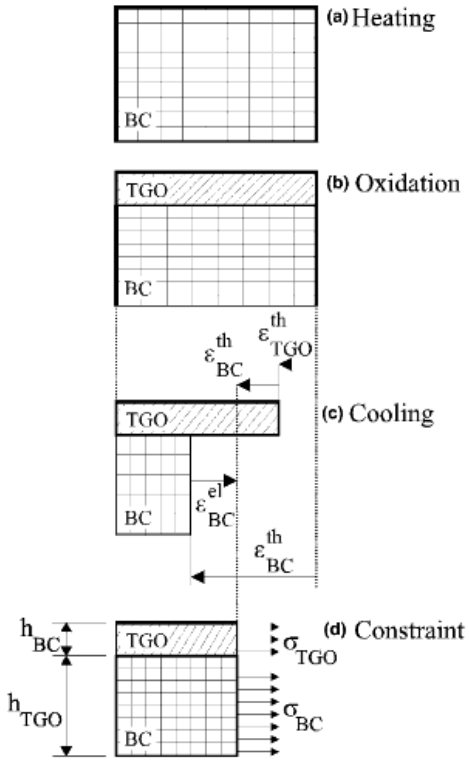

Figure 2.20 Schematic illustration of the main steps that lead to the field stress due to oxide formation [106].

Busso et al. [105] thought of a methodology to predict the lifetime of EB-PVD/TBC based on stress measurements, which uses three steps:

- Step 1: Quantifying TBC damage and integrating this information into a model. This links the damage measurements at each time to a critical roughness for a given thermal cycle.
- Step 2: Interpolating the finite element results to obtain a relationship between time and the accumulation of local stress responsible for crack initiation.
- Step 3: Predict lifetime by using a curve generated by finite element analysis.

Such TBC system finite element models are unfortunately often simplified (Figure 2.21) and do not take into account the uneven roughness and growth of the TGO or the imperfections found into the oxide layer which may make estimations, if not inaccurate, then at least have a high error margin. The system is often assumed to be in a stress-free state before oxidation even though residual stresses exist in an APS coating [96].

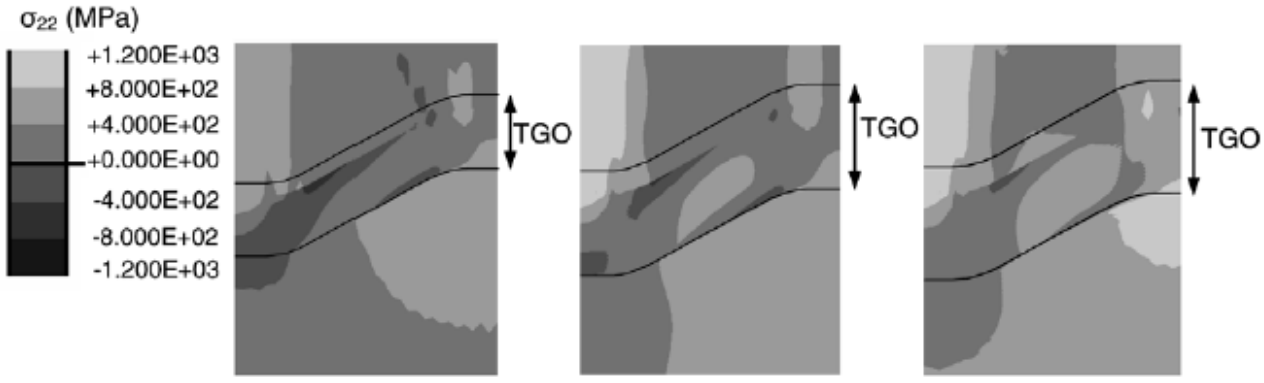

Figure 2.21 Finite Element model of the out-of-plane stress in a component cooled down from 1000°C to room temperature for 61, 167 and 241 hours (from left to right) [105].

2.4.2 Models based on elemental diffusion

The rate and mechanism of consumption of the Al reservoir from the BC as been proven to influence greatly the lifetime of the whole system (e.g. through an inability to re-heal protective oxide layers or formation of less protective oxides rich in Cr, Co or Ni). Numerical models describing the diffusional transport through the different layers of the scale and coating can bring further understanding to the growth mechanisms of the oxide layers and also predict when the system will reach a critical shortage of crucial elements [72,108,109].

These diffusional processes are described by the well known Fick's laws of diffusion:

$$J = -D\frac{\partial C}{\partial X} \ \ (First\ Law) \ \ (2)$$

and,

$$\frac{\partial C}{\partial t} = \frac{\partial}{\partial X}\left(D\frac{\partial C}{\partial X}\right) \ (Second\ Law) \ (3)$$

Where J is the flux and C is the concentration of the diffusing element, D is the appropriate diffusion coefficient, and X and t refer to distance and time respectively. Often, D is assumed independent of the concentration and the second Fick's law can be written:

$$\frac{\partial C}{\partial t} = D\left(\frac{\partial^2 C}{\partial X^2}\right) \qquad (4)$$

When D cannot be assumed to be independent of concentration, the equation becomes:

$$\frac{\partial C}{\partial t} = D\frac{\partial^2 C}{\partial X^2} + \frac{\partial D}{\partial C}\left(\frac{\partial C}{\partial X}\right)^2 \qquad (5)$$

Solutions to Fick's laws can describe many situations involving high-temperature processes such as solute oxidation in binary or ternary alloys, internal oxidation and moving boundaries. However, simplifying assumptions for the diffusion coefficients, the isothermal conditions, the geometry and the boundary condition are required for such models to be solved [108]. Recently Renusch et al. [72] proposed a model to predict the failure of the TBC system due to the depletion of the aluminium. They used the Fick's laws to describe the diffusion of Al to both the BC and the substrate (Figure 2.22(a)) and then related it to the growth and stress generation of the TGO layer, thus allowing the prediction of the end-of-life of the coating (Figure 2.22(b)). In a general manner, such models have demonstrated that TBC life should be longest for coatings with the highest amount of Al in the BC [114].

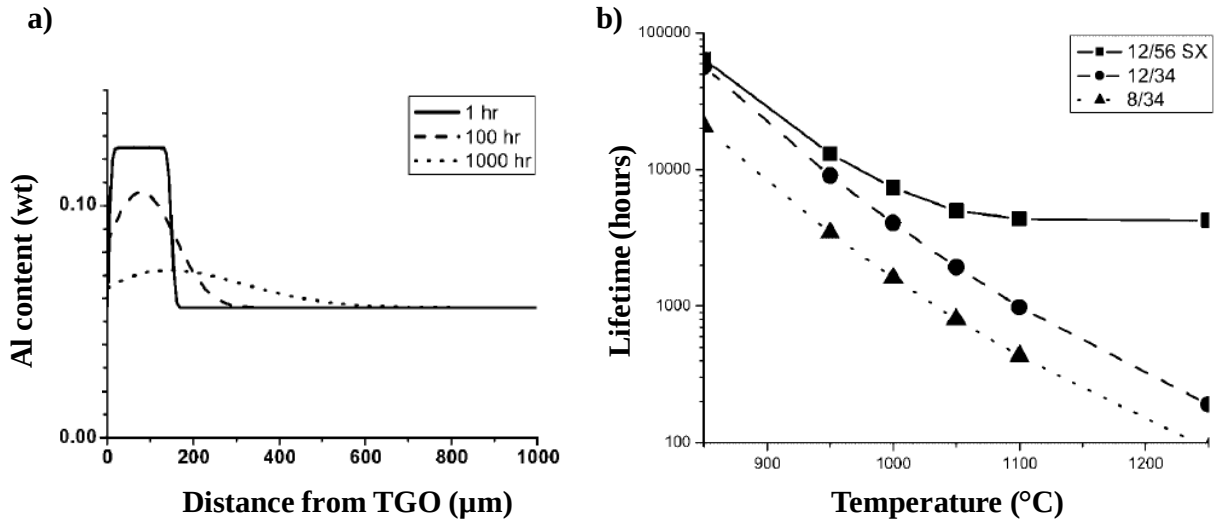

Figure 2.22 (a) Plots of Al diffusion into the substrate and consumed by TGO growth, and (b) spallation lifetime due to BC depletion of Al with internal oxidation of different APS/TBC systems at 850-1250 °C (CMSX4 coated with 150 µm Abler Ni 192-8; IN738 coated with 150 µm Abler Ni 192-8 and IN738 coated with 150 µm SC2231) [72].

2.4.3 Models based on the TGO growth

Initial crack growth is believed to be related to the thickness of the TGO on the BC. After exceeding a critical thickness, crack propagation is governed by stresses induced by thermal mismatch and TGO growth [58]. Lifetimes can be predicted using equations taking into account the oxide growth rate, the initial Al content, oxide adherence and the component geometry [110]. This semi-empirical method requires the data from long term oxidation of commercial and/or model TBC systems.

Such models can be based on the mass gain of samples caused by the growth of the TGO and use the equations describing the growth kinetics of the oxide layer:

$$\Delta m^2 = k_p t \quad (6)$$

where Δm is the mass gain per unit area at time t and k_p the parabolic rate constant [111-113]. The parabolic rate constant k_p is temperature dependant and follows the Arrhenius law:

$$k_p(T) = C \,.exp\left(\frac{-Q}{R.T}\right) \quad (7)$$

where the parameters C and Q are determined and used for the interpolation of k_p and R is the gas constant [58]. Newer models consider the two stages of oxidation, the transient stage which has a higher rate and coincides with the formation of θ-Al_2O_3 (and other transient oxides) followed by the steady-state stage characterised by the slow growth of α-Al_2O_3 using two equations [1]:

$$\left(\frac{\Delta w_\theta}{A}\right)^2 = \left(k_{p\theta}.t\right) + C \;\; (if\; t < t_c) \quad (8)$$

$$\left(\frac{\Delta w_\alpha}{A}\right)^2 = \left(\frac{\Delta w_{\theta c}}{A}\right)^2 + k_{p\alpha}(t - t_c)\; (if\; t > t_c) \quad (9)$$

where Δw is the mass change in mg, A the material surface area in cm^2, $k_{p\theta}$, the rate constant for the θ-Al_2O_3 in mg^2/cm^4h, $k_{p\alpha}$ the rate constant for the α-Al_2O_3 in mg^2/cm^4h, w_c the critical weight in mg/cm^2, t the time, t_c the critical time and C an integration constant. This model was used by Nalin [1] and reproduced accurately the mass gain of coated systems oxidized at 850°C and 900°C, but was less accurate at higher temperatures. Also a gradual transition between the two oxidation rates is not taken into account.

Another attempt to describe the mechanism of α-Al_2O_3 failure and to predict lifetime was made by considering both the diffusion of Al from a FeCrAlY material to α-Al_2O_3 and the thickening of this oxide layer (e.g. through the mass gain of samples) [112,115]. The model is formulated based on certain understanding such as:

- A FeCrAlY, with a density of ρ_m and a surface to volume ratio of *V/A*, initially gains mass due to the uptake of oxygen in forming a surface scale of density ρ_{ox}(formation of α-Al_2O_3),
- The scale growth leads to the loss of Al from the alloy,
- After a critical time t_c, the Al content of the alloy may decrease below some critical level C_c such that α-Al_2O_3 can no longer form (i.e. the beginning of breakaway oxidation).

In this model, the onset of chemical failure is predicted by modelling the rate of Al depletion in the alloy. An accelerated rate of depletion caused by the spallation of the oxide scale (and growth of new oxide on freshly exposed depleted alloy) is also accounted for. The equation is composed of two terms, one describing the oxide spallation and the other the oxide growth and goes as follow:

$$\beta \frac{k_p t_c}{\Delta x} + (1-\beta)\left(k_p t_c\right)^{1/2} = 0.89 \frac{\rho_m}{\rho_{ox}} \frac{(C_o - C_c)}{(1-C_c)} \frac{V}{A} \quad (10)$$

where β is the statistical function that defines the likely fraction of surface area to spall and Δx the mean oxide thickness that spalls. If no spallation occurs, β=0 and if it dominates, β approaches 1 and equation (10) suggests a linear relationship between the time to breakaway and the geometry of the sample (V/A). It is important to note that in this study, kp is in $\mu m^2/s$ in equation (10) meaning that it is calculated from the oxide thickness [112,115]. It could be similarly calculated from mass change data. The second term describing the oxide growth is based on the following equation and equation (6):

$$Al\ reservoir = \rho_m \frac{V}{A} \cdot \frac{(C_0 - C_c)}{(1-C_c)} \quad (11)$$

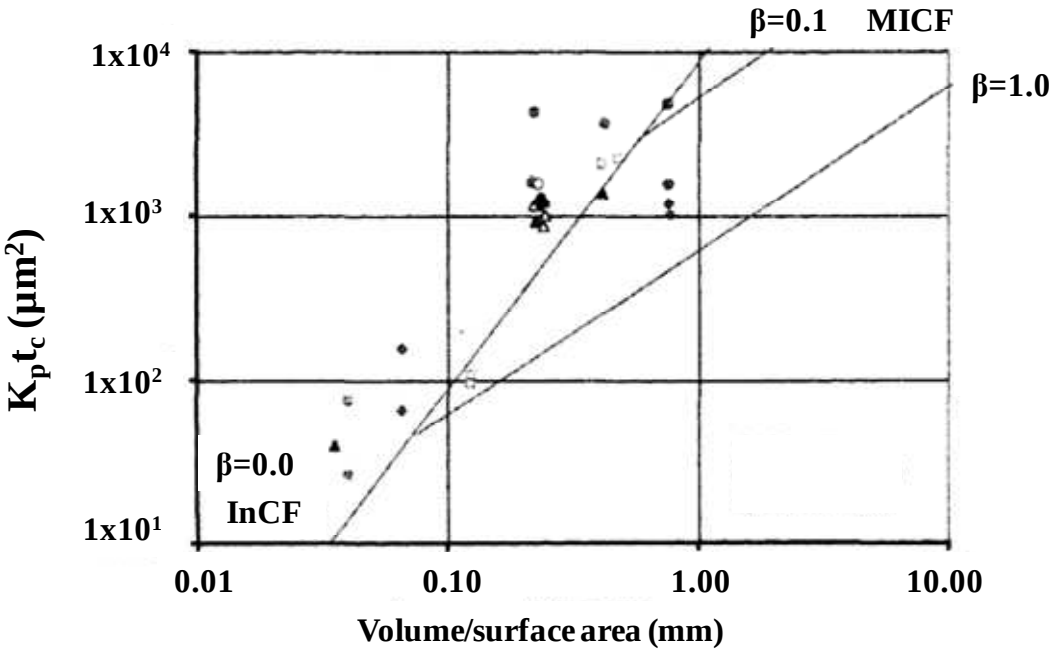

Figure 2.23 Model of breakaway oxidation, based on equation (10) [115].

A simplified validation of the model is provided in Figure 2.23. Data for a range of FeCrAl alloys are plotted at 1300 °C. The empty symbols represent samples that did not go into breakaway oxidation while filled symbols represent the ones that did. MICF and InCF refer to the different mechanisms of the coating system failure caused by Al depletion [73]. Prior to the onset of spalling, the TGO growth follows a generalised rate law. However, in areas that have spalled, the oxide repairs following either parabolic or sub-parabolic kinetics. To allow this model to be correct, several assumptions on the Al diffusion, the initial condition and the oxidation were made (given in reference [115]).

CHAPTER III – AIM AND OBJECTIVES

3.1 1st part: Experimental evaluation of the integrity of APS/TBCs

The first task of this thesis was to obtain quantitative data on the failure modes that can lead APS/TBCs to spallation after exposure at temperatures similar to those found in gas turbines (900-1000 °C). The thesis focuses on the effect of the components' shape, i.e. macro and micro geometry, as it has appeared recently that the bulk sample shape affects the TBC's integrity (Section 2.3.5).

The modelling of the modified aerofoil-shaped samples' behaviour will be established from the data obtained from their oxidation and observation of the progression of TBC spallation. Moreover, assessing the behaviour of several features such as the TGO, spinels, the β-phase in the BC, TC microstructure and crack propagation, will enable the understanding of the role of aerofoils' curvature. With exposure to high temperatures, the change of the different layers' microstructure, of the TGO thickness and the evolution of stress states influence the integrity of the whole system in ways that were more or less explained in literature. Indeed, the separate mechanisms happening in the BC, TC and TGO are in general well understood. However, the way they interact, coupled with the effect of geometry still needs to be investigated. In addition improving an existing TGO growth model with this input will enable the prediction of their lifetime in industrial gas turbines.

3.2 2nd part: Improving the efficiency of MCrAlY bond coats undergoing oxidation

As a second task of the thesis, different MCrAlY BC compositions were obtained by magnetron sputtering and were analyzed. The extensive research that has been undertaken over many years to find the best BC composition has been targeted at aero-engines and so assumed bond coat temperatures over 1000 °C. Few studies have been carried out at temperatures encountered in industrial gas turbines (e.g. bond coat temperatures of 900 – 1000 °C).

This is why, a profile indicating the best composition resisting 900-950°C oxidation will be drawn. This will include mass change data and the mapping of the oxides created at those temperatures. An improved BC, tailored to be used in industrial gas turbines will results from this project, added to a better understanding of the effect of composition and temperature on the nature of oxides grown on the coatings. Also, the manufacturability of such coatings using 2 or 3 target magnetron co-sputtering will be assessed as well as the limitations of this technique.

CHAPTER IV - EXPERIMENTAL PROCEDURE AND EQUIPMENT

4.1 Oxidation of the modified aerofoil-shaped samples

4.1.1 The modified aerofoil-shaped samples

Modified aerofoil-shaped samples were designed and manufactured (by Siemens Industrial Turbomachinery Ltd) to recreate curvatures found on industrial gas turbine blades (Figure 4.1). A CoNiCrAlY BC was deposited on the CMSX4 Ni-superalloy substrates (Table 4.1) by HVOF spraying of AMDRY 995 powder (Table 4.1). On top of the BC an YSZ TC was deposited by APSing. TC and BC were deposited by Praxair Surface Technologies Ltd. The manufacturing process caused the TC and BC thicknesses to vary with curvature. The BC thickness measured between 50 and 135 μm, while the TC measured between 130 and 250 μm (Table 4.2). In the as-sprayed conditions, the ceramic coatings were grey. This can be explained by the formation of Zr_2O_3 in the reduced gas atmosphere during APSing. It depends on the Ar/H_2 ratio during deposition [116-118]. The TC regained its white colour during exposure (oxygen stoichiometry restored). The locations' curvatures (Table 4.2) chosen around the modified aerofoil-shaped samples for observation are the inverse of the radii calculated from the samples' design sheet (Appendix I).

Alloy	Ni	Cr	Co	Al	W	Ti	Mo	Ta	Re	Hf	Y
CMSX-4	base	6.5	9.6	5.6	6.4	1	0.6	6.5	3	0.1	
AMDRY 995	32	21	base	8							0.5

Table 4.1 Composition (in wt%) of modified aerofoil-shaped sample's substrate and BC.

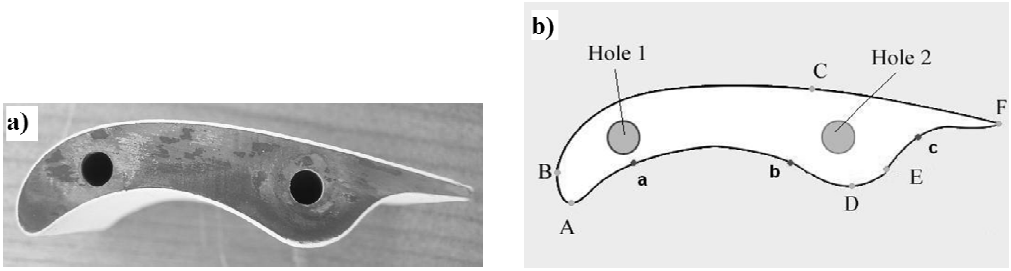

Figure 4.1 Picture of a modified aerofoil-shaped sample (a) and its schematic representation (b). Upper case letters correspond to convex areas, lower case to concave. This figure can also be found at the end of thesis (Appendix I).

Location	TC thickness (µm)	BC thickness(µm)	Curvature (mm^{-1})
A	190	90	0.85
B	190	50	0.14
C	220	110	0.01
D	210	100	0.18
E	170	80	Theoretical 0
F	130	50	2.86
a	220	130	-0.06
b	230	130	-0.05
c	250	135	-0.20

Table 4.2 TC, BC thicknesses and curvatures at different positions around the modified aerofoil-shaped sample (Approximation after measurements carried out on 23 samples (Appendix C). Upper case design convex curvatures and lower case concave ones.

4.1.2 Experimental procedure

Laboratory oxidation experiments consisted of exposing the samples in furnace assemblies for various temperatures and times of exposure, under oxidative conditions similar to those found within operating gas turbines. Long cycle exposure tests were carried out on 37 samples in resistance heated furnaces from 900 to 1000 °C. After each cycle, lasting 150, 250 or 500 hours depending on temperature (Table 4.3), the samples were slowly removed from the hot furnace over a 20 minute period and cooled in air. Selected samples were removed for destructive examination after periods of 100, 300,

1050, 1500, ~ 3000, 4000, 7000, 10,000, 15,000 and 20,000 hours (Table 4.3). Table 4.4 summarises the oxidation conditions for every sample. The oxidation tests employed horizontal tube furnaces in which the samples were located within a zone where the temperature is within ±5ºC of the target test temperature.

Oxidation temperature (°C)	Cycle length (hours)	Total exposure time (hours)
900	250 then 500	≤ 20,000
925	250	≤ 10,000
950	250	≤ 5000 (failure)
975	150	≤ 4000 (failure)
1000	150	≤ 1500 (failure)

Table 4.3 Exposure of APS/TBC system on modified aerofoil-shaped samples.

81-BSYA-	Oxidation Temp. (°C)	Total exposure time (hours)	81-BSYA-	Oxidation Temp. (°C)	Total exposure time (hours)
1	900	4000	20	1000	1050
2	900	10,000	21	1000	1050
3	900	2780	22	1000	1050
4	900	2780	23	1000	1500
5	900	20,000	24	1000	1050
6	900	4000	25	925	10,000
7	900	7000	26	925	100
8	900	15,000	27	925	4000
9	950	4000	28	925	>10,000
10	950	5000	29	925	2740
11	950	5000	30	925	2740
12	950	2780	31	925	7000
13	950	4000	32	925	>10,000
14	950	2780	33	975	4000
15	950	5000	34	975	3000
16	950	5000	35	975	300
17	1000	1500	36	975	3000
18	1000	1050	37	975	2700
19	1000	1500			

Table 4.4 Modified aerofoil-shaped samples' identifications, oxidation temperatures and total exposure times.

Metrology was applied to the samples before and after exposure. This consisted of an accurate measurement of samples dimensions to quantify material degradation in terms of mass gain. The most useful data for accurate and reliable material life time predictions were identified as oxide thickness gain, interdiffusion zone thicknesses, β-depletion depths and TC/BC microstructures; this information could only be collected through a destructive method of analysis.

Both scanning electron microscopy (SEM) and energy dispersive X-ray spectroscopy (EDX) were used to observe sample cross-sections in order to characterize their microstructure (as described in Section 4.3). Selected samples were etched for 5 seconds with a solution of hydrochloric acid and copper sulphate diluted in distilled water to reveal and then observe the grain boundaries in the BC.

4.1.3 Additional curved samples

Additional APS/TBC samples were provided by Rolls-Royce (RR) in order to gather more information on the initial stages of oxidation. The BC deposited on top of the CMSX-4 substrate is a diffused Al coating coupled with a LPPS MCrAlY. The BC was heat treated for 1h at 1100°C before deposition of TBC which is an APS YSZ. As shown in Figure 4.2, each sample comprises 2 flat areas and a concave bend enabling the study of the geometry effects if needed.

In order to investigate the initial stages of oxidation, those samples were oxidised isothermally for a short time, specified in Table 4.5. Similarly to the modified aerofoil shaped samples, the RR samples were weighed before oxidation and between cycles. SEM and EDX were used to observe cross-sections' microstructure.

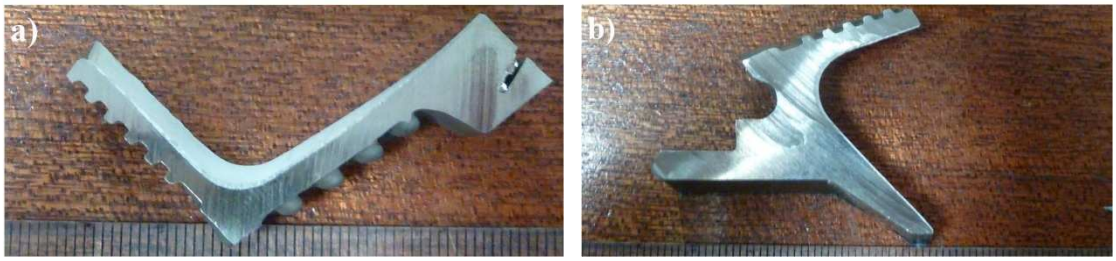

Figure 4.2 Pictures of as received Rolls-Royce samples, (a) RR1 and (b) RR5.

RR-	Oxidation Temperature (°C)	Total exposure time (hours)
1	925	0
2	925	0
3	925	0
4	925	50
5	925	200
6	925	150
7	925	100
8	925	100
9	925	150
10	925	50
11	925	200

Table 4.5 RR samples identification, oxidation temperatures and total exposure times.

4.1.4 Flash Pulsed Thermography

4.1.4.1 Flash pulsed thermography system

The flash thermography system used was based at the National Physical Laboratory (NPL). It consisted of a 316 x 255 pixel Pheonix FLIR system MWIR camera, 12 bit data, 50 Hz frame rate infrared camera with a Thermalwave commercial image processing software package called Mosaic. The total pulse duration was measured to be 31 ms, with a radiant power of 2815 Wm^{-2}. The wavelength distribution

of the emitted light ranges between 350 nm to 1800 nm with some 80 % in the region 400 to 800 nm [119].

4.1.4.2 Principle of flash pulsed thermography

Flash thermography looks at a sample's thermal response to heating (or cooling) to determine the presence of subsurface defects and/or the material properties of the target. Thermography (Figure 4.3(a)) is based on measuring the temperature loss on a sample surface after heat is applied with a pulsed light. The heat is gradually conducted through the sample and an infrared camera records changes in the surface temperature. Irradiating the cold TBC sample with infra-red radiation causes its surface to warm up quickly, because its thermal capacity is small and its thermal conductivity low (Figure 4.3(b)). The coating conducts some of this heat to the substrate below [120,121].

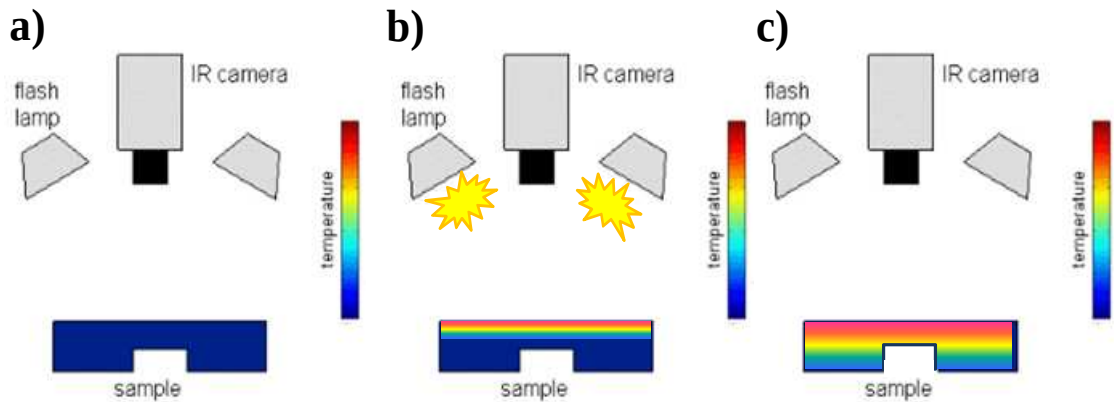

Figure 4.3 Representation of pulsed flash thermography [122].

As the sample cools down, any loss of bonding in the coating creates additional interfaces that interfere with the heat flow through the system, so that the local surface temperature is affected by internal flaws such as disbinding, voids or inclusions

(Figure 4.3(c)). In the absence of any defects, the surface cools down uniformly. If the propagating heat encounters a defect with different thermal properties, it will flow either faster (if it has higher thermal diffusivity) or more slowly (lower diffusivity). The camera, which can only see the surface temperature, makes such defects appear with a different contrast on the pictures taken of the cooling sample surface. [120,121].

4.2 Deposition of new BC compositions

4.2.1 Principle of magnetron sputtering

The mechanism of sputtering consists of ejecting of atoms from a target (cathode) which then land on a substrate. To be more accurate, the charged ions travel through an Ar plasma where they acquire energy from the voltage drop. Then, they hit the target's surface with a momentum that is immediately transferred to the cathode material. Neutral atoms are therefore ejected from this surface, fly back through the plasma and are deposited on the substrate.

The most important concern in sputter deposition is to enhance the ion bombardment rate on the cathode so that a good deposition rate can be achieved. That is why means to increase the secondary electron production are designed to improve the sputtering rate. The invention of magnetron sputtering (Figure 4.4), where the use of an electromagnetic field improves the trapping of electrons, greatly assisted the deposition rate and made sputtering the leading technique for physical vapour deposition (PVD) [123].

In magnetron sputtering, the electrons are confined close to the cathode (which they normally tend to move away from), making it much easier to sustain an electrical discharge at low pressure. Consequently, the required residual gas pressure can be

reduced to enable the transfer of sputtering material without so many collisions. A better deposition rate is reported, as well as a good quality coating [124].

Instead of applying a direct current (DC) field to create the plasma, a radio frequency (RF) field can be used to achieve sputtering. In the latter case, only electrons can respond to the alternating current whereas the ions act as if the field was DC. The advantage of rf sputtering is that no charge accumulates at the target since the electrons are oscillating with the field. The RF technique is mostly used for deposition on insulating or semi-conducting materials [123]. Another way to raise the deposition rate is to provide an additional amount of power to the Ar plasma. Most of this power is absorbed by the target which needs to be water-cooled.

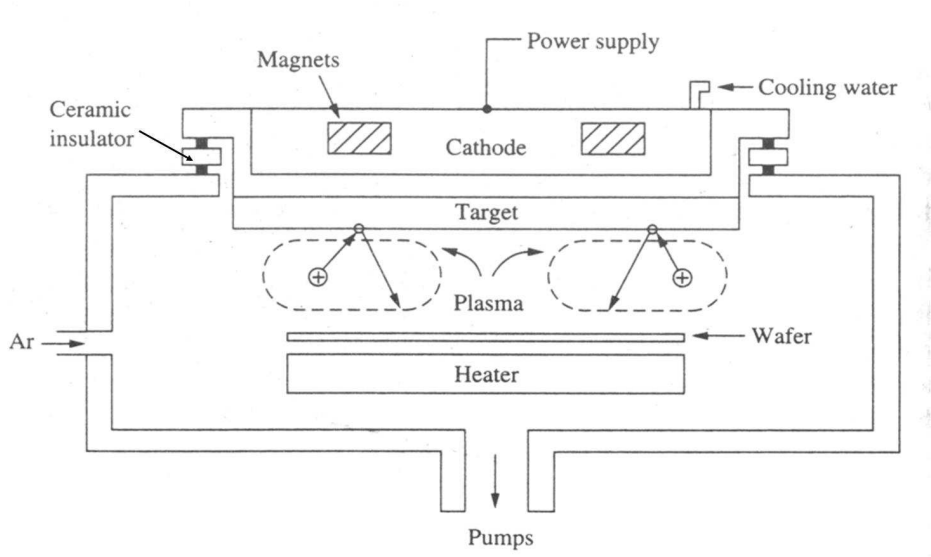

Figure 4.4 A schematic representation of a DC-magnetron sputtering system [120].

In the case of magnetron co-sputtering, several targets (up to 3 in this thesis), connected to different power supplies, are used at the same time in order to create coatings that are composed of a blend of the targets' compositions. For example, in Figure 4.5, substrates located beneath target 1 are expected to be rich in elements

present in that target. Reciprocally, samples placed close to target 2 will be rich in elements from this target. Such process allows depositing a range of compositions depending on the location of the substrate with respect to the targets. The fact that magnetron sputtering achieves deposition atom by atom, and due to the high amount of energy involved in the process, coatings created via co-sputtering are homogeneous. Each target however behaves differently and needs to be calibrated separately. The interaction between plasmas, while running the equipment, also affects deposition rates and must therefore be taken into account during calibration. 3 target co-sputtering is shown in Figure 4.6.

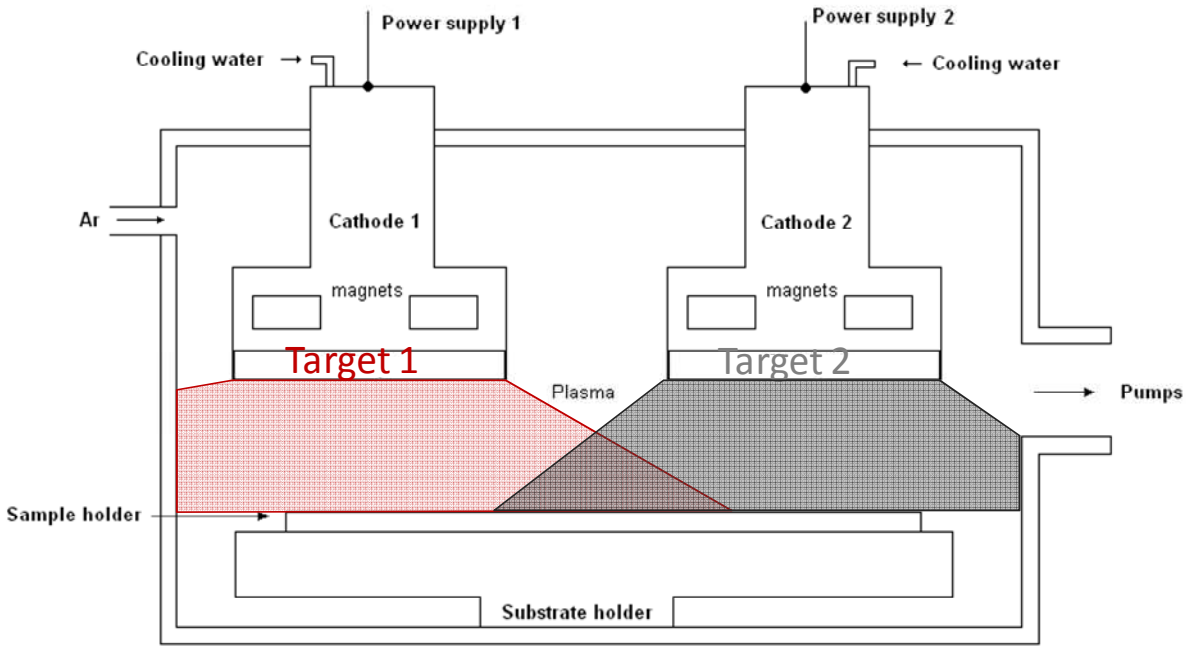

Figure 4.5 Schematic representation of a deposition chamber in a 2 targets co-sputtering system (side view).

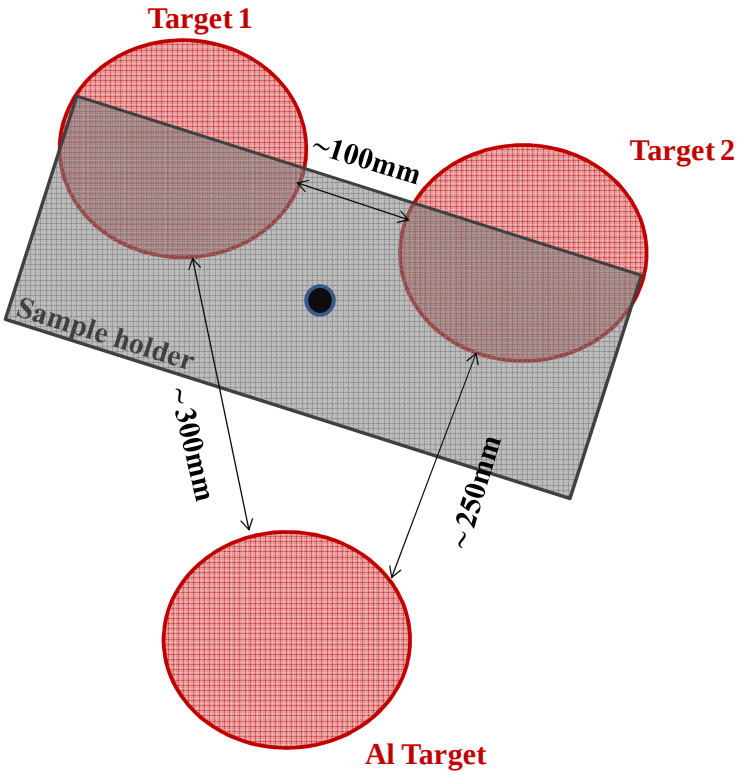

Figure 4.6 Schematic representation of the 3 targets co-sputtering process (top view).

4.2.2 Sapphire substrates

A PVD technique, magnetron sputtering, was used to deposit the coatings. A range of Ni-Cr-Al-Co coatings have been deposited onto 10 mm diameter and 3 mm thick sapphire substrates. Sapphire substrates were chosen instead of metallic alloy to reduce diffusion between the MCrAlY and substrate. They were manufactured by Pi-Kem Ltd.

4.2.3 Magnetron sputtering equipment

Research work was undertaken in CVCI (Figure 4.7(a)) and Leybold L560® (Figure 4.7(b)) coaters equipped with two and three 3-inch (75mm) magnetrons respectively.

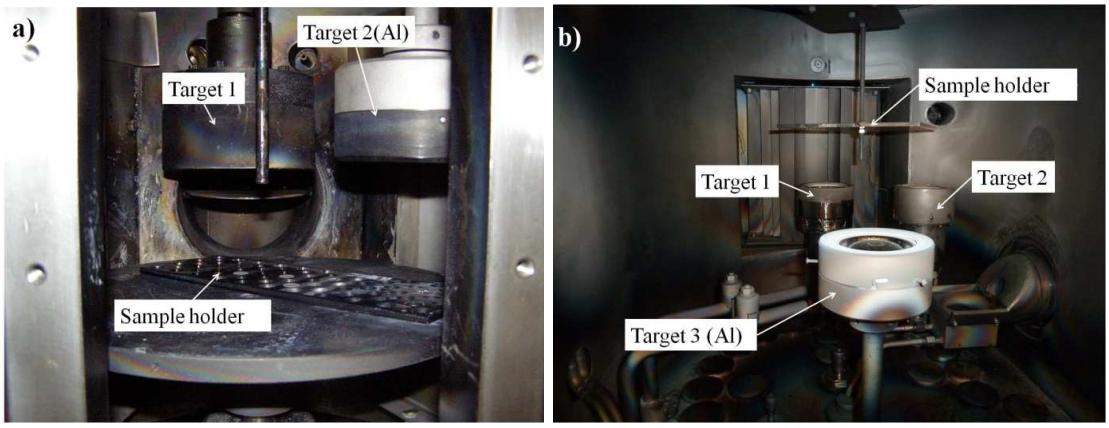

Figure 4.7 Picture of deposition chambers of (a) CVC I (2 target co-sputtering) and (b) Leybold (3 target co-sputtering).

The first stage of experimentation using only 2 target co-sputtering was achieved sputtering of 76.2 mm diameter and 6.35 mm thick targets: (1) either a Ni-10wt%Cr, Ni-20wt%Cr, Ni-50wt%Cr, Ni-20wt%Co-40wt%Cr or Ni-20wt%Co-40wt%Cr target (changed between successive deposition runs) and (2) pure Al target. Targets were supplied by Testbourne and Pi-Kem (Table 4.6).

Ni, Ni-10wt%Cr, Ni-20wt%Cr, and Ni-50wt%Cr targets (coupled with a pure Al target) were chosen for these combinatorial studies because they allow investigation of the different potential oxidation behaviours in the Ni-Cr-Al system. Figure 4.8 presents a ternary diagram, superimposed on Figure 2.9, where the dotted lines represent the alloy ranges obtained with the different target combinations (Ni + Al, Ni-10%Cr + Al, Ni-20%Cr + Al).

Deposition	Target 1	Target 2	Target 3
Set 1	Ni	Al	
Set 2	Ni-10wt%Cr	Al	
Set 3	Ni-20wt%Cr	Al	
Set 4	Ni-50wt%Cr	Al	
Set 5	Ni-20wt%Co-40wt%Cr	Al	
Set 6	Ni-40wt%Co-20wt%Cr	Al	
Set 7	Ni-10wt%Cr	Ni-50wt%Cr	Al

Table 4.6 Targets used to deposit NiAl, NiCrAl and NiCoCrAl coatings using co-sputtering.

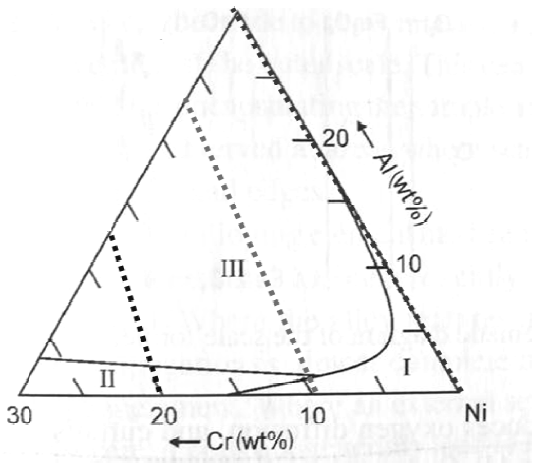

Figure 4.8 Composition lines of deposit superimposed on Ni-Cr-Al ternary oxidation diagram [12, 40, 63].

The addition of Co, with the use of the Ni-20wt%Co-40wt%Cr or Ni-40wt%Co-20wt%Cr targets, was intended to extend these studies to quaternary systems in order to deposit coatings with compositions closer to commercial MCrAlYs.

4.2.5 Sample holders

In this combinatorial study, 150 samples with varying compositions were produced by magnetron sputtering. They were produced in batches of 20 to 40, with the substrates arranged between two sputtering targets of different compositions, to produce a range of BC compositions. Specially designed sample holders, shown in Figures 4.9 and 4.10, allowed precise substrate location. This figure also shows the sample labeling scheme used in this study.

4.2.6 Calibration

Several deposition runs were carried out on glass slides instead of sapphire discs in order to find the best parameters to give a large range of coating compositions, as well as the best deposition rates. It was not possible to deposit very thick films of the Ni-Al alloys using magnetron sputtering because the paramagnetic nature of Ni reduced the Ni deposition rate. To achieve deposition, the chamber was pumped to a vacuum of 23 mTorr under the inert Ar gas. A DC plasma was used with plasma densities of 0.8 x 10^4 - 1.7 x 10^4 W/m^2 (details in Table 4.7). Once, the best deposition parameters were found, sapphire discs were used. Energy dispersive X-ray (EDX) analysis was used to characterize the exact composition of each sample prior to oxidation. Compositions are plotted for each set of experiment in Figures 4.11 to 4.15. The compositions of the samples used for exposure can be found in Tables from Chapters VIII and IX.

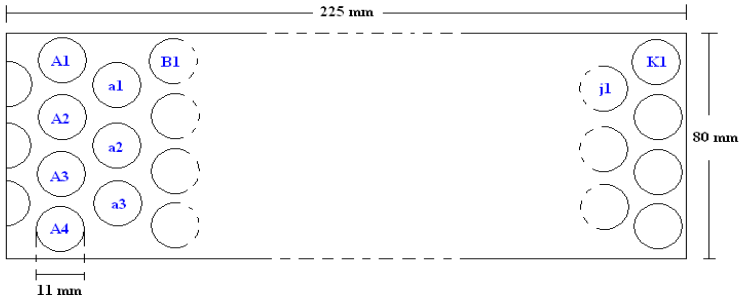

Figure 4.9 Location of samples on the sample holder used for 2 target co-sputtering.

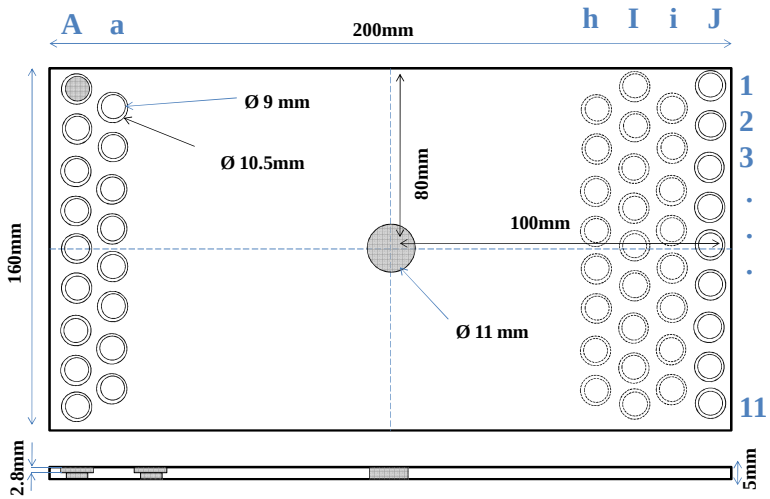

Figure 4.10 Location of samples on the sample holder used for 3 target co-sputtering.

Set	Target 1	Power density (W/m^2)	Target 2	Power density (W/m^2)	Target 3	Power density (W/m^2)
1	Ni	1.7×10^4	Al	0.5×10^4		
2	Ni-10wt%Cr	1.4×10^4	Al	1.1×10^4		
3	Ni-20wt%Cr	1.4×10^4	Al	1.1×10^4		
4	Ni-50wt%Cr	0.9×10^4	Al	1.1×10^4		
5	Ni-20wt%Co-40wt%Cr	1.4×10^4	Al	0.8×10^4		
6	Ni-40wt%Co-20wt%Cr	1.1×10^4	Al	1.1×10^4		
7	Ni-10wt%Cr	5.5×10^3	Ni-50wt%Cr	10×10^4	Al	1.4×10^4

Table 4.7 Process conditions used to deposit Ni-Al, Ni-Cr-Al and Ni-Co-Cr-Al coatings using 2 and 3 targets co-sputtering (chamber pressure 23 mTorr and 10mTorr respectively).

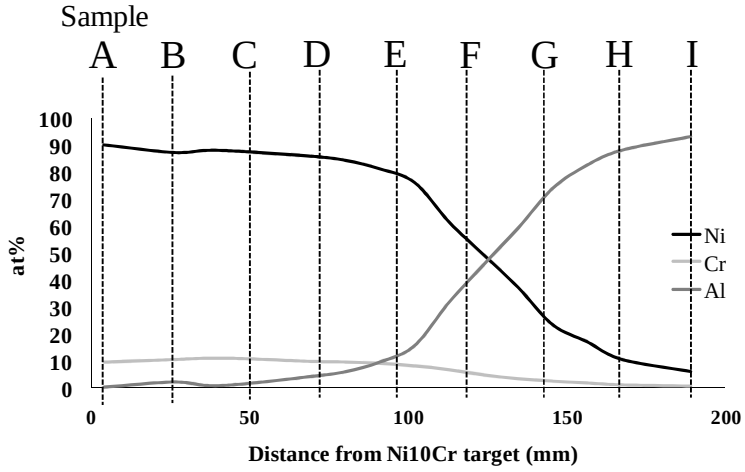

Figure 4.11 Compositions along the sample holder for 2 target co-sputtering (Ni-10wt%Cr+Al).

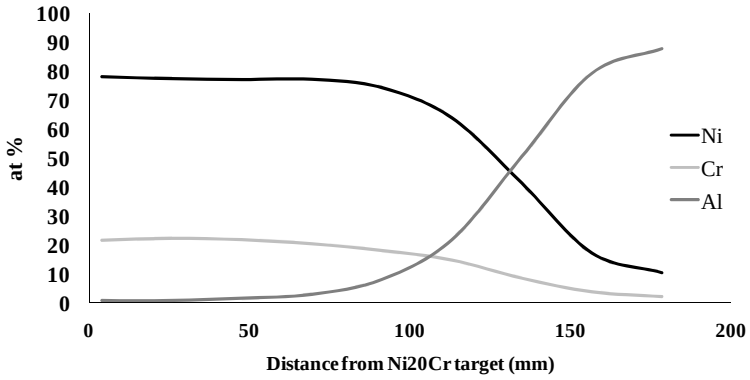

Figure 4.12 Compositions along the sample holder for 2 target co-sputtering (Ni-20wt%Cr+Al).

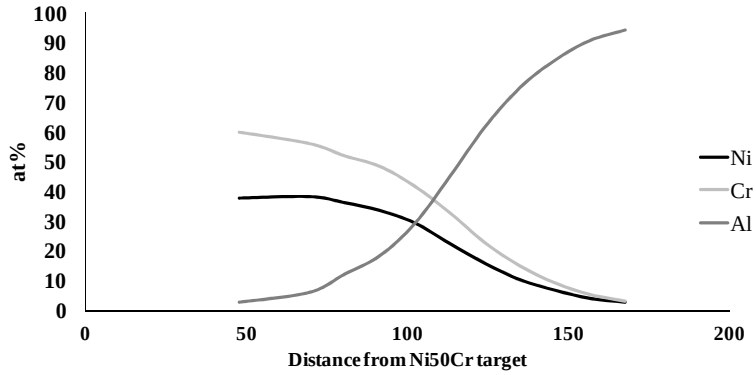

Figure 4.13 Compositions along the sample holder for 2 target co-sputtering (Ni-50wt%Cr+Al).

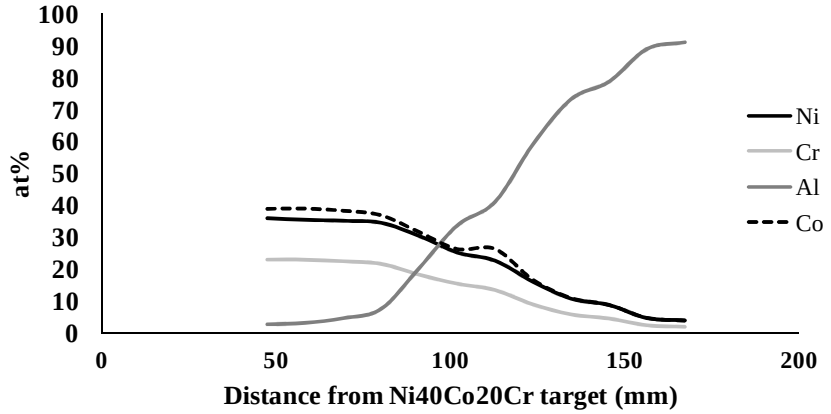

Figure 4.14 Compositions along the sample holder for 2 target co-sputtering (Ni-40wt%Co-20wt%Cr+Al).

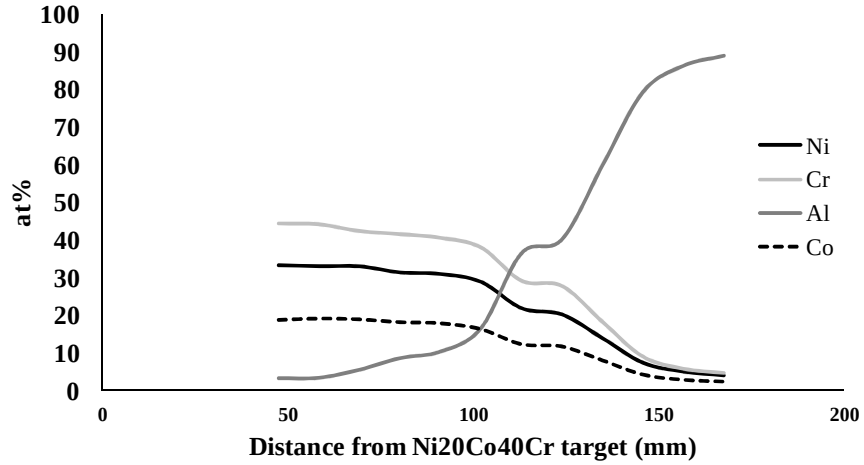

Figure 4.15 Compositions along the sample holder for 2 target co-sputtering (Ni-20wt%Co-40wt%Cr+Al).

The X-axis of the graphs in Figures 4.11 to 4.15 represent the locations of the samples between the targets; 0 being under the Ni-XCowt%-Ywt%Cr target (X= 0, 20 or 40 and Y=10, 20 or 40) and 200 being under the Al target. For example in Figure 4.11, sample A has got the following composition: ~90 at% Ni, ~10 at% Cr and ~0 at% Al. Similarly, sample F would have the following composition: ~ 55 at% Ni, ~ 5 at% Cr

and 45 at% Al. The variation of composition vertically along the sample holder was found to be negligible.

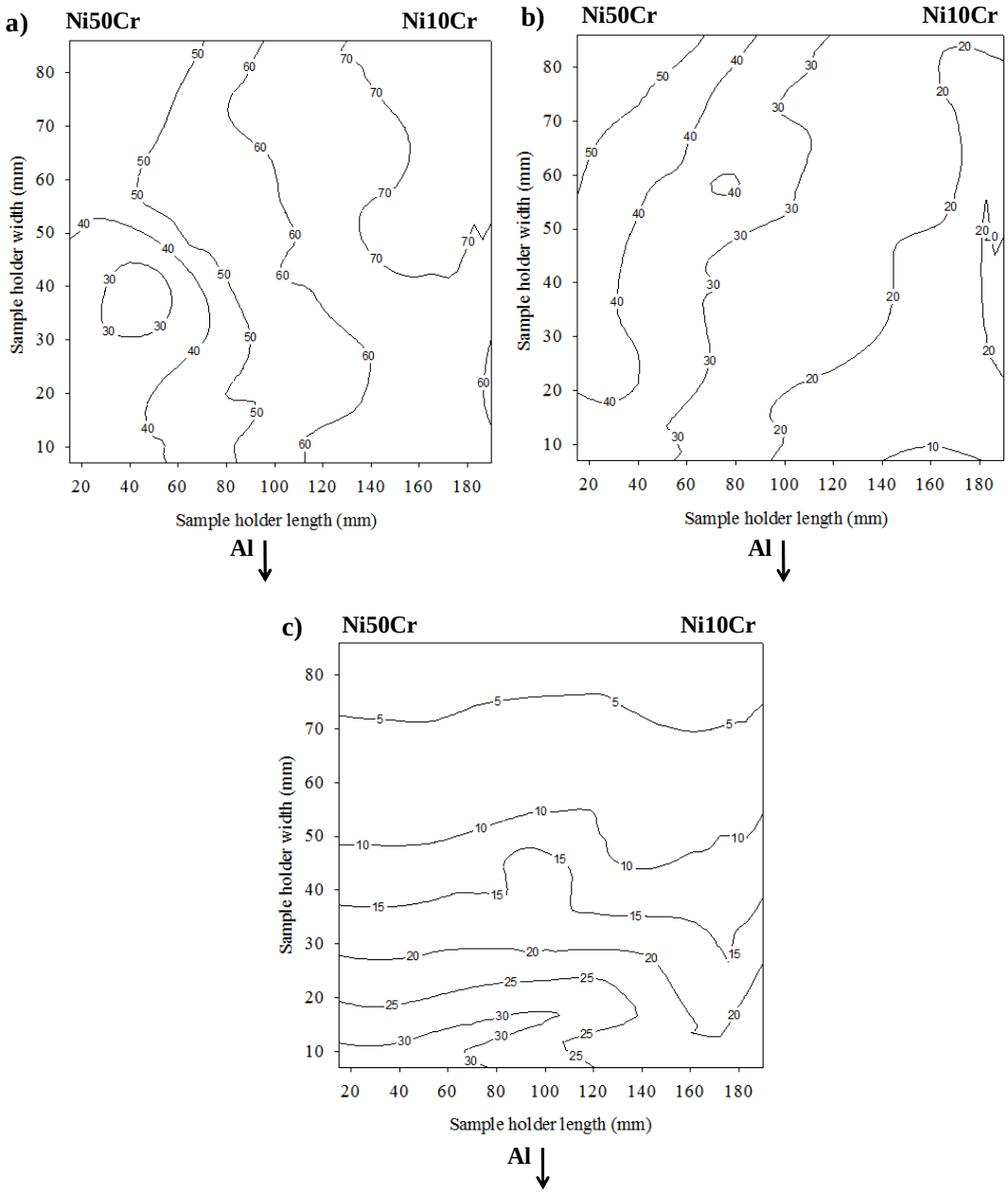

Figure 4.16 Atomic Percentage of Ni (a), Cr (b) and Al (c) along the sample holder for 3 targets co-sputtering (Ni-wt%10Cr+Ni-50wt%Cr+Al). The top left corner of the sample holder is located above the Ni-50wt%Cr target and the top right corner above the Ni-wt%10Cr target.

Figure 4.16 shows the gradient of elemental composition along the sample holder, measured with EDX analysis of the samples' surface, used during the 3 target co-sputtering deposition of coatings (with the Ni-10wt%Cr, Ni-50wt%Cr and Al targets).

4.2.7 Oxidation of coated sapphire discs

Sample metrology showed that the magnetron co-sputtering method successfully deposited 30 to 50 µm thick coatings depending on substrate placement. The coatings were then isothermally oxidised in air for 500 hours in furnaces set at 900 and 950 °C. All samples were weighed every 20 hours, which allowed the evaluation of the oxidation kinetics. Energy dispersive X-ray (EDX) analysis was used to characterise the composition of the oxides post-exposure. Additionally, X-ray diffraction (XRD) was used to identify the oxides formed during these exposures. The selective growth of protective Cr_2O_3 or Al_2O_3 oxides, or less protective NiO, CoO and mixed oxides, was observed depending on the initial coating composition.

4.3 Analytical and observation tools

4.3.1 Scanning Electron Microscopy (SEM)

SEM was extensively used in this study because sample preparation is fast and high magnifications allow the observation of features present in TBC systems which can measure less than a micron.

Two different kind of SEM were used during the project: first by a SFEG-SEM (FEG stands for Field Emission Gun): FEI XL30 SFEG. This alternative to a classical SEM with a W filament source of electrons, gives a much narrower electron beam allowing high resolution pictures, up to 300,000X. Secondly an ESEM (Environmental Scanning Electron Microscope): FEI KL30 ESEM. This SEM uses a classical source of electrons, but the chamber can be doped with water vapour, which allows observations to be carried out in a relatively low vacuum. It also makes it possible to image non-conductive materials, as water vapour prevents electron charge build up; this was used for surface observations on oxidised samples, which could not be coated with a conductive carbon or gold/palladium coating. However the resolution of this SEM is lower than the SFEG's.

Energy Dispersive X-ray Analysis (EDX) was extensively used to identify and quantify the chemical species in the substrate, coatings or oxide scales. The X-Ray detector is an addition to the SEM chamber. The atoms of the material react to the electron irradiation caused by the X-Ray bombardment by releasing a photon during the energy relaxation of electrons from the electronic cloud surrounding the atom core. The energy of the dispersed photon is equal to the difference in energy level between the excited and the standard status of the concerned electron, which is typical for each element of the periodic table [125]. The size of the region observed using the EDX is $1\mu m^2$ for the SEM whereas spatial resolution is $0.2nm^2$ in TEM.

Modified aerofoil-shaped samples were mounted in hard resin (filled with glass beads (ballotini)) in a specially design mould (Appendix A), cut in half, polished and then coated with a thin coating of Au and Pd before being put in the SFEG-SEM chamber. Observations were usually carried using settings of 20 KV and a spot size of

5. Single point quantitative analysis, concentration line profiles (number of points per line depending on the area to characterise) and mapping were carried out using EDX.

NiCoCrAl coatings deposited on sapphire discs were observed under the ESEM and their compositions characterised using single point EDX quantitative analysis. Since they are metallic coatings, they did not require the application of any conducting film. Cross-sections were mounted in Durocit resin and polished.

4.3.2 X-Ray Diffraction (XRD)

XRD was used as an analytical tool. XRD of coated sapphire discs, as deposited, or oxidised were carried out in order to make a qualitative analysis of the compounds or oxides in the system. The diffractometer was mainly used with a typical $\theta/2\theta$ layout in vertical diffractometer mode. The XRD system is a Siemens D5005 loaded with a Cu K-alpha X-ray tube [125]. 2-2-1 slits were used during this project.

4.3.3 Focussed ion beam (FIB)

FIB system use a finely focused beam of gallium ions that can be operated at low beam currents for imaging or high beam currents for site specific sputtering or milling (unlike SEMs that use a beam of electrons). At low current, typically between 1 and 70pA, FIB is used for imaging, as the sputtering yield is very low for these values. Above 70pA, the beam is energetic enough to noticeably mill the substrate. Increasing the current transfers more energy to the surface: increasing the current reduces the milling time. However, it increases the thermal affected zone around the milled section.

The FIB facility at Cranfield is a single beam FIB: more recent systems have a dual beam with integrated SEM in the chamber (available at Bristol University (FEI Helios) and used for this thesis as well). This allows the user to observe the sample while it is sputter etched by the ion beam. This feature is particularly useful for transmission electronic microscope (TEM) sample manufacturing. On Cranfield apparatus, the operator works "blindly": imaging of the sample at low current, then programming the milling pattern, and closing the detector when actually milling (the high contrast created by high energy milling would burst the single secondary electron detector). [125]

FIB was used in Bristol University to prepare samples for TEM analysis. They were lifted-out from the cross-sections through the exposed and mounted modified-aerofoil shaped samples in order to observe the TC/TGO and TGO/BC interfaces. The manufacture of the TEM samples was very delicate because it had to mill 3 different types of materials (YSZ, Al_2O_3 and MCrAlY). Pt was deposited on the area of interest (20 x 1 um). High beam current was used to mill and extract the slice (6.5nA operating at 30kV). When the lift-out section was 1-2 µm, the current was lowered to prevent cracking of the sample in the YSZ layer or complete disappearance of the sample (because of the faster milling rate of the metal layer) (Figure 4.17(a)). The sample is tilted in order to cut the section so it is almost free standing, it is attached to a microscopic needle with platinum in order to be lifted out (Figure 4.17(b)) and welded on a Cu grid. It is then further thinned down (0.28 nA, 93pA and 48pA) until it reaches a thickness of 100 nm. The FIB lift-out is then attached in-situ to a sample holder in order to be transported to the TEM.

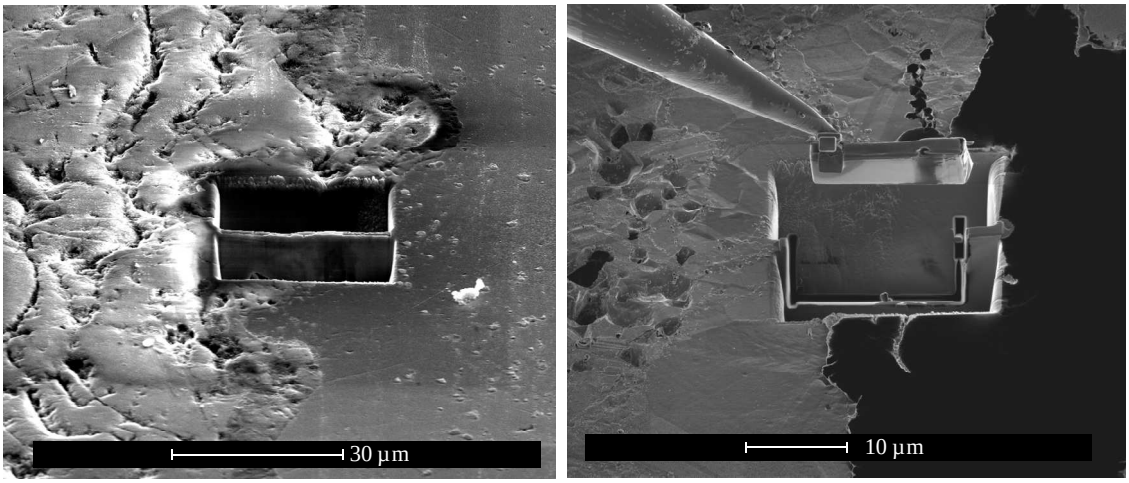

Figure 4.17 FIB images of the preparation of a lift-out sample. (a) the thin section at the TC/TGO and TGO/BC interface being thinned down and (b) the sample being lifted-out.

4.3.4Transmission electronic microscopy (TEM)

TEM is used for high resolution imaging, and can go up to a magnification of 1000kX in transmission mode with the facility used. TEM was not extensively used in this study, and observations were carried out with a specialised operator. The machine used was a Philips CM20 transmission Electron Microscopecouple with an Oxford Instruments INCA X-ray Microanalysis system (EDX).

The samples lift-out using the FIB were observed using the TEM and had to be extremely thin. For observations, the beam of high energy electrons was driven through a series of electromagnetic lenses, through the substrate and then focused onto a screen. The acceleration voltage was 200kV.

PART I - EFFECT OF THE SAMPLE GEOMETRY ON THE APS/TBC SYSTEM'S OXIDATION BEHAVIOUR

The effect of aerofoil geometry on the behaviour of TBC systems at the microscopic scale is of interest due to its possible effect on their life. Coating detachments have been noted on blades' leading edges, pressure sides and trailing edges [100]. To account for this DeMasi and Sheffler [103] stated that normal stresses could be introduced to a curved surface's coating by the tangential compressive stresses present and these could result in ceramic spallation.

The oxidative degradation mechanisms of an APS/TBC coated superalloy and the effect the aerofoil shape had on its behaviour has been investigated. Details of the TGO's microstructural evolution, the BC and the interdiffusion between the BC and

substrate were characterized (Chapter V). In order to detect and track the spread of cracks beneath the TBCs before spalling, flash thermography, a novel non-destructive examination (NDE) technique was used (Chapter VI). The following results describe the experimentation done on a range of modified aerofoil-shaped samples, coated with a HVOF sprayed BC plus an APS/TBC and tested under conditions appropriate for an industrial gas turbine TBC system (exposure in the temperature range of 900 to 1000 ºC). While initially focussing on the effect of curvature, the investigations expanded to consider the effect of BC and TC thicknesses and interface roughnesses on the diffusion behaviour of the different elements present in the coating system. An attempt to explain the intricate influence of curvature, thickness and roughness of both BC and TC is presented in this chapter (Chapter VII).

To begin with, the damage evolution on the modified aerofoil-shaped samples is presented along with the results of the pulsed flash thermography experiments. Then, after explaining the evolution of the BC microstructure with exposure time and temperature, the effect of curvature will be compared to BC behaviour. Part of the following discussion is aimed at explaining why the geometry affects the BC and how it modifies the lifetime of the whole system, by focussing on the TGO growth (protective Al_2O_3 and less-protective spinels/mixed oxides) and Al diffusion as well as the TC microstructure. Some of the work in this chapter has been presented in a published paper (Materials at High Temperatures) [126].

CHAPTER V- THE INFLUENCE OF CURVATURE ON FAILURE, DIFFUSION AND OXIDE GROWTH MECHANISMS

5.1 The influence of geometry on the failure of modified aerofoil-shaped samples

The effect of the modified aerofoil-shaped samples' geometry on the behaviour of the APS/TBC system subject to oxidation at 900-1000 °C was investigated. The initiation and propagation of cracks on samples were observed using NDE methods (i.e. optical microscopy and pulsed flash thermography) and destructive methods (i.e. SEM). Coating characteristics such as the BC, TGO and spinels were compared as a function of curvature. The different features of the modified aerofoil-shaped samples are described using the nomenclature given in Figure 4.1, or in a reference sheet in Appendix I. In figures describing the samples, the concave side refers to the pressure side of the blade and convex to the suction side.

5.1.1 Evolution of damage on the oxidised modified aerofoil-shaped samples

Important damage occurred on samples oxidised above 950 °C and was characterised by the appearance of cracks initiating at the edges of the samples. Figure 5.1 depicts the evolution of cracks on sample 81-BSYA-15, oxidised at 950 °C for up to 5000 hours. Cracks were first spotted on this sample after 1350 hours (Figure 5.1(a)) and were located on the leading edge of the blade (locations A and B). After 4000 hours, these cracks had propagated toward the suction side of the blade (Figure 5.1(b)). Finally after 5000 hours, damage appeared at location D and E of the sample and after a day out of the furnace, critical delamination of the

ceramic TC happened on the blade's suction side. Damage was located at the same location on the sample oxidised at 1000 °C, as shown in Figure 5.2. In these pictures of sample 81-BSYA-23, the TBC coating gradually delaminated at location D and E, between 1350 and 1500 hours.

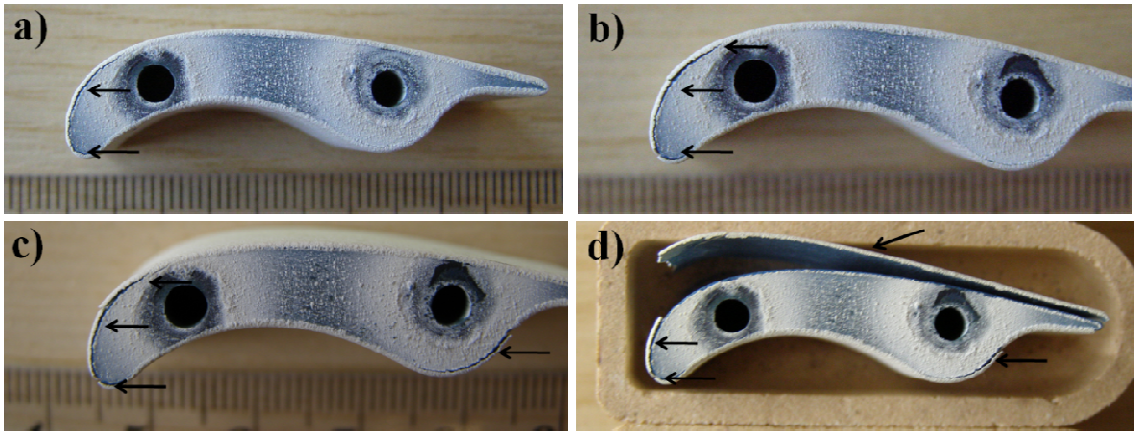

Figure 5.1 Photographs of sample 81-BSYA-15 oxidised at 950 °C for (a) 3750, (b) 4000, and (c) (d) 5000 hours. Black arrows point to coating delamination.

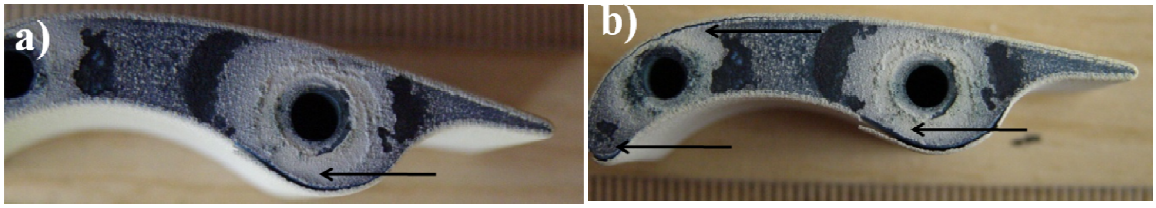

Figure 5.2 Photographs of sample 81-BSYA-23 oxidised at 1000 °C for (a) 1350, and (b) 1500 hours. Black arrows point to coating delamination.

Such damage could be seen when the cracks propagated greatly and samples approached the end of their life. Ordinary characterisation methods do not enable the extent of failure propagation to be checked without destroying the sample. This is why a novel NDE technique (called pulse flash thermography) was used to observe the extent of cracking beneath the ceramic TC.

5.1.2 Pulsed flash thermography of the modified aerofoil-shaped samples

Samples were regularly taken to NPL to observe internal damage using pulsed flash thermography. As a result of the alteration of heat conduction with cracks present beneath the ceramic, the IR camera could detect damage. On the thermographs, flaws appeared with a different contrast to the rest of the sample, making identification easy.

The damage evolution on modified aerofoil-shaped samples oxidised at 1000°C is shown in Figures 5.3 to 5.5. The light grey colour represents cracking in the coating. The dark grey colour represents coating delamination. Samples were observed after 1050, 1350 and 1500 hours oxidation. Looking at Figure 5.3, after 1050 hours of oxidation of sample 81-BSYA-17, a small crack appeared at B (position given in Figure 4.1 and Appendix I) on the right hand side of the sample (Figure 5.3(a)). 300 hours later, the crack in B propagated and another initiated in A (Figure 5.3(b)). After 1500 hours of oxidation, the crack starting at A and B joined. The sample also began to be damaged at D and E (Figure 5.3(c)).

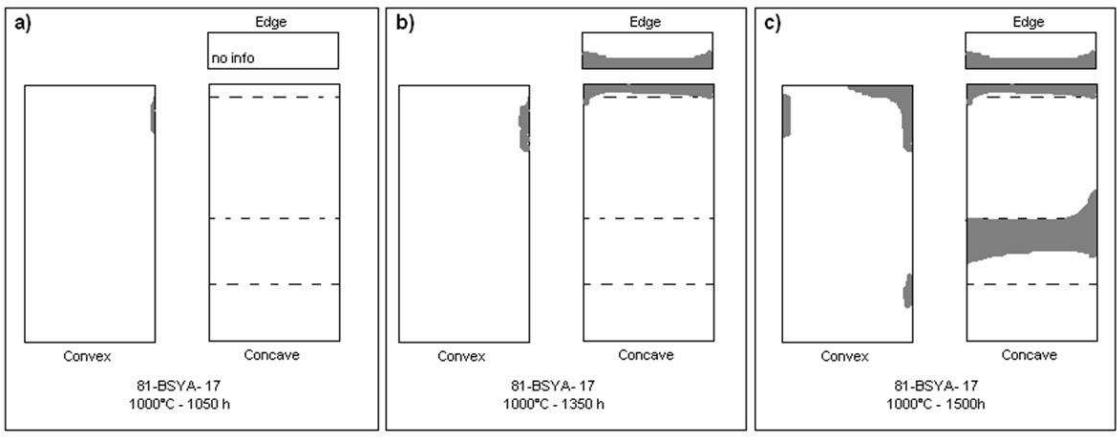

Figure 5.3 Schematic representation of the damage evolution in sample 81-BSYA-17 oxidised at 1000 °C. Sample was oxidised for (a) 1050; (b) 1350; and (c) 1500 hours. Damage beneath the ceramic TC appears in grey.

Unlike sample 81-BSYA-17, sample 81-BSYA-19 (Figure 5.4) showed damage in D and E after 1050 hours of oxidation while no damage could be observed in A or B (Figure 5.4(a)). After further oxidation, cracks on the "bump" propagated and some appeared in A, as for the other sample (Figure 5.4(b)). Finally after 1500 hours, large cracking occurred at region F on the sample's convex (suction) side. The damage at D and A did not seem to propagate. New cracks appeared in region B (Figure 5.4(c)). It was considered that sample 81-BSYA-17 had failed after 1500 hours of oxidation since damage covered more than 20% of its surface.

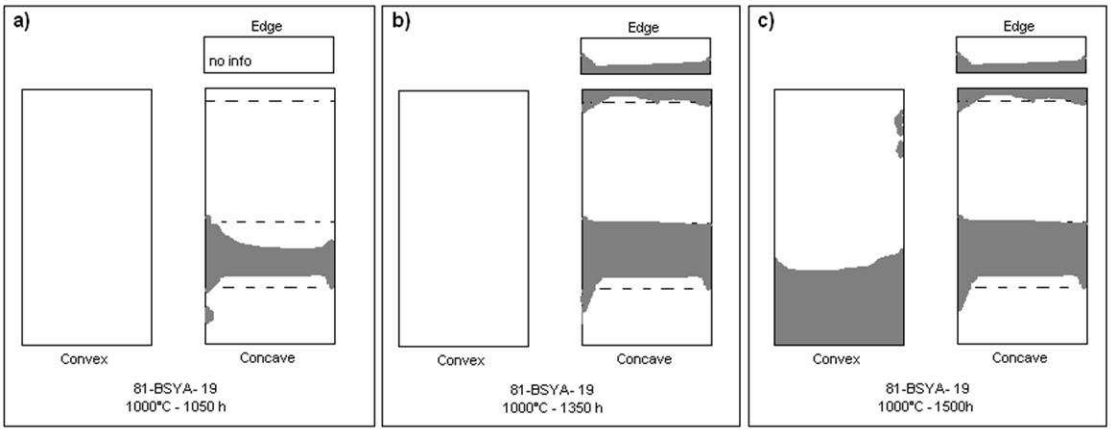

Figure 5.4 Schematic representation of the damage evolution in sample 81-BSYA-19 oxidised at 1000 °C. Sample was for oxidised for (a) 1050; (b) 1350 and (c) 1500 hours. Damage beneath the ceramic TC appears in grey.

Sample 81-BSYA-23 was more damaged than the two other samples when it was first analysed after 1050 hours. In Figure 5.5(a), damage could be seen in region B on both edges of the sample. On the left hand side, the cracks extended towards A. Like the other samples, damage was present in regions D and E. After 1350 hours, in Figure 5.5(b), propagation occurred through regions A and B and started on the suction side following the edges. Cracks were also entirely covering regions D and E. After 1500 hours, parts of the coatings detached from the substrate in D, E and A (as represented by

dark grey colour in Figure 5.5(c)). Cracks propagated on the suction side of the sample and in region F.

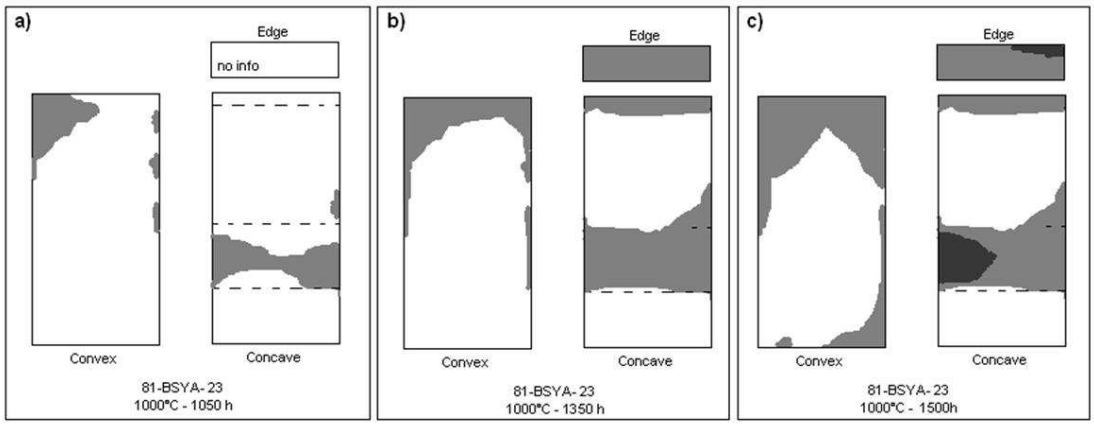

Figure 5.5 Schematic representation of the damage evolution in sample 81-BSYA-23 oxidised at 1000 °C. Sample was oxidised for (a) 1050; (b) 1350; and (c) 1500 hours. Damage beneath the ceramic TC appears in grey. Delamination of the ceramic TC appears in dark grey.

The damage evolution in samples oxidised at 975 °C is shown in Figures 5.6 and 5.7. For sample 81-BSYA-36, after 1950 hours of exposure, the first signs of cracking could be seen in locations A and B (Figure 5.6(a)). In location A, the crack propagated across the leading edge of the sample. Damage could be also observed on the pressure side of the blade in region a. After further oxidation, it did not propagate and was therefore considered not to be caused by high temperature exposure. The cracks propagated greatly between 1950 and 2850 hours and covered most of the suction side of the sample as well as location D, E and c on the pressure side (Figure 5.6(b)). Finally after 3000 hours, when the sample exposure was terminated, the damage propagated on the bump and initiated at location F (Figure 5.6(c)).

In sample 81-BSYA-37 (also oxidised at 975 °C), cracks similarly propagated on the convex side of the blade and on the bump (Figure 5.7). After 2850 hours, damage could be spotted in location F (Figure 5.7(b)). The extent of oxidation of this sample

after 2700 hours, was much more significant than sample 81-BSYA-36 since none of the convex side of the sample was free of cracking (Figure 5.7(c)).

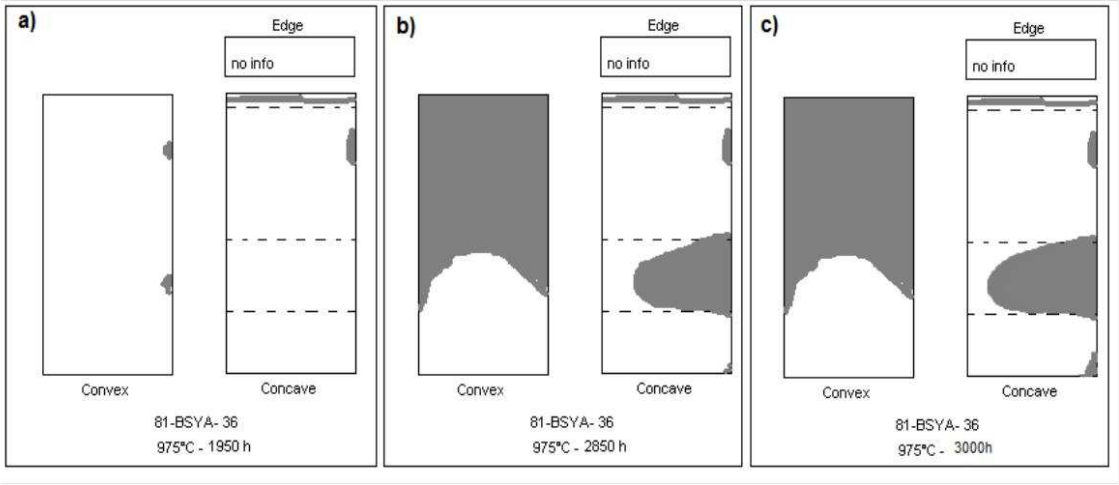

Figure 5.6 Schematic representation of the damage evolution in sample 81-BSYA-36 oxidised at 975 °C. Sample was oxidised for (a) 1950; (b) 2850; and (c) 3000 hours. Damage beneath the ceramic TC appears in grey.

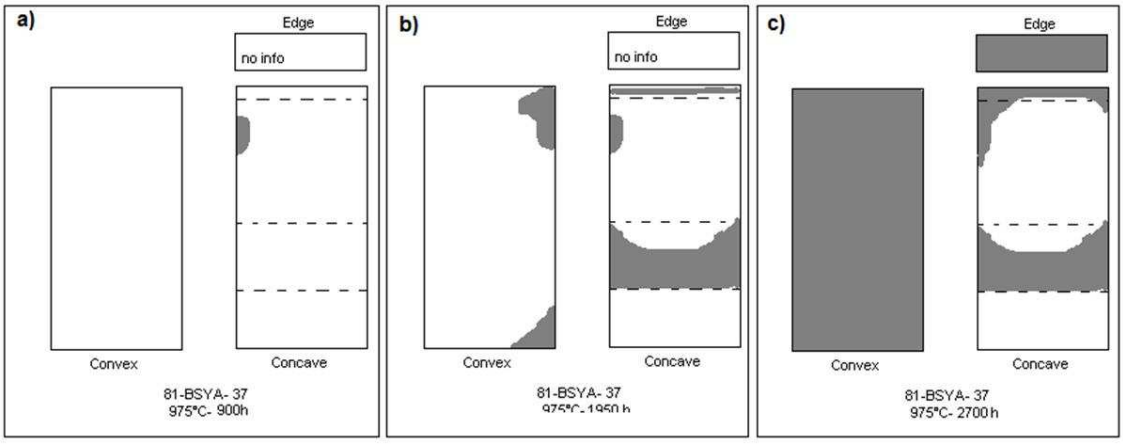

Figure 5.7 Schematic representation of the damage evolution in sample 81-BSYA-37 oxidised at 975 °C. Sample was oxidised for (a) 900; (b) 1950; and (c) 2700 hours. Damage beneath the ceramic TC appears in grey.

The damage evolution on modified aerofoil-shaped samples oxidised at 950 °C are shown in Figures 5.8 and 5.9. Samples were observed after 4500 and 4760 hours of oxidation. Figure 5.8 describes the evolution of damage in 81-BSYA-10. After 4760

hours, damage had initiated in region B on the right hand edge of the sample (Figure 5.8(b)). This was similar to sample 81-BSYA-17 in Figure 5.3 oxidised at 1000°C. No other damage could be seen in this sample.

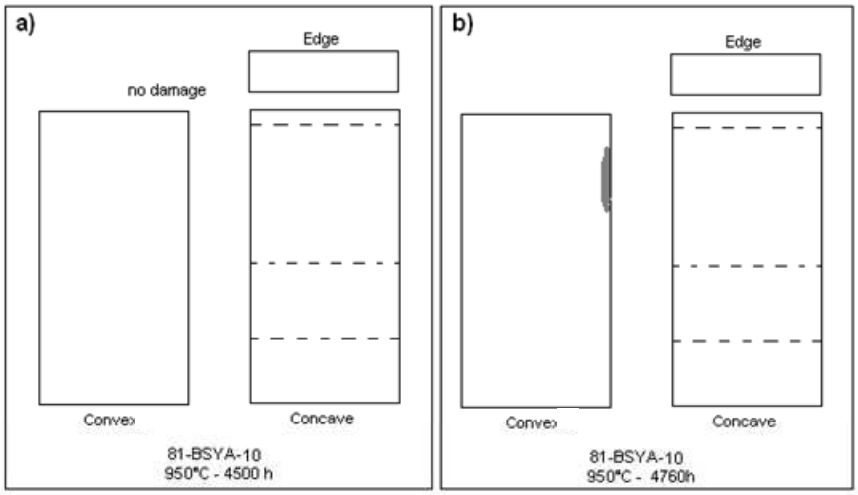

Figure 5.8 Schematic representation of the damage evolution in sample 81-BSYA-10 oxidised at 950 °C. Sample was oxidised for (a) 4500; and (b) 4760 hours. Damage beneath the ceramic TC appears in grey.

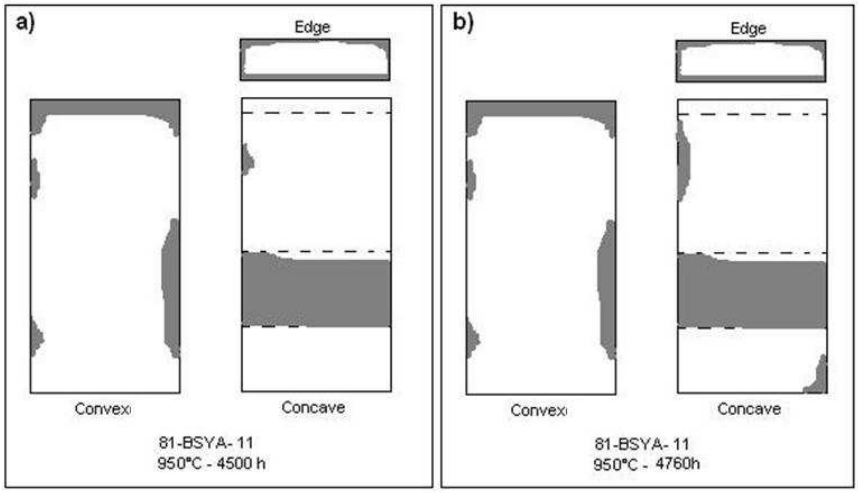

Figure 5.9 Schematic representation of the damage evolution in sample 81-BSYA-11 oxidised at 950 °C. Sample was oxidised for (a) 4500; and (b) 4760 hours. Damage beneath the ceramic TC appears in grey.

Much more cracking was recorded on sample 81-BSYA-11 exposed at 950 °C (Figure 5.9). After 4500 hours oxidation, damage was observed at regions A, D and E. There were also cracks on the right hand side of region C. Cracks were always located on the edges of the sample (Figure 5.9(a)). After another cycle, these cracks had not spread much but new ones had appeared in region F (Figure 5.9(b)).

The evolution of cracks at 950 °C was slower than at 975 and 1000°C. Cracks usually initiated in regions A and B first, then in D and E.

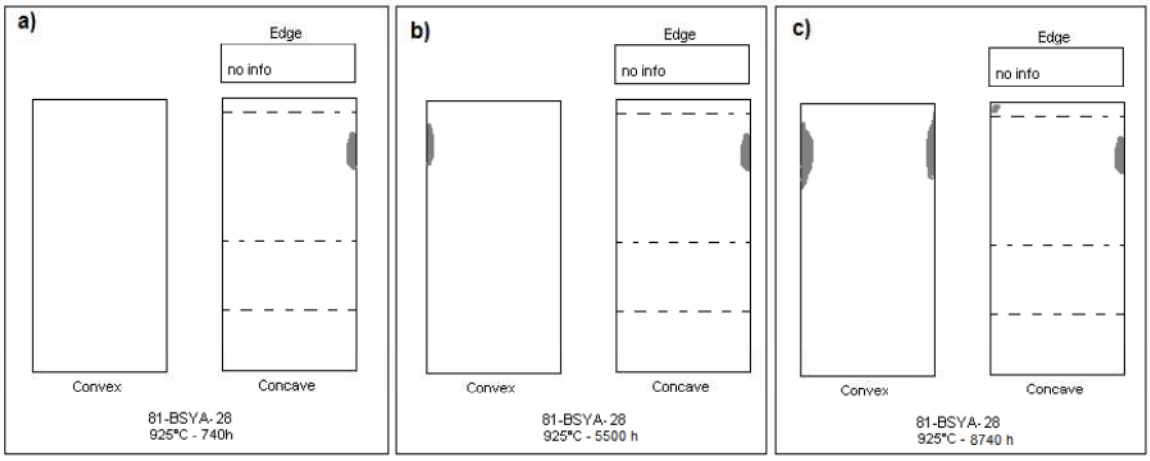

Figure 5.10 Schematic representation of the damage evolution in sample 81-BSYA-28 oxidised at 925 °C. Sample was oxidised for (a) 740; (b) 5500; and (c) 8740 hours. Damage beneath the ceramic TC appears in grey.

At 925°C samples, against expectations, some small damage could be observed on the concave side of the blade at region a after 740 hours of oxidation (Figure 5.10(a)). After further oxidation, this damage did not propagate and was therefore considered not to be high temperature exposure/cycling induced cracking. As for a similar feature observed at 975 °C, it was supposed to be damage caused during the manufacturing of the sample. The first signs of exposure induced cracking appeared after 5500 hours of exposure and were located on the left hand edge at location B (Figure 5.10(b)). After 8740 hours, this crack propagated and another one appeared on

the right hand edge of the sample at location B (Figure 5.10(c)). After 18,000h of oxidation, no damage could be seen on samples oxidised at 900 °C.

The presence of cracks identified by flash thermography was partly verified by optical microscopy on the edges of samples, as shown in Figure 5.11 which shows microcracks at location B and location E of the sample. Cracking away from the edges was later confirmed by the observation of polished cross-sections through the samples.

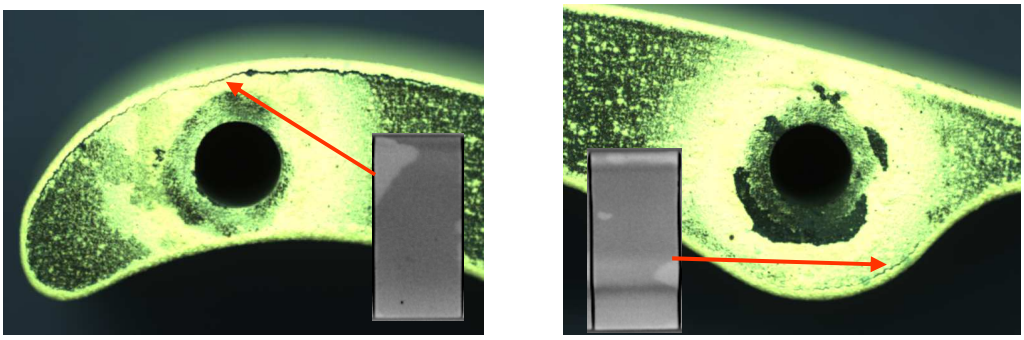

Figure 5.11 Optical microscope image of cracks in a modified aerofoil shaped sample exposed at 950 °C for 3000 hours with flash thermography data.

5.1.3 Observations of crack development using SEM

A range of crack profiles were observed, around the samples' cross sections using a SEM (Figure 5.12). The coatings' oxidation temperature, exposure time and curvature did not seem to induce a particular pattern of failure. Cracks ran through the TGO (Figure 5.12(a)), at the TGO/BC interface (Figure 5.12(b)) or at the TBC/TGO interface (Figure 5.12(c)) and in some cases cracks ran through spinels (Figure 5.12(e)). When a lot of TGO surface undulation was present, cracks ran through the TBC (Figure 5.12(d)). Echsler et al. [98] observed similar crack profiles. The only apparently consistently observed crack feature influenced by curvature was the vertical cracking through the TC at the trailing edge (Figure 5.12(f)) [126].

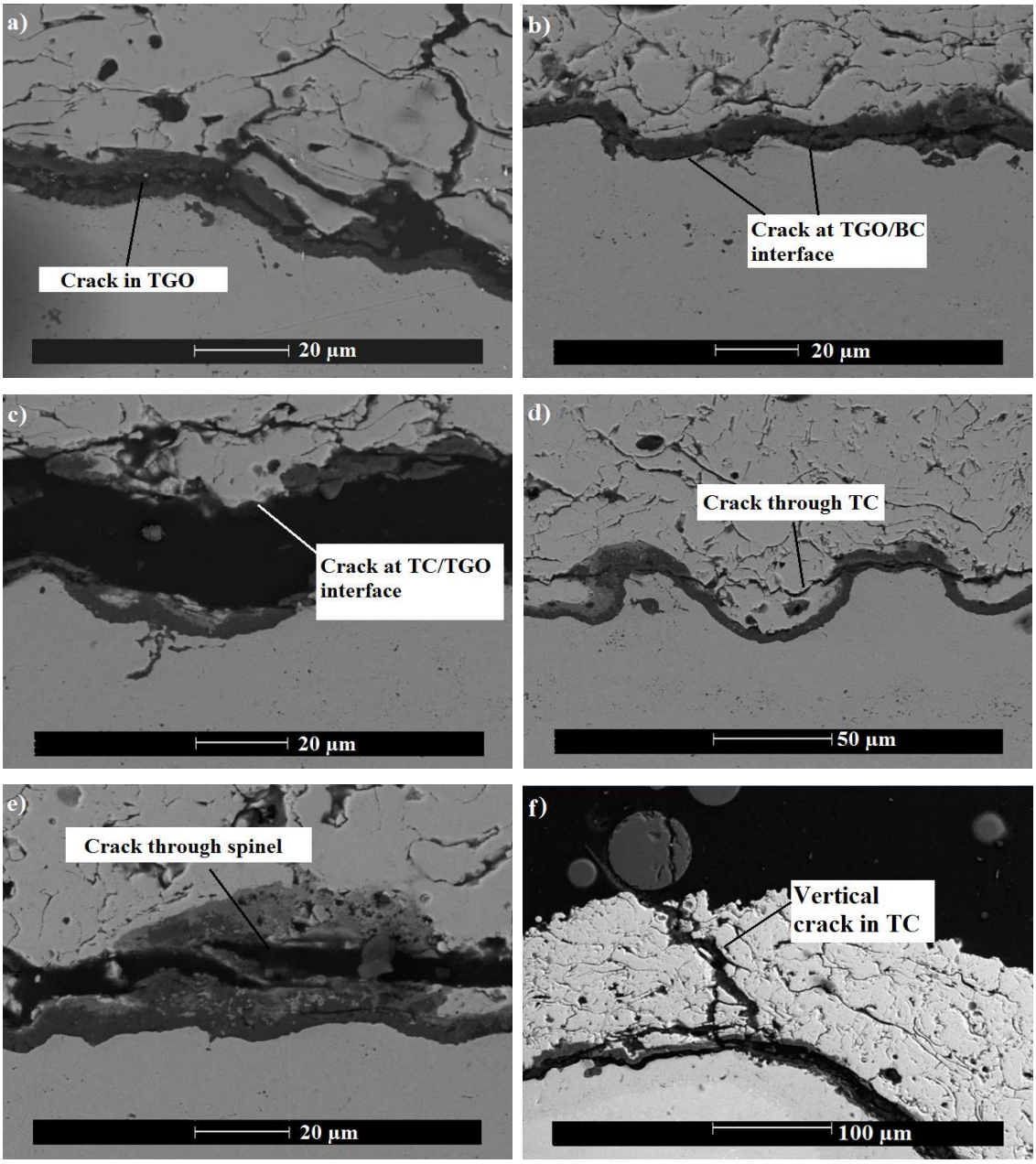

Figure 5.12 SEM image of a crack running (a) through the TGO (b) at the TGO/BC interface (c) at the TGO/TC interface (d) through the TC (e) through spinel and (f) vertically through the TC.

5.1.4 Summary

To summarise, the use of flash thermography showed that at high temperatures cracks initiated first at the leading edge and at the "bump" (region D) and then

propagated along the edges and across the samples. Damage also propagated at the trailing edge and finally on the flat convex surface of the sample (Figures 5.13 and 5.14). This indicates that the sample shape has an influence on crack initiation and propagation. The amount of damage varied between samples with the same exposure times/temperatures [126].

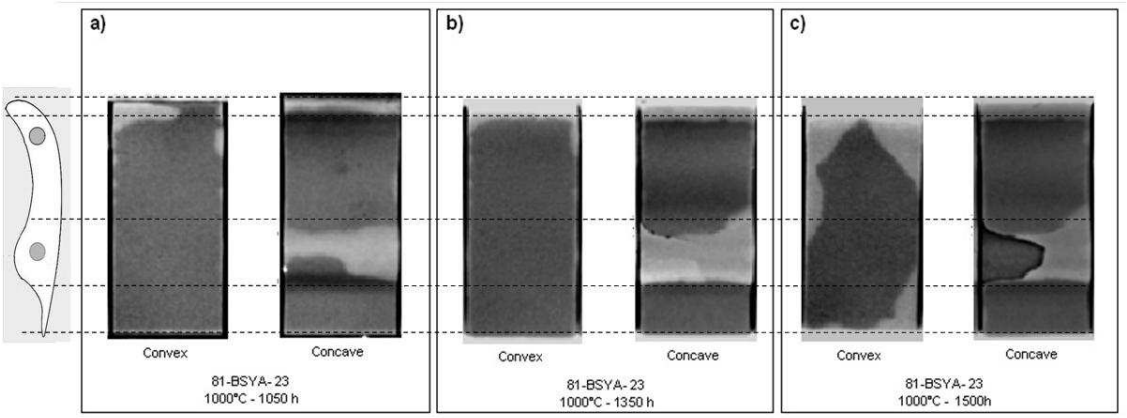

Figure 5.13 Flash thermography data showing damage evolution in a sample isothermally oxidised at 1000 °C for exposure times of (a) 1050; (b) 1350; and (c) 1500 hours. Light contrast indicates sub-surface damage.

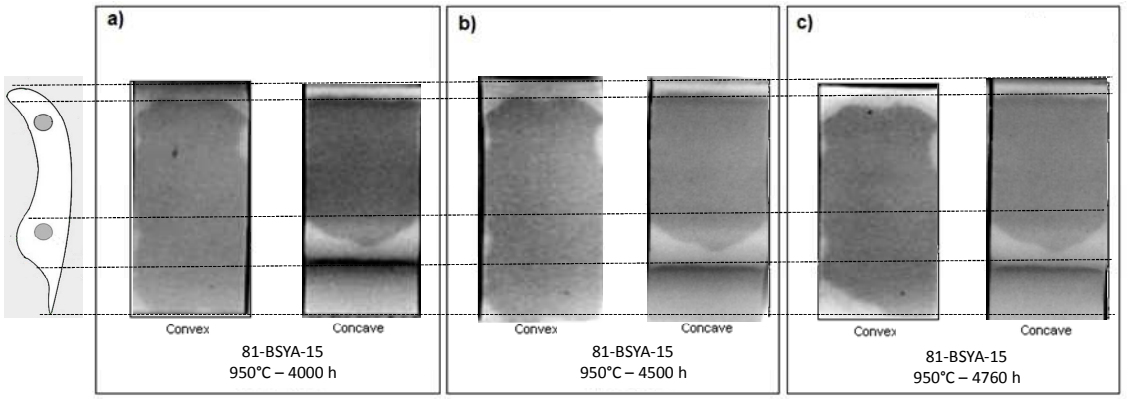

Figure 5.14 Flash thermography data showing damage evolution in a sample isothermally oxidised at 950 °C for exposure times of (a) 4000; (b) 4500; and (c) 4760 hours. Light contrast indicates sub-surface damage.

5.2 Influence of the curvature on the evolution of the BC microstructure

5.2.1 Understanding the effect of exposure time on the oxidation behaviour of an APS/TBC system

All TBC coating systems exposed to high temperature have a common oxidation behaviour which is well established in literature (Chapter II). In this section, the basic diffusion/inter-diffusion mechanisms occurring in the modified aerofoil-shaped samples, such as the BC depletion of the β-NiAl phase, the TGO growth and the SRZ formation, are characterised, described and explained. The first stage of observation ensures that samples have behaved as expected from previously reported research carried out on similar materials, in order to allow a comparison of the results. Furthermore, testing the modified aerofoil-shaped samples at a range of temperatures (900-1000 °C) enabled the comparison of oxidation mechanisms under different exposure conditions.

5.2.1.1 Depletion of the β-NiAl phase and the growth of the protective Al_2O_3 layer with exposure

Within the MCrAlY BC, the β-NiAl phase constitutes the Al reservoir which is used to grow the protective Al_2O_3 during exposure at high temperatures [12]. As the TGO thickens, the amount of Al in the BC reduces causing the gradual depletion of the β-phase. Figure 5.15 depicts the evolution of BCs at location C (with this region chosen as an example because of its relatively flat curvature) in samples oxidised at 925 °C for up to 7000 hours. Before exposure, the β-phase grains, in dark grey contrast within the BC (Figure 5.15(a)), were fine and evenly distributed in the layer. At this stage, the TGO was non-existent (or very thin) and the SRZ, which was formed during

manufacturing, smaller than 10 µm. After 100 hours exposure (Figure 5.15(b)), the β-NiAl grains present in the BC increased in size and a zone free of β-phase, of 15 µm thickness at the outer edge of the BC, accompanied by the growth of the TGO layer, in dark grey contrast, at the TC/BC interface. The oxide layer (TGO) at this stage was 1.5 µm thick.

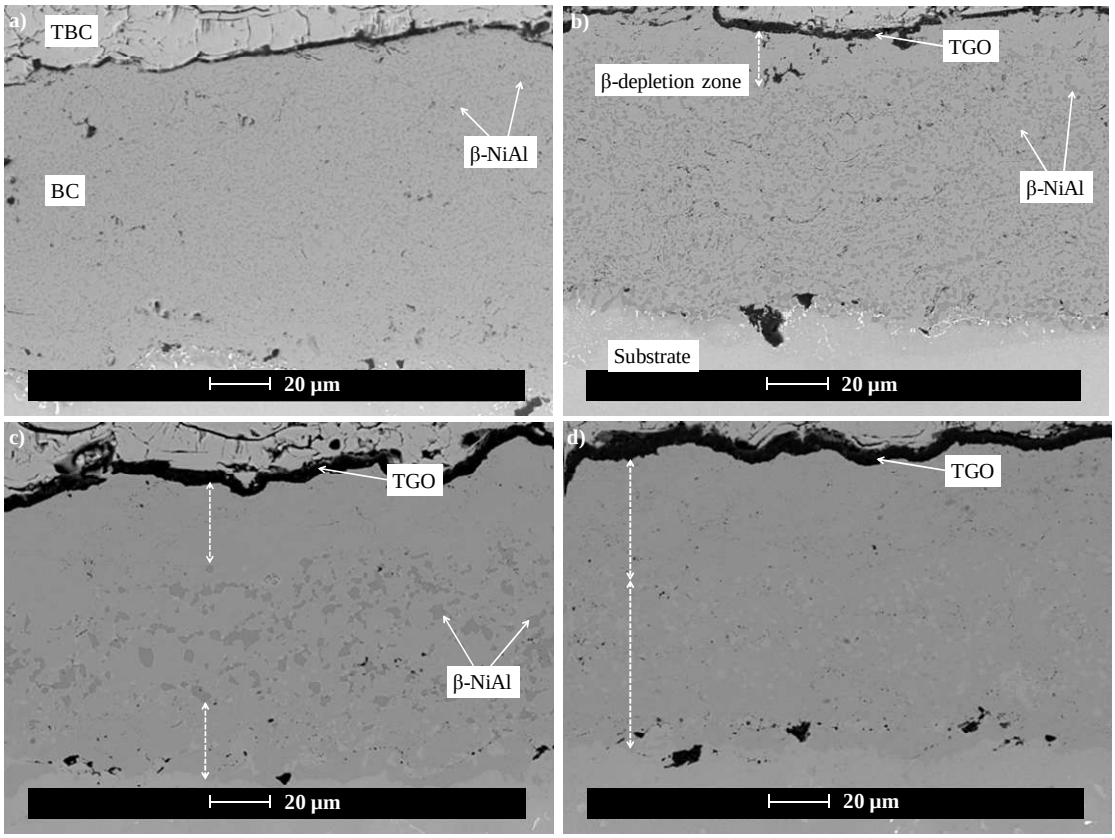

Figure 5.15 Evolution of the APS/TBC system under oxidation at 925 °C. SEM images of the BC and TGO in location C of (a) an as-deposited sample; and samples exposed for (b) 100 hours; (c) 4000 hours; and (d) 7000 hours. Dotted white arrows indicated β-depletion zones.

This β-depleted zone, called the outward depletion zone, has a γ-Ni matrix (confirmed by EDX analysis), and is created by the diffusion of Al from the BC to the TGO. Beneath the BC, the SRZ remained the same size and no inward β-depletion, from the BC to the substrate, could be observed. After 4000 hours (Figure 5.15(c)), β-NiAl grains continued to increase in size and appear more scattered than on as-

deposited coatings. The outward β-depletion zone progressed deeper into the BC, 22 µm thick, as the TGO thickened up to 3.7 µm. Close to the BC/substrate interface, an inward β-depletion zone, characterising the diffusion of Al to the substrate, appeared and measured 35 µm. This zone has a γ-Ni/γ'-Ni_3Al matrix (confirmed by EDX analysis). Finally, after 7000 hours (Figure 5.15(d)), the outward and inward β-depletion zone joined together, leaving the BC totally depleted in β-NiAl. The TGO was 5.3 µm thick.

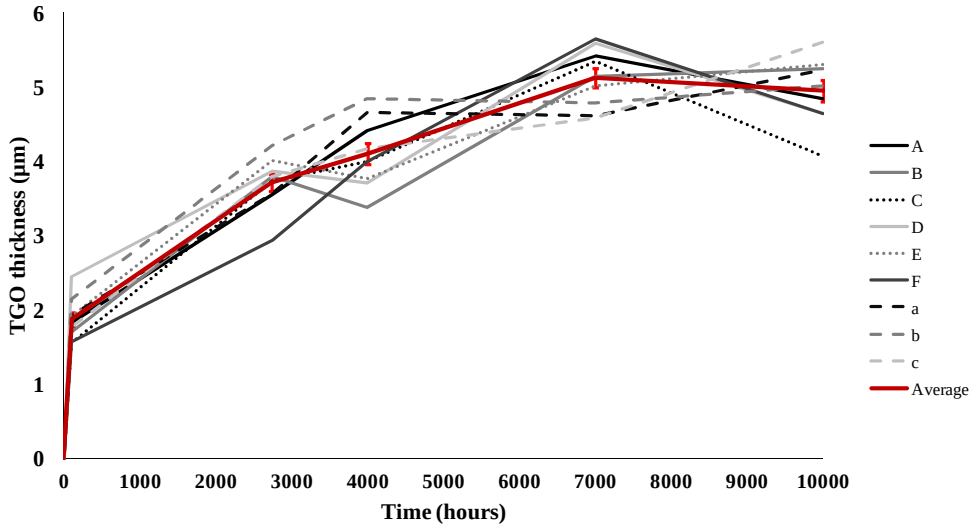

Figure 5.16 Median TGO thickness at different location around samples oxidised at 925 °C against time. Plain, dotted and dashed lines respectively correspond to convex, flat and concave curvatures.

The growth of the TGO, which was measured at every location around the modified aerofoil-shaped samples (Appendix D), was divided in two stages, as seen on Figure 5.16. In the graph, the trend appears as a sub-parabolic curve which is composed of a first part with a higher slope and a second part that was less steep. The fast oxidation rate described by the high slope, the transient stage, correspond to the rapid growth of transient θ-Al_2O_3 and it is followed by the steady-state stage, second part of the curve, during which stable slow growing α-Al_2O_3 replaces totally or partially

(depending on temperature) the transient oxides. The trend is the same at every location around the sample meaning that growth mechanisms remain identical regardless of geometry. This aspect will be investigated in greater details later in this chapter.

5.2.1.2 Identifying the less protective mixed oxides/spinels in the TGO layer

The depletion of Al from the BC, as a result of selective oxidation to maintain the protective Al_2O_3 layer, causes a compositional change in the TGO from α-Al_2O_3 to include a mixture of chromia and spinels ($(Cr,Al)_2O_3$) and ($Ni(Cr,Al)_2O_4$)). Under the SEM those less protective oxides appear in a lighter contrast than the Al_2O_3 layer (Figure 5.17). Usually located close to the TGO/TC interface as isolated clusters or more rarely a continuous layer, they are made of one single phase ($(Co,Ni)(Cr,Al)_2O_4$) (Figure 5.17(a)) or of two phases ($(Co,Ni)(Cr,Al)_2O_4$ and (Co,Ni)O) (Figure 5.17(b)). In the Al_2O_3 layer, Ti associates with Al to form Ti aluminate precipitates which appear as white phases in the dark TGO layer. These different phases were identified using EDX analysis (Figures 5.18 and 5.19).

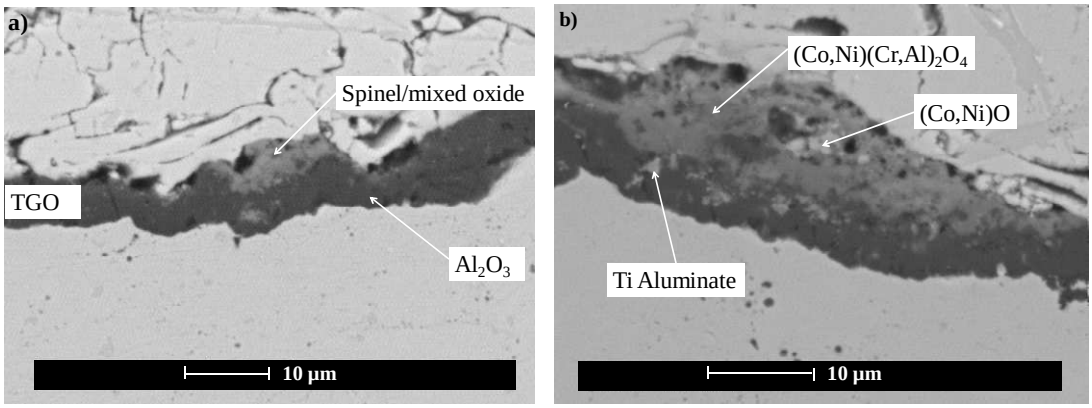

Figure 5.17 SEM images of TGO layer in sample oxidised at 950 °C for 4000 hours. Pictures of spinels/mixed oxides at (a) location D and (b) location c.

EDX mapping highlighted the concentration of Co and Cr in the spinel/mixed oxide. Spinels/mixed oxides contain very small amounts of Al and Ni concentrated at their cores (Figure 5.18). The compositions of each phase are given in Figure 5.19. The compositions of these mixed oxides are consistent with observations made by Chen et al. [36] who found levels of Ni+Co up to 5-16 at% and Al+Cr of 28-43 at%.

These less protective oxides have a detrimental effect on the coating's life as they are believed to help the initiation and propagation of cracks [36,50,78,79]. However, their presence highlights a change of diffusion behaviour in the coating and can be used to understand oxidation mechanisms. Indeed, they require different oxygen partial pressure to grow compare to Al_2O_3 [12], they need more space between the TC and the oxide due to their larger volume change and their location seems to be dictated by the TC microstructure as well as the TC/TGO interface profile [36,56,80]. Even though they are extensively described in literature, their effect on the coating system's lifetime still needs to be clarified. This will be discussed later in Chapter VI.

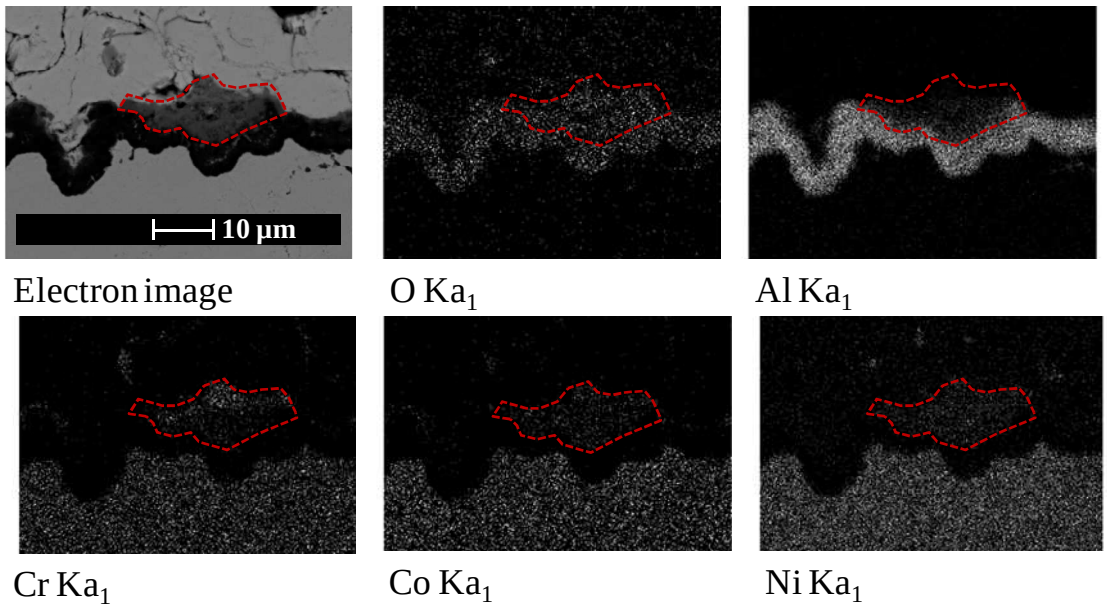

Figure 5.18 EDX mapping of spinel/mixed oxides in TGO from location a in sample oxidised at 925 °C for 7000 hours. Spinel/mixed oxide is circled in red.

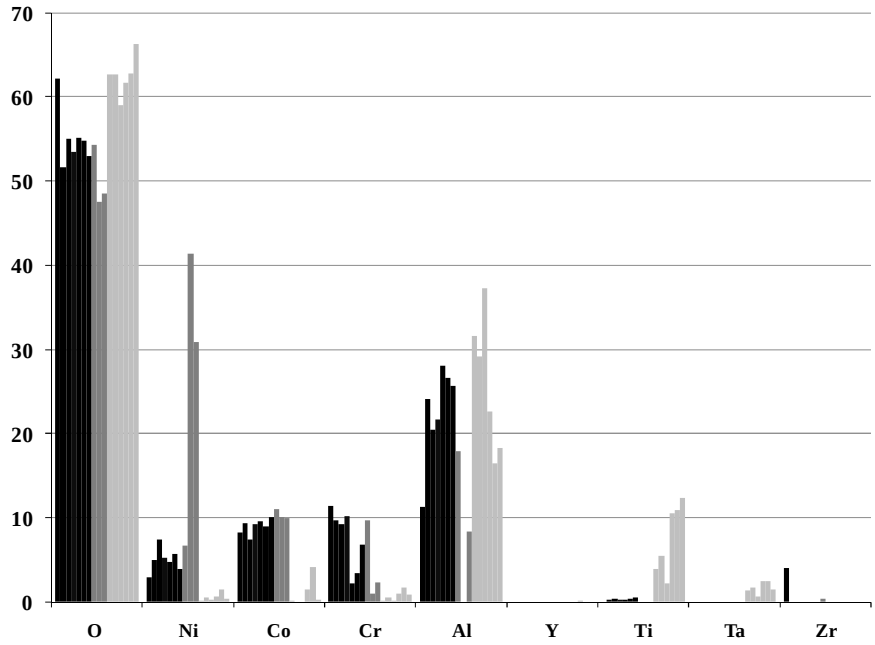

Figure 5.19 Composition in at% of different phases constituting a spinel/mixed oxide and precipitates present in the TGO. The black bars show the composition of the dark grey phase. The dark grey bars show the composition of the light grey phase. The light grey bars show the composition of a white precipitate.

5.2.1.3 Evolution of the SRZ at the BC/Substrate interface with exposure

The diffusion of Al from the BC to the substrate leads to an increase of the SRZ thickness with time at the BC/substrate interface. Initially the SRZ was only a few microns thick and composed of the substrates' γ'-Ni_3Al (light grey phase), β-NiAl (dark grey phase) and intermetallic TCP phases, rich in heavy elements such as W, Ta or Re (white phase) (Figure 5.20(a)). With further exposure time at 900-1000 °C the SRZ increased in size and changed microstructure. Figure 5.20(b) shows the microstructure of the SRZ after 7000 hours at 900 °C and is representative of most samples. The size of the SRZ increased greatly with exposure time, reaching 57 µm thick after 15,000 hours (Figure 5.20(c)). Under the BC/substrate interface a zone free of TCP phases formed

and in the rest of the SRZ light grey precipitates appeared and the white precipitates increased in size.

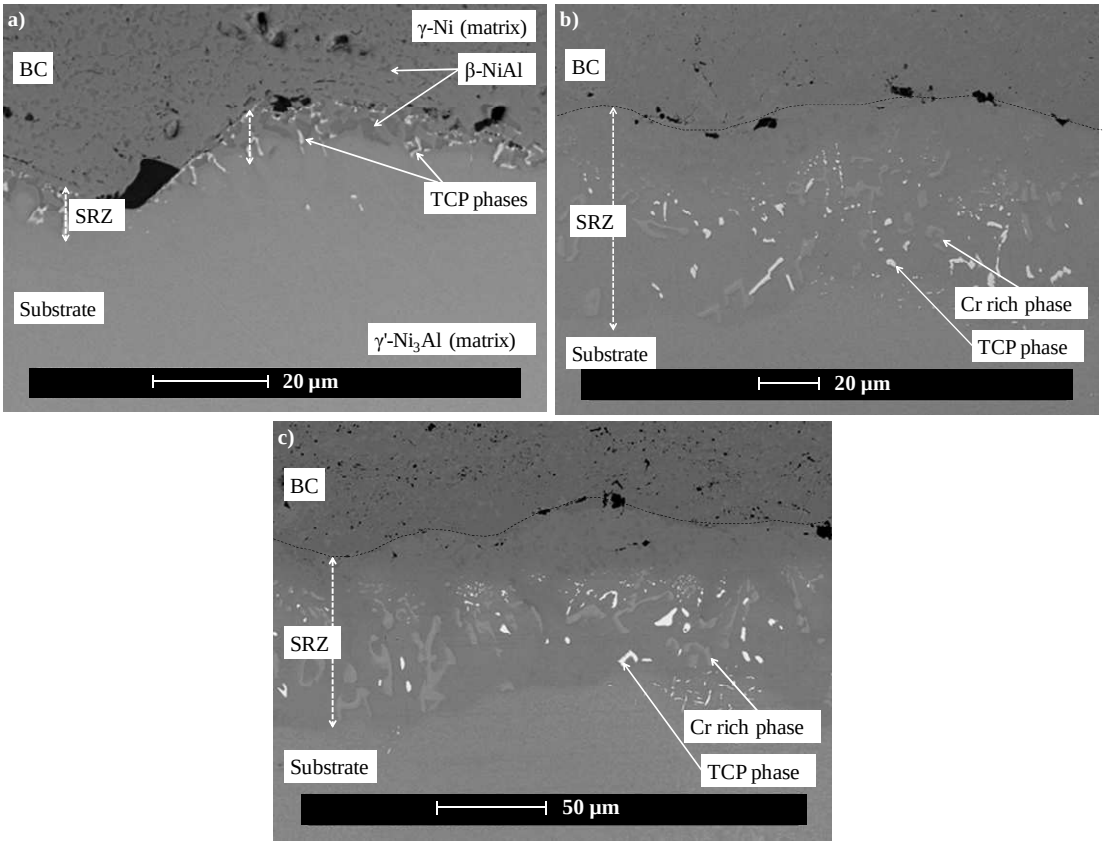

Figure 5.20 Evolution of SRZ with time. SEM images of BC/Substrate interface in location C on as-deposited sample (a) and samples exposed at 900 °C for 7000 hours (b); and 15,000 hours (c).

Figure 5.21 shows the results of EDX mapping done on the SRZ at location F on the same sample. The sample was etched in order to see the phase structure of the BC and the SRZ. The analysis showed the SRZ was composed of a Ni and Al-rich matrix (γ' phase, which was etched away leaving raised phases marking grain boundaries). Indeed accordingly to the composition of the CMSX-4 substrate and the AMDRY 995 BC (which can be found in Table 4.1), more Ni was counted in the SRZ and more Cr was present in the BC. However, more Al should be observed in the BC rather than in

the SRZ, confirming that Al had diffused from one layer to the other and that the SRZ is partly made of γ'-Ni_3Al.

A phase rich in Cr and low in Al and Ni (α-Cr) gathers at the grain boundaries. EDX analysis showed that the white phases appearing on Figure 5.21(f) were intermetallic TCP phases, rich in W and Ta. Later during exposure, the SRZ was still made of two zones and increased in size, reaching 81 µm after 15,000 hours (Figure 5.20(c)). The grain size of the precipitates also seemed bigger but this was not the case for every sample and quantifying their size to confirm the trend could not be achieved accurately enough.

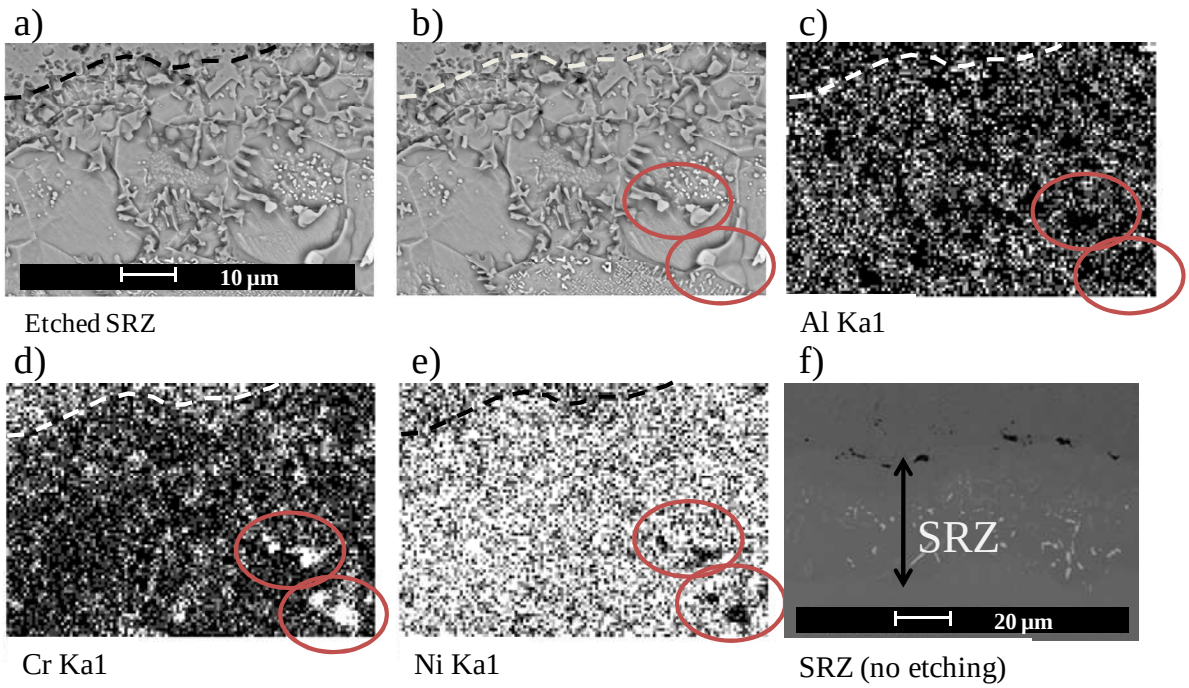

Figure 5.21 EDX mapping of the SRZ. Image of location F on an etched sample exposed for 7000 hours at 900 °C. (a) and (b) are SEM images of an etched sample. (c),(d) and (e) are the scans of (a) and (b). (f) is a SEM image of the SRZ at location F before etching. Dotted lines represent the limit between the SRZ and the BC. Red circles correspond to a Cr rich precipitate in the SRZ.

The thickness of the SRZ in samples exposed at 900 °C was measured at every location around the sample (Appendix H) and plotted against time in Figure 5.22 (the

SRZ thickness of the samples exposed at higher temperatures can be found in Figure 5.29). While the TGO growth followed a sub-parabolic behaviour, the SRZ's evolution was described by parabolic trend composed of a fast and a steady state. The fast growth rate in the first stages of oxidation might be exaggerated by the heat treatment processes carried out before deposition of the TC. This increase of the SRZ with time is common to each modified aerofoil shaped sample regardless of the exposure temperature. Even though TGO and SRZ follow a different growth trend, if we suppose that they both grow parabolically (as described by equation (1)), the growth rate $k_{(TGO)}$ of the TGO would average around $1.5x10^{-6}$ $\mu m^2/s$ while the SRZ growth rate $k_{(SRZ)}$ would average around $4.0x10^{-4}$ $\mu m^2/s$.

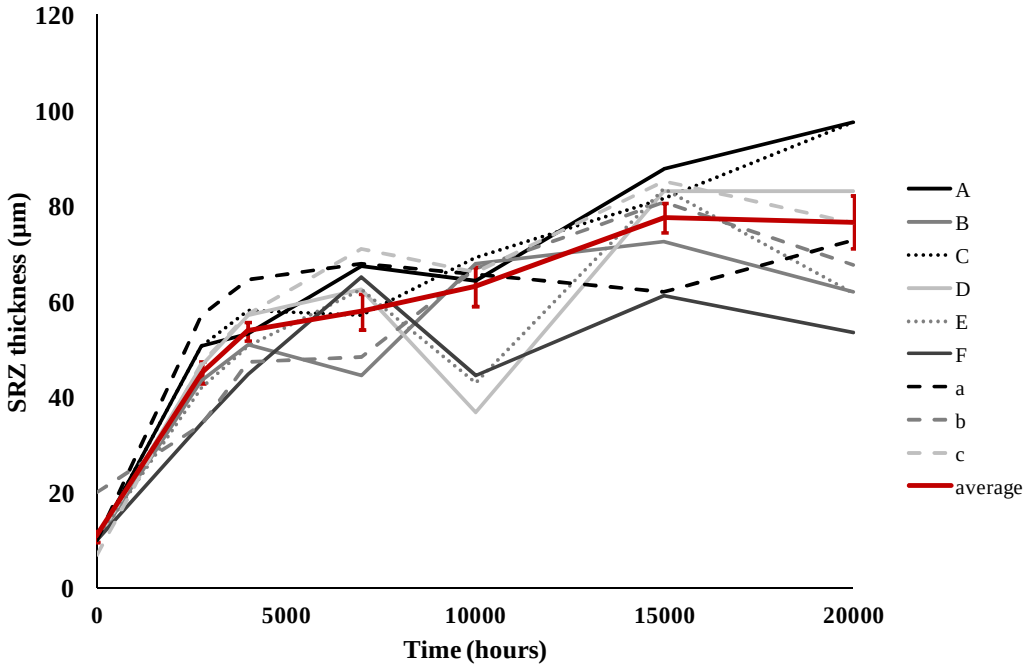

Figure 5.22 SRZ thickness as a function of time in samples oxidised at 900 °C. Plain, dotted and dashed lines respectively correspond to convex, flat and concave curvatures. See nomenclature on reference sheet at end of thesis.

5.2.2 Understanding the effect of exposure temperature on the oxidation behaviour of an APS/TBC system

5.2.2.1 The effect of exposure temperature on the TGO growth

Modified aerofoil-shaped samples were exposed at temperatures between 900 and 1000 °C to allow the investigation of the effect of temperature on the oxidation behaviour of the APS/TBC system.

The samples were weighed regularly between each oxidation cycle (Appendix B) to give an indication of the extent of oxide growth for each sample. The average mass gain of the samples at each temperature, between 900 and 1000 °C, is plotted against time in Figure 5.23. For each temperature in the graph, the trends appeared as a combination of parabolic and linear curves which were composed of a first part with a higher slope and a second part that was less steep. For the first hundred hours of oxidation, the mass gain was quick, correlating with the fast growth of the θ-Al_2O_3 oxide during the transient stage of oxidation. Then the mass gain slowed down in accordance to the formation of the slow growing α-Al_2O_3. As the temperature increased, the mass gain rate increased as well which can be explained by looking at the TGO growth equation found in literature [1]:

$$h^2 = 2k_p t + C \qquad (1)$$

where h is the thickness, t time and k_p the parabolic rate constant. Since k_p follows the Arrhenius law, the increase of temperature will greatly influence the rate at which the TGO grows and so, the mass gain of the samples. The Arrhenius equation for k_p is [1]:

$$k_p = k_o \exp\left(-{}^{E}/_{RT}\right) \qquad (12)$$

where k_0 is the standard rate constant, T is the temperature, E the activation energy (J/mol) and R the gas constant (J/mol/K). The actual TGO thickness of the modified

aerofoil-shaped samples can be seen in Figure 5.24. The similar trend of the curves confirms the relation between mass gain and TGO growth. Modelling of the TGO growth is described in more detail in Chapter VII.

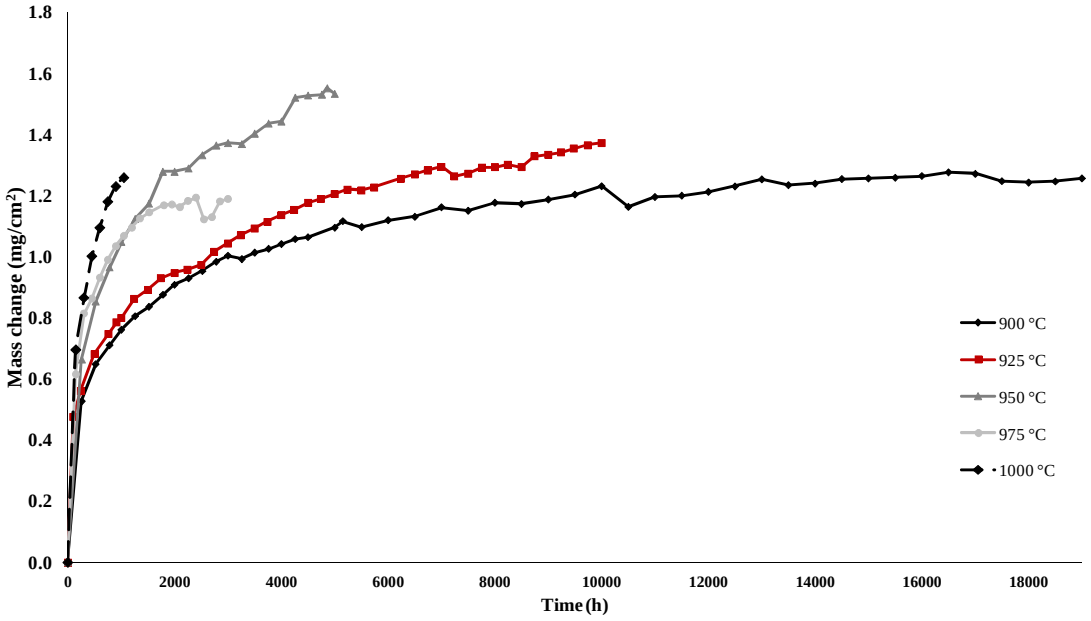

Figure 5.23 Average mass change of samples exposed to temperatures between 900 and 1000 °C as a function of time.

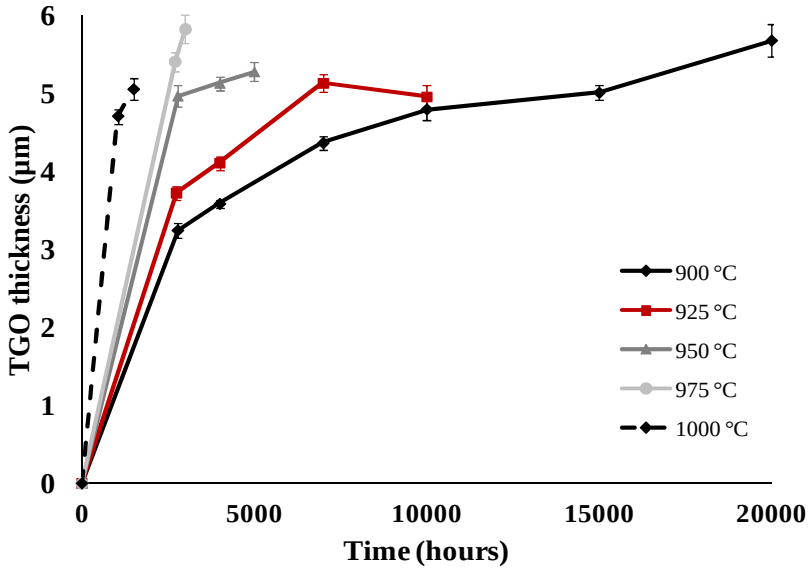

Figure 5.24 Average TGO thicknesses of samples exposed to temperatures between 900 and 1000 °C as a function of time. Errors bars represent the standard deviation.

5.2.2.2 The effect of exposure temperature on the β-depletion and the SRZ

The accelerated growth of the TGO with temperature which was shown by the accelerated mass gain (Figure 5.23) and TGO thickness (Figure 5.24) was accompanied by an accelerated depletion of the β-NiAl phase from the BC (Appendix F). Figure 5.25 plots the amount of β-phase remaining in the BC at location C as a function of time for temperatures between 900 and 950 °C. The time for the samples' BC to be depleted decreased as the temperature increased. Samples oxidised at 950 °C were completely depleted after 4000 hours of exposure while the ones oxidised at 900 °C were completely depleted after 15,000 hours. The percentage of β-NiAl remaining in the BC of samples oxidised over 950 °C could not be plotted because at the time the samples were taken out to be observed under the SEM, in most cases the BC was already totally depleted.

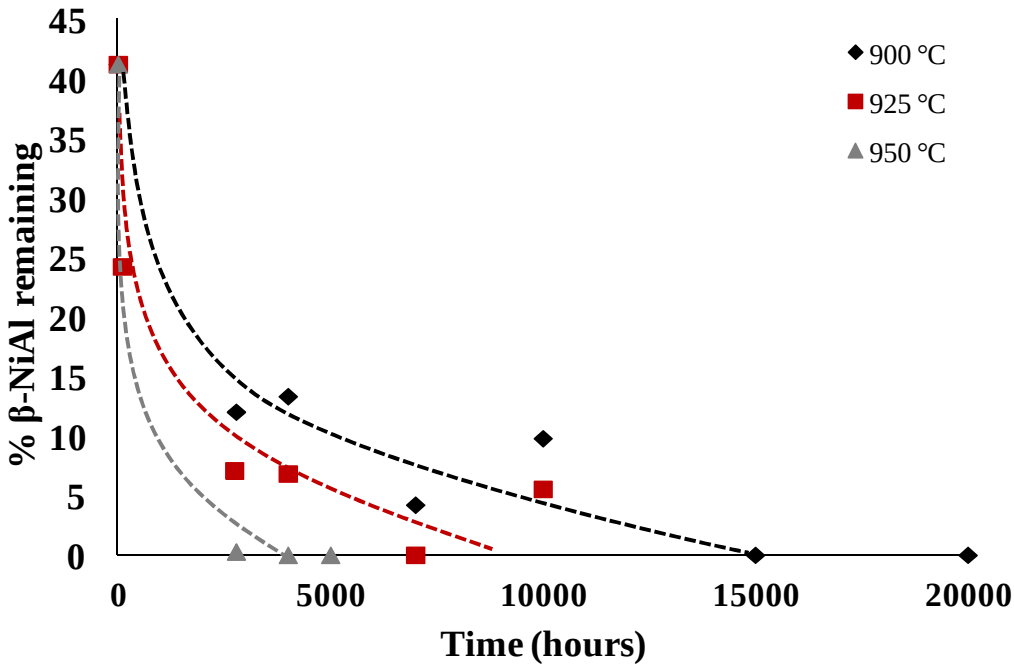

Figure 5.25 β-NiAl depletion in location C on samples oxidised at temperatures between 900 and 950°C. The dotted line is an estimation of the β-depletion trend.

As well as accelerating the depletion of β-NiAl from the BC, the oxidation temperature seemed to modify the diffusion mechanisms of Al from phases other than β in the BC. It is important to note that according to the Ni-Al binary phase diagram (Figure 5.26), as the fraction of Al diminishes in the Ni-Al system at constant temperature, starting from the β-NiAl phase, it gradually transforms into γ'-Ni_3Al and then into γ-Ni.

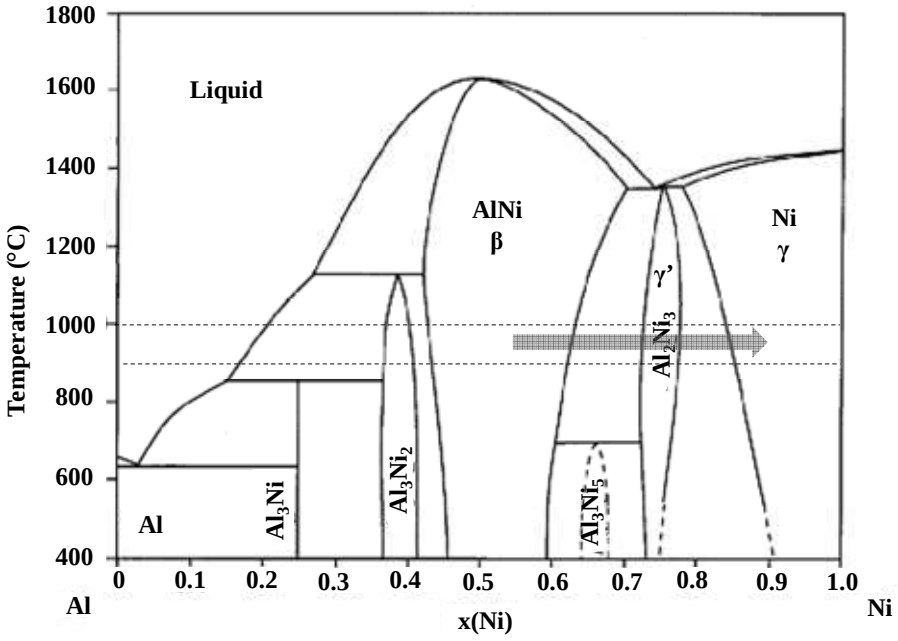

Figure 5.26 Al-Ni binary phase diagram [127]. Added dashed lines represent the temperatures of 900 and 1000 °C. Grey arrow represents the phase change when the amount of Al decreases.

In Figure 5.27 SEM images with enhanced contrast BCs are shown with similar thickness at location C in samples oxidised at 900, 975 and 1000 °C. The exposure times of 15,000, 2700 and 1050 hours, respectively, were chosen because they were close to the end of samples' life or the start of failure. Also, the TGO thickness, around 5 µm thick, was similar on each of them meaning that a similar amount of Al diffused from the BC to form the oxide layer. Below 950 °C, the β-NiAl depleted BC was

divided into two different zones (Figure 5.27(a)). First, a zone close to the BC surface contained only the γ-Ni matrix, whose Al level is the lowest in the BC (around 10 at%), as Al had been used to grow the TGO. This zone can be associated with the outward β-NiAl depletion zone and measured around 35 µm. Then, the second zone, beneath the Al-depleted one, was made of a mix of γ-Ni and γ'Ni_3Al, appearing as a light grey phase on the SEM image. Because this zone's boundary coincided with the boundary of the outward Al depletion zone on a large majority of the SEM pictures, it was considered to correspond to the inward β-depletion zone (in case of a totally depleted BC).

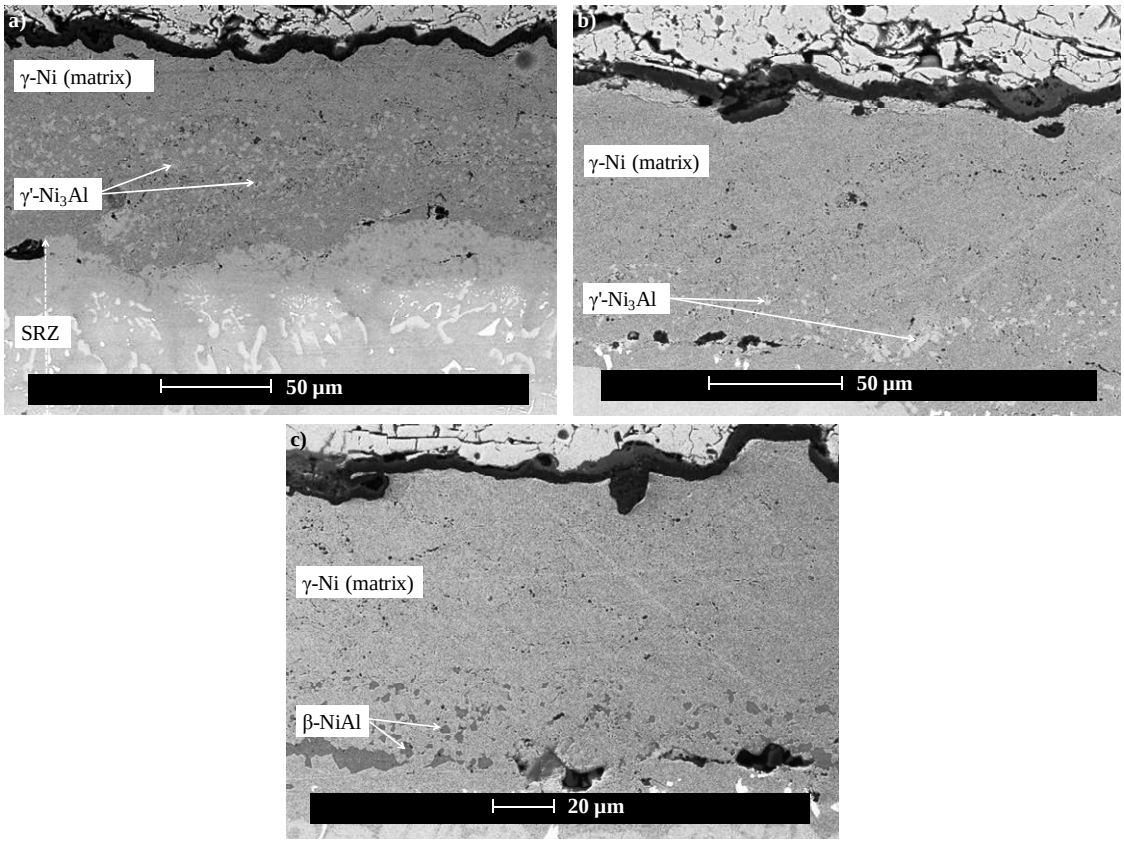

Figure 5.27 SEM images of phases present in the BC in location C on samples exposed at (a) 900 °C; (b) 975 °C; and (c) 1000 °C for 15,000, 3000 and 1050 hours respectively (samples are close to failure). Black arrows correspond to the outward and inward depletion zones.

In parallel with the change of diffusion behaviour in the BC with increasing temperature, made obvious by the re-precipitation of the β-phase from the substrate to the BC, a modification of the microstructure in the SRZ at the BC/substrate interface was observed.

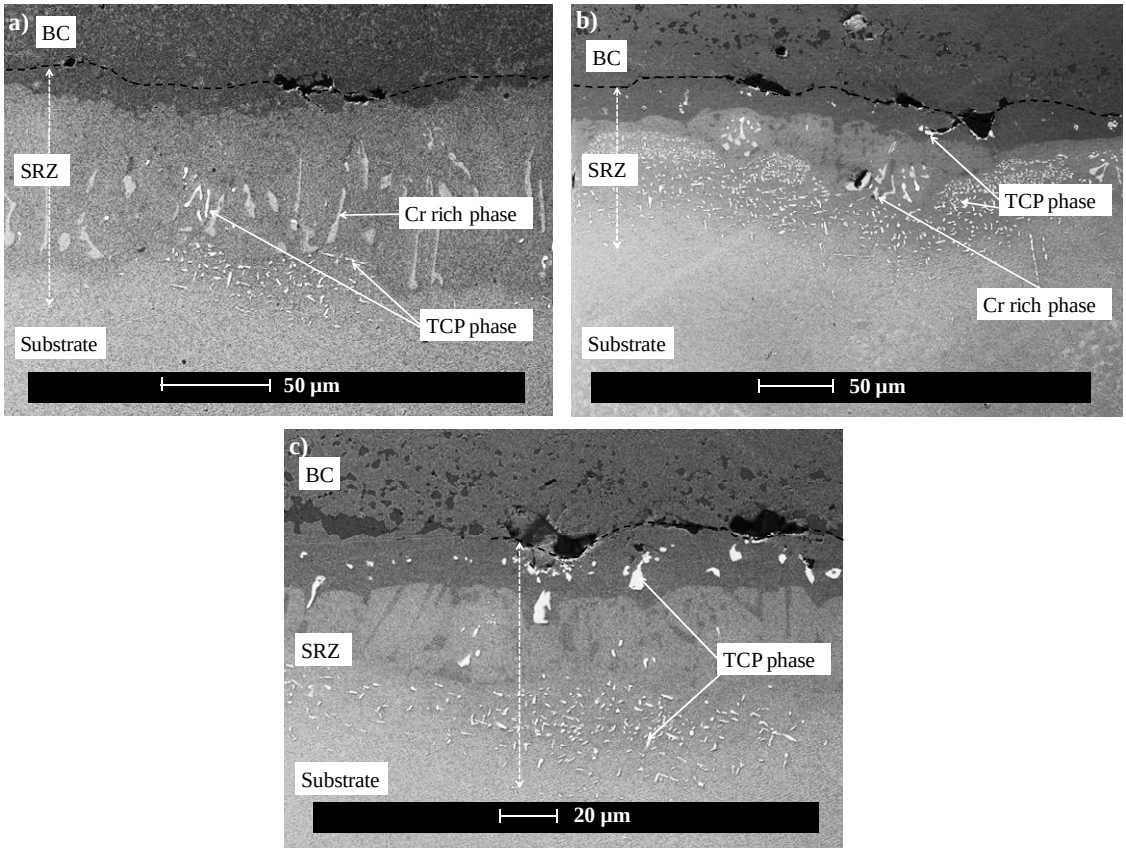

Figure 5.28 Effect of the temperature on the microstructure of the SRZ. SEM images (enhanced contrast) of the BC/substrate interface in location C on (a) samples exposed at 950 °C for 4000 hours (b) exposed at 975 °C for 2700 hours; (c) and exposed at 1000 °C for 1050 hours. The black dotted lines represent the BC/Substrate interface. The white arrows represent the SRZ.

Figure 5.28 shows the SEM images, with enhanced contrast, of SRZ at location C, at increasing temperature in samples close to the end of their lifetime. With increasing temperature, the amount of TCP close to the BC/Substrate interface rose, indicating a more pronounced diffusion of heavy elements towards the BC. The precipitation of the white phase could be caused by an increase in Al content since Al

reduces the solubility of some heavy elements, such as Ta [47]. At the same time, TCP close to the SRZ/substrate interface possessed a dot-like microstructure and seemed evenly scattered unlike at lower temperatures (Figure 5.20) suggesting a change of lattice orientation. Moreover the progression from the BC to the SRZ of the γ-Ni phase, characterised by the dark grey matrix, accompanied by the disappearance of the light grey γ'-Ni_3Al, confirms the diffusion of Al (mechanisms will be explained in section 6.1). Finally, as a remark, the absence of Cr-rich phase in Figure 5.28(c), is not representative of other samples. As for the TGO, the growth rate of the SRZ increases with temperature (Figure 5.29). The growth rate calculated from the SRZ thickness data, considering the behaviour parabolic (as described by equation (1) and shown in Figure 5.29), the growth rate $k_{(SRZ)}$ increased from 7.7×10^{-5} µm²/s at 900 °C to 9.8×10^{-4} µm²/s at 1000 °C (Table 5.1).

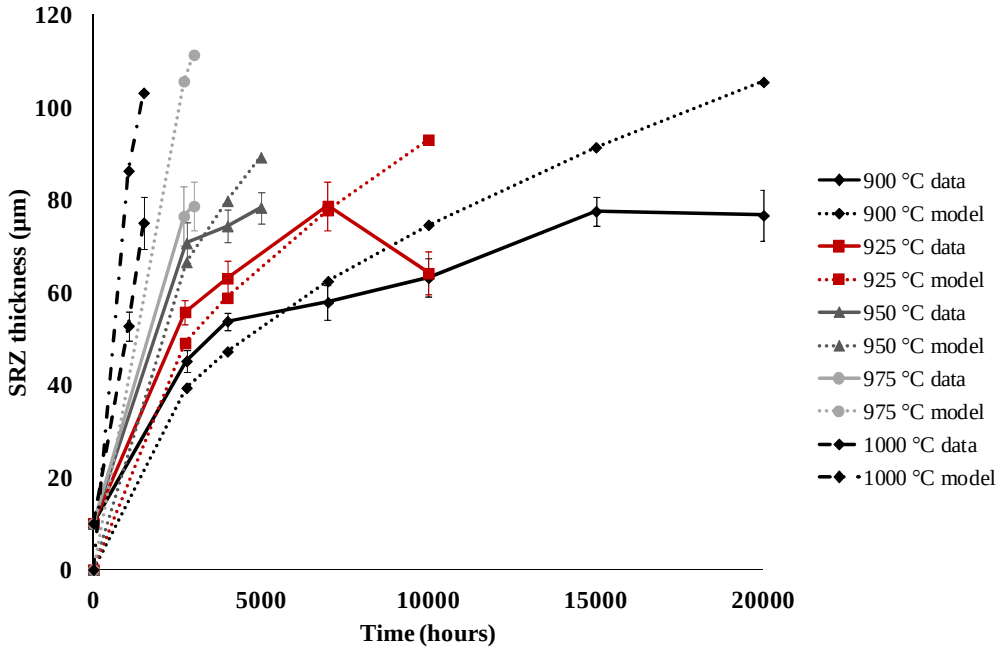

Figure 5.29 Average SRZ thicknesses of samples exposed to temperatures between 900 and 1000 °C compared to a model derived from a parabolic behaviour (Equation (1)) as a function of time. Error bars represent standard error.

Temperature (°C)	900	925	950	975	1000
$k_{(SRZ)}$ **(µm²/s)**	7.7E-05	1.2E-04	2.2E-04	5.7E-04	9.8E-04

Table 5.1 Table 1 Value of SRZ Growth rate with temperature.

The measured inward and outward β-depletion zone thicknesses are plotted against time in Figure 30. Important scatter in the data was caused by the rough TGO/BC and SRZ/BC interfaces. However, generally the trend described by the outward β-depletion zone thickness as a function of time was similar to the trends obtain from the TGO thickness data in Figure 5.24 while the trend described by the inward β-depletion zone thickness as a function of time is similar to the SRZ growth trend shown in Figure 5.29. This is in accordance with known TGO and SRZ growth mechanisms which rely respectively on the outward and inward Al diffusion from the BC.

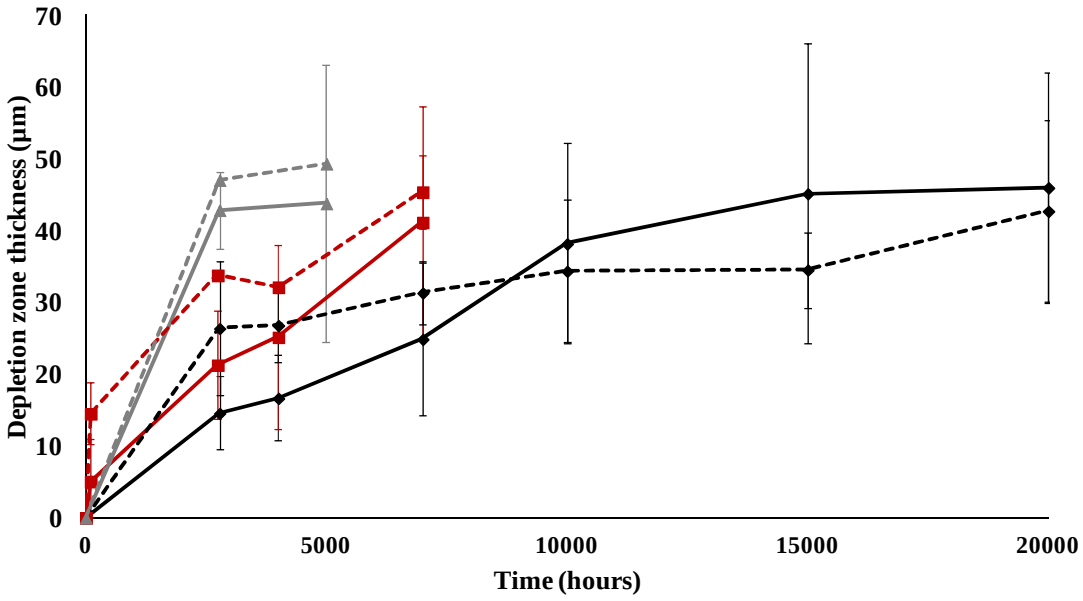

Figure 5.30 Inward (plain line) and outward (dashed line) β-depletion zone thickness at 900 (black), 925 (red) and 950 (grey) as a function of time.

5.2.3 Discussion

Most of the observations made in section 5.2 were in accordance with previous results found scattered across the literature. The growth of the TGO was sustained by the diffusion of Al from the β-NiAl phase [44,45] which caused the creation of an Al outward diffusion zone close to the TGO/BC interface [12,48]. In parallel, Al also diffused to the substrate, creating the SRZ, composed of γ/γ', α-Cr and TCP phases [17,19,21,44,46]. An Al inward diffusion zone close to the substrate resulted from this diffusion. After longer exposure, the β-phase disappeared completely from the BC [48].

The effect of temperature was in accordance with modelling equations found in literature [12,21,57,58]. Higher temperatures accelerated the diffusion mechanisms resulting into faster depletion of the β-NiAl phase and faster growth of the TGO and SRZ (more detail in section 7.2).

The depletion of Al and the growth of the TGO are considered as important factors leading to the failure of APS/TBC systems [68]. Indeed the lack of Al in the BC, augments the risks of growing less protective oxides (spinels/mixed oxides) in the TGO, and prevents the oxide layer re-healing in case of cracking; while the growth of the TGO increases the stresses between the different layers of the coating system. As a consequence, with increasing temperature, the failure of samples occurred earlier (Figure 5.31). The first sign of damage in samples exposed at 1000 °C were noticed after 1050 hours whereas samples exposed at 900 °C started cracking after 15,000 hours. Moreover, the extent of damage was greater at higher temperatures. At 1000 °C, the first cracks were spotted after 900 hours of exposure and samples were then removed after 1500 hours due to significant ceramic TC delamination;, meaning that critical failure was reached within 600 hours of initial cracking. At 975 °C this

happened between 1950 and 4000 hours, and at 950 °C between 2780 and 5000 hours. At those temperatures, critical failure was reached within 2050 and 2220 hours of first cracking observation respectively. Under 950 °C, samples still haven't experienced critical failure.

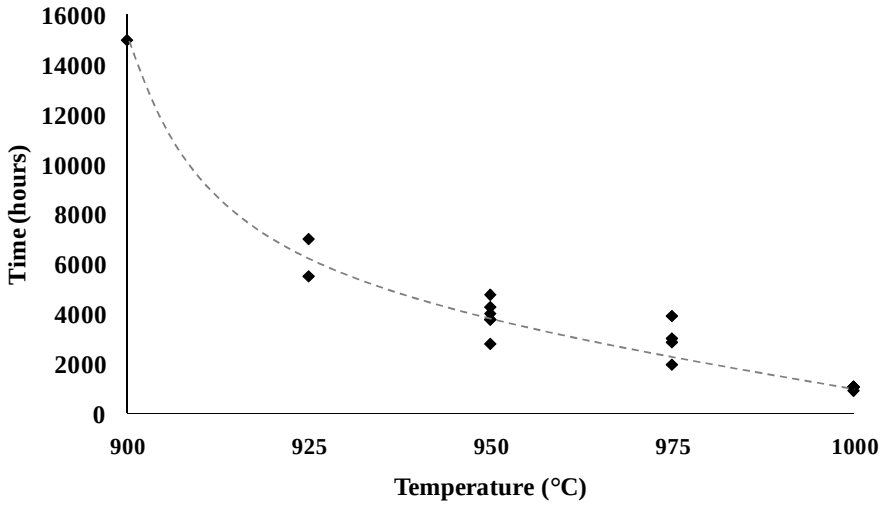

Figure 5.31 Time of exposure after which damage was observed for the first time (by eye, under SEM or using pulsed flash thermography) for samples oxidised at temperatures between 900 and 1000 °C.

5.2.4 Summary

To summarise, when an APS/TBC system is exposed to high temperature oxidation, the amount of β-NiAl phase, whose purpose is to provide Al for the growth of the protective Al_2O_3 layer, reduces with exposure. This produces two β-depletion zones: one close to the TGO/BC interface (outward depletion of Al) and another close to the BC/substrate interfaces (inward depletion of Al). Lack of Al leads to the formation of spinels/mixed oxides in the TGO which are believed to promote the coating system's failure. Moreover, in parallel to the TGO growth at the TC/BC

interface, a SRZ is produced at the BC/Substrate interface. The difference in Al activity between the coating and the substrate cause the Al to deplete from the BC toward the substrate. It was also found that, increasing the oxidation temperature increased the oxidation rate of the coated system. This is a direct consequence of the accelerated diffusion of Al and other elements with temperature. The mechanisms of oxidation change with increasing temperature. This was suggested by different microstructure observed in the BC and SRZ.

Knowing the basic behaviour of the modified aerofoil-shaped samples, it is now possible to investigate the effect of the samples' geometry on the integrity of the coating system.

5.3 Quantification of APS/TBC features as a function of curvature

The curvature of nine different locations around the samples (Table 4.2 or Appendix I) was calculated to investigate their influence on the TC and BC thicknesses, β-NiAl phase depletion and TGO and spinel growth. Curvature was defined as the inverse of the radius. Many of the results have been published in a journal paper (see [126]).

5.3.1 Influence of curvature on TC and BC thicknesses

Plotting TC and BC thicknesses against sample curvature showed that at any temperature, the more convex the surface, the thinner the TC and BC (Figures 5.32 to 5.36). Only the BC in location B with a curvature of 0.14 mm^{-1}, did not follow this tendency and appeared thinner (regardless of exposure time and temperature).

These results reflect the nature of the coating application processes used in the manufacture of these samples. The decreasing trends approximated in Figures 5.32 to 5.36 seem almost parallel and are similar for each temperature confirming that the thickness reduction with curvature was a result of the reproducibility of manufacture and how the coating thickness varied with angle of incidence and deposition efficiency. More details about the manufacturing process in section 6.2.

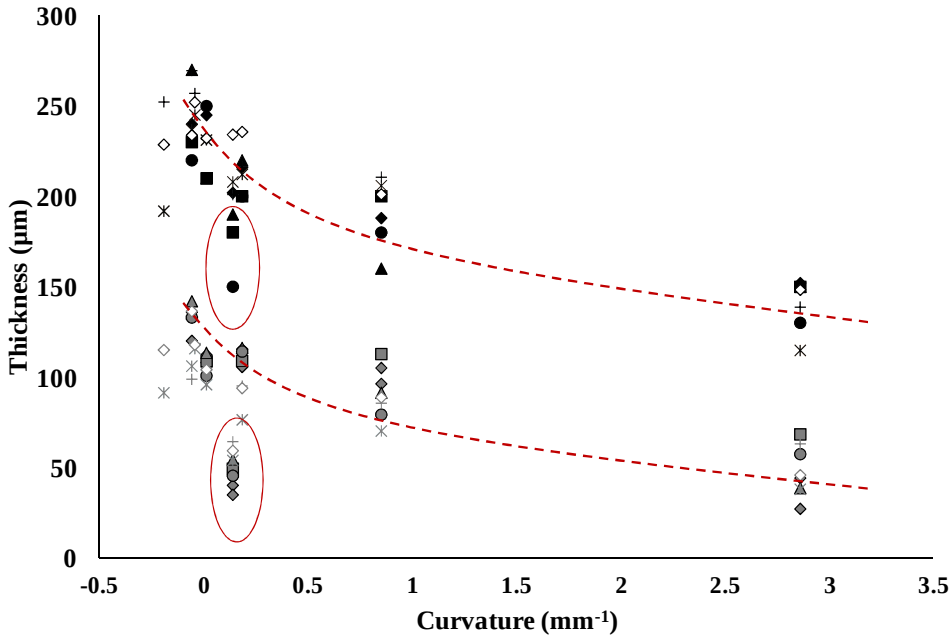

Figure 5.32 Thickness of the TC (black symbols) and the BC (grey symbols) as a function of sample curvature. As deposited sample (diamond) and samples oxidised at 900 °C for 2780 (squares), 4000 (triangles), 7000 (circles), 10,000 (crosses), 15,000 (stars) and 20,000 hours (empty diamonds). Red circles highlight location B and red dashed line is a trend estimation, excluding the data at location B.

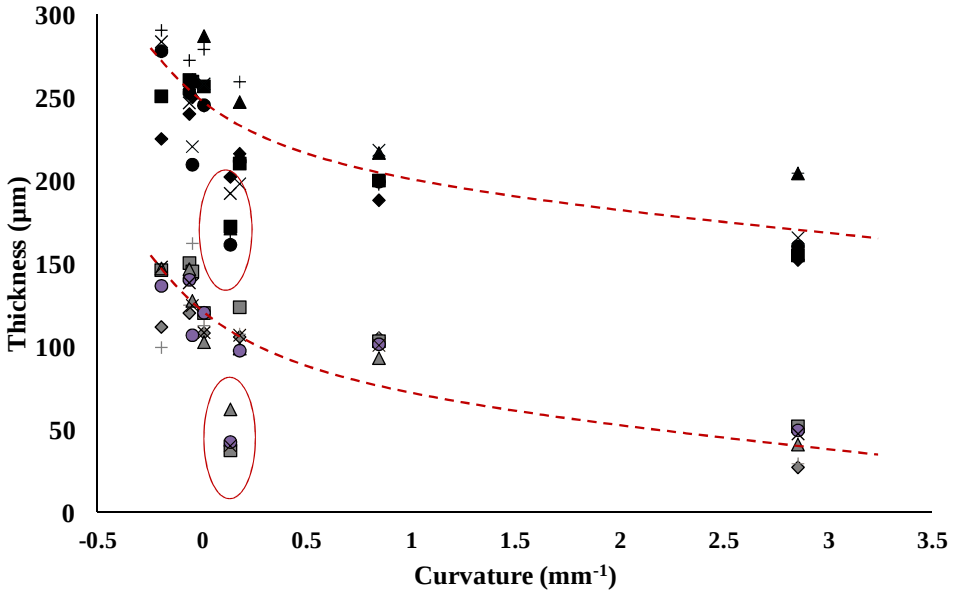

Figure 5.33 Thickness of the TC (black symbols) and the BC (grey symbols) as a function of sample curvature. As deposited sample (diamond) and samples oxidised at 925 °C for 100 (cross,) 2740 (squares), 4000 (triangles), 7000 (circles) and 10,000 hours (stars). Red circles highlight location B and red dashed line is a trend estimation, excluding the data at location B.

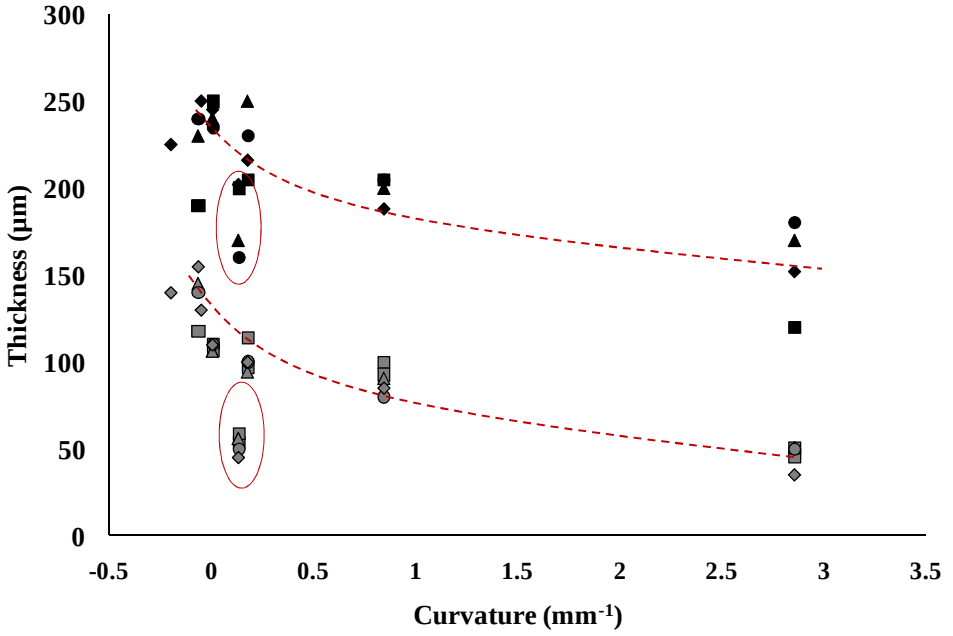

Figure 5.34 Thickness of the TC (black symbols) and the BC (grey symbols) as a function of sample curvature. As deposited sample (diamond) and samples oxidised at 950 °C for 2780(squares), 4000 (triangles) and 5000 hours (circles). Red circles highlight location B and red dashed line is a trend estimation, excluding the data at location B.

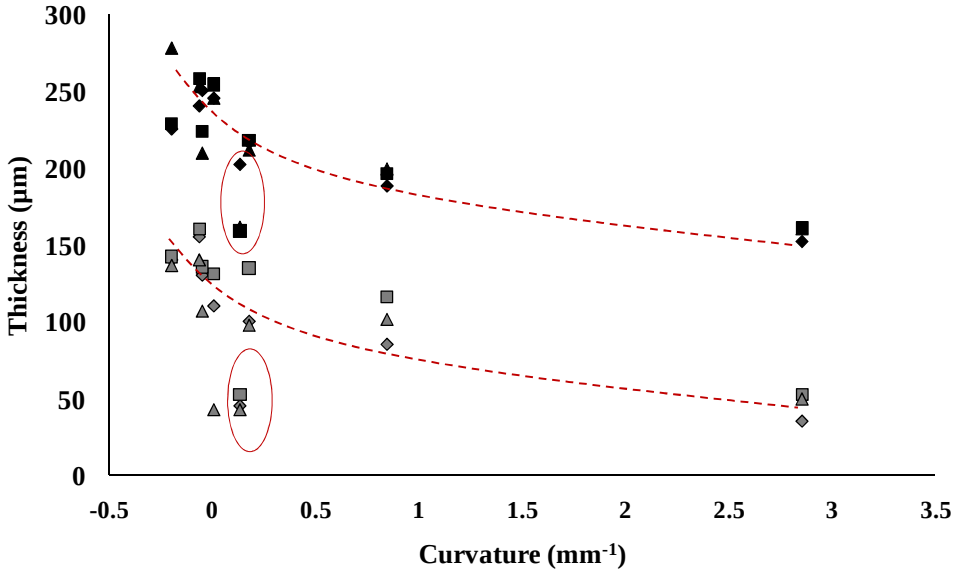

Figure 5.35 Thickness of the TC (black symbols) and the BC (grey symbols) as a function of sample curvature. As deposited sample (diamond) and samples oxidised at 975 °C for 2700 (squares) and 4000 hours (triangles). Red circles highlight location B and red dashed line is a trend estimation, excluding the data at location B.

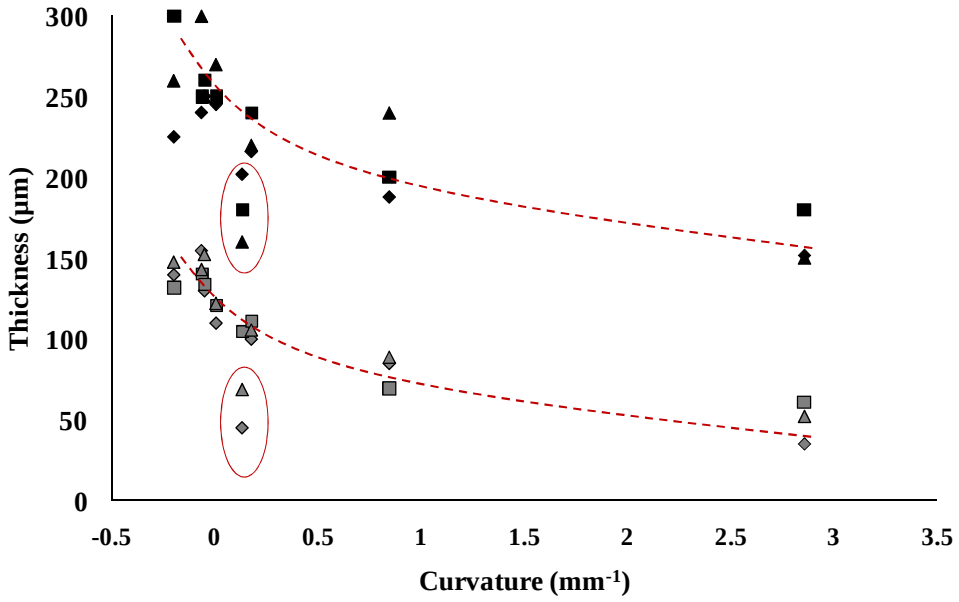

Figure 5.36 Thickness of the TC (black symbols) and the BC (grey symbols) as a function of sample curvature. As deposited sample (diamond) and samples oxidised at 1000°C for 1050 (squares) and 1500 hours (triangles). Red circles highlight location B and red dashed line is a trend estimation, excluding the data at location B.

5.3.2 Influence of curvature on the β-phase

The amount of β-NiAl remaining in the BC was quantified using an image analysis software (Image J) (Appendix F), where different phases were distinguished by their different gray scale values, and was linked to the BC thickness as well as exposure time/temperature (Figures 5.37 to 5.39). β-NiAl remaining in the BC was measured at 900, 925 and 950 °C, i.e. in samples where β-phase was not completely depleted, after various exposure times.

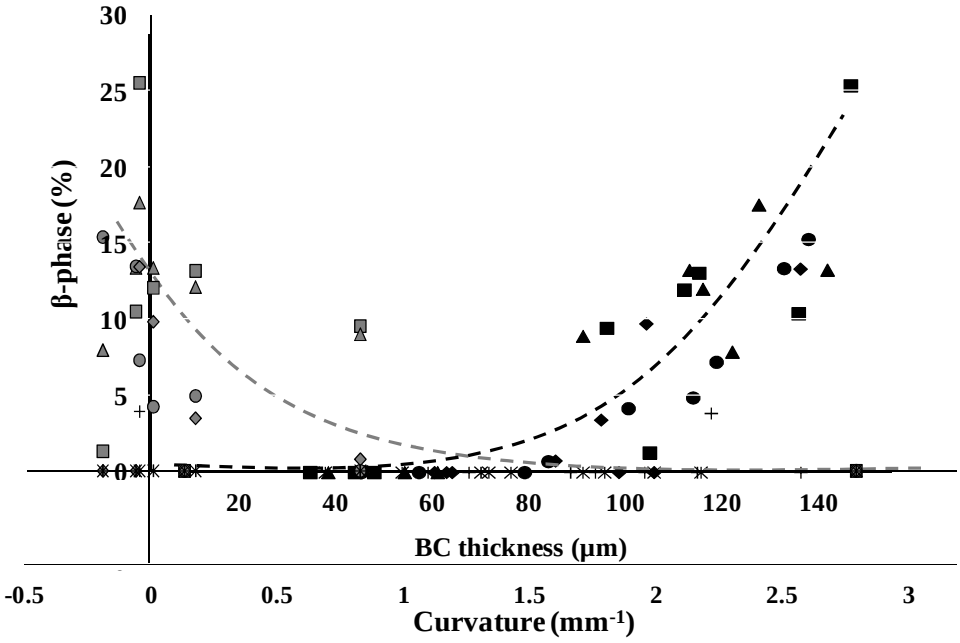

Figure 5.37 Comparison of the β-NiAl concentration with the BC thickness (black symbols) and the β-NiAl concentration with the sample curvature (grey symbols). Samples oxidised at 900 °C for 2780 (squares), 4000 (triangles), 7000 (circles), 10,000 (diamonds), 15,000 (stars) and 20,000 hours (crosses). Dashed lines are trend estimations.

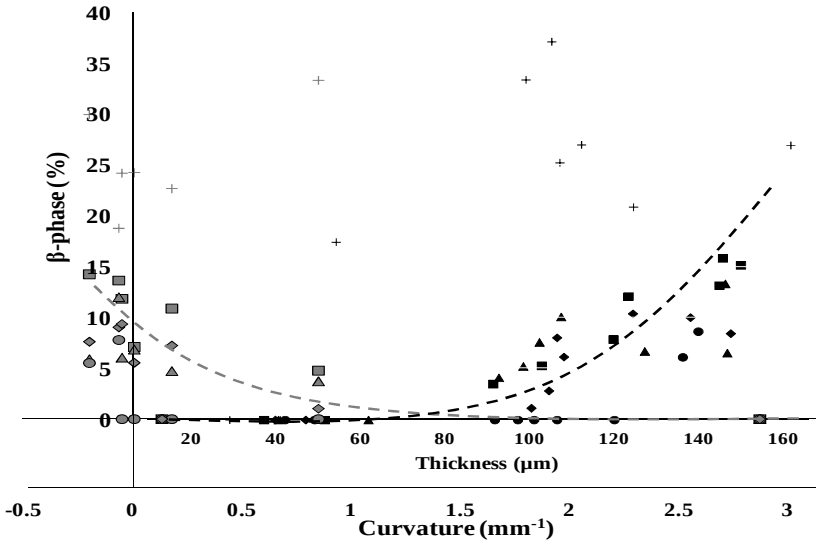

Figure 5.38 Comparison of the β-NiAl concentration with the BC thickness (black symbols) and the β-NiAl concentration with the sample curvature (grey symbols). Samples oxidised at 925 °C for 100 (cross), 2740 (squares), 4000 (triangles), 7000 (circles) and 10,000 hours (diamonds). Dashed lines are trend estimations.

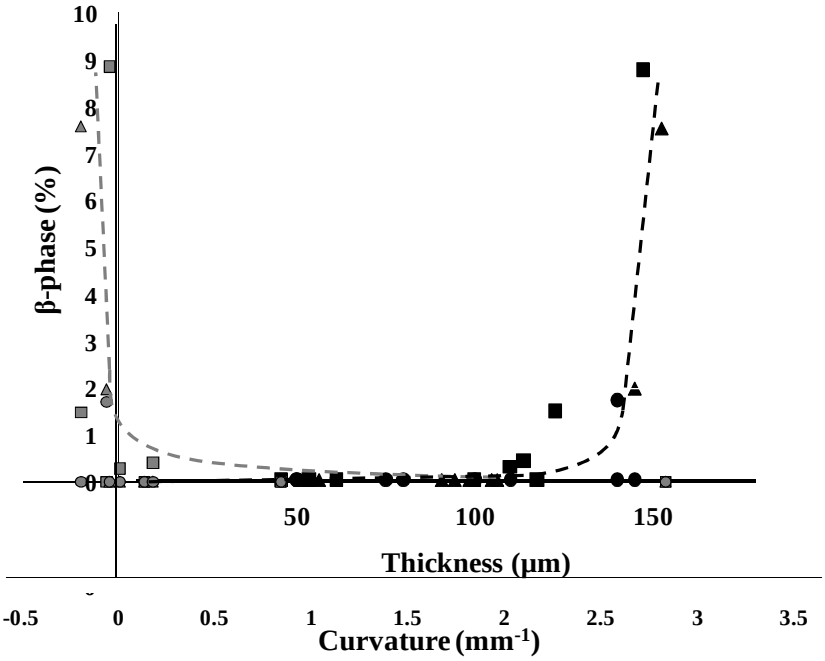

Figure 5.39 Comparison of the β-NiAl concentration with the BC thickness (black symbols) and the β-NiAl concentration with the sample curvature (grey symbols). Samples oxidised at 950°C for 2780 (squares), 4000 (triangles), and 5000 hours (circles). Dashed lines are trend estimations.

For short exposure times, curvature did not affect the amount of β-phase present in the BC. However, after further exposure, the amount of β-phase remaining was related to sample curvature and it was found that, the more convex the curvature, the less β-NiAl was present. As well as being smaller in thin BC, the Al reservoir in convex locations can be affected by faster oxidation rates caused by a more rapid transport of oxygen through the thinner TC [116], explaining the reduced amount of β-phase observed in thin/convex regions.

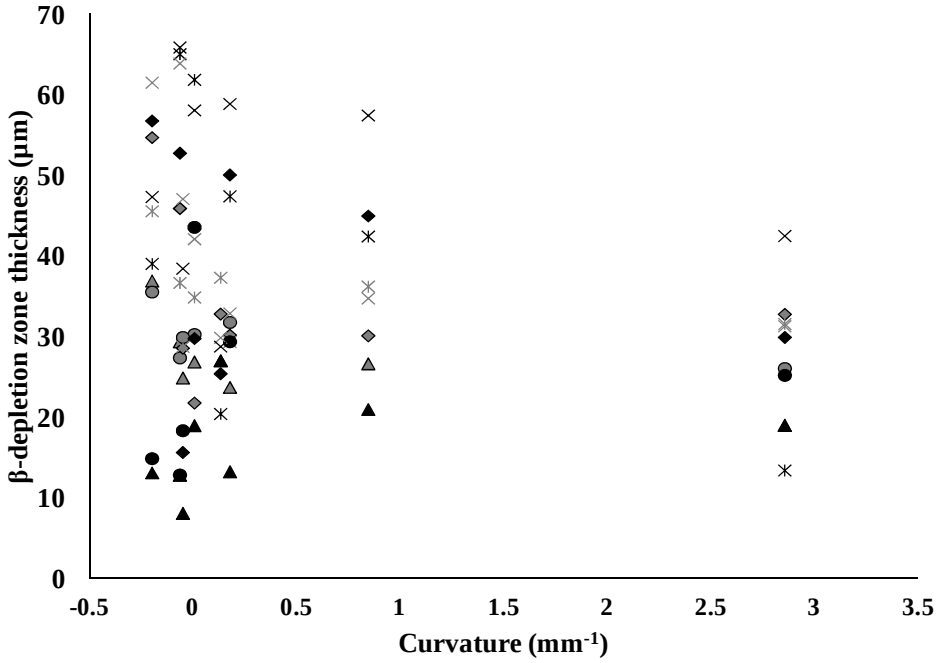

Figure 5.40 Thickness of the β inward depletion zone (black symbols) and the β outward depletion zone (grey symbols) as a function of sample curvature. Samples oxidised at 900 °C for 4000 (triangles), 7000 (circles), 10,000 (diamonds) 15,000 (stars) and 20,000 hours (crosses).

The depletion zones' thicknesses were also compared to the curvature (Figures 5.40 to 5.43) (Appendix E). At 900 °C, the outward diffusion from the BC to the TGO did not appear to follow any pattern related to curvature. For less than 7000 hours of exposure, the inward diffusion did not follow any pattern either. However after 7000

hours, the inward diffusion of Al from the BC to the substrate reduced for more convex curvatures (Figure 5.40).

Similarly at 925 °C, the outward diffusion from the BC to the TGO did not follow any obvious pattern with respect to curvature. Under 4000 hours of exposure, the inward diffusion did not follow any obvious pattern either. However after 7,000 hours, the inward diffusion of aluminium from the BC to the substrate reduced for more convex curvatures (Figure 5.41). At 100 hours of exposure, the data does not follow any trend and this may be explained by the system being in the transient stage of oxidation rather than the steady-state stage. The abnormally thin microstructure of the β-phase grains might also have lead to inaccuracy in the measurements.

At 950 °C, there was a clear trend for the inward diffusion of Al from the BC to the substrate, which reduced for more convex curvatures, whereas the outward diffusion from the BC to the TGO did not follow any obvious pattern related to curvature as shown in Figure 5.42. Due to the high oxidation rate of the coating over 950 °C, only a few data could be measured for samples oxidised at 975 °C and 1000 °C. In Figure 5.43 it can be seen that the outward and inward diffusion of Al from the BC to the substrate reduced for more convex curvatures.

Generally, the diffusion of Al did not seem to follow any obvious pattern as a function of curvature. Diffusion is expected to be influenced by the micro-geometry (roughness) of the interfaces between the different layers of the TBC systems rather than the macro-geometry (curvature) of the samples.

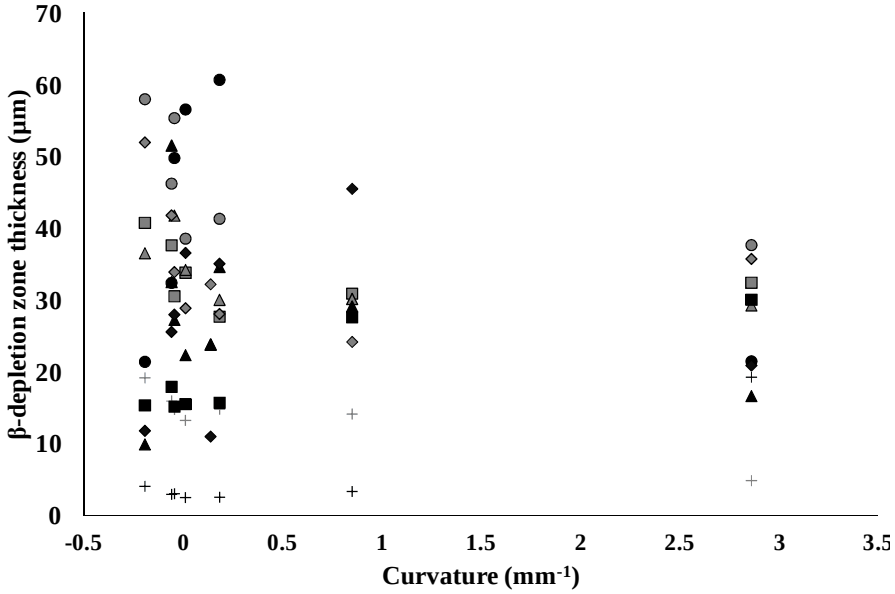

Figure 5.41 Thickness of the β inward depletion zone (black symbols) and the β outward depletion zone (grey symbols) as a function of sample curvature. Samples oxidised at 925 °C for 100 (crosses), 2740 (squares), 4000 (triangles), 7000 (circles) and 10,000 hours (diamonds).

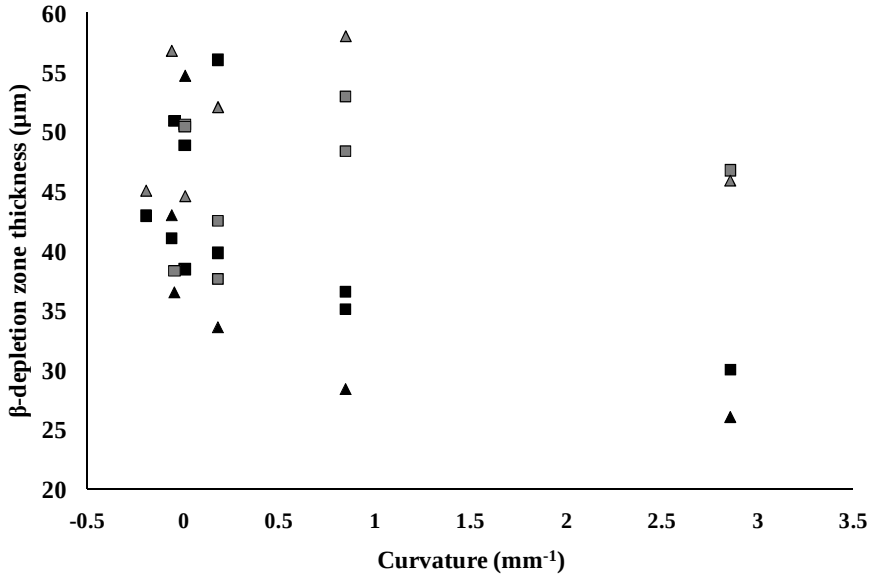

Figure 5.42 Thickness of the β inward depletion zone (black symbols) and the β outward depletion zone (grey symbols) as a function of sample curvature. Samples oxidised at 950 °C for 2780 (squares,) and 4000 hours (triangles).

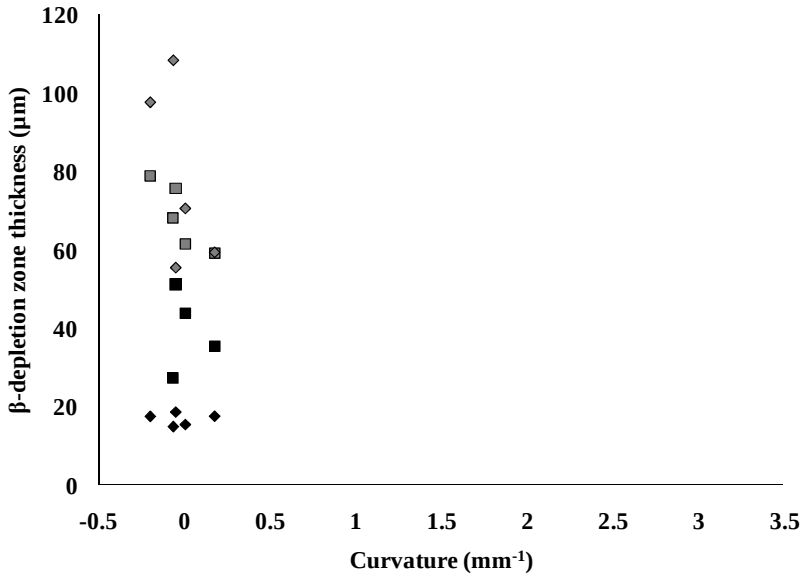

Figure 5.43 Thickness of the β inward depletion zone (black symbols) and the β outward depletion zone (grey symbols) as a function of sample curvature. Samples oxidised at 975 °C for 2700 hours (squares) and at 1000 °C for 1050 hours (diamonds).

5.3.3 Influence of curvature on TGO growth

The TGO thickness was observed not to vary with sample curvature (Figure 5.44). The outward diffusion of Al from the β-phase, that supported the growth of the TGO, was not influenced by the geometry of the sample; hence the lack of any noticed trend in the TGO thickness with curvature.

The values of k_p for different exposure temperatures and locations around the modified aerofoil shaped samples were also calculated (Table 5.2 and Figure 5.45). At temperature below 950 °C, the oxidation kinetics did not vary with curvature. However, scatter in the results can be seen above 950 °C. This can be explained by the few data obtained from the samples exposed at higher temperature because of their early failure. Moreover, important cracking on these samples induced errors in the measurement of the TGO thickness.

At each temperature, the values of k_p seemed to decrease slightly for curvatures close to 0 (Table 5.2). Higher TGO/BC roughness of increasingly concave locations and the extreme convex geometry of location F explain why the oxidation kinetics increased in these regions (see Chapter VI for further explanation).

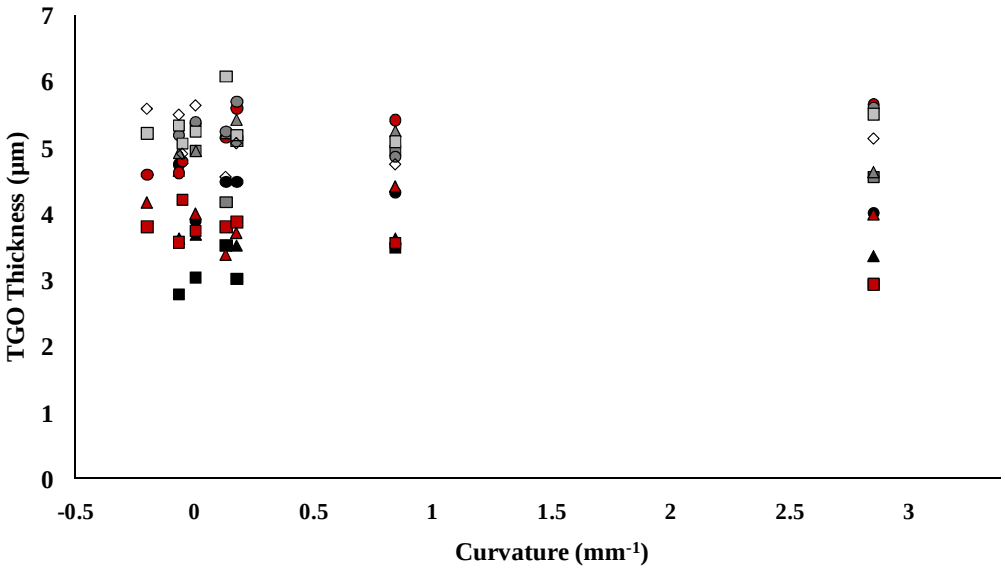

Figure 5.44 Thickness of the TGO thickness as a function of sample curvature. Samples oxidised at 900 (black symbols), 925 (dark grey symbols), 950 (mid grey symbols), 975 (light grey symbols) and 1000 °C (empty symbols) for 1500 (diamond), ~ 2700 (squares), 4000 (triangles) and 5000 hours (circles).

Location	Curvature (mm^{-1})	k_p ($\mu m/s^2$)				
		Exposure temperature (°C)				
		900	925	950	975	1000
A	0.85	4.1E-07	7.2E-07	1.5E-06	3.6E-06	4.3E-06
B	0.14	3.2E-07	7.8E-07	1.6E-06	3.5E-06	4.3E-06
C	0.01	5.7E-07	5.7E-07	1.6E-06	2.8E-06	5.6E-06
D	0.18	3.9E-07	6.5E-07	1.8E-06	3.1E-06	5.0E-06
E	Theoretical 0	3.3E-07	7.6E-07	1.3E-06	3.4E-06	3.9E-06
F	2.86	4.9E-07	7.4E-07	1.7E-06	2.7E-06	5.2E-06
a	-0.06	3.5E-07	7.1E-07	1.5E-06	2.6E-06	5.6E-06
b	-0.05	2.6E-07	6.5E-07	1.7E-06	2.3E-06	4.7E-06
c	-0.20	4.8E-07	8.0E-07	1.7E-06	2.5E-06	6.0E-06

Table 5.2 Oxidation kinetics (values of k_p) at different locations and exposure temperatures of the BCs on the modified aerofoil-shaped samples.

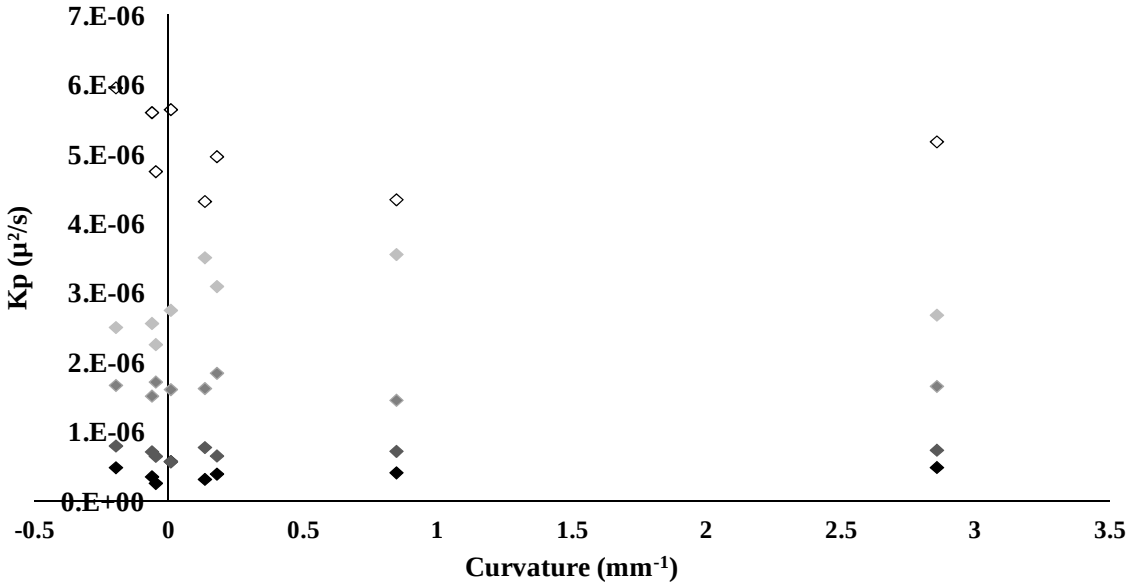

Figure 5.45 Values of kp at 900 (black symbols), 925 (dark grey symbols), 950 (mid grey symbolss), 975 (light grey symbols) and 1000 °C (empty symbols) as a function of curvature.

It was observed that the amount of spinel at 900 and 950 °C reduced significantly for more convex curvatures (Figure 5.46) (Appendix G). The high fraction of spinels in location F, with a curvature of 2.86, can be explained by the relatively sharp trailing edge geometry. Al depletion in this region occurred more rapidly because of diffusion in multiple directions to support TGO growth resulting in more rapid β-phase depletion, spinels form earlier and are at higher concentration than in other areas of the samples.

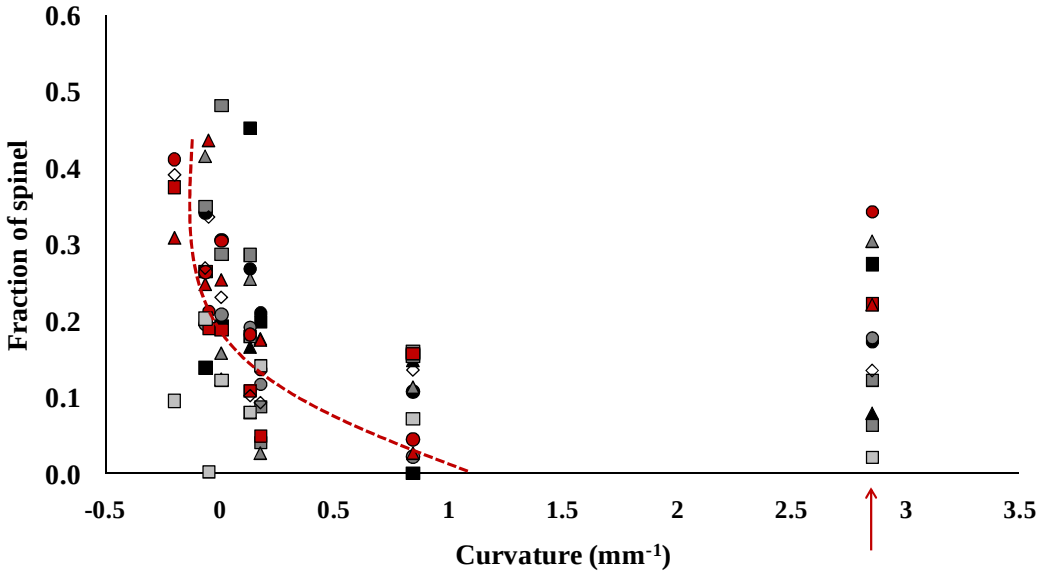

Figure 5.46 Fraction of spinel as a function of sample curvature. Samples oxidised at 900 (black symbols), 925 (red symbols), 950 (mid grey symbols), 975 (light grey symbols) and 1000 °C (empty symbols) for 1500 (diamond), ~ 2700 (squares), 4000 (triangles) and 5000 hours (circles). Red arrow points to the curvature of location F.

5.3.4 Distinction between effect of BC thickness and effect of curvature

The graphs in Figures 5.32 to 5.46 indicate that for more convex curvatures, the BC and TC thicknesses, β-NiAl fraction and spinel fraction all decrease. However, because of the relationship between the BC thickness and the β-NiAl fraction it is not possible to separate geometry effects from BC microstructure and BC thickness itself. To investigate the actual influence of geometry, two regions on the samples, which have approximately the same BC thickness but a different curvature (Figure 5.47), were compared. In this comparison, the temperature and time of exposure were not taken into account but rather the relative behaviour at locations C and D. It was found that irrespective of exposure conditions (Table 5.3) the curvature did not influence the inward Al diffusion (Figure 5.48), the outward Al diffusion (Figure 5.49) or the TGO

thickness (Figure 5.50). However, the fraction of spinels appeared to be greater in location C, in most cases (Figure 5.51).

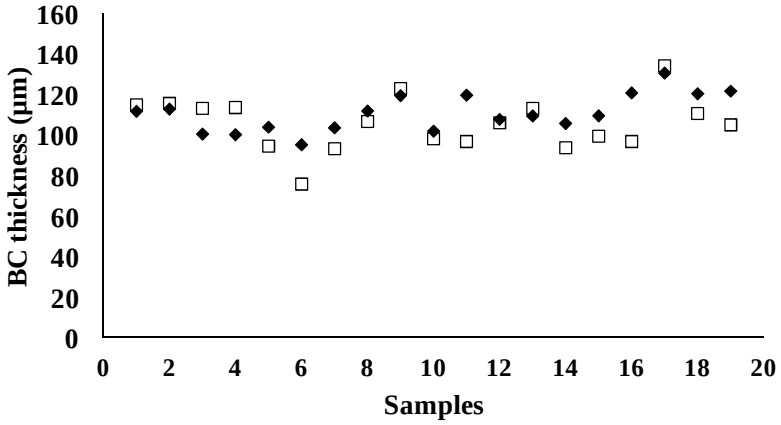

Figure 5.47 Relative comparison of the BC thickness in region C (diamonds) and D (squares).

Sample	Temperature (°C)	Time of exposure (hours)
1	900	2780
2	900	2780
3	900	4000
4	900	7000
5	900	10,000
6	900	15,000
7	900	20,000
8	925	100
9	925	2740
10	925	4000
11	925	7000
12	925	10,000
13	950	2780
14	950	4000
15	950	5000
16	975	300
17	975	2700
18	1000	1050
19	1000	1500

Table 5.3 Oxidation conditions of data used in Figures 5.45 to 5.49.

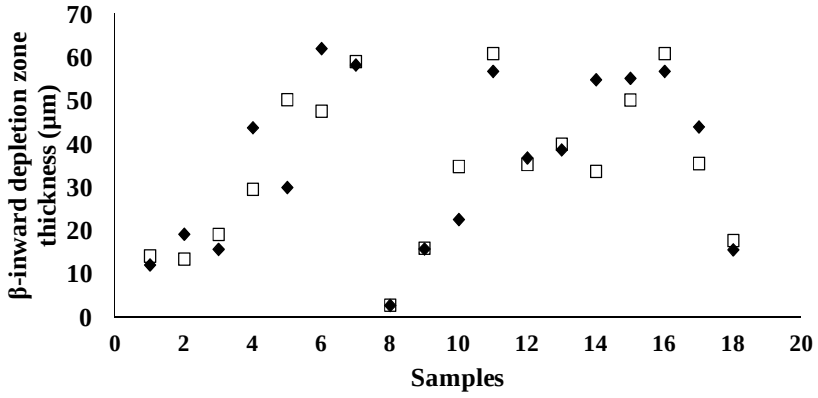

Figure 5.48 Relative comparison of the β-inward diffusion depletion zone thickness in region C (diamonds) and D (squares).

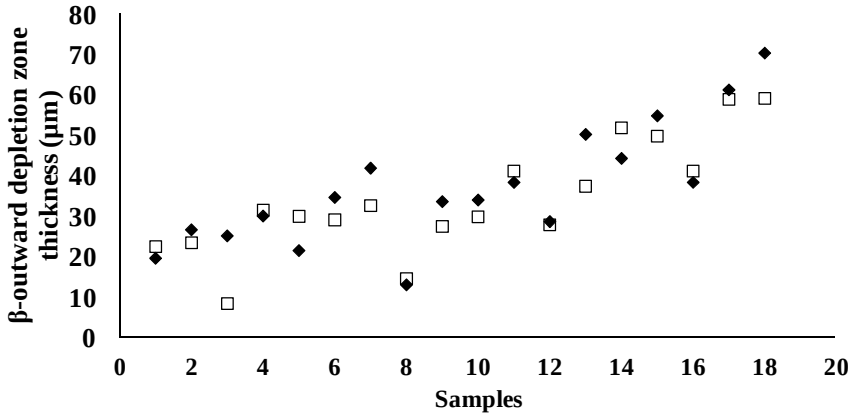

Figure 5.49 Relative comparison of the β-outward diffusion depletion zone thickness in region C (diamonds) and D (squares).

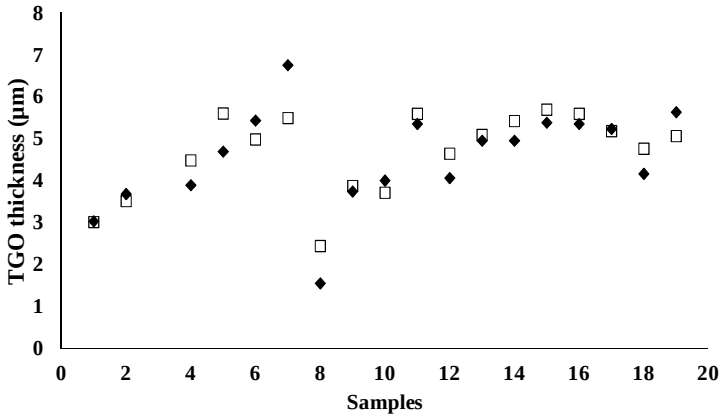

Figure 5.50 Relative comparison of the median TGO thickness in region C (diamonds) and D (squares).

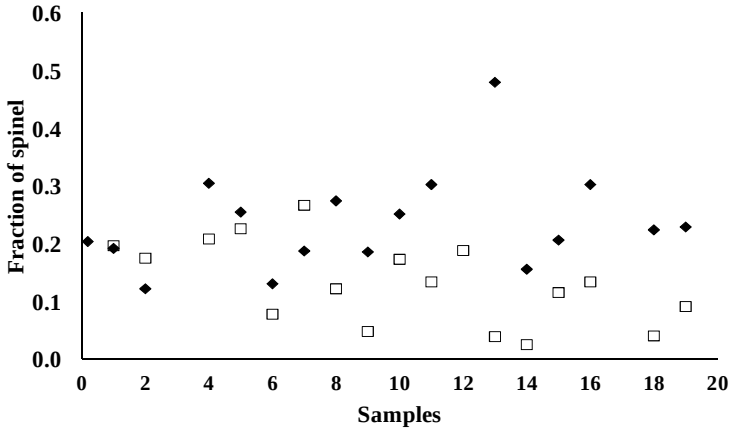

Figure 5.51 Relative comparison of the amount of spinel in the TGO in region C (diamonds) and D (squares).

In Figures 5.47 to 5.51, samples have been arranged by severity of oxidation, plotting the data by increasing exposure temperatures and exposure times. Oxidation conditions of each set of data were summarised earlier in Table 5.3. By considering this table of exposures, further remarks to the effect of temperature and time on the behaviour of the coatings may be made. For example, looking at Figure 5.49, the outward diffusion of Al for the formation of the TGO seemed to be depended of the severity of oxidation. Increasing oxidation temperature and time increased, almost linearly, the depletion in the BC of β-NiAl phase. However, this trend was not followed by the inward diffusion of Al to the substrate which seemed rather parabolic with time for each temperature examined, as seen in Figure 5.48 (ignoring point 8 because of the low exposure time). Finally, the TGO growth reached a plateau when thickness exceeded 5 μm (Figure 5.50). This did not coincide with the linear growth of the outward β-depletion zone in the BC suggesting that an excess of Al was used for other purposes than growing Al_2O_3.

5.3.5 Discussion - Why is spinel and mixed oxide formation influenced by curvature?

Figure 5.52 shows the state of the TGO around the "bump" (location D/E/c) of the modified aerofoil shaped samples after 2740 hours of exposure at 925 °C. Travelling from region D (Figure 5.52(a)), to E (Figure 5.52(b)) and to c (Figure 5.52(c)), the curvature becomes gradually more concave; while the TGO thickness remained essentially unchanged, its undulations and irregularities were observed to increase.

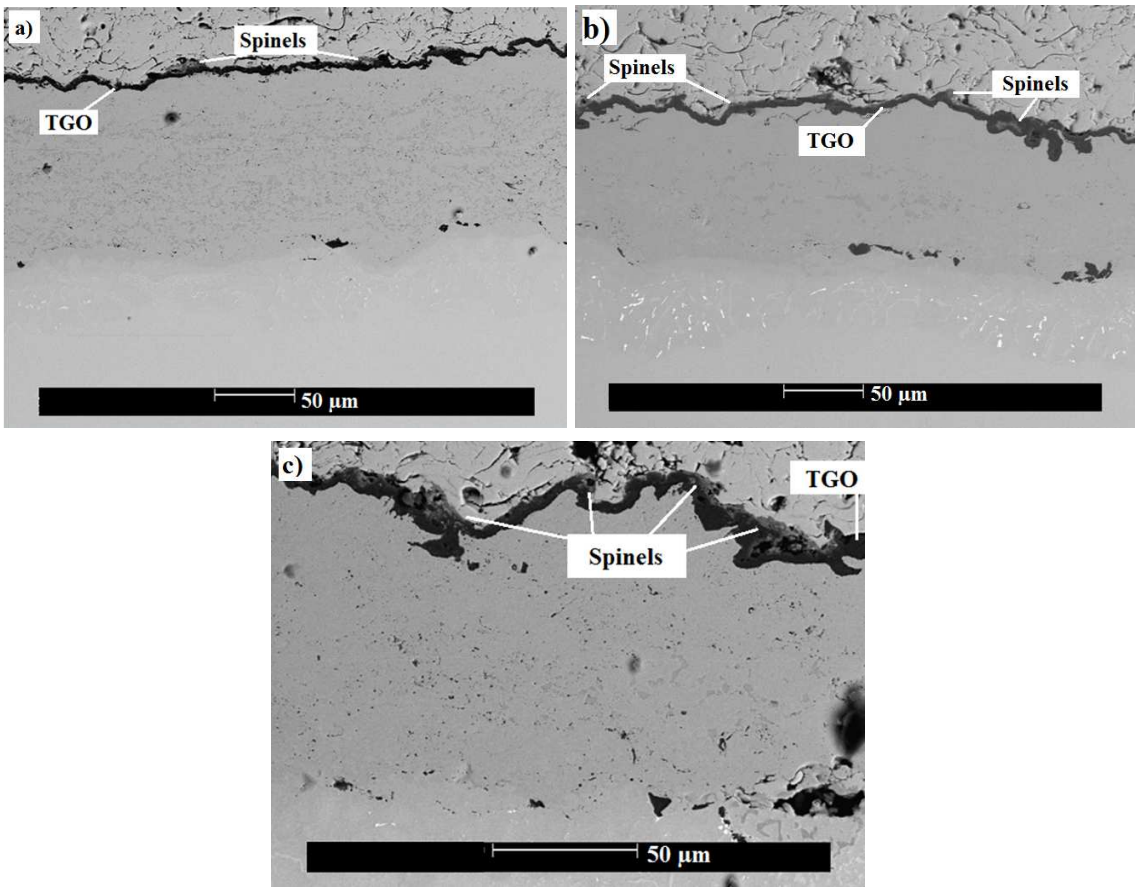

Figure 5.52 SEM images of a TGO and spinels in samples exposed at 925 °C for 2740 hours at (a) location D, (b) location E and (c) location c.

Spinels and/or mixed, less protective, oxides in the form of clusters, were more frequently identified in concave regions. These spinels were observed to form at the

TC/TGO interface as well as within the TGO itself. EDX analysis showed that spinels and mixed oxides growing at the interface contained Ni and Cr as well as Al i.e. $(Cr,Al)_2O_3$ and $Ni(Cr,Al)_2O_4$ while the phase formed within the alumina layer was Ti rich (Figure 5.19). Unlike the TGO, the β-phase outward diffusion zone border did not undulate which could be explained by Taylor et al.'s [74] theory of an accelerated Al depletion in asperities. Naumenko et al. [68] highlighted the influence of TGO roughness on the growth behaviour of various oxides. They found that TGO "peaks" consisted mainly of pure Al_2O_3 occasionally covered with spinel nodules and they associated it with a faster depletion of Y and Al under those regions compared with TGO "valleys". The influence of the geometry of the modified aerofoil shaped samples on the observed fraction of spinels may be associated with the increased undulation of the TGO in the concave locations.

5.3.6 Summary

To summarise, decreasing TC and BC thicknesses as a function of curvature indicated that geometry of the modified aerofoil-shaped samples had an impact on the deposition process of the coating, which in turn also influenced the depletion of the β-phase. However, further investigation showed that this phenomenon was related to thickness of the BC rather than the curvature of the substrate. Concave geometries around the sample (and the sharp trailing edge) seemed to be more prone to spinel formation. The influence of the geometry of the modified aerofoil shaped samples on the concentration of spinels could be associated with an increased undulation of the TGO in the concave locations. This statement however leads to further questions:

- How does BC thickness and TC/BC interface roughness interact with each other?
- Why do spinels/mixed oxides grow more easily in concave region where the Al reservoir in the BC is more important?
- Cracking of the coating system does not appear to happen in concave regions. What factor, more important that the spinel/mixed oxide concentration, reduces the lifetime of the samples as a function of geometry?

Focus needs to be drawn on the mechanisms occurring in different regions of the samples in order to identify the intricate effects of curvature, thickness and roughness on the behaviour of the different layers of the APS/TBC coating system and finally understand why failure location seems dictated by geometry. In parallel, the change of TC structure, and consequent effect on the coating integrity, with curvature needs to be identified. The following sections explore the results and corresponding discussions on a more detailed study of the influence of the roughness of the TC/BC interface and the BC thickness on the behaviour of the TBC system.

CHAPTER VI – INFLUENCE OF BC, TC/BC INTERFACE AND TC MICROSTRUCTURE ON THE BEHAVIOUR AND FAILURE OF APS/TBC

6.1 Influence of Roughness of the TBC/BC interface and BC thickness

This chapter shows how blade curvature influences BC thickness and TC/BC roughness during manufacture and how this affects the behaviour of the system during oxidation. In an attempt to separate the effect of thickness and roughness, thin and thick BCs with various TC/BC interface roughness were characterised. Ultimately, the purpose of this investigation is to show whether BC thickness affects the failure mechanisms of the TBC system and in what way. Samples oxidised at 900 °C were chosen to study the influence of interface roughness and BC thickness, since all mechanisms happened more slowly at 900 °C than at higher temperatures. Also, these samples were exposed for up to 20,000 hours, allowing the collection of more pictures and data to support this analysis.

6.1.1 Roughness as a function of curvature

HVOF thermal spraying has been found to deposit relatively smooth coatings compared to plasma spray techniques (e.g. LPPS or shrouded air plasma spraying) [31]. The TC/BC interface at most locations around the modified aerofoil-shaped samples had small undulations and was relatively smooth as shown in Figure 6.1(a). However, roughness increased greatly on concave sample features (Figure 6.1(b)) (Chapter V). Generally, during manufacture, the spraying gun is programmed to travel around the sample and deposit an equal amount of molten powder in every location. As a molten

particle hits the sample surface, it creates a splat. Around convex sample features, a small part of the splat might spatter the adjacent concave side. That could explain the greater BC thickness as well as greater interface roughness on such concave features. The two SEM images in Figure 6.1 were taken from a convex and a concave region of the same sample. In location c, a concave region, the TGO undulated more and was also highly uneven in thickness. On the contrary, in location D, a convex region, the TGO was relatively smooth and even in thickness.

As the geometry of the sample is the main parameter influencing BC thickness and roughness, the TGO microstructure at locations with different curvatures was characterised in order to investigate the influence of thickness and/or roughness on the diffusion behaviour of the coating system. The volume fraction and size of spinels/mixed oxides in the scale increased the more concave the location (section 5.3). Even early during exposure (4000 hours), their microstructures were more complex than those found at more convex locations (microstructure similar to an example at 950 °C is illustrated in Figure 5.17).

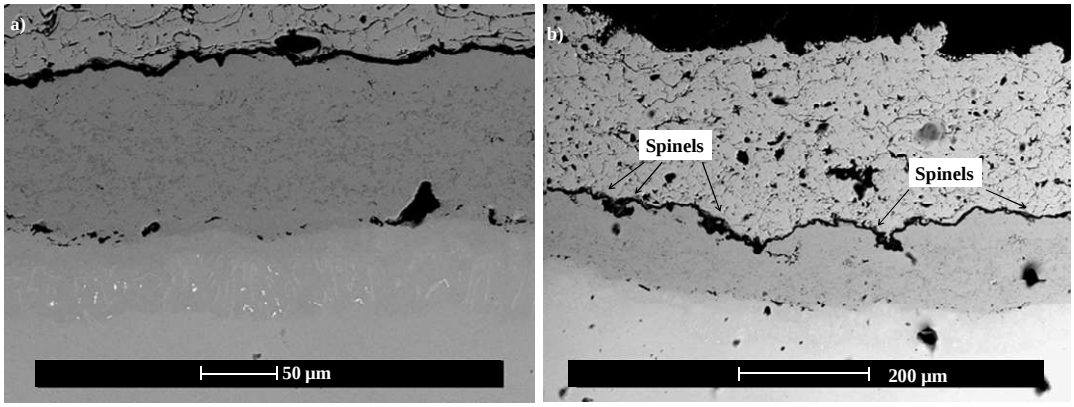

Figure 6.1 SEM images of the TGO and spinels in a sample exposed at 900 °C for 4000 hours. (a) 110 µm thick BC at convex region D and (b) 125 µm thick BC at concave region c.

Thick BCs seemed to be associated with greater roughness and greater roughness was accompanied by the formation of less protective oxides. The high fraction of spinels/mixed oxides suggested that the Al diffusion was also influenced by the roughness of the TC/BC interface.

The growth of Al_2O_3, with large fractions of spinels/mixed oxides in the TGO of thicker BC, was a strong indication that the coating layer was either critically depleted in Al or physically defective. Two phases of spinel/mixed oxides started to appear in the TGO at locations with thicker BC on exposed samples after 4000 hours, when the β-NiAl outward depletion zone measured around 30 µm. On locations with slightly thinner and smoother BCs, two spinel phases were observed after 7000 hours of exposure. In that case, the depletion zone was around 30 µm thick, as well and for these reasons, 30 µm was considered the critical outward depletion width of β-NiAl promoting the chemical failure for this study.

6.1.2 The influence of BC thickness: the case of thin BCs

6.1.2.1 Can β-depleted thin BCs grow an Al_2O_3 scale?

In location B, the BC was only 50 µm thick on average and the absence of the dark grey phase in SEM pictures showed that it was depleted of β-phase after only 2780 hours of exposure at 900°C (Figure 6.2(a)). Critical Al depletion was assumed to have been reached in an early stage of exposure. Because the depletion of the β-NiAl phase is often associated to the formation of less protective oxide according to literature [68-71], it was expected that a high fraction of spinels/mixed oxides would grow in this region of the sample and that chemical failure would ultimately occur very rapidly. However, not only did the sample continue to resist oxidation up to 20,000 hours at 900 °C without

major failure, but from examination of cross-sections, the TGO was found to grow steadily and mostly formed a protective Al_2O_3 scale (Figure 6.2).

Figure 6.3 is a plot of the TGO thickness in the nine locations around the sample as a function of exposure time. The TGO at location B was as thick as the TGO at any other region of the sample, within measurement error. This suggested that the TGO grew at the same rate at location B as around the rest of the modified aerofoil-shaped sample, indicating that the TGO fed on a source of Al other than solely the β-NiAl phase. This source could be the γ-Ni rich phase of the BC and/or the γ'- Ni_3Al phase of the substrate as they both contain Al.

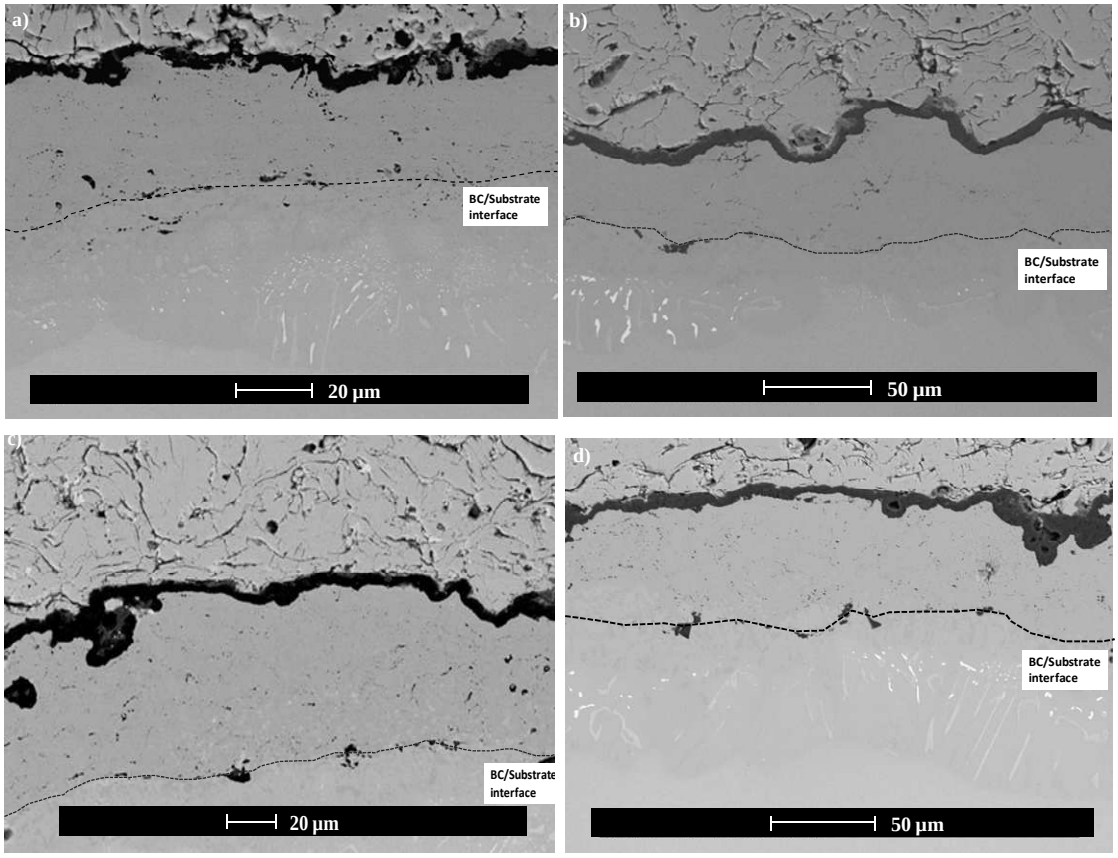

Figure 6.2 SEM images of location B's BC in samples exposed at 900 °C for (a) 2780 hours; (b) 7000 hours; (c) 10,000 hours and (d) 15,000 hours. The BC is respectively 54, 45, 64, and 54 µm thick on average.

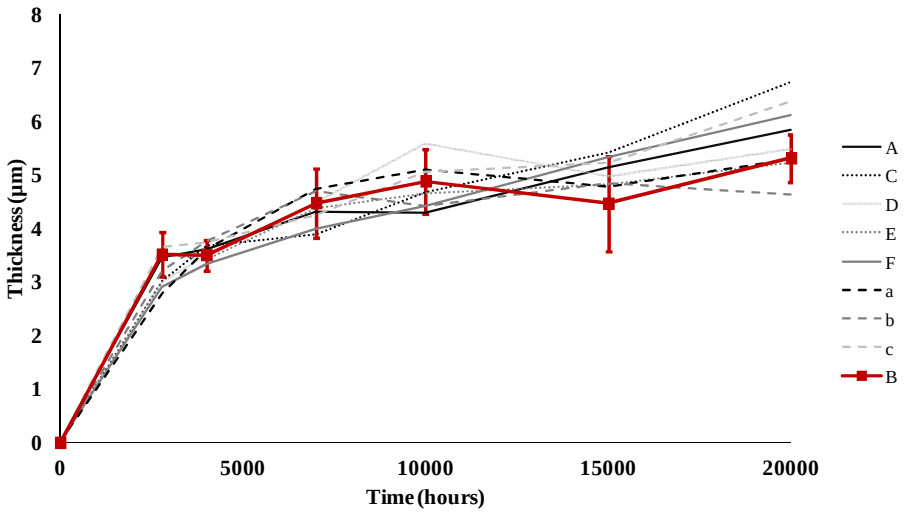

Figure 6.3 TGO thicknesses against exposure time at 900 °C for different locations around the modified aerofoil-shaped samples. Plain, dotted and dashed lines respectively correspond to convex, flat and concave curvatures.

In location F, where the BC was found to measure as little as 20 µm for some samples, the TGO growth followed the same tendency as the other regions. The particular geometry of the trailing edge suggested that Al could diffuse laterally as well as inward and outward. Added to the hypothesis of secondary Al reservoirs, this can explain how the thin coating (20 µm) could maintain its oxide and integrity.

6.1.2.2 In thin BCs, where does the additional Al diffuse from?

The Al concentration EDX line traces recorded across location B's depleted BC are presented in Figure 6.4. Between 7 and 10 points were measured across the BC from the TGO/BC interface to the BC/substrate interface in order to record the amount of Al present in the BC. The amount of Al in the middle of the BC decreased from ~12 at% after 2780 hours of exposure to ~4 at% after 7000 hours of exposure. This tendency was confirmed after further exposure to 15,000 hours. The Al concentration was observed to increase again close to the substrate as a result of the inward diffusion which occurred

in the first stages of high temperature exposure leading to the formation of the SRZ. The continued TGO growth observed in Figure 6.3, despite the low levels of Al in the centre of the BC means that some Al from the γ-phase must have been used to sustain TGO growth and repair it when damaged. EDX analysis performed on other depleted locations around the modified aerofoil-shaped samples indicated that the amount of Al remaining in these depleted areas had generally fallen to around 8 to 10 at%. After 20,000 hours of exposure, no significant reduction of the amount of Al in the BC was found. This implied that the source of Al was not the γ-phase in the BC and that this was also being replenished with the Al from another phase.

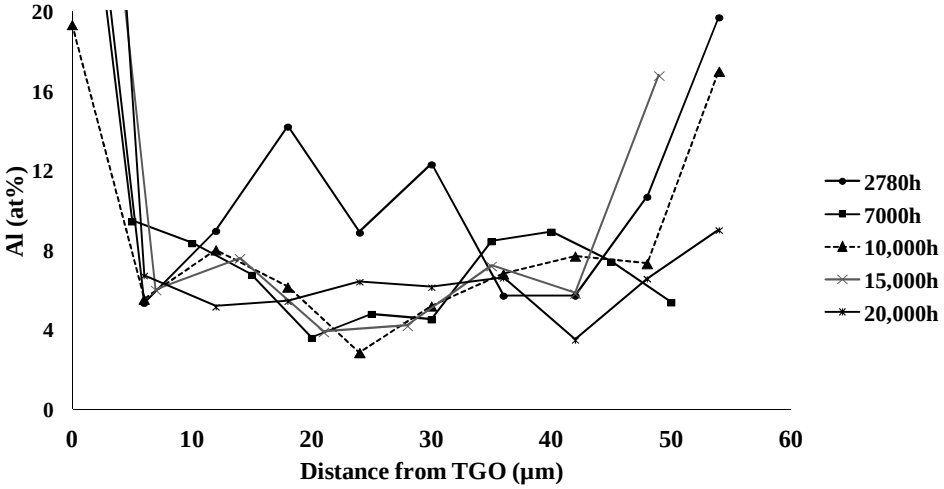

Figure 6.4 Amount of Al (at%) in depleted BCs at location B from the TGO/BC to the BC/substrate interface after exposure at 900 °C for 2780 to 20,000 hours.

The possible source of Al to sustain the TGO growth could be the substrate itself. In section 5.2.2.2, evolution of the SRZ with time and temperature highlighted the existence of a zone rich in γ'- Ni_3Al close to the BC/SRZ interface. Etching of BCs helped identify 3 different phases present in the different layers. β-NiAl left deep pores (appearing black in contrast) in the BC, while γ'- Ni_3Al, in the SRZ and BC could be seen as light grey cavities (Figure 5.21). The presence of the γ'-phase in the BC close to

the BC/SRZ interface (Figure 5.27(a)) indicated either that less Al diffused, transforming β- into γ'- instead of the γ-phase, or that the Al could diffuse from the SRZ back into the BC.

The evolution of the BC in location B with time is shown in Figure 6.5. Before oxidation (Figure 6.5(a)), location B had the same microstructure as other locations around the sample. The BC was made of a γ matrix with β-NiAl precipitates (no γ'-Ni_3Al observed) and the SRZ was composed of a mix of γ, γ', β and TCP phases.

Black inclusions at the BC/substrate interface, caused by grit-blasting before deposition of the MCrAlY, are an indication of the interface between the BC and the SRZ, which is delimited by the red dashed line. After 4000 hours at 900 °C, the BC was depleted of β-NiAl and left a γ/γ' mix, as explained in section 5.2.2.2. In the SRZ, the TCP phase was observed to form further into the CMSX-4 substrate, and this element diffusion left a zone composed of γ' and γ only close to the BC (Figure 6.5(b)). In the BC, the γ'-Ni_3Al phase disappeared after 7000 hours of exposure, due to the inward diffusion of Al into the SRZ (Figure 6.5(c)). Also, the amount of dark grey phase in the γ'/γ zone of the SRZ seemed to increase, suggesting a transformation of γ' into γ. At this point, the BC was only composed of the γ phase, therefore containing very low levels of Al. However, pictures of the BC in location B after 15,000 hours showed that only Al_2O_3 was growing on the BC. At the BC/SRZ interface, propagation of γ'-phase back into the BC could be seen, and this is more evidence for the hypothesis of reversed diffusion of Al back into the BC (Figure 6.5(d)).

To summarise, the TGO grew in locations B and F of the BC for 20,000 hours without critical crack formation, despite complete β-depletion after 2780 hours. As the oxide layer only had a low fraction of less-protective oxides, the low amounts of Al (~4

at%), coming from the γ'-Ni_3Al in the substrate, in the BC/substrate were sufficient enough to grow and heal the Al_2O_3 TGO.

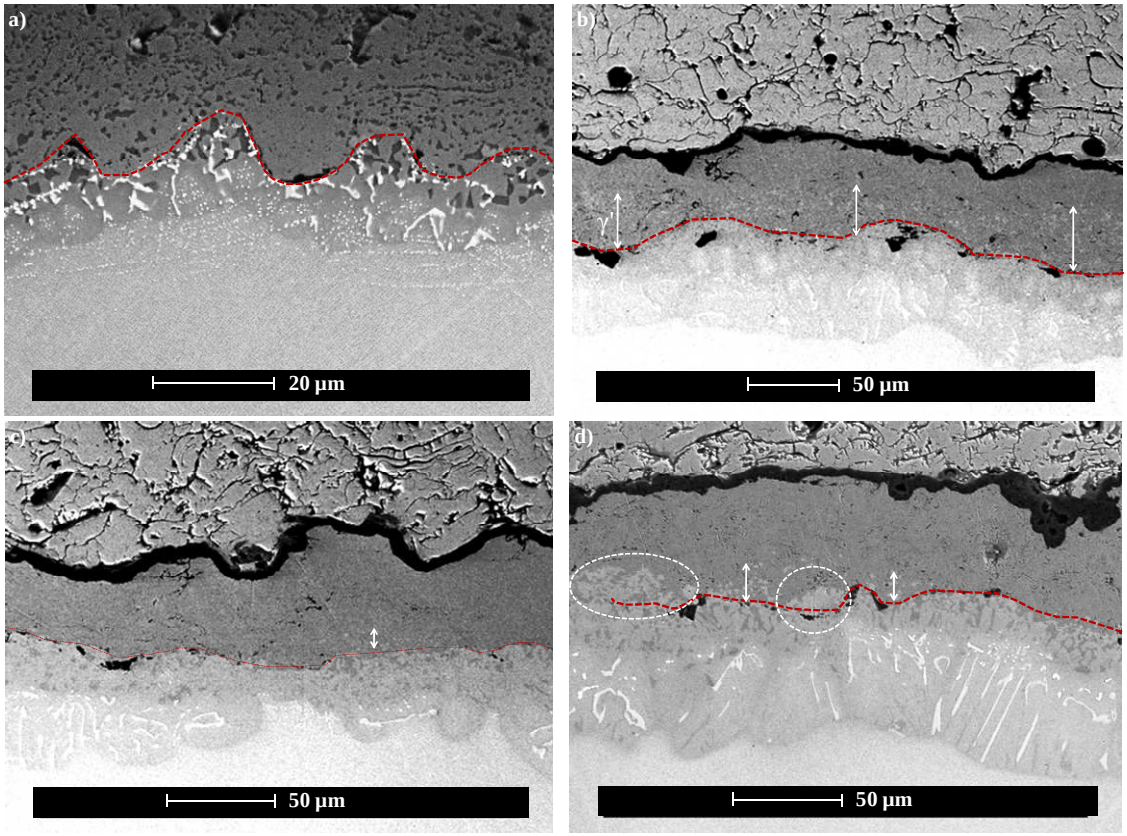

Figure 6.5 SEM images of BC and SRZ at Location B on (a) as-deposited sample and on samples exposed at 900 °C for (b) 4000, (c) 7000 and (d) 15,000 hours. Red dashed line delimits the BC/SRZ interface. White arrows represent the propagation of the γ'-Ni_3Al phase. White circle indicate intrusion of SRZ into BC.

6.1.3 The influence of BC thickness: the case of thick BCs

Thicker BCs were shown to be located in concave areas of samples (section 5.3) and their interfaces with the TC had a high probability of being rougher than other interfaces around the sample. This is why the diffusion behaviour of Al in thicker BCs differs from that observed in thinner BC [126].

Cross-sectional images from samples around areas with thick BCs showed that the inner interface of the outward β-depletion zone did not follow the undulations of the TGO. In Figure 6.6 it can be seen that more Al was consumed under the TGO "peak" (2) than in a place where the TGO did not undulate (1). The TGO "peak" grew protective Al_2O_3 as well as less protective spinel/mixed oxides (circled). Also, while the Al consumed in (1) was used to grow Al_2O_3 only, the Al provided by the same amount of β-depletion allowed a much thicker TGO with spinel/mixed oxides to be grown at (3) and a thinner TGO with spinel/mixed oxides at (4). From a 3D point of view, this difference in Al diffusion might be explained by the 3D roughness of the TBC/BC interface, which increases the surface-to-volume ratio in contact with the supply of oxygen locally. This changes the local Al activity forcing the Al to diffuse in all directions down activity gradients. A lack of Al would result in the growth of less-protective oxides.

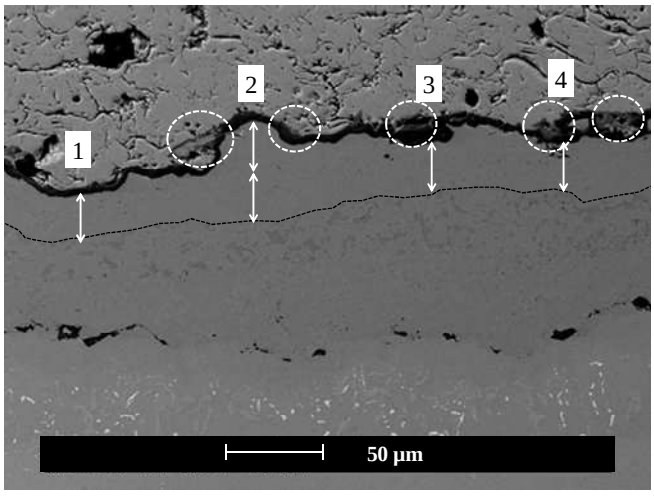

Figure 6.6 SEM image of location C's BC in a sample exposed at 900 °C for 7000 hours. Dashed line indicates limits of outward β-depletion. Dashed circles indicate spinels/mixed oxides. White arrows are used as reference to show the distance between the TGO and the limit of the β-depletion zone.

Grains of the γ- and β-phases in the BC could be observed on etched samples (Figures 6.7 and 6.8). On as-coated samples (Figure 6.7), the γ- and β- phase grains are fine and evenly distributed in the BC but etching with phosphoric acid did not allow the two phases to be distinguished easily.

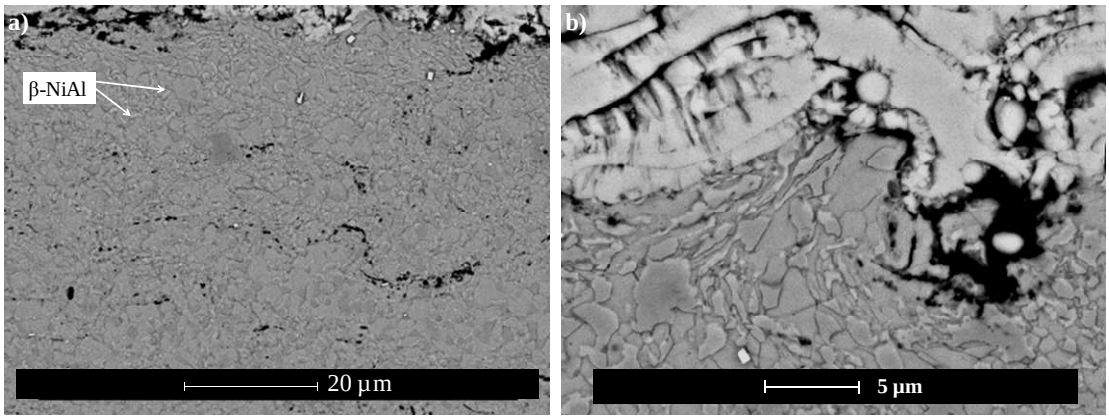

Figure 6.7 SEM image of (a) the BC and (b) the TC/BC interface at location A on as-coated sample etched with phosphoric acid.

At the TC/BC interface, before the formation of the TGO, the grains looked deformed and elongated as if they were following the rough geometry of the interface. This was caused by the HVOF deposition of the MCrAlY, during which the molten particle travels with enough energy to deform the microstructure of the alloy upon impact. After oxidation, as shown in Figure 6.8, the grains generally measured between 1 and 6 µm in diameter. In most cases, smaller grains (all γ-Ni) were present close to the TGO (Figure 6.8(a)) and BC asperities usually contained very fine grains (Figure 6.8(b)).

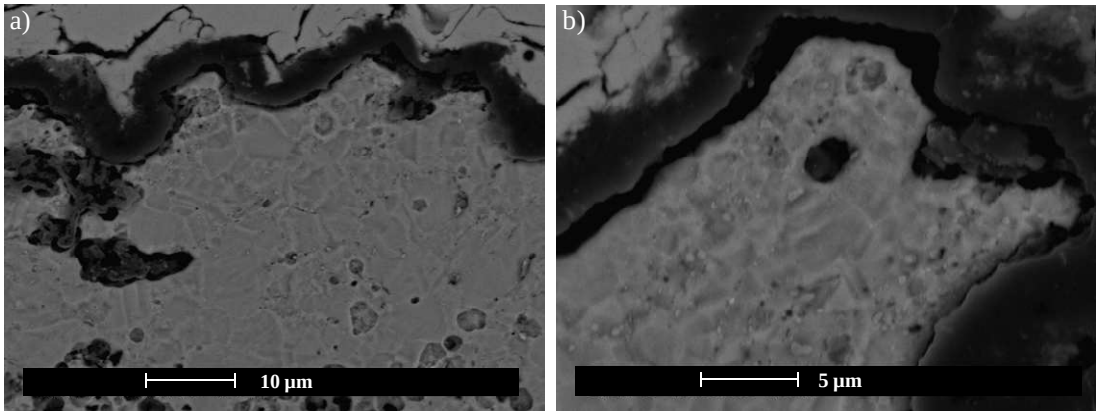

Figure 6.8 SEM image of the BC in (a) location D and (c) location c in an etched sample oxidised at 900 °C for 2780 hours (cracking caused by etching with hydrochloric acid).

6.1.4 FIB results and study of TGO/BC interface grain boundaries.

To look at grain microstructure in more detail a cross-sectional TEM sample of a sample oxidised at 900 °C 15,000 hours taken from location B, was prepared using focused ion beam (FIB) thinning. The location and orientation was chosen so that the FIB lift-outs would comprise three different layers of the TBC system: BC, TGO and TC, enabling both interfaces to be examined on the same sample (Figure 6.9).

In Figure 6.10, the TC appears in dark grey contrast at the top of the image. Beneath it, in light grey contrast, is the TGO whose two microstructures can be seen clearly. Close to the BC, appearing in dark grey contrast at the bottom of the picture, the TGO scale has the typical columnar α-Al_2O_3 microstructure [29,30,68,134] with an overlying fine-grained layer which has been identified in literature as a mixed θ-Al_2O_3-ZrO_2 zone (confirmed by EDX analysis) [128]. EDX analysis of this zone detected ~ 45 at% of Al, ~ 45at% of O, ~ 1 at% of Zr and traces of Cr, Co and Ni. Pores at the TGO/BC interface appeared in a very light contrast in TEM imaging (Figures 6.10 and 6.11). They can also be seen on the SEM image in Figure 6.15.

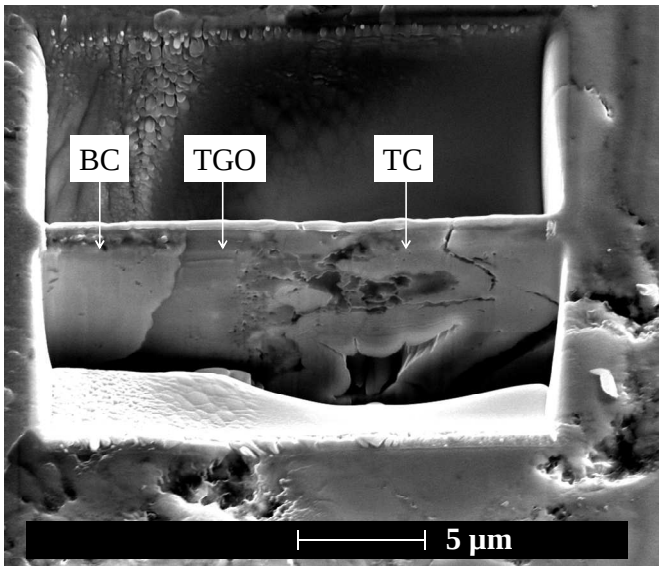

Figure 6.9 FIB image of a lift-out being cut.

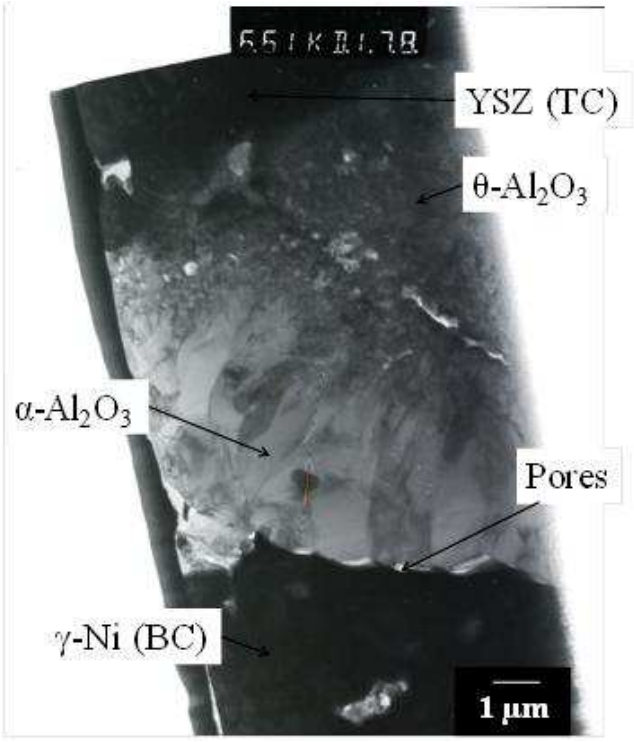

Figure 6.10 TEM image of a FIB lift-out from sample 81-BSYA-8 exposed for 15,000 hours at 900 °C. Light grey contrast corresponds to α-Al_2O_3, dark grey at the top of the image to the ceramic TC and at the bottom of the image to the BC.

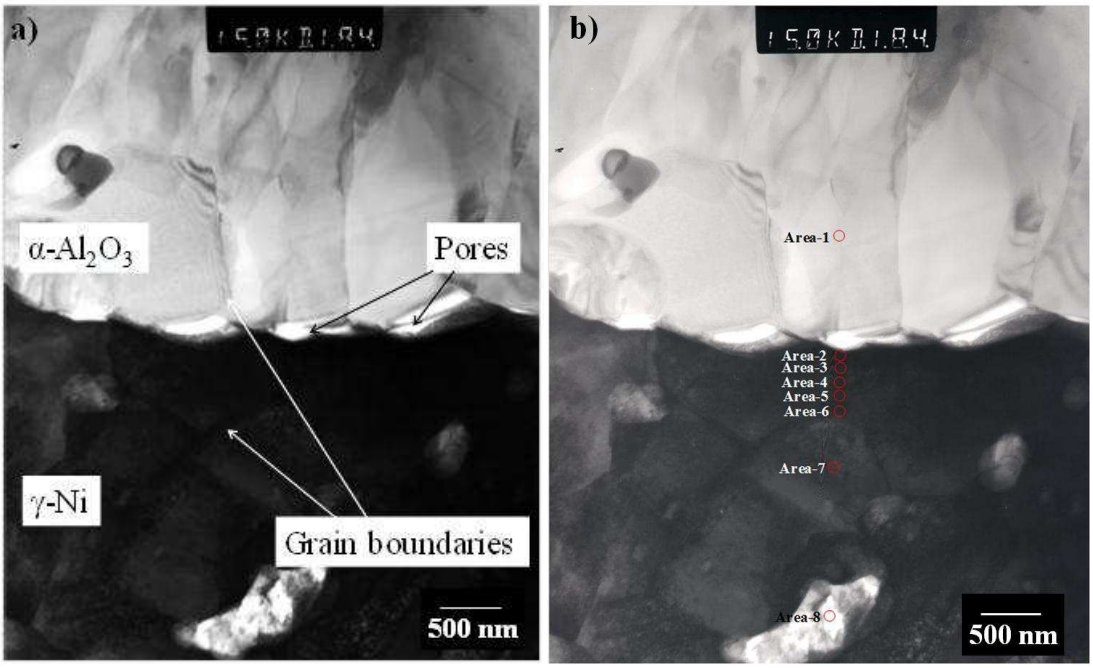

Figure 6.11 TEM image of a FIB lift-out from sample 81-BSYA-8 exposed for 15,000 hours at 900 °C. (a) Light grey contrast corresponds to α-Al_2O_3 and dark grey to γ-Ni. Areas analysed by EDX appear in red in (b).

As well as revealing the TGO's microstructure, TEM imaging enabled the observation of the grains inside the BC (Figure 6.11(a)). These were fine grains measuring around 1 µm. To verify if grain boundaries have a direct effect on an accelerated diffusion of Al, EDX analysis was performed along these grain boundaries as shown in Figure 6.11(b). The aim of these measurements was to check the variation of the Al amount between the grains and their boundaries. Results are summarised in Table 6.1.

Analysis of area 1 in the TGO, confirmed the presence of pure Al_2O_3, containing only traces of Cr and Ni. Moving on to the BC, the amount of Al drastically diminished from 54.2 at% in the Al_2O_3 TGO to 2.6 at%, representative of the γ-Ni phase. The difference in Al values detected using the EDX in the SEM, where around 8 at% of Al was found (Figure 6.4), and the EDX system in the TEM, can be explained by the

reduced depth of analysis in the TEM. Cr, Ni and Co levels were much higher in the BC. Traces of heavy elements, such as Re, W, Ta and Y, were detected as well, but their fraction did not exceed 2 at%. The presence of Zn, S and Si might be contamination of the sample.

	Area 1	**Area 2**	**Area 3**	**Area 4**	**Area 5**	**Area 6**	**Area 7**	**Area 8**
distance from TGO (nm)	**-1000**	**0**	**100**	**200**	**300**	**400**	**900**	**2250**
O	45.0	2.6	2.5	1.9	1.7	2.1	1.8	40.8
Al	54.2	3.6	3.2	2.7	2.7	2.6	2.8	27.5
Cr	0.6	25.7	26.0	26.2	26.3	25.9	25.8	9.3
Ni	0.2	37.0	37.7	37.3	37.7	38.4	37.4	11.0
Co	0.0	27.9	28.3	28.6	29.2	29.0	28.4	8.7
Zn	0.0	1.0	0.0	1.2	0.0	0.0	1.3	0.0
W	0.0	1.5	1.5	1.5	1.3	1.3	1.4	0.0
Re	0.0	0.2	0.9	0.0	1.1	0.9	0.0	0.0
S	0.0	0.5	0.0	0.0	0.0	0.0	0.0	0.0
Ta	0.0	0.0	0.0	0.7	0.0	0.0	0.7	0.0
Y	0.0	0.0	0.0	0.0	0.0	0.0	0.4	0.0
Si	0.0	0.0	0.0	0.0	0.0	0.0	0.0	2.7

Table 6.1 Results of EDX analysis conducted on areas indicated in Figure 6.11.

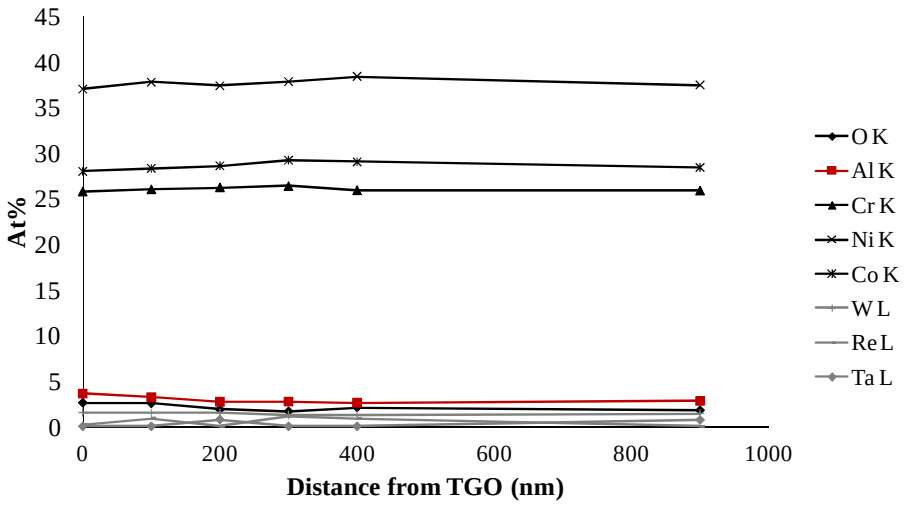

Figure 6.12 Element composition along a grain boundary in the BC.

The graph in Figure 6.12 plots the change of the elemental concentration along the grain boundary, moving away from the TGO and compares it to the composition of a grain (area 7). The horizontal lines show that there was no difference between boundaries and centre of grains, in terms of elemental composition.

6.1.5 Discussion – Difference in Al diffusion behaviour depending on BC thickness.

In section 6.1.2, the study of thin locations around the modified aerofoil-shaped samples, showed that, despite a smaller Al reservoir and the reported possibility of accelerated oxidation because of thinner TCs [116], the TGO grew as quickly as at any other location around the samples. Observation of SEM images at location B, led to the conclusion that after long exposure times Al diffusion from the substrate to the BC could be maintaining the Al flux and thus the integrity of the TGO. Following these observations, a mechanism for Al diffusion in thin BCs is proposed in Figure 6.13. In as-coated samples, the system starts with a BC composed of β-NiAl and γ-Ni phases and a thin SRZ made of β-NiAl, γ'-Ni_3Al, γ-Ni and TCP phases. The substrate is characterised by a dendritic γ + γ' structure (Figure 6.13). Pictures (Figure 6.14) of BCs taken in the transient stage of oxidation showed that in the first stages of oxidation (Figure 6.13(b)), Al from the β-phase diffused outwardly to form the TGO and inwardly towards the SRZ with precipitation of the γ'-Ni_3Al phase being observed towards the BC/SRZ interface. Figure 6.13(b) also shows the γ+γ'+TCP layer being thicker. The microstructure of the SRZ itself did not change much but an increase in thickness (~10 µm +/- 5) was observed. During the steady-state stage of oxidation, corresponding to the growth of stable α-Al_2O_3 above the BC, two β-depletion zones

were observed: one close to the TGO and the other close to the SRZ (Figure 6.13(c)). The outward depletion zone thickened with time and consisted of γ phase, while the inward depletion zone, whose thickness also increased, had a γ/γ' mix. At this point, in the SRZ, the TCP were found to be located further into the substrate, rather than close to the BC interface and α-Cr started to appear. The TCP phase free zone, close to the BC interface, was composed of the γ'/γ phases (Figure 6.13(c)). Steps (b) and (c) were only observed in thick BCs but may have happened in thin BCs too rapidly to be detected within the time steps used. Figure 6.13(d) represents the completely β- phase depleted BC, at which point the outward and inward depletion zones join in the BC. The size of the BC's γ/γ' zone decreased with time as the outward and inward diffusion of Al continued. In the SRZ, the amount of γ phase in the TCP phase free zone increased. Finally, in the case of thin BCs, the diffusion of Al from the BC to the SRZ reversed and the γ'-Ni_3Al phase was observed to form back into the BC (Figure 6.13(e)). Reduction in Al concentration in the SRZ was also highlighted by the increase in γ phase (Ni rich) in the TCP phase free zone. This new source of Al to the BC maintains the growth of the TGO on thin BCs and, therefore, the integrity of thin coating systems. If we consider that the concentration gradient between the BC and the substrate provides a driving force for Al diffusion [128], then the diffusion of Al back into the depleted BC appears likely.

It is believed that TBC systems with larger Al reservoirs have longer lifetimes [129,130]. Al Badairy et al. [129] studied the breakaway oxidation of FeCrAlY wedge samples and observed that an increased Al concentration led to an increase in alloy life. Chemical failure along with crack initiation would always occur at the thinnest part of their samples. They associated an increase of surface-to-volume ratio with an increase

of Al depletion during exposure [129]. Renusch et al. [130] developed a model confirming the effect of the Al reservoir on the system's lifetime. They also proposed a hypothesis that the substrate could provide the TGO with Al. Results shown in section 6.1.2 and Figure 6.13 confirm that, when considering the Al depletion, the BC's γ-phase and the substrate's γ'-phase must also be taken into account.

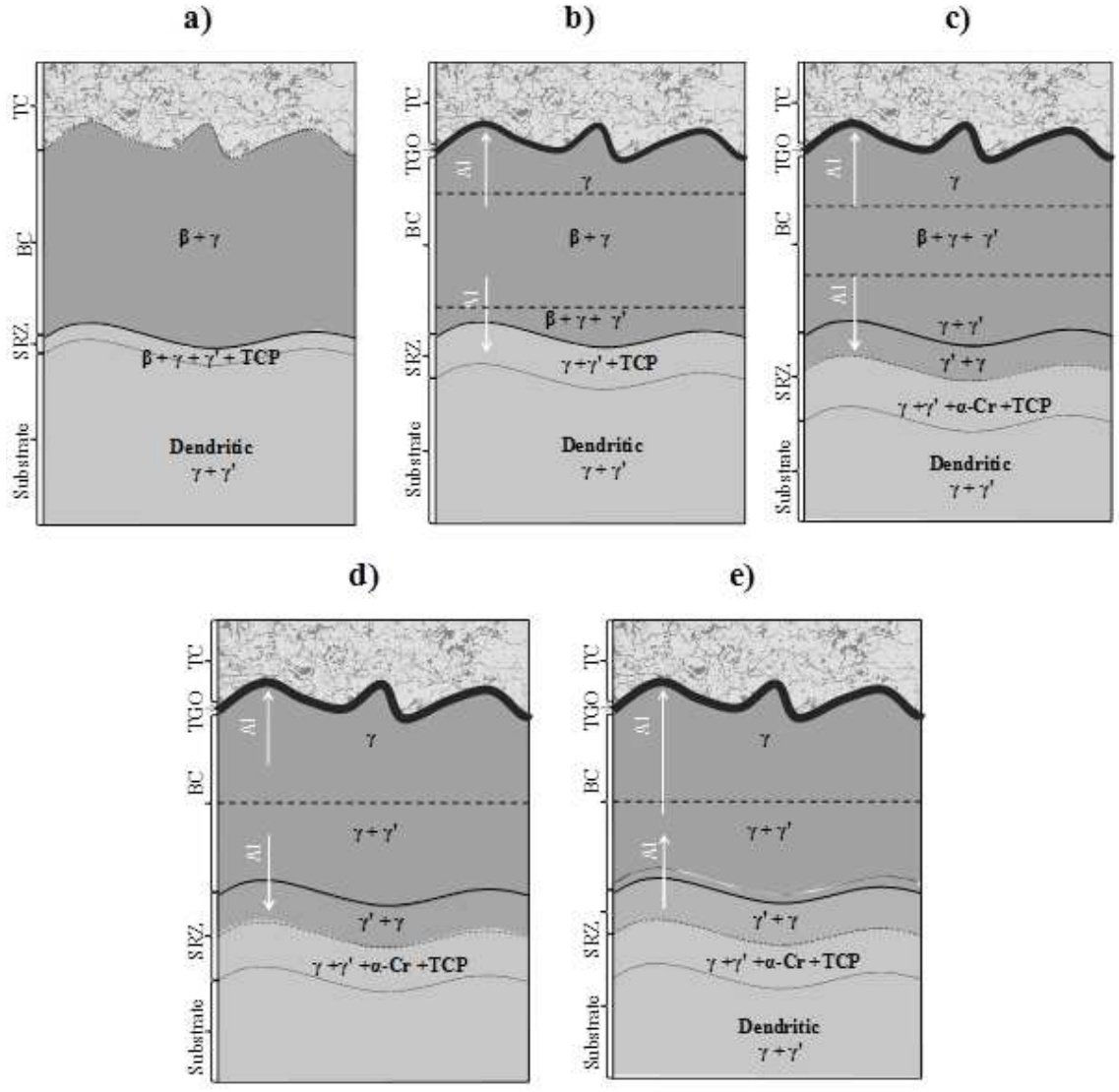

Figure 6.13 Schematic mechanism of the evolution of phases caused by the diffusion of Al in thin BC. (a) Represents the coating system as-deposited, (b) to (d) show the evolution of phases with exposure and (e) illustrates the hypothesis of reverse diffusion of Al after Al depletion of the BC reduces levels to below those in the substrate.

Diffusion of Al from the substrate to the BC does not prevent failure of the system, but only delays its onset. Indeed, cracking of the modified aerofoil-shaped samples oxidised at 900 °C was first spotted on the trailing edge, after 15,000 hours of exposure. It probably initiated at the tip of the trailing edge where the BC and TC were the thinnest. The crack then propagated along the TGO/BC interface by the coalition of microcracks (Figure 6.15).

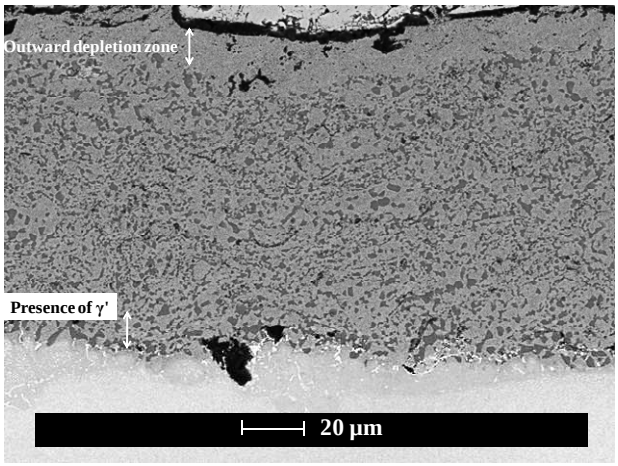

Figure 6.14 SEM image of BC at location C after oxidation at 925 °C for 100 hours. Arrows represent the Al outward diffusion depletion zone and the zone containing γ' close to the BC/SRZ interface.

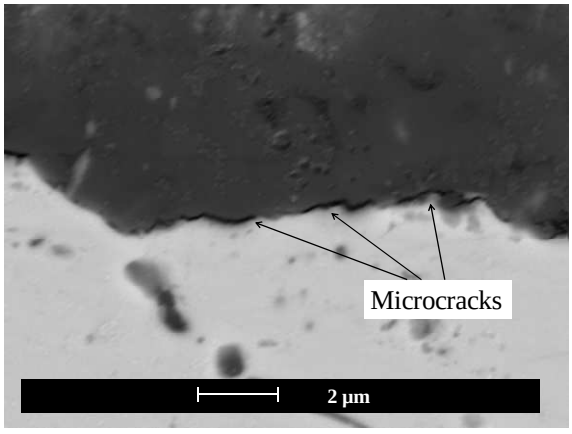

Figure 6.15 SEM image of the tip of a crack propagating at the TGO/BC interface at location F in a sample oxidised at 900 °C for 15,000 hours.

In section 6.1.3, the greater roughness of the BC/TGO interface on the thicker coatings, corresponding to concave locations, was found to locally affect the diffusion of Al. Taylor et al. [74] proposed a model to explain the rapid depletion of Al and the formation of less protective oxides around TGO peaks. They assumed that "the Al concentration was determined by the balance between the flux of Al entering the oxide layer and that arriving at the asperity from the bulk of the coating". The high surface-to-volume ratio at TGO peaks would accelerate Al depletion, resulting in a steeper gradient of Al concentration. Their model predicted the bulk of the asperity could only contain 1 at% Al.

Figure 6.16 shows that this model needs to be reconsidered and that the mechanisms of Al diffusion in rough coatings are more complex than for those with a smooth interface. EDX line scans performed through two BC asperities and into the BC show that the level of Al was constant, within the resolution of the scan, from the TGO/BC interface to the middle of the BC (at around 10 at%). No or very little Al gradient could be observed. Another explanation for the rapid β-phase depletion in BC asperities must be found and the answer may well be held by the grain microstructure of the BC near the TGO/BC interface.

SEM images of etched samples revealed the presence of finer grains close to the TGO (Figure 6.7 and 6.8). Diffusion of elements happens faster when grain boundaries are more numerous. Indeed, the expected bulk diffusion of elements, switches to short-circuit diffusion at the grain boundaries as the size of the grains is reduced. This could explain why Al depletion happened faster in asperities and thus when the TGO/BC interface was rough. Moreover, as Pint et al. [128] observed while studying the relationship between the adhesion of Al_2O_3 and substrate composition, spallation

resistance was affected by the BC grain size. Their results showed that finer grains in the BC were more likely to lead to spallation of the TGO at 1150 °C than similar BCs with larger grains [128].

TEM coupled with EDX analysis did not give any indication on how boundaries affected the diffusion of elements such as Al and Cr only demonstrating that the composition was constant and consistent both within the grains and at the grain boundary. However, it enabled a better view of the TC/TGO (discussed later in section 6.2.3) and TGO/BC interfaces. For this coating system, the chemical bonding of Al_2O_3 seemed stronger with the ZrO_2 than with the MCrAlY and this might explain why cracks appeared first at the TGO/BC interface.

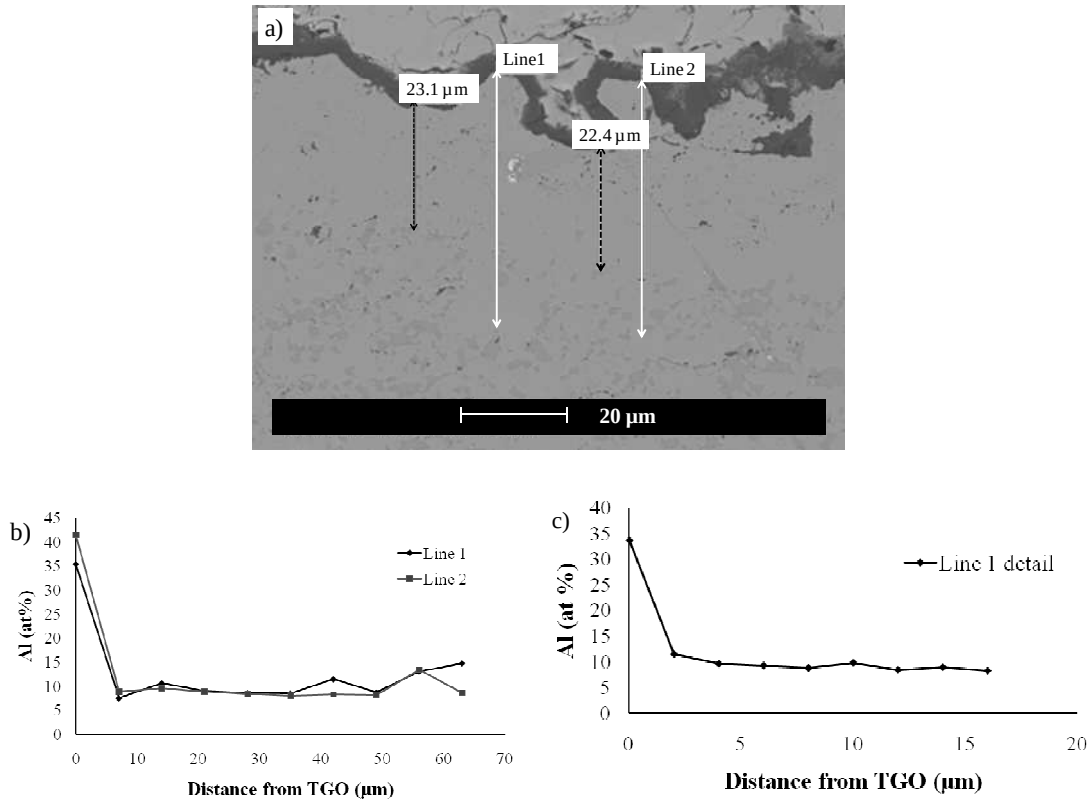

Figure 6.16 SEM image of BC asperities in location D on a sample oxidised at 900 °C for 7000 hours (a) and measurements of Al concentration along Line 1 and Line 2 (b). Line 1 was repeated at higher magnification in (c).

6.1.6 Summary

Thick BCs were observed to be more likely to have spinel/mixed oxide formation, but the BC roughness and TGO undulations in this region were believed to aid the growth of those less-protective oxides. Thin BCs were able to maintain the integrity of their TGO by using Al from other sources after the β-phase depletion (Al from γ-phase in BC and then Al from the substrate).

The depletion of Al at rough interfaces is believed to be eased by the abundance of fine grains in BC asperities. However, this assumption could not be verified using the SEM and the TEM. In general, γ-phase grains were smaller close to the TGO. However, in thick BCs, larger grains were found away from the TGO whereas in thin BCs, grains had the same size from the TGO/BC interface to the BC/substrate interface. This probably explains why Al diffuses more easily across thin plasma or thermally sprayed BC to sustain the TGO layer (Figure 6.8).

Finally, it is important to consider the BC thickness when assessing the lifetime of an APS/TBC system. Thin and thick BCs give rise to different mechanisms of failure (Chapter V). It is essential to study the oxidation of BCs to identify failure mechanisms since the TGO growth and change in microstructure is known to promote interfacial debonding. However, to understand fully the APS/TBC system, it is also important to study the ceramic TC as well.

6.2 Effect of the modified aerofoil-shaped sample's geometry on the behaviour of the TC and the TC/BC interface.

TCs' particular microstructure, composed of deposition splats, inter-splat boundaries, microcracks and pores (Figure 6.17(a)), makes the APS YSZ a delicate material to study. Indeed, the presence of those defects affects local residual stresses, oxygen diffusion and as a consequence, failure mechanisms (as well as heat transfer through the coating). Moreover, the porous microstructure makes mechanistic experimentation difficult and induces a large scatter in results.

Section 6.2 presents the results of the observations of modified aerofoil-shaped samples' TCs and the impact of geometry on their microstructure and behaviour. The main focus is on the ceramic layer as a whole and also on the region close to the TC/TGO interface. As for the work on BCs, the effect of TC thickness and interface roughness is looked at and failure mechanisms (via the propagation of cracks) taking those parameters into account are suggested.

Samples oxidised at 925 °C were used as a representative example because the kinetics of the mechanisms were slow at this temperature and data on the transient stage of oxidation was available (from a sample taken out after 100 hours of exposure). The fast growth of the oxide during the transient stage of oxidation and the large volume change that this involved, between the BC and TC, might result in a particular TC behaviour, and so is worth considering. For this purpose, additional samples provided by Rolls-Royce (section 4.1.3) were exposed at 925 °C for up to 200 hours and the TGO growth behaviour as a function of roughness was investigated (section 6.2.3).

6.2.1 Influence of the geometry on TC microstructure

6.2.1.1 Flat locations

Because of its flat curvature, TC's microstructure at location C was taken as a reference. Figure 6.17 shows the evolution of the TC between 0 and 7000 hours. Features common to plasma sprayed coatings, such as horizontal splat boundaries, microcracks into the splats and pores could be observed (Figure 6.17(a)). 6 deposition layers separated by thick splat boundaries were counted (Figure 6.17(b)). They were created as the powder particles cooled down between each passage of the spray gun during manufacturing. In early stages of exposure (Figure 6.17(c)), a lot of short splat boundaries, microcracks and pores were present in the TC.

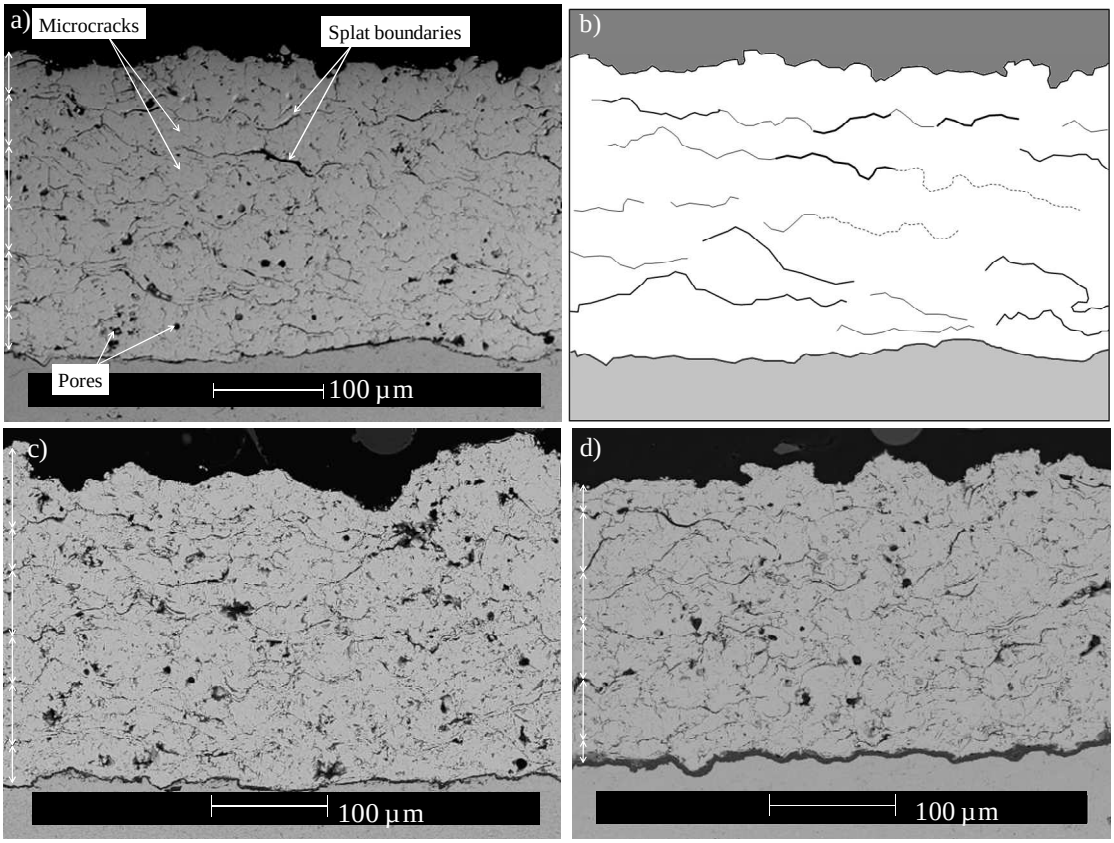

Figure 6.17 SEM image of TC in location C in (a) as-deposited sample and (b) its schematical representation as well as SEM images of samples oxidised at 925 °C for (c) 100 hours and (d) 7000 hours. White arrows on left hand side represent deposition layers.

After 7000 hours (Figure 6.17(d)), the number of splat boundaries decreased but their length increased suggesting the coalescence of those splats, or the formation of cracks linking them together. Also, fewer microcracks and fewer pores indicated a reduction of porosity (slight sintering).

6.2.1.2 Convex locations

The ceramic microstructure in convex areas of the modified aerofoil-shaped sample was different to that found on flat regions, as highlighted by images taken at location A, representative of a sample's convex feature (Figure 6.18). As for areas of flat curvature, 6 deposition layers could be counted. In the early stages of exposure, the ceramic TC contained numerous short inter-splat boundaries that seemed to link together with exposure. Simultaneously, the pores and microcracks, very present in Figure 6.18(a), disappeared with further oxidation. However, unlike flat regions, splat boundaries were not all parallel to the BC surface but present in a more random organisation.

After 7000 hours, cracks started to propagate along the TGO/BC interface of the sample's convex regions. At the same time, the ceramic started to crack vertically, driving inter-splat boundaries of different deposition layers to link together (Figure 6.18(c)). The widening of these vertical cracks, from the BC to the surface, associated with cracking in the TGO, promoted delamination and then the coating system's failure. Wide vertical cracks through the TC were only observed on convex regions.

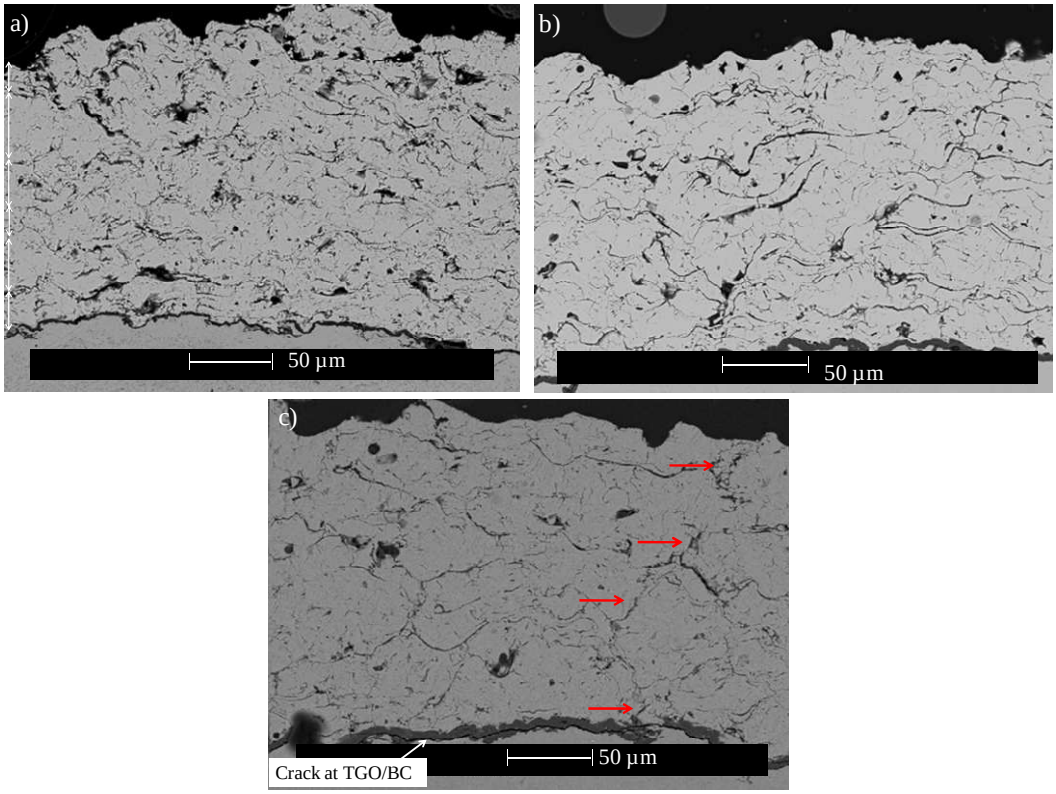

Figure 6.18 SEM image of TC in location A in sample oxidised at 925 °C for (a) 100, (b) 4000 and (c) 7000 hours. White arrows on left hand side (a) represent deposition layers. Red arrows (c) point at vertical cracking.

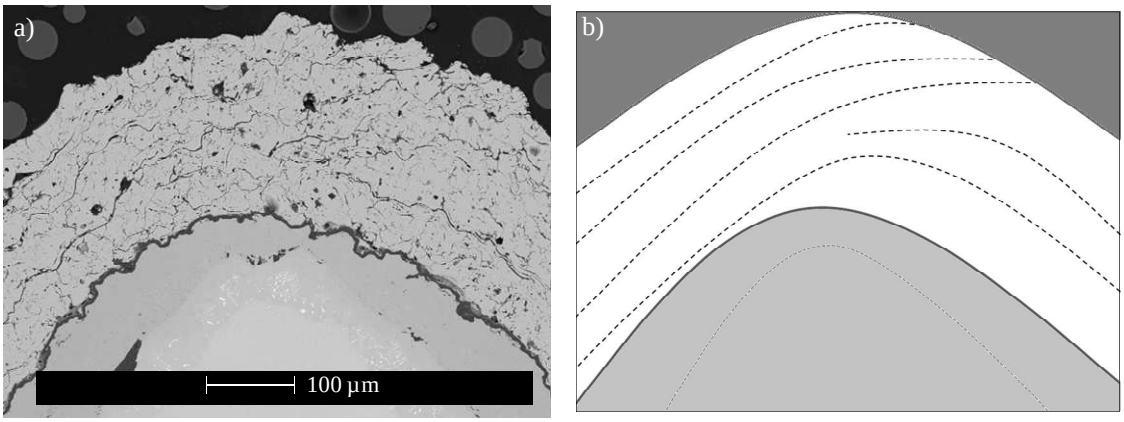

Figure 6.19 (a) SEM image of TC in location F in sample oxidised at 925 °C for 4000 hours and (b) its schematic representation.

Moving on to the trailing edge (location F), where the curvature is extremely convex, the deposition layers, which amount reduced to 5 rather than 6, did not follow

the thin geometry of the blade (Figure 6.19). Instead, inter-splat boundaries linked with the surface. This feature of the manufacturing process was not observed at less convex curvatures (presumably as a result of the motion of the spray gun around the sample). Large inter-splat boundaries or microcracks open to the surface would be expected to ease the propagation of cracks trough the TC at that location and the eventual spallation of the TC during the course of the exposure.

6.2.1.3 Concave locations

Concave curvatures, as explained in section 6.1, have the potential to be rougher than other areas (because of the spraying process).

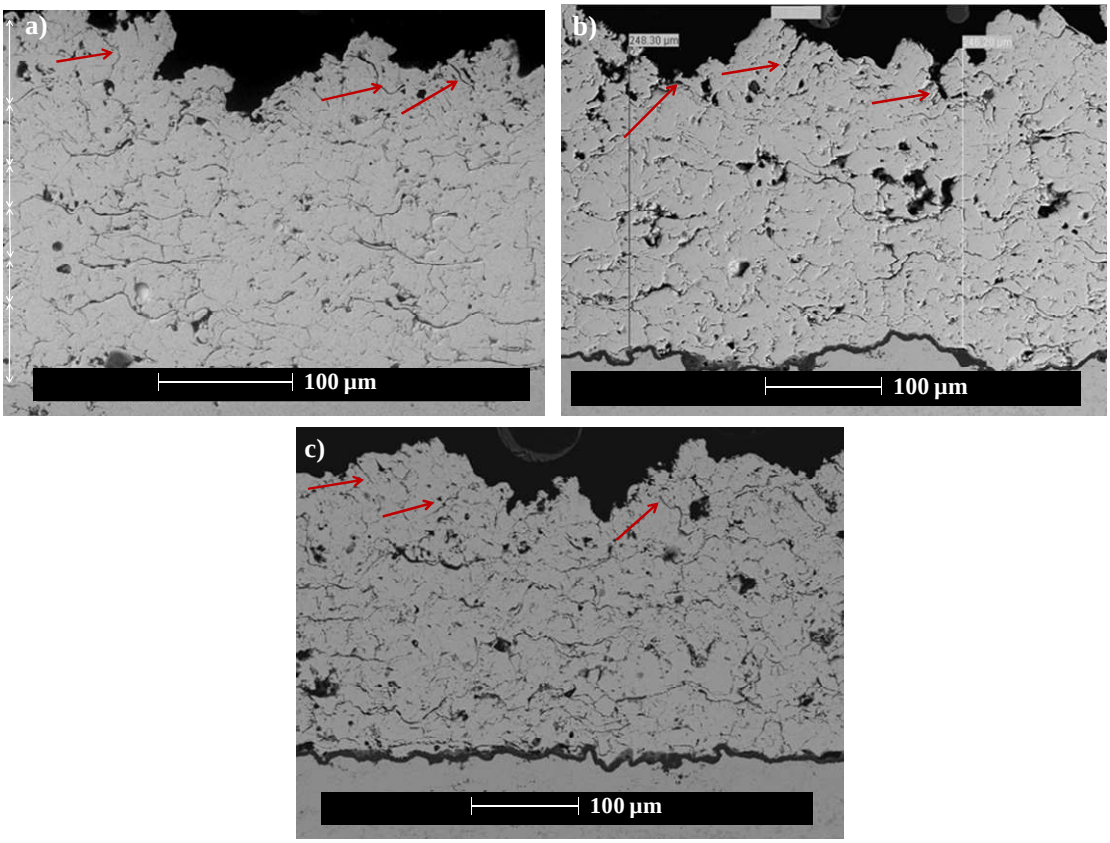

Figure 6.20 SEM image of TC in location a in (a) an as-deposited sample and samples oxidised at 925 °C for (b) 2740 and (c) 7000 hours. Red arrows point at vertical micro cracks.

Counting deposition layers was more difficult because of this roughness, but seemed to be around 6 in most cases. The TC surface roughness amplitude can be seen in Figure 6.20. Roughness seemed to be related to the formation of vertical cracks at the surface of the TC (red arrows on Figure 6.20). During the first 2740 hours of exposure, these vertical cracks grew open (Figure 6.20(b)). After 7000 hours, it was more difficult to observe these cracks, suggesting that a combination of compressive stresses and the concave curvature had forced their closure. The vertical cracks did not propagate to the lower region of the TC. It is not clear if these cracks have a detrimental effect on the lifetime of the coating.

The particular microstructures observed on samples exposed at 925 °C were also spotted on the modified aerofoil-shaped samples oxidised at other temperatures, as is summarised in Table 6.2. Vertical microcracks in concave TCs were present on all the concave locations of every modified aerofoil-shaped sample used for experimentation. The manufacturing features found at the trailing edges were more difficult to observe but were present in most cases. Concerning the vertical macro- cracking of the TC in convex locations; these could not be observed on samples oxidised at 900 °C and most of the ones exposed at 925 °C because they had not reached the end of their life at the time of observation. These preliminary results tend to show that convex features promote the development of critical cracks in the TCs, which eventually lead to failure (section 6.2.4).

Temperature (°C)	Time (hours)	Vertical microcracks in concave TC	Abnormal deposition layers in convex TC	Vertical crack through convex TC
0	0	+	+	+
900	2780	+	+	
	4000	+		
	7000	+		
	10,000	+	+	
	15,000	+	+	
	20,000	+	+	
925	100	+	+	
	2740	+	+	
	4000	+	+	
	7000	+	+	+
	10,000	+	+	
950	2780	+	+	+
	4000	+		+
	5000	+		+
975	300	+		
	2700	+	+	+
	3000	+	+	+
1000	1050	+	+	+
	1500	+	+	+

Table 6.2 Summary of observations of particular features observed in ceramic TCs depending on curvature, made in samples oxidised from 900 °C to 1000 °C.

6.2.2 The TC/TGO interface's microstructure

6.2.2.1 YSZ splats configuration at the TC/TGO interface

In APS/TBC systems, the roughness of the TC/BC interface is one of many factors promoting the failure of the whole coating system. One explanation is that rough surfaces produce convoluted scales with higher out-of-plane stress, contributing to spallation [128] (section 2.3.3.2). To investigate the effect of roughness at the TC/BC interfaces, SEM images at every location around the samples oxidised at 925 °C were compared.

As a result, four types of TC protrusion into the BC were observed. Their microstructures depended on the splat particles layout (Figure 6.21).

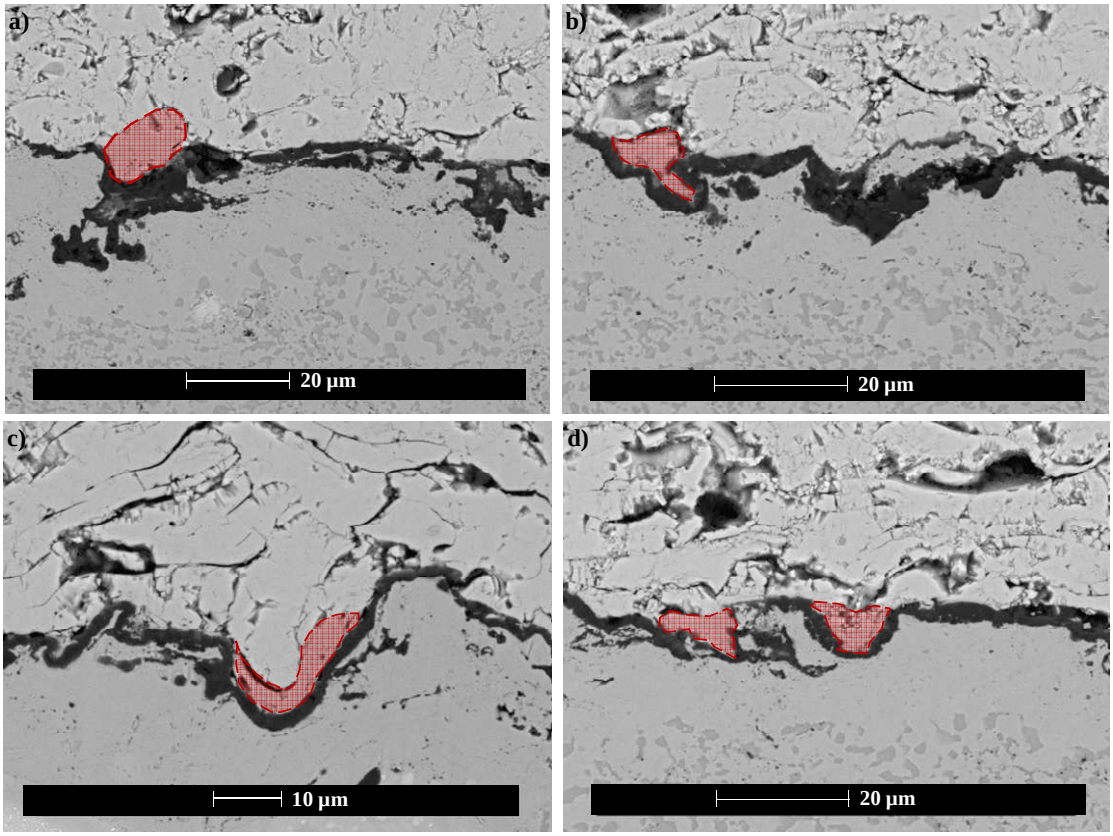

Figure 6.21 SEM image of TC/BC interface from (a) location B, (b) location D, (c) location F and (d) location A, in sample oxidised at 925 °C for 100 hours. Highlighted areas represent YSZ powder particles.

Type 1, in Figure 6.21(a), occurred on deep and broad undulations filled by a single splat particle. This type of protrusion appeared during manufacture when a single molten TC powder particle was deposited on the bare BC. After exposure, the TGO contoured that protrusion. Type 2 protrusions, in Figure 6.21(b), were also filled by a single splat particle but unlike Type 1, the protrusion was convoluted and small. This configuration was the result of an initial rough BC surface on which the YSZ molten particle landed, coupled to TGO growth stresses created during oxidation causing the protrusion to deform and the ceramic to be trapped by Al_2O_3. Type 3 in Figure 6.21(c)

occurred when the protrusion was deep and broad with splats particles following the shape of the BC surface. Unlike Type 1, the particle did not keep a round shape but flattened and elongated. Type 4 protrusions, Figure 6.21(d), were observed to be shallow and narrow undulations filled with one or several small splat particles; with the upper boundary of the splat usually being aligned with the edges of the protrusion. These four types, (and their combinations), describe almost all the kinds of TC asperities encountered at the TC/BC interface. The stresses gradient generated between the TC and the TGO is most likely to differ around various kinds of protrusions, leading to different crack profiles as shown in Figure 6.22.

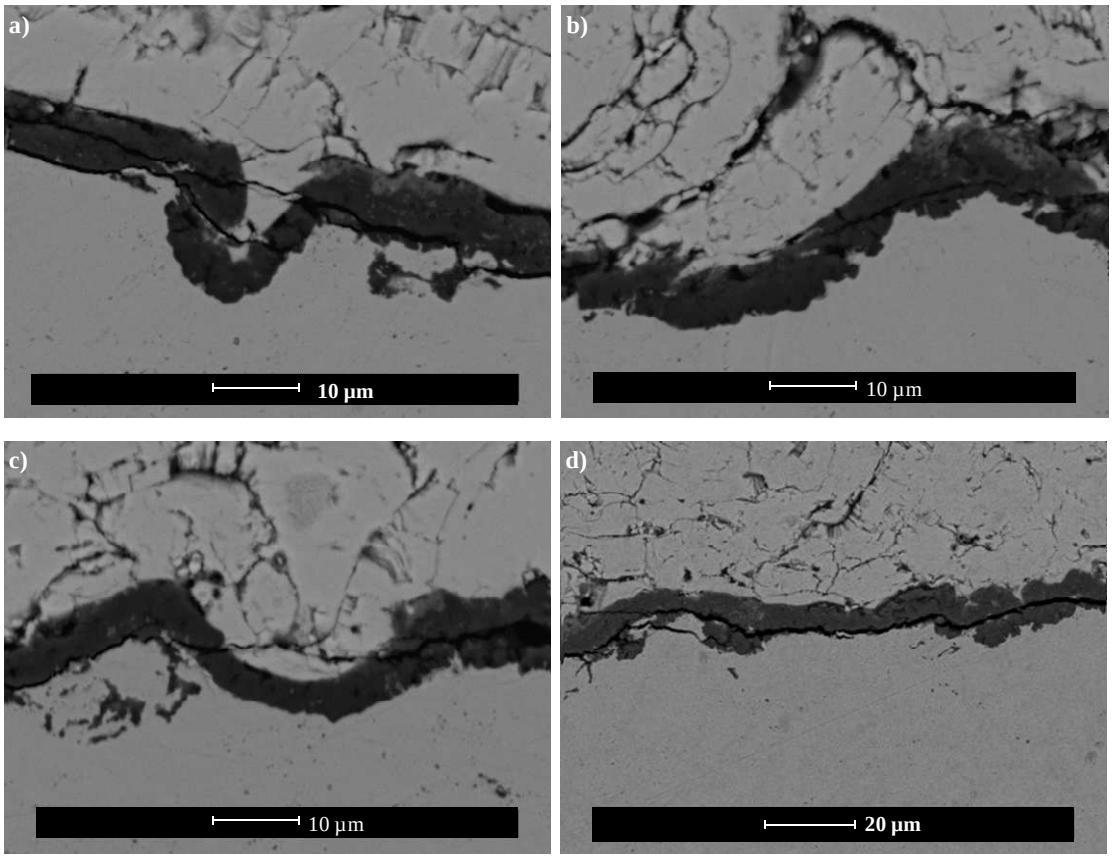

Figure 6.22 SEM image of cracks running into the TGO at TC/TGO in the case of (a) Type 2, (b) Type 3 and (c) Type 4 microstructures. (d) Without TGO undulation cracks were located at TGO/BC interface.

In Figure 6.22(a), Type 2 protrusions caused a crack initially propagating in the TGO (or at the TGO/BC interface, depending on propagation direction), to travel through the TC and caused the ceramic to crack. In the presence of a Type 3 asperity (Figure 6.22(b)), the crack followed the inter-splat boundary and travelled through the TC instead of propagating in the TGO. For Type 4 (Figure 6.22(c)), undulation of the TGO was wider than a Type 2 layout, but acted in the same way. No examples were found of cracks encountering a Type 1 asperity, suggesting that they do not promote the formation and/or propagation of cracks. When the TGO was less rough, cracks would propagate along the TGO/BC interface as seen in Figure 6.22(d).

6.2.2.2 Presence of spinels at the TC/TGO interface

Spinel/mixed oxides change the mechanical properties of the TC and the TGO and reduce the TC/TGO and TGO/BC adhesion [36,50,51,78,79]. Added to the large volume change of those particles at the TC/BC interface, recognised to induce stresses, the Ni, Co and Cr contained in the spinels (especially large ones in concave locations of samples) grew into the TC (infiltrating micro-cracks) and created oxides in the cracks and/or splat boundaries (Figures 6.23(a) and 6.24). It locally increased the amount of stress in the TC eventually leading to cracking into the TC (Figure 6.23(b)).

It was interesting to notice that in almost all of cases, spinels/mixed oxides were connected to a crack/splat boundary in the TC (Figure 6.25). The isolated islands of spinel present into the TC suggested that spinels diffused along such cracks. The oxygen partial pressure was higher in these areas, which could help the growth of spinels instead of Al_2O_3 (Al_2O_3 needs a lower minimum oxygen partial pressure to form

[12]). Although, spinels were associated with cracks, cracks did not always lead to spinel formation.

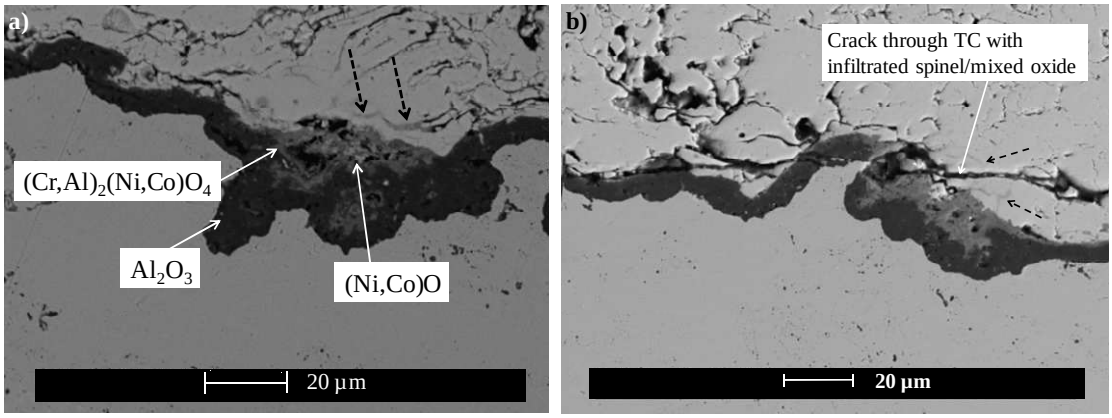

Figure 6.23 SEM image of (a) spinel/mixed oxides in TGO at location b in sample oxidised at 925 °C for 7000 hours and (b) crack propagating through infiltrated TC at location c in sample oxidised at 975 °C for 2700 hours. Black dashed arrows point to diffusion of oxide into the ceramic TC.

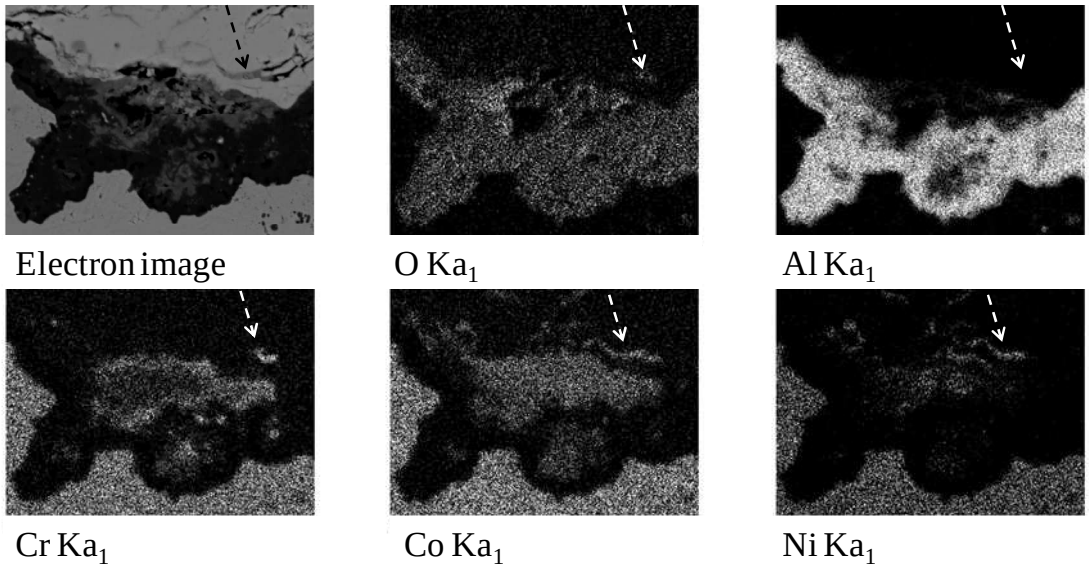

Figure 6.24 EDX mapping of oxide showed in Figure 6.23(a).

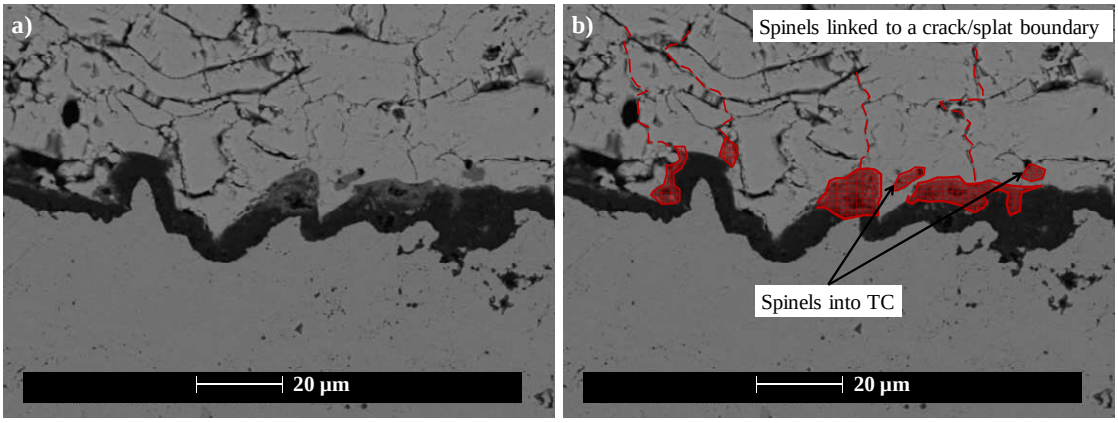

Figure 6.25 SEM image of spinel/mixed oxides in TGO from location a in sample oxidised at 925 °C for 7000 hours. (a) Original image. (b) Red dashed lines are cracks/splat boundaries linked to spinels.

The same features were observed on samples oxidised at other temperatures as summarised in Table 6.3. The different types of TC asperities were not observed at every temperature or exposure time which might suggest that stress states and/or oxidation mechanisms change with exposure conditions (Type 2 asperities) and that some Types of asperities have lower probability to be formed during manufacture (Type 1 and Type 3). Lower temperature oxidation (e.g. at 900 °C) involves longer exposure times which could leave enough time for the TC/TGO and TGO/BC interfaces to accommodate stresses. Also, ceramic TCs oxidised at high temperatures (1000 °C) are more likely to sinter, making it more difficult to observe micro-cracks and pores in the YSZ.

Temp. (°C)	Time (hours)	Type 1 TC asperity	Type 2 TC asperity	Type 3 TC asperity	Type 4 TC asperity	Spinel into TC	Spinel linked to TC crack
0	0	+	+	+	+		
900	2780		+	+	+	+	+
	4000	+	+	+	+	+	+
	7000	+	+	+	+	+	+
	10,000	+	+	+	+	+	+
	15,000		+	+	+	+	+
	20,000	+	+	+	+	+	+
925	100	+	+	+	+	+	+
	2740	+	+	+	+	+	+
	4000	+	+	+	+	+	+
	7000	+	+	+	+	+	+
	10,000	+	+	+	+	+	+
950	2780			+	+	+	+
	4000		+		+	+	+
	5000	+	+	+	+	+	+
975	300	+			+	+	+
	2700		+	+	+	+	+
	3000			+	+	+	+
1000	1050		+		+	+	+
	1500		+		+	+	+

Table 6.3 Summary of observation, made in samples oxidised from 900 °C to 1000 °C, of particular features observed at the TC/BC interface.

6.2.3 Study of the initial stages of oxidation (Rolls-Royce samples)

6.2.3.1 Evolution of TC/BC interface and TGO on Rolls-Royce samples

Additional APS/TBC samples were provided by Rolls-Royce in order to gather more information on the initial stages of oxidation. The areas of main interest were around the interface between the YSZ TC and MCrAlY BC, and the adhesion between the two layers. Moreover, the evolution of the TGO in the first hours of oxidation would provide information on how the microstructures of the TC and the BC influence the

nature of the TGO and could promote the growth of less-protective oxides. These samples were exposed at 925 °C for up to 200 hours (section 4.1.3).

SEM observations of an as-coated sample showed that before exposure a TGO was already present between the TC and BC. This 0.3 to 0.5 µm thick layer was mostly continuous (Figure 6.26(a)), but could become discontinuous in some places (Figure 6.26(b)). This was due to a significant difference between the manufacturing of the Rolls-Royce and modified aerofoil-shaped samples (heat treatment before deposition of TBC). EDX analysis detected the presence of Al (7 to 28 at%), Zr (2 to 20 at%), Co (1 to 13 at%), Ni (1.5 to 14.5 at%) and Cr (2.5 to 13 at%) oxides suggesting that the TGO was a mix of Al_2O_3, ZrO_2 and spinels in various places. Similar mixed oxide layers were observed in the literature between EBPVD/TBCs and MCrAlYs and were found to be caused by the BC heat treatment before deposition of the ceramic [134-137].

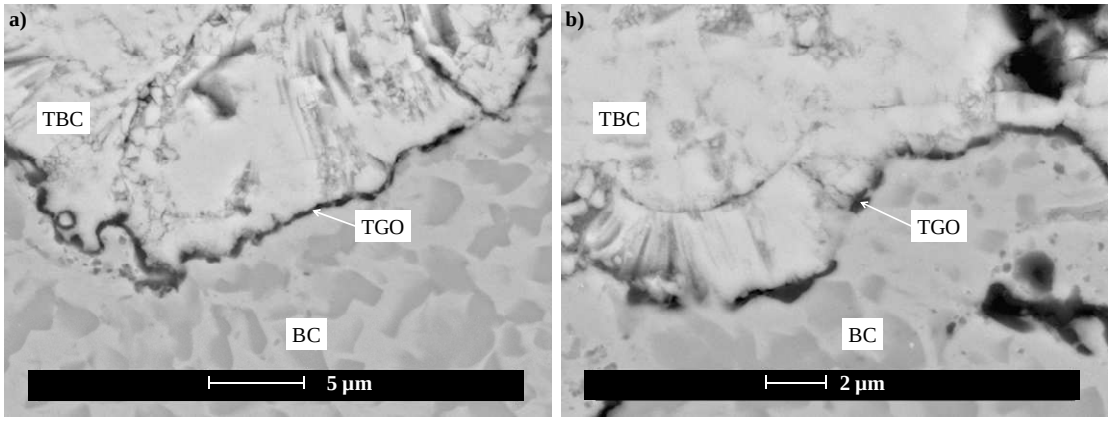

Figure 6.26 SEM images of as-received RR sample, taken at a flat location, showing a (a) continuous and (b) discontinuous TGO between the APS/TBC and BC.

According to Murphy et al. [135], the formation of the Al_2O_3+ZrO_2 mixed zone is promoted by the presence of transient Al_2O_3 (γ or θ). This was confirmed by Levi et al. [135], as well as Jarayam et al. [138], who stated that ZrO_2 is much more soluble in metastable Al_2O_3 than in stable α-Al_2O_3. Indeed, an initial layer of γ-Al_2O_3 could

dissolve and contain up to 17 mol% YSZ; and θ-Al_2O_3 up to 40 mol%. Levi et al. [135] made the hypothesis that Zr and Y were able to slow down the conversion from γ- to α-phases and thus delay the transition between TGO growth mechanisms by Al outward diffusion and O inward diffusion [134]. Exposures in these studies were usually over 1000 °C [134-137], making the solid state diffusion of elements easier between the two layers. However, the Rolls-Royce samples in this thesis were exposed at 925 °C, suggesting that the initial mixed zone was created during a short heat treatment at 1100 °C (carried out during the manufacturing process) and further growth of the mixed zone would be more a physical phenomena (growth of oxides in TC micro-cracks) than a chemical one (interdiffusion of Zr and Al). The thermodynamically stable θ-Al_2O_3 phase present in the TGO at this temperature grew between the micro-cracks in the TC, this creating a fine network of Al_2O_3 and ZrO_2.

In concave areas of the RR samples, what initially appeared to be TGO in some places was just in fact an absence of cohesion between the BC and TC (no TGO) (Figure 6.27). Also, the high roughness of the TC/BC promoted the presence of pores in the BC and at the interface (Figure 6.28(a)).

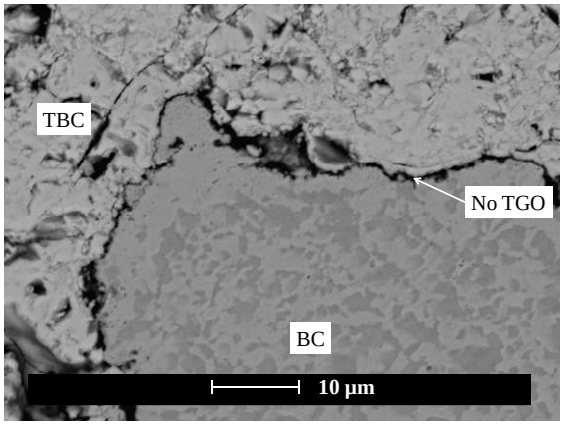

Figure 6.27 SEM image of as-received RR sample, taken at a concave location, showing the absence of TGO between the TBC and BC.

Upon further oxidation, the gradual growth of TGO into big pores at the TC/BC interface caused splats of MCrAlY to be stuck between oxides and ceramic (Figure 6.28(b)). These islands were good candidates to grow spinels with further oxidation. After 150 hours of exposure, they were almost completely depleted of β-NiAl (Figure 6.28(c)).

At the same time, the TGO layer at the TBC/BC interface became more continuous and it reached thicknesses of between 1.5 and 4 µm after 200 hours at 925 °C. SEM images of the oxide layer showed that it was not composed of pure Al_2O_3. Indeed, diffusion of elements from the TBC into the TGO and/or diffusion of elements from the BC into the TGO seem to be occurring according to the network of light contrast into the dark Al_2O_3 (Figures 6.29).

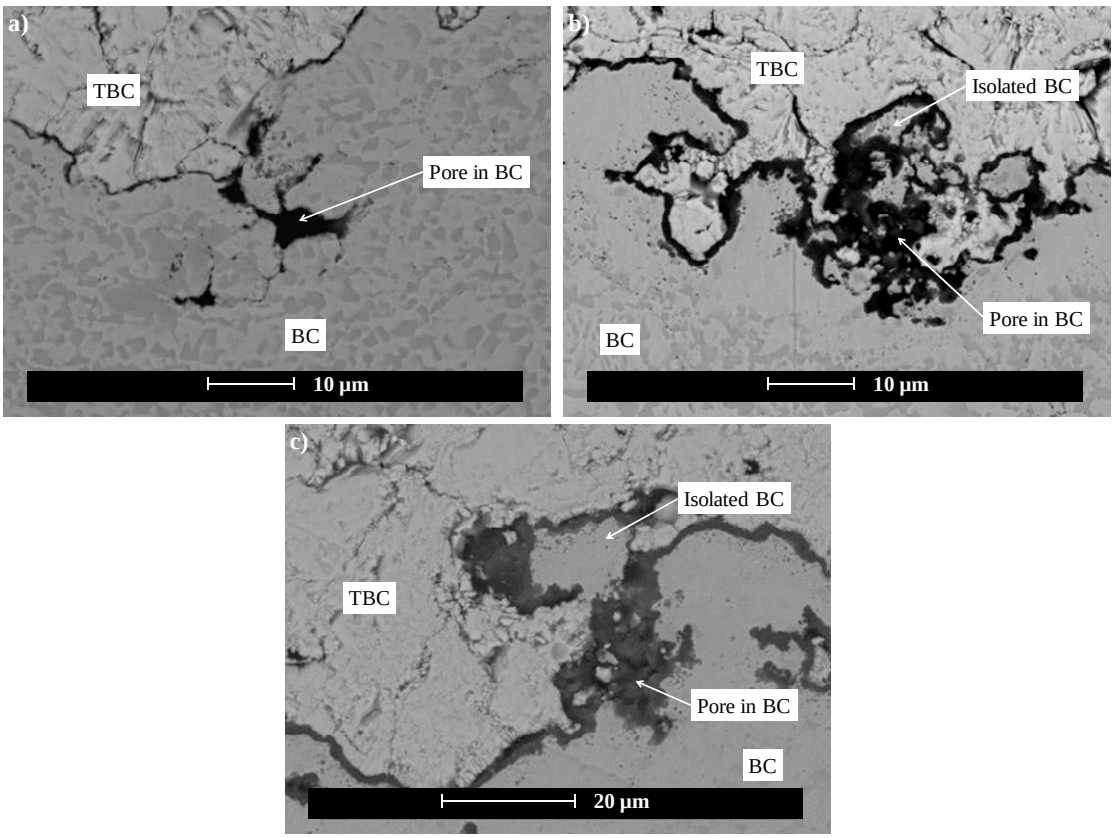

Figure 6.28 SEM images of (a) as-received RR sample and samples exposed for (b) 50 and (c) 150 hours at 925 °C, showing the presence of pores in the BC close to the TBC/BC interface.

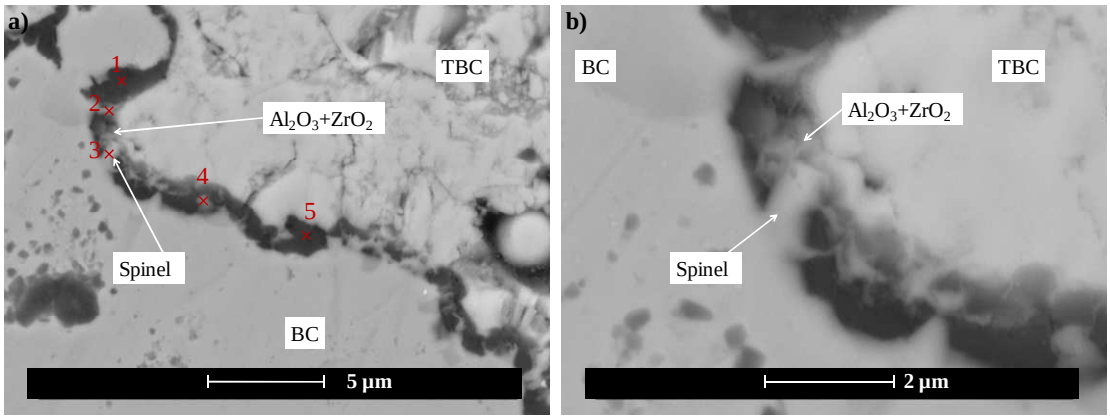

Figure 6.29 SEM images of RR sample exposed for 50 hours, taken at a flat location, of the TGO (a). Image is magnified in (b). Red numbers indicate location of EDX analysis.

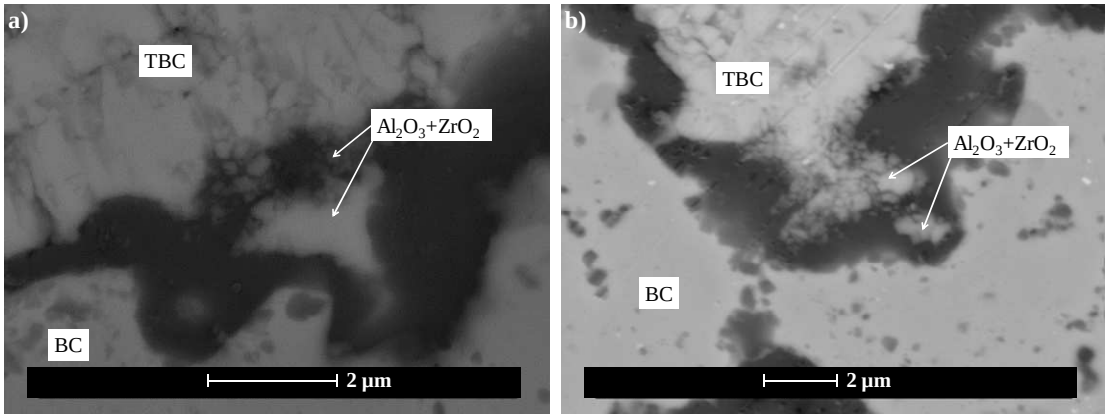

Figure 6.30 SEM images of samples exposed for (a) 150 and (b) 200 hours, taken at a flat location, of the interdiffusion between TC and TGO.

The local roughness of the interface between the TC and the TGO was found to influence greatly the interdiffusion between the TC and the TGO. Indeed, in the presence of fine protrusions of ceramic into the TGO, the Al_2O_3 seemed to infiltrate deeper into the YZS than around areas of lesser roughness or bigger undulations by filling physical holes present in the TC. In some cases, it led to the isolation of TC islands into the TGO as in Figure 6.30(a), or to a protrusion of TC laced with channels

of Al_2O_3 as shown in Figure 6.30(b). The question is: has this mixed zone a detrimental effect on the coating's adhesion and integrity or not? (section 6.2.4)

6.2.3.2 Comparison with the modified aerofoil-shaped samples

The observations made on the Rolls Royce APS/TBC samples were compared to the modified aerofoil-shaped samples, concentrating on features such as the mixed zones, the presence of pores caused by the roughness of the TC/BC interface and the growth of spinels. Some TGO was present on the modified aerofoil shaped samples before exposure at 925 °C. However, it was not continuous (Figure 6.31(a) and (b)) and internal oxidation seemed to prevail (Figure 6.31(c) and (d)) regardless of the location around the sample.

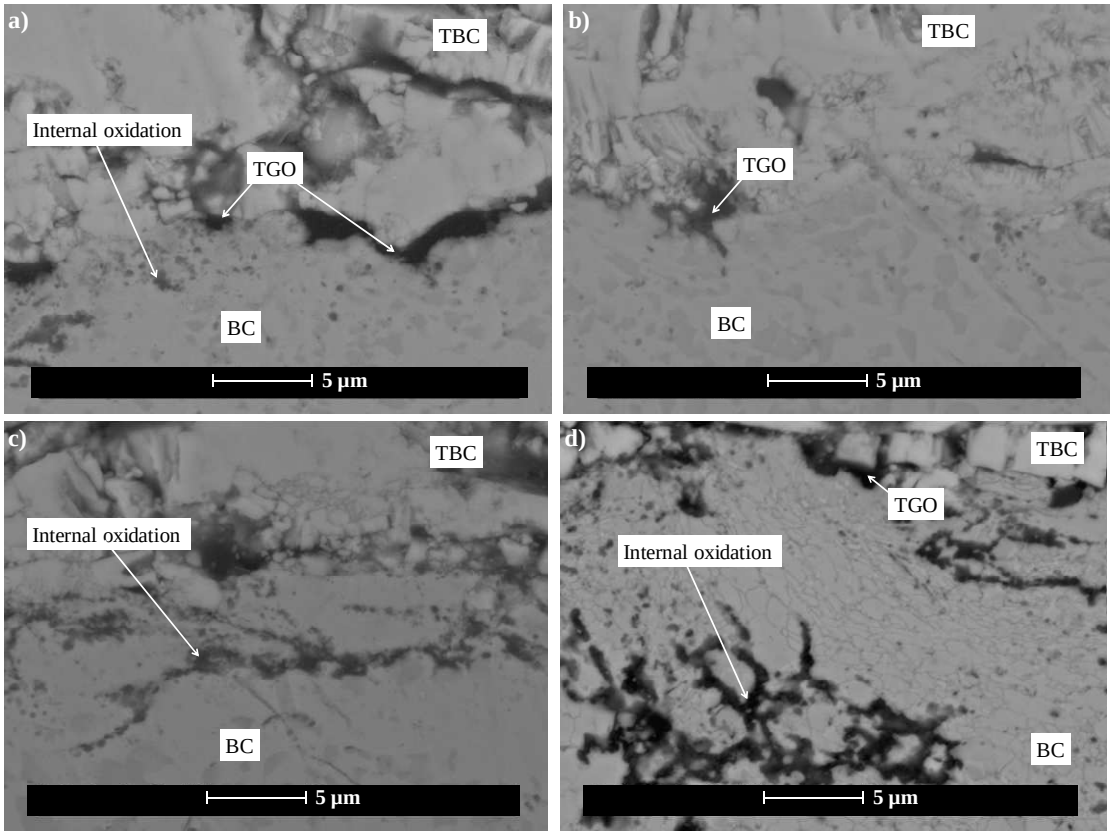

Figure 6.31 SEM images of as-coated modified aerofoil-shaped samples' TC/BC interface at locations (a) B, (b) C, (c) c and (d) F. Sample shown in (d) was etched using phosphoric acid.

This level internal oxidation causes some islands of BC to be isolated from the rest of the MCrAlY with exposure, as seen in Figure 6.32. In the case of the Rolls-Royce samples, the isolation of these islands seemed to be as a consequence of the roughness of the TC/BC interface (Figure 6.28), whereas for the modified aerofoil-shaped samples, it happened around relatively flat interfaces.

The Al_2O_3-ZrO_2 mixed zone was observed on the 925 °C modified aerofoil-shaped sample exposed for 100 hours indicating the presence of transient Al_2O_3 in the first stages of oxidation. Figure 6.33(a) shows that most of the TGO layer was made of the Al_2O_3-ZrO_2 mixed zone. The infiltration of Al_2O_3 into Zr is characterised by its lighter contrast. After longer exposure at 900 °C (comparable to 925 °C), the thickness of the Al_2O_3-ZrO_2 mixed zone was equal or smaller than the one of α-Al_2O_3 and not present all around the samples suggesting that some of it was converted into the most stable form of Al_2O_3. However, some particles of Zr could still be observed in the TGO as well as some diffusion of Al_2O_3 into the TC as shown in Figures 6.33(b) and 6.34.

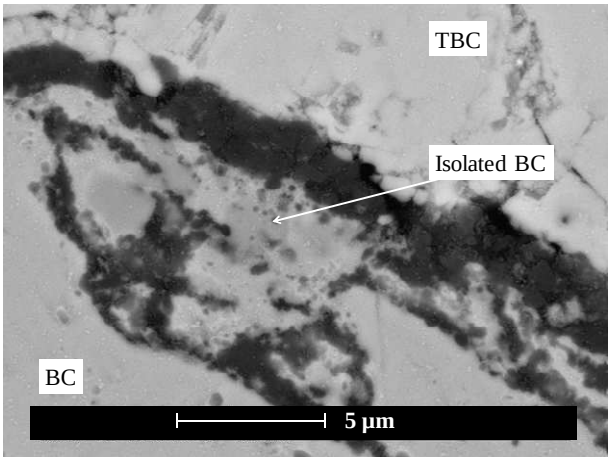

Figure 6.32 SEM image of internal oxidation isolating islands of BC on a modified aerofoil-shaped sample exposed for 100 at 925 °C.

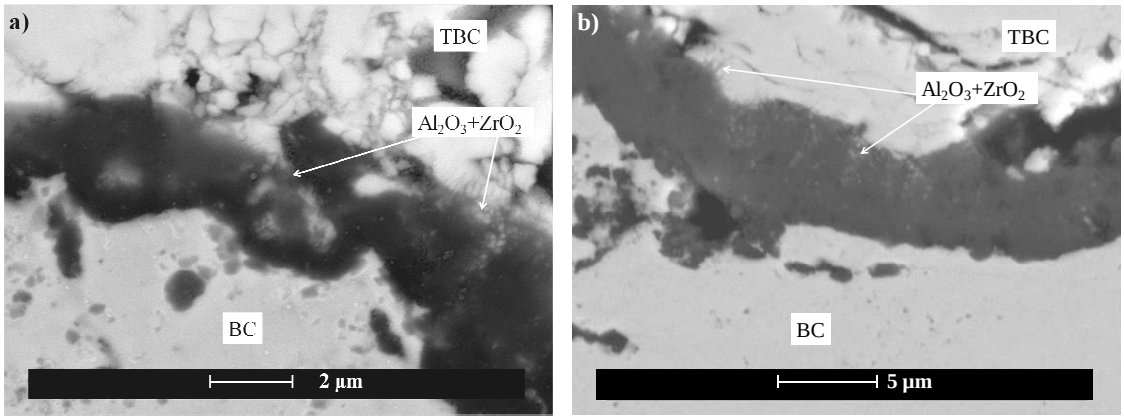

Figure 6.33 SEM images of the interdiffusion between TC and TGO on modified aerofoil-shaped samples exposed (a) for 100 hours at 925 °C and (b) for 7000 hours at 900 °C.

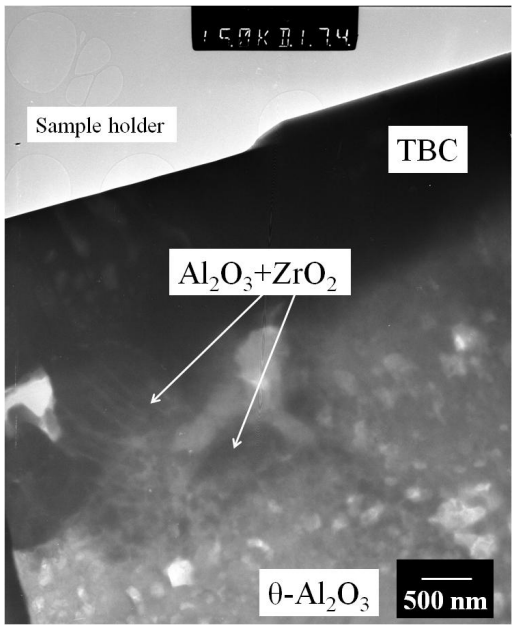

Figure 6.34 TEM image of the TC/TGO interface taken on sample exposed for 15,000 hours at 900 °C.

A series of EDX analysis were carried out along a line through the interdiffusion zone observed on the TEM sample shown in Figure 6.34. These results are summarized in Figure 6.35 and show that the amount of Zr, which initially reached ~45at%,

gradually diminished until disappearing in the α-Al_2O_3. At the same time the fraction of Al gradually increased on going from the TC to the TGO (increasing from ~1 at% to ~45at%). Only traces of Cr, Co and Ni were detected, confirming the absence of spinel in the area investigated.

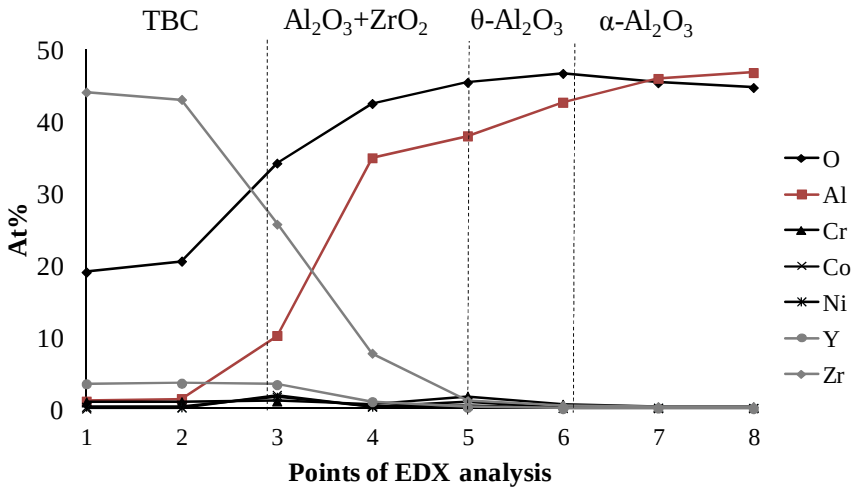

Figure 6. 35 EDX measurements along a line through the TBC, mixed zone and Al_2O_3.

Another feature shared by the Rolls-Royce and modified aerofoil-shaped samples was that pores at the TC/BC interface were filled by the growing TGO (Figure 6.36). After short exposure times big pores were found at the TC/BC interface, as shown in Figure 6.36(a) taken on a sample oxidised for 100 hours at 925 °C. The BC surface around these pores grew Al_2O_3 more or less thick depending on the roughness of the surface. Depletion of the β-NiAl from the BC around these pores was believed to be more important. Also, the pores can be filled with particles of ceramic which become embedded into the growing Al_2O_3. As the exposure continued, these pores were completely filled by a mixed of Al_2O_3 and spinel/mixed oxide, as shown in Figure 6.36(b) taken on a sample exposed at 925 °C for 4000 hours.

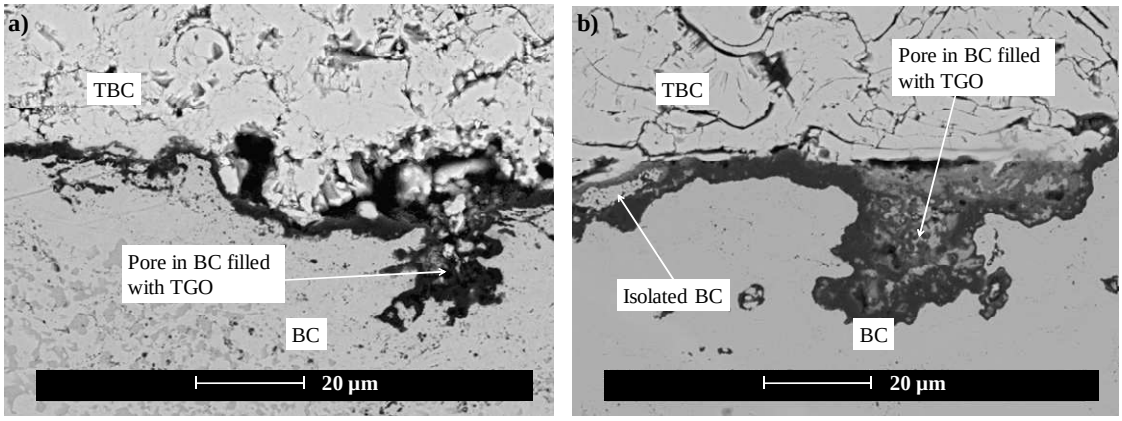

Figure 6.36 SEM images of modified aerofoil-shaped samples exposed for (a) 100 and (b) 4000 hours at 925 °C, of pores between TC and BC being filled by the growth of the TGO.

Comparison of the Rolls Royce and modified aerofoil-shaped samples showed that although they were initially different due to manufacturing processes (a heat treatment growing an initial TGO on the RR samples), similarities were found on samples after exposure for a few hours. These similarities comprised the presence of an Al_2O_3-ZrO_2 mixed zone in the TGO close to the TC, the formation of isolated islands of spinels and the formation of thick clusters of TGO because of the growth of the TGO into large pores between the BC and the TC.

6.2.4 Discussion – The effect of micro and macro geometry on the TC/BC interface behaviour.

Observation of the TC in flat locations on the modified aerofoil shaped samples in section 6.2.1, showed that the amount of small cracks in the ceramic reduced with exposure at 925 °C. Residual stress measurements, on the modified aerofoil-shaped samples, done using Raman Spectroscopy in Bristol University [131], showed that the ceramic was becoming more and more compressive with oxidation. Tensile stresses in

the first stages of oxidation could promote the appearance of pores and the creation of microcracks while compressive stresses (caused by the growth of TGO and thermal cooling) later during exposure explained the closure of microcracks and pores. The linking together of TC splats indicated stress relaxation. Thompson and Clyne [132] also observed an increase of stiffness with exposure to temperatures higher than 1000 °C, divided in two stages: a rapid initial increase followed by a more progressive rise. This change in mechanical properties was associated with sintering of the ceramic [75]. Generally expected at temperatures above 1400 °C, sintering was detected at temperatures as low as 800 °C [133].

The macro-geometry of the substrate seemed to greatly affect the microstructure of the TC which in turn affected parameters such as stress generation and relaxation, crack initiation and propagation, as well as the transport of oxygen. Irregularities in manufacture, caused by the different curvatures around the modified aerofoil shaped samples, produced ceramic coatings with varying thickness and roughness which eventually promoted the localised generation of vertical and life limiting cracks. Moreover in literature, thin TCs were found to enhance the gas permeation of oxygen because of a greater density of interconnected microcracks shortening diffusion paths [116] which would eventually affect the oxidation rate of the system. Spallation of the ceramic did not happen on concave regions of the samples (observed through pulse flash thermography in section 5.1). Failure happened first on the convex features of the sample, and then propagated along the flat curvature (suction side). Propagation through the concave locations was more difficult and always happened last. To understand fully how cracks were created in the coating system, it was necessary to study the TC/BC

interface which micro-scale topology is now well known to affect the way cracks initiate and propagate.

On the effect of local TC/BC interface roughness, Singh et al. [90] observed the damage evolution at the TC/BC interface of a similar TBC system and found that damage was preferentially initiated in areas where the ZrO_2 protruded into the BC because of the different stress state of the ceramic and Al_2O_3 layer. Combination of the compressive stress in the TGO and the tensile stress in TC protrusion (because of shrinkage caused by sintering), made the convoluted interfaces preferred damage initiation sites. They added that spallation occurred through the linkage of micro-cracks rather than because of the rapid propagation of a single crack [90].

In line with the findings of Singh et al. [90], the investigation of the BC/TC interface was focussed on TC asperities into the BC. In section 6.2.2, 4 recurrent TC asperity types were found to affect the crack propagation at the TC/TGO interface (Figure 6.22). Figure 6.37 is a schematic representation of the 4 asperity types. The red arrows represent the crack paths observed on SEM pictures. Type 1 did not allow cracks to propagate through the TC. The large asperity, the absence of short splat boundaries, and the unlikely formation of micro-cracks, made the propagation of a crack difficult into this asperity. In that case, the crack would be expected to travel around through the TGO. It is highly likely that Type 2 allowed a lot of stress to concentrate in a small area of the TC. Micro-cracks often developed in the asperity's convoluted space and cracks propagating in the TGO continued their path at the splat boundary as well as across the fine strip of ceramic. The large undulation encountered in Type 3 did not stop cracks from propagating at the splat boundary. However, if that splat boundary was too far away from the TGO/TC interface (bringing them closer to Type 1), cracking occurred in

the TGO. In Type 4, again a lot of stresses were gathered within the asperity causing the formation of micro-cracks. A propagating crack from the TGO would travel along the splat boundary at the edge of the asperity. The linkage of microcracks with the asperity was also observed. Finally, in the absence of undulation, the cracks propagated mainly at the TGO/BC interface or in the middle of the TGO (Figure 6.22).

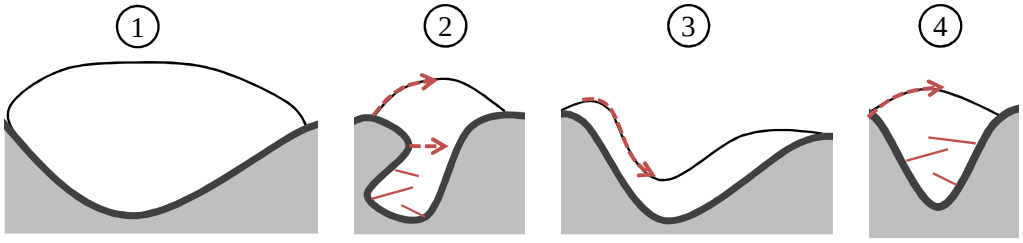

Figure 6.37 Schematic representation of YSZ splats configurations found in TC protrusions into the BC. Red arrows and lines are potential cracks paths.

The residual stresses around the different types of protrusions were measured by D. Liu as part of a collaborative work done between Bristol University and Cranfield University on the modified aerofoil-shaped samples. It was found that the local geometry had a large effect on the stress interaction between the TGO and the TC resulting in large stress mismatches and leading to a physical stress accommodation (closure or opening of micro-cracks in the TC) or to debonding of the two layer and crack imitation. The nature of the TC/TGO interface (pure Al_2O_3 or a mix of Al_2O_3-ZrO_2) greatly affected the stress accumulated in the two layers. In a general manner, it was found that the protrusion of TC into the TGO resulted in a large residual stress difference between the two layers which, when reaching a high value, led to cracking, either in the TC or at the TC/TGO interface depending on the local geometry.

Work done by Karadge et al. [139] can help explain how cracks propagating at either the TC/TGO or the TGO/BC interface manage to link when they encounter highly

convoluted features in the oxide layer (Figure 6.22 (a) and (c)). Karadge et al. [139] studied the microstructure of the oxides growing in EB-PVD and APS/TBC systems and found that cracks nucleated either at the TC/TGO or at the TGO/BC interfaces, but were able to traverse inter-granularly across the TGO thickness around severely rumpled geometries (in the case of EB-PVD/TBCs). Also, their research showed that the texture of the TGOs in APS/TBC systems led to large inter-granular stresses that could explain micro-cracking in the oxide layer [139].

Added to the local undulation of the interface, the presence of an Al_2O_3-ZrO_2 mixed zone in the TGO, affected the integrity of the APS/TBC system. At temperatures over 1000 °C, because of the rapid transformation of the γ-Al_2O_3 and θ-Al_2O_3 into α-Al_2O_3 [53], the mixed zone is only formed during the early stages of oxidation and is therefore very thin [134-137]. However, between 900 and 1000 °C, transient and stable forms of Al_2O_3 can thermodynamically co-exist [53], thus enabling ZrO_2 to stay dissolved into the TGO. The TEM images of a sample exposed at 900 °C for 15,000 hours in Figures 6.10 and 6.34 showed the large fraction of mixed zone present in the TGO. Moreover, the mixed zone was found to form more easily around fine protrusions of TC into the TGO (Type 2) which would be expected to have a large affect on the stress states at the TGO/TC interface and therefore act as potential decohesion points.

Tuan et al. [140] studied the mechanical properties of Al_2O_3-ZrO_2 composites and reported that the toughness of Al_2O_3 was enhanced by adding t-ZrO_2 or m-ZrO_2 but at the same time, reduced its strength. They found that increasing the ZrO_2 content led to a reduced densification of the Al_2O_3, a reduction in its elastic modulus and refined its grain microstructure [140]. Moreover, Leyens et al. [136] reported some spinel formation between the mixed oxide and the TC, as well as some pronounced pore

formation within the mixed oxide helping crack propagation. This has led to the suggestion that the Al_2O_3-ZrO_2 can in some cases promote the diffusion of species such as Cr, Co and Ni which will eventually convert into spinels at the interface between the TGO and TC.

The effect of the TC/BC interface geometry on the formation of spinels/mixed oxides was also investigated. The islands of BC created in the early stages of oxidation, by the internal growth of Al_2O_3 around BC protrusions into the TC (Figure 6.38(c)) were believed to be one route for the formation of spinels/mixed oxides. To explain this hypothesis, it is important to go back to thermodynamics of oxide formation. The stability of oxide product for the Ni-Al-O system is presented in Figure 6.38.

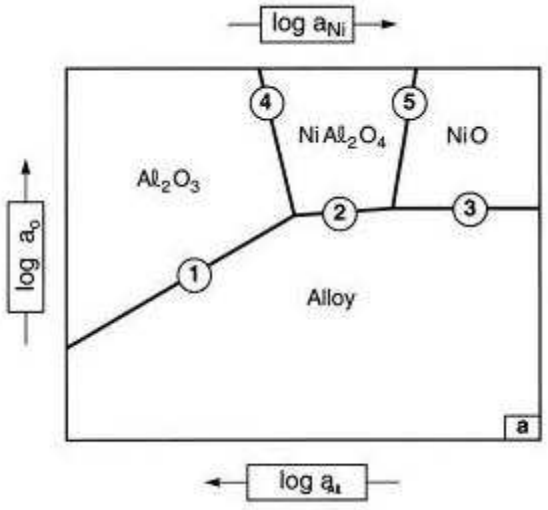

Figure 6.38 Thermodynamic stability diagram of the Ni-Al-O system [21].

The diagram represents the equilibrium between the Al_2O_3, $NiAl_2O_4$, NiO and Ni-Al phases with the oxygen activity, a_o and the Al activity a_{Al}. In the diagram, the important equilibria are as follow:

- (1) represents Al_2O_3 in equilibrium with Ni-Al by the reaction: $2Al + 3O = Al_2O_3$;

- (2) refers to $NiAl_2O_4$ in equilibrium with the alloy by the reaction: Ni + 2Al + 4O = $NiAl_2O_4$;

- (3) involves NiO in equilibrium with the alloy by the reaction: Ni + O = NiO;

- (4) is defined by the reaction: 3Ni + 4 Al_2O_3 = 3 $NiAl_2O_4$ + 2Al;

- and (5) is defined by the reaction: 3 Ni + $NiAl_2O_4$ = 4 NiO + 2Al [21].

In the BC islands at the beginning of exposure, the parameters assure that reaction (1) (Figure 6.38) is occurring. The oxygen activity is too low at the interface to form oxides other than Al_2O_3. However, as the amount of Al in the BC reduces, the oxygen activity increases along line 1 in Figure 6.38. At the intersection of lines 1 and 2 the Al_2O_3 converts into $NiAl_2O_4$. Thermodynamics might explain as well the presence of spinels/mixed oxides close to microcracks and pores at the TC/TGO interface in the modified aerofoil-shaped samples. Indeed Fox and Clyne [116] found that the permeation of oxygen through the TC was enhanced by the presence of these flaws in the ceramic, as they act as discrete oxygen delivery sites and shorten the diffusion path. This would increase p_{O_2} locally and promote the growth of spinels/mixed oxides.

The diffusion of Al out of these BC islands to grow Al_2O_3 changed the initial composition of the MCrAlY which may eventually mean that the mixed $(Al,Cr)_2O_3$ become the more stable oxide to grow. Referring back to the Ni-Cr-Al oxidation diagram in Figure 2.9 (Wallwork et al. [12,65]), at temperatures of over 1000 °C, the amount of Ni, Cr and Al present in the BC influence the nature of the growing oxide.

Figure 6.39 is a schematic representation of the formation of spinel/mixed oxides in the particular case of BC islands. After a short exposure time, the TGO (mainly transient oxides) is thin and follows the undulations of the TC/BC interface,

with the BC being rich in β-NiAl phase (Figure 6.39 (a)). After longer exposures, the TGO thickens as a result of the outward diffusion of Al from the β-NiAl phase reacting with the oxygen to form transient Al_2O_3. As observed on the Rolls-Royce samples, internal oxidation occurred in the BC close to the TGO, narrowing the asperity's neck (Figure 6.39 (c)). Further exposure caused the complete isolation of the upper part of the undulation, creating a BC island still rich in Al (Figure 6.39(d)).

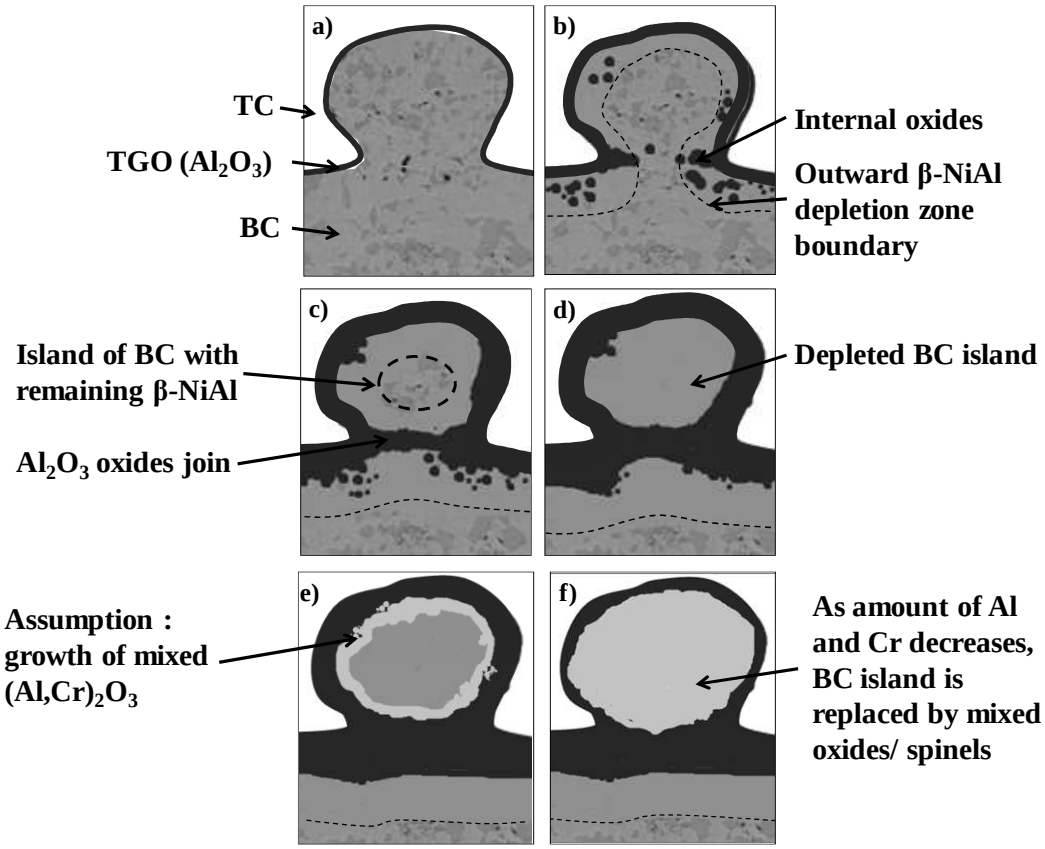

Figure 6.39 Schematic representation of spinels/mixed oxides growth in isolated BC islands with exposure at high temperatures (chronologically from (a) the initial stage of oxidation to (f) the final form of the spinel/mixed oxide).

The increasing thickness of the TGO eventually led to the depletion of the β-phase from the BC island (Figure 6.39(d)), thus reducing the Al activity and promoting the formation of MCrAlY increasingly rich in Cr growing $(Al,Cr)_2O_3$ (Figure 6.39(e))

and then the formation of spinels in a second time until the whole coating is converted (Figure 6.39(f)).

Liang et al [142], studied the grow mechanisms of Cr_2O_3 and $NiCr_2O_4$ on NiCoCrAlYs at the lattice scale and found that the lattice mismatch between the γ-Ni/γ'-Ni_3Al phases and Cr_2O_3 was less than for the γ-Ni/γ'-Ni_3Al phases and Al_2O_3 [142]. This meant that, Cr_2O_3 would grow more easily on a depleted BC, giving another reason why (added to the fact that the BC is running out of Al) the creation of Al_2O_3 is replaced by the creation of mixed $(Al,Cr)_2O_3$. As the BC is further depleted in Al and Cr, the growth of (Co,Ni)O becomes possible and the reaction between (Ni,Co)O and $(Al,Cr)_2O_3$ forms the spinels. Going back to the EDX mapping of a spinel/mixed oxide in Figure 6.24, this would explain the presence of $(Al,Cr)_2O_3$ oxides with changing Al contents on the outer region of the spinel/mixed oxide, and the core of the spinel/mixed oxide being rich in Ni. The study of model BC deposited by magnetron sputtering in Part II of this thesis will show the influence of BC composition on the nature of the oxide and that the Cr/Al ratio dictates the fraction of $(Al,Cr)_2O_3$ created on the surface.

6.2.5 Summary

On the effect of the substrate macro-geometry, it was found that life limiting vertical cracking happened more easily on convex features. The initiation of these vertical macro-cracks happened after cracking of the TC/TGO and TGO/BC interfaces. In the case of extreme convex curvature (trailing edge), a particular TC microstructure could be observed; the deposition layers did not follow the geometry of the blade around the trailing edge. Concave curvatures were very rough and as a consequence, vertical micro-cracking was located at the surface of the ceramic. These cracks,

however, did not seem to propagate towards the BC. With exposure, pores and micro-cracks present in the coating closed and inter-splat boundaries grew in size, suggesting stress accommodation and maybe sintering.

Looking at the TC/BC interface, 4 types of TC asperities into the BC could be recognised, caused by the interface roughness. These different configurations are believed to change crack propagation paths and eventually to promote the formation of vertical macro-cracks into the ceramic layer. Spinels/mixed oxides were found to form by diffusion into the ceramic coating, changing the mechanical properties of the interface and also giving an indication of the diffusion mechanisms occurring around the TC/TGO and TGO/BC interfaces. The high oxygen partial pressure at the TC micro-cracks and splat boundaries promoted the formation of spinels. The roughness of the TC/BC interface in concave curvatures was also found to be important in promoting the formation of thick TGO and spinels/mixed oxides. An extension on the study of spinels at lower exposure temperatures is presented in Part II.

Finally, the fraction of Al_2O_3-ZrO_2 mixed zone in the TGO is expected to have an effect on the adhesion of the coating, the residual stress concentration and on the formation the spinels/mixed oxides by helping the diffusion of species such as Cr, Ni and Co toward the TC/TGO interface.

CHAPTER VII – GENERAL DISCUSSION (PART I)

7.1 Why does failure of the modified aerofoil-shaped samples occur in convex locations?

In section 5.1, Flash Thermography showed that the modified aerofoil-shaped samples delaminated (and cracked) at the leading and trailing edges and at the "bump", i.e. around convex features. Then the comparison of features such as TC and BC thicknesses, Al diffusion and TGO growth (section 5.2) against curvature, highlighted the role of geometry on the physical quality of the coating (section 5.3). Indeed, the thicknesses of the TC and BC were highly dependent on curvature, and TGOs in convex areas grew less spinels/mixed oxides than concave regions of the samples.

7.1.1 Thickness of BC influences the type of failure

The results in sections 5.3 and 6.1 led to the following conclusions:

- Substrate curvature, TC/BC interface roughness and BC thickness are factors that affect each other and influence the behaviour of the TBC coating system.
- In thin BCs, more likely to be found around convex curvatures, inward Al diffusion mechanisms eventually reverse in order to maintain the growth of the TGO.
- In thick BCs, more likely to be found around concave curvatures, the high roughness of the TC/BC interface seems to increase the amount of mixed oxides/spinels in the TGO despite a larger Al reservoir. More rapid depletion of

Al in BC asperities was explained by short-circuit diffusion promoted by finer grains close to the TGO.

One question is: how does BC thickness (and indirectly the substrate's curvature) influences the failure of the TBC system?

In the case of thin BCs, where the supply in Al depends on phases other than β-NiAl, the diffusion rate from the γ and γ' phases might be too slow to grow Al_2O_3 in case of cracking. Indeed when the partial pressure of oxygen increases i.e. formation of crack, a minimum amount of Al is needed to repair the oxide layer. This critical amount is likely to be in the range of 4 to 5 at% Al [74]. For that reason, thin BCs are more vulnerable to the formation of cracks which would cause the rapid growth of less protective oxide and eventually the failure of the coating system, i.e. mechanically induced chemical failure (MICF).

MICF and intrinsic chemical failures (InCF) are the two types of failure associated with the depletion of Al from the BC. Eschler et al. [75] affirmed that those two types of failure, when leading to spallation, had different mechanisms with different temperature dependences. InCF was based on BC properties while MICF depends mostly on the TC properties. Evans et al. [73] suggested that MICF happened before intrinsic chemical failure if the Al_2O_3 layer cracked. If the integrity of the Al_2O_3 layer was maintained, MICF could not be initiated and the system lifetime would depend on InCF. They also wrote that chemical failure would occur at different times around a sample because of different deposition splat sizes, formed during manufacturing of the BC.

In thick BCs, often associated with high roughness, failure of the coating was associated with InCF. Indeed, depletion of the Al reservoir happened faster in BC asperities and using sources of Al other than the β-phase seemed more difficult because of the higher distance to diffuse through. Thick BCs were more prone to form spinels and/or mixed oxides. This might be explained by the grain size of the γ-phase in the BC. Figure 7.1 shows two SEM pictures taken in location F of an etched sample. They were taken on the tip of the trailing edge where the BC became thicker. In the thin BC at location F, it was very difficult to distinguish the grains even with higher magnification suggesting that they were very small. On the contrary, in thick BC away from location F, the grains were coarser. Bigger grains would make it difficult for elements like Al to diffuse quickly across the BC due to the relative reduction in grain boundaries explaining why thicker BCs do not benefit from the diffusion of Al from phases other than the β-phase as much as thin coatings do. That could be a reason why the failure mechanisms of thin and thick coatings are different.

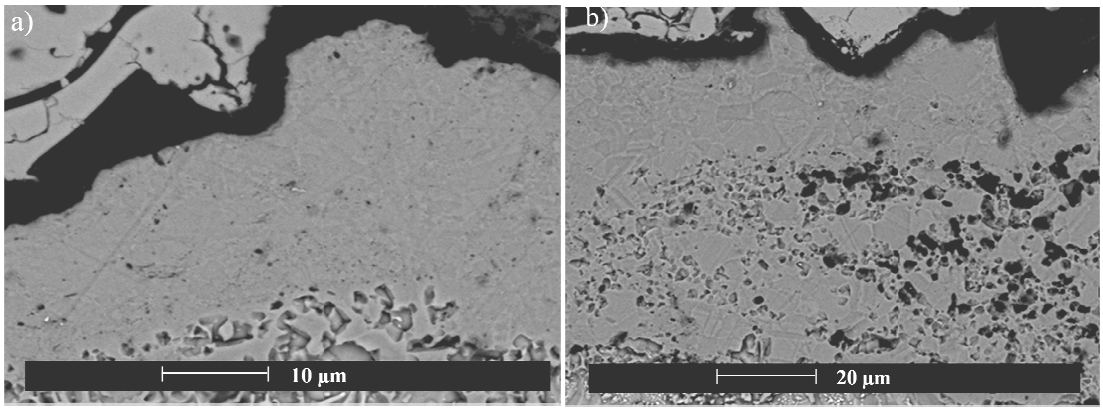

Figure 7.1 SEM image of the BC in location F on an etched sample oxidised at 900 °C for 2780 hours. Tip of the trailing edge (a) and adjacent to the tip of trailing edge (b).

7.1.2 Higher probability of failure in convex areas

The results in section 6.2 led to the following conclusions:

- TCs in convex curvatures were more likely to cracks vertically through their thickness.
- TCs in concave curvature did not promote the propagation of vertical cracks through the ceramic.
- Undulation of the TC/BC interface and different TC asperity microstructures influence the propagation of cracks. Cracks into the TC promote the critical failure of the TBC system by initiation life limiting vertical macro-cracks into the ceramic.
- High roughness of the TC/BC interface promotes the presence of large pores which in turn promote the growth of large Al_2O_3 clusters mixed with spinels/mixed oxides.

Crack initiation and propagation mechanisms are complex as they depend on several parameters, such as: the stress state of the 3 different layers of the system, their microstructure and the local geometry. Those factors are in turn influenced by oxidation temperature and time. Mechanisms suggested in literature [21,68,94,98] (section 2.3.4) agree that the stress caused by the growth of the TGO could cause the initiation of cracks in the TC and/or the TGO, and that undulation of the interface create out-of plane and shear stresses causing micro-cracks to link and propagate. It was also agreed that cracks preferentially propagated at the TC/TGO, TGO/BC interface, through the TGO and in the TC depending on the local roughness [67,98]. Researchers understand the importance of roughness on failure mechanisms. However, little research, if any, has

been carried out into the effect of the layout of discrete splats in the TC at the TC/TGO interface on the residual stress state of the APS/TBC system. In this study, the particular layout of the YSZ splats and the TGO were found to have a great effect on crack propagation. This, in turn, was dependent on the macroscopic geometry of the turbine blade.

Indeed, in regions of concave curvature, the roughness of the TC/BC interface was more important and the amplitude of the TGO undulation between the two layers was higher than in regions of convex curvature. Larger amplitudes were more likely to promote Type 1 and Type 3 ceramic microstructures (Figure 6.37), configurations making cracks formation and propagation more difficult. The flash thermography experiments confirmed this hypothesis by showing that damage at concave locations of the samples did not propagate as quickly as in convex areas. Moreover, when critical failure happens, the TBC coatings in concave regions usually stayed attached to the BC (Figure 7.2).

On the other hand, the TC/BC interfaces at convex curvatures were more likely to promote Type 2 and Type 4 (Figure 6.37) TC asperities because of the smaller amplitude of the TGO undulations dictated by a smaller roughness. These two types of TC microstructure at the TC/BC interface were found to promote cracking into the TC, the creation of an Al_2O_3-ZrO_2 mixed zone and high residual stress gradient between both sides of the interface. The probability of crack propagation inside the ceramic when the curvature of the coating was convex was therefore higher. Figure 7.3 is an SEM image of a cross-section through the trailing edge of a modified aerofoil shaped samples (location F) and shows how a crack propagating inside the TGO continued its path in the ceramic when encountering a Type 4 protrusion. The 3 concave undulations

highlighted in red demonstrate the fact that around these protrusions, the cracks do not always continue propagating into the TC but only increase the probability of creating a critical crack into the ceramic.

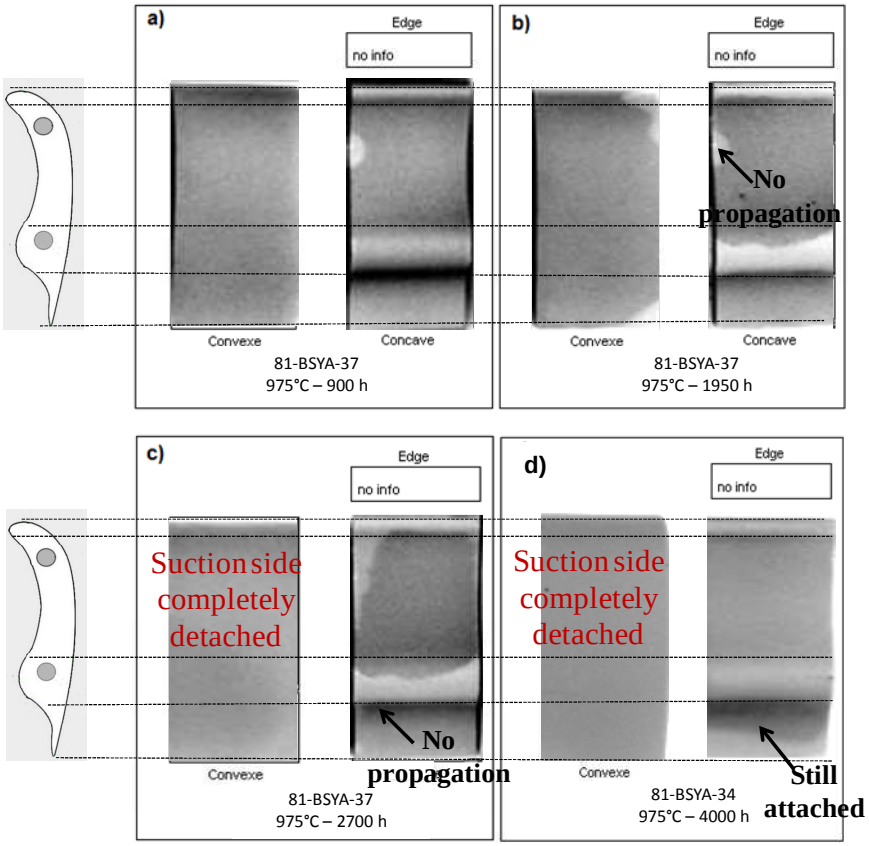

Figure 7.2 Thermographs of sample 81-BSYA-37, oxidised at 975 °C for 4000 hours. Light grey contrast corresponds to detached ceramic.

The higher probability of cracks generating critical damage close to the TC/TGO interface at convex features of the modified aerofoil-shaped sample, combined with the poorer physical state of the whole TC caused by the spray deposition in these areas (thinner coating not following the geometry of the blade), make it a preferential location for critical cracking which will dictate the lifetime of the entire system.

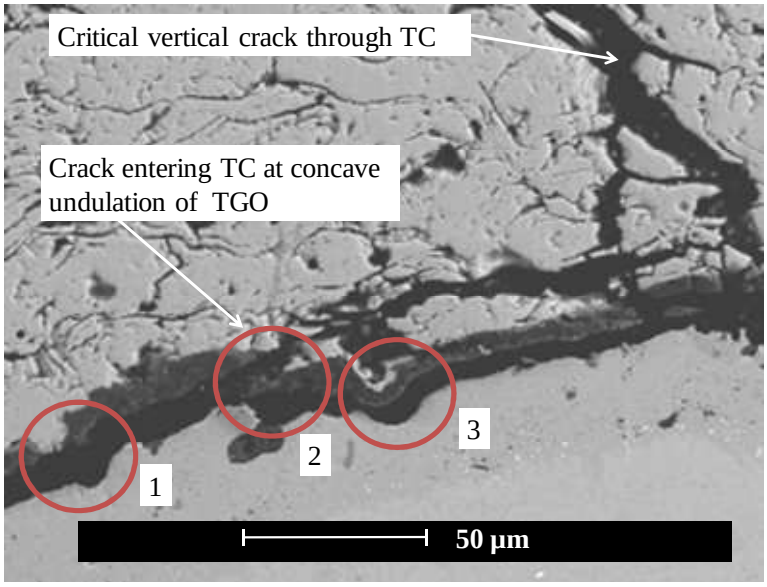

Figure 7.3 SEM image taken at location F of samples oxidised for 2780 hours at 950 °C showing cracks propagating at TGO/BC interface and through the TC. Red circles highlight TC protrusions into the TGO.

7.2 TGO thickness development model

7.2.1 Modelling the TGO growth on the modified aerofoil-shaped samples

The oxidation at 5 different temperatures between 900 and 1000 °C for times up to 20,000 hours on modified aerofoil-shaped samples has enabled the collection of significant data to improve the modelling of TGO development in industrial gas turbine conditions (Chapter 5).

In the literature [1,58,110-113,115], modelling the oxidation behaviour was conducted by considering that the ideally parabolic trend was actually composed of two stages: a transient stage, which had a higher rate and corresponded to the formation of θ-Al_2O_3, followed by a steady state stage corresponding to the α-Al_2O_3 formation. The entire process deriving from the transition of one stage to the other can be described by the following equations [1]:

$$\left(\frac{\Delta w\theta}{A}\right)^2 = \left(k_{p\theta}.t\right) + C \qquad if\ t < t_c \qquad (8)$$

$$\left(\frac{\Delta w_\alpha}{A}\right)^2 = \left(\frac{w_{\theta c}}{A}\right)^2 + k_{p\alpha}\,(t - t_c) \qquad if\ t > t_c \qquad (9)$$

Where, Δw is the mass change (mg); A the material surface (cm^2); kp_θ the rate constant for θ-Al_2O_3 ($mg^2/(cm^4\ h)$); kp_α the rate constant for α-Al_2O_3 ($mg^2/(cm^4\ h)$); $w_\theta c$ the critical weight for θ-Al_2O_3 (mg/cm^2); t the time; and t_c the critical time for the θ- to α-Al_2O_3 transformation to happen. The first equation describes the growth of θ-Al_2O_3 and the second, the growth of α-Al_2O_3.

In this simple initial model, the influence of temperature on $w_{\theta c}$ (critical weight at which θ-Al_2O_3 starts transforming into α-Al_2O_3) was not taken into account. It meant that the mass of the grown oxide at the transition point between formation of θ- and α-Al_2O_3 was the same at every temperature. However, it is well known, that the stability of metastable Al_2O_3 and their rate of transformation is highly dependent on temperature [53]. This assumption led to an inaccurate description of growth behaviour as it can be seen in Figure 7.4. In this first trial, the experimental data was well represented by the model for the first stages of the oxidation but was not for the second stage especially for temperatures above 925 °C.

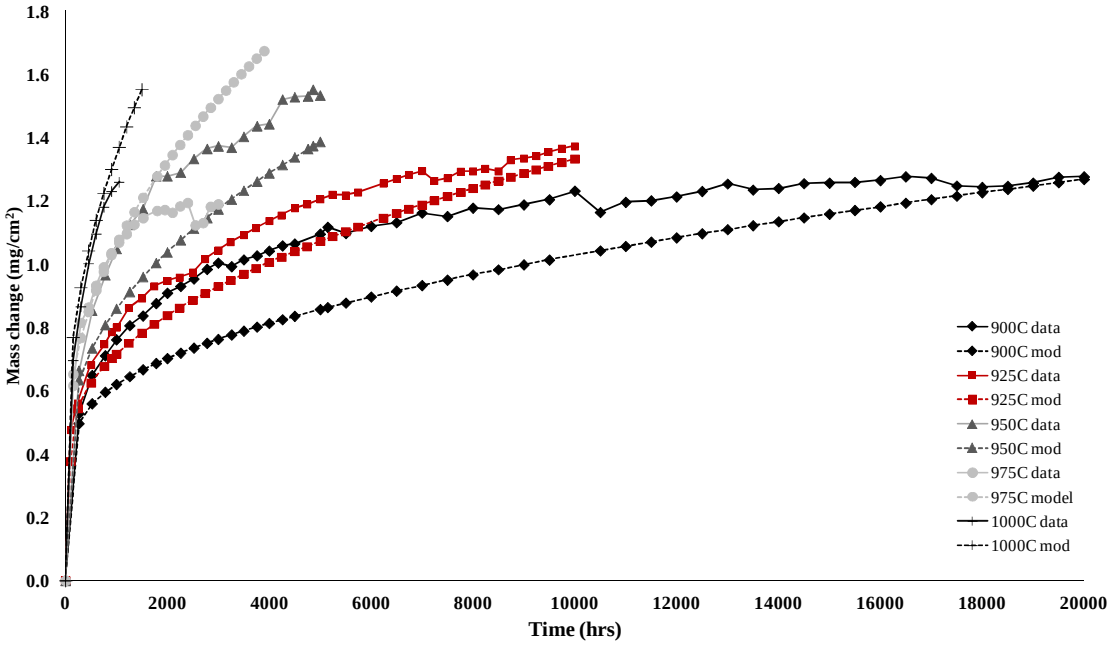

Figure 7.4 Inaccurate comparison of experimental mass change data and model.

Figure 7.5 shows the model after temperature specific values of $w_{\theta c}$ were calculated. The new model describes the mass change of samples oxidised at 900, 925 and 1000 °C much better. The new values of $w_{\theta c}$ are plotted against temperature in Figure 7.6.

The critical mass of the oxides, at which the transition between θ-Al_2O_3 and α-Al_2O_3 happened, reduced when the exposure temperatures were higher. The inaccuracy remaining at temperatures 950 and 975 °C could be explained by a change of oxidation mechanism and means that further adjustments of the model are needed. Changes could include the rate constant kp_{α} in function of the temperature or even transposing the parabolic trend to a cubic one.

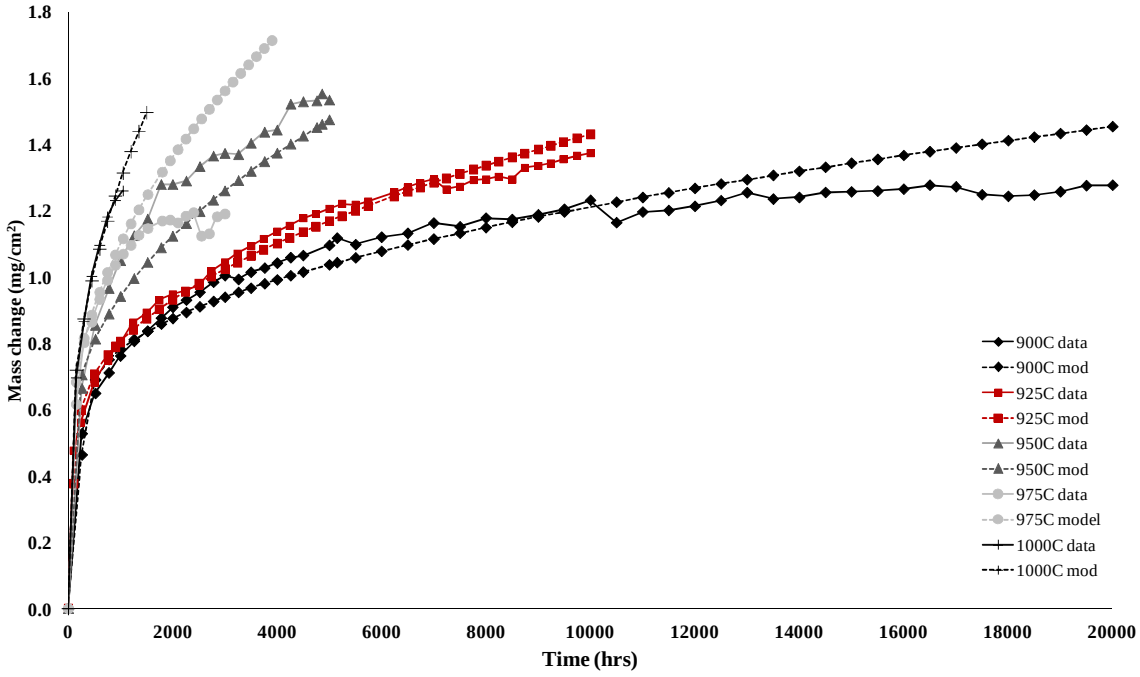

Figure 7.5 Comparison of experimental mass change data and corrected model.

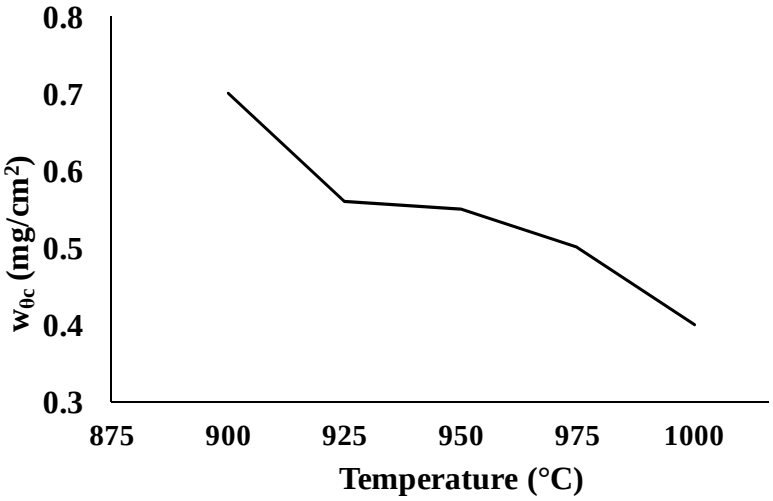

Figure 7.6 w_{0c} as a function of temperature.

7.2.2 Modelling the transition between θ- Al_2O_3 and α- Al_2O_3

The critical weight $w_{\theta c}$, represents the weight at which the transformation of the transient Al_2O_3 occurs during the oxidation. More than a weight term, $w_{\theta c}$ can be interpreted as a time and temperature term, describing the nucleation and growth kinetics of α-Al_2O_3. Indeed, plotting $\ln(w_{\theta c}(T))$ against 10000/T describes an Arrhenius function as seen in Figure 7.7.

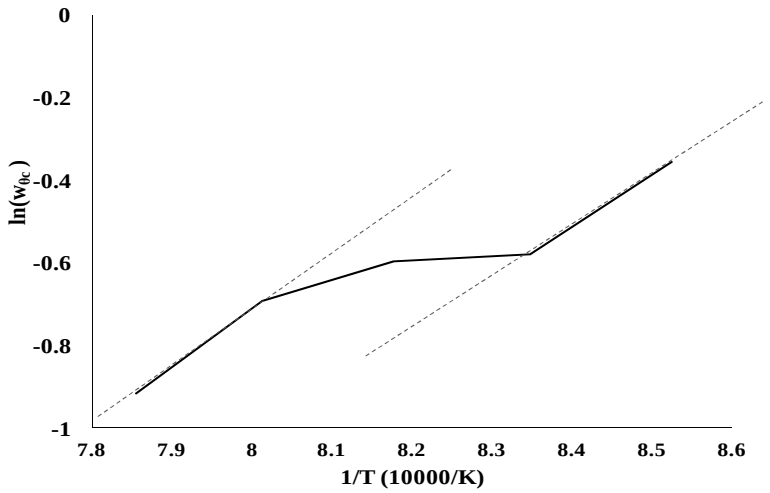

Figure 7.7 Arrhenius plot of $\ln(w_{\theta c})$ for the oxidation of the APS/TBC system.

The transformation of θ- into α-Al_2O_3 is a solid-state transformation whose kinetics, for a set temperature, can be described by the Avremi equation as follow [141]:

$$y = 1 - e^{-kt^n} \quad (12)$$

where *k* and *n* are time-independent constants describing the reaction. The Arrhenius function must be incorporated into equation (12) in order to add the temperature factor to the phase transformation of Al_2O_3, which leads to equation (13):

$$w_{\theta c} = Ax\left(\frac{10{,}000}{T}\right) - Bx\left(1 - \exp(-Cx(\frac{10{,}000}{T})^n)\right) \quad (13)$$

where, according to the data, A = 0.7267, B = 6.5744, C = 0.05 and n = 6.

7.3 Conclusion (Part I)

An advanced approach was developed for the understanding of complex coating systems, taking into account metallurgical, microstructural and mechanical evolutions. It is now possible to predict where failure will occur first around an aerofoil shape, potentially making gas turbines overhaul quicker and more efficient. The effect of different coating shapes on as-deposited coatings, showing the dependence on curvature, highlighted the importance of having a well controlled manufacturing route. Despite the high level of interest in TBCs, there has been relatively little work on the TC/TGO interface geometry of APS/TBC systems and its effect on mechanisms of crack initiation and propagation [90,91]. This present work highlighted the effect of local TC/BC interface geometry on the state of the ceramic layer and the propagation of cracks in and around the TGO.

The improvement of NDE techniques and their possible application in industry will save time during gas turbine maintenance, and thus reduce costs, by quickly indicating which blades are still serviceable or need to be changed. Shorter shut-downs and better estimation of damage on the blades will reduce the downtime and increase the availability of industrial gas turbines.

Plasma spraying imperfections, causing a scatter in the TC and BC thicknesses of the TBC systems were found to cause preferential and then critical failure on convex features of modified aerofoil-shaped samples, i.e. leading and trailing edges. During operation, the temperature experienced by a single turbine blade can vary from 600 to a maximum of 1100 °C around the different geometries because hot streaks from the

combustor flow into the turbine making the temperature field highly heterogeneous [1,18,99,143]. Furthermore, modelling of the aerodynamics of turbine blades, carried out by researchers specialised in Computational Fluids Dynamics (CFD) [143,144], showed that hot spots were generally concentrated on the leading edge of turbine blades (Figure 7.8).

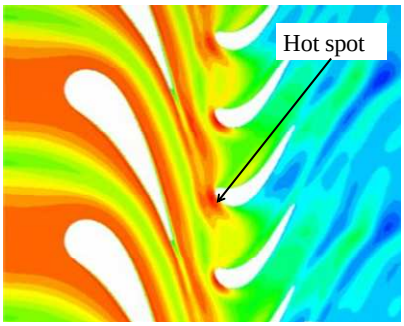

Figure 7.8 CFD simulation of hot spots in a high pressure turbine stage [143].

Past studies on the coating failure on turbine blades also indicated that compressive stresses states were modified by aerofoil geometry, explaining the spallation of the protective ceramic generally being found on convex and flat surfaces as well as on sharp edges [100,101,103,104].

The combination of higher temperatures and higher stress gradients on the leading edge of blades make such locations highly vulnerable. It is therefore crucial to improve the spraying process of the BC and TBC in order to avoid the deposition of thin coatings in areas likely to experience the most severe conditions during service.

PART II - OPTIMISING BOND COATINGS FOR GAS TURBINE APPLICATION

Overlay coatings, or BCs in the presence of a TBC, provide different protection properties depending on their composition because of the nature of the oxides growing on them. The time and temperature of their exposure also greatly influences the oxide layers created. Ni-Cr-Al and Co-Cr-Al ternary systems undergoing oxidation have been the subject of extensive studies. Since researchers usually operate at high temperatures in order to accelerate the oxidation of samples, and because of the important support and interest of aeronautical industry, the behaviour of these alloys above 1000 °C is well understood and mapped [12,40,63,65,66]. However, this is not the case for oxidation at lower temperatures. Information on the Co-Ni-Cr-Al system is also difficult to find.

New coating compositions deposited by magnetron sputtering (method described in Chapter IV) were oxidised in order to achieve a better knowledge of MCrAlYs behaviour under oxidation in industrial gas turbine operating conditions. Oxidation rate for the Ni-Co-Cr-Al system and determination of oxide types at 900 and 950 °C have been outputs from these experiments. Studying a range of Ni-Cr-Al and Ni-Co-Cr-Al has also highlighted the role of each element concentration on the preferential oxidation and the growth of protective oxides (such as Cr_2O_3 and Al_2O_3) or less protective oxides (such as $NiCr_2O_4$).

Firstly the results of the oxidation and analysis of Ni-Cr-Al coatings exposed at 950 then 900 °C are presented: including, mass gain curves, EDX and XRD analysis. This leads to the creation of oxide predominance Ni-Cr-Al maps at both the exposure temperatures, and a comparison of the coatings behaviour with exposure temperature and composition.

Secondly, the effect of Co addition to the Ni-Cr-Al system has been investigated. Again, mass change curves, EDX analysis and XRD graphs are presented and their analysis has led to the creation of oxide predominance maps at 900 and 950°C. Some of the work presented in this chapter has been published in a paper in Surface and Coating Technology [145].

CHAPTER VIII – OXIDATION OF Ni-Cr-Al COATINGS AT 900 – 950 °C

8.1 Oxidation of Ni-Cr-Al systems at 950 °C

Around 10 samples from each batch of the two target co-sputtering deposition experiments were chosen and oxidized in air at 950 °C in a horizontal furnace for exposure times of up to 500 hours. They were unloaded every 20 hours for weighing, XRD and visual inspection. Samples with apparent cracking and/or significant weight loss were taken out of the experiment. The compositions of the samples produced using the Ni-10wt%Cr+Al, Ni-20wt%Cr+Al and Ni-50wt%Cr+Al targets are presented in Table 8.1. A dozen samples were sufficient to represent the range of compositions deposited by sputtering from each combination of targets.

8.1.1 Physical changes of samples with exposure

Pictures of the sapphire discs were taken regularly between exposure cycles (Figures 8.1 to 8.3). Before oxidation all coatings had a homogeneous grey colour, the shade of which depended on the amount of Al present. The more the Al the lighter the grey shades. In the Figures 8.1 to 8.3, 4 to 5 samples were chosen as representative examples of the physical changes happening during oxidation. They are described in terms of increasing amounts of Al. Samples from the Ni-10wt%Cr+Al batch are shown in Figure 8.1. Sample 130510B3 (10.6 at%Cr, 1.9 at% Al), rich in Ni, had an increasingly rough surface with ongoing exposure.

Targets	Sample		Ni (at%)	Cr (at%)	Al (at%)	Cr/Al	Exposure (hours)
Ni-10wt%Cr +Al	130510	B3	87.5	10.6	1.9	5.58	220
	170510	d2	84.5	9.7	5.8	1.67	200
	130510	E2	81.4	9.2	9.4	0.98	300
	130510	e3	76.3	8.2	15.5	0.53	500
	170510	F2	61.6	6.7	31.7	0.21	500
	170510	f3	49.5	4.7	45.8	0.10	500
	170510	G3	37.3	3.3	59.4	0.06	100
	170510	g2	23.5	2.3	74.2	0.03	500
	130510	H2	15.9	1.6	82.4	0.02	500
	130510	h2	10.7	0.9	88.4	0.01	20
	130510	i2	6.0	0.4	93.6	0.00	20
Ni-20wt%Cr +Al	080710	B2	77.4	22.1	0.5	44.20	80
	080710	D2	77.2	20.2	2.6	7.77	500
	080710	F2	63.9	14.6	21.5	0.68	500
	080710	f2	52.5	11.5	36.0	0.32	500
	080710	G2	41.2	8.4	50.4	0.17	500
	080710	g2	29.1	6.1	64.8	0.09	80
	080710	H2	17.1	3.7	79.2	0.05	500
	080710	h2	14.0	2.5	83.5	0.03	500
	080710	i1	8.4	2.1	89.5	0.02	500
Ni-50wt%Cr +Al	290610	C3	37.7	59.7	2.7	22.53	500
	290610	D2	38.1	55.9	6.0	9.36	500
	290610	d3	36.1	51.8	12.1	4.28	500
	290610	E3	33.5	48.2	18.2	2.64	500
	290610	F2	22.5	44.9	32.6	1.38	500
	290610	f3	15.8	22.5	61.6	0.37	500
	290610	G2	10.3	14.7	74.9	0.20	60
	290610	H3	4.1	5.1	90.8	0.06	500
	290610	h2	2.8	2.8	84.4	0.03	500

Table 8.1 Compositions of Ni-Cr-Al coatings resulting from 2 target co-sputtering and oxidised at 950 °C.

Detachment of the coating happened after 200 hours at 950 °C as indicated by the red arrow. Sample 130510e3 (8.2 at% Cr, 15.5 at% Al), obtained a green coloration after 20 hours of oxidation which became more pronounced after 500 hours. 170510 F2 (6.7 at% Cr, 31.7 at% Al), kept a grey colour throughout its exposure. Finally, 130510h2 (0.9 at% Cr, 88.4 at% Al), composed mainly of Al, was cracked and seemed to have melted at high temperature and solidified during cooling. Overall, samples changed colour during the first stages of oxidation and then stayed unchanged during the reminder of the 500 hours exposure (or until failure).

Samples from the Ni-20wt%Cr+Al batch are shown in Figure 8.2. Similarly to 130510B2, 080710B2 (22.1 at% Cr, 0.5 at% Al), became rougher with exposure. However before cracking at 80 hours, green crystals precipitated on the surface of the coating and then disappeared. This could be explained by the higher amount of Cr in this sample. With increasing amount of Al, in sample 080710D2 (20.2 at% Cr, 2.6 at% Al), the green coloration was not observed anymore. Instead the progressive growth of a light grey oxide occurred, and after 500 hours, covered the entire surface of the coating. Like 170510F2, 080710F2, composed of 21.5 at% Al and 14.6 at% Cr, kept the same grey colour throughout its exposure at 950 °C. Also similar to the Ni-10wt%Cr+Al batch, samples with a high amount of Al, represented by 080710h2 (2.5 at% Cr, 83.5 at% Al), showed a molten then solidified surface. However, its higher amount of Cr seemed to have avoided cracking and failure. Again no difference could be spotted between the transient stage and the steady-state stage of oxidation at 950 °C.

The samples from the Ni-50wt%Cr+Al batch showed that high amounts of Cr (above 45 at%) resulted in a green surface coloration (Figure 8.3). Indeed on sample 290610d3, containing 51.8 at% of Cr and 12.1 at% Al, a green oxide grew progressively

toward the edges of the sapphire disc between 300 and 500 hours, while on sample 290610E3, with 48.2 at% of Cr and 18.2 at% Al, the edge of the disc also became green. As previously, higher amount of Al (above 30 at%) lead to grey coloured surfaces, as seen on sample 260910F2 (44.9 at% Cr, 32.6 at% Al) and very high level of Al (above 75 at%) lead to molten coatings (290610H3 with 5.1 at% Cr and 90.8 at% Al). Most of the samples from the Ni-50wt%Cr+Al batch lasted 500 hours, indicating that higher amounts of Cr in the coating provided better adhesion properties and /or oxidation protection.

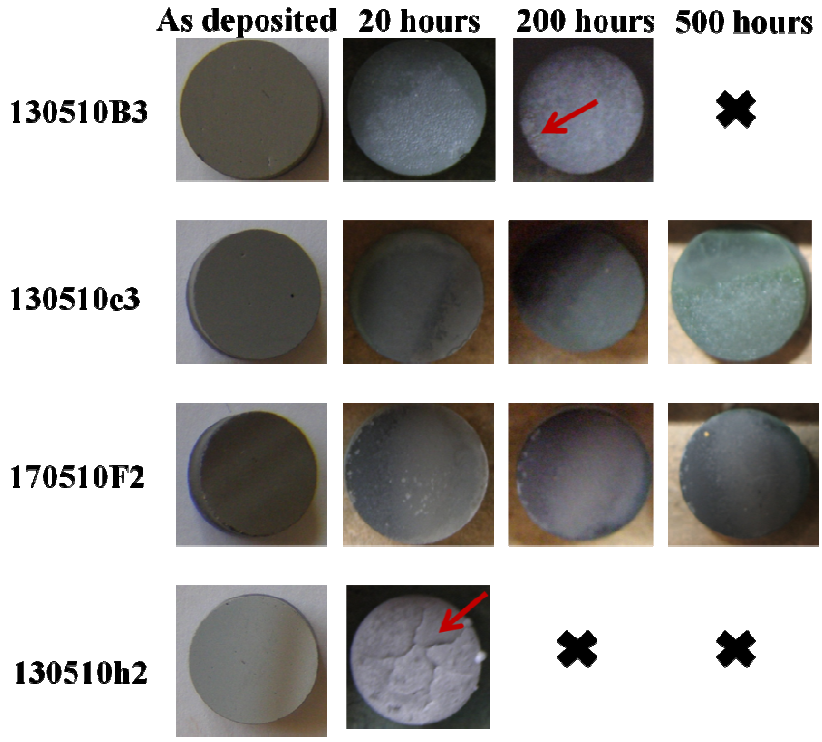

Figure 8.1 Pictures showing evolution of 130510B3 (10.6 at%Cr, 1.9 at% Al), 130510e3 (8.2 at% Cr, 15.5 at% Al), 170510F2 (6.7 at% Cr, 31.7 at% Al) and 130510h2 (0.9 at% Cr, 88.4 at% Al) (Ni-10wt%Cr+Al) with exposure time at 950 °C. Red arrows point at damage in coatings.

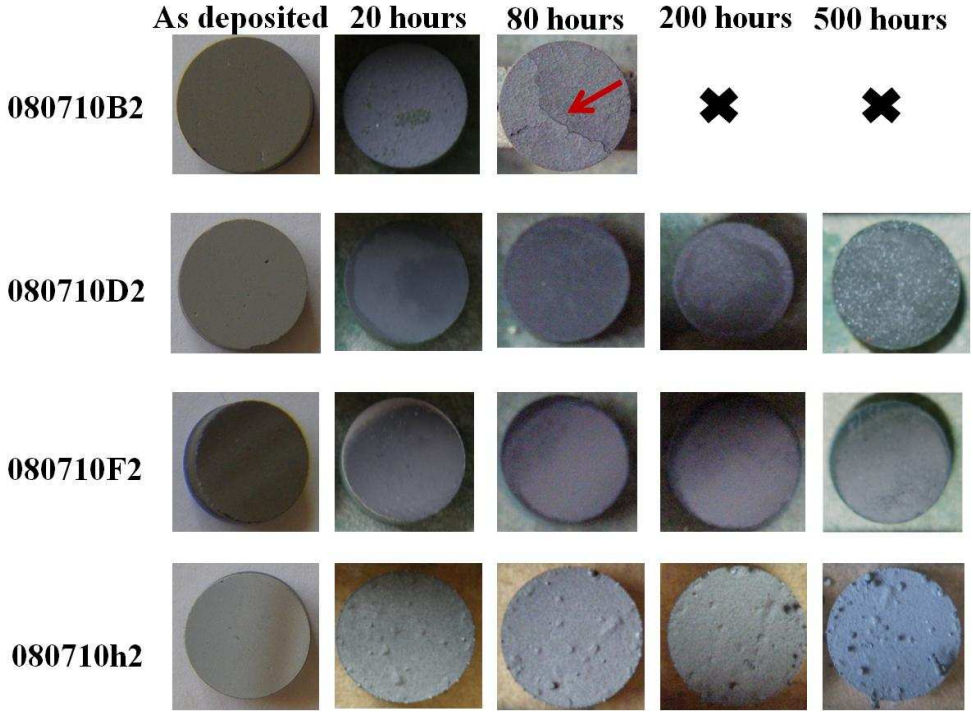

Figure 8.2 Pictures showing evolution of the oxides on 080710B2 (22.1 at% Cr, 0.5 at% Al), 080710D2 (20.2 at% Cr, 2.6 at% Al), 080710F2 (14.6 at% Cr, 21.5 at% Al) and 080710h2 (2.5 at% Cr, 83.5 at% Al) (Ni-20wt%Cr+Al) with exposure time at 950 °C. Red arrows point at damage in coatings.

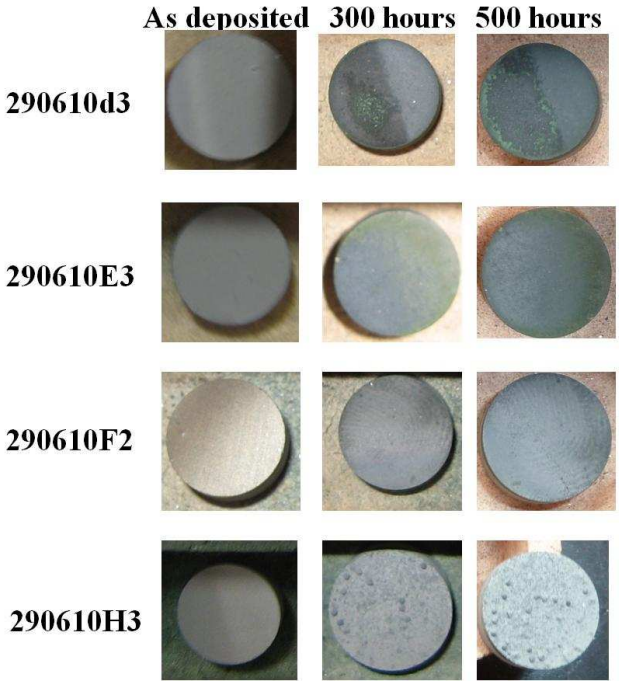

Figure 8.3 Pictures showing evolution of the oxides on 290610d3 (51.8 at% Cr, 12.1 at% Al), 290610E3 (48.2 at% Cr, 18.2 at% Al), 290610F2 (44.9 at% Cr, 32.6 at% Al) and 290610H3 (5.1 at% Cr, 90.8 at% Al) (Ni50Cr+Al) with exposure time at 950 °C.

8.1.2 Mass change of samples

Weighing the coated sapphire discs allowed calculation of the sample mass changes, which are representative of oxide growth. Different types of oxides have different oxidation rates. Therefore, mass change graphs plotted against time can be correlated with the nature of the oxide growing on the coating.

Figure 8.4 presents the mass changes as a function of time for the Ni-10wt%Cr+Al coatings. Two types of behaviour could be observed. Oxides on samples containing large amounts of nickel, 130510B3 (10.6 at%Cr, 1.9 at% Al) for example, grew very quickly, while oxides on samples with a large amount of Al, 170510F2 (6.7 at% Cr, 31.7 at% Al), grew slowly. Slow growing oxide curves were divided in two parts: an initial fast growing part followed by a steady growth part. This describes the two stages of Al_2O_3 growth well (transient oxide growth, e.g. θ-Al_2O_3 or possibly NiO, followed by α-Al_2O_3). An abrupt reduction of a sample's mass corresponded to the spallation of part of the oxide or coating. Sample 130510e3 (8.2 at% Cr, 15.5 at% Al) is believed to have had a particularly unusual behaviour. Indeed, XRD analysis (which will be presented later in this chapter), showed that a mix of NiO and transient θ-Al_2O_3 grew on the coating's surface. The presence of NiO would suggest a quick mass gain, however, this sample behaved like a slow growing Al_2O_3 former.

The mass change of the Ni-20wt%Cr+Al coatings, represented in Figure 8.5, showed the same behaviour apart from sample 080710H2 (3.7 at% Cr, 79.2 at% Al) which did not appear to follow the trend. 080710H2 falls into the composition range that is expected to be molten at the 950 °C test temperature and this is believed to account for the high observed oxidation rate for this sample [61,147]. In Figure 8.5, 080710h2 (2.5 at% Cr, 83.5 at% Al) does not follow this trend, even if it contains a

large concentration of Al. At 950 °C, it might form a different liquid or partially liquid phase which behaves differently than the other phases formed by the rest of the batch.

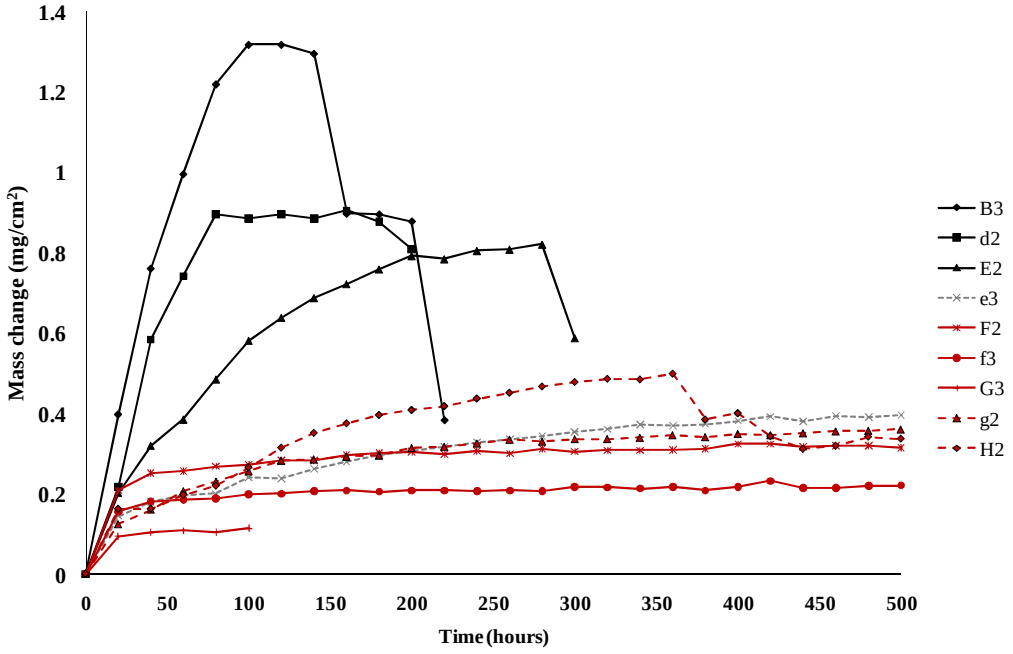

Figure 8.4 Mass change of Ni-10wt%Cr+Al coatings against time of exposure at 950 °C. Red curves represent samples growing protective oxides.

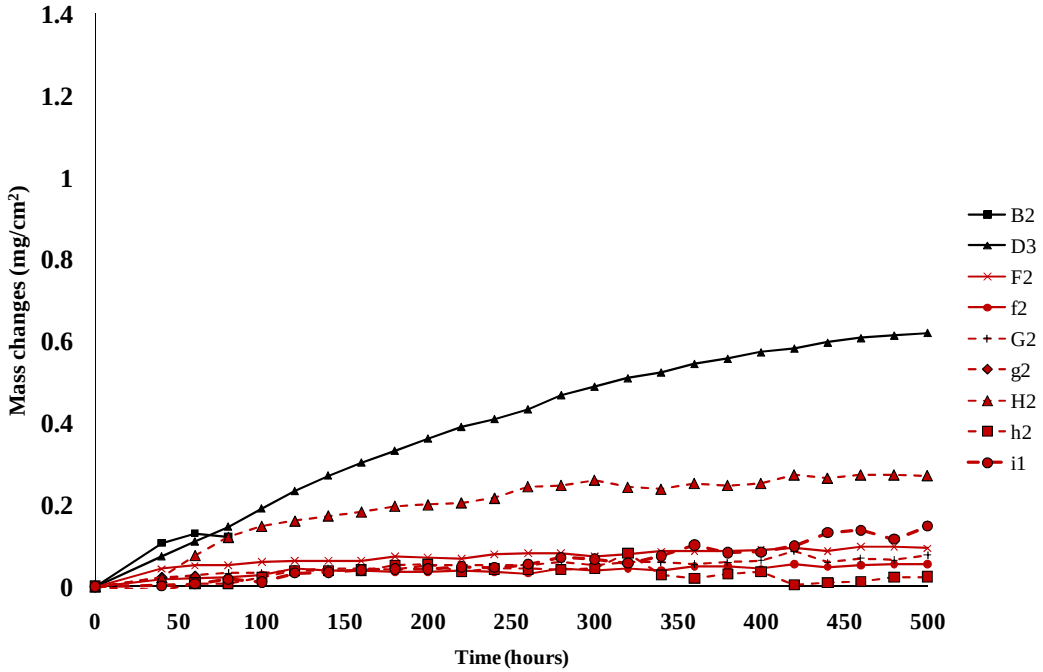

Figure 8.5 Mass change of Ni-20wt%Cr+Al coating against time of exposure at 950 °C. Red curves represent samples growing protective oxides.

The addition of Cr to the alloy system reduced the extent of oxidation. Indeed, in Figure 8.4 (Ni-10wt%Cr + Al), the mass change of samples mainly growing Al_2O_3 reached 0.2 to 0.4 mg/cm^2 after 500 hours of exposure while in Figure 8.5 (Ni-20wt%Cr + Al) their masses only went up by 0.1 mg/cm^2. Cr-rich coatings from the Ni-50wt%Cr+Al batch produced slow growing oxides with a maximum weight gain of 0.35 mg/cm^2 after 200 hours of exposure (Figure 8.6), presumably as a result of these compositions favoring the growth of Cr_2O_3 and Al_2O_3 scales over faster growing NiO. Samples 290610C3 (59.7 at% Cr, 2.7 at% Al) and 290610D2 (55.9 at% Cr, 6.0 at% Al) produced Cr_2O_3; sample 290610d3 (51.8 at% Cr, 12.1 at% Al) produced a mix of Cr_2O_3 and Al_2O_3; the rest of the Ni-50wt%Cr+Al batch tested, grew Al_2O_3. In Figure 8.6 it can be seen that Cr_2O_3, even if protective, grows slightly faster than Al_2O_3 over 500 hours. The Ni-50wt%Cr + Al samples growing Al_2O_3 (and not melting) only reached a maximum gain weight of 0.1 mg/cm^2, comparable to the mass change seen in Figure 8.6.

Although plotting the mass changes against time identified coating compositions that produced slow growing oxides, it did not show which samples had the lowest extent of oxidation. To this end, mass changes were plotted against the Cr/Al fractions in the coatings (Figure 8.7). Low levels of Al led to higher levels of oxidation, as did high levels of Al. From the three graphs, the optimum Cr/Al fraction (at%) producing the least oxidation was between 0.1 and 0.5. The corresponding samples are listed in Table 8.2 [145].

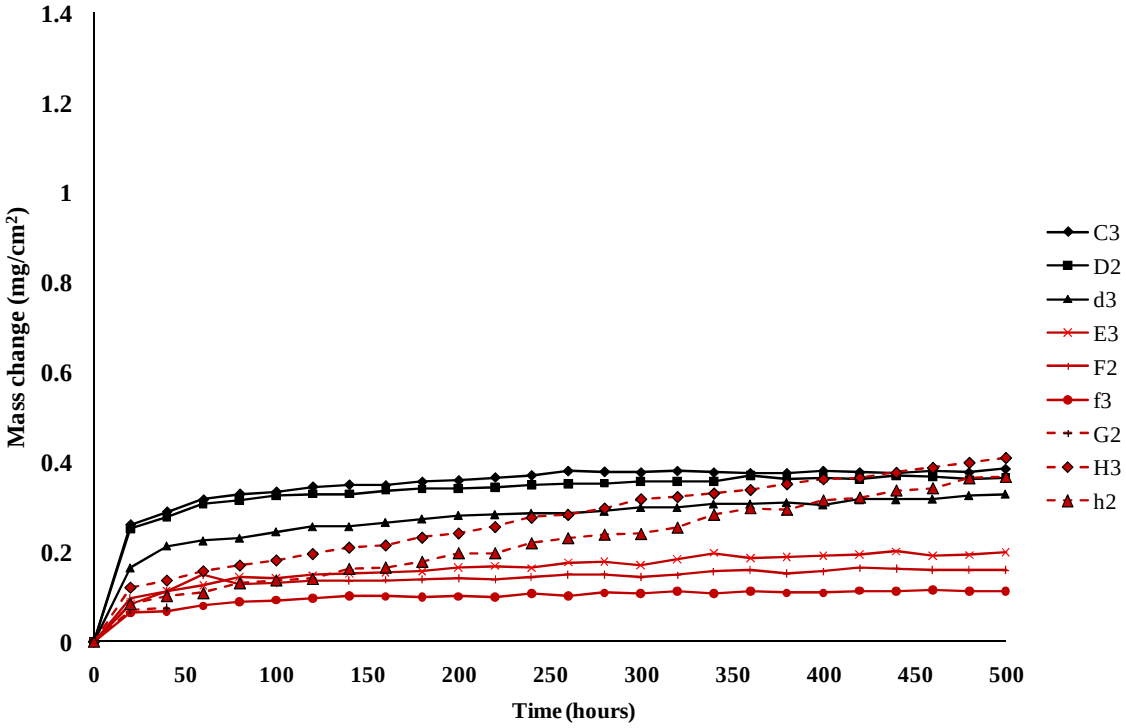

Figure 8.6 Mass change of Ni-50wt%Cr+Al coating against time of exposure at 950 °C. Red curves represent samples growing protective oxides.

Targets	Sample	Ni (at%)	Cr (at%)	Al (at%)	Cr/Al
	F2	61.60	6.70	31.70	0.21
Ni-10wt%Cr+Al	f3	49.50	4.70	45.80	0.10
	f2	52.50	11.50	36.00	0.32
Ni-20wt%Cr+Al	G2	41.20	8.40	50.40	0.17
	F2	22.45	44.93	32.61	1.38
Ni-50wt%Cr+Al	f3	15.83	22.54	61.63	0.37

Table 8.2 Ni-Cr-Al samples producing slow lowest oxidation levels.

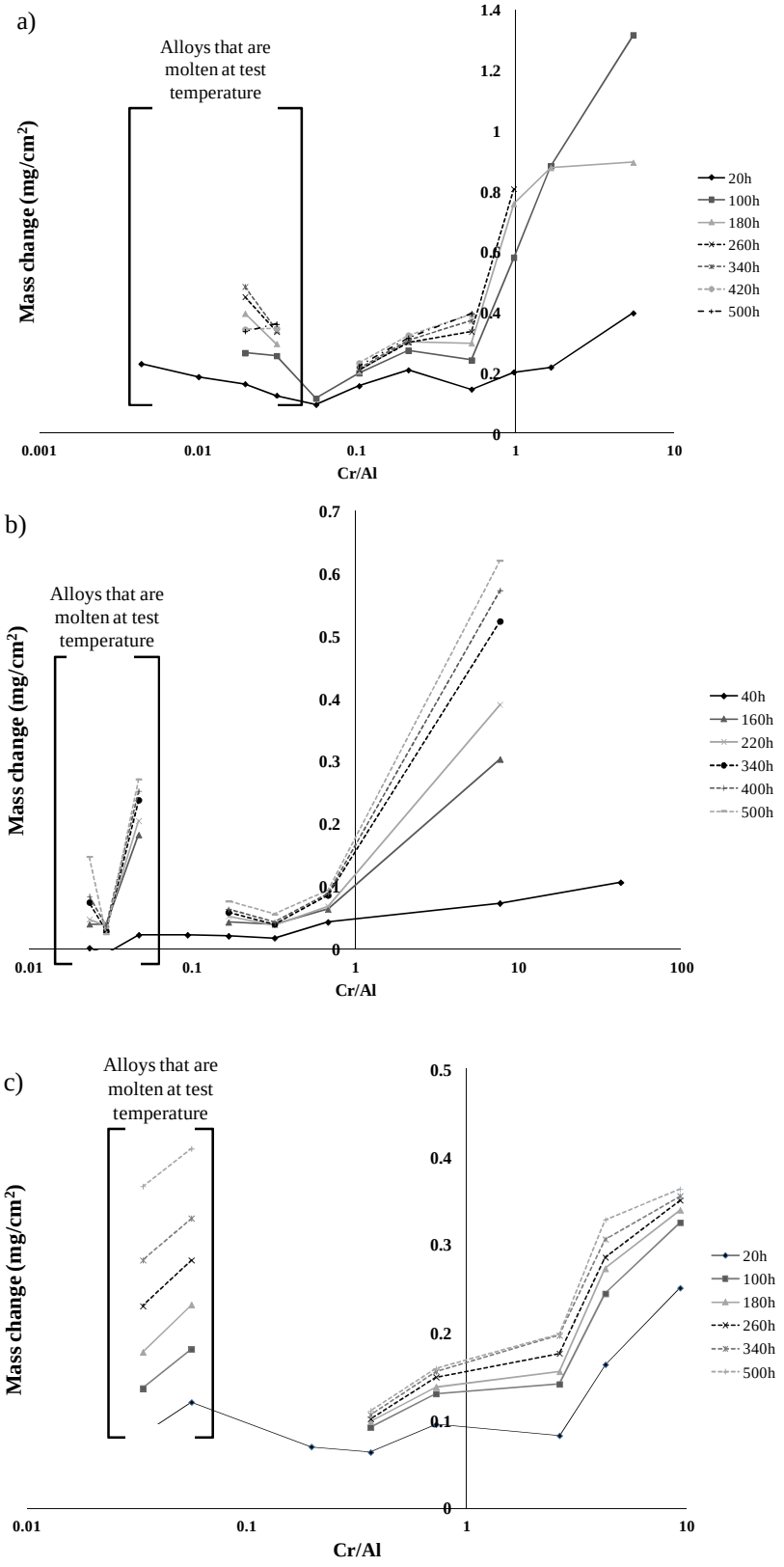

Figure 8.7 Mass change of (a) Ni-10wt%Cr+Al, (b) Ni-20wt%Cr+Al and (c) Ni-50wt%Cr+Al coatings against Cr/Al content (in at %). Gaps in the curve correspond to sample failure (absence of data).

8.1.3 Identification of oxides

XRD was used to identify the oxides present on the coatings after exposure. High concentrations of Ni in the samples led to the growth of NiO oxides (Figure 8.8). High concentrations of Cr were needed in order to form Cr_2O_3 instead (Figure 8.9). No Cr_2O_3 was formed on samples containing less than 20 at% Cr. The first traces of Al_2O_3 were observed on sample 130510e3 (8.2 at% Cr, 15.5 at% Al) (Figure 8.10). However, the high amount of Ni in the composition of this coating led to the formation of NiO as well, which reduced the oxidation protection properties of the coating. Pure and protective Al_2O_3 was observed on samples F2 (from the Ni-10wt%Cr+Al and Ni-20wt%Cr+Al batches) as shown in Figures 8.11 and 8.12. When the amount of Cr was low (6.7 at%) , 32 at% Al was needed to form Al_2O_3. However, higher amounts of Cr (14.6 at%) reduced the required Al to 21.5 at%. At high Cr levels (56 at%), Al_2O_3 oxides were found when the alloy contained 6 at% Al (Figure 8.13). This tendency is described in literature, where it is called the “third element effect” [63] and is consistent with current understanding of the oxidation performance of Ni aluminide coatings and MCrAlY overlay coatings used in industrial gas turbines. XRD analysis of samples 170510F2 (6.7 at% Cr, 31.7 at% Al) and 080710F2 (14.6 at% Cr, 21.5 at% Al) detected the presence Al_2O_3 with two different microstructures, hexagonal and monoclinic. A study from Levin and Brandon [147] identified the hexagonal Al_2O_3 as α-Al_2O_3 and the cubic one as θ-Al_2O_3. This confirms that, at temperatures below a 1000°C, the oxide layer is constituted of two different forms of Al_2O_3. Higher amounts of Al led to α-Al_2O_3 forming coatings [145].

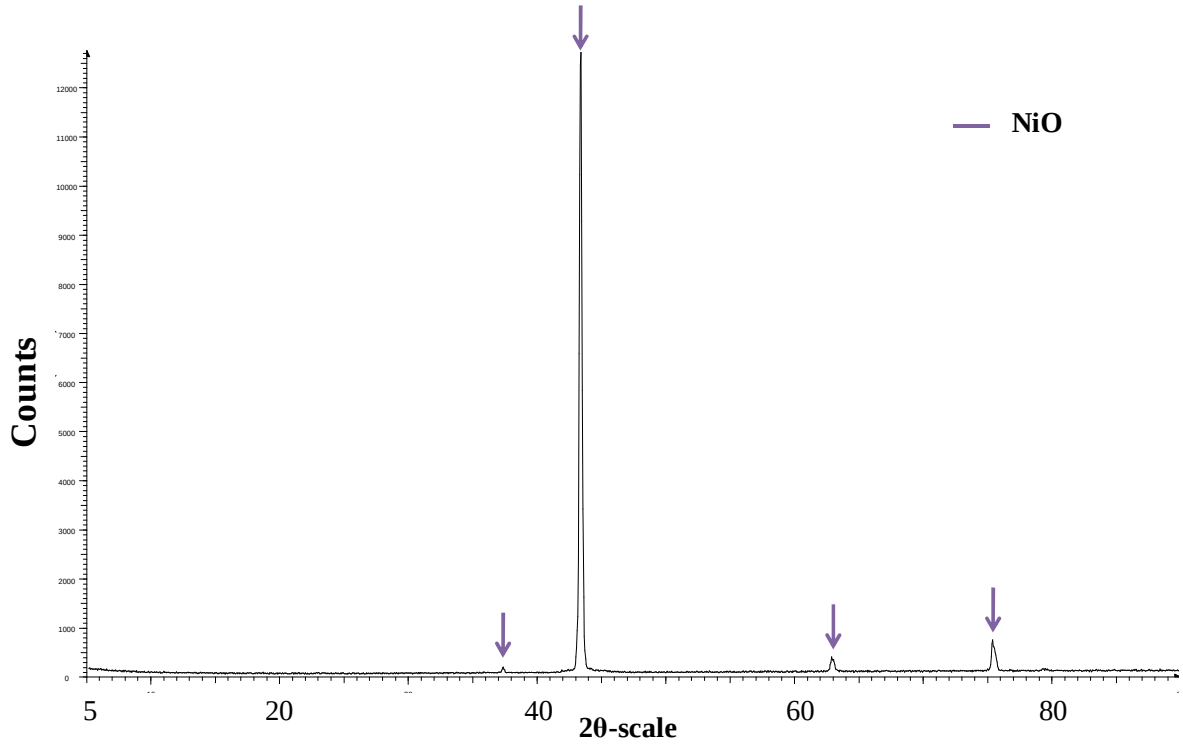

Figure 8.8 XRD spectrum from the surface of sample 130510B3 (10.6 at% Cr, 1.9 at% Al)(Ni-10wt%Cr + Al) after 220 hours exposure showing the presence of NiO.

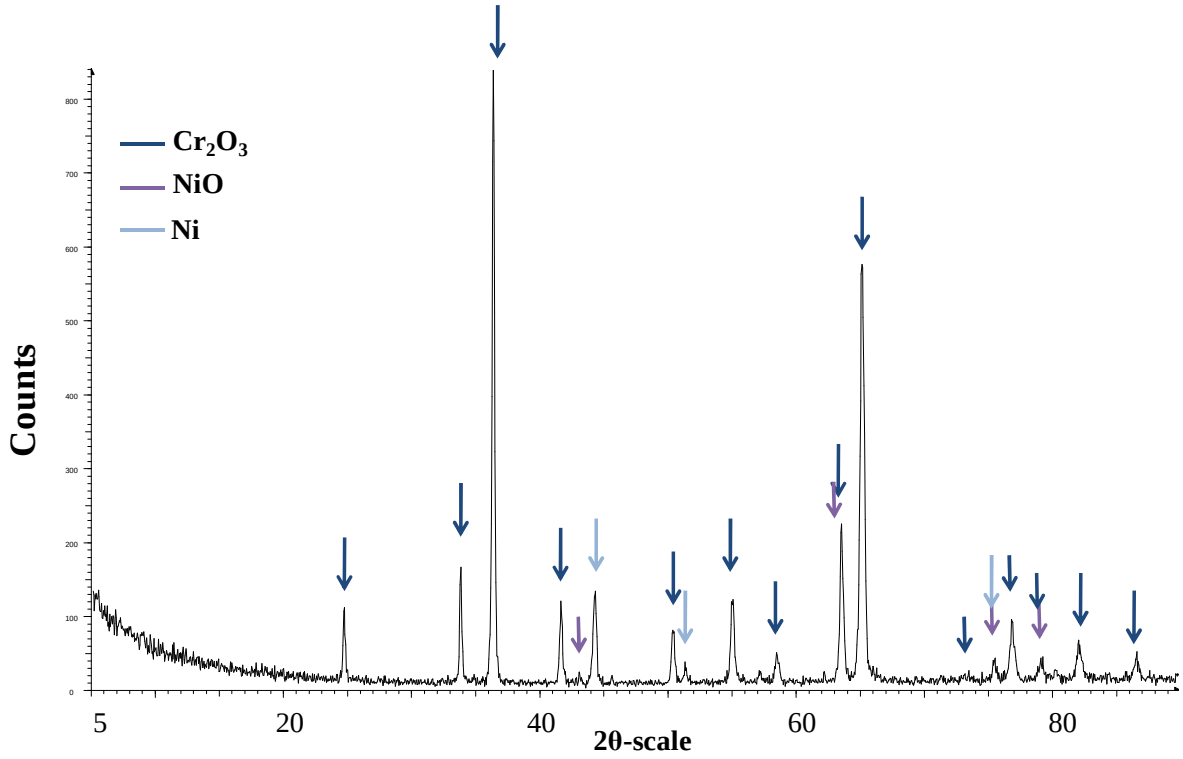

Figure 8.9 XRD spectrum from the surface of sample 290610D2 (55.9 at% Cr, 6.0 at% Al)(Ni-50wt%Cr + Al) after 500 hours exposure showing the presence of NiO and Cr_2O_3.

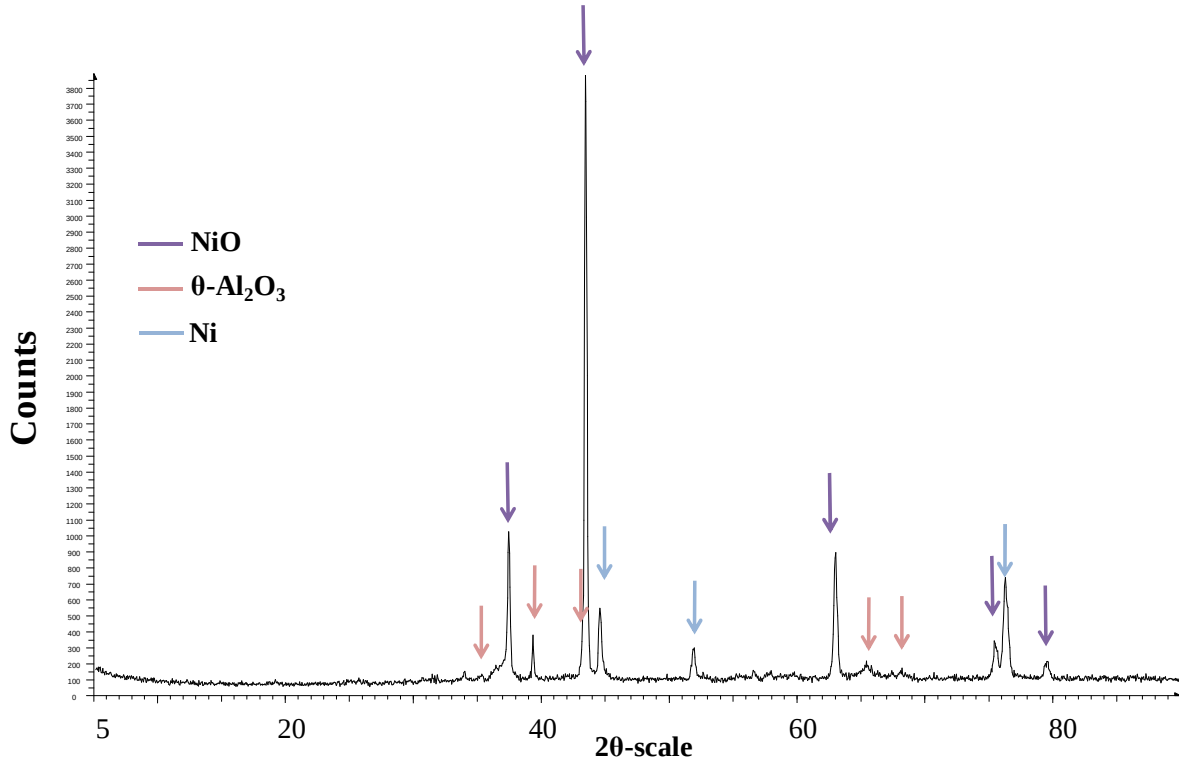

Figure 8.10 XRD spectrum from the surface of sample 130510e3 (8.2 at% Cr, 15.5 at% Al)(Ni-10wt%Cr + Al) after 500 hours exposure showing the first traces of Al_2O_3.

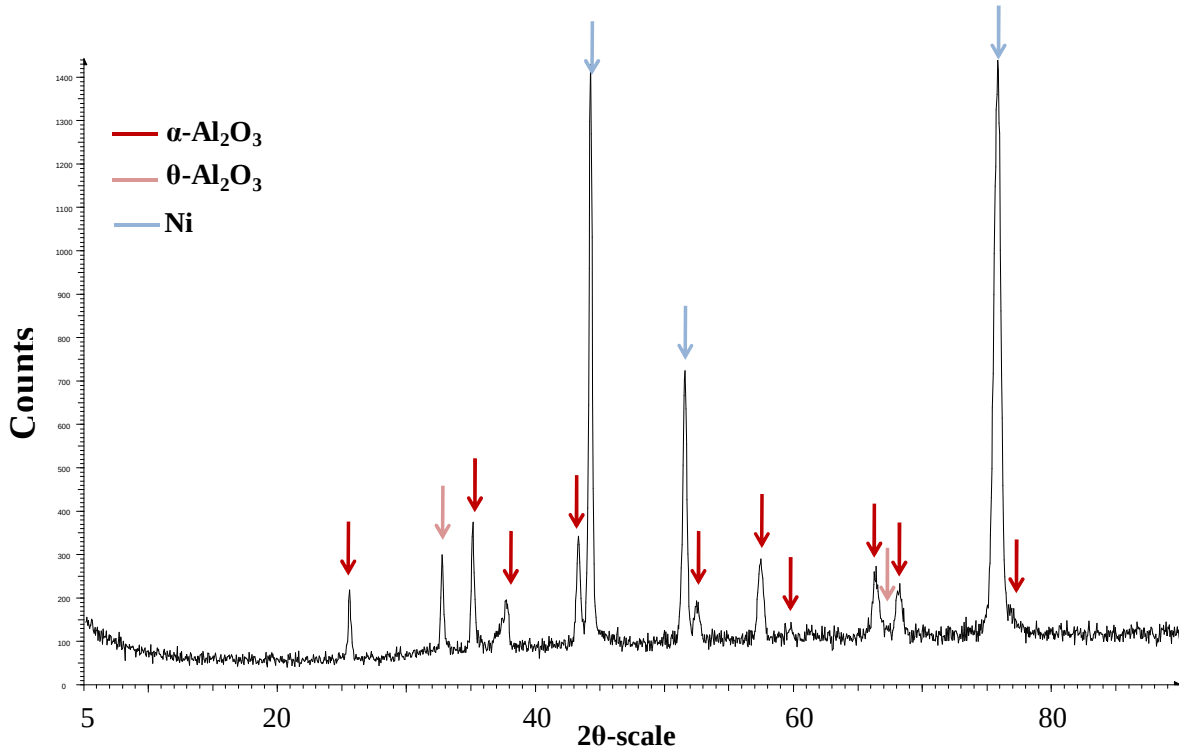

Figure 8.11 XRD spectrum from the surface of sample 170510F2 (6.7 at% Cr, 31.7 at% Al)(Ni-10wt%Cr + Al) after 500 hours exposure showing Al_2O_3.

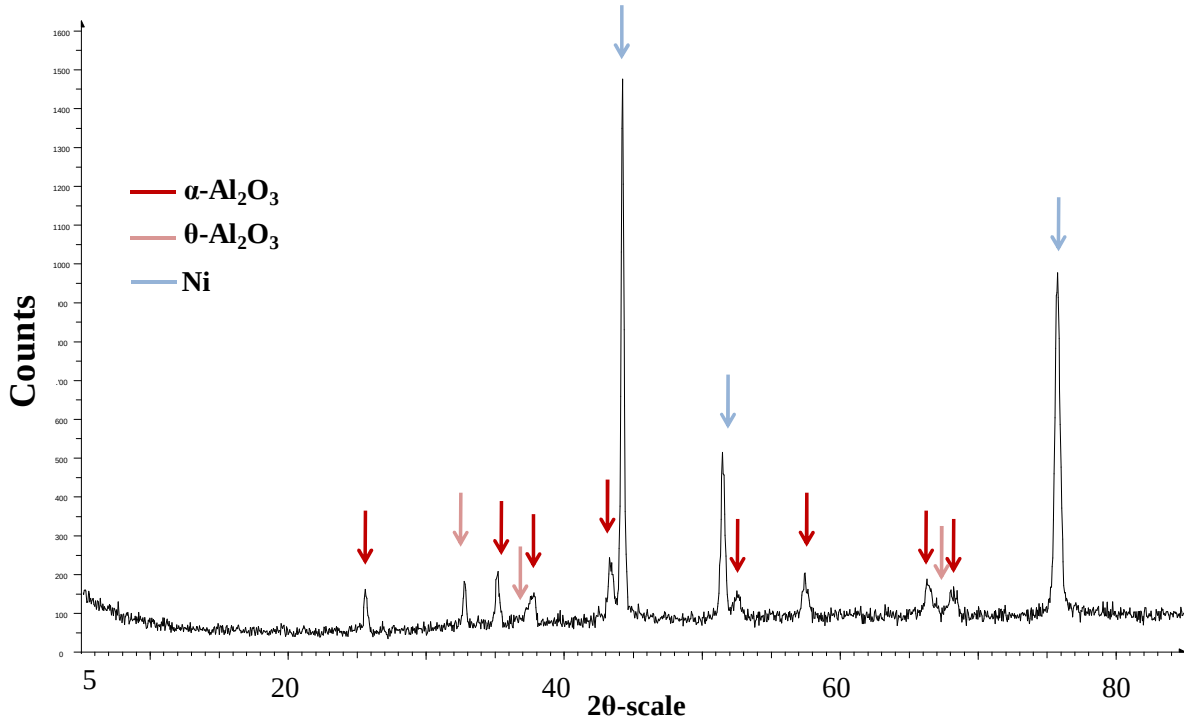

Figure 8.12 XRD spectrum from the surface of sample 080710F2 (14.6 at% Cr, 21.5 at% Al) (Ni-20wt%Cr + Al) after 500 hours exposure showing Al_2O_3.

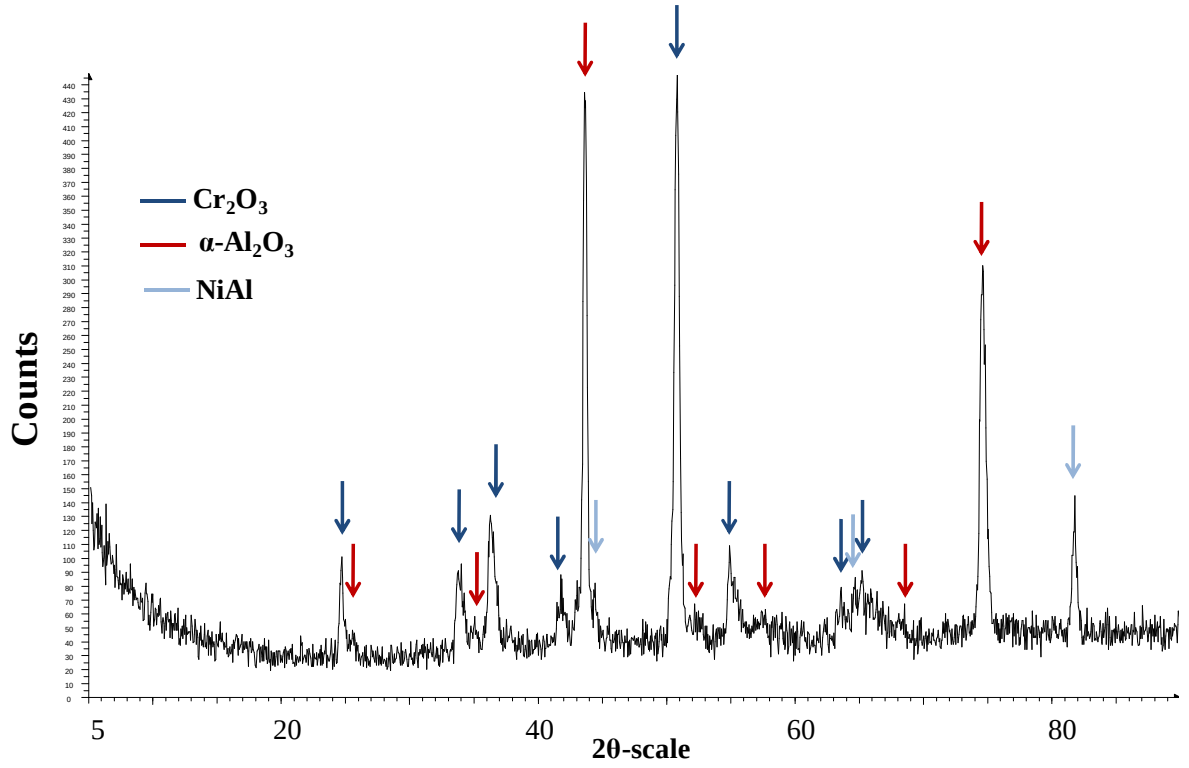

Figure 8.13 XRD spectrum from the surface of sample 290610E3 (48.2 at% Cr, 18.2 at% Al)(Ni-50wt%Cr + Al) after 500 hours exposure showing the first traces of Al_2O_3 growing with Cr_2O_3.

A few samples grew less protective oxides, such as $NiCr_2O_4$ and $NiAl_2O_4$ spinels or $NiO.Cr_2O_3$ oxides. Spinels observed on samples having failed prematurely may be a result of transient oxidation, such as sample 080710B2 (22.1 at% Cr, 0.5 at% Al)(Figure 8.14). However, after longer exposure, the formation of spinel between the coating and the substrate may well reflect Al exhaustion after 500 hours of oxidation testing at 950 °C (Figure 8.15). At 950 °C, less protective oxides were observed on a few samples with Cr contents higher than 5 at% (in the absence of NiO). Samples oxidised at 950 °C indicate either that these oxidation conditions do not promote the formation of spinels, or that exposure at this temperature might help the transformation of transient spinels and mixed oxides into protective Al_2O_3 or Cr_2O_3 [145].

The XRD results for all the samples oxidised at 950 °C are summarised in Table 8.3.

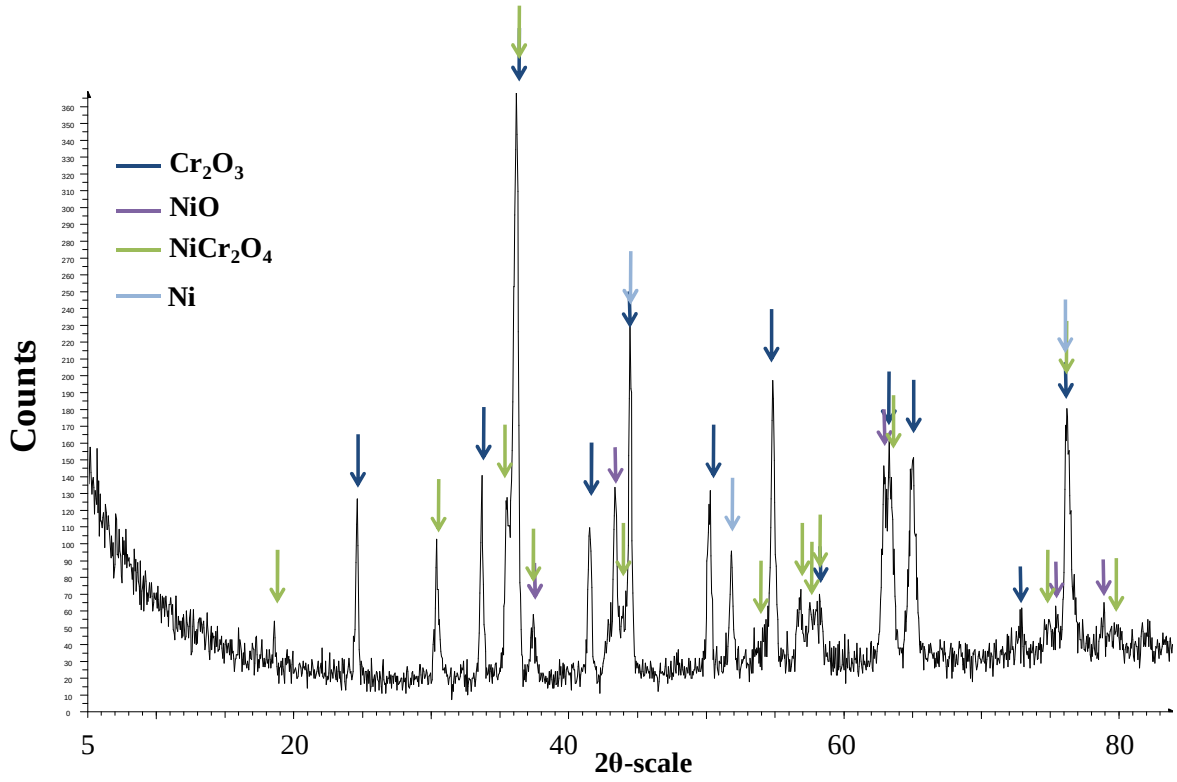

Figure 8.14 XRD spectrum from the surface of sample 080710B2 (22.1 at% Cr, 0.5 at% Al)(Ni-20wt%Cr + Al) after 80 hours exposure showing the presence of Cr_2O_3 as well as spinels.

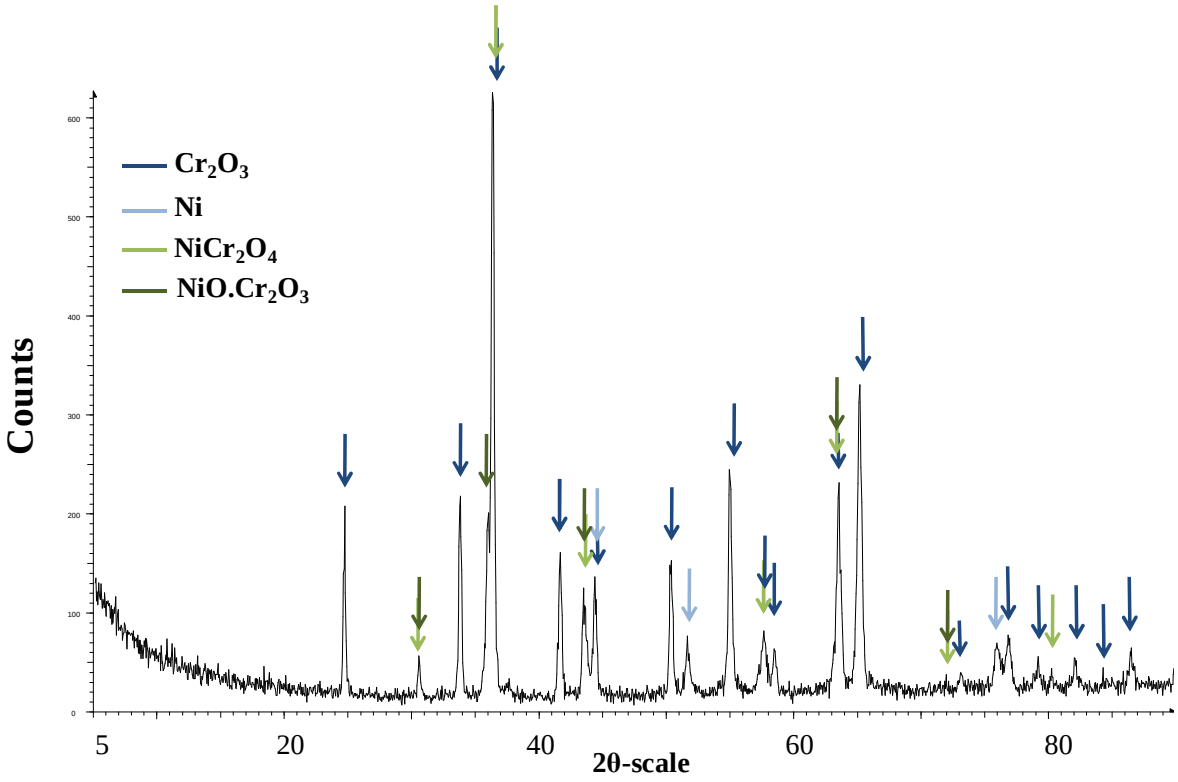

Figure 8.15 XRD spectrum from the surface of sample 290610d3 (51.8 at% Cr, 12.1 at% Al)(Ni-50wt%Cr + Al) after 500 hours exposure showing the presence of Cr_2O_3 , as well as spinels and mixed oxides.

The cross-sections through samples from the Ni-10wt%Cr+Al, Ni-20wt%Cr+Al and Ni-50wt%Cr+Al batch were mounted and observed under the SEM (Figures 8.16 to 8.18). According to literature [63], the magnetron sputtering had deposited coatings with a columnar microstructure because of the roughness of the sapphire substrates. Even if the deposition rate was dependant on the target, all the coatings were between ~30 and ~50 µm thick. As Figure 8.17(a) shows, adhesion between the Ni-Cr-Al and the sapphire disc was more or less adequate depending on composition, which might explain why some coatings detached earlier than others during exposure.

Targets	Sample		NiO	Cr_2O_3	Al_2O_3	Mixed oxides	Spinels
Ni-10wt%Cr+Al	130510	B3	+				
	170510	d2	+				
	130510	E2	+				
	130510	e3	+				
	170510	F2			α-,θ-		
	170510	f3			α-,θ-		
	170510	G3			α-		
	170510	g2			α-		
	130510	H2			α-		
	130510	h2			α-		
	130510	i2			α-		
Ni-20wt%Cr+Al	080710	B2	+	+			$NiCr_2O_4$
	080710	D3	+	+			
	080710	F2			α-,θ-		
	080710	f2			α-		
	080710	G2			α-		
	080710	g2			α-		
	080710	H2			α-,θ-		
	080710	h2			α-		
	080710	i1			α-		
Ni-50wt%Cr+Al	290610	C3		+			
	290610	D2	+	+			
	290610	d3	+	+		$NiO.Cr_2O_3$	$NiCr_2O_4$
	290610	E3		+	α-		
	290610	F2			α-,θ-		$NiCr_2O_4$
	290610	f3			α-,θ-		
	290610	G2			α-		
	290610	H3			α-		$NiCr_2O_4$
	290610	h2			α-		

Table 8.3 Different oxide phases identified using XRD on the samples exposed at 950 °C.

Figure 8.16(a) shows a cross-section through sample 170510d2, from the Ni-10wt%Cr+Al batch which was initially rich in Ni (85 at% Ni, 9.7 at% Cr, 5.8 at% Al). The oxide scale that grew on the coating surface was composed of an external NiO layer above a mixed Cr_2O_3+Al_2O_3 layer. An external NiO layer above a Cr_2O_3 layer is consistent with the literature [40,43,59]. Indeed, the establishment of the Cr_2O_3 would have happened when the partial pressure of O_2 was reduced by the growth of NiO.

Figure 8.16(b) highlights the fact that oxide could also grow between the columns constituting the coating and at the coating/substrate interface. The high oxidation rate of the oxide could be an explanation for the formation of pores inside the Ni-Cr-Al overlay coating. Decreasing the amount of Ni to 81 at % in sample 170510E2 (9.2 at% Cr, 9.4at%Al) still led to the formation of a NiO layer. The $(Al,Cr)_2O_3$ was thicker on this sample and failure occurred between the two different oxide layers. Gradual increase of the Al content caused the external NiO layer to disappear, being replaced by a two layered $(Al,Cr)_2O_3$ oxide with different Cr contents (Figure 8.16(c)). With still more Al (31.7 at%), a pure Al_2O_3 layer formed (Figure 8.16(d)).

Sample 080710D3 (20.2 at% Cr, 2.6 at% Al), from the Ni-20wt%Cr+Al batch, is shown in Figure 8.17(b). $(Cr,Al)_2O_3$ and NiO were identified on this sample by XRD analysis and this was confirmed with EDX analysis. The oxide layer typically measured around 20 µm. Figure 8.17(c), presents an image from a cross-section through sample 080710G2 (8.4 at% Cr, 50.4 at% Al), which was found to grow Al_2O_3 and traces of spinels. The oxides were typically very thin, < ~ 5µm thick, and grew on top on the Ni-Cr-Al, between the columns and at the interface with the sapphire substrate. The spinels were usually found close to the substrate which indicated that the Al concentration was very low in this region of the coating. Finally, Figure 8.17(d) shows the picture of a sample containing a high amount of Al, 080710H2 (3.7 at% Cr, 79.2 at% Al). In this case the growth of the oxide consumed most of the Ni-Cr-Al to create an Al_2O_3 which did not survive sample preparation. The growth of this oxide was promoted by the melting of the coating.

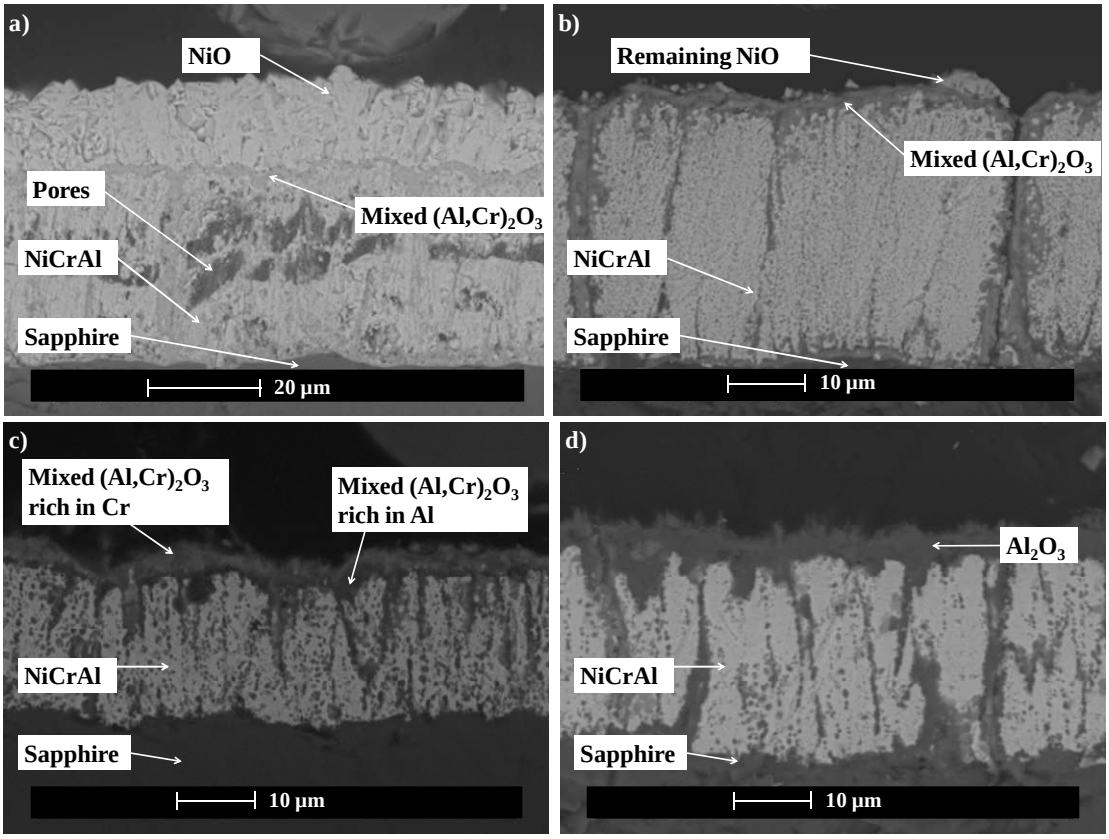

Figure 8.16 Cross sections SEM images of (a) 170510d2, (b) 130510E2, (c) 130510e3 and (d) 170510F2.

Cross-sections of samples chosen from the Ni-50wt%Cr+Al batch are shown in Figure 8.18. High amounts of Cr avoided the formation of an external NiO layer and led to the growth of a mixed $(Al,Cr)_2O_3$ layer (Figure 8.18(a)). Increasing the initial fraction of Al up to 32.61 at%, enabled the growth of a pure Al_2O_3 layer as seen on the cross-section through sample 290610F2 (44.9 at% Cr, 32.6 at% Al) in Figure 8.18(b).

The use of analytical techniques, to identify the nature of the oxides growing on the Ni-Cr-Al coatings, confirmed the hypothesises from the weight change data. Indeed, the various extents of oxidation shown by the different mass gain curves, reflected well the oxides formed. The only feature that mass change measurements did not show was the presence of spinels or mixed oxides beneath an outer oxide layer.

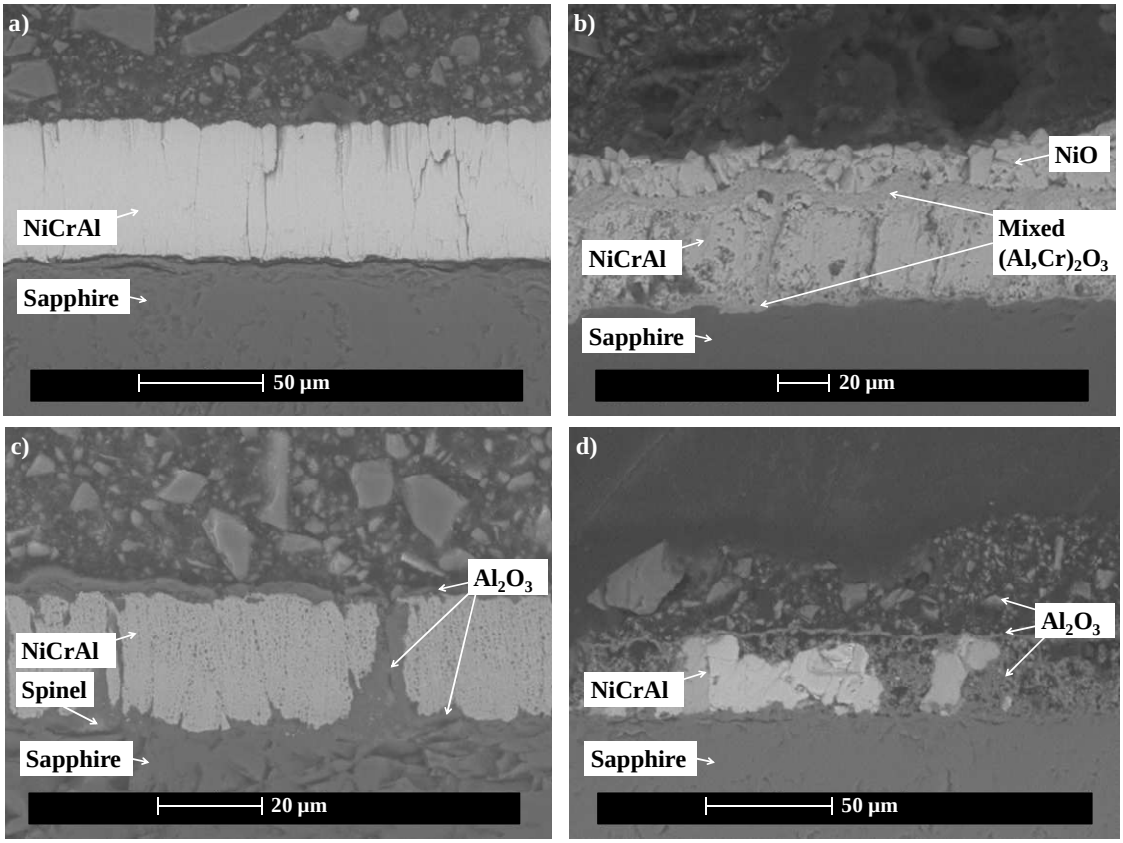

Figure 8.17 Cross sections SEM images of as deposited (a) 080710A2, (b) 080710D3, (c) 080710G2 and (d) 080710H2.

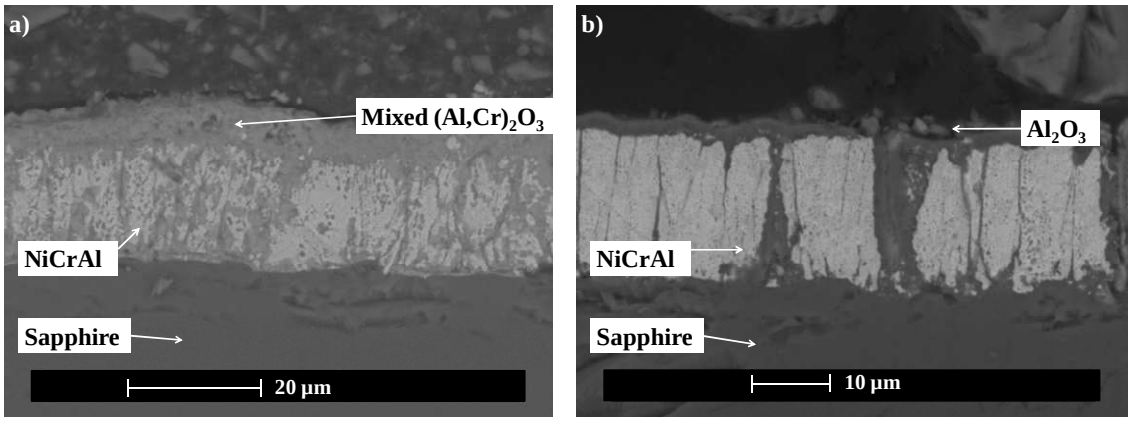

Figure 8.18 Cross sections SEM images of (a) 290610d3, and (b) 290610 F2.

The chemical composition obtained by EDX analysis of the oxide layers observed on example samples are summarised in Table 8.4.

Sample		Oxide	O (at%)	Ni (at%)	Cr (at%)	Al (at%)
130510	B3	outer layer	52.5	32.9	1.1	13.5
		inner layer	57.2	14.9	13.9	14.0
170510	d2	outer layer	52.8	25.7	1.9	19.7
		inner layer	56.2	16.2	8.3	19.3
130510	E2	outer layer	52.3	33.0	2.3	12.5
		inner layer	50.4	17.0	8.9	23.7
130510	e3	outer layer	52.9	23.9	2.1	21.2
		inner layer	53.2	12.6	8.4	25.9
170510	F2	single layer	61.2	3.9	1.2	33.7
170510	f3	single layer	62.0	1.8	0.9	35.2
170510	g2	single layer	61.6	1.8	0.0	36.6
080710	D3	outer layer	53.2	25.6	1.5	19.4
		inner layer	62.0	8.5	14.1	15.5
080710	F2	single layer	60.3	3.2	1.6	35.0
080710	f2	single layer	56.0	4.8	2.6	36.7
080710	G2	single layer	58.5	2.4	2.0	37.1
080710	H2	single layer	60.3	1.7	0.4	37.6
290610	d3	single layer	62.1	1.5	18.7	17.7
290610	E3	single layer	54.4	3.4	10.8	31.4
290610	F2	single layer	54.0	2.1	8.4	35.5

Table 8.4 Composition (obtained by EDX analysis) of the oxide layers observed on the cross-sections of selected Ni-Cr-Al samples exposed at 950°C.

Table 8.4, indicated that, all the oxide layers contained variable levels of Ni. Comparison with Table 8.1 shows that this depended on the initial amount of Ni in the deposited coating. Lower levels of Ni could be from the beam spread in the EDX. High initial amounts of Ni (130510B3) led to the formation of a two layered oxide scale, whose outer layer was composed of 32.9 at% Ni and 13.5 at% Al (mixed $NiO.Al_2O_3$) and inner layer was composed of 14.9 at% Ni, 14 at% Al and 13.9 at% Cr ($NiO + (Al,Cr)_2O_3$). The reduced amount of Ni in samples from the Ni-50wt%Cr+Al batch coupled with the high fraction of Cr, avoided the formation of a double layered oxide.

Increasing the initial amount of Al in the coatings led to mixed $(Cr,Al)_2O_3$ layers increasingly richer in Al until the layer formed was mainly pure Al_2O_3 (Figure 8.19). SEM and EDX did not allow identifying different forms of Al_2O_3.

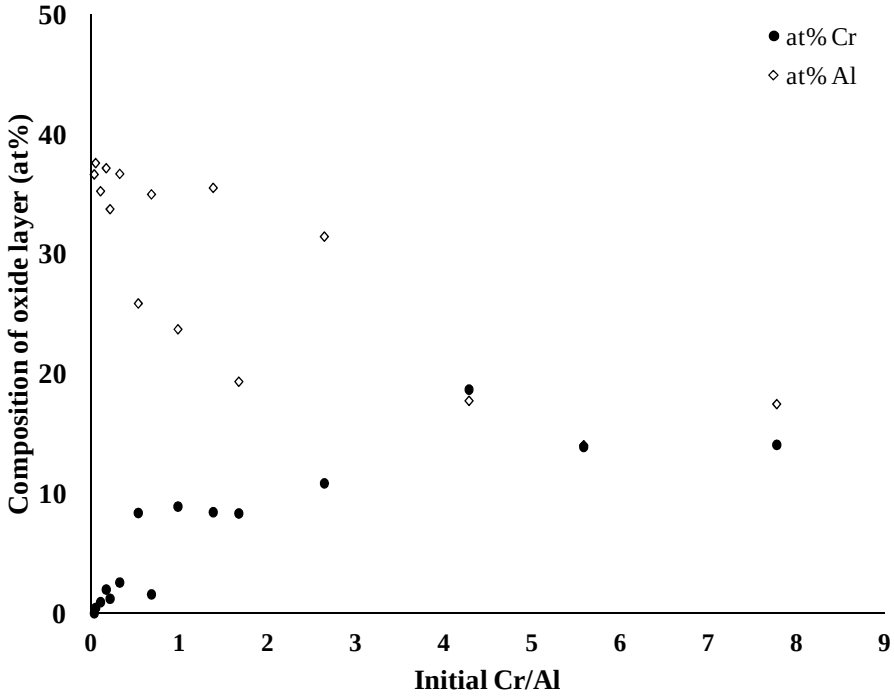

Figure 8.19 Effect of the initial Ni-Cr-Al coating composition on the $(Cr,Al)_2O_3$ oxides formed at 950°C.

8.1.4 Oxidation of the coatings obtained from 3 target co-sputtering

To complete the information provided by these 29 samples, 9 additional samples from the Ni-10wt%Cr+Ni-50wt%Cr+Al 3 targets co-sputtering batch were also exposed at 950 °C. The composition of the coatings selected for the oxidation at 950 °C, are in Table 8.5.

Sample	Ni (at%)	Cr (at%)	Al (at%)
251111_02	46.3	20.7	33.1
251111_06	32.4	28.9	38.7
251111_07	55.2	16.3	28.5
251111_08	30.7	38.0	31.3
251111_16	44.8	28.4	26.8
251111_20	57.6	26.0	16.4
251111_24	48.9	37.8	13.3
251111_25	45.4	33.7	21.0
251111_27	44.2	39.4	16.4

Table 8.5 Ni-Cr-Al compositions of coatings resulting from 3 targets co-sputtering and oxidised at 950 °C

After verification under the SEM, it was found that prior to oxidation, the coatings were only 10 µm thick, despite modifying deposition parameters. Therefore, to avoid their complete destruction, the samples were oxidised for 40 hours instead of 500. They were then analysed using XRD. A summary of the oxides detected in the samples is shown in Table 8.6. A majority of the transient Al_2O_3 present consisted of δ- Al_2O_3 instead of the θ-Al_2O_3 obtained on the previous samples after 500 hours exposure suggesting that the θ- phase appears later during oxidation. Also, few spinels were observed. Few spinels were detected on the samples' surface.

Sample	NiO	Cr_2O_3	α-Al_2O_3	transient Al_2O_3	spinels
251111_02		+	+	θ-Al_2O_3	
251111_06			+	δ-Al_2O_3	
251111_07	+	+	+	δ-Al_2O_3	
251111_08		+	+	δ-Al_2O_3	$Ni(Cr,Al)_2O_4$
251111_16		+	+	δ-Al_2O_3	
251111_20	+	+			$NiCr_2O_4$
251111_24		+	+		
251111_25		+	+	δ-Al_2O_3	
251111_27		+	+	δ-Al_2O_3	

Table 8.6 Different oxide species identified using XRD on the samples exposed at 950 °C for 40 hours.

8.1.5 Discussion - Ni-Cr-Al ternary oxidation map at 950 °C

Figure 8.20 summarises the oxides found on the coatings after oxidation at 950 °C for 500 hours of exposure. It shows that the higher the amounts of Al, the more likely Al_2O_3 will grow on the coating. Samples 170510g2 (2.3 at% Cr, 74.2 at% Al) and 130510H2 (1.6 at% Cr, 82.4 at% Al) from the Ni-10wt%Cr + Al batch differ from this tendency, but both of these coatings are expected to be molten when tested at 950 °C [61,146]. Superimposed on Figure 8.20 is a proposed boundary defining the limiting coating composition for Al_2O_3 scale formation at 950 °C. It should noted that at high concentrations and temperature's Al tends to react with the Ni to form intermetallics and that this will modify the Al_2O_3 activity and therefore the propensity of the coating to form Al_2O_3 scales. XRD showed the presence of Ni_3Al or NiAl phases in the coatings initially containing more than 60 at% Al. Oxidation of Ni_3Al at 950 °C does not encourage the growth of Al_2O_3 [148] and this could explain the presence of spinels in some of the samples. An Al depletion, caused by either the formation of Al_2O_3 in the first stages of oxidation or the formation of intermetallics, may have led to the growth of Ni oxides and mixed oxides towards the end of the oxidation tests. Moreover, because of the columnar microstructure of the sputtered coating, in some cases oxides grew between the substrate and the BC, between columns and on top of the BC. The higher oxygen partial pressure at the bottom of the BC caused by the growth of Al_2O_3 between columns, could contribute the growth of Ni oxides, and therefore the formation of $NiAl_2O_4$, instead of Al oxides as the Al reservoir in the coating is depleted as the oxidation progresses [145].

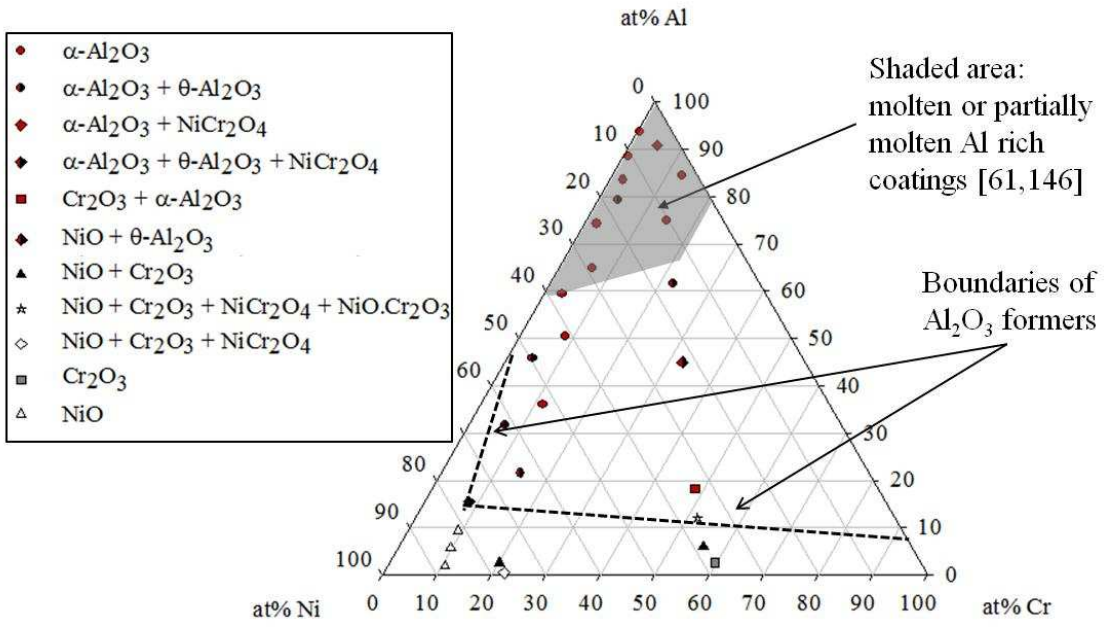

Figure 8.20 Oxide compositions grown on Ni-Cr-Al coatings after 500 hours at 950 °C (diagram in at%).

In 1989, Nicholls et al. [63] also oxidized sputtered Ni-Cr-Al discs at 950 °C and studied the rates of oxidation and the oxides formed. Coatings of similar thickness to those studied for this thesis (i.e. over 30 µm thick), showed the first traces of Al_2O_3 on samples containing 52.4 at% Al and 6.4 at% Cr (although, from the performances of commercially available BCs they anticipated that the boundary may well exist at 35 at% Al and 7 at% Cr, which is very comparable with the results of this study as can be seen from Figure 8.21).

For coatings with higher amounts of Cr, the amount of Al needed to form Al_2O_3 was only 15 at%; comparable to the results obtained in this thesis. However, Nicholls et al. [63] were able to observe Cr_2O_3 oxides even with low concentrations of Cr (4 at%) in their alloys, in contrast to the data obtained for this thesis (Figure 8.21). Typical commercial Ni-Cr-Al-Y coatings have 18 – 22 at% Cr and 16 – 24 at% Al, and so they are expected to grow Al_2O_3 when oxidized at temperatures of 950 °C. In the ternary

diagram (Figure 8.21), these coatings would be located above and right of the two hypothetical Al_2O_3 boundaries. In addition, the high amount of Cr in the most oxidation protective compositions found in this study might signify that such coatings would be capable of both oxidation and hot corrosion protection. This would be very useful for an industrial gas turbine application [145].

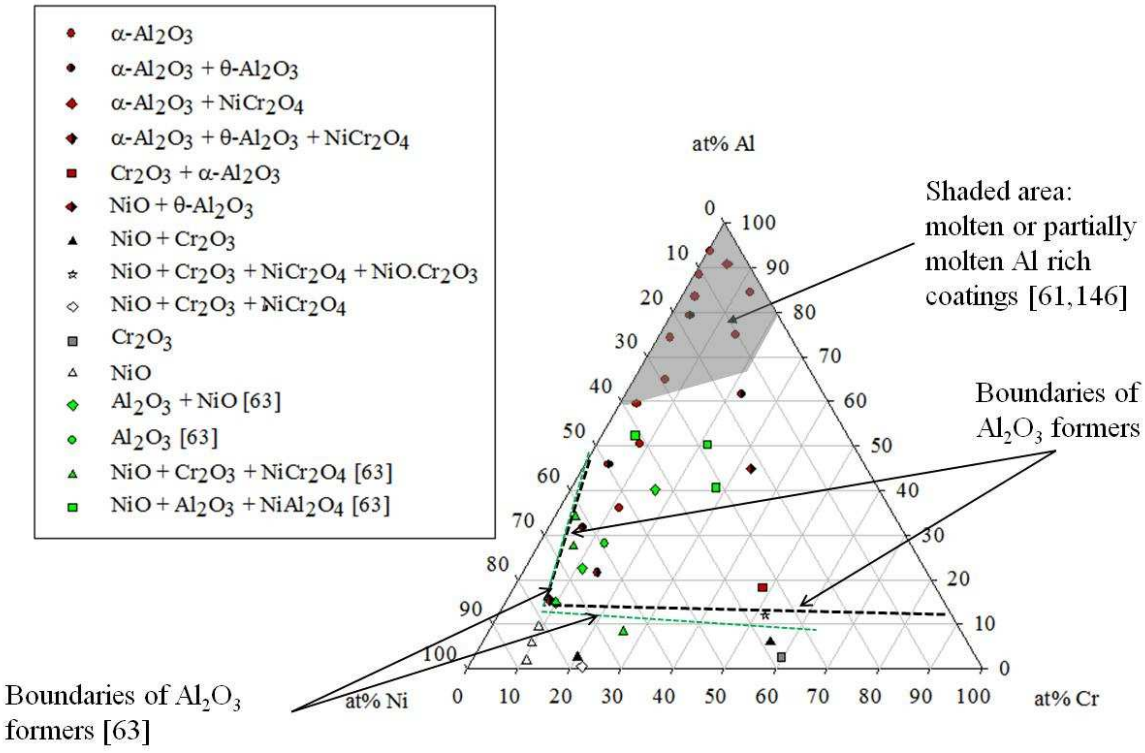

Figure 8.21 Oxide compositions grown on Ni-Cr-Al coatings after 500 hours at 950 °C compared to data obtained by Nicholls et al. [63](diagram in at%).

Data obtained from the oxidation of the coatings deposited with 3 targets was added to the previous ternary map and are shown in Figure 8.22. Apart from the exception circled in red, samples confirm the Al_2O_3 former domain boundaries drawn in Figure 8.20.

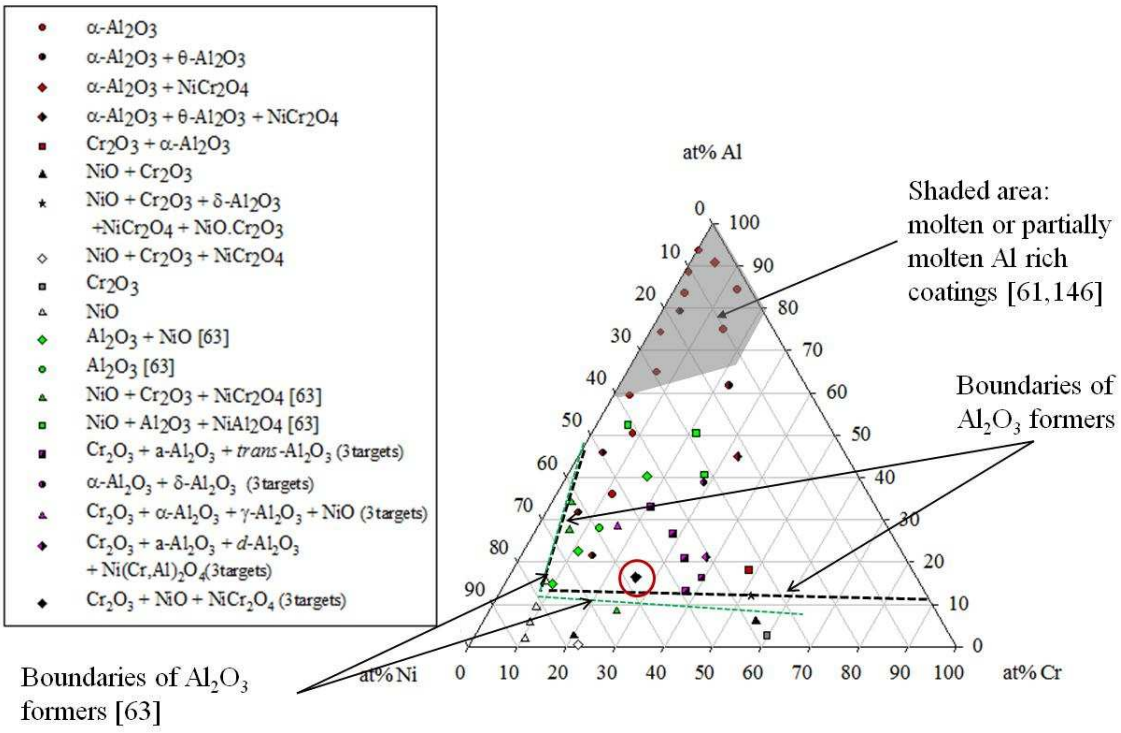

Figure 8.22 Oxide compositions grown on Ni-Cr-Al coatings after 500 hours at 950 °C completed with the data obtained from 3 target co-sputtering and compared to data obtained by Nicholls et al. [63](diagram in at%).

8.2 Oxidation of Ni-Cr-Al systems at 900 °C

As for the experiments carried out at 950 °C, around 10 samples from each batch of the 2 target co-sputtering deposition experiments were chosen and oxidized in air at 900 °C in a horizontal furnace for exposure times of up to 500 hours. They were unloaded every 20 hours for the same inspections as previously. Samples with apparent cracking and/or significant weight loss were taken out of the experiment. The compositions of the samples from the Ni-10wt%Cr+Al, Ni-20wt%Cr+Al and Ni-50wt%Cr+Al targets are presented in Table 8.7. Compositions as close to the ones chosen previously were taken for exposure in order to compare the behaviour of the coatings at different temperatures.

Targets	Sample		Ni (at%)	Cr (at%)	Al (at%)	Cr/Al	Exposure (hours)
Ni-10wt%Cr+Al	130510	D2	86.1	9.9	4.0	2.49	100
	130510	d2	84.5	9.7	5.8	1.67	120
	170510	E3	81.4	9.2	9.4	0.98	*60*
	170510	E2	81.4	9.2	9.4	0.98	460
	130510	e2	76.3	8.2	15.5	0.53	*60*
	170510	e2	76.3	8.2	15.5	0.53	100
	170510	F3	61.6	6.7	31.7	0.21	500
	170510	f2	49.5	4.7	45.8	0.10	500
	130510	i3	6.0	0.4	93.6	0.00	500
Ni-20wt%Cr+Al	080710	c2	77.2	20.9	1.9	11.00	100
	080710	d3	77.0	18.5	4.5	4.11	500
	080710	E3	74.3	17.9	7.8	2.31	220
	080710	e2	69.1	16.3	14.6	1.11	500
	080710	F3	63.9	14.6	21.5	0.68	500
	080710	f3	52.5	11.5	36.0	0.32	500
	080710	G3	41.2	8.4	50.4	0.17	500
	080710	h3	14.0	2.5	83.5	0.03	500
	080710	i4	10.2	2.1	87.7	0.02	100
Ni-50wt%Cr+Al	290610	C2	37.7	59.7	2.7	22.53	500
	290610	c3	37.9	57.8	4.3	13.41	500
	290610	D3	38.1	55.9	6.0	9.36	500
	290610	E2	33.5	48.2	18.2	2.64	500
	290610	e3	29.7	41.6	29.1	1.43	500
	290610	F3	22.5	32.6	44.9	0.73	500
	290610	G3	10.3	14.7	74.9	0.20	60
	290610	g3	6.8	9.0	84.2	0.11	500
	290610	H2	4.1	5.1	90.8	0.06	500

Table 8.7 Compositions of Ni-Cr-Al coatings resulting from 2 target co-sputtering and oxidised at 900 °C. Numbers in italic correspond to samples removed prematurely for observation purposes.

8.2.1 Physical changes of samples with exposure

Lowering the exposure temperature from 950 to 900 °C caused the oxidation mechanisms to slow down, leading to particular physical changes of the coatings surfaces. Pictures of the samples at different exposure times are shown in Figures 8.23 to 8.25.

Samples from the Ni-10wt%Cr+Al batch are presented in Figure 8.23. As at 950 °C, light grey crystals grew on the surface of coatings containing over 85 at% Ni (130510 D2 (9.9 at% Cr, 4 at% Al)). Increasing the Al concentration led to a spectacular change of colour during the first stages of oxidation. The surfaces of samples 170510E2 (9.2 at% Cr, 9.4 at% Al) and 170510 e2 (8.2 at% Cr, 15.5 at% Al) evolved from grey to iridescent pinks and greens. These colourful shades disappeared with further exposure to leave a light grey colour. On the other hand, samples with higher amounts of Al (over 30 at%), like 170510F3 (6.7 at% Cr, 31.7 at% Al), became black in the first stages of oxidation. Finally, as for samples oxidised at 950 °C, the samples essentially composed of Al such as 130510i3 (0.4 at% Cr, 93.6 at% Al), showed a molten/re-solidified profile. The early detachment of most of the coatings from the Ni-10wt%Cr+Al batch at 900 °C confirm that low amounts of Cr are life limiting.

Only pictures of the transient stage of oxidation were taken for the samples from the batches of Ni-20wt%Cr+Al (Figure 8.24) and Ni-50wt%Cr+Al (Figure 8.25). They show the unchanged coloration of 080710d3 (18.5 at% Cr, 4.5 at% Al), the slightly iridescent edge of 080710E3 (17.9 at% Cr, 7.8 at% Al) and the black shade of 080710e2 (16.3 at% Cr, 14.6 at% Al) which confirmed the different nature of the oxides growing on those three samples. The iridescent shade on 080710E3 disappeared with oxidation

as it was observed on sample 130510E2. As for samples from the Ni-10wt%Cr+Al batch, 080710h3 (2.5 at% Cr, 83.5 at% Al) showed a molten/re-solidified profile.

The same observations were made for samples taken from the Ni-50wt%Cr+Al batch (Figure 8.25). As the amount of Al in the coating increased, samples went from a grey (290610D3 (55.9 at% Cr, 6.0 at% Al)), to an iridescent (290610 E2 (48.2 at% Cr, 18.2 at% Al)), to a dark colour (290610F3 (32.6 at% Cr, 44.9 at%Al). Again, the iridescent colour, faded with exposure. This is an effect of oxide thicknesses when they are approximately the same as the wavelength of light. Finally high amounts of Al (91 at%) lead to the same molten/re-solidified coatings (290610 H2 (5.1 at% Cr, 90.8 at5 Al).

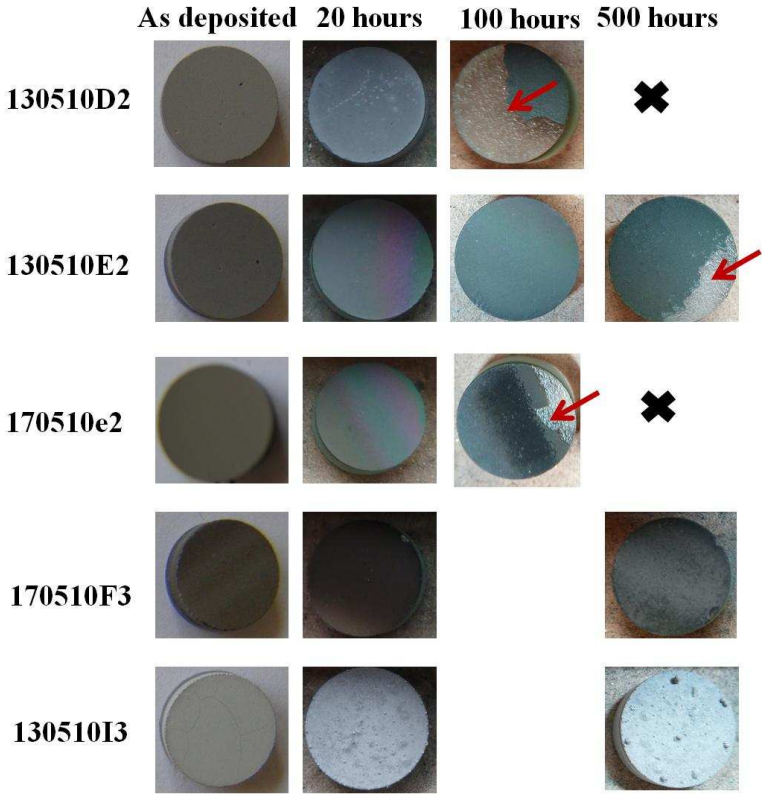

Figure 8.23 Pictures showing the evolution of the oxides on 130510D2 (9.9 at% Cr, 4 at% Al), 170510E2 (9.2 at% Cr, 9.4 at% Al), 170510e2 (8.2 at% Cr, 15.5 at% Al), 170510F3 (6.7 at% Cr, 31.7 at% Al) and 130510i3 (0.4 at% Cr, 93.6 at% Al)(Ni-10wt%Cr+Al) with exposure at 900 °C. Red arrows point at damage in coatings.

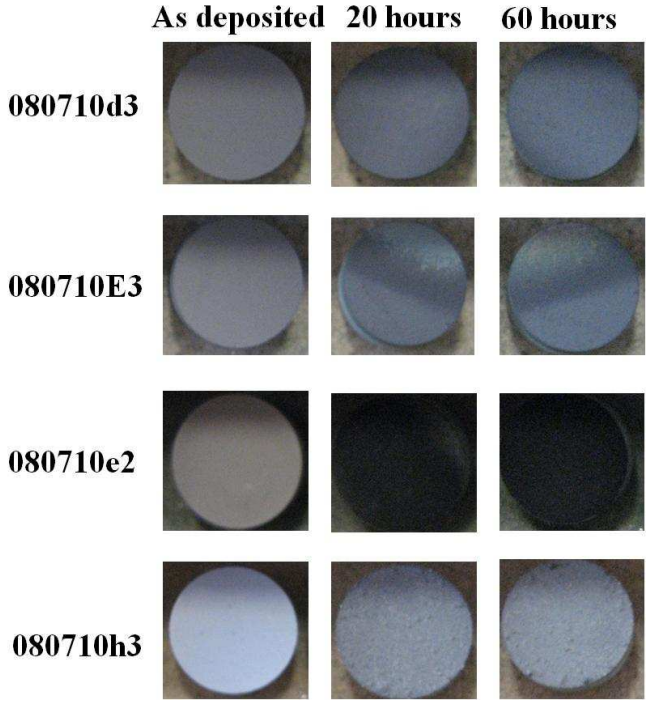

Figure 8.24 Pictures showing the evolution of the oxides, during the first stage of oxidation, on 080710d3 (18.5 at% Cr, 4.5 at% Al), 080710E3 (17.9 at% Cr, 7.8 at% Al), 080710e2 (16.3 at% Cr, 14.6 at% Al) and 080710h3 (2.5 at% Cr, 83.5 at% Al)(Ni-20wt%Cr+Al) with exposure at 900 °C.

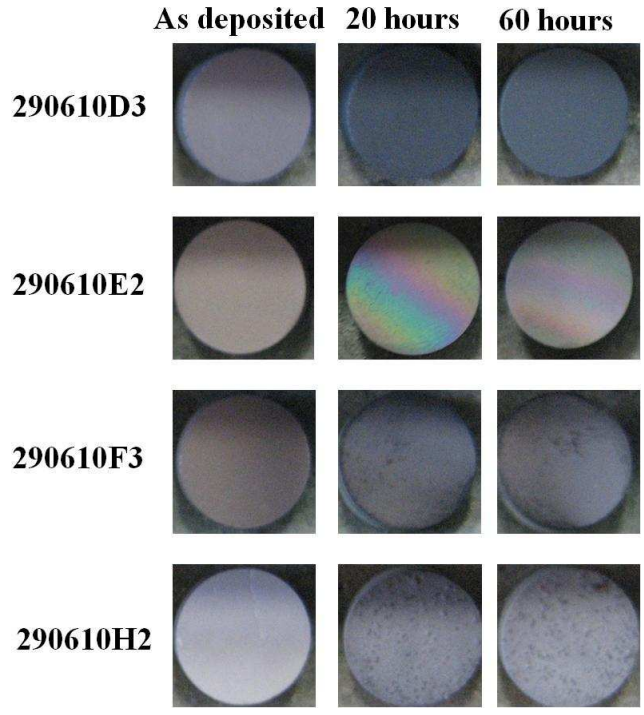

Figure 8.25 Pictures showing the evolution of the oxides, during the first stage of oxidation, on 290610D3 (55.9 at% Cr, 6.0 at% Al), 290610E2 (48.2 at% Cr, 18.2 at% Al), 290610F3 (32.6 at% Cr, 44.9 at%Al) and 290610H2 (5.1 at% Cr, 90.8 at5 Al) (Ni-50wt%Cr+Al) with exposure at 900 °C.

8.2.2 Mass change of samples

Once again, weighing the coated sapphire discs allowed the sample mass changes to be calculated. Different types of oxides had different oxidation rates. Therefore, the mass change graphs of sample over a period of 500 hours could be correlated with the nature of the oxide growing on the coating.

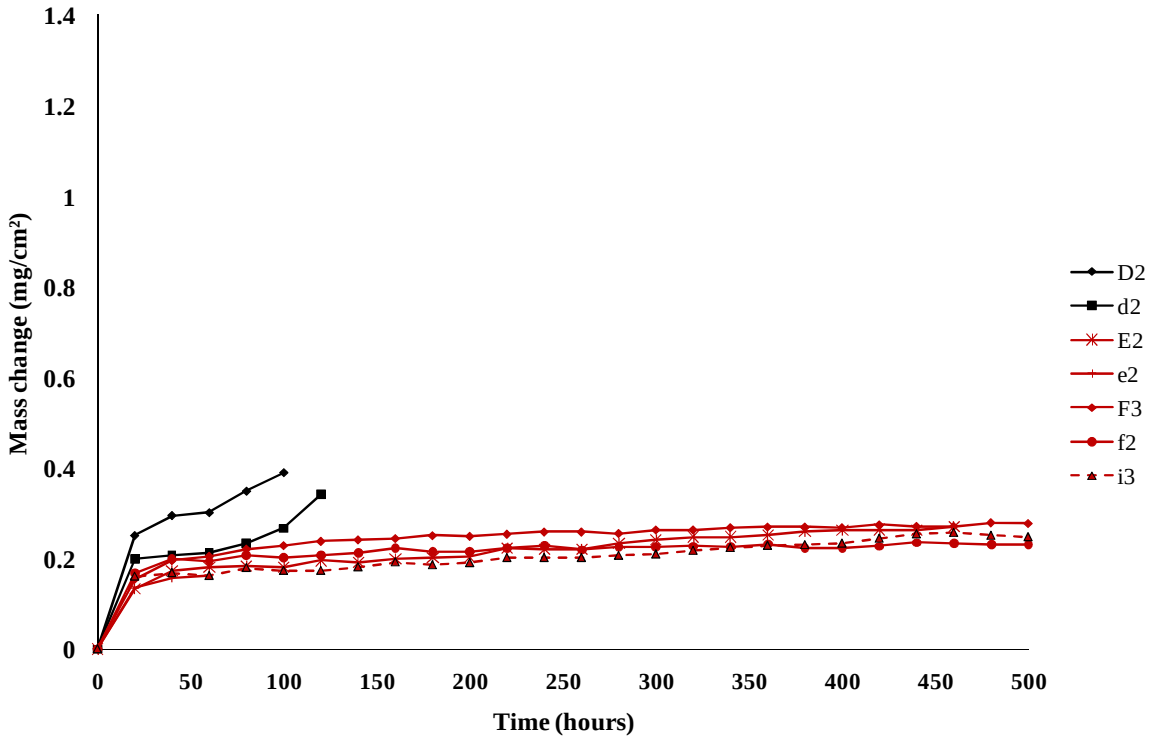

Figure 8.26 Mass change of Ni-10wt%Cr+Al coating against time of exposure at 900 °C.

Figure 8.26 presents the mass changes of the Ni-10wt%Cr+Al coatings. As at 950 °C, two types of behaviour were observed. However, the mass changes associated with these two behaviours were very close to each other, reaching from 0.2 to 0.4 mg/cm^2 after 100 hours. Oxides on samples containing over 80 at% of Ni, 130510D2 (9.9 at% Cr, 4 at% Al) for example, grew quickly while oxides on samples with

contents around and above 9 at% Al, 170510E2 (9.2 at% Cr, 9.4 at% Al), grew more slowly. The mass change curves were once again divided in two parts: an initial fast growing part followed by and a steady growth part. This describes the two stages of Al_2O_3 growth (transient oxide growth, e.g. θ-Al_2O_3 or possibly NiO, followed by α-Al_2O_3). The particular behaviour of 130510d2 (9.7 at% Cr, 5.8 at% Al) can be explained by a late appearance of NiO oxides which changed the oxidation mechanisms after 80 hours of exposure until failure of the sample at 120 hours. Reducing the oxidation temperature did not reduce the mass gain of the coatings. The average mass change remained around 0.2 mg/cm^2 after 500 hours.

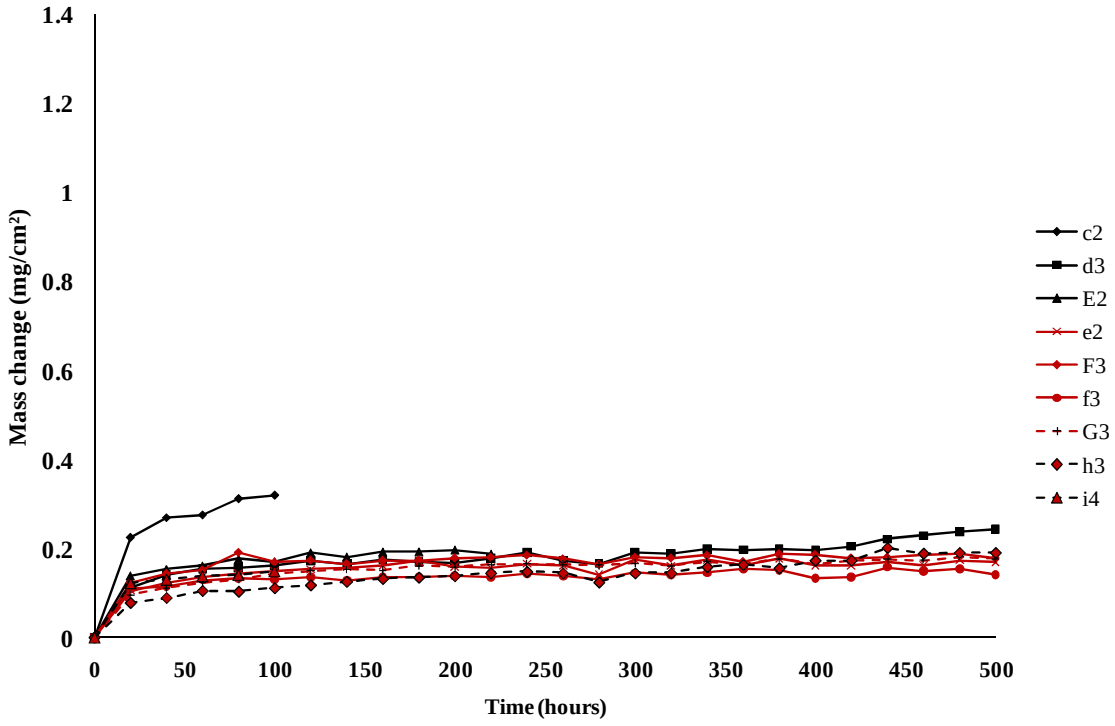

Figure 8.27 Mass change of Ni-20wt%Cr+Al coating against time of exposure at 900 °C.

The mass change of the Ni-20wt%Cr+Al coatings, represented in Figure 8.27, showed a similar behaviour to the Ni-10wt%Cr+Al ones apart from samples 080710d3

(18.5 at% Cr 4.5 at% Al) and 080710E2 (17.9 at% Cr, 7.8 at% Al) which, even if they were later found not to grow pure Al_2O_3 (XRD analysis), still had a very slow growing oxide. Samples falling into the composition range that were expected to be molten at the 950 °C test temperature (red and black data points on graph) did not show a high oxidation rate at 900 °C. However, pictures of these coatings confirmed that they had melted during exposure indicating that it might form a different liquid or partially liquid phase which behaves differently compared to the other phases.

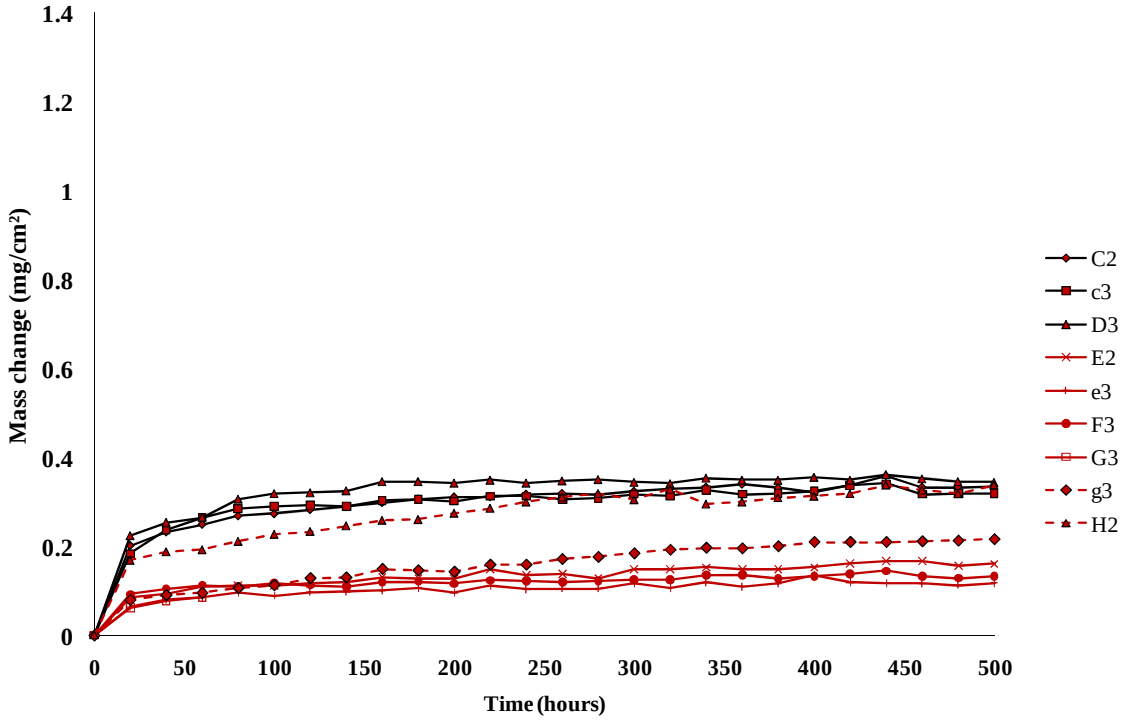

Figure 8.28 Mass change of Ni-50wt%Cr+Al coating against time of exposure at 900 °C.

The addition of up to 50 at% Cr to the alloy system reduced the extent of oxidation at 900 °C in a less dramatic manner than for samples exposed at 950 °C. Indeed, in Figure 8.26 (Ni-wt%10Cr+Al), the mass change of samples mainly growing Al_2O_3 reached 0.2 mg/cm^2 after 500 hours of exposure while in Figure 8.27 (Ni-

20wt%Cr+Al) their masses only increased by 0.1-0.2 mg/cm^2. Cr-rich coatings from the Ni-50wt%Cr+Al batch produced slow growing oxides with a maximum weight gain of 0.35 mg/cm^2 after 500 hours of exposure (Figure 8.28), presumably as a result of these compositions favoring the growth of Cr_2O_3 and Al_2O_3 scales over faster growing NiO. The Ni-50wt%Cr+Al samples growing Al_2O_3 (and not melting), such as 290610F3 (32.6 at% Cr, 44.9 at%Al) only reached a maximum gain weight of 0.1 mg/cm^2, comparable to the mass change seen in Figure 8.28, and similarly to samples exposed at 950 °C (Figure 8.6).

8.2.3 Identification of oxides

XRD analysis was used to identify the oxide phases present on the coatings after exposure. On samples from the Ni-10wt%Cr+Al batch, high concentrations of Ni (over 80 at%) in the samples led to the growth of NiO oxides and Cr_2O_3 (Figures 8.29 and 8.30). A peak typical of γ-Al_2O_3 was even observed on sample 130510d2's (9.7 at%Cr, 5.8 at% Al) spectrum but the presence of this oxide could not be confirmed (Figure 8.29). Increasing the concentration of Al up to ~9 at% led to the formation of $NiO.Al_2O_3$ and a further increase, to 15.5 at% Al, to the formation of α-Al_2O_3 (Figure 8.31). The composition of the Al_2O_3 oxide layer seemed more diverse when the initial amount of Al in the coating was around 32 at% as various transient forms of the Al oxide were observed on 170510 F3 (6.7 at% Cr, 31.7 at% Al)(Figure 8.32).

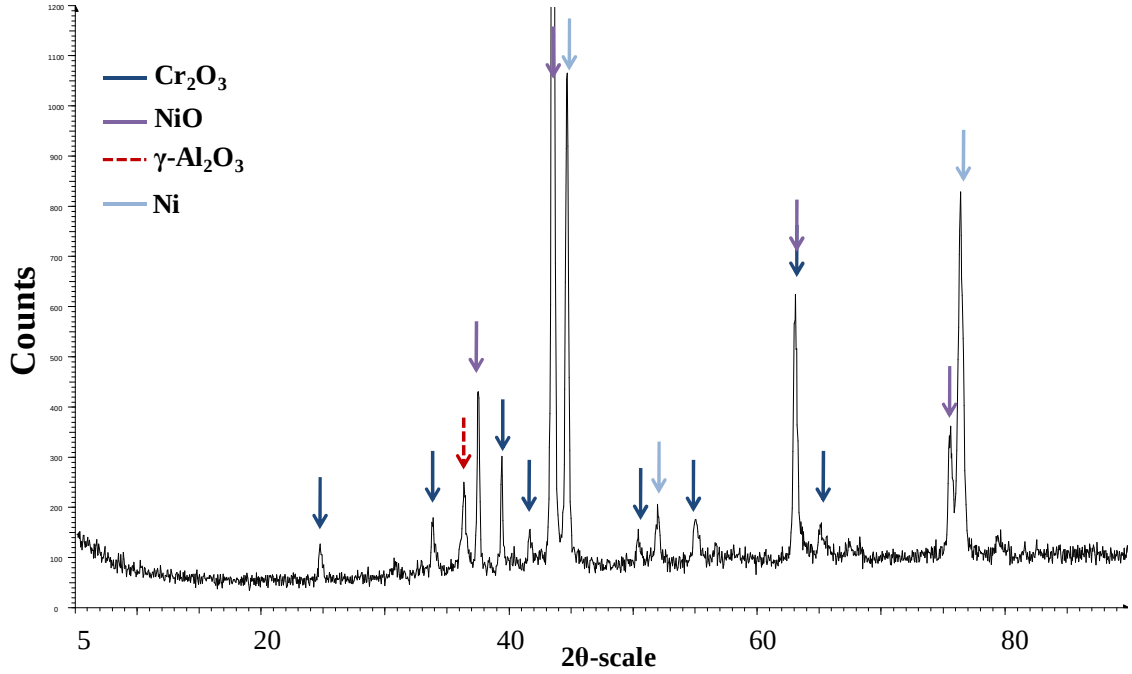

Figure 8.29 XRD spectrum from the surface of sample 130510d2 (9.7 at% Cr, 5.8 at% Al) (Ni-10wt%Cr+Al) after 120 hours exposure, showing the presence of Cr_2O_3, NiO and presumably transient γ-Al_2O_3.

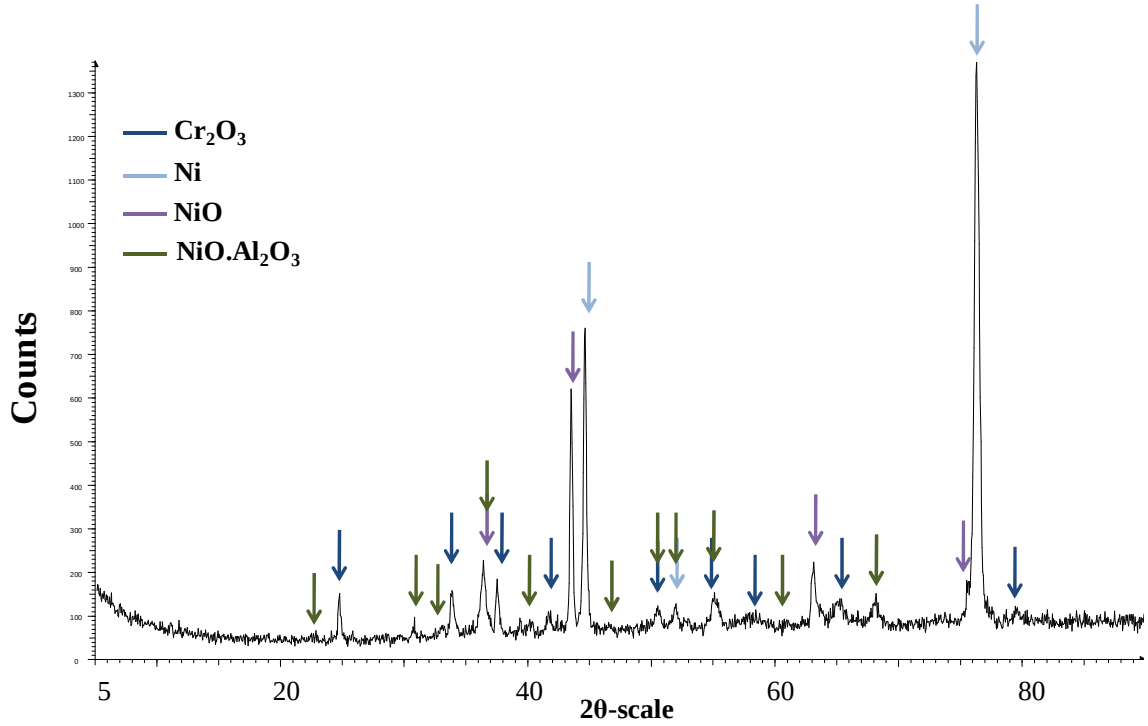

Figure 8.30 XRD spectrum from the surface of sample 170510E2 (9.2 at% Cr, 9.4 at% Al) (Ni-10wt%Cr+Al) after 500 hours exposure, showing the presence of Cr_2O_3, NiO and mixed oxides.

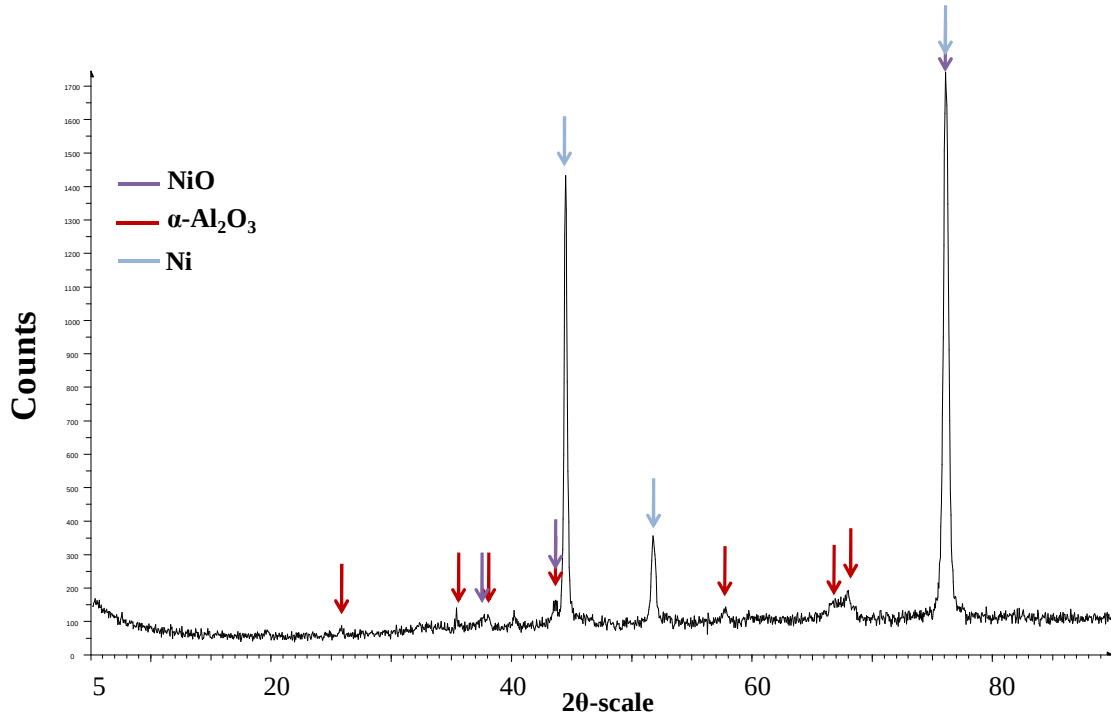

Figure 8.31 XRD spectrum from the surface of sample 130510e2 (8.2 at% Cr, 15.5 at% Al)(Ni-10wt%Cr+Al) after 100 hours observation, showing the presence of NiO and α-Al_2O_3.

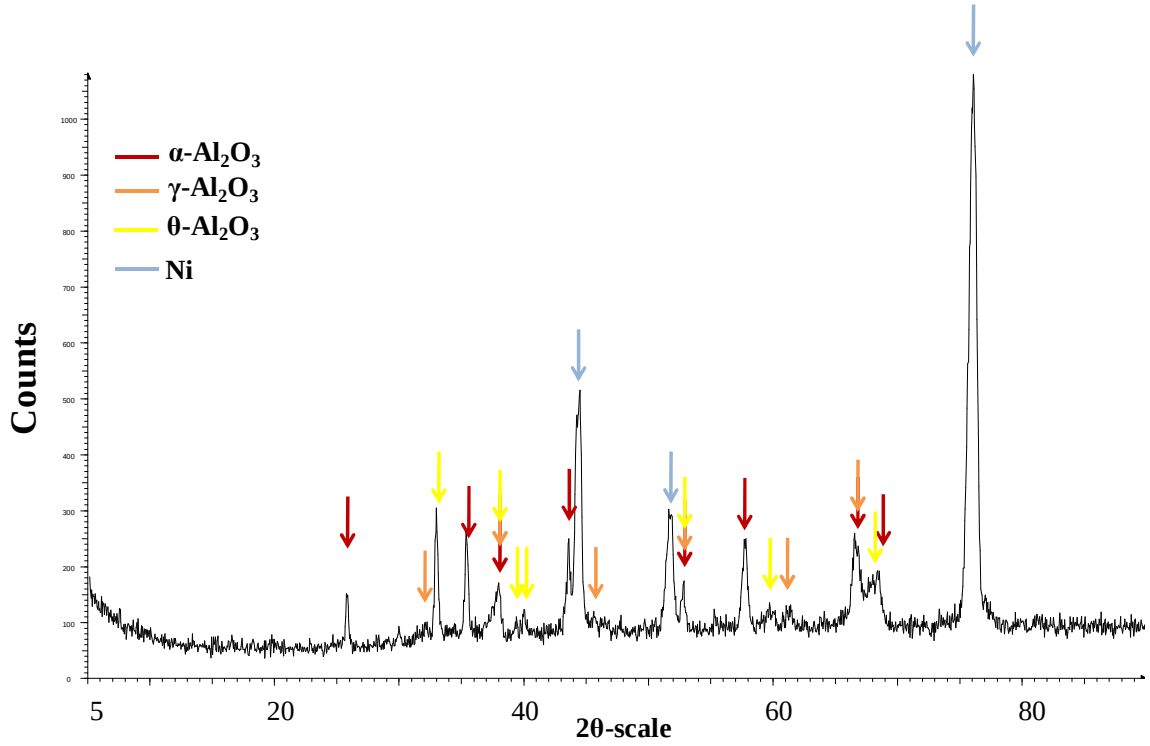

Figure 8.32 XRD spectrum from the surface of sample 170510F3 (6.7 at% Cr, 31.7 at% Al) (Ni-10wt%Cr+Al) after 500 hours oxidation, showing the presence of transient γ- and θ-Al_2O_3 as well as α-Al_2O_3.

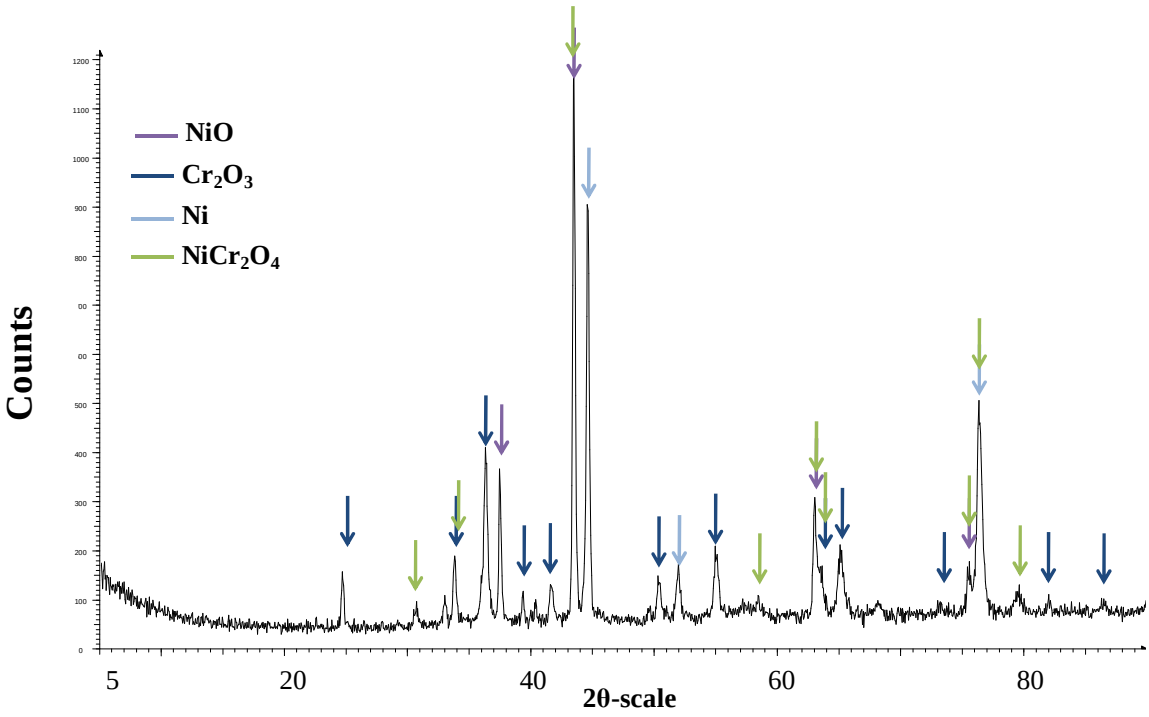

Figure 8.33 XRD spectrum from the surface of sample 080710d3 (18.5 at% Cr, 4.5 at% Al) (Ni-20wt%Cr+Al) after 500 hours exposure, showing the presence of Cr_2O_3, NiO and spinels.

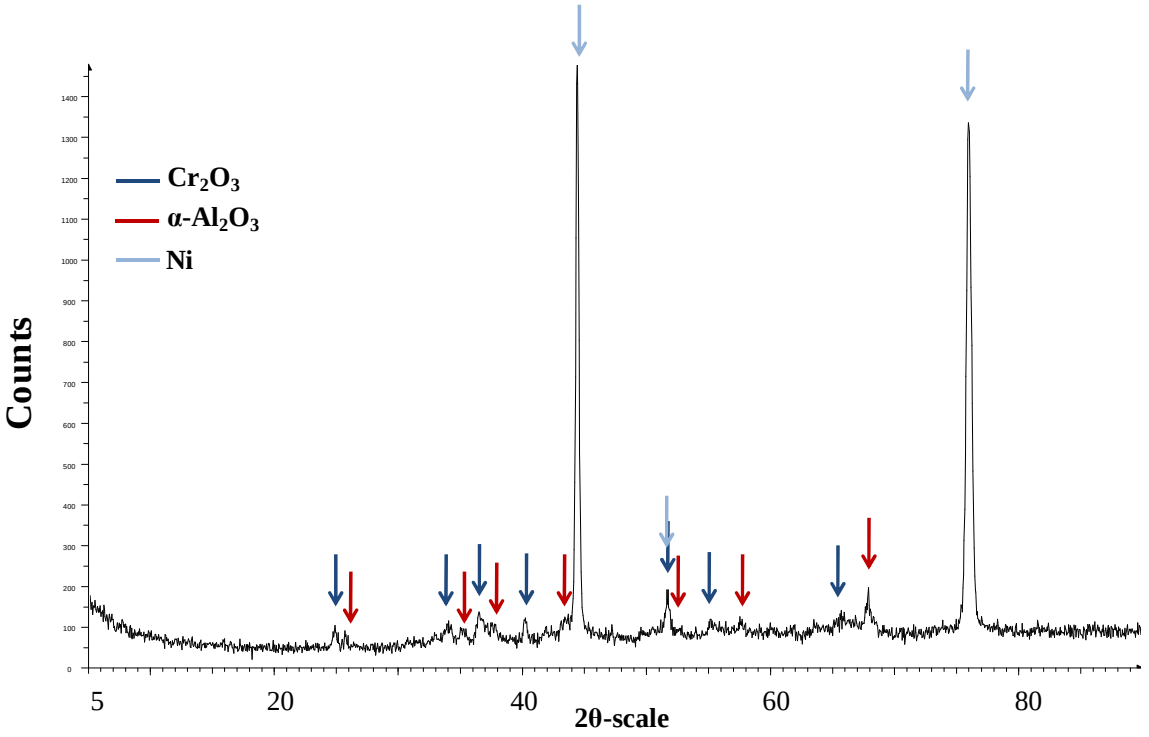

Figure 8.34 XRD spectrum from the surface of sample 080710e2 (16.3 at5 Cr, 14.6 at% Al) (Ni-20wt%Cr+Al) after 500 hours exposure, showing the presence of Cr_2O_3 and α-Al_2O_3.

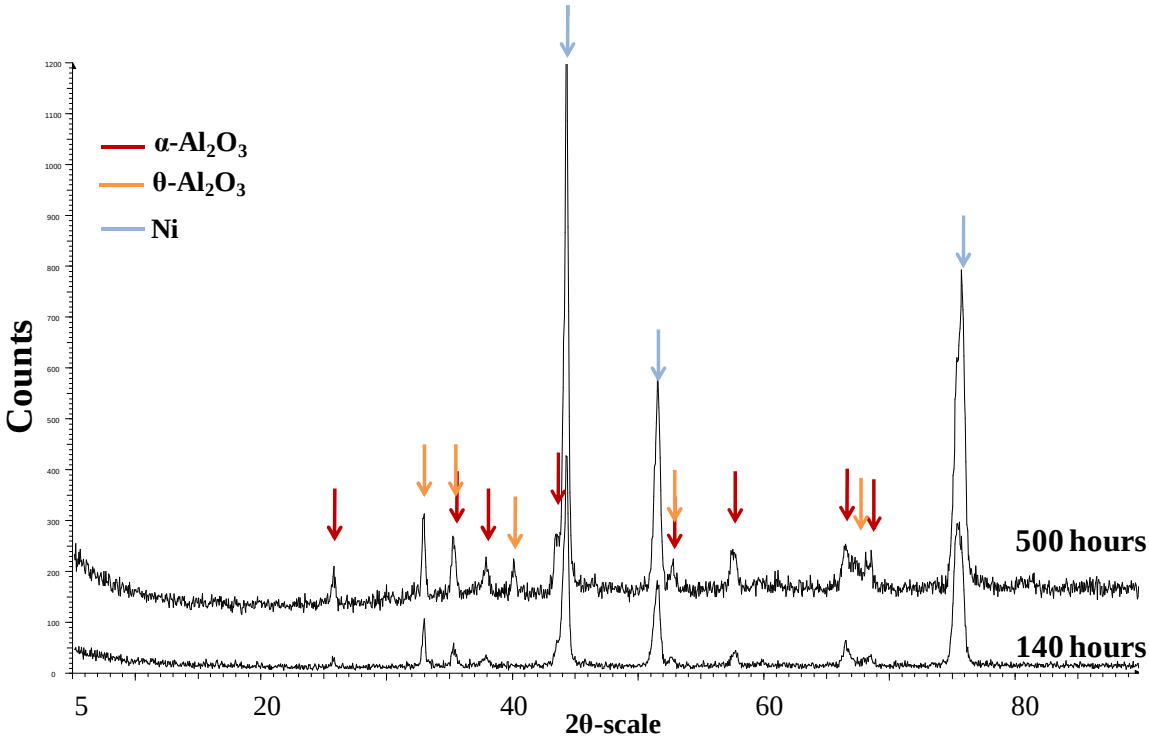

Figure 8.35 XRD spectrum from the surface of sample 080710F3 (14.6 at% Cr, 21.5 at% Cr) after 140 and 500 hours exposure (Ni-20wt%Cr+Al) showing the presence of transient θ-Al_2O_3 as well as α-Al_2O_3.

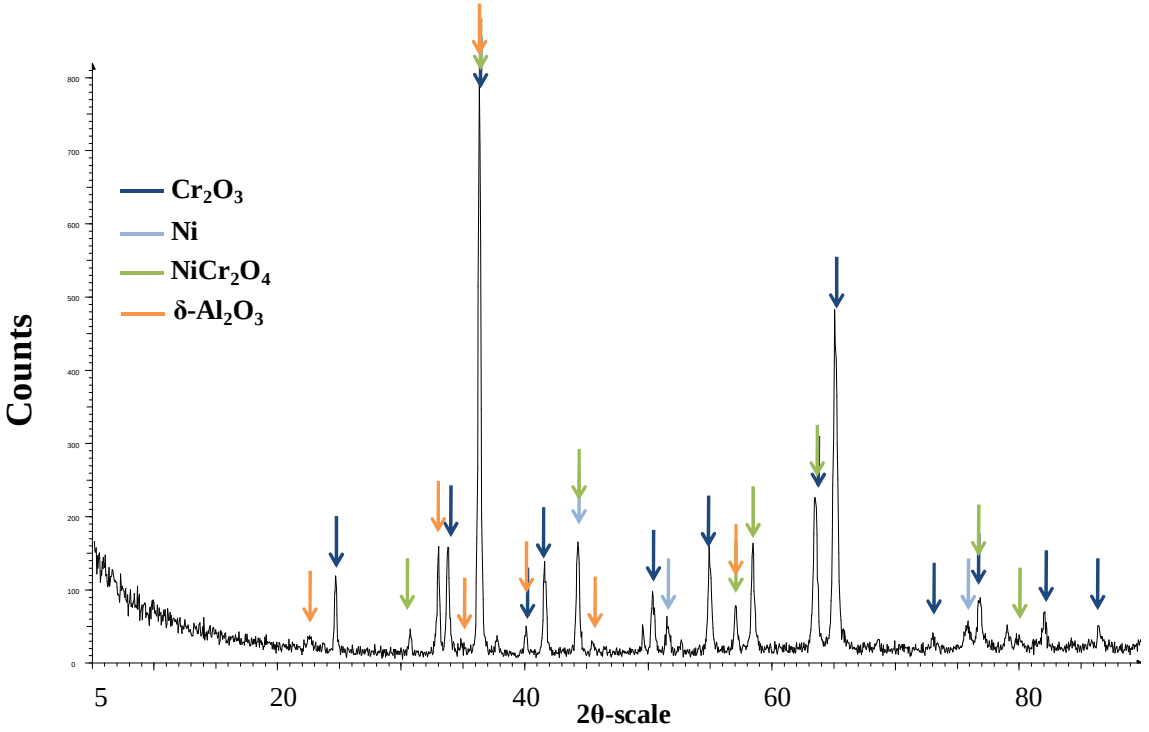

Figure 8.36 XRD spectrum from the surface of sample 290610D3 (55.9 at% Cr, 6.0 at% Al) (Ni-50wt%Cr+Al) after 500 hours exposure, showing the presence of Cr_2O_3, transient δ-Al_2O_3 and spinels.

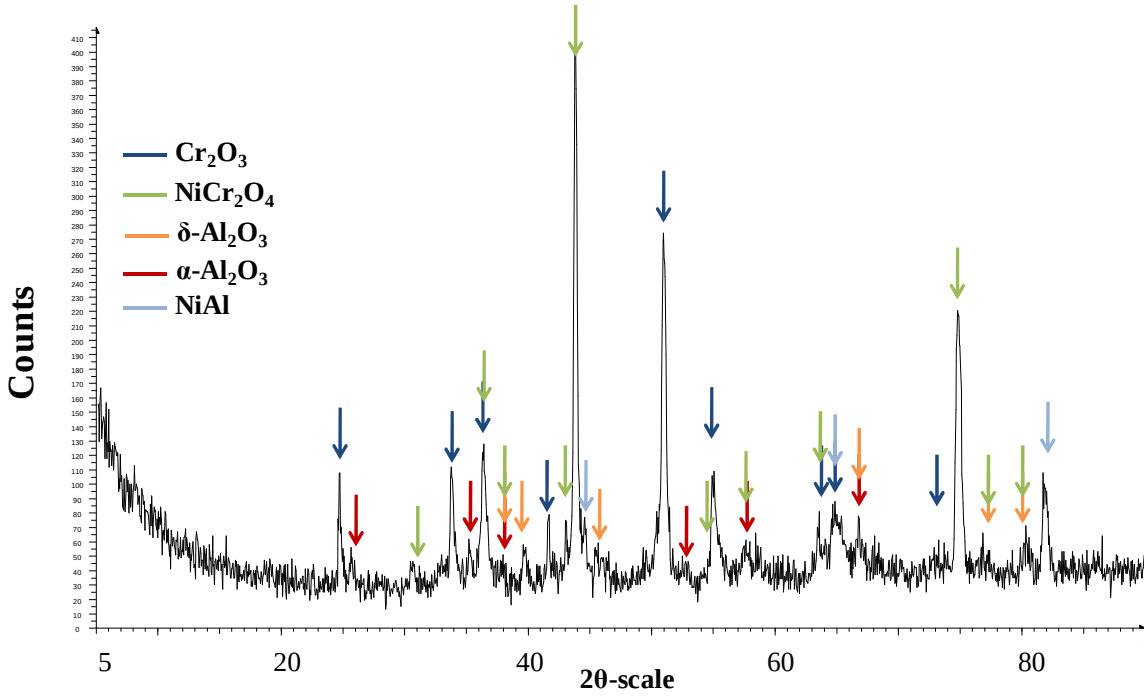

Figure 8.37 XRD spectrum from the surface of sample 290610E2 (48.2 at% Cr, 18.2 at% Al) (Ni-50wt%Cr + Al) after 500 hours exposure, showing the presence of Cr_2O_3, transient δ-Al_2O_3, α-Al_2O_3 and spinels.

Low concentrations of Cr (minimum of 5 at%) were needed in order to form Cr_2O_3 (Figures 8.29, 8.30, 8.31, 8.32, 8.36 and 8.37). On the Ni-20wt%Cr+Al batch, the first evidence of Al_2O_3 was observed on sample 080710e2 (16.3 at% Cr, 14.6 at% Al) as shown in Figure 8.34. Once again, increasing the amount of Al up to 21.5 at%, lead to the growth of the transient θ-Al_2O_3 along with α-Al_2O_3 (Figure 8.35). Figure 8.35 also highlights the growth of the Al_2O_3 oxides with time. Between 140 and 500 hours, the transient phases seemed to grow as much as the stable α-phase which confirms that at the lower temperature different forms of Al_2O_3 can co-exist.

Finally on the samples from the Ni-50wt%Cr+Al batch, Al_2O_3 was first spotted on 290610D3 (55.9 at%Cr, 6.0 at% Al) (Figure 8.36). Generally, a higher initial amount of Cr reduced the amount of Al necessary to form Al_2O_3, as was observed at 950 °C, but

also seemed to increase the probability of forming spinels/mixed oxides. Indeed, most of the samples for this batch grew $NiCr_2O_4$ or $NiO.Al_2O_3$ (Figures 8.30, 8.33, 8.36 and 8.37).

The XRD results for all the samples oxidised at 900 °C are summarised in Table 8.8.

Targets	Sample		NiO	Cr_2O_3	α-Al_2O_3	Mixed oxides	Spinels
Ni-10wt%Cr+Al	130510	D2	+	+			
	130510	d2	+	+			
	170510	E3	+	+			
	170510	E2	+	+		Al_2O_3.NiO	
	130510	e2	+		α-		
	170510	e2	+		α-		
	170510	F3			α,γ,θ-		
	170510	f2			α,δ,θ-		
	130510	i3			α-		
Ni-20wt%Cr+Al	80710	c2	+	+			$NiCr_2O_4$
	80710	d3	+	+			$NiCr_2O_4$
	80710	E2		+		Al_2O_3.NiO	
	80710	e2			α-		
	80710	F3			α,θ-		
	80710	f3			α,θ-		
	80710	G3			α,γ-		
	80710	h3			α-		
	80710	i4			α-		
Ni-50wt%Cr+Al	290610	C2	+	+			
	290610	c3		+			
	290610	D3		+	δ-		$NiCr_2O_4$
	290610	E2		+	α,γ-		$NiCr_2O_4$
	290610	e3			α-	Al_2O_3.NiO	$NiCr_2O_4$
	290610	F3			α-		$NiCr_2O_4$
	290610	g3			α,θ-	Al_2O_3.NiO	
	290610	H2			α,γ-		

Table 8.8 Different oxide phases identified using XRD on the samples exposed at 900 °C.

The first traces of Al_2O_3 were observed on samples 130510e2 (8.2 at% Cr, 15.5 at% Al), 080710e2 (16.3 at%Cr, 14.6 at% Al) and 290610D3 (55.9 at%Cr, 6.0 at% Al),

showing that the amount of Al needed to grow this protective oxide decreased with increasing proportions of Cr. Three different transient Al_2O_3 (δ, γ, and θ) were detected but they did not seem to depend on the composition of the coating (for example, a lower amount of Al did not lead to a particular transient phase). Initial contents of Cr above 18 at% increased the chance of detecting spinels into the oxide layer and mixed Al_2O_3.NiO oxides were present even with high amounts of Al (maximum of 84.2 at%).

The oxide microstructure of the exposed coatings was observed under the SEM and is shown in Figures 8.38 to 8.40. It confirmed that coating were generally between ~20 and ~50 µm thick.

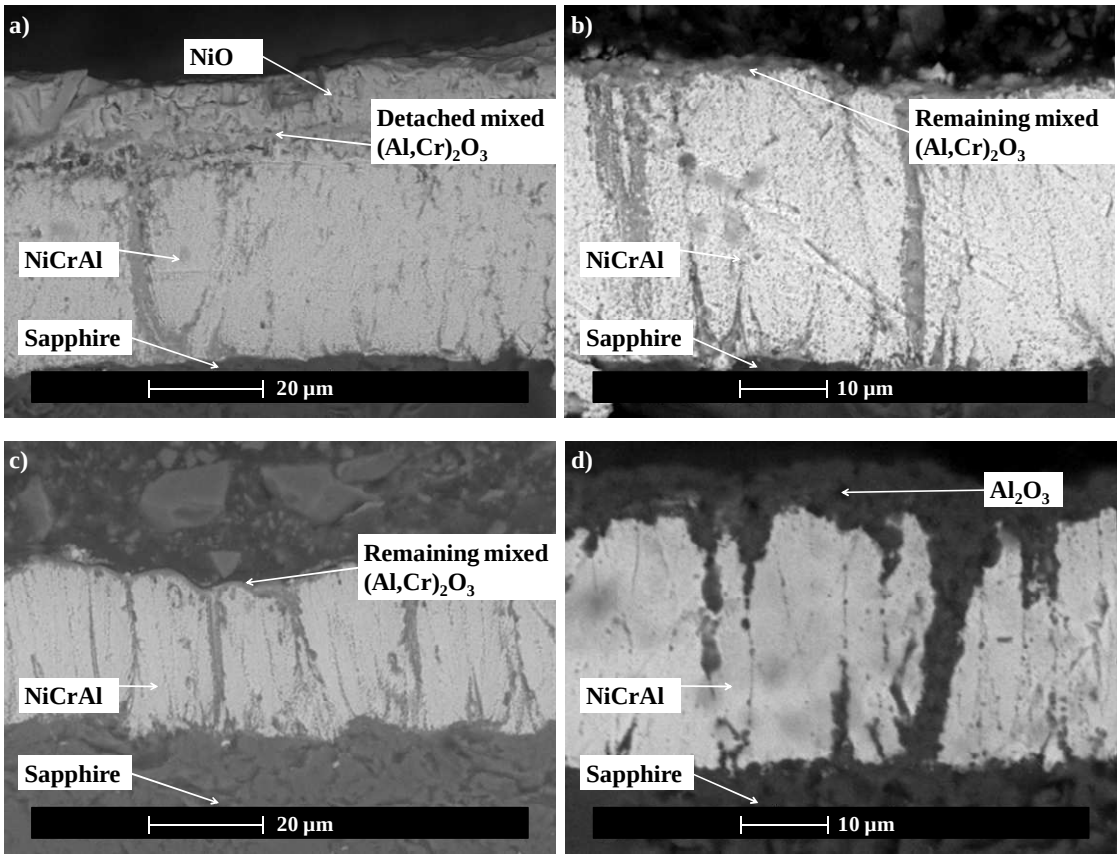

Figure 8.38 Cross sections SEM images of (a) 130510d2, (b) 170510E2, (c) 130510e2 and (d) 170510F3.

The first pure Al_2O_3 layer in the Ni-10wt%Cr+Al batch was observed on sample 170510F3 (6.7 at% Cr, 31.7 at% Al) (Figure 8.38(d)) and contained 38.6 at% of Al.

Samples containing high amounts of Ni (over 84 at%) grew a two layered TGO composed of an outer mixed $NiO.Al_2O_3$ layer and an inner mixed $(Al,Cr)_2O_3$ layer (Figure 8.38(a)). Increasing the initial Al contents from 5.8 to 9.4 at% in the coating led to the growth a mixed $(Al,Cr)_2O_3$ layer (Figure 8.38(b) and (c)). Samples 170510E2 (9.2 at% Cr, 9.4 at% Al) and 130510e2 (8.2 at% Cr, 15.5 at% Al) respectively failed after 460 and 100 hours of exposure, explaining the very thin remaining oxide layer. This indicates either that failure occurred within the oxide layer or at the oxide/coating interface and was followed by re-growth of the oxide.

From the Ni-20wt%Cr+Al batch, a pure Al_2O_3 layer could not be seen at compositions lower than sample 080710F3 (14.6 at% Cr, 21.5 at% Al) (Figure 8.39(d)). Lower amounts of Al (14.6 at%) led to the formation of a mixed $Cr_2O_3.Al_2O_3$ layer, the composition of which was dependent on the initial composition of the coating (Figures 8.39(b) and 8.39(c)). Even with high amount of Ni in 080710d3 (18.5 at% Cr, 4.5 at% Al), the double oxide layer system made of NiO and Cr_2O_3 could not be found as easily as on samples oxidised at 950 °C (Figure 8.39(a)). Also, spinels were largely present on the coatings and usually had two sorts of microstructures. They could appear as very voluminous oxides consuming most of the overlay coating as in Figures 8.39(a) and 8.39(d), or be very small and located in the oxide layer next to the overlay coating as in Figure 8.39(b) and 8.39(c).

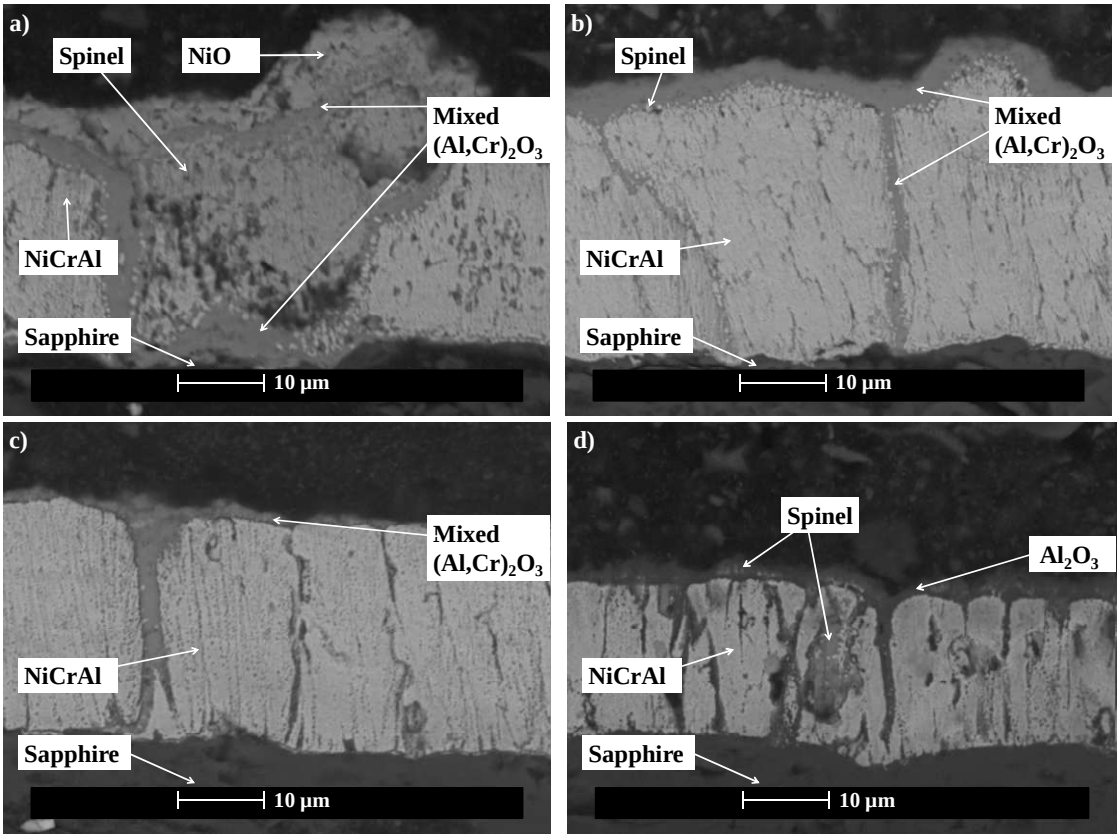

Figure 8.39 Cross sections SEM images of (a) 080710d3, (b) 080710E2, (c) 080710e2 and (d) 080710F3.

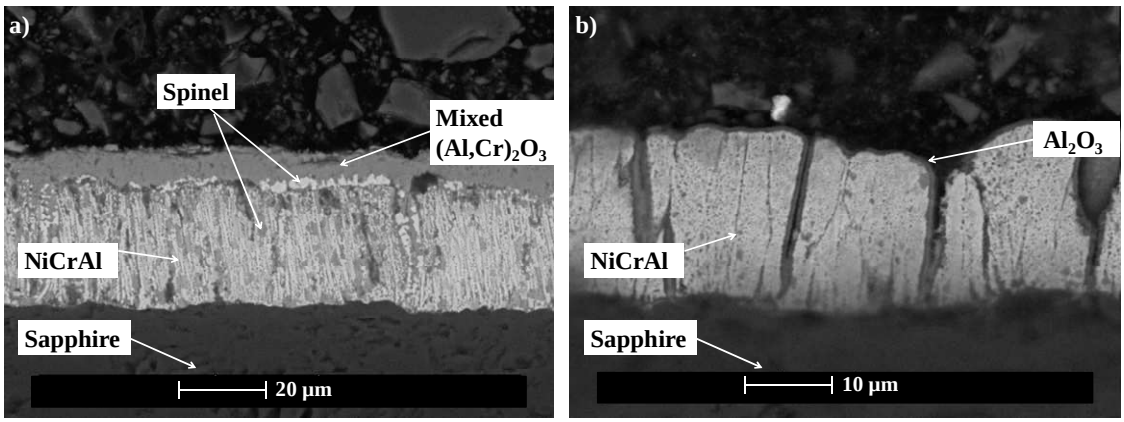

Figure 8.40 Cross sections SEM images of (a) 290610D3 and (b) 290610E2.

Cross-sections through samples from the Ni-50wt%Cr+Al batch showed that a pure Al_2O_3 layer could not be observed on samples with an amount of Al smaller than

18 at% as in 290610 E2 (48.2 at% Cr, 18.2 at% Al) (Figure 8.40(b)). Even if traces of Al_2O_3 were found on 080710D3 (55.9 at% Cr, 6.0 at% Al) using XRD analysis, SEM coupled with EDX analysis showed that the oxide layer was rich in Cr and Al instead (mix of Cr_2O_3 and Al_2O_3) (Figure 8.40(a)). The size of spinels in the oxide layer increased and they also seem to be present more inside the overlay coating.

Sample		Oxide	O (at%)	Ni (at%)	Cr (at%)	Al (at%)
130510	d2	outer layer	50.2	30.9	1.4	17.5
		inner layer	54.7	19.2	9.2	16.9
170510	E2	outer layer	46.4	21.5	8.4	23.7
130510	e2	outer layer	54.4	9.2	2.7	33.6
170510	F3	outer layer	56.2	4.2	1.2	38.4
080710	d3	outer layer	55.3	5.0	20.7	19.0
080710	E2	outer layer	57.1	4.0	22.8	16.2
080710	e2	outer layer	58.9	5.5	13.9	21.8
080710	F3	outer layer	52.6	3.8	2.6	41.
290610	D3	outer layer	59.4	1.8	18.8	20.1
290610	E2	outer layer	59.2	2.6	6.8	31.5
290610	e2	outer layer	43.8	8.6	14.5	33.1
290610	F3	outer layer	57.9	1.7	4.0	36.4

Table 8.9 Composition (obtained by EDX analysis) of the oxide layers observed on the cross-sections of selected Ni-Cr-Al samples exposed at 900°C.

The compositions of the oxide layers were determined using EDX analysis and the results are summarised in Table 8.9. As for the results in Table 8.4, all the oxide layers contained a fraction of Ni (probably because of the resolution of the EDX which is around 3-5 µm). High initial amounts of Ni (130510d2 with 9.7 at% Cr and 5.8 at% Al) led to the formation of a two layered oxide scale, whose outer layer was composed of 30.9 at% Ni and 17.5 at% Al (mixed $NiO.Al_2O_3$) and inner layer was composed of 19.2 at% Ni, the same amount of Al and 9.2 at% Cr (mixed $(Cr,Al)_2O_3$ enriched in Ni).

The amount of Ni present in the oxides layers reduced with the lesser amounts of Ni in the coating before oxidation.

At the same time, as for coatings exposed at 950 °C (Figure 8.19), increasing the initial amount of Al in the coatings led to mixed $(Cr,Al)_2O_3$ layers increasingly richer in Al until the layer formed was mainly pure Al_2O_3 (Figure 8.41). SEM and EDX did not allow identifying different forms of Al_2O_3.

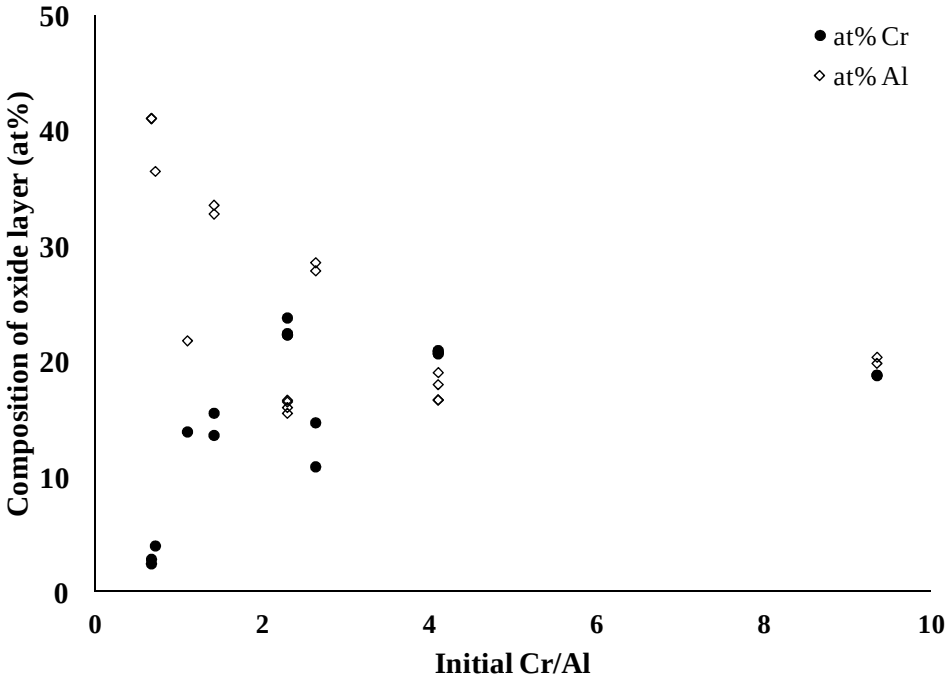

Figure 8.41 Effect on the initial composition on the oxides formed at 900°C.

8.2.4 Oxidation of the coatings obtained from 3 target co-sputtering

To complete the information provided by these 27 samples, 8 additional samples from the Ni-10wt%Cr+Ni-50wt%Cr+Al 3 target co-sputtering batch were also exposed at 900 °C. The compositions of the coatings selected for the oxidation at 900 °C are given in Table 8.10.

Sample	Ni (at%)	Cr (at%)	Al (at%)
251111_01	41.1	39.8	19.1
251111_04	39.3	36.3	24.5
251111_09	52.3	23.2	24.6
251111_10	39.4	45.3	15.3
251111_12	35.9	39.9	24.2
251111_15	30.5	33	36.5
251111_17	60.9	15.2	23.9
251111_23	44.1	42.8	13.1

Table 8.10 Ni-Cr-Al compositions of coatings resulting from 3 targets co-sputtering and oxidised at 900 °C.

After verification under the SEM, it was found that prior to oxidation the coatings were only 10 µm thick, despite modifying deposition parameters. Therefore, to avoid their complete destruction, these samples were oxidised for 40 hours instead of 500 hours. They were then analysed using XRD. A summary of the oxides detected in the samples is shown in Table 8.11. The majority of the transient Al_2O_3 present consisted of δ-Al_2O_3 instead of the θ-Al_2O_3 obtained on the previous samples after 500 hours exposure, suggesting that this phase appears later during oxidation at this temperature. Also, spinels were detected on most of the samples.

Sample	NiO	Cr_2O_3	a-Al_2O_3	transient Al_2O_3	spinels
251111_01		+	+	δ-Al_2O_3	$NiCr_2O_4$
251111_04		+	+	δ-Al_2O_3	$NiCr_2O_4$
251111_09		+	+	δ-Al_2O_3	$NiCr_2O_4$
251111_10		+	+	δ-Al_2O_3	$NiCr_2O_4$
251111_12		+	+	δ-Al_2O_3	$NiCr_2O_4$
251111_15		+	+	δ-Al_2O_3	$NiCr_2O_4$
251111_17	+	+	+		
251111_23		+	+	θ-Al_2O_3	

Table 8.11 Different oxide species identified using XRD on the samples exposed at 900 °C for 40 hours.

8.2.5 Discussion- Ni-Cr-Al ternary oxidation map at 900 °C.

Superimposed on Figure 8.42 is a proposed boundary defining the limiting composition for Al_2O_3 scale formation at 900 °C. Samples identified to grow any form of Al_2O_3 are represented in red in the diagram. As for the oxidation at 950 °C, an increase in the Cr fraction in the initial coating reduced the amount of Al needed to grow Al_2O_3, extending the Al_2O_3 domain toward the Cr rich corner.

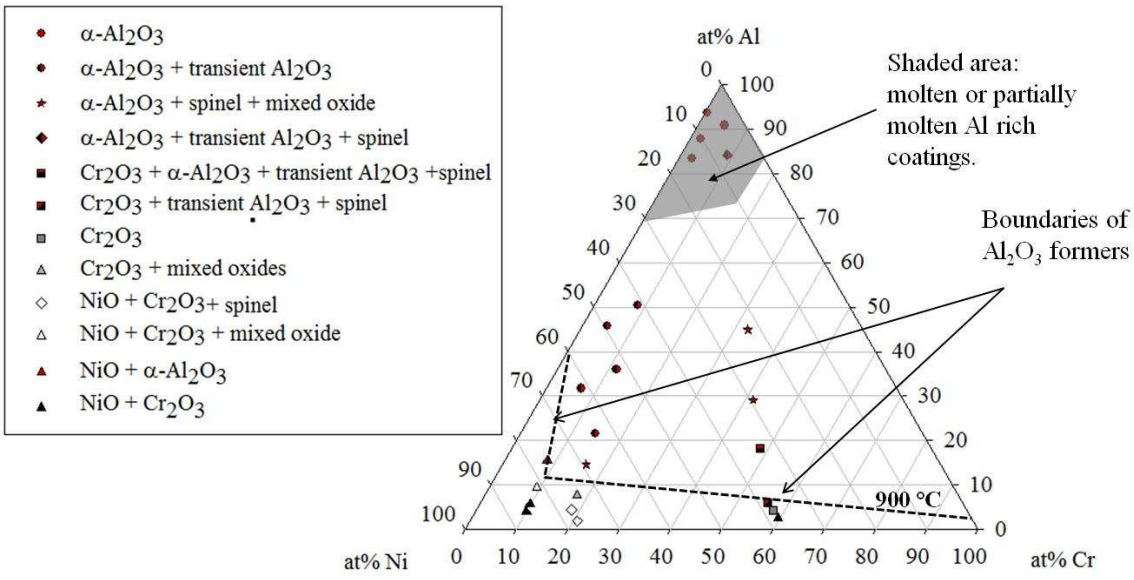

Figure 8.42 Oxide compositions grown on Ni-Cr-Al coatings after 500 hours at 900 °C (diagram in at%).

Less melting of the Al rich samples was noticed at 900 °C suggesting that the melting domain in the Al rich corner is smaller compared to the one at 950 °C (Figure 8.42 compared to Figure 8.20). Spinels were present more in coatings with a high initial Cr content while transient Al_2O_3 seemed to form more easily with lower amounts of Cr and Al (Figure 8.42).

Data obtained from the oxidation of the coatings deposited with 3 targets was added to the previous ternary map and are shown in Figure 8.43. These data confirm the boundaries drawn by the results from the coatings deposited by 2 target co-sputtering. The presence of Cr_2O_3 in the Al_2O_3 domain could be explained by the fact that the coatings were only exposed for 40 hours. At low temperatures such as 900 °C, the conversion of the Cr_2O_3, spinels and transient Al_2O_3 might be too slow to disappear after short exposure times [12,149]. It can be assumed that the Cr_2O_3 will cause the O_2 partial pressure at the surface of the BC to reduce thus promoting the formation of Al_2O_3. This needs to be confirmed by depositing thicker coatings and oxidizing them for longer periods of time.

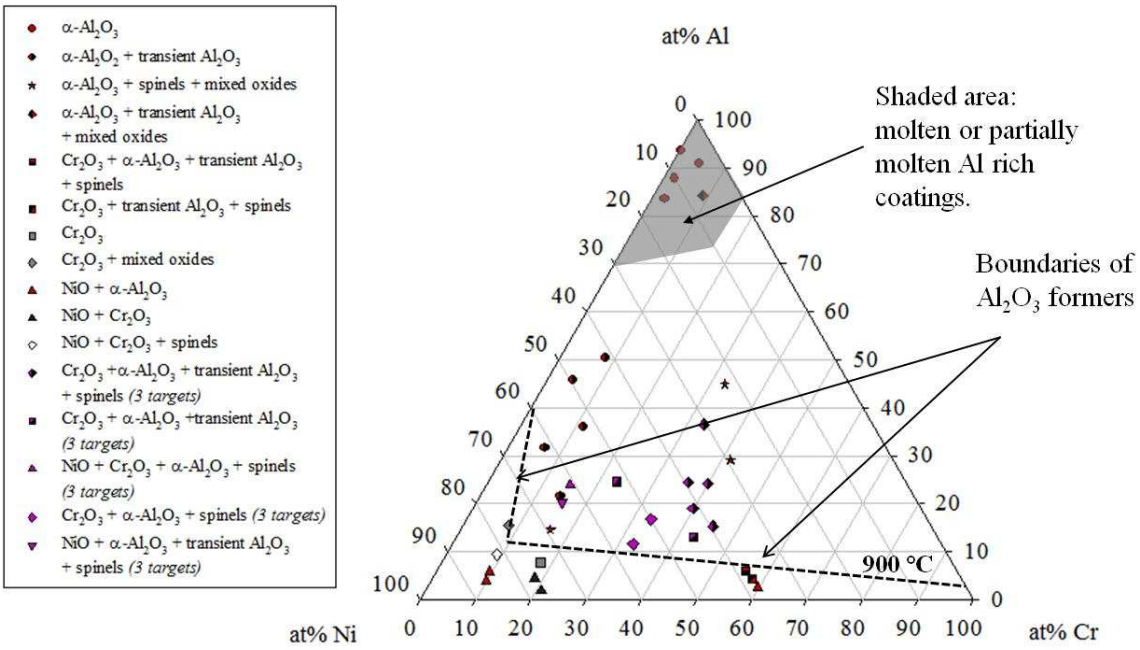

Figure 8.43 Oxide compositions grown on Ni-Cr-Al coatings after 500 hours at 900 °C including the data obtained from 3 target co-sputtering(diagram in at%).

8.3 Discussion - Influence of Ni-Cr-Al compositions and exposure temperature on the nature and growth of oxides.

Both domains for the samples oxidised at 900 and 950 °C are drawn on the Ni-Cr-Al diagram in Figure 8.44. Reducing the oxidation temperature expanded the Al_2O_3 formers domain a little, promoted formation of transient Al_2O_3 and reduced the transition to stable Al_2O_3. The difference of oxidation behaviour increased with an increasing amount of Cr in the initial coating. Indeed, less Al was needed at 900 °C to grow Al_2O_3 than at 950 °C for the same amount of Cr. However, going back to the mass gain graphs in Figures 8.6 and 8.28 showing the evolution of the oxide layer for the Ni-50wt%Cr+Al batch of samples, at both temperatures the behaviour was almost identical, unlike the Ni-10wt%Cr+Al and Ni-20wt%Cr+Al samples (Figure 8.4, 8.5, 8.26 and 8.27).

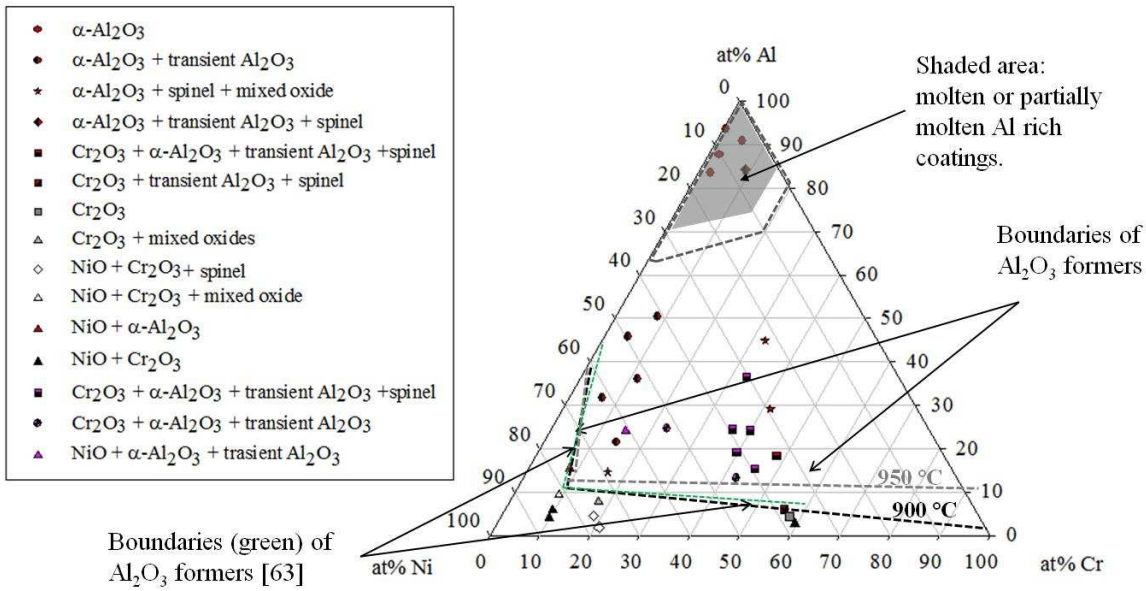

Figure 8.44 Oxide compositions grown on Ni-Cr-Al coatings after 500 hours at 900 °C Boundaries of Al_2O_3 formers are compared to those obtained at 950 °C in this work and by Nicholls et al. [63](diagram in at%).

This leads to the idea that at high Cr contents, the same quantity of oxygen had reacted at both temperatures, but the slower oxidation mechanisms allowed the growth of different oxides. Or, the slower oxidation mechanisms enabled transient Al_2O_3 to remain in the oxide layer, instead of being replaced by a continuous layer of Cr_2O_3, as at 950°C. For lower amounts of Cr, reducing the oxidation temperature reduced the overall mass gain of the samples and did not affect the nature of oxide grown on the surface. Unlike Brumm and Grabke [52], the beneficial effect of Cr on the transformation of transient Al_2O_3 into stable Al_2O_3 was not observed here.

At the lower temperature, more forms of transient Al_2O_3 were observed (Table 8.8). This is consistent with research carried out on the oxidation of NiAl which showed that with decreasing temperature transient forms of Al_2O_3 could co-exist with α-Al_2O_3 because of their slower oxidation kinetics (Figure 2.7) [52]. Lowering the temperature from 950 to 900 °C, increased the probability of the system being in the transient domain of this diagram (Figure 2.7) and thus the likelihood of forming different phases of Al_2O_3.

Reducing the oxidation temperature from 950 to 900 °C also reduced the extent of the melting samples domain in the ternary diagram. This enables higher amounts of Al to be included in coatings if a very pure Al_2O_3 layer is needed for protection purposes at lower temperatures. However, in real life operation, these coatings are exposed to the risk of overheating and too high a content of Al will lead to melting and premature failing of the system.

At both temperatures, the domain of protective oxide formers (Cr_2O_3, Al_2O_3 or a mix of the two), comprises the usual Ni-Cr-Al-Y composition found commercially (18-22 wt%Cr, 8-12 at% Al) which suggests that even if they are not the most efficient

composition available for overlay and BCs at lower temperature, they will still grow protective oxides and extend the lifetime of the substrate they are supposed to protect.

Lowering the temperature from 950 to 900 °C also affected the formation of spinels and mixed oxides. More $NiCr_2O_4$ and Al_2O_3.NiO were detected using XRD (comparing Tables 8.3 and 8.8) at 900 °C. This could be caused by the lower oxidation kinetics at 900 °C delaying the formation of continuous and protective Al_2O_3 and/or Cr_2O_3 layer(s) and thus promoting the formation of spinels [12]. Or it could be caused by the higher amounts of transient Al_2O_3 at 900 °C, helping the diffusion of Ni and Cr species to form less protective oxides [136].

The data gathered from the samples with the Ni-10wt%Cr+Al, Ni-20wt%Cr+Al and Ni-50wt%Cr+Al coatings were also compared to the work reported by Wallwork et al. [65] on samples oxidised at 1000 °C and over (Figure 2.9). In this case, instead of just taking into account the growth of Al_2O_3, the Ni-Cr-Al compositions were divided into 3 categories: (I) the NiO formers; (II) the Cr_2O_3 formers; and, (III) the Al_2O_3 formers. The diagram for the samples exposed at 950 °C is shown in Figure 8.45: boundaries between the 3 different domains at 1000 °C are in black, while the ones at 950 °C are traced in red. Domain sizes changed greatly with the reduction of temperature from 1000 to 950 °C. Indeed, the external NiO domain was much bigger at the lower temperature and more Al was needed to grow an external layer of Al_2O_3.

Reducing the exposure temperature to 900 °C (Figure 8.46) altered the domain boundaries in a similar way as for 950 °C. Another difference is that at 1000 °C, it was stated that the oxides were composed of two layers, even in domain II, which was found in the literature [40] to grow an external layer of Cr_2O_3 and an internal layer of Al_2O_3. At lower temperatures, only the coatings containing a high amount of Ni grow an outer

layer of NiO above a layer of mixed $(Cr,Al)_2O_3$. In other cases, only one mixed oxide layer was created at the lower temperatures and its composition varied with the initial Cr/Al ratio.

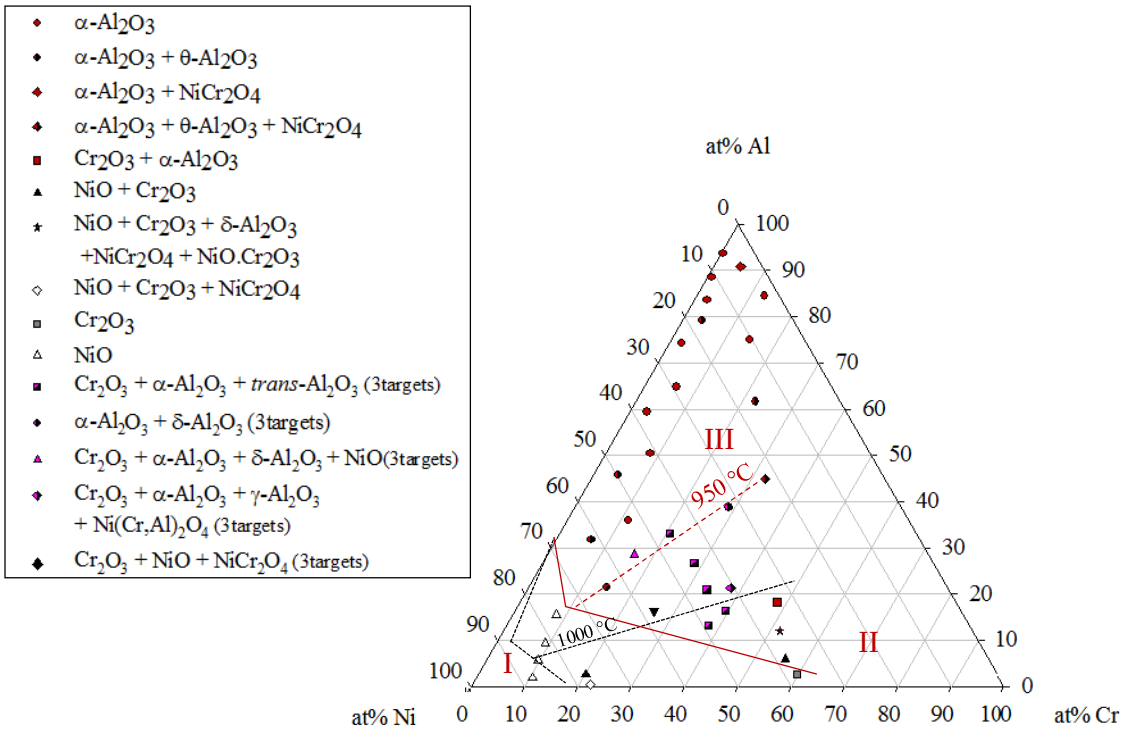

Figure 8.45 Compositional effects on the oxidation of Ni-Cr-Al ternary alloys, at over 1000 °C [65], cited in reference [12] and [63], compared to the data gathered at 950 °C on the coated sapphire discs. Black doted lines represent the boundaries at 1000 °C and the red ones, the boundaries at 950 °C. I) NiO + internal oxidation of Al and Cr ; II) Cr_2O_3 + internal oxidation of Al ; III) an Al_2O_3 external scale.

Boundaries between domains II and III in Figure 8.45 and 8.46 were established according to the data obtained from the 3 target co-sputtered coatings. Because these samples were only exposed 40 hours, the oxide layer was essentially composed of transient oxides (NiO, spinels, Cr_2O_3 and transient Al_2O_3). Therefore, the red dotter boundaries on the ternary diagrams might shift toward lower Al concentrations with longer exposure. Indeed, research carried out on Ni-Cr-Al samples at 1000 °C in the

literature [12, 149] showed that the initial formation of NiO, spinels and Cr_2O_3 was gradually replaced by stable α-Al_2O_3 because of the reduction of the O_2 partial pressure. This transformation is expected to take place more slowly at lower temperatures.

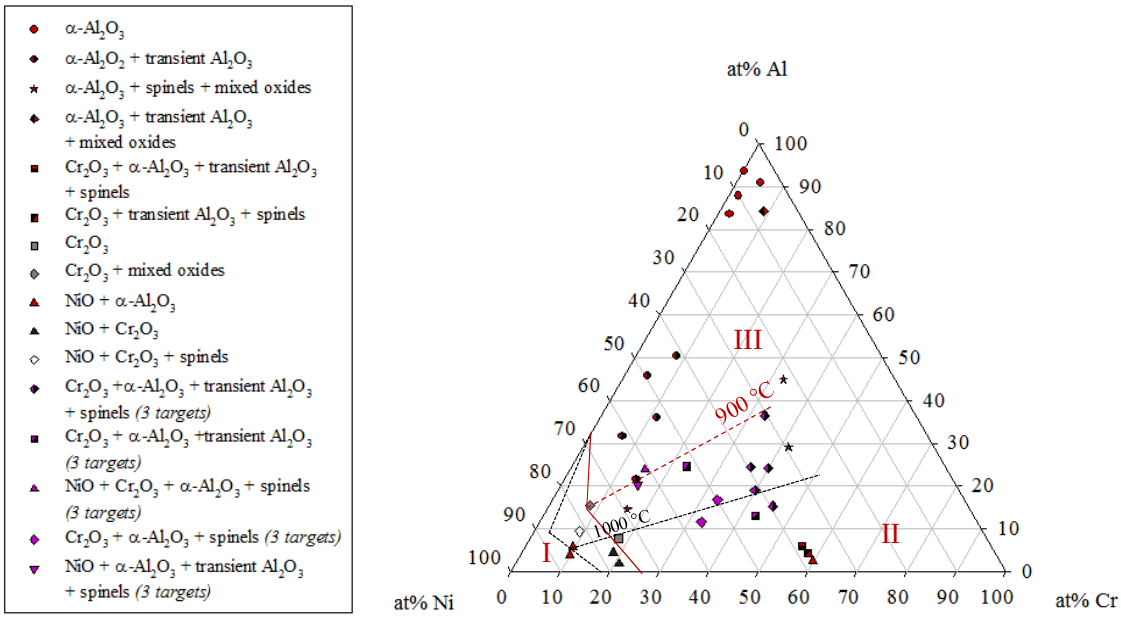

Figure 8.46 Compositional effects on the oxidation of Ni-Cr-Al ternary alloys, at over 1000 °C [65], cited in reference [12] and [63], compared to the data gathered at 950 °C on the coated sapphire discs. Black doted lines represent the boundaries at 1000 °C and the red ones, the boundaries at 950 °C. I) NiO + internal oxidation of Al and Cr ; II) Cr_2O_3 + internal oxidation of Al ; III) an Al_2O_3 external scale.

8.4 Summary

The physical vapour deposition technique, magnetron sputtering, has been used successfully to deposit a range of Ni-Cr-Al coatings on 10 mm diameter sapphire substrates. This was achieved through co-sputtering from two targets: a Ni10Cr, Ni20Cr, Ni50Cr target (changed between deposition runs) and a pure Al target. X-ray diffraction (XRD) was used to identify the oxides formed during exposures at 900 and 950 °C. The selective growth of protective Cr_2O_3 or Al_2O_3 oxides (depending on the

initial coating composition) was observed. At 950 °C, the first traces of Al_2O_3 were observed on samples containing 32 at% Al (at a low Cr concentration, 6.7 at%) and 21.5 at% Al (at a higher Cr concentration, 14.6 at%). Increasing the Cr content to 56 at% confirmed that for all high Cr alloys the critical Al level to form Al_2O_3 was below 6 at%. Decreasing the exposure temperature to 900 °C decreased the amount of Al needed to form Al_2O_3.The first traces of Al_2O_3 were observed on samples containing 15.5 at% Al (at a low Cr concentration, 8.2 at%), 16.3 at% Al (at a medium Cr concentration, 14.6 at%) and 6 at% Al (at a high Cr concentration, 56 at%). Decreasing the oxidation temperature promoted the formation of transient Al_2O_3 and spinels.

CHAPTER IX – OXIDATION OF THE Co-Ni-Cr-Al COATINGS AT 900-950 °C

9.1 Study of the Co-Ni-Cr-Al system – oxidation at 950 °C

The addition of Co, with the use of the Ni-20wt%Co-40wt%Cr or Ni-40wt%Co-20wt%Cr targets, was intended to extend these studies to quaternary systems in order to deposit coatings with compositions closer to commercial MCrAlYs. Similar oxidation experiments were conducted on the Ni-40wt%Co-20wt%Cr+Al and Ni-20wt%Co-40wt%Cr+Al samples. The names, compositions and exposure times of the coated sapphire discs are collated in Table 9.1.

Targets	Sample		Co(at%)	Ni(at%)	Cr(at%)	Al(at%)	Cr/Al	Co/Ni
Ni-	130910	d3	18.3	31.3	41.6	8.8	4.75	0.58
20wt%Co-	130910	E2	18.0	30.9	40.6	10.5	3.88	0.58
40wt%Cr	130910	e2	16.4	28.8	38.1	16.7	2.28	0.57
+Al	130910	F2	12.3	21.9	29.2	36.6	0.80	0.56
	130910	f3	11.8	20.2	27.8	40.2	0.69	0.58
	130910	G2	7.9	14.0	18.3	59.8	0.31	0.57
	130910	g3	4.2	7.5	9.0	79.3	0.11	0.56
	130910	H2	2.7	5.2	5.8	86.3	0.07	0.53
	130910	i4	1.7	2.8	3.1	92.4	0.03	0.57
Ni-	160810	d2	36.6	34.4	21.6	7.4	2.93	1.06
40wt%Co-	160810	E4	31.4	30.3	18.2	20.1	0.91	1.03
20wt%Cr	160810	e3	26.0	25.1	15.4	33.5	0.46	1.04
+Al	160810	F4	24.0	21.7	13.4	40.9	0.33	1.16
	160810	f2	16.3	15.8	8.9	59.0	0.15	1.03
	160810	G4	10.7	10.5	5.8	73.0	0.06	1.02
	160810	g1	8.5	8.5	4.5	78.5	0.06	1.00
	160810	H1	4.4	4.4	2.4	88.8	0.03	1.01
	160810	h1	3.5	3.6	1.9	91.0	0.02	0.99

Table 9.1 Compositions of Co- Ni-Cr-Al coatings resulting from 2 target co-sputtering and oxidised at 950 °C.

9.1.1 Physical changes of samples with exposure

Pictures of the Ni-40wt%Co-20wt%Cr+Al and Ni-20wt%Co-40wt%Cr+Al samples were taken regularly between exposure cycles and are shown respectively in Figures 9.1 and 9.2.

Fractions of Co above 30 at% in the initial coating, led to very specific coating morphology. Indeed on samples 160810d2 (21.6 at% Cr, 7.4 at% Al) and 160810E4 (18.2 at% Cr, 20.1 at% Al) in Figure 9.1, after 20 and 40 hours of exposure, features looking like crystals started to nucleate on the coatings' surface and grow with time. These crystals eventually covered the whole sample surface. Increasing the initial amount of Al to 16.7 at% created a grey surface which did not change during exposure. Failure on sample 160810e3 (15.4 at% Cr, 33.5 at% Al) started on the edges of the sapphire disc after 280 hours at 950 °C. As for the Ni-Cr-Al system (section 8.1.1), coatings containing a very high content of Al (above 75 at%) melted at 950 °C. Sample 160810H1 (2.35 at% Cr, 88.8 at% Al) has got a molten and re-crystallised layer (as previously observed on Ni-Cr-Al samples).

Physical changes on the coatings from the Ni-20wt%Co-40wt%Cr+Al batch, shown in Figure 9.2, were not as spectacular as the ones presented above (Figure 9.1) but still depended on their initial compositions. High levels of Cr (around 40 at%) grew green oxidation products whose colour became more intense with exposure, indicating a thickening of the oxide layer (e.g. 130910 d3 with 41.6 at% Cr and 8.8 at% Al).

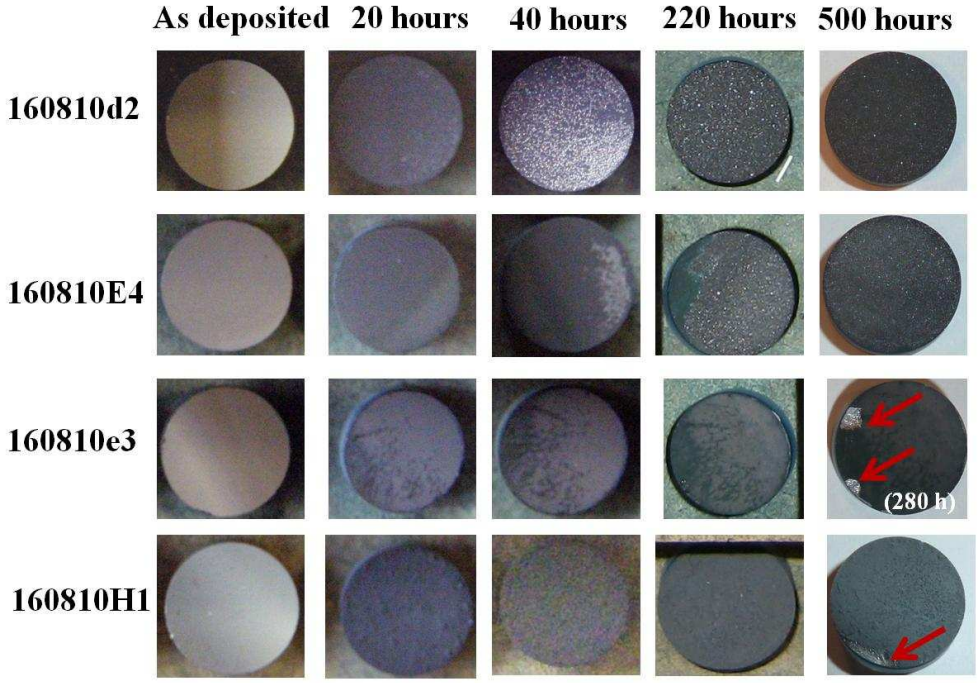

Figure 9.1 Pictures showing the evolution of oxides on 160810d2 (21.6 at% Cr, 7.4 at% Al), 160810E4 (18.2 at% Cr, 20.1 at% Al), 160810e3 (15.4 at% Cr, 33.5 at% Al) and 160810H1(2.35 at% Cr, 88.8 at% Al) (Ni-40wt%Co-20wt%Cr+Al) with exposure at 950 °C. Red arrows point at damage in coatings.

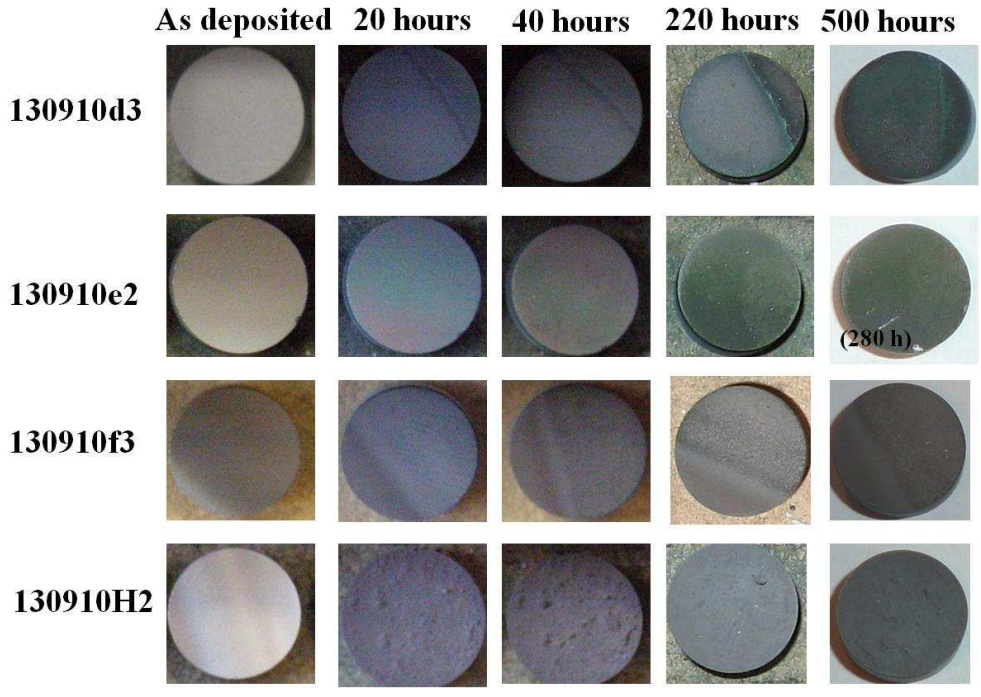

Figure 9.2 Pictures showing the evolution of oxides on 130910d3 (41.6 at% Cr, 8.8 at% Al), 130910e2 (38.1 at% Cr, 16.7 at% Al), 130910f3 (27.8 at% Cr and 40.2 at% Al) and 130910H2 (5.8 at% Cr and 86.3 at% Al) (Ni-20wt%Co-40wt%Cr+Al) with exposure at 950 °C. Red arrows point at damage in coatings.

Sample 130910e2 (38.1 at% Cr, 16.7 at% Al) became slightly iridescent in the first stages of exposure and then turned green, which suggests a thickening oxide (interference colours). Again, increasing the amount of Al led to the formation of grey surface oxide layers (130910f3 with 27.8 at% Cr and 40.2 at% Al)) and melting occurred on samples with the fraction of Al exceeding 80 at% (130910H2 with 5.8 at% Cr and 86.3 at% Al)).

9.1.2 Mass change of samples

As carried out previously for the Ni-Cr-Al system (sections 8.1.2 and 8.2.2), the samples mass changes were plotted against time. For samples coated with the Ni-20wt%Co-40wt%Cr and Al targets, no obvious trend in behavior could be deduced (Figure 9.3), except that samples 130910f3 (27.8 at% Cr and 40.2 at% Al) and 130910G2 (18.3 at% Cr, 59.8 at% Al) which resulted in the slowest oxidation and corresponded to a Cr/Al atomic ratio between 0.31 and 0.69. It should be noted that all the samples had alternatively high Cr and/or Al contents, thus all would be expected to produce relatively slow growing oxides.

As previously reported, the high Al concentration coatings may well be molten at the test temperature of 950 °C. Indeed, while 130910i4 (3.1 at% Cr, 92.4 at% Al) was the sample with the most Al, its mass increased by 0.15 mg/cm^2 after 500 hours of exposure while sample 130910f3, with less Al, only increased by 0.1 mg/cm^2.

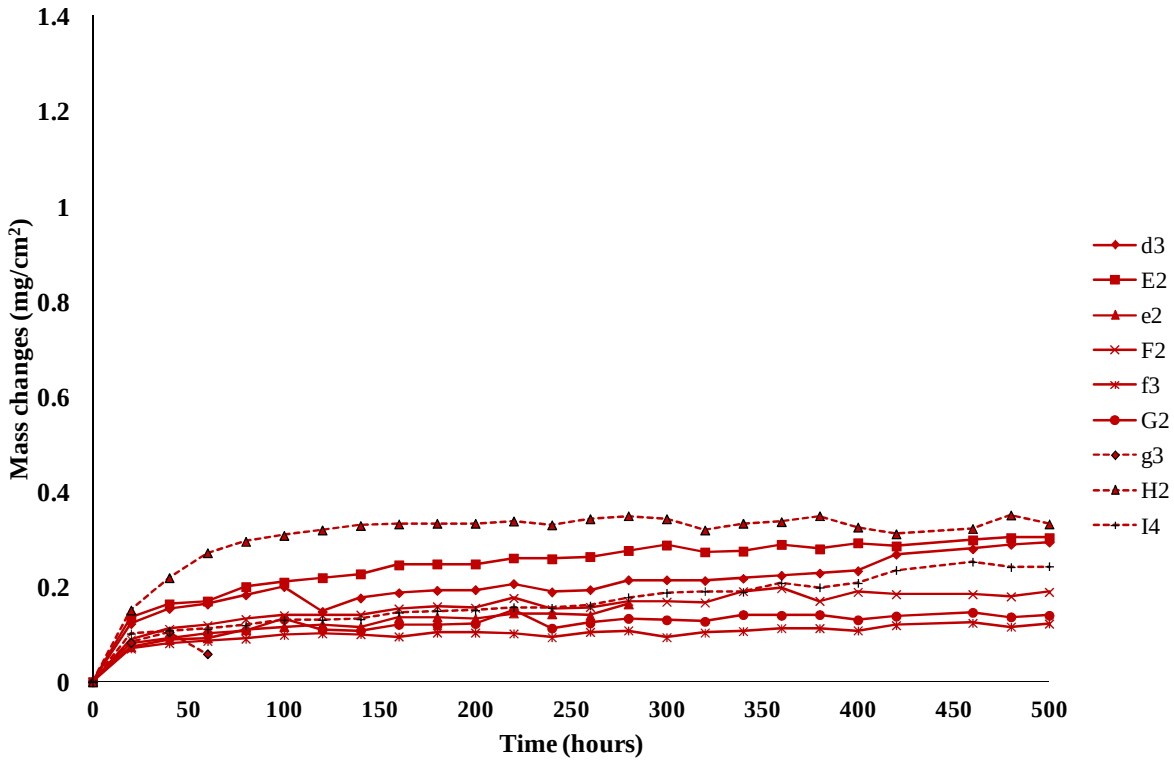

Figure 9.3 Mass change of Ni-20wt%Co-40wt%Cr+Al coating against time of exposure at 950 °C.

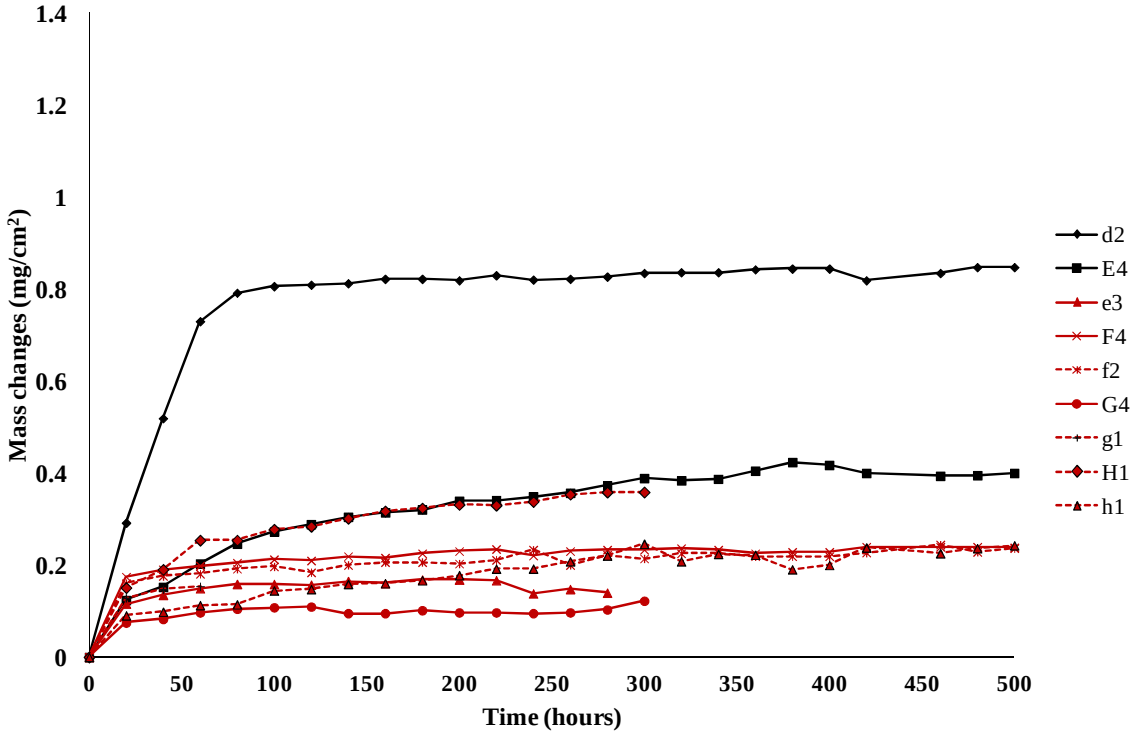

Figure 9.4 Mass change of Ni-40wt%Co-20wt%Cr+Al coating against time of exposure at 950 °C.

In systems containing more Co, two rates of oxidation could be observed (Figure 9.4). The faster growing oxides on sample 160810d2 (21.6 at% Cr, 7.4 at% Al) were believed to be the result of a mix of CoO and NiO. The lowest level of oxidation was obtained with sample 160810G4 (5.8 at% Cr, 73.0 at% Al), a coating which contained a very high amount of Al and on Cr/Al atomic ratio of 0.06. The sample with the second lowest oxidation, 160810e3, contained 33.5 at% Al and 15.4 at% Cr, giving a Cr/Al atomic ratio of 0.45. Both of these high Al coatings would be expected to be brittle [146].

9.1.3 Identification of oxides

XRD was used to identify the oxides present on the coatings after exposure. On samples from the Ni-20wt%Co-40wt%Cr+Al batch, high concentrations of Cr in the samples led to the growth of Cr_2O_3. In sample 130910d3 (41.6 at% Cr, 8.8 at% Al) (Figure 9.5), 31 at% Ni and 18 at% Co were enough to grow NiO and CoO. The spinel $NiCr_2O_4$ was also detected. Against expectations, 8.8 at% Al led to the formation of transient δ-Al_2O_3. It was surprising because in the Ni-50wt%Cr+Al system (section 8.1.3) a minimum of 18 at% Al was needed to grow Al_2O_3 at 950 °C. Increasing the fraction of Al, as shown in the spectrum of sample 130910F2 (29.2 at% Cr, 36.6 at% Al) in Figure 9.6, decreased the strength of the Cr_2O_3 peaks while increasing the strength of the Al_2O_3 peaks (both α- and transient δ-phases). Although no Co and Ni oxides could be detected on 130910F2, a further increase of Al in sample 130910f3 (27.8 at% Cr, 40.2 at% Al) (Figure 9.7) created mixed (Co,Ni)O oxides and CoO. Finally, coatings containing a very high levels of Al (above 80 at%) grew Al_2O_3.

Depending on the sample, both transient and stable phases could be detected, or only α-Al_2O_3 was present. The composition of spinels changed from $NiCr_2O_4$ to $NiAl_2O_4$ because of the low amount of Cr in coatings such as 130910H2 (5.8 at% Cr, 86.3 at% Al) (Figure 9.8).

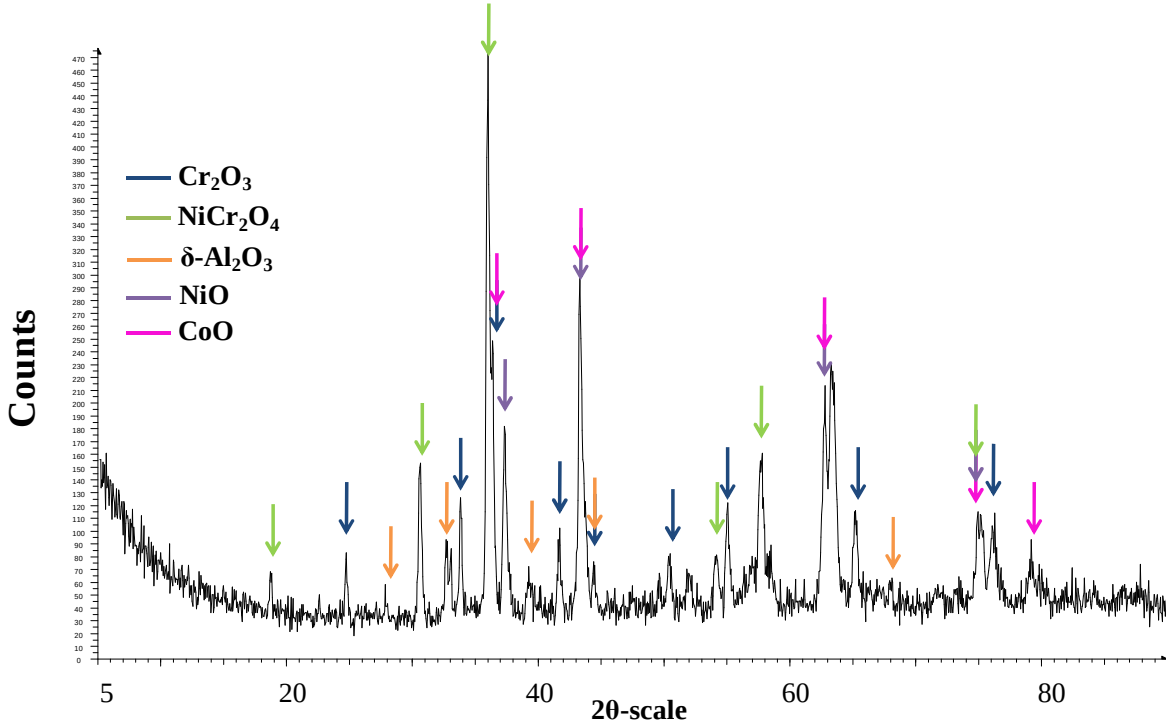

Figure 9.5 XRD spectrum from surface of sample 130910d3 (41.6 at% Cr, 8.8 at% Al) (Ni-20wt%Co-40wt%Cr+Al) after 500 hours exposure, showing the presence of Cr_2O_3, transient δ-Al_2O_3, spinels, NiO and CoO.

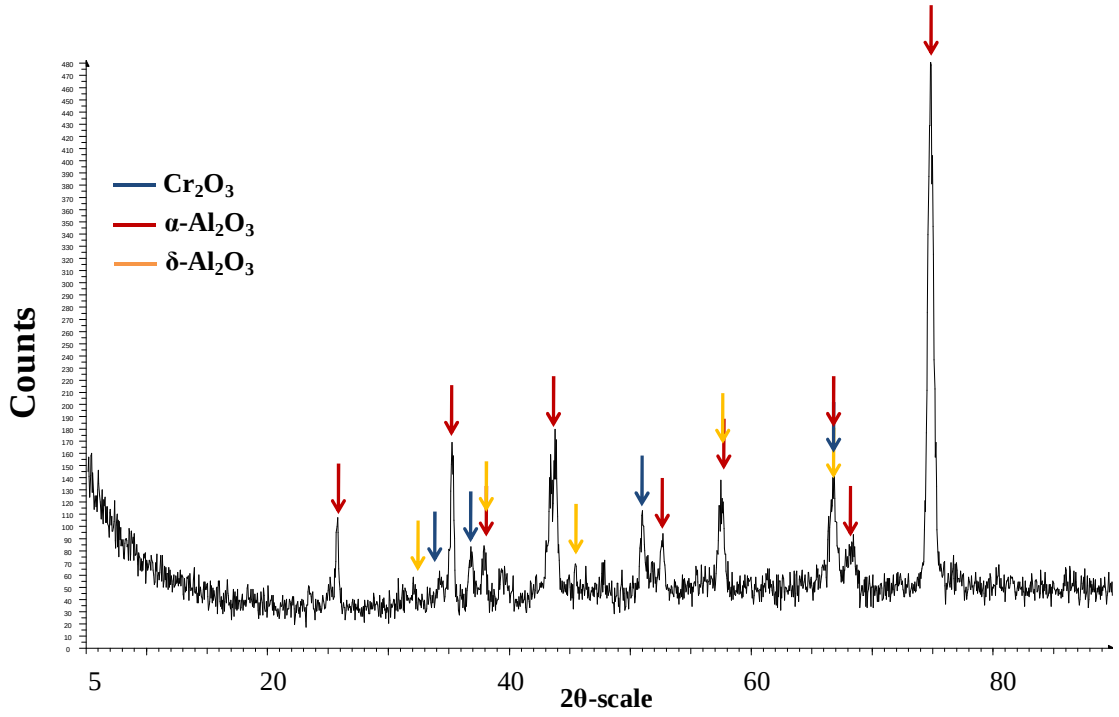

Figure 9.6 XRD spectrum from surface of sample 130910F2 (29.2 at% Cr, 36.6 at% Al) (Ni-20wt%Co-40wt%Cr+Al) after 500 hours exposure, showing the presence of Cr_2O_3, transient δ-Al_2O_3 and α-Al_2O_3.

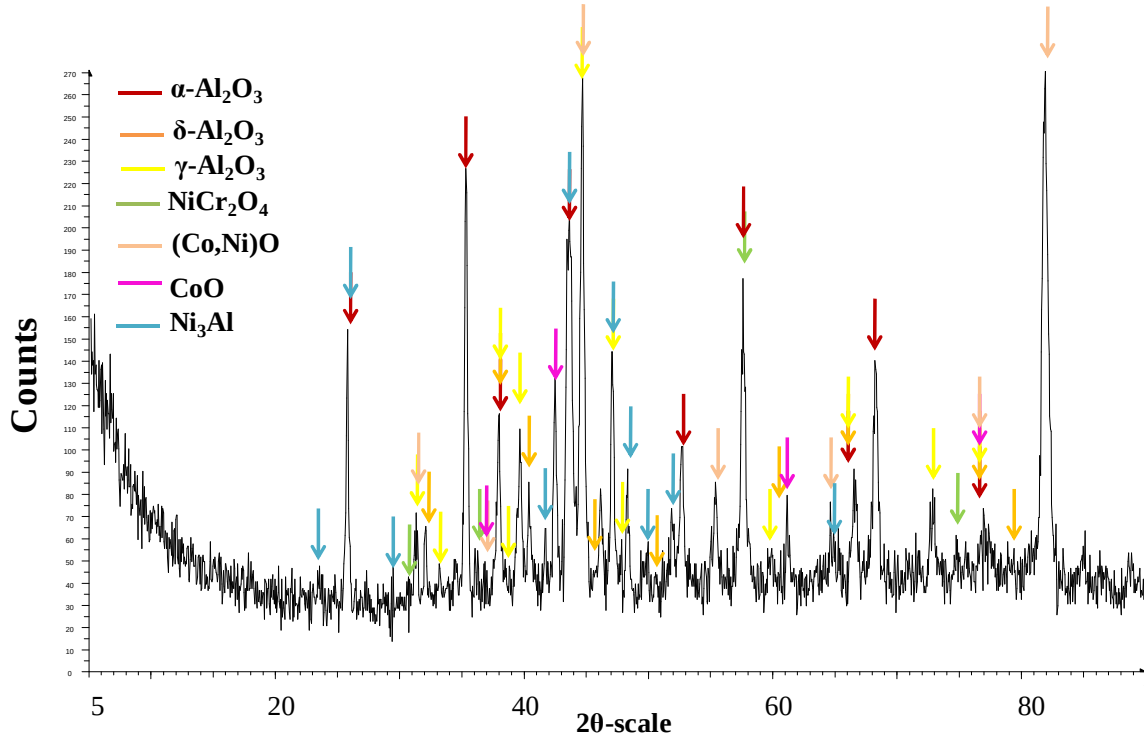

Figure 9.7 XRD spectrum from surface of sample 130910f3 (27.8 at% Cr, 40.2 at% Al) (Ni-20wt%Co-40wt%Cr+Al) after 500 hours exposure, showing the presence of transient δ and γ-Al_2O_3, α-Al_2O_3, spinels and CoO.

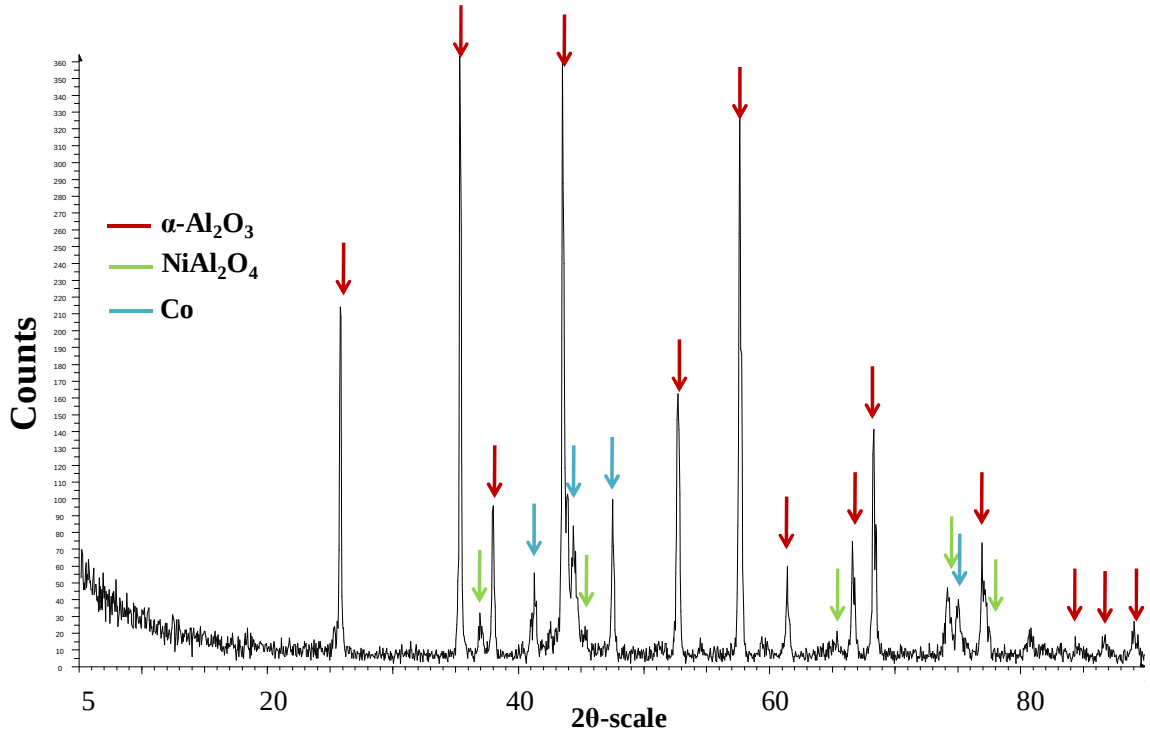

Figure 9.8 XRD spectrum from surface of sample 130910H2 (5.8 at% Cr, 86.3 at% Al) (Ni-20wt%Co-40wt%Cr+Al) after 500 hours exposure, showing the presence α-Al_2O_3 and spinels.

The high content of Co in the coatings coming from the Ni-40wt%Co-20wt%Cr+Al batch led to the formation of NiO, CoO and mixed (Co,Ni)O oxides (Figure 9.9). No Cr_2O_3 could be detected with the high amount of Co (36.6 at%) and Ni (34.4 at%) present in coating 160810E4 (18.2 at% Cr, 20.1 at% Al). The non-protective oxide layer growing on these coatings might be too thick to detect an underlying Cr_2O_3 layer. A mix of $NiCr_2O_4$ and $CoCr_2O_4$ spinels was detected as well in Co and Ni rich coatings. Higher levels of Al (a minimum of 41 at%) enabled the coatings to grow α-Al_2O_3 (160810F4 with 13.4 at% Cr and 40.9 at% Al).

Another sort of Co oxide was also detected on few coatings: Co_3O_4 (Figure 9.10). Only on two samples, 160810f2 (8.9 at% Cr, 59.0 at% Al) and 160810g1 (4.4 at% Cr, 78.5 at% Al), were transient forms of Al2O3 observed (Figure

9.11). In both case, their crystal structure was monoclinic, characteristic of the θ-phase, according to Levi and Brandon [147]. On sample 160810g1, containing 4.4 at% Cr, peaks of tetragonal Cr_2O_3 were detected. These are different from the usual hexagonal form present in oxidised coatings (Figure 9.11).

All the oxides observed on the Ni-20wt%Co-40wt%Cr+Al and Ni-40wt%Co-20wt%Cr+Al samples using XRD analysis are summarised in Table 9.2.

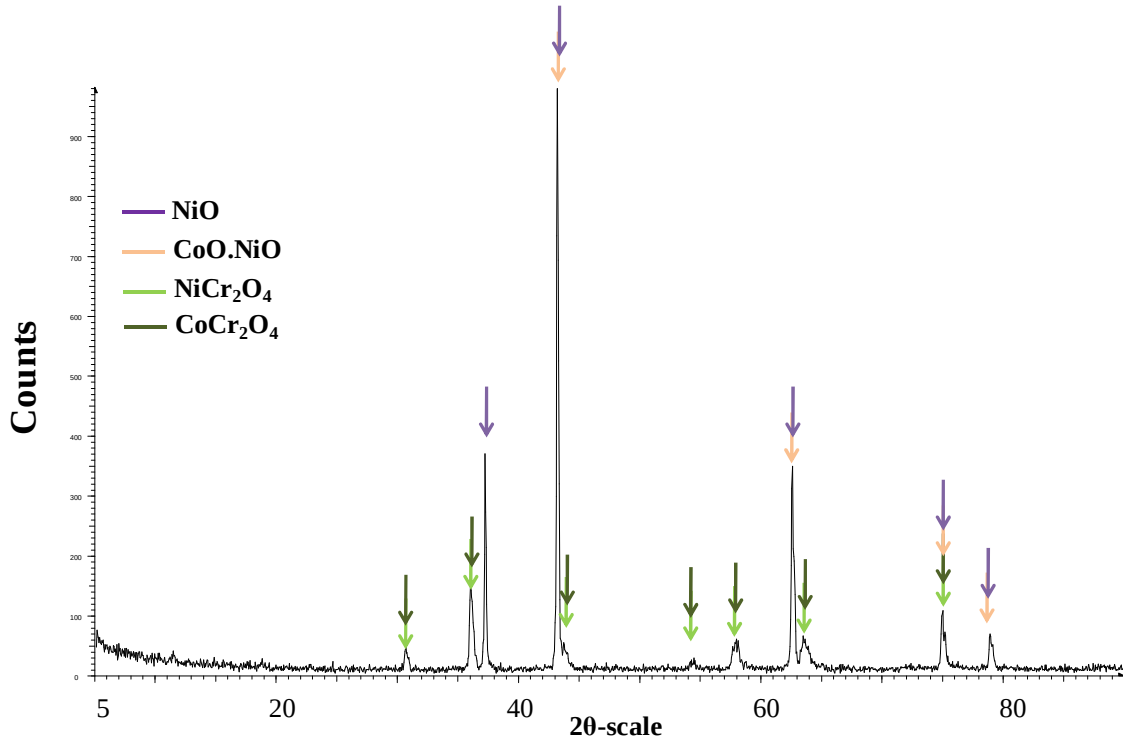

Figure 9.9 XRD spectrum from surface of sample 160810E4 (18.2 at% Cr, 20.1 at% Al) (Ni-40wt%Co-20wt%Cr+Al) after 500 hours exposure, showing the presence of NiO, mixed (Co,Ni)O and spinels.

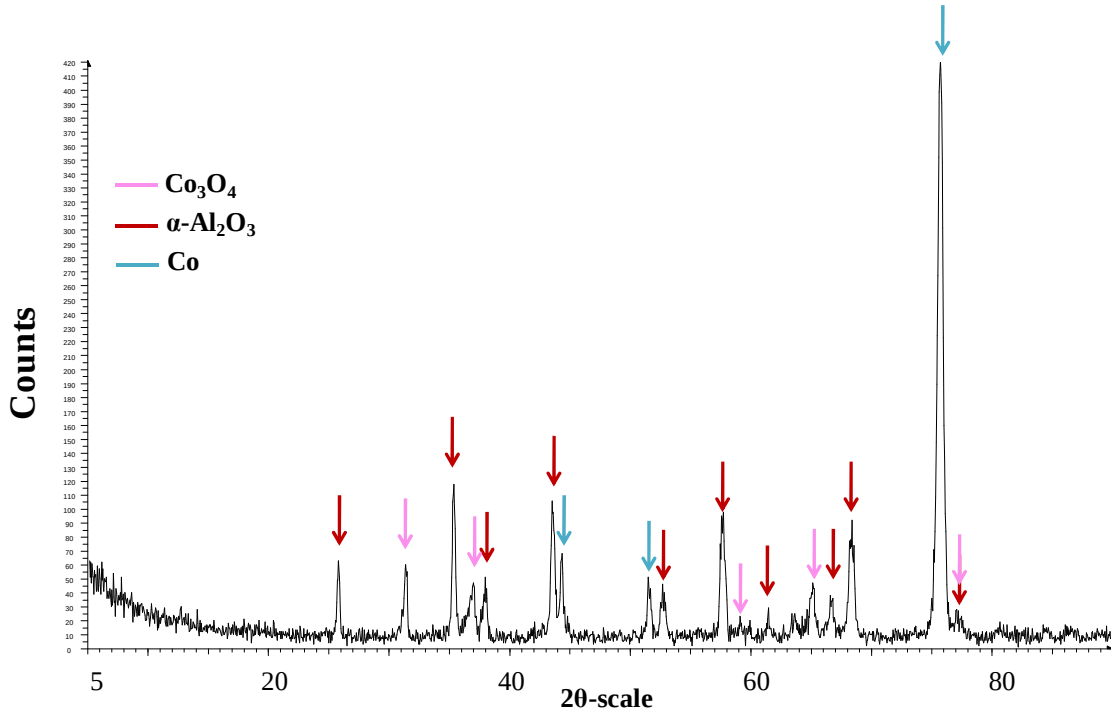

Figure 9.10 XRD spectrum from surface of sample 160810F4 (13.4 at% Cr, 40.9 at% Al) (Ni-40wt%-Cowt%20Cr+Al) after 500 hours exposure, showing the presence of α-Al_2O_3 and Co_3O_4.

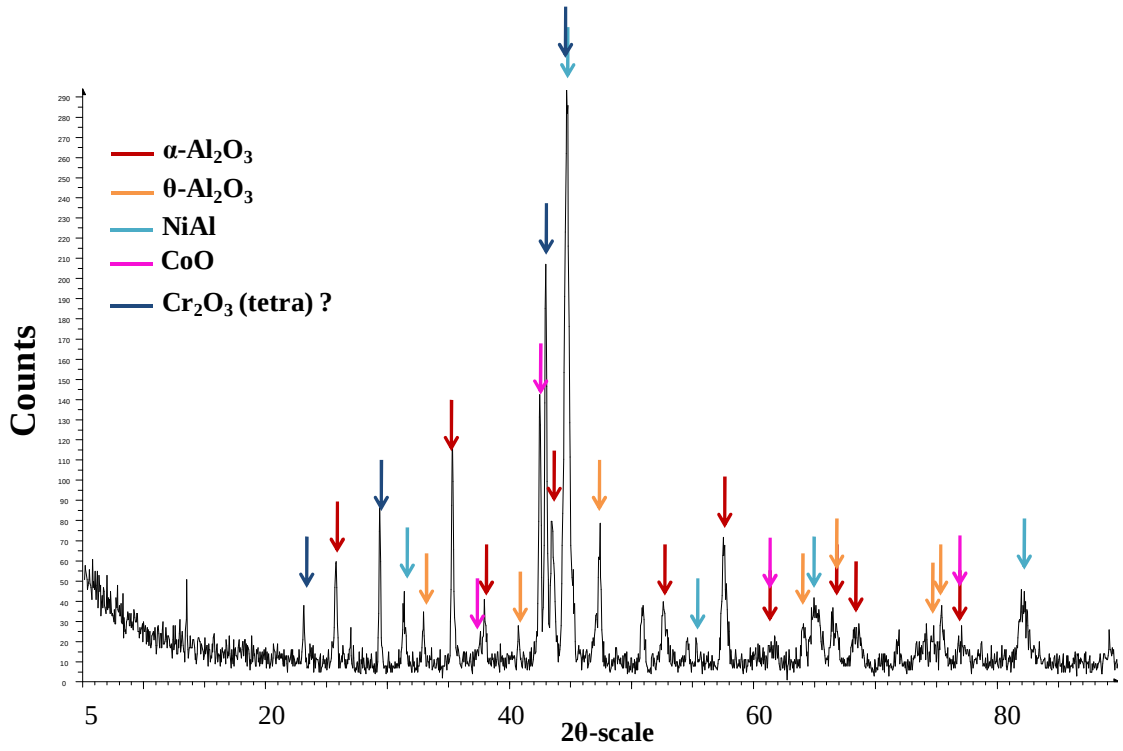

Figure 9.11 XRD spectrum from surface of sample 160810g1(4.4 at% Cr, 78.5 at5 Al) (Ni-40wt%Co-20wt%Cr + Al) after 500 hours exposure, showing the presence of α-Al_2O_3 , transient θ-Al_2O_3 CoO and Cr_2O_3.

Targets	Sample		NiO/CoO	NiO.CoO	Cr_2O_3	Al_2O_3	Spinels
Ni-	130910	d3		+	+	δ-	$NiCr_2O_4$
20wt%Co-	130910	E2			+	θ-	$NiCr_2O_4$
40wt%Cr	130910	e2			+	α-	
+Al	130910	F2				α,γ,θ-	
	130910	f3		+		α,γ,θ-	$NiCr_2O_4$
	130910	G2				α-	
	130910	g3				α-	
	130910	H2				α-	$NiAl_2O_4$
	130910	I4				α-	
Ni-	160810	d2	NiO	+			$NiCr_2O_4$
40wt%Co-	160810	E4		+			$(Ni,Co)Cr_2O_4$
20wt%Cr	160810	e3				α-	
+Al	160810	F4	Co_3O_4			α-	
	160810	f2	CoO			α-	
	160810	G4		+		α,θ-	
	160810	g1				α-	
	160810	H1				α,θ-	
	160810	h1				α-	

Table 9.2 Different oxide species identified using XRD on the surface of samples exposed at 950 °C.

The oxide microstructures in cross-sectioned Co-Ni-Cr-Al coatings after exposure at 950 °C were observed under the SEM and are shown in Figures 9.12 and 9.13. These confirmed that coating were generally between 20 and 30 µm thick.

In the Ni-20wt%Co-40wt%Cr+Al batch of samples, the oxides had formed in a single mixed layer. High initial amounts of Cr (41.6 at%) led to the growth of a mixed $(Al,Cr)_2O_3$ layer whose thickness varied between 3 and 12 µm due to the presence of oxide "lumps" (Figure 9.12(a)). Increasing the initial Al fraction to 16 at% still created a layer of mixed $(Al,Cr)_2O_3$. However, the Cr content in this layer reduced to an average of 5 at%, with the amount of Al increasing up to 35 at%. Also, the thickness of the oxide layer was thinner (1.5 µm) and more homogeneous (Figure 9.12(b)).A further increase in Al (36.6 at%) led to similar results (Figure 9.12(c)).

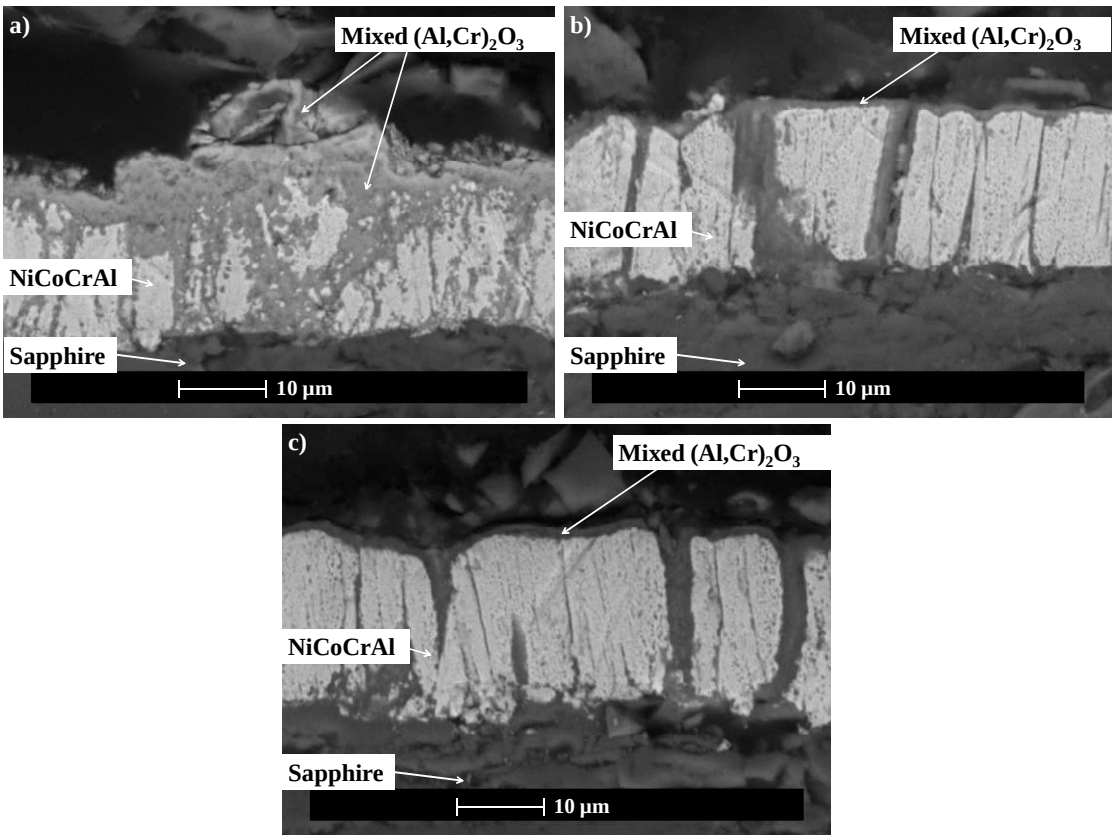

Figure 9.12 Cross sections SEM images of (a) 130910d3, (b) 130910e2 and (c) 130910F2.

High fractions of Co in the initial composition of coatings from the Ni-40wt%Co-20wt%Cr+Al batch led to different oxide microstructures. Above 26 at% Co, a two-layered oxide grew on the surface (Figure 9.13(a)). EDX analysis identified the upper layer as a mix of (Co,Ni)O while the lower one was mixed $(Al,Cr)_2O_3$. The upper layer corresponded to the coloured crystals appearing on the surface of the sample, as shown in Figure 9.1, but was not continuous. Their high porosity indicated that they were fast growing oxides and therefore not protective against oxidation. With increasing initial amounts of Cr (15.4 at%) and Al (33.5 at%), and decreasing amounts of Ni (25.1 at%), the upper oxide layer disappeared and only a mixed $(Al,Cr)_2O_3$ oxide was formed. On sample 160810e3 (15.4 at% Cr, 33.5 at% Al), which was identified as the first

sample growing Al_2O_3, a discontinuous double layered oxide was observed. The compositions of the two layers were very similar, but the inner one contained a little less Cr (7.7 at%), Co (1.6 at%) and Ni (2.2 at%) than the outer one (Figure 9.13(b)). The higher the initial Al content, the purer the Al_2O_3 layer. Indeed sample 160810F4 (13.4 at% Cr, 40.9 at% Al) grew pure Al_2O_3 together with few spinels, while 160810f2 (8.9 at% Cr, 59.0 at% Al) did not produce any of the less-protective oxides. Unlike XRD results, no CoO or Co_3O_4 were found on 160810F4 and 160810f2 under the SEM. The Co detected by XRD might correspond to the metal coating instead of the actual oxide layer grown during exposure.

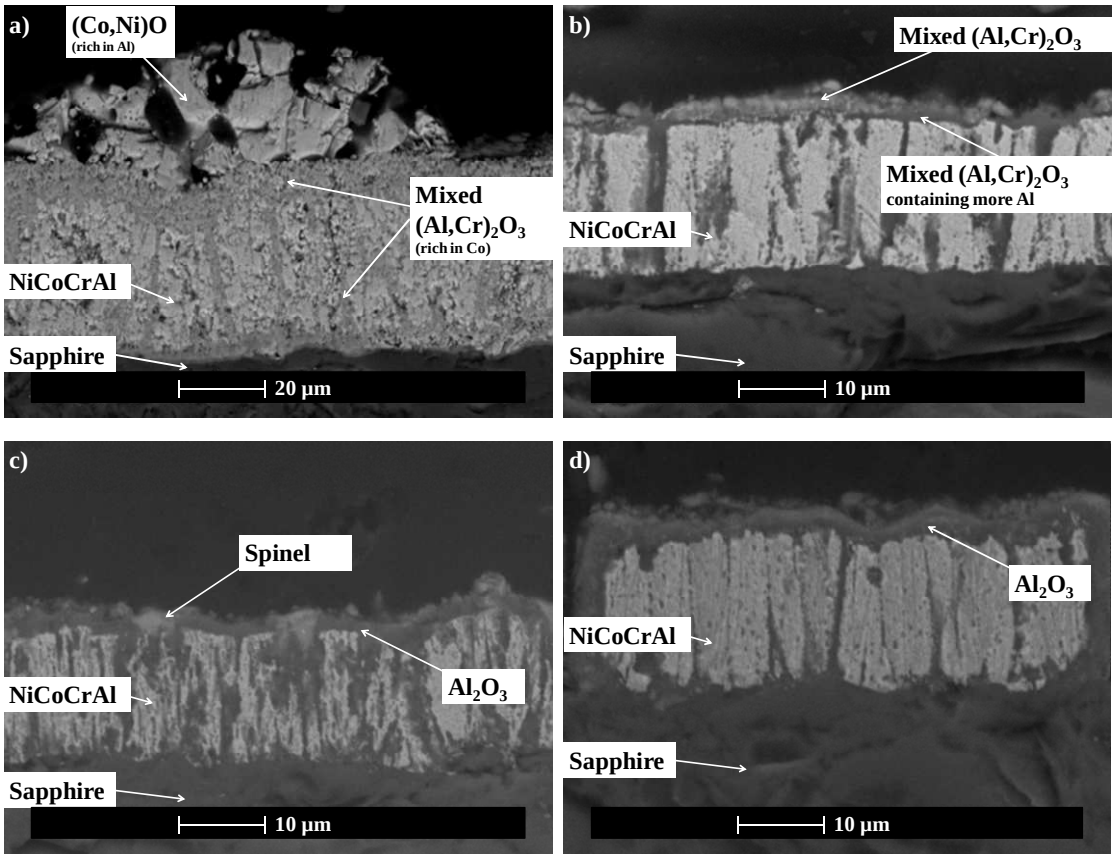

Figure 9.13 Cross sections SEM images of (a) 160810d2, (b) 160810e3, (c) 160810F4 and (d) 160810f4.

The results of EDX analysis carried out on the oxides of selected samples are summarised in Table 9.3. They showed that the layers of "pure" Al_2O_3 in fact contained

small amounts of Cr (~2 to 6 at%). Samples containing less initial amounts of Cr (from the Ni-40wt%Co-20wt%Cr+Al batch) formed purer Al_2O_3. The double oxide layers formed on samples with high initial amounts of Co (above 30 at%) were composed of an outer layer containing equal contents of Co and Ni. However, the inner oxide layer contained around 10 at% Co and no Ni amongst ~ 15at% of Cr and Al. Co had a better affinity with the mixed $(Al,Cr)_2O_3$ oxide than Ni.

Sample		Oxide	O (at%)	Co (at%)	Ni (at%)	Cr (at%)	Al (at%)
130910	d3	single layer	57.7	4.9	2.5	17.2	17.8
130910	e2	single layer	57.6	1.1	2.4	5.5	33.5
130910	F2	single layer	57.0	1.6	3.1	6.4	31.8
160810	d2	outer layer	50.1	12.9	18.2	2.2	16.7
		inner layer	56.6	10.1	3.1	15.8	14.5
160810	e3	single layer	58.8	1.6	2.2	7.7	29.7
160810	F3	single layer	63.0	0.8	0.8	1.3	34.2
160810	f4	single layer	61.7	1.5	0.6	2.5	33.4

Table 9.3 Composition (obtained by EDX analysis) of the oxide layers observed on the cross-sections of selected Co-Ni-Cr-Al samples at 950°C.

9.1.4 Discussion - An attempt to map the oxide composition as a function of the Ni-Co-Cr-Al content at 950 °C.

The identification of the oxide layers grown on the Co-Ni-Cr-Al coatings at 950 °C are summarised in Figure 9.14, in a graph plotting Cr/Al against Co/Ni atomic ratios. The domain under the red dotted line on the graph represents the Co-Ni-Cr-Al compositions capable of forming α-Al_2O_3 after 500 hours when exposed at 950 °C. The black dotted line delimits the samples capable of forming transient forms of Al_2O_3. Samples needed a ratio of Cr/Al (in at%) under 5 with Co/Ni equal to 0.5 to grow a pure α-Al_2O_3 layer at 950 °C. Without Co present this Cr/Al ratio did not change much and was still around 5. Increasing the amount of Co increased the amount of Al needed to grow Al_2O_3 and no Cr_2O_3 could be produced. Ni and Co oxides were more likely to be

formed with a higher initial Co level and some of these non protective oxides could be found in the Al_2O_3 domain. Not appearing in the graph, mixed oxides and spinels were observed in a lot of samples (more details in Figure 9.28(a)). Adding Co to the Ni-Cr-Al increased the likelihood for the formation of spinels/mixed oxides (see Figure 9.28(a)).

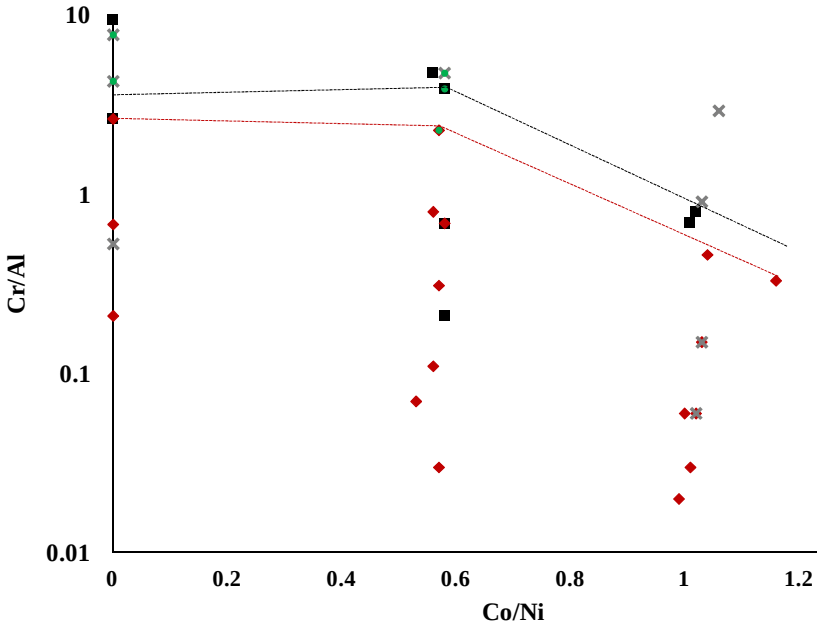

Figure 9.14 Effect of Cr/Al and Co/Ni ratios (at%) on oxide compositions observed after 500 hours at 950 °C. Red diamonds correspond to α-Al_2O_3, black squares to transient Al_2O_3, green dots to Cr_2O_3 and grey crosses to Ni or Co oxides. Beneath black dotted line are samples capable of forming transient Al_2O_3. Beneath red dotted line are samples capable of forming α-Al_2O_3.

9.2 Study of the Co-Ni-Cr-Al system – oxidation at 900 °C

Two other sets of Ni-20wt%Co-40wt%Cr+Al and Ni-40wt%Co-20wt%Cr+Al samples were exposed at 900 °C for up to 500 hours. Their denominations and compositions are given in Table 9.4.

Targets	Sample		Co (at%)	Ni(at%)	Cr(at%)	Al(at%)	Cr/Al	Co/Ni
Ni	130910	c2	19.1	33.0	44.3	3.6	12.46	0.58
-20wt%Co	130910	d2	18.3	31.3	41.6	8.8	4.75	0.58
-40wt% Cr	130910	E1	18.0	30.9	40.6	10.5	3.88	0.58
+Al	130910	e3	16.4	28.8	38.1	16.7	2.28	0.57
	130910	F3	12.3	21.9	29.2	36.6	0.80	0.56
	130910	f2	11.8	20.2	27.8	40.2	0.69	0.58
	130910	G1	7.9	14.0	18.3	59.8	0.31	0.57
	130910	g1	4.2	7.5	9.0	79.3	0.11	0.56
	130910	H1	2.7	5.2	5.8	86.3	0.07	0.53
Ni	160810	c2	38.7	35.4	22.9	3.0	7.69	1.09
-40wt%Co	160810	D3	38.0	35.1	22.4	4.5	5.02	1.08
-20wt%Cr	160810	E2	31.2	30.3	18.2	20.1	0.91	1.03
+Al	160810	E3	31.2	30.3	18.2	20.1	0.91	1.03
	160810	e2	26.0	25.1	15.4	33.5	0.46	1.04
	160810	F1	23.2	22.5	13.4	40.9	0.33	1.16
	160810	f3	16.5	15.8	8.9	59.0	0.15	1.03
	160810	G2	7.9	14.0	18.3	59.8	0.06	1.02
	160810	g3	4.2	7.5	9.0	79.3	0.06	1.00

Table 9.4 Compositions of Co-Ni-Cr-Al coatings resulting from 2 target co-sputtering and oxidised at 900 °C.

9.2.1 Physical changes of samples with exposure

Pictures of the Ni-40wt%Co-20wt%Cr+Al and Ni-20wt%Co-40wt%Cr+Al samples exposed at 900 °C are shown in Figures 9.15 and 9.16.

Initial levels of Co above 30 at% in the Ni-40wt%Co-20wt%Cr+Al samples (Figure 9.15) led to the formation of shiny crystals on the coatings surface. In sample 160810c2 (22.9 at% Cr, 3.0 at% Al) these crystals started to appear after 100 hours

exposure while in sample 160810D3 (22.4 at% Cr, 4.5 at% Al) they nucleated after only 40 hours exposure. The coverage increased with further exposure until the samples' surface was fully covered. Sample 160810E2 (18.2 at% Cr, 20.1 at% Al) grew two distinct types of oxides, because of an initial composition gradient across its surface. The half of the coating with a higher Co and Cr content grew a green oxide which was later covered by the same sort of shiny crystals, while the part of the coating with an higher Al content grew a grey oxide. After 300 hours exposure, failure was located on the grey half of 160810E2.

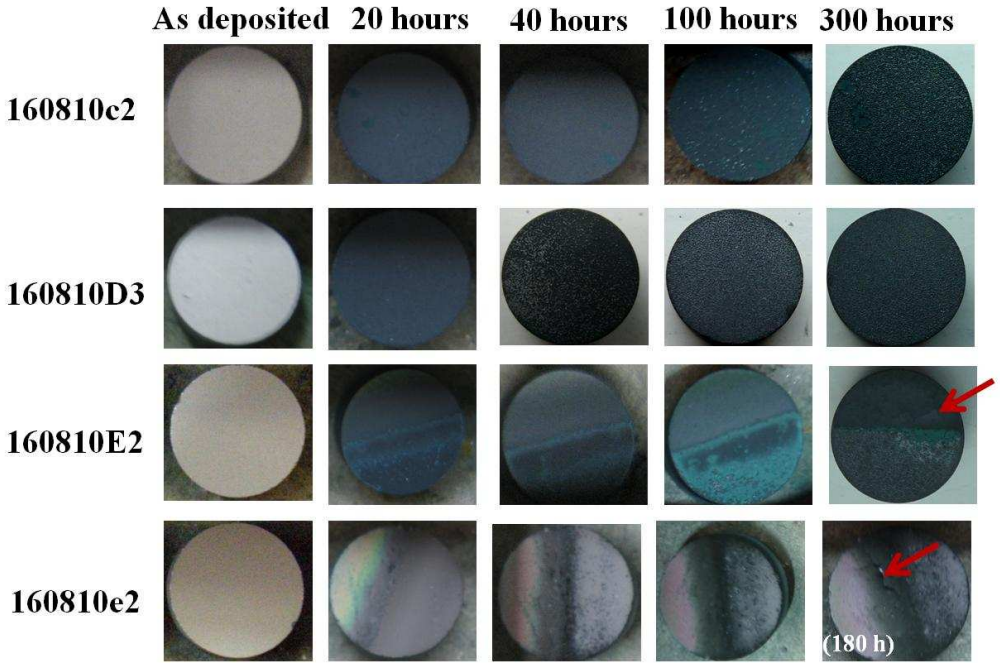

Figure 9.15 Pictures showing the evolution of oxides on 160810c2 (22.9 at% Cr, 3.0 at% Al), 160810D3 (22.4 at% Cr, 4.5 at% Al), 160810E2 (18.2 at% Cr, 20.1 at% Al) and 160810e2 (15.4 at% Cr, 33.5 at% Al) (Ni-40wt%Co-20wt%Cr+Al) with exposure at 900 °C. Red arrows point at damage in coatings.

Similarly 160810e2 (15.4 at% Cr, 33.5 at% Al), even if it could not be seen on the as-deposited coating, had a gradient of composition which led to the growth of different oxides in different areas. The oxide formed went from light grey to a mix of

pink, dark grey and light grey depending on the amount of Al present initially. Failure at the sapphire/coating interface occurred after 180 hours in the dark grey area in the coating while other parts stayed attached to the sapphire substrate.

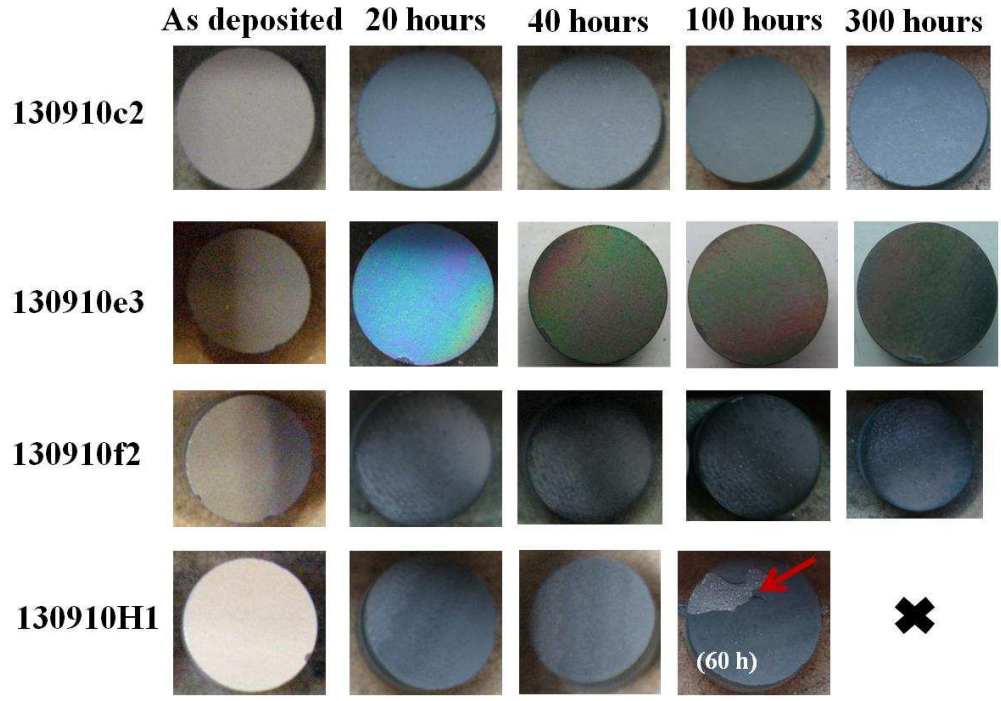

Figure 9.16 Pictures showing the evolution of oxides on 130910c2 (44.3 at% Cr, 3.6 at% Al), 130910e3 (38 at% of Cr, 16.7 at% of Al), 130910f2 (27.8 at% Cr, 40.2 at% Al) and 130910H1 (5.8 at% Cr, 86.3 at% Al) (Ni-20wt%Co-40wt%Cr+Al) with exposure at 900 °C. Red arrows point at damage in coatings.

Increasing the amount of Cr in all coatings up to 44 at% led to the growth of homogeneous grey oxides (e.g. 130910c2 with 44.3 at% Cr and 3.6 at% Al in Figure 9.16). 130910e3, containing 38 at% of Cr and 16.7 at% of Al, grew a very vivid blue oxide during the first 20 hours of exposure at 900 °C. The colour faded with further exposure, to be replaced by an iridescent coloured oxide. Higher amounts of Al (over 30 at%) created grey to black surface colours, e.g. on 130910f2 (27.8 at% Cr, 40.2 at% Al). Finally, excessive amounts of Al (over 80 at%), limited the lifetime of the coatings

to a few cycles. 130910H1 (5.8 at% Cr, 86.3 at% Al), only lasted 60 hours. The coating did not have the molten profile that could be observed on samples from the Ni-Cr-Al system, suggesting that the Co had changed its melting point, however, the short lifetime of the coating still indicated that the high level of Al had limited its mechanical properties.

9.2.2 Mass change of samples

The mass change data from the Co-Ni-Cr-Al coatings exposed at 900 °C were plotted against time. Figure 9.17 shows the results obtained with samples deposited with the Ni-20wt%Co-40wt%Cr and Al targets. Most of the samples lasted until 500 hours, apart from 130910H1 (5.8 at% Cr, 86.3 at% Al) which initially contained a high fraction of Al. The oxides grew slowly and could be split into two categories. Oxides from the coatings with a higher amount of Cr (above 40 at%) reached a maximum growth of 0.3 mg/cm^2 after 500 hours while the ones grown on coating with a higher amount of Al (above 16 at% Al) did not exceed 0.1 mg/cm^2. This indicated that coatings 130910c2 (44.3 at% Cr, 3.6 at% Al) to 130910E1(40.6 at% Cr, 10.5 at% Al) grew oxides with compositions dominated by Cr_2O_3 and coatings 130910e3 (38.1 at% Cr, 16.7 at% Al) to 130910g1 (9 at% Cr, 79.3 at % Al) grew purer Al_2O_3.

The batch of samples resulting from sputter deposition using the Ni-40wt%Co-20wt%Cr and Al targets showed a range of diverse behaviours (Figure 9.18). The most peculiar was observed on sample 160810c2 (22.9 at% Cr, 3.0 at% Al), which initially contained 38 at% Co. Starting at a slow rate until 20 hours exposure, the mass of the oxide increased almost exponentially until 200 hours when it slowed down again. At that point the curve showed a parabolic trend, corresponding to the growth of protective

oxides. This radical change of behaviour could be explained by the appearance and propagation of the crystals on the surface of the coatings as seen in Figure 9.15. The growth rate of the oxide slowed down when those crystals covered the whole surface of the sample. However, sample 160810D3 (22.4 at %Cr, 4.5 at% Al) also grew these crystals but the mass gain curve described a parabolic behaviour divided into an initial rapid growth (up to 100 hours) and a second part where the sample didn't gain much weight. After 500 hours, the mass gain of the sample with the most Co reached 1.3 mg/cm^2 while the other one reached 0.8 mg/cm^2.

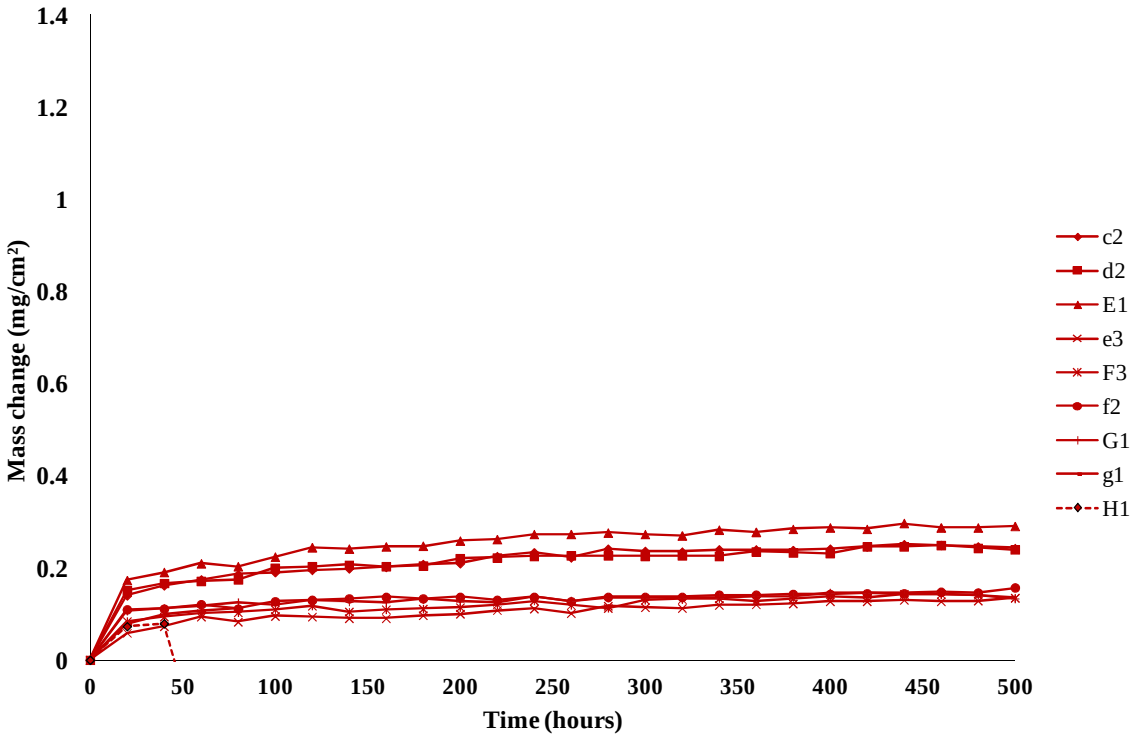

Figure 9.17 Mass change of Ni-20wt%Co-40wt%Cr+Al coating against time of exposure at 900 °C.

Increasing the amount of Al (over 20 at%) changed the nature of the oxides growing on the coatings and therefore reduced the extent of oxidation. Samples

160810E2 and E3 (18.2 at% Cr, 20.1 at% Al), which had the same composition grew oxides at a different rate. Samples that were expected to grow Al_2O_3, red curves in the graph, reached an average growth of 0.2 mg/cm^2 after 500 hours.

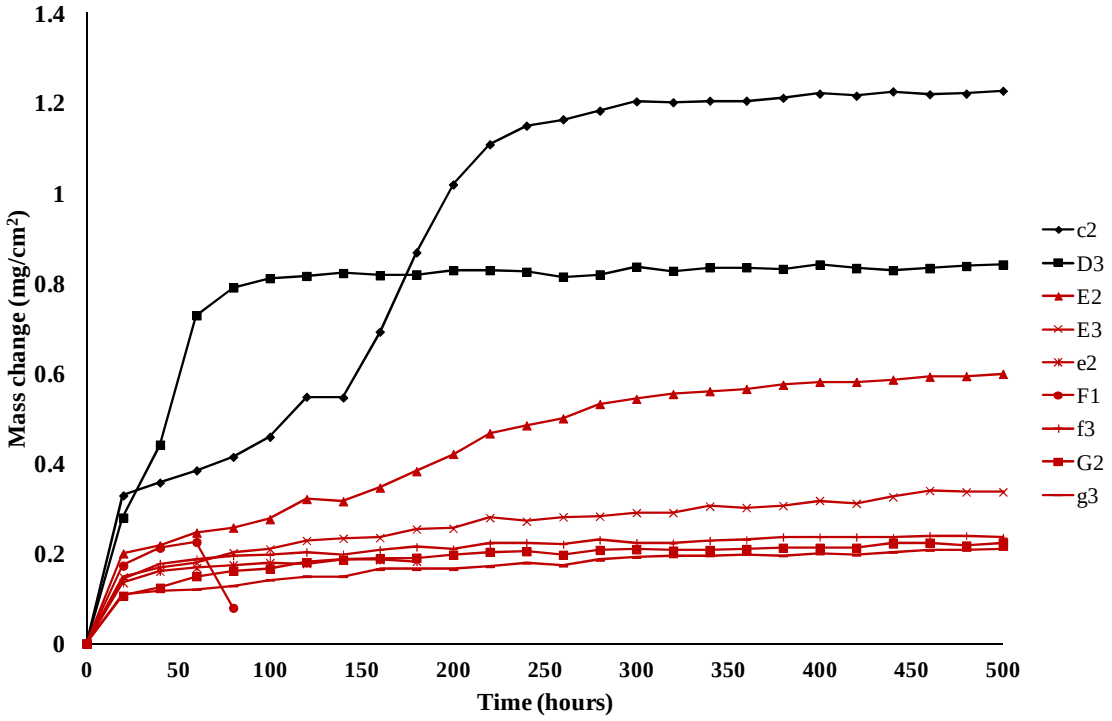

Figure 9.18 Mass change of Ni-20wt%Co-40wt%Cr+Al coating against time of exposure at 900 °C.

9.2.3 Identification of oxides

XRD spectra of selected Ni-20wt%Co-40wt%Cr+Al samples exposed at 900°C are shown in Figures 9.19 to 9.21. High amounts of Cr (44.3 at%) added to the presence of Co (19.2 at%) enabled the formation of transient Al_2O_3 with very low initial contents of Al (3.6 at%). Indeed XRD analysis of sample 130910c2 (Figure 9.19) detected the presence of δ-Al_2O_3 as well as Cr_2O_3 and spinels. No fast growing oxides such as NiO or CoO were detected on the coating's surface. The first traces of α-Al_2O_3 were observed on sample 130910e3 (38.1 at% Cr, 16.7 at% Al), as seen in Figure 9.20. At the

same time, the peaks corresponding to transient Al_2O_3 lose intensity compared to Figure 9.20. Coating that were possibly molten during exposure, because of their high level of Al (over 80 at%), grew a mix of stable and transient Al_2O_3. $NiCr_2O_4$ spinels could also be detected (Figure 9.21). No Cr_2O_3 was observed with such low levels of Cr (below 10 at%) in these coatings.

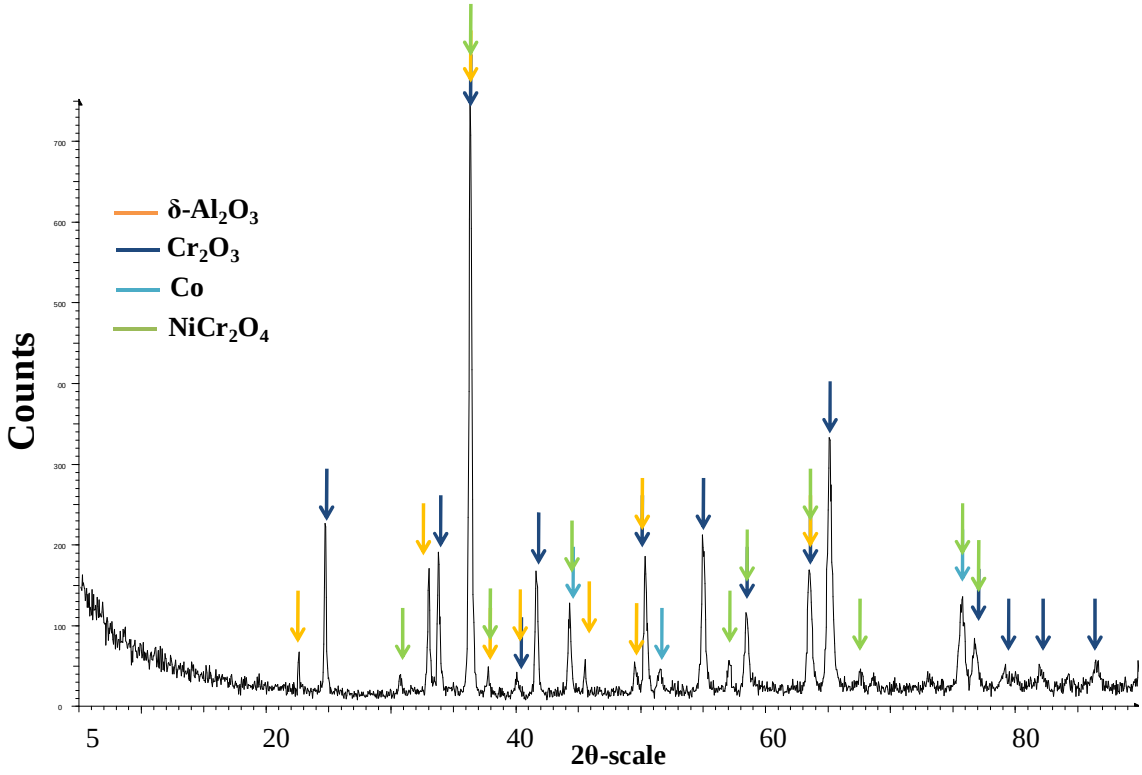

Figure 9.19 XRD spectrum from surface of sample 130910c2 (44.3 at% Cr, 3.6 at% Al) (Ni-20wt%Co-40wt%Cr + Al) after 500 hours exposure, showing the presence of δ-Al_2O_3, Cr_2O_3 and $NiCr_2O_4$.

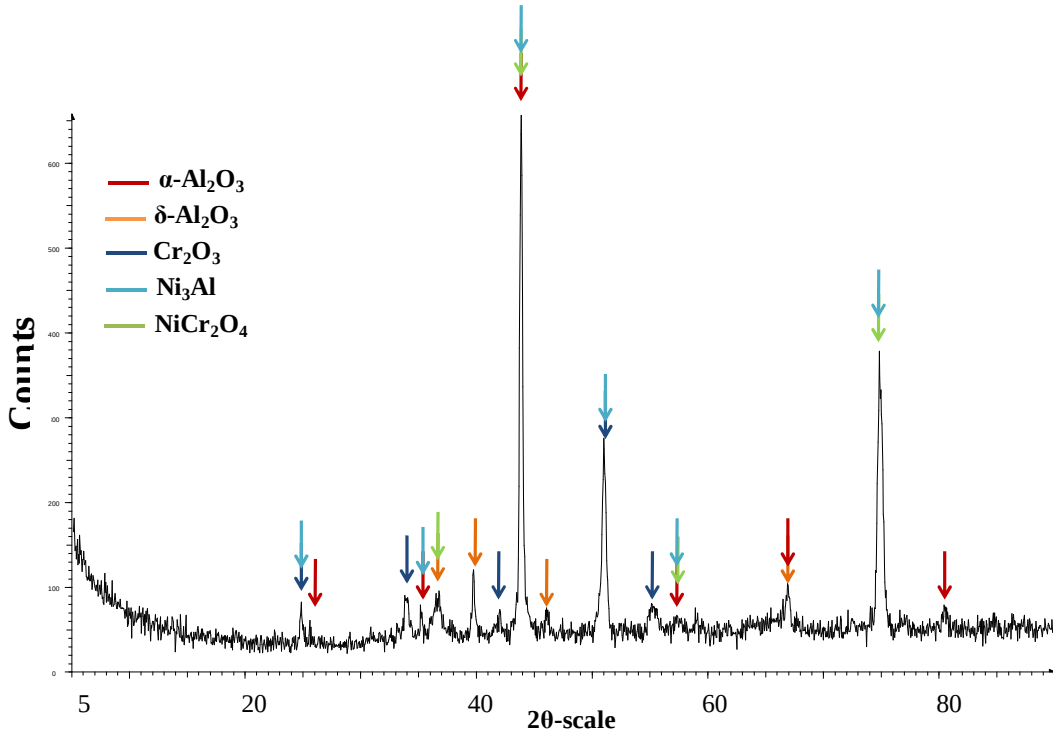

Figure 9.20 XRD spectrum from surface of sample 130910e3 (38.1 at% Cr, 16.7 at% Al) (Ni-20wt%Co-40wt%Cr + Al) after 500 hours exposure, showing the presence of α-Al_2O_3 δ-Al_2O_3, Cr_2O_3 and $NiCr_2O_4$.

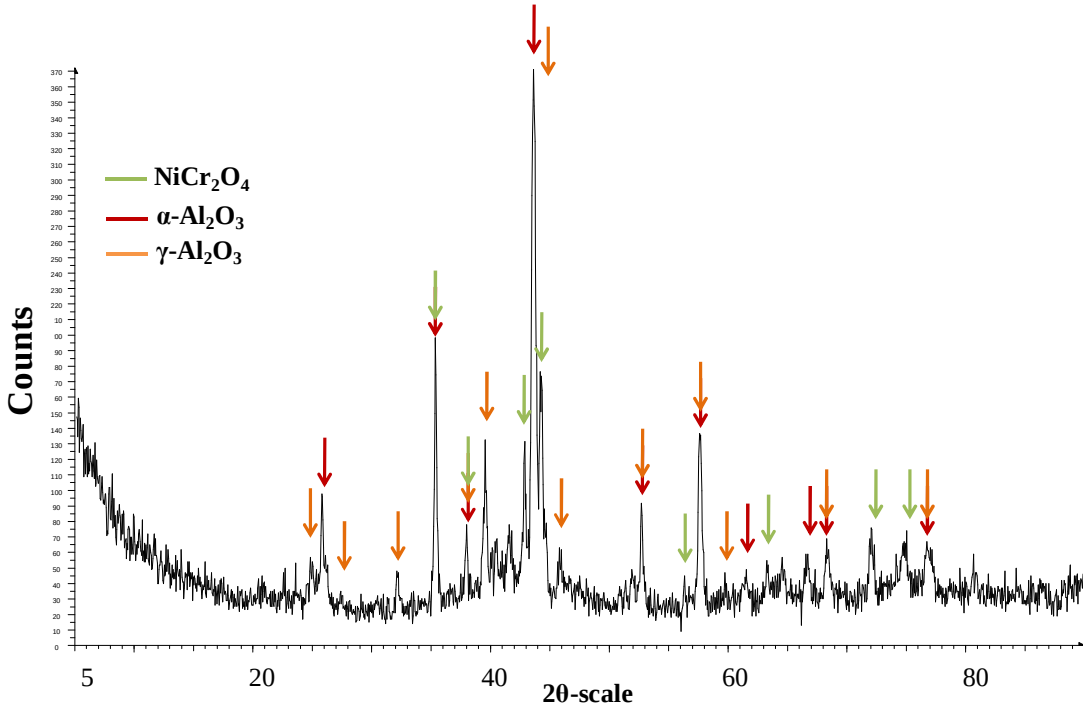

Figure 9.21 XRD spectrum from surface of sample 130910H1 (5.8 at%Cr, 86.3 at% Al) (Ni-20wt%Co-40wt%Cr + Al) after 500 hours exposure, showing the presence of γ-Al_2O_3, α-Al_2O_3 and $NiCr_2O_4$.

XRD spectra of selected samples from the Ni-40wt%Co-20wt%Cr+Al batch are shown in Figures 9.22 to 9.24. High amounts of Co (38.7 at%) in sample 160810c2 (22.9 at% Cr, 3.0 at% Al) enabled the formation of a range of Co oxides, including CoO, mixed (Ni,Co)O and Co_2O_3 (Figure 9.22). Peaks of Cr_2O_3 were weak compared to the Co oxides ones, suggesting that the Cr oxides form an inner layer beneath a thick (Ni,Co)O outer layer. The first traces of Al_2O_3 were detected on sample 160810E2 (18.2 at% Cr, 20.1 at% Al), as shown in Figure 9.23. At these levels of Co, Cr and Al, the coating still grew an outer layer of non-protective CoO, this time above an inner layer of mixed $(Cr,Al)_2O_3$. Spinels were detected as well. Initial levels of Co needed to be reduced to 26.1 at%, e.g. in sample 160810e2 (15.4 at% Cr, 33.5 at% Al) (Figure 9.24), to avoid formation of the fast growing external layer. At the same time, the increased amount of Al enabled the formation of stable α-Al_2O_3 as well as transient γ-Al_2O_3. The absence of Cr_2O_3 suggests that the oxide layer is essentially made of pure Al_2O_3.

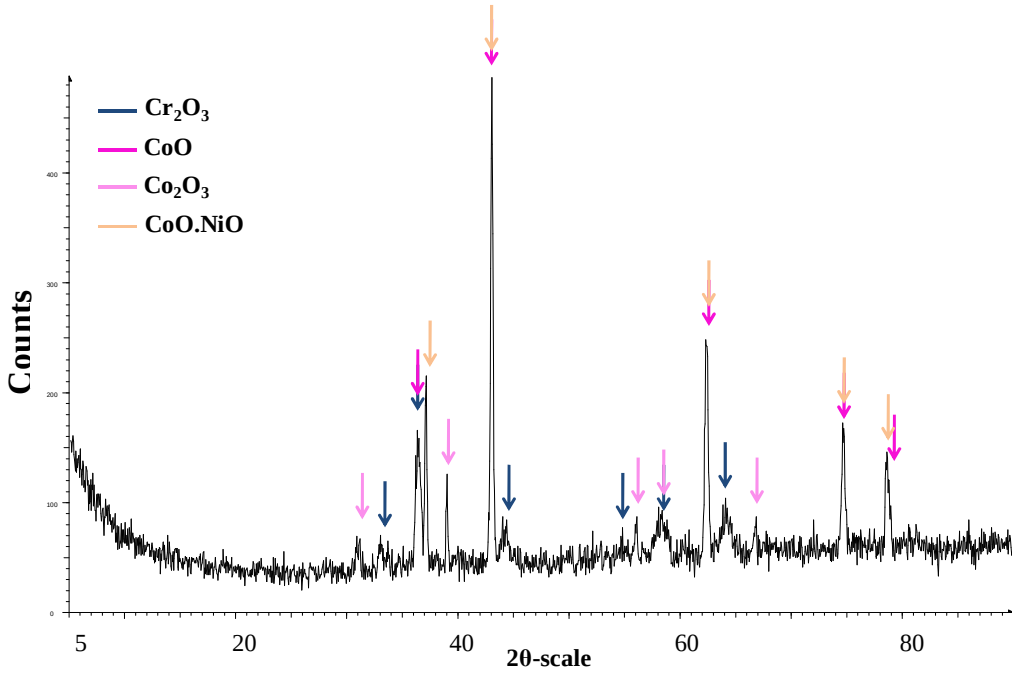

Figure 9.22 XRD spectrum from surface of sample 160810c2 (22.9 at% Cr, 3.0 at% Al) (Ni-40wt%Co-20wt%Cr + Al) after 500 hours exposure, showing the presence of Cr_2O_3, CoO, (Co,Ni)O and Co_2O_3.

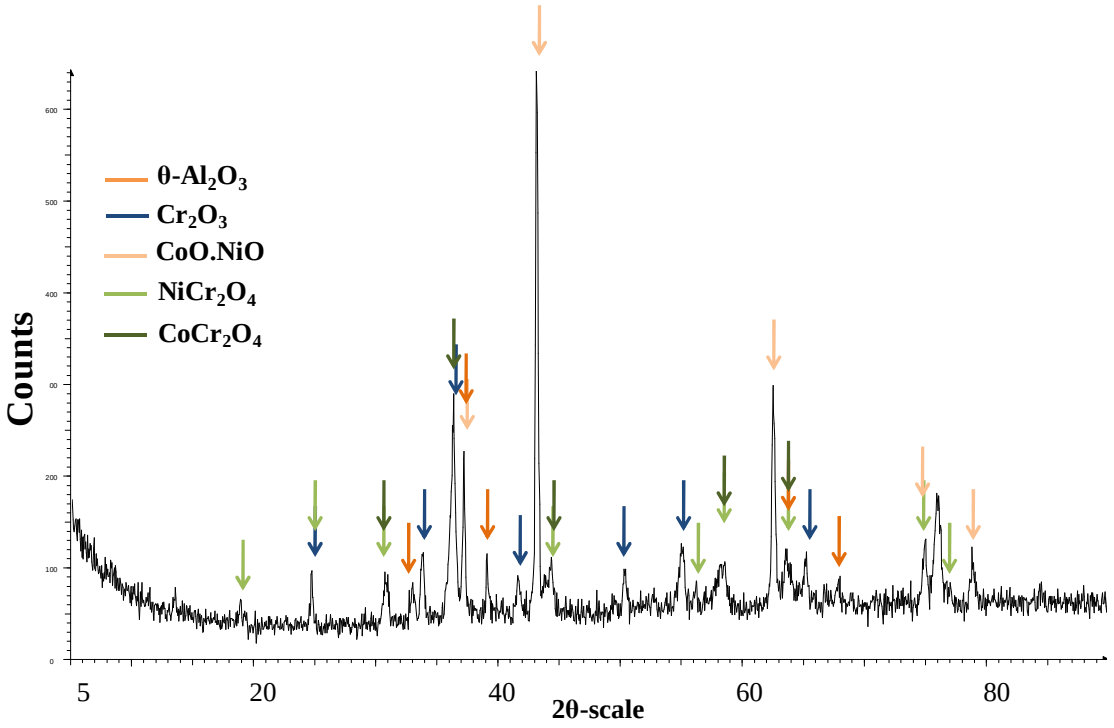

Figure 9.23 XRD spectrum from surface of sample 160810E2 (18.2 at% Cr, 20.1 at% Al) (Ni-40wt%Co-20wt%Cr + Al) after 500 hours exposure, showing the presence of θ-Al_2O_3, Cr_2O_3, (Co,Ni)O and (Co,Ni)Cr_2O_4.

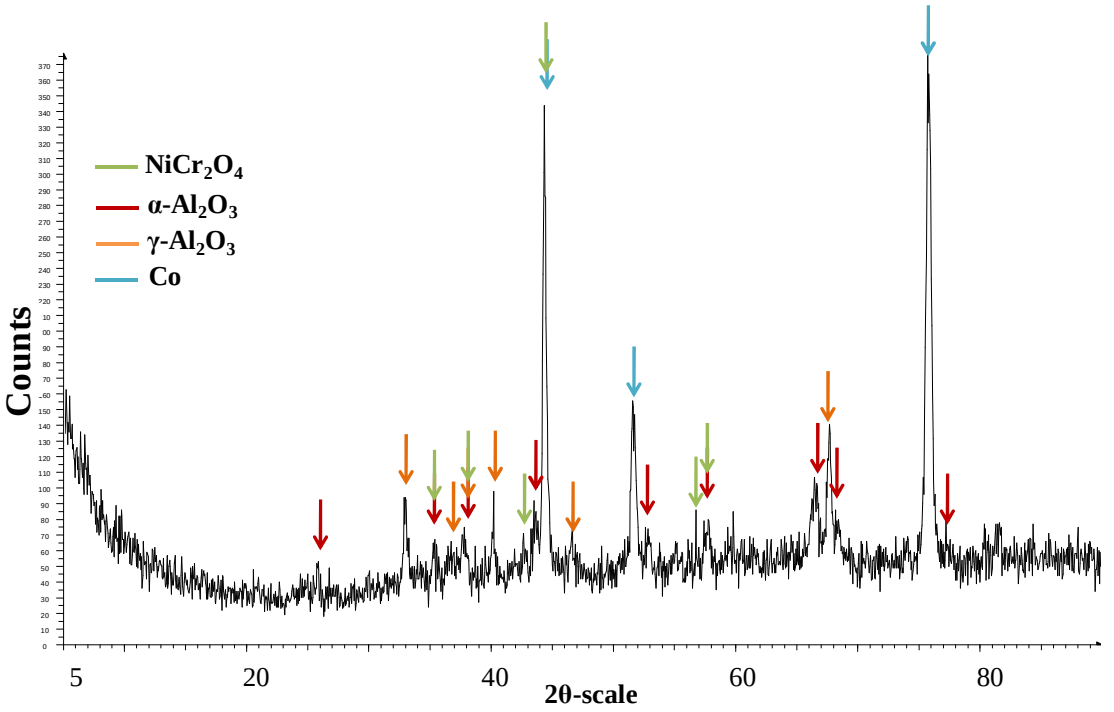

Figure 9.24 XRD spectrum from surface of sample 160810e2 (15.4 at% Cr, 33.5 at% Al) (Ni-40wt%Co-20wt%Cr + Al) after 500 hours exposure, showing the presence of γ-Al_2O_3, α-Al_2O_3 and $NiCr_2O_4$.

Table 9.5 is a summary of all the oxides observed on the Ni-Co-Cr-Al samples exposed at 900 °C. Most of the samples from the Ni-Co-Cr-Al batch formed spinels as well as their other oxides. Ni-20wt%Co-40wt%Cr+Al samples only formed $NiCr_2O_4$, while adding more Co (30 at%) led to the growth of $CoCr_2O_4$ as well. Coatings from the Ni-20wt%Co-40wt%Cr+Al batch grew transient Al_2O_3 with only low initial levels of Al and an increased fraction of Al was needed to grow stable α-Al_2O_3. The same phenomenon could be observed on the Ni-40wt%Co-20wt%Cr+Al coatings, with the only difference being that more Al was needed to start growing any form of Al_2O_3. Co and Cr oxides gradually disappeared as the initial fraction of Al increased.

Targets	**Sample**		**NiO/CoO**	**NiO.CoO**	**Cr_2O_3**	**Al_2O_3**	**Spinels**
Ni-	130910	c2			+	δ-	$NiCr_2O_4$
20wt%Co	130910	d2			+	δ-	
40wt%Cr	130910	E1			+	δ-	
+Al	130910	e3				α-	$NiCr_2O_4$
	130910	F3				α-	$NiCr_2O_4$
	130910	f2				α-	$NiCr_2O_4$
	130910	G1				α-	$NiCr_2O_4$
	130910	g1				α,θ-	$NiCr_2O_4$
	130910	H1				α,γ-	$NiCr_2O_4$
Ni-	160810	c2	CoO,Co_2O_3	+	+		
40wt%Co	160810	D3	CoO	+	+		
20wt%Cr	160810	E2		+	+	θ-	CoCr2O4
+Al	160810	E3			+	δ-	$(Ni,Co)Cr_2O_4$
	160810	e2				α,θ,δ-	$NiCr_2O_4$
	160810	F1				α,δ-	$Ni(Cr,Al)_2O_4$
	160810	G2				α,θ-	$NiCr_2O_4$
	160810	g3				α,γ-	$NiAl_2O_4$

Table 9.5 Different oxide species identified using XRD on the samples exposed at 900 °C.

The oxide microstructures of the exposed Ni-Co-Cr-Al coatings at 900 °C were observed under the SEM and are shown in Figures 9.25 and 9.26. These images confirmed that coatings were generally between 20 and 30 µm thick.

Cross-sections of samples from the Ni-20wt%Co-40wt%Cr+Al batch are shown in Figure 9.25. High initial amounts of Cr in sample 130910d2 (41.64 at% Cr, 8.8 at% Al) led to the formation of a single layer of mixed $(Al,Cr)_2O_3$. The presence of spinel was also identified (Figure 9.25(a)). Decreasing the initial amount of Cr down to 40.6 at% in the coating and increasing Al to 10.5 at%, gave similar results. The mixed $(Al,Cr)_2O_3$ contained a small fraction of Co (~ 2at%) and Ni (~ 3 at%) (Figure 9.25(b)). The first layer of Al_2O_3 was observed on sample 130910e3 (38.1 at% Cr, 16.7 at% Al) (Figure 9.25(c)). A further increase in the initial level of Al in the coating, reduced the amount of Cr in the Al_2O_3 layer, as shown for example on sample 130910F3 which contained only ~ 6 at% of Cr in its Al_2O_3 layer (Figure 9.25(d) and Table 9.6).

The microstructures of the oxides grown on samples from the Ni-40wt%Co-20wt%Cr+Al batch are shown in Figure 9.26. As for the samples exposed at 950 °C, high amounts of Co in the initial composition (over 32 at% Co) of samples exposed at 900 °C led to the formation of double layered oxides. On the top, a porous mixed (Co,Ni)O containing ~10 at% Al. Beneath this layer was a mixed $(Al,Cr)_2O_3$ (Figure 9.26(a)). Amongst the range of composition across the coating on sample 160810E2 (average of 18.2 at% Cr and 20.1 at% Al), is the threshold over which a double layer is no longer formed and is replaced by a single layer of mixed $(Al,Cr)_2O_3$. Clusters of mixed oxides rich in Co are still present (Figure 9.26(b)). A further increase in the initial Al content enables the growth of an Al_2O_3 layer, as observed on sample 160810e2 (15.4 at% Cr, 33.5 at% Al). Although small spinels precipitated within the

Al_2O_3 layer, the latter was almost pure, containing only 2 at% or less of Co,Ni and Cr (Figure 9.26(c)).

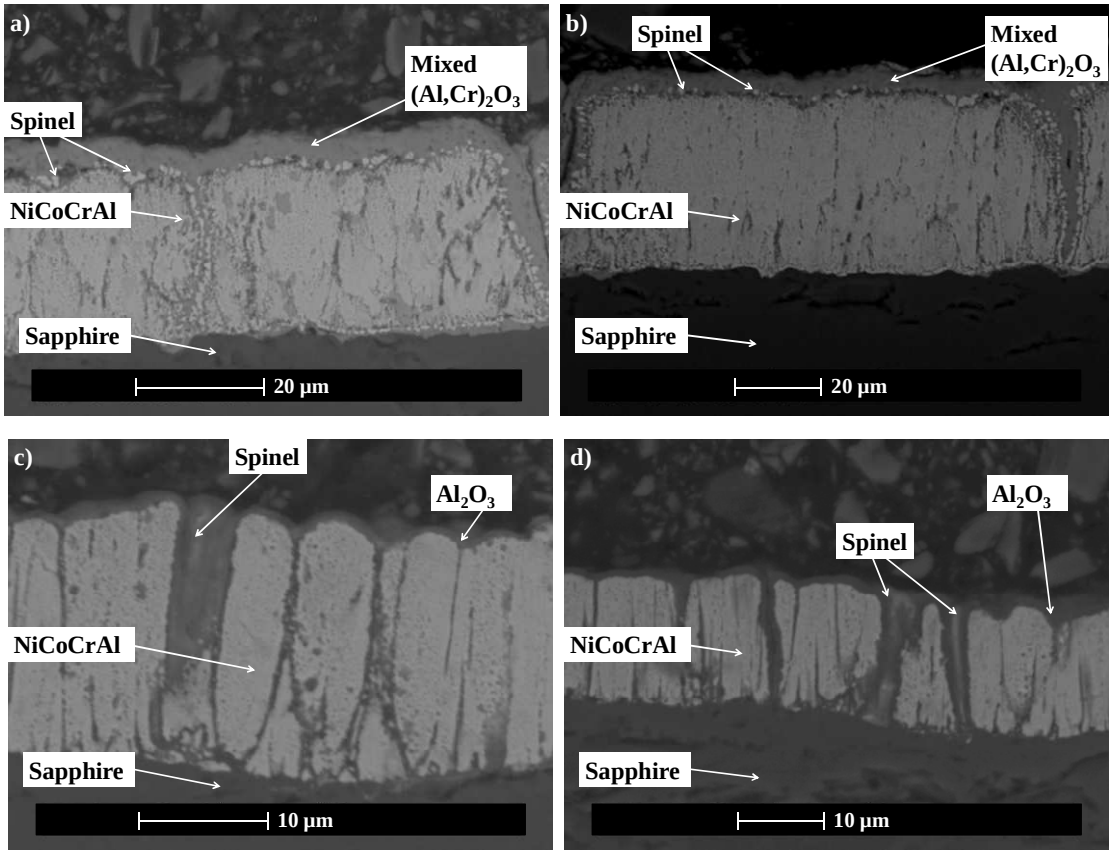

Figure 9.25 Cross sections SEM images of (a) 130910d2, (b) 130910E1, (c) 130910e3 and (d) 130910F3.

The results of EDX analyses carried out on the oxides of the selected samples are summarised in Table 9.6. Oxides growing at the surface of the Ni-20wt%Co-40wt%Cr+Al batch samples always contained very small amounts of Co (> 2 at%) and Ni (> 4 at%) and as the Cr/Al atomic ratio decreased, the amount of Al present in the oxide increased, making the Al_2O_3 layer purer. The two layers of oxide growing on samples from the Ni-40wt%Co-20wt%Cr+Al batch contained a significant amount of Al which increased with the increasing initial fraction of Al in the coating. Ultimately, when reaching an initial fraction of Al of ~33.5 at%, the oxide layer becomes almost

pure Al_2O_3. Also, at equal initial fractions of Co and Ni, upon exposure, the outer oxide layer formed was always richer in Ni.

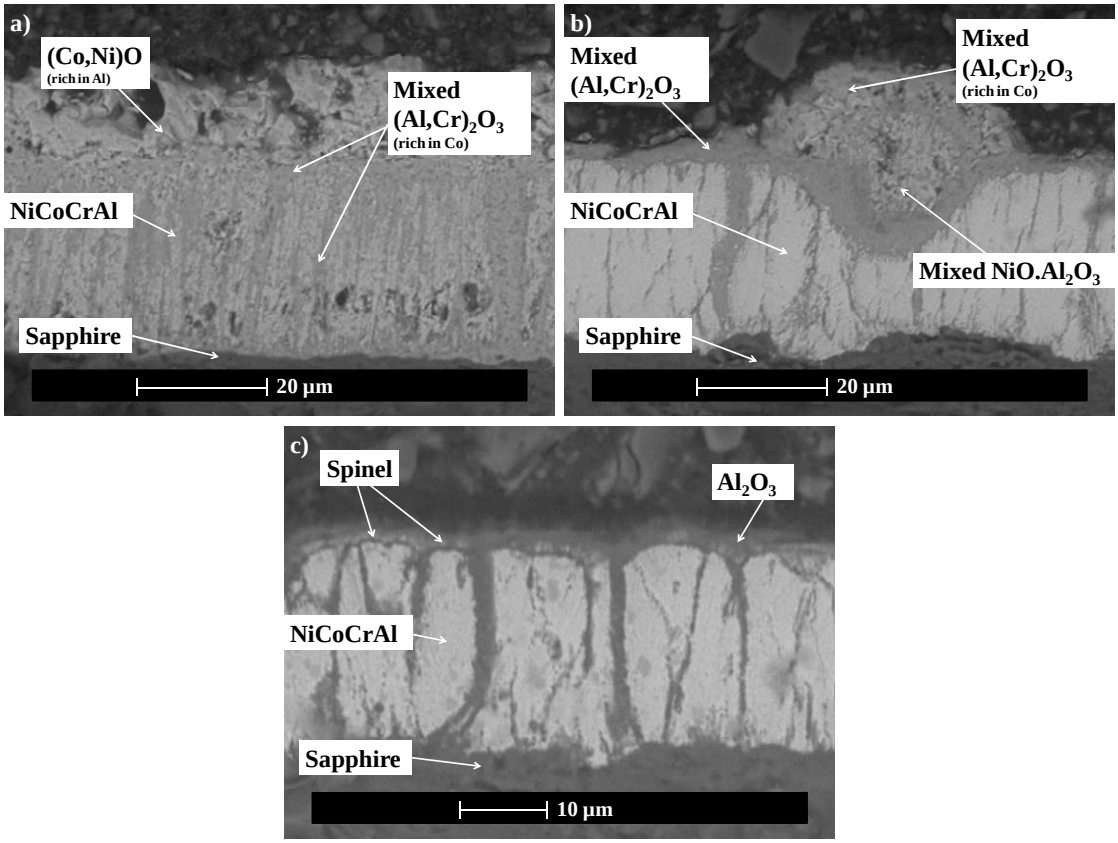

Figure 9.26 BSE SEM images of cross-sections through (a) and (b) 160810E2, and (c) 160810e2.

Sample		Oxide	O (at%)	Co (at%)	Ni (at%)	Cr (at%)	Al (at%)
130910	d2	single layer	60.9	0.6	1.2	19.2	18.1
130910	E1	single layer	55.8	1.9	3.9	20.1	18.3
130910	e3	single layer	53.3	1.4	4.0	10.0	31.3
130910	F3	single layer	55.8	1.0	1.9	4.6	36.9
160810	D3	outer layer	54.1	11.6	17.8	1.6	14.9
		inner layer	58.6	10.7	3.8	13.8	13.2
160810	E2	outer layer	53.6	10.6	12.0	1.5	22.3
		inner layer	58.7	2.6	2.4	15.5	20.9
160810	e2	single layer	59.9	1.6	1.6	1.9	34.9

Table 9.6 Composition (obtained by EDX analysis) of the oxide layers observed on the cross-sections through selected Co-Ni-Cr-Al samples at 900°C.

9.2.4 Discussion-An attempt to map the oxide composition as a function of the Ni-Co-Cr-Al content at 900 °C.

The results concerning the analysis of the Co-Ni-Cr-Al samples exposed at 900 °C are summarised in Figure 9.27. The domain under the red dotted line on the graph represents the Co-Ni-Cr-Al compositions capable of forming α-Al_2O_3 after 500 hours when exposed at 900 °C. The black dotted line delimits the sample capable of forming transient forms of Al_2O_3. Samples needed a ratio of Cr/Al (in at%) under 5 with Co/Ni equal to 0.5 to grow a pure α-Al_2O_3 layer at 950 °C. Without Co present this Cr/Al ratio did not change much and was still around 5. The growth of transient Al_2O_3 as 900°C seems to be promoted by the addition of Co, increasing the Cr/Al ratio up to around 7.

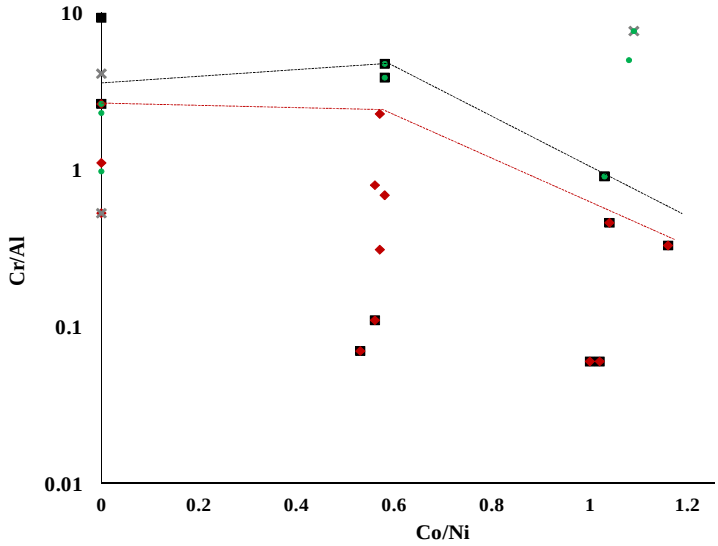

Figure 9.27 Effect of Cr/Al and Co/Ni ratios (at%) on oxide compositions observed after 500 hours at 900 °C. Red diamonds correspond to α-Al_2O_3, black squares to transient Al_2O_3, green dots to Cr_2O_3 and grey crosses to Ni or Co oxides. Beneath black dotted line are samples capable of forming transient Al_2O_3. Beneath red dotted line are samples capable of forming α-Al_2O_3.

However this tendency reverses with further increases of the initial Co concentration. More Co also increased the amount of Al needed to grow α-Al_2O_3. Not appearing in the graph, mixed oxides and spinels were observed in a lot of samples

(more details in Figure 9.28 (b)). Adding Co to the Ni-Cr-Al increased the likelihood for the formation of mixed oxides (see Figure 9.28(b)).

9.3 Discussion - Effect of Co-Ni-Cr-Al compositions and temperature on the coating behaviour

9.3.1 The effect of temperature on the Co-Ni-Cr-Al system

Comparison of Tables 9.2 and 9.5, summarising the peaks identified using the XRD, shows that the nature of the oxides changed with exposure temperature.

The coatings from the Ni-20wt%Co-40wt%Cr+Al batch grew more (Co,Ni)O oxides when exposed at 950 °C than at 900 °C. For example, sample 130910d3 (18.3 at% Co, 41.6 at% Cr, and 8.8 at% Al) grew an external layer of mixed $(Al,Cr)_2O_3$ containing less Co (5 at% less) than the similar 130910d2 that was oxidised at 900 °C (Tables 9.3 and 9.6). Similarly, samples from the Ni-40wt%Co-20wt%Cr+Al which were more likely to grow NiO and/or CoO, did not form as much of these fast growing oxides when oxidised at lower temperatures. Indeed at 900 °C, samples initially containing below 30 at% Co, did not grow CoO oxides while they were detected on samples initially containing as little as 8 at% Co at 950 °C. More Cr_2O_3 oxides were observed on samples oxidised at 900 °C. They grew on samples from the Ni-40wt%Co-20wt%Cr+Al with an initial Cr content above 18 at%, unlike at 950 °C.

Changing the exposure temperature did not affect the formation of α-Al_2O_3 (Tables 9.2 and 9.5). The first traces of the stable oxide where observed on samples 130910e2 and 130910e3 (38.1 at% Cr, 16.7 at% Al) for the Ni-20wt%Co-40wt%Cr+Al batch, and on samples 160810e3 and 160810e2 (15.41 at% Cr, 33.5 at% Al) for the Ni-40wt%Co-20wt%Cr+Al batch. However, at the lower temperature, transient Al_2O_3 were

detected earlier on samples containing less initial Al and Cr (e.g. 160810E2 with 18.22 at% Cr and 20.1 at% Al).

Finally, a lot more spinels were detected at 900 °C than at 950 °C (Tables 9.2 and 9.5). This phenomenon is more pronounced in samples from the Ni-40wt%Co-20wt%Cr+Al coating batch. The coatings only formed $NiCr_2O_4$ and $(Ni,Co)Cr_2O_4$ on the samples containing the most initial Co at 950 °C (160810d2 (36.6 at% Co) and 160810E4 (31.3 at% Co)) while at 900 °C, spinels grew on most of the samples. Also the nature of the spinels varied depending on the initial amounts of Al and Cr. Gradually, more initial Al led to the formation of $NiAl_2O_4$, and more Cr to $NiCr_2O_4$. This is discussed further in Chapter X.

An alternative method of comparing the oxidation data obtained from the sputtered coatings is presented in Figure 9.28. Instead of plotting the Cr/Al ratio over the Co/Ni ratio as in Figures 9.14 and 9.27, data was organised in a ternary diagram similar to the ones used for the study of the Ni-Cr-Al system. To simplify the quaternary system into a ternary one, the atomic Co and Ni contents were added together. Also, the experimental data were compared to commercial Co-Ni-Cr-Al-(Y) compositions found in literature and summarised in Table 9.7 [60,150,151]. The ternary diagrams show that decreasing the oxidation temperature increased the Al_2O_3 formers domain for coatings containing less Cr in their initial composition. It could be assumed that the domain is also larger for coatings containing around 50 at% Cr, but more data is needed to confirm this assumption.

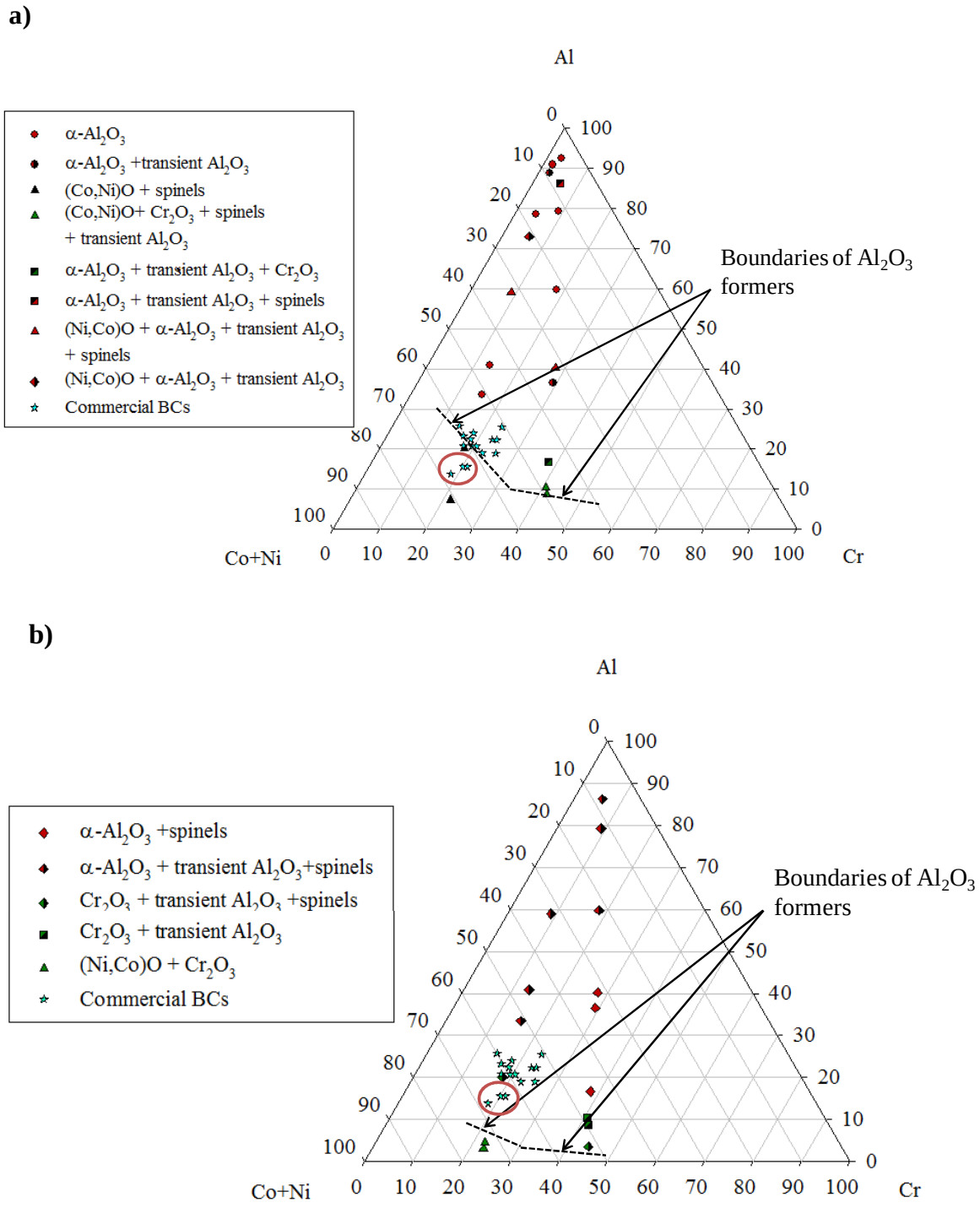

Figure 9.28 Compositional effects on the oxidation gathered at (a) 950 °C and (b) 900 °C on the coated sapphire discs. Black doted lines represent the Al_2O_3 formers boundaries and the circles highlight commercial coatings out of Al_2O_3 formers domain at 950 °C.

At 950 °C, commercial Co-Ni-Cr-Al-Y caotings that are expected to grow Al_2O_3 upon exposure, did not coincide with the results found with the coated sapphire discs exposed at 950 °C (circled in red on Figure 9.28(a)). Indeed, three compositions corresponding to AMDRY 995/LC022, LN21 and LC029 are out of the Al_2O_3 formers domain at 950 °C. This could indicate that those coatings are not ideal for exposure at 950°C or that they behave differently when used as BCs instead of overlay coatings. Covered by a YSZ TC, these coatings might grow protective oxides because of the reduced oxygen partial pressure. This could also indicate that the real BC surface temperature are lower than 950 °C, as at 900 °C, the compositions are well within the Al_2O_3 domain.

	Co(at%)	Ni (at%)	Cr (at%)	Al (at%)	Reference
AMDRY 995	34.7	28.6	21.2	15.5	-
LN11	20.0	40.3	16.4	23.3	[150]
LN21	21.3	42.9	20.2	15.6	[150]
LN33	0.0	59.7	19.5	20.7	[150]
LN46	13.7	45.5	18.4	22.4	[150]
LN49	12.7	45.1	18.2	24.0	[150]
LC07	54.5	0.0	23.2	22.3	[150]
LC022	34.7	28.6	21.2	15.5	[150,151]
LC022Al	33.6	25.1	20.5	20.7	[150]
LC029	67.7	0.0	18.4	13.8	[150]
LC040	55.5	0.0	25.6	18.9	[150]
LC049	24.4	35.5	14.3	25.7	[150]
TM309	21.7	36.7	22.7	19.0	[150]
Talboom et al.	50.9	0.0	23.6	25.5	[60]
ATD2B	53.6	0.0	24.1	22.3	[151]
ATD5B	61.5	0.0	17.7	20.8	[151]
ATD10	0.0	59.7	19.5	20.7	[151]

Table 9.7 Commercial overlay coatings used as commercial reference in ternary diagrams in Figure [60,150,151]. Y (at%) is not taken into account.

9.4 Summary

As for the Ni-Cr-Al system, magnetron sputtering has been used successfully to deposit a range of Co-Ni-Cr-Al coatings onto 10 mm diameter sapphire substrates. This was achieved through co-sputtering from two targets: a Ni-20wt%Co-40wt%Cr or Ni-40wt%Co-20wt%Cr target (changed between deposition runs) and a pure Al target. XRD was used to identify the oxides formed during oxidation exposure at 900 or 950 °C for 500 hours. High levels of Co in the coatings promoted the formation of (Co,Ni)O oxides at both temperatures. At 950 °C, the first traces of Al were observed on samples containing 33.5 at% Al (at low Cr concentration, 15.4 at%) and 9 at% Al (at high Cr concentration, 41.6 at%). At 900 °C, the first traces of Al were observed on samples containing 33.5 at% Al (at low Cr concentration, 15.4 at%) and 20 at% Al (at high Cr concentration, 18 at%). Lowering the oxidation temperature increase the size of the Al_2O_3 formers domain (larger composition range for Al_2O_3 formers) and prevented the formation of (Co,Ni)O oxides (with high concentrations of Cr). Adding Co to the Ni-Cr-Al systems promoted the formation of diverse spinel phases the compositions of which depended on the initial compositions of the coatings.

CHAPTER X – GENERAL DISCUSSION (PART II)

10.1 How does composition and temperature affect spinel/mixed oxide formation?

Looking at Figures 9.14 and 9.27 (from sections 9.1.4 and 9.2.4), adding Co to the Ni-Cr-Al gradually required more initial Al concentration (at lower Cr contents) to enable the exposed coating to grow a protective Al_2O_3 layer. While the system was not affected by up to 20 at% Co, increasing the amount up to 40 at% led to a diminution of the Al_2O_3 formers domain area. This is confirmed by the ternary diagrams in Figure 9.28 (section 9.3) which shows that as the Ni+Co content increases, the amount of Al needed to grow Al_2O_3 is higher (the effect of Co and Ni are separated by comparing Figure 9.28 to Figure 8.44). Thermodynamic studies of the effect of Co in MCrAlY, carried out by several groups of researchers (such as Ma and Schoenung [152] and Liang et al. [153]), led to the conclusion that increasing the amount of Co in the Co-Ni-Cr-Al system reduced the formation of γ'-Ni_3Al phase and increased the fraction of β-NiAl and γ-Ni. As a consequence, Co additions increased the oxidation resistance of the different alloys studied. These conclusions contradict the result found in this chapter and could be explained by the fact that it is not possible, using the data generated in this thesis, to separate the effect of the increase of the Co fraction and the decrease of the Cr fraction. Indeed in Chapter VIII, it was found that increasing the amount of Cr in the coating, was reducing the amount of Al needed to grow Al_2O_3. Reciprocally, by decreasing the amount of Cr, a higher amount of Al should be required to grow the protective oxide layer.

In order to investigate the effect of Co additions on the growth of the oxide, samples with similar Cr and Al initial contents from the Ni-Cr-Al and Co-Ni-Cr-Al batches were compared. The samples chosen are summarised in Table 10.1.

Temperature (°C)	Sample		Co (at%)	Ni (at%)	Cr (at%)	Al (at%)	Oxides formed (XRD)
950	080710	B2	0.0	77.4	22.1	0.5	NiO, Cr_2O_3, $NiCr_2O_4$
	080710	D3	0.0	77.2	20.2	2.6	NiO, Cr_2O_3
	160810	d2	36.6	34.4	21.6	7.4	NiO, (Co,Ni)O, $NiCr_2O_4$
	080710	F2	0.0	63.9	14.6	21.5	α-Al_2O_3, θ- Al_2O_3
	160810	e3	26.1	25.1	15.4	33.5	α- Al_2O_3
	080710	h2	0.0	14.0	2.5	83.5	α- Al_2O_3
	160810	H1	4.5	4.4	2.4	88.8	α- Al_2O_3, θ- Al_2O_3
900	080710	c2	0.0	77.2	20.9	1.9	NiO, Cr_2O_3, $NiCr_2O_4$
	080710	d3	0.0	77.0	18.5	4.5	NiO, Cr_2O_3, $NiCr_2O_4$
	160810	c2	38.7	35.4	22.9	3.0	NiO, (Co,Ni)O, Co_2O_3, Cr_2O_3
	160810	D3	38.0	35.1	22.4	4.5	NiO, (Co,Ni)O, Cr_2O_3
	080710	F3	0.0	63.9	14.6	21.5	α- Al_2O_3, θ- Al_2O_3
	160810	e2	26.1	25.1	15.4	33.5	α- Al_2O_3, δ,θ- Al_2O_3, $NiCr_2O_4$
	290610	g3	0.0	6.8	9.0	84.2	α- Al_2O_3, θ- Al_2O_3, Al_2O_3.NiO
	130910	g1	4.2	7.5	9.0	79.3	α-Al_2O_3, θ- Al_2O_3, $NiAl_2O_4$

Table 10.1 Chosen samples for comparisons between the Ni-Cr-Al and Co-Ni-Cr-Al systems, their compositions and oxide formed.

At 950 °C, the comparison of sample with a high Co and/or Ni content, medium Cr content and low Al content (samples 080710B2 (22.1 at% Cr, 0.5 at% Al), 080710D3 (20.2 at% Cr, 2.6 at% Al) and 160810d2 (21.6 at% Cr, 7.4 at5 Al)) showed that XRD could not detect Cr_2O_3 in the sample containing Co (Tables 8.3 and 9.2 from sections 8.1.3 and 9.1.3). However, SEM cross-sections confirmed the presence of a mixed $(Cr,Al)_2O_3$ layer beneath the (Co,Ni)O outer layer (Figures 8.17(b) and 9.13(a) in section 8.1.3 and 9.1.3). In the three cases, the Cr content of the mixed layer was around

15 at% (Tables 8.4 and 9.3 from sections 8.1.3 and 9.1.3) suggesting that the effect of Co addition here is to grow a thicker outer oxide layer. A comparison of the images of the outer oxide layers in both systems revealed that addition of Co create a more porous and discontinuous outer oxidelayer (Figures 8.17 (b) and 9.13 (a)).

At 950 °C, samples with medium initial contents of Cr and Al (080710F2 (14.6 at% Cr, 21.5 at% Al) and 160810 e3 (15.4 at% Cr, 33.5 at% Al)) both grew Al_2O_3 (Figure 8.12 and Table 9.2). In the sample with no Co (080710F2), XRD detected the presence of transient Al_2O_3. More Al was needed to grow the Al_2O_3 on the coating containing Co and microstructure of the oxide layer observed under the SEM revealed that the layer contained Cr, unlike the layer grown on the Ni-Cr-Al coating (Tables 8.4 and 9.3). Also, the sample containing Co failed early, after only 260 hours of exposure (Figure 9.4 in section 9.1.2), suggesting weaker oxide adhesion properties.

At 950 °C, samples containing high levels of Al (080710h2 (2.5 at% Cr, 83.5 at% Al) and 160810H1 (2.4 at% Cr, 88.8 at% Al) grew similar α-Al_2O_3 layers. Transient θ-Al_2O_3 was detected on the surface of the Co-Ni-Cr-Al coating (Table 8.3 and 9.2).

At 900 °C, medium Cr contents and low Al content (080710 c2 (20.9 at% Cr, 1.9 at% Al), 080710d3 (18.5 at% Cr, 4.5 at% Al) and 160810 d2 (22.9 at% Cr, 3.0 at% Al) led to the growth of a double layered oxide on both Ni-Cr-Al and Co-Ni-Cr-Al coatings (Tables 8.8 and 9.5 and Figure 8.39(a) in sections 8.2.3 and 9.2.3). XRD detected Cr_2O_3 on each samples suggesting that the outer layers have similar thicknesses, and EDX quantified the content of Cr in the mixed $(Al,Cr)_2O_3$ layer to be around 18 at% in the case of 080710d3 and 14 at% in the case of 160810d2 (Tables 8.9

and 9.6 in sections 8.2.3 and 9.2.3). The external non-protective oxide layer was continuous in both cases.

At 900 °C, for samples with an higher level of Al (080710F3 and 160810e2), the oxide layers present in both cases were mixes of transient and stable Al_2O_3 coupled with some $NiCr_2O_4$ spinels (as detected by the XRD and confirmed by SEM). Both layers were very similar (Figures 8.39(d) and 9.26(b) in section 9.2.3). As for the samples containing very high amounts of Al exposed at 900 °C (290610g3 and 130910g1), XRD detected similar Al_2O_3 oxides layers and $NiAl_2O_4$ on both the Ni-Cr-Al and Co-Ni-Cr-Al sample (Tables 8.9 and 9.5).

In a general manner, comparing the Al_2O_3 domains (in ternary phase diagrams) drawn from the data obtain from the sputtered coatings (Figure 10.1), adding Co to the Ni-Cr-Al system promoted the formation of protective Al_2O_3. Indeed, for higher Cr concentrations, at 900 and 950 °C, the amount of Al needed to grow Al_2O_3 was reduced by adding Co to the coatings.

In Chapter VIII, the oxidation of the Ni-Cr-Al coating systems showed that the spinels/mixed oxides grown (and identified using XRD) were essentially $NiCr_2O_4$ (Tables 8.3 and 8.8). Lowering the oxidation temperature promoted their formation, as did increasing the initial amount of Cr in the coating (Figures 8.22 and 8.43). The Ni-Cr-Al coatings with enough Al to start growing Al_2O_3, formed a mixed $(Al,Cr)_2O_3$ layer instead of pure Al_2O_3 (at Cr levels of 6.7, 14.6 and 56 at% at 950 °C and 8.2, 14.6 and 56 at% at 900 °C). The initial Cr/Al ratio needed to achieve a pure protective Al_2O_3 layer needed to be below 1, meaning that the initial amount of Al had to be quite high (Figures 8.19 and 8.41).

In Chapter IX, after the oxidation of the Co-Ni-Cr-Al, a more diverse selection of spinel/mixed oxides was detected. Depending on the initial amount of Co, Cr and Al, the spinels could be $CoCr_2O_4$, $NiCr_2O_4$ or $NiAl_2O_4$ (Tables 9.2 and 9.5). Also, the formation of an outer (Ni,Co)O layer prevented the formation of spinels at 900 °C. In the absence of this outer layer, adding Co to the Ni-Cr-Al system inhibited the formation of a mixed $(Al,Cr)_2O_3$ layer. Indeed, the Al_2O_3 formed always contained around or less than 2 at% Cr (Tables 9.3 and 9.6).

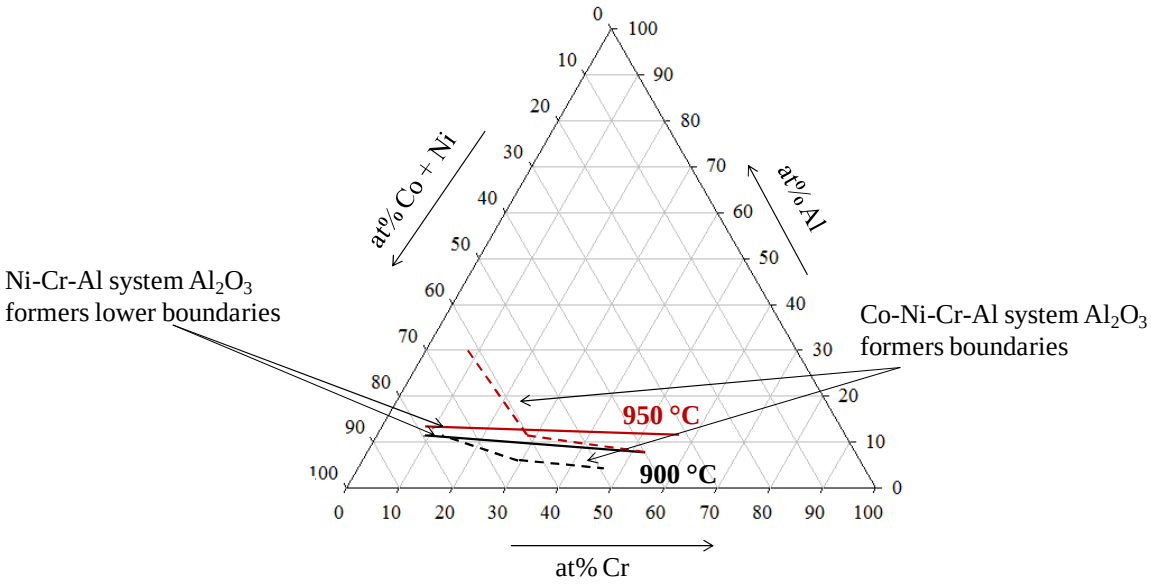

Figure 10.1 Comparison of the Al_2O_3 forming domains at 900 (black) and 950 °C (red) for the Ni-Cr-Al (plain lines) and the Co-Ni-Cr-Al systems (dotted lines).

The temperature shift of the Al_2O_3 former boundaries on the Ni-Cr-Al and Co-Ni-Cr-Al ternary diagrams are significant in terms of the compositions chosen for commercial MCrAlYs and also for BC temperatures used in industrial gas turbines. Relating to the study of the modified aerofoil-shaped samples exposed at 900 to 1000 °C in Part I, this could explain the formation of NiO and $(Al,Cr)_2O_3$ clusters instead of

the expected protective Al_2O_3. For Ni-Cr-Al and Co-Ni-Cr-Al systems, as oxidation goes on and the Al depletes from the coating, the local fraction of Cr increases and promotes the localised growth of mixed oxides.

In the literature, various types of commercial overlay and bond coatings have been exposed at temperatures above 1000 °C [36,48,50,51,77-81]. The results concerning spinels and mixed oxides that were reported, whether they were obtained from EXD, XRD analysis or SEM imaging, were more or less precise. However, they showed that Ni-Cr-Al-Y coatings promoted the formation of a double layer of mixed $(Al,Cr)_2O_3$ over α-Al_2O_3 with small amounts of NiO and $NiAl_2O_4$ [51,80]. Observation of oxidised Ni-Co-Cr-Al-Y highlighted the presence (or not) of a mixed $(Al,Cr)_2O_3$ layer above a protective α-Al_2O_3 as well, but no spinels were mentioned [77,79]. More research carried out on Co-Ni-Cr-Al-Y coatings at 1000 °C and above, and describes the TGO as a mix of α-Al_2O_3, and clusters of mixed $(Al,Cr)_2O_3$, spinels and (Ni,Co)O [77,78]. Different types of spinels were detected and reported as $(Co,Ni)(Al,Cr)_2O_4$ [36], and the mixed oxides/spinels seemed to form more easily as clusters rather than continuous layers [36,48,77,78,81]. It was also found that depositing YSZ on top of the overlay coatings promoted the formation of spinels and mixed/oxides [51,81]. Thickness measurements of the TGOs grown on different types of BCs did not show which was more inclined to form more spinels/mixed oxides [50]. The results found in literature showed that above 1000 °C, adding Co to the Ni-Cr-Al system promoted the formation of spinels and correlate with the behaviour observed on the coatings deposited on the sapphire discs using magnetron sputtering and exposed at lower temperature in this study.

The amount of spinels/mixed oxides, growing on modified aerofoil shaped samples used in Part I (Figure 5.44) after exposure at 900 to 1000 °C, was measured in 9 different locations on 26 samples. The fraction of spinels/mixed oxides in the TGO decreased from ~21 to ~16% as the temperature increased. This would help confirm the effect of temperature on the formation of spinels found with the coated sapphire discs, but the scatter in the measured data (error of +/- 5%) were too important to take this result into account.

10.2 What would be the best coating?

The coatings compositions growing the slowest oxides (minimum mass gain after 500 hours) and without NiO and/or CoO oxides are summarised in Table 10.2 for 950 °C, and Table 10.3for 900 °C. From an oxidation point of view, these coatings are considered to have the most suitable compositions for a use in industrial gas turbines.

In order to eliminate more candidates, mechanical, thermal stability (interdiffusion) and corrosion properties must be taken into account as well as oxidation properties. High levels of Al are expected to produce a high volume fraction of β-NiAl which is a desirable phase to form a protective oxide but could also be detrimental by making the coating too brittle. At high operating temperatures, high brittleness is avoided due to the brittle to ductile transition, but in gas turbines, the coatings have to survive thermal cycling (start up and shut downs) which would expose them to lower temperatures. Moreover, at high temperatures, Co-Ni-Cr-Al coatings containing contents of Al that are too high will melt (Figure 8.44) [151]. Achar et al. [154], modelled the phase equilibria in different MCrAlY alloys at 950, 1000 and 1050 °C.

Their work proved that the phase constitution of these alloys changed with temperature, which could partly explain why in Part II of this thesis, the oxides formed differed somewhat with temperature. From their study of Ni-Cr-Al alloys [154] it can be deduced that 170510F2 microstructure would be of a mix of β-NiAl + γ'-Ni_3Al phases, 170510f3 and 080710G2 would be made of β-NiAl phase and 080710f2 of α-Cr + β-NiAl + γ'-Ni_3Al (Table 10.2). It is not possible to determine the phases present in 290610F2 and 290610f3 from their work, but it can be estimated that they would contain α-Cr and β-NiAl.

Along with Ma and Schoenung [152] and Liang et al. [153], Achar et al. [154] found that Co additions stabilised the γ and β phases, explaining why lower levels of Al are needed to grow Al_2O_3. They also added that levels of Co around 10 at% promoted the formation of α-Cr [154]. Mechanical testing of Ni-Cr-Al-Y and Co-Ni-Cr-Al-Y alloys proved that the former crept faster at low stress than the latter, but that the tendency reversed in the case of high stresses [155], showing that either type of BC could be desirable from a mechanical point of view.

Sample	Co (at%)	Ni (at%)	Cr (at%)	Al (at%)	Spinels	Weight gain (mg/cm^2)
170510F2	0.0	61.6	6.7	31.7		0.31
170510f3	0.0	49.5	4.7	45.8		0.22
080710f2	0.0	52.5	11.5	36.0		0.05
080710G2	0.0	41.2	8.4	50.4		0.07
290610F2	0.0	22.5	44.9	32.6		0.11
290610f3	0.0	15.8	22.5	61.6	+	0.15
130910G2	7.9	14.0	18.3	59.8	+	0.13

Table 10.2 Coating compositions forming Al_2O_3, with the lower final mass gain after 500 hours at 950 °C.

Sample	Co (at%)	Ni (at%)	Cr (at%)	Al (at%)	Spinels	Weight gain (mg/cm^2)
170510f2	0.0	49.5	4.7	45.8		0.23
080710e2	0.0	69.1	16.3	14.6		0.16
080710F3	0.0	63.9	14.6	21.5		0.17
080710f3	0.0	52.5	11.5	36		0.14
290610e3	0.0	29.7	41.6	29.1		0.12
290610F3	0.0	22.5	44.9	32.6	+	0.13
160810E3	31.2	30.3	18.2	20.1	+	0.33
160810f3	16.5	15.8	8.9	59.0	+	0.23
130910e3	16.4	28.8	38.1	16.7	+	0.13
130910F3	12.3	21.9	29.2	36.6	+	0.13

Table 10.3 Coating compositions forming Al_2O_3, with the lower final mass gain after 500 hours at 900 °C.

Adding in this information, at 950 °C, the best BC compositions for industrial gas turbine use are, in terms of high temperature protection properties, Ni-11.5Cr-36Al and Ni-6.7Cr-31.7Al (in at%).

At 900 °C, higher levels of Cr are preferable because such low temperature could induced corrosion attacks (in the presence of deposits and corrosive gas) as well as oxidation one. Contents of Co above 10 at% are also needed in order to stabilize the β-NiAl phase. This is why, the best BC composition, in order of oxidation protection efficiency is, Ni-12.3Co-29.2Cr-36.6Al (at%).

10.3 Conclusion (part II)

In Part II, the oxidation of a range of MCrAl compositions at 900 and 950 °C confirmed the effect of temperature on the high temperature protection of these coatings and the potential to use alternative alloys in industrial gas turbines where the exposure temperatures are lower than those for which commercial BCs are designed. The new BC, needs to contain more Cr and Al than the ones exposed at 1000 °C or over.

On an (Ni+Co)-Cr-Al ternary diagram, commercial BC are located near to the boundaries (at 900 °C) or out of the Al_2O_3 former domain (at 950 °C) meaning that they would be susceptible to forming species less protective than the desired Al_2O_3 during exposure (mixed $(Cr,Al)_2O_3$ or spinels).

Magnetron co-sputtering was found to be an efficient method to deposit a large quantity of small samples with different compositions. However, it was not a good technique for the deposition of Ni alone, because of the paramagnetic nature of this metal. Films containing contents of Cr higher than 40wt% were also less adhesive. Targets of any chosen composition can be used in magnetron sputtering, making this technique very flexible to coat small parts. It is limited by the deposition rate of the coatings, which is quite slow (20 hours to deposit ~20 µm) and by the size of the substrate (dependant on the size of the deposition chamber).

CHAPTER XI – CONCLUSIONS

TBCs are a key part of the high temperature protection of industrial gas turbines parts. Although they are extensively used in industry, many challenges still remain in understanding their failure mechanisms and in developing better performing materials.

This PhD project was divided in two parts. Firstly, the effect of the bulk geometry of the components on the microstructural evolution of APS/TBC systems and their failure was studied. Secondly, new BC compositions, which could be used as coatings for high temperature protection of industrial gas turbines, were manufactured and investigated.

In part I, 40 modified aerofoil-shaped samples were exposed in air at 900, 925, 950, 975 and 1000 °C for up to 20,000, 15,000, 5000, 3000, and 1500 hours respectively. Pulsed (flash) thermography has been successfully used to detect cracked and delaminated areas below APS/TBCs on modified aerofoil shaped samples. Multiple samples cracked at the leading edge and on a convex feature on the “pressure side”, suggesting an impact of geometry on coating failure. SEM and EDX characterisation enabled to gather data at 9 different locations of varying curvature around the sample on the different layers of the TBC system. Concave geometries around the sample promoted the formation of less protective oxides; spinels and mixed oxides. BC roughness and TGO undulations were found to cause the growth of those less-protective oxides. The overall sample curvature also affected the quality of manufacturing explaining the higher thicknesses and higher roughnesses on concave features. In the case of extremely convex geometry, TBC deposition layers did not follow the substrate curvature resulting in uneven coatings which could ease crack formation and

propagation. Thinner BCs at convex locations were able to grow Al_2O_3 at the same rate as thicker BCs by using the Al from the γ'-Ni_3Al instead of the β-NiAl phase. They were however found to be more sensitive to mechanically induced failure which made convex locations more likely to crack first. Additionally, the investigation of the TC/TGO interface highlighted the significant effect of the splat layout on the residual stress state at the interface and therefore the initiation and propagation of cracks.

The oxidation of samples at 900 to 1000 °C for up to 20,000 hours, enabled the collection of an important amount of data, which in turn, allowed the optimisation of an existing oxidation prediction model. It highlighted the dependence of the transition to stable Al_2O_3 growth on temperature and the importance of this in the model.

Premature failure of the APS/TBC at the leading and trailing edge of a blade, which are locations subject to higher temperatures and stresses in the gas turbine, could be reduced by monitoring the manufacture of the coating more effectively. Roughness of the TC/BC interface is compulsory for the adhesion properties of the APS/TBC so cannot be avoided. However, the difference of TC and BC thicknesses around the blades should be reduced to prevent preferential cracking at the thinner locations.

In part II of this thesis, the PVD technique, magnetron sputtering, has been used successfully to deposit a range of potential Co-Ni-Cr-Al coatings on sapphire substrates. Around 200 samples were created using this technique and half of them were exposed in air at 900 and 950 °C for up the 500 hours. The selective growth of protective Cr_2O_3 or Al_2O_3 oxides or other non-protective oxides (depending on the initial coating composition) was observed. The oxidation temperature was found to have great effect on the nature of the oxides formed on the coating surfaces. It increased the domain (on ternary phase diagrams) of NiO formers for coatings containing low levels of Cr while

increasing the Al_2O_3 formers domain for higher initial levels of Cr. Lowering the oxidation temperature from 950 to 900 °C promoted the formation of transient Al_2O_3 and spinels. At the same time, adding Co to the Ni-Cr-Al system allowed coatings to form Al_2O_3 with lower Al levels (at 900 °C) and also encouraged spinels growth.

At 900 °C, the composition with the lowest extent of oxidation and therefore the best oxidation protection properties was (in at%) Ni-12.3Co-29.2Cr-36.6Al. This coating contained less Al and more Cr than the most efficient coatings at 950°C which were Ni-11.5Cr-36Al and Ni-6.7Cr-31.7Al. All these compositions have high levels of Al suggesting that the most oxidation resistant coatings at 950 and 900°C contain high volume fractions of nickel/cobalt aluminides.

Recommendations for further work:

The work presented in this thesis opens many directions for further investigations:

- The deposition and oxidation of APS/TBC systems with equal thicknesses all around aerofoil-like samples will verify whether the preferential cracking on convex locations is caused by geometry or by the thickness of the coating.
- Further investigations of the transient stage of oxidation at 900-950 °C using FIB and TEM techniques would generate detailed information about the growth mechanisms of γ- and θ-Al_2O_3 and spinel/mixed oxides, as well as their chemical interaction with the YSZ TC and the resulting creation of the Al_2O_3-ZrO_2. More studies are needed to understand the effect of the Al_2O_3-ZrO_2 mixed zone on the integrity of the TBC coating systems at lower temperatures.

- Nano-indentation should be used to evaluate the mechanical properties of the TC/BC interface and verify the effect of the TC splat size/shape on the toughness of the TC material. Also, the elastic moduli of YSZ reported in literature are not representative of the TC material due to the defects present in the TC ceramic.
- New BC compositions should be deposited onto a metallic substrate to study the effect of interdiffusion on the nature of the oxide(s) grown on the overlay coating during exposure. A variety of CoCr targets should be used in magnetron co-sputtering to investigate further the effect of Co on the oxidation protection properties of CoNiCrAl systems. They should then be coated with an APS/TBC in order to verify their efficiency under conditions closer to the ones encountered in practise.

REFERENCES

[1] Nalin L., *Degradation of environmental protection coatings for gas turbine materials* (2008 MPhil Thesis), Cranfield University, Bedfordshire, UK.

[2] Enerdata, electricity domestic consumption data by region in 2010, http://yearbook.enerdata.net/world-electricity-production-map-graph-and-data-in-2010.html#/electricity-domestic-consumption-data-by-region-in-2010.html.

[3] International Energy Agency, Key World Energy Statistics 2010.

[4] Commission of the European Communities (2007), Communication from the commission to the European council and the European parliament – An energy policy for Europe, Report SEC(2007)12, Brussel.

[5] Keenan R. (2010), "Statistical aspects of the energy economy in 2009", *Eurostat.*

[6] Oakey J.E., Simms N.J., Allen D.H. (2004), "Environmental degradation issues in gas turbines and their relevance to plant life extension – R&D initiatives", *Environmental*
degradation in gas turbine, OMMI 3, Issue 1.

[7] Boyce M.P. (2008), *Gas turbine engineering handbook* (third edition), Gulf professional publishing, Boston.

[8] Simms N.J., Oakey J.E., Stephenson D.J., Smith P.J., Nicholls J.R. (1995),"Erosion-corrosion modelling of gas turbine materials for coal-fired combined cycle power generation", *Wear*, vols. 186-187, pp. 247-255.

[9] Driver D., Hall D.W., Meetham G.W. in Meetham G.W. (ed.) (1981), *The development of gas turbine materials*, Applied Science Publishers Ltd., London, pp.1-30.

[10] Stringer J. (2002), "High temperature corrosion in energy-related systems", *Materials Research*, vol. 7, pp. 1-9.

[11] Eon Course – Introduction to the options for power generation.

[12] Birks N., Meier G.H., Pettit F.S.(2006), *Introduction to the high-temperature oxidation of metals* (Second edition), Cambridge University Press, Cambridge.

[13] Nicholls J.R., Lawson K.J., Rickerby D.S., Morell P. (1997), "Advanced processing of TBC's for reduced thermal conductivity", AGARP REPORT R-823, Aalborg, Denmark.

[14] Taylor R., Brandon J.R., Morell P. (1991), "Microstructure, composition and property relationship of plasma-sprayed thermal barrier coatings", *Surface and Coatings Technology*, vol. 50, pp. 141-149.

[15] Nicholls J.R. (2000), "Design of oxidation-resistant coatings", *Journal of the Minerals, Metals and Materials Society*, vol. 52, pp. 28-35.

[16] Okazaki M. (2001), "High-temperature strength of Ni-base superalloy coatings", *Science and Technology of Advanced Materials*, vol. 2, pp. 357-366.

[17] Donachie M.J. and Donachie S.J. (2002) *Superalloys: a technical guide* (Second edition), ASM international, Ohio.

[18] Betteridge W. (1959), *The nimonic alloys*, Edward Arnold Ltd., London.

[19] White C.H. in Meetham G.W. (ed.) (1981), *The development of gas turbine materials*, Applied Science Publishers Ltd., London, pp.89-120.

[20] Smith W.F (1981) *Structure and properties of engineering alloys*, McGraw-Hill, New York, p. 458.

[21] Evans A.G., Mumm D.R., Hutchinson J.W., Meier G.H., Pettit F.S.(2001), "Mechanisms controlling the durability of thermal barrier coatings", *Progress in Materials Science*, vol. 46, pp. 505-553.

[22] Kingery W.D., Bowen H.K., Ulhmann D.R. (1976), *Introduction to ceramics* (Second edition), Wiley-Interscience, New York. Cited in [6]

[23] Gleeson B. (2005), "Thermal barrier coatings for aeroengine applications", *Journal of Propulsion and Power*, vol. 22, pp. 375-383.

[24] Nicholls J.R, Simms N.J. (2010), "Gas turbine oxidation and corrosion", *Shreir's Corrosion*, vol. 1, pp. 518-540.

[25] Weisenburger A., Rizzi G., Scrivani, Mueller G., Nicholls J.R.(2007), "Pulsed electron beam treatment of MCrAlY bondcoats for EB-PVD TBC systems part 1 of 2: Coating production", *Surface and Coatings Technology*, vol. 202, pp. 704-708.

[26] Smeggil J.G. (1987), "Some comments on the role of yttrium in protective oxide scale adherence", *Materials Science and Engineering*, vol. 87, pp. 261-265. Cited in [6].

[27] Smialek J.L., Jayne D.T., Schaeffer J.C., Murphy W.H. (1994), "Effect of hydrogen
annealing, sulphur segregation and diffusion on the cyclic oxidation of superalloys – a review", *Thin Solid Films*, vol. 253, pp. 285-292. Cited in [6].

[28] Saunders S.R.J., Nicholls J.R. (1989), "Coatings and surface treatments for high temperature oxidation resistance", *Materials Science and Technology*, vol. 5, pp. 780-798.

[29] Christensen R.J., Tolpygo V.K., Clarke D.R. (1996), "The influence of the reactive element yttrium on the stress in alumina scales formed by oxidation", *Acta Materialia*, vol.45, pp. 1761-1766.

[30] Jedlinski J. (2005), "Local and microstructure-related effects affecting the high temperature oxidation of alumina formers: a brief survey", *Materials at High Temperature*, vol.22, pp. 485-495.

[31] Ding Z., Knight R., Smith R.W. (2002), "Effect of bond coat processes and surface characteristics on the failure mechanism of thermal barrier coatings" in Berndt C.C. (ed.), Thermal spray 2001 : New Surface for a New Millennium, ASM international, Ohio, pp.173-177.

[32] *Mom A.J.A. (1981),* "High Temperature Coatings for Gas Turbines, an overview", *NLR report MP 81003U*, Amsterdam.

[33] Prescott R., Graham M.J. (1991) "The formation of aluminum oxide scales on high-temperature alloys", Oxidation of Metals, vol. 38, pp. 233-253.

[34] Wright P.K., Evans A.G. (1999), "Mechanisms governing the performance of thermal barrier coatings", *Current Opinion in solid State and Materials Science*, vol. 4, pp. 255-265.

[35] Evans A.G., Clarke D.R., Levi C.G. (2008), "The influence of oxides on the performance of advanced gas turbines", *Journal of the European Ceramic Society*, vol. 28, pp. 1405-1419.

[36] Chen W.R., Wu X., Marple B.R., Patnaik P.C. (2006), " The growth and influence of thermally grown oxide in a thermal barrier coating", *Surface and Coatings Technology*, vol. 201, pp 1074-1079.

[37] Armijo J.S. The kinetics and mechanism of solid-state spinel formation – A review and critique. *Oxidation of metals* **1**, 171- 198 (1969).

[38] Zhao X., Shapiro I.P., Xiao P (2007), “Spinel formation in thermal barrier systems with a Pt-enriched γ-Ni + γ’-Ni_3Al bond coat”, *Surface and Coatings Technology,* vol. 202, pp. 2905-2916 (2007).

[39] Pieraggi B. (1997), “Fundamental aspects of reactions at the metal/scale interface during scaling”, *Materials Science Forum*, vols. 251-254, pp. 299-312.

[40] Kvernes I.A., Kofstad P. (1972), “The oxidation behaviour of some Ni-Cr-Al alloys at high temperatures”, *Metallurgical Transactions*, vol. 3, pp. 1511-1519.

[41] Gesmundo F. (1997), “Mathematical modeling of alloy oxidation”, *Material Science Forum*, vols. 251-254, pp. 3-18.

[42] Rahmel A., Wood G.C., Kofstad P., Douglas D.L. (1985), “International Workshop on 'Critical issues concerning the mechanisms of high-temperature corrosion'”, *Oxidation of Metals*, vol. 23, pp. 251-338.

[43] Wood G.C. (1970), “High-temperature oxidation of alloys”, *Oxidation of Metals*, vol. 2, pp. 11- 57.

[44] Karuaratne M.S.A, Ogden S.L, Kenny S.D., Thomson R.C. (2009), “ A multicomponent diffusion model for prediction of microstructural evolution in coated Ni based superalloy”, Materials Science and Technology, vol. 25, pp. 287-299.

[45] Taylor M.P (2005), “An oxidation study of an MCrAlY overlay coating”, *Materials at high temperatures*, vol. 22, pp. 433-436.

[46] Li M., Sun X., Zhang Z., Hu W., Hou G., Guan H., Hu Z. (2004), “Element diffusion and interface characteristics between NiCrAlY coating and Ni-based single crystal superalloy”, *Rare Metal Materials and Engineering*, vol. 33, pp. 55-58.

[47] Taylor M.P., Pragnell W.M., Evans H.E. (2004), "Evidence for the formation of Al-rich reservoir phase resulting from the interdiffusion between MCrAlY coating and Ni-based substrate", *Materials Science Forum*, vol. 461-464, pp. 239-246.

[48] Rabiei A., Evans A.G. (2000), "Failure mechanisms associated with the thermally grown oxide in plasma-sprayed thermal barrier coatings", *Acta materialia*, vol. 48, pp. 3963-3976.

[49] Okada M., Hisamatsu T., Kitamura T. (2008), "Temperature estimation and Al content prediction focusing on microstructural change in a thermal barrier coating", *Journal of Thermal Spray Technology*, vol. 18, pp. 90-95.

[50] Wu F., Jordan E.H., Ma X., Gell M. (2008), "Thermally grown oxide growth behaviour and spallation lives of solution precursor plasma spray thermal barrier coatings", *Surface and Coatings Technology*, vol. 202, pp 1628-1635.

[51] Haynes J.A., Rigney E.D. (1996), "Oxidation and degradation of plasma-sprayed thermal barrier coating system", *Surface and Coatings Technology*, vol. 86, pp. 102-108.

[52] Brumm M.W., Grabke H.J. (1992), "The oxidation behaviour of NiAl-I. Phase transformations in the alumina scale during oxidation of NiAl and NiAl-Cr alloys", *Corrosion Science*, vol.33, pp. 1677-1690.

[53] Grabke H.J. (1999), "Oxidation of NiAl and FeAl", *Intermatallics*, vol. 7, pp. 1153-1158.

[54] Jedlinski J. (2009), "Growth mechanism vs matter transport in thermally growing oxides on high temperature materials: a brief survey based on the case study of alumina formers", *Defect and Diffusion Forum*, vols. 289-292, pp. 385-395.

[55] Rybicki G.C. and Smialek J.L. (1989), Effect of the θ-α-Al_2O_3 transformation on the oxidation behaviour of β-NiAl + Zr", *Oxidation of Metals*, vol. 31, pp. 275-304.

[56] Klumpes R., Marée C.H.M., Schramm E., de Wit J.H.W. (1997), "The influence of chromium on the oxidation of β-NiAl at 1000 °C", in H.J Grabke and M. Schütze (ed.), Oxidation of Intermetallics, Wiley-VCH,Weinheim, pp. 99-107.

[57] Niranatlumpong P., Ponton C.B., Evans H.E. (2000), "The failure of protective oxides on plasma-sprayed NiCrAlY overlay coatings", *Oxidation of Metals*, vol. 53, pp. 241-258.

[58] Beck T., Herzog R., Trunova O., Offermann M., Steinbrech R.W., Singheiser L. (2008), "Damage mechanisms and lifetime behavior of plasma sprayed thermal barrier coating systems for gas turbines-Part II: Modeling", *Surface and Coatings Technology*, vol. 202, pp 5901-5908.

[59] Li M.H., Zhang Z.Y., Sun X.F., Li J.G., Yin F.S., Hu W.Y., Guan H.R., Hu Z.Q. (2003), "Oxidation behavior of sputter-deposited NiCrAlY coating", *Surface and Coatings Technology*, vol. 165, pp. 241-247.

[60] F.T Talboom, R.C. Elam, L.W. Wilson, Evaluation of advanced superalloy protection systems, Report CR7813, NASA, Houston, TX (1970).

[61] Grainger S. (1989) *Engineering coatings – design and application*, Abington Publishing, Cambridge, p.79.

[62] Hou P.Y. (2010), "Oxidation of metals and alloys", in T.S.A Richardson (ed.), Shreir's corrosion, vol. 1, 1st ed., Elsevier, Manchester, 2010, pp. 215-224.

[63] Nicholls J.R., Hancock P., Al Yasiri L.H. (1989), "Optimising oxidation resistance of MCrAl coating systems using vapour phase alloy design", *Materials Science and Technology*, vol. 5, pp. 799-805.

[64] P.F. Tortorelli and M.P. Brady (2010), “Design of high temperature alloys”,in T.S.A. Richardson (ed.), Shreir’s Corrosion, vol.1,Elsevier, Manchester, p. 541-557.

[65] Wallwork G.R., Hed A.Z. (1971),” Mapping of oxidation products in ternary Co-Cr-Al system”, *Oxidation of Metals*, vol. 3, pp. 213.

[66] Rhouta B., Hajjaji M., Oquab D., Pieraggi B. (1997), “ Oxydation à haute température de poudres d’alliages MCrAlY (M=Co,Ni) à différentes teneurs en aluminium”, *Materials Science Forum*, vols 251-254, pp. 49-56.

[67] Trunova O., Beck T., Herzog R., Steinbrech R.W., Singheiser L. (2008), “Damage mechanisms and lifetime behavior of plasma sprayed thermal barrier coating systems for gas turbines-Part I: Experiments”, *Surface and Coatings Technology*, vol. 202, pp 5027-5032.

[68] Naumenko D., Shemet V., Singheiser L., Quadakkers W.J. (2009), “ Failure mechanisms of thermal barrier coatings on MCrAlY-type bondcoats associated with the formation of the thermally grown oxide”, Journal of Materials Science, vol. 44, pp. 1687-1703.

[69] Schlichting K.W., Padture N.P., Jordan E.H., Gell M. (2003), “Failure modes in plasma-sprayed thermal barrier coatings”, *Material Science and Engineering*, vol. A342, pp. 120-130.

[70] Shillington E.A.G. and Clarke D.R. (1998), “Spalling failure of a thermal barrier coating associated with aluminum depletion in the bond-coat”, *Acta Materialia*, vol. 47, pp. 1297-1305.

[71] Yi H.C., Smeltzer W.W., Petric A. (1996), “Oxidation of γ’-Ni_3Al and γ’-$Ni_3Al(Si)$ intermetallic compounds at low-oxygen pressures”, *Oxidation of Metals*, vol.45, pp. 281-299.

[72] Renusch D., M., Schütze M. (2008), "The role that bond coat depletion of aluminium has on the lifetime of APS=TBC under oxidizing conditions", *Materials and Corrosion*, vol. 59, pp.547-555.

[73] Evans H.E. and Taylor M.P. (2001), "Diffusion cells and chemical failure of MCrAlY bond coats in thermal-barrier coating systems", *Oxidation of Metals*, vol. 55, pp. 17-34.

[74] Taylor M.P., Pragnell W.M., Evans H.E. (2008), "The influence of bond coat surface roughness on chemical failure and delamination in TBC systems", *Materials and Corrosion, vol* 59, pp. 508-513.

[75] Eschler H., Renusch D. and Schütze M. (2004), "Bond coat oxidation and its significance for life expectancy of thermal barrier coating systems", *Materials Science and Technology*, vol.20, pp. 307-317.

[76] Taylor M.P. and Evans H.E. (2003), "Formation of diffusion cells in LPPS MCrAlY coatings", *Materials at High Temperatures*, vol. 20, pp. 461-465

[77] Brandl W., Grabke H.J., Toma D., Krüger J. (1996), "The oxidation behaviour of sprayed MCrAlY coatings", *Surface and Coatings Technology*, vol. 86-87, pp 41-47.

[78] Chen W.R., Wu X., Marple B.R., Lima R.S., Patnaik P.C. (2008), " Pre-oxidation and TGO growth behaviour of an air-plasma-sprayed thermal barrier coating", *Surface and Coating Technology*, vol. 202, pp. 3787-3796.

[79] Moskal G., Swadźba L., Mendala B., Góral M., Hetmańczyk M. (2009), "Degradation of the TBC system during the static oxidation test", *Journal of Microscopy*, vol. 237, pp. 450-455.

[80] Ajdelsztajn L., Picas J.A., Kim G.E., Bastian F.L., Schoenung J., Provenzano V. (2002), "Oxidation behaviour of HVOF spryed nanocrystalline NiCrAlY powder", *Materials Science and Engineering A*, vol. A338, pp. 33-34.

[81] Ogawa K., Masuda T., Shoji T. (2001), "Kinetics of thermally grown oxide at interface between thermal barrier coatings and MCrAlY bond coatings", in Berndt C.C., Khor K.A. and Lugscheider E.F. (eds.), *Thermal Spray 2001 : New Surfaces for a New Millennium*, ASM international, Ohio, pp. 187-194.

[82] Gil A., Shemet R., Subanovic M., Toscano J., Naumenko D., Singheiser L., Quadakkers W.J. (2006), "Effect of surface condition on the oxidation behaviour of MCrAlY coatings", *Surface and Coatings Technology*, vol. 201, pp 3824-3828.

[83] Che C., Wu G.Q., Qi H.Y., Huang Z., Yang X.G. (2009), "Uneven growth of thermally grown oxide and stress distribution in plasma-sprayed barrier coatings", *Surface and Coatings Technology*, vol. 203, pp. 3088-3091.

[84] Tang F. and Schoenung J. (2004), "Local accumulation of thermally grown oxide in plasma-sprayed thermal barrier coatings with rough top-coat/bond-coat interfaces", *Scripta Materialia*, vol. 52, pp. 905-909.

[85] Gong X.Y and Clarke D.R. (1998), "On the measurement of strain in coatings formed on a wrinkled elastic substrate", *Oxidation of Metals*, vol.50, pp.355-376.

[86] Tolpygo V.K. and Clarke D.R. (1997), " Competition between stress generation and relaxation during oxidation of an Fe-Cr-Al-Y alloy", *Oxidation of Metals*, vol.49, pp.187-212.

[87] Bull S.J. (1997), "Modeling of residual stress in oxide scales", *Oxidation of Metals*, vol. 49, pp. 1-17.

[88] DeMasi-Marcin J.T., Sheffler K.D., Bose S. (1990), "Mechanisms of degradation and failure in plasma-deposited thermal barrier coating", *Journal of Engineering for Gas Turbines and Power*, vol. 112, pp. 521-526.

[89] Bäker M., Rösler J., Heinze G. (2004), "A parametric study of the stress of thermal barrier coatings Part II: cooling stresses", *Acta Materialia*, vol. 53, pp. 469-476.

[90] Singh J.P., B.G. Nair, D.P. Renusch, M.P. Sutaria, M.H Grimsditch (2001), " Damage evolution and stress analysis in Zirconia thermal barrier coatings during cyclic and isothermal oxidation", *Journal of American Ceramic Society*, vol. 84, pp. 2385-2393.

[91] Hsueh C-H., Haynes J.A., Lance M.J., Becher P.F., Ferber M.K, Fuller E.R., Langer S.A., Carter W.C., Cannon W.R. (1999), "Effects of interface roughness on residual stresses in thermal barrier coatings", *Journal of the American Ceramic Society*, vol. 82, pp. 1073-1075.

[92] Miller R.A. and Lowell C.E. (1982), "Failure mechanisms of thermal barrier coatings exposed to elevated temperatures", *Thin Solid Films*, vol. 95, pp. 471-482.

[93] Goswani G., Ray A.K., Sahay S.K. (2003), "Thermal barrier coating system for gas turbine application – A review", *High Temperature Materials and Processes*, vol. 23, pp. 73-92.

[94] Sohn Y.H., Biederman R.R., R.D Sisson Jr. (1994), "Isothermal oxidation of physical vapour deposited partially stabilized zirconia thermal barrier coatings", *Journal of Materials Engineering and Performance*, vol. 3, pp. 55-60.

[95] Teixeira V., Andritschky M., Buchkremer H.P., Stöver D. (1998), "Failure mechanisms in thermal cycled TBC's" in Lecomte-Beckers J., Schubert F. and Ennis P.J. (eds.), Materials for advanced power engineering 1998 Part III, Forschungszentrum Jülich, Jülich, pp. 1601-1610.

[96] Bäker M., Rösler J., Heinze G. (2004), “A parametric study of the stress state of thermal barrier coatings part II: cooling stresses”, *Acta Materialia*, vol. 53, pp. 469-476.
[97] Eschler H., Renusch D., Schütze M. (2004), “Mechanical behaviour of as sprayed and sintered air plasma sprayed partially stabilised zirconia”, *Materials Science and Technology*, vol. 20, pp. 869-876.

[98] Echsler H., Shemet V., Schütze M., Singheiser L., Quadakkers W.J. (2006), “Cracking in and around the thermally grown oxide in thermal barrier coatings: A comparison of isothermal and cyclic oxidation”, *Journal of Materials Science*, vol. 41, pp. 1047-1058.

[99] Mezzedimi V., Giorni E., Tognarelli L., Pratesi F., Zonfrillo G., Giannozzi M., Innocenti M. (1998), “Assessment of turbine hot gas path components”, ” in Lecomte-Beckers J., Schubert F. and Ennis P.J. (eds.), Materials for advanced power engineering 1998 Part III, Forschungszentrum Jülich, Jülich, pp. 1601-1610.

[100] Sjöström S. and Brodin H. (2010), “Influence of TBC end geometry on the TMF of an APS TBC”, *Procedia Engineering*, vol. 2, pp. 1363-1371.

[101] Sohn Y.H., Lee E.Y., Nagaraj B.A., Biederman R.R, Sisson Jr. R.D. (2001), “Microstructural characterization of thermal barrier coatings on high pressure turbine blades”, *Surface and Coatings Technology*, vol. 147-147, pp. 132-139.

[102] Altuncu E., Karaali E.I., Erdogan G., Ustel F., Turk A. (2009), “ The effect of samples geometry and thermal cycling on the thermal shock behaviour of plasma sprayed TBCs”, *Plasma Processes and Polymers*, vol. 6, pp. S711- S715.

[103] Demasi J.T. & Sheffler K.D. Thermal barrier coating life prediction model development. In: NASA Contract Rep. 175087, National Aeronautics and Space Administration (1986).

[104] Koomparkping T., Damrongrat S., Niranatlumpong P. (2004), "Al-rich precipitation in CoNiCrAlY bondcaot at high temperature", *Journal of Thermal Spray Technology*, vol. 14, pp. 264-267.

[105] Busso E.P., Wright L., Evans H.E., McCartney L.N, Saunders S.R.J, Osgerby S., Nunn J. (2007), "A physics-based life prediction methodology for thermal barrier coating systems", *Acta Materialia*, vol. 55, pp. 1491-1503.

[106] Martena M., Botto D., Fino P., Sabbadini S., Gola M.M., Badini C. (2005), "Modelling of TBC system failure: Stress distribution as a function of TGO thickness and thermal expansion mismatch", *Engineering Failure Analysis*, vol. 13, pp. 409-426.

[107] Renusch D., Eschler H., Schütze M. (2001), "New approach to the understanding of failure and lifetime prediction of thermal barrier coating systems", in Schütze, M., Quadakkers, W.J., Nicholls, J.R.(eds), *Lifetime Modelling of High Temperature Corrosion Processes 34*, Proceedings of an EFC Workshop, Maney, pp. 324-336.

[108] Nesbitt J.A. (1995), "Numerical modeling of high-temperature corrosion processes", *Oxidation of Metals*, vol. 44, pp. 309-338.

[109] Krukovski P., Kolarik V., Tadlya K., Rybnikov A., Kryukov I., Juez-Lorenzo M. (2001), " Theoretical and experimental approach for long term modeling of oxidation and diffusion processes in MCrAlY coatings", in Schütze, M., Quadakkers, W.J., Nicholls, J.R.(eds), *Lifetime Modelling of High Temperature Corrosion Processes 34*, Proceedings of an EFC Workshop, Maney, pp. 231-245.

[110] Gurrappa I., Weibruch S., Naumenko D., Quaddakers W.J. (2000), " Factors governing breakaway oxidation of FeCrAl-based alloys", *Materials and Corrosion*, vol. 51, pp. 224-235.

[111] Monceau D. and Pieraggi B. (1998), "Determination of parabolic rate constants from a local analysis of mass-gain curves", *Oxidation of Metals*, vol. 50, pp. 477-493.

[112] Strehl G., Guttmann V., Naumenko D., Kolb-Telieps A., Borchardt G, Quaddakers W.J., Klöwer J., Beaven P.A., Nicholls J.R. (2001), "The influence of sample geometry on the oxidation and chemical failure of FeCrAl(RE) alloys", in Schütze, M., Quadakkers, W.J., Nicholls, J.R.(eds), *Lifetime Modelling of High Temperature Corrosion Processes 34*, Proceedings of an EFC Workshop, Maney, pp. 107-122.

[113] Gurrappa I., Weibruch S., Naumenko D., Quaddakers W.J. (2000), "Factors governing breakaway oxidation of FeCrAl-based alloys", *Materials and Corrosion*, vol. 51, pp. 224-235.

[114] Nesbitt J.A. and Heckel R.W. (1984), "Modeling degradation and failure of Ni-Cr-Al overlay coatings", *Thin solid Films*, vol. 119, pp. 281-290.

[115] Nicholls J.R., Newton R., Bennett M.J., Evans H.E., Al-Badairy H., Tatlock G.J., Naumenko D., Quadakkers W.J., Strehl G, Borchardt G. (2001), "Development of a life prediction model for the chemical failure of FeCrAl(RE) alloys in oxidizing environments", in Schütze, M., Quadakkers, W.J., Nicholls, J.R.(eds), *Lifetime Modelling of High Temperature Corrosion Processes 34*, Proceedings of an EFC Workshop, Maney, pp. 83-106.

[116] Fox A.C. and Clyne T.W. (2004), "Oxygen transport by gas prmeationthrough the zirconia layer in plasma sprayed thermal barrier coatings", *Surface and Coatings Technology*, vol. 184, pp. 311-321.

[117] Ingo G.M., Paparazzo E., Bagnarelli N., Zaccheti N. (1990), " XPS studies on cerirum, zirconium and yttrium valence states in plasma-sprayed coating", *Surface and Interface Analysis*, vol. 16, pp. 515-519 cited in [149].

[118] Ingo G. (1991), "Origin of sarkening in 8wt% yttria-zirconium plasma-sprayed thermal barrier coatings", *Journal of the American Ceramic Society*, vol. 74, pp. 381-386.

[119] Kidd G., Nunn J. (2011), "Application of pulsed thermography to quality assurance of thermal barrier coatings", to be published *in Journal of Aerospace Engineering*.

[120] Sun J.G. Thermal Imaging Characterization of Thermal Barrier Coatings. *American Ceramic Society's 31st International Cocoa Beach Conference & Exposition on Advanced Ceramics & Composites*, Daytona Beach, FL, Jan. 21-26 (2007).

[121] Nunn J, Saunders S., Banks J. (2005), Application of thermography in the evaluation of early signs of failure of thermal barrier coating systems. *Materials at High Temperatures*, vol. 22, 385-392.

[122] Thermal Wave Imaging Inc. (2009), thermography basics at http://www.thermalwave.com/technology.php

[123] Chang C.Y & Sze S.M. (1996), "ULSI technology", *New York: McGraw-Hill*

[124] Danson N., Safi I., Hall G.W., Howson R.P. (1997), "Techniques for the sputtering of optimum indium-tin oxide films on to room-temperature substrates", *Surface & Coatings Technology*, vol. 99. pp. 147-160.

[125] Carlin M., *Design, manufacture, and high temperature behaviour of α-phase bondcoat for thermal barrier coating* (2007 PhD Thesis), Cranfield University, Bedfordshire, UK.

[126] Seraffon M., Simms N., Sumner J., Nicholls J. (2011) ,"Performance of thermal barrier coatings in industrial gas turbine conditions", *Materials at High Temperatures*, vol. 28, pp.309-314.

[127] Okamoto H., Desk handbook phase diagrams for binary alloys, ASM, Ohio, 2000, p.38.

[128] Pint B.A., Wright I.G., Lee W.Y., Zhang Y., Prüβner K., Alexander K.B. (1998), "Substrate and bond coat compositions: factors affecting alumina scale adhesion", *Materials Science and Engineering A*, vol. 245, pp. 201-211.

[129] Al-Badairy H., Tatlock G.J., Bennett J. (2000), "A comparison of breakaway oxidation in wedge-shaped and parallel sided coupons of FeCrAl alloys", *Materials at high temperature*, vol. 17, pp. 101-107.

[130]Renusch D., Schorr M., Schütze M. (2008), "The role that bond coat depletion of aluminium has on the lifetime of APS-TBC under oxidizing conditions", *Materials and Corrosion*, vol 59, pp 547-555.

[131] Liu D., Flewitt P.E.J., Hallam K.R. (2011), "The measurement of residual stresses in thermal barrier coated model aerofoils", *Key Engineering Materials*, vols 488-499, pp. 9-12.

[132] Thompson J.A., Clyne T.W. (2001), "The effect of heat treatment on the stiffness of zirconia top coats in plasma-sprayed TBCs", *Acta Materialia*, vol. 49, pp. 1565-1575.

[133] Wesling K.F, Darrell F.S., Beardsley B. (1994), "Fatigue of thick thermal barrier coatings", *Journal of the American Ceramic Society*, vol. 77, pp. 1863-1868.

[134] Murphy K.S., More K.L., Lance M.J. (2001), "As-deposited mixed zone in thermally grown oxides beneath a thermal barrier coating", *Surface and Coatings Technology*, vol.146-147, pp. 152-161.

[135] Levi C.G., Sommer E., Terry S.G., Catanoiu A., Rühle M. (2003), "Alumina grown during deposition of thermal barrier coatings on NiCrAlY", *Journal of the American Ceramic Society*, vol. 86, pp. 676-685.

[136] Leyens C., Schulz U., Fritscher K. (2003), "Oxidation and lifetime of PYSZ and CeSZ coated Ni-based substrates with MCrAlY bond layers", *Materials at High Temperature*, vol. 20, pp. 475-480.

[137] Yang Y.Q., Leyens C., Schuls U., Dudek H.J., Kaysser W.A. (2000), Proc. Materials Week, Munich, Germany.

[138] Jayaram V., Levi C.G., Whitney T., Mehrabian R. (1990), "Charaterisation of Al_2O_3-ZrO_2 powders produces by electrohydrodynamic atomization", *Materials Science and Engineering A*, vol. 124, pp. 65-81.

[139] Karadge M., Zhao X., Preuss M., Xiao P. (2006), "Microtexture of the thermally grown alumina in commercial thermal barrier coatings", *Scripta Materialia*, vol. 54, pp. 639-644.

[140] Tuan W.H., Chen R.Z., Wang T.C., Cheng C.H., Kuo P.S. (2002), "Mechanical properties of Al_2O_3/ZrO_2 composites", *Journal of the European Ceramic Society*, vol. 22, pp. 2827-2833.

[141] Callister W.D. (ed.), (2007), *Materials Science and Enginerring – An introduction* (7^{th} edition), John Wiley & Sons, USA.

[142] Liang G.Y, Zhu C., Wu X.Y, Wu Y. (2010), "The formation model of Ni-Cr oxides on NiCoCrAlY-sprayed coating", *Applied Surface Science*, vol. 257, pp. 6468-6473.

[143] Wlassow F., Leonard T., Duchaine F., Gourdain N., CERFACS (2010), http://www.cerfacs.fr/8-26772-Aerothermie-des-turbines.php.

[144] Shyam V., *3-D unsteady simulation of a modern high pressure turbine blade : analysis of heat transfer and flow*, (2010 PhD thesis), Ohio State University, Ohio, USA.

[145] Seraffon M., Simms N.J., Sumner J., Nicholls J.R. (2011), "The development of new bond coat compositions for thermal barrier coating systems operating under gas turbine conditions", *Surface and Coatings Technology*, vol. 207, pp. 1529-1537.

[146] Rosell-Laclau E., Durand-Charre M., Audier M. (1996), "Liquid-solid equilibria in the aluminium-rich corner of the Al-Cr-Ni system", *Journal of Alloys and Compounds*, vol. 233, pp. 246-263.

[147] Levin I., Brandon D. (1998), "Metastable alumina polymorphs: crystal structures and
transition sequences", *Journal of the American Ceramic Society*, vol. 81, pp. 1995-2012.

[148] Sauthoff G. (1995), "Intermetallics", 1st Ed., *VCH, Weinheim*, p.38 .

[149] Kear B.H., Pettit F.S., Forwalt D.E, Lemaire L.P. (1971), "On the transient oxidation of a Ni-15Cr-6Al alloy", *Oxidation of Metals*, vol.3, pp.557-569.

[150] Taylor T.A., Walsh P.N. (2004), "Thermal expansion of MCrAlY alloys", *Surface and Coatings Technology*, vol. 177-178, pp. 24-31.

[151] Nicholls J.R., Lawson K.J, Al Yasiri L.H., Hancock P. (1993), "Vapour phase alloy design of corrosion resistant overlay coatings", *Corrosion Science*, vol. 35, pp. 1209-1223.

[152] Ma K., Schoenung J.M. (2010), "Thermodynamic investigation into the equilibrium phases in the NiCoCrAl system at elevated temperatures", *Surface and Coatings Technology*, vol. 205, pp. 2273-2280.

[153] Liang J.J., Wei H., Zhu Y.L., Sun X.F., Jin T., Hu Z.Q., Dargusch M.S., Yao X. (2011), "Influence of Co addition on constituent phases and performance of a NiCrAlYRe alloy system", *Surface and Coatings Technology*, vol. 205, pp. 4968-4979.

[154] Achar D.R.G, Munoz-Arroyo R., Singheiser L., Quadakkers W.J. (2004), "Modelling of phase equilibria in MCrAlY coating systems", *Surface and Coatings Technology*, vol. 187, pp. 272-283.

[155] Thompson J.A., Tsui Y.C., Reed R.C., Rickerby D.S., Clyne T.W.(2000), "Creep of plasma sprayed CoNiCrAlY and NiCrAlY bond coats and its effect on residual atresses during thermal cycling of thermal barrier coating systems", High Temperature Surface Engineering, Proceedings of 6th International Conference on Engineering the Surface, Edinburgh, UK.

APPENDIX A – MOUNTING MOULD (DESIGN)

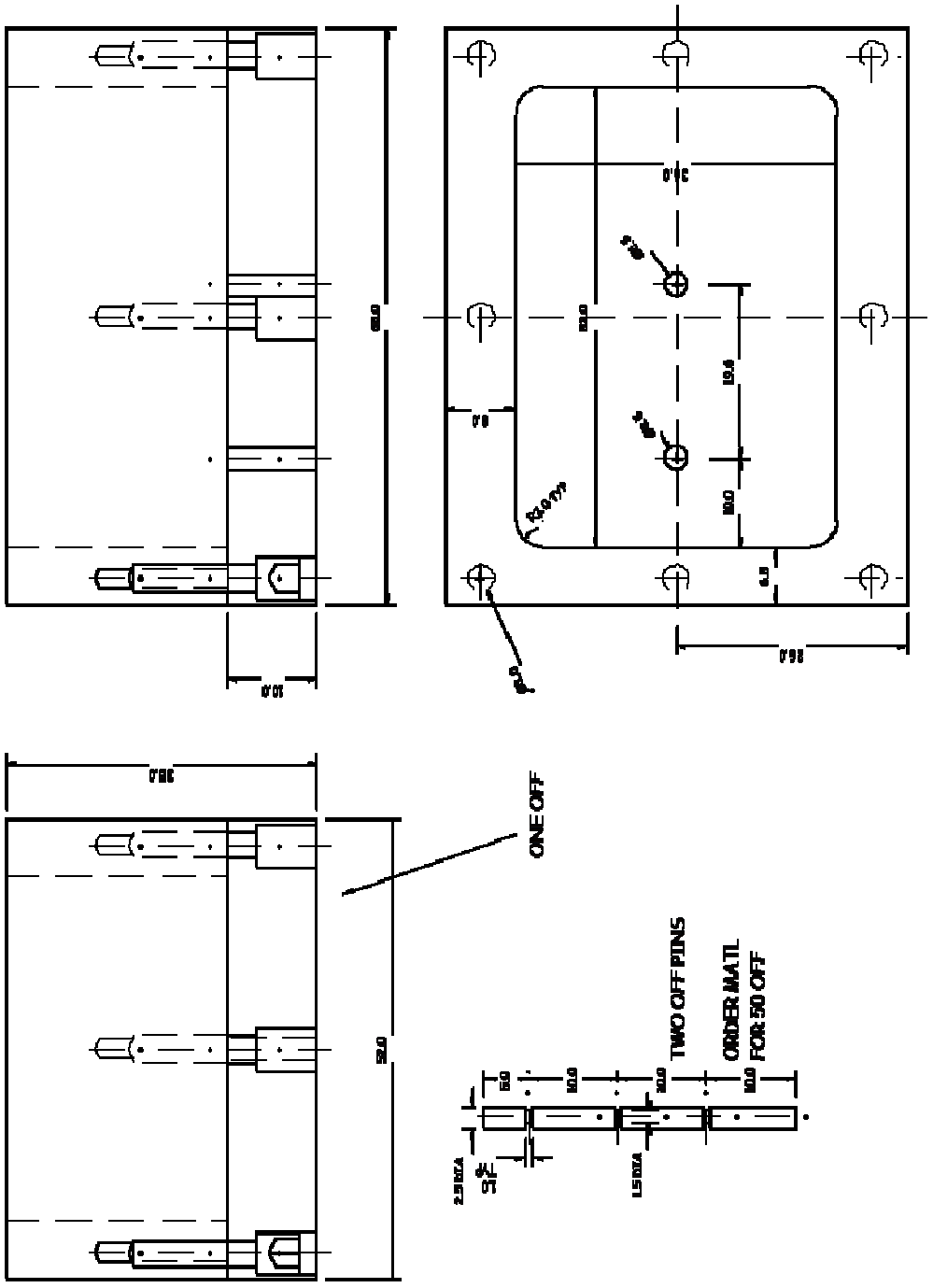

APPENDIX B – MASS CHANGE CURVES OF MODIFIED AEROFOIL-SHAPED SAMPLES

Data at 900 °C:

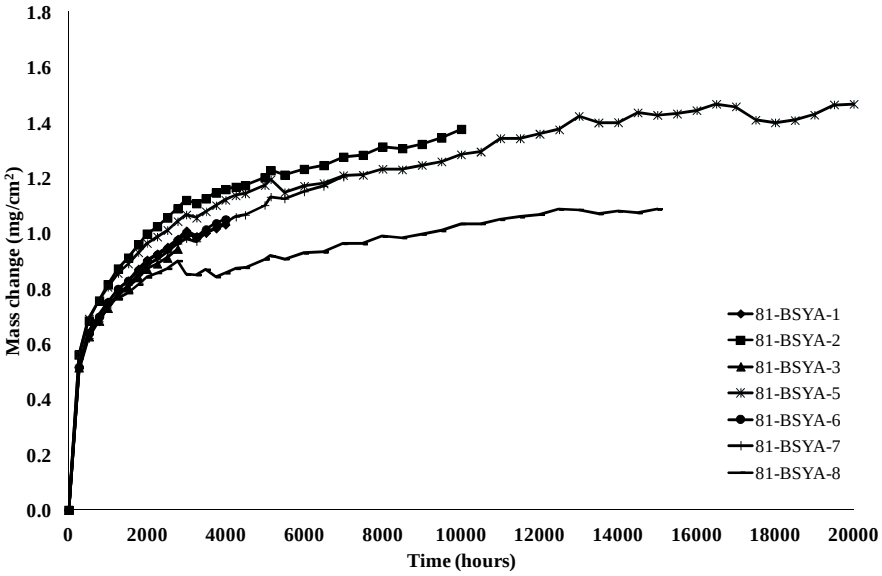

Data at 925 °C:

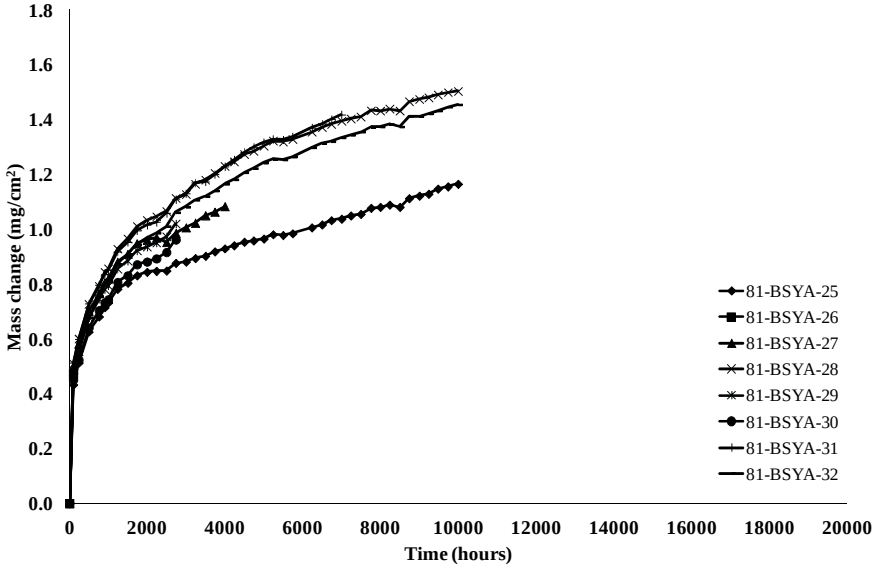

Data at 950 °C:

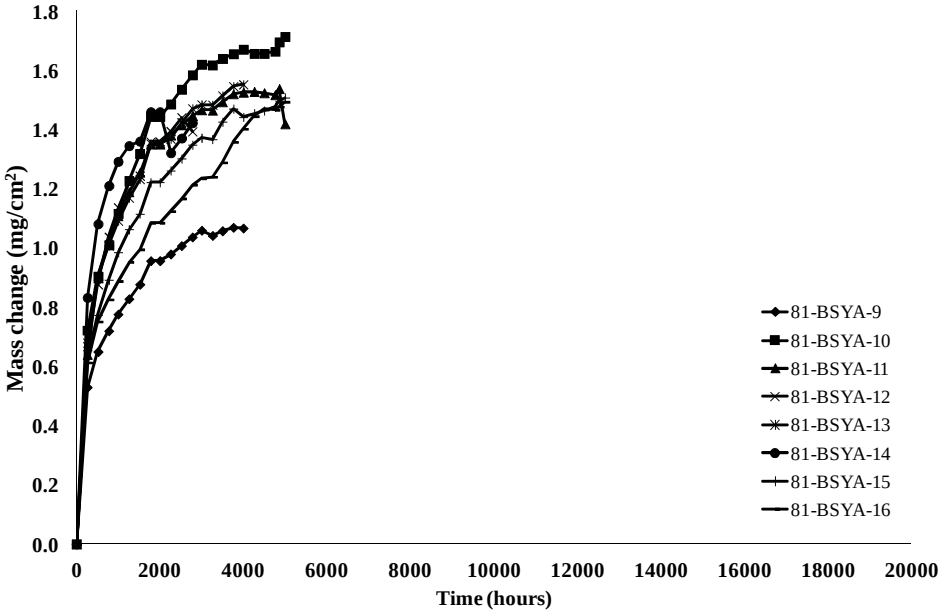

Data at 975 °C:

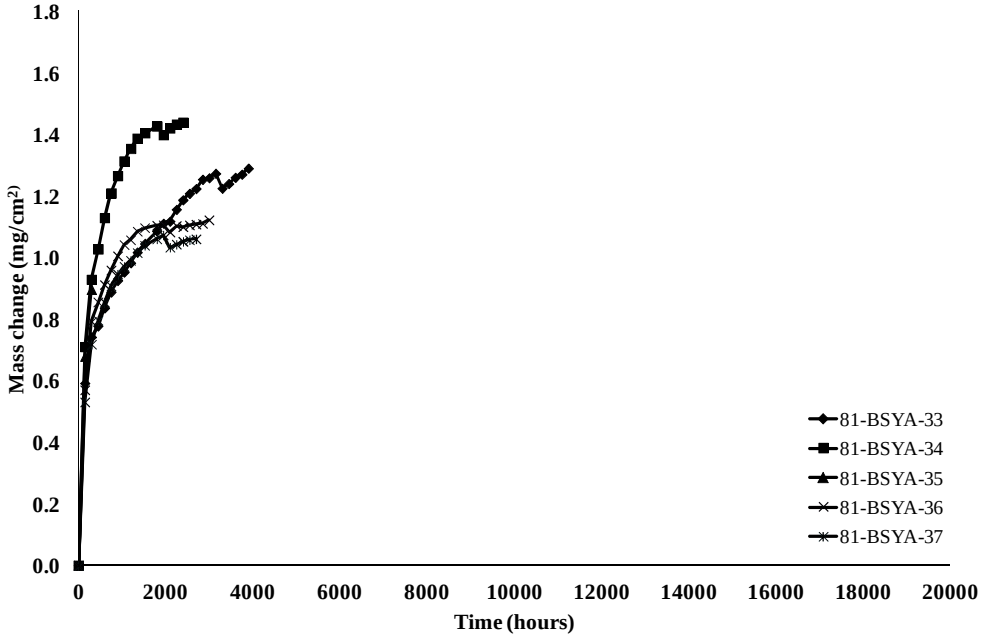

Data at 1000 °C:

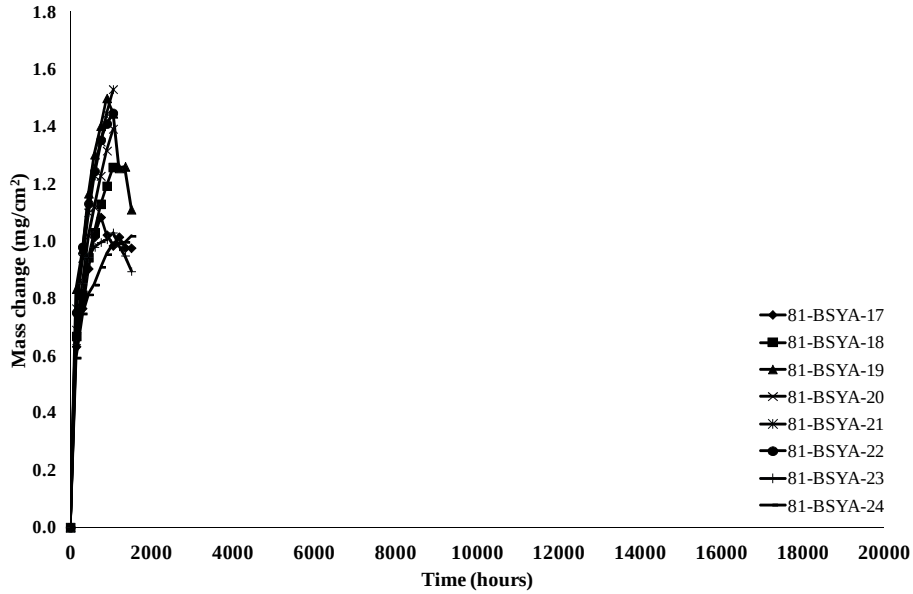

APPENDIX C – MEASURED BOND COAT AND TOP COAT THICKNESSES ON MODIFIED AEROFOIL-SHAPED SAMPLES (µm)

na: data non available

BOND COAT:

Sample (81-BSYA)	**ref**	**1**	**2**	**3**	**4**	**5**	**6**	**7**	**8**
Temperature (°C)	0	900	900	900	900	900	900	900	900
Exposure time (hours)	0	4000	10,000	2780	2780	20,000	4000	7000	15,000
A	105	91.3	85.6	112.7	96.2	88.7	97.1	79.2	70.1
B	40	54.3	64.2	49.3	34.8	59.2	58.5	45.4	53.8
C	108	113.3	104.4	108.7	112.3	104.1	101.0	100.7	95.8
D	105.6	116.1	95.0	108.9	115.4	93.8	113.7	114.1	76.4
E	48.6	61.2	60.5	117.9	48.0	67.6	112.0	84.1	71.7
F	27	38.5	63.0	68.3	44.0	45.7	88.6	57.3	37.9
a	120	141.9	98.7	na	135.9	136.4	na	132.9	106.0
b	141	127.7	136.3	na	146.8	117.9	na	118.9	115.7
c	111.6	122.2	106.0	na	105.1	115.0	na	138.0	91.3

Sample (81-BSYA)	**12**	**13**	**14**	**15**	**18**	**19**
Temperature (°C)	950	950	950	950	1000	1000
Exposure time (hours)	2780	4000.0	2780.0	5000	1050	1500
A	99.8	90.7	92.7	80	69.1	88.7
B	53.5	56.1	58.5	50	104.4	68.7
C	109.9	106.3	106.8	110	120.9	122.2
D	113.7	94.3	97.2	100	111.1	105.6
E	61.1	104.7	79.3	75	84.6	82.0
F	45.6	50.8	50.4	50	60.8	52.0
a	117.5	145.0	na	140	140.4	143.2
b	147.2	98.5	na	140	133.7	152.4
c	122.5	152.5	139.3	145	131.6	147.7

Sample (81-BSYA)	**25**	**26**	**27**	**29**	**31**	**35**	**36**	**37**
Temperature (°C)	925	925	925	925	925	975	975	975
Exposure time (hours)	10,000	100	4000	2740	7000	300	3000	2700
A	105.4	100.6	92.9	103.0	101.2	104.6	106.8	116.1
B	41.2	40.0	62.0	37.3	42.3	58.8	49.0	52.2
C	112.4	108.2	102.5	120.0	120.0	121.3	120.0	131.1
D	107.3	106.6	98.6	123.5	97.4	100.0	129.4	134.7
E	54.3	104.7	107.6	91.5	91.9	108.5	60.5	105.6
F	29.2	47.2	40.7	51.7	49.3	50.0	45.9	52.4
a	124.7	138.2	146.5	150.1	140.1	153.6	157.1	160.1
b	161.9	124.6	127.4	145.1	106.6	146.0	165.7	135.6
c	99.3	147.7	146.9	145.9	136.4	154.1	96.7	142.1

TOP COAT:

Sample (81-BSYA)	**ref**	**1**	**2**	**4**	**5**	**7**	**8**
Temperature (°C)	0	900	900	900	900	900	900
Exposure time (hours)	0	4000	10,000	2780	20,000	7000	15,000
A	188	160	211	200	201	180	206
B	202	190	201	180	234	150	208
C	245	210	232	210	232	250	231
D	216	220	216	200	236	200	212
E	202	190	172	170	166	210	201
F	152	150	139	150	148	130	115
a	240	270	270	230	234	220	237
b	250	250	257	230	252	200	245
c	225	250	252	250	229	220	192

Sample (81-BSYA)	**12**	**13**	**16**	**18**	**19**
Temperature (°C)	950	950	950	1000	1000
Exposure time (hours)	2780	4000	5000	1050	1500
A	205	200	205	200	240
B	200	170	160	180	160
C	250	240	235	250	270
D	205	250	230	240	220
E	170	210	180	180	180
F	120	170	180	180	150
a	190	230	240	250	300
b	230	235	240	260	250
c	245	290	300	300	260

Sample (81-BSYA)	**25**	**26**	**27**	**29**	**31**	**35**	**36**	**37**
Temperature (°C)	925	925	925	925	925	975	975	975
Exposure time (hours)	10,000	100	4000	2740	7000	300	3000	2700
A	198	218	216	200	199	235	196	196
B	169	192	171	172	161	250	175	159
C	279	258	287	257	245	270	255	254
D	259	198	247	210	212	220	204	218
E	204	193	216	218	184	170	212	213
F	204	165	204	155	160	198	148	161
a	272	247	258	260	253	256	235	258
b	261	220	253	260	209	258	226	224
c	290	284	307	251	278	246	97	228

APPENDIX D – TGO THICKNESSES MEASURED ON MODIFIED AEROFOIL-SHAPED SAMPLES (µm)

Data in red: presence of cracks

na: data non available

Sample ID	Thickness at location (µm)								
81-BSYA-1	**A**	**B**	**C**	**D**	**E**	**F**	**a**	**b**	**c**
900°C	2.51	3.11	3.21	2.6	2.8	2.86	3.09	2.43	3.16
4000 hours	2.53	3.23	3.28	3.23	2.96	2.96	3.28	3.38	3.52
	3.09	3.36	3.29	3.34	3.04	3.15	3.47	3.45	3.53
	3.58	3.4	3.6	3.34	3.21	3.34	3.57	3.67	3.61
	3.62	3.51	3.68	3.51	3.42	3.35	3.62	3.77	3.74
	3.65	3.53	3.72	3.56	3.59	3.48	3.76	3.96	3.79
	3.8	3.64	3.8	3.6	3.63	3.5	3.76	4.18	3.83
	3.81	3.84	4.14	3.88	3.76	3.66	3.88	4.2	3.83
	4.15	3.87	4.44	4.07	3.77	3.71	3.96	4.29	4.51
	4.51	3.98	4.93	4.16	3.91	3.83	4.6	5.43	4.55

Sample ID	Thickness at location (µm)								
81-BSYA-2	**A**	**B**	**C**	**D**	**E**	**F**	**a**	**b**	**c**
900°C	3.82	3.96	2.7	4.38	3.09	3.75	3.94	3.49	4.46
10,000 hours	3.91	4	3.43	5.11	4.2	3.92	4.41	3.76	4.61
	3.98	4.04	3.92	5.11	4.42	4.1	4.62	3.92	4.76
	4.03	4.54	4.16	5.11	4.64	4.29	4.87	4.06	4.76
	4.29	4.89	4.69	5.6	4.65	4.42	5.1	4.42	5.06
	4.53	5.22	4.78	5.84	4.86	4.65	5.66	5.03	5.21
	4.96	5.22	5.23	6.57	4.87	4.78	5.68	5.82	5.36
	5.25	5.22	5.39	7.3	5.08	4.95	6.39	5.94	5.8
	5.51	5.41	5.88	7.54	5.08	5.5	6.49	6.33	5.95
	5.77	5.45	6.01	8.03	5.52	5.79	7.66	7.34	6.55

Sample ID	Thickness at location (µm)								
81-BSYA-3	**A**	**B**	**C**	**D**	**E**	**F**	**a**	**b**	**c**
900°C	2.82	2.27	2.69	2.83	2.62	3	na	na	na
2780 hours	3.1	2.61	2.93	3.03	2.68	3.06	na	na	na
	3.14	2.66	2.97	3.19	2.69	3.07	na	na	na
	3.2	2.83	3.02	3.41	3.01	3.27	na	na	na
	3.47	2.9	3.12	3.42	3.09	3.32	na	na	na
	3.53	3.22	3.28	3.5	3.21	3.36	na	na	na
	3.56	3.34	3.45	3.55	3.29	3.95	na	na	na
	3.69	3.41	3.51	3.56	3.43	3.96	na	na	na
	3.79	3.7	3.69	3.58	3.61	4.53	na	na	na
	4.38	3.99	3.78	3.82	3.75	4.61	na	na	na

Sample ID	Thickness at location (µm)								
81-BSYA-4	**A**	**B**	**C**	**D**	**E**	**F**	**a**	**b**	**c**
900°C	2.68	2.53	2.25	2.49	2.72	2.65	2.01	2.65	2.68
2780 hours	2.75	3.07	2.48	2.57	3.01	2.78	2.13	2.9	3.38
	3.09	3.2	2.61	2.57	3.2	2.83	2.69	3.07	3.39
	3.39	3.51	2.98	2.62	3.36	2.88	2.74	3.18	3.61
	3.48	3.52	3.03	3.01	3.54	2.92	2.78	3.21	3.67
	3.67	3.57	3.04	3.14	3.64	3.01	2.86	3.31	3.97
	3.79	3.62	3.09	3.14	3.74	3.13	3.14	3.82	4.22
	4.16	3.73	3.38	3.31	3.78	3.2	3.44	3.83	4.51
	4.24	3.84	3.49	3.79	4.04	3.36	3.46	3.85	4.73
	4.98	3.9	3.54	3.8	4.76	3.37	3.64	4.3	5.23

Sample ID	Thickness at location (µm)								
81-BSYA-5	**A**	**B**	**C**	**D**	**E**	**F**	**a**	**b**	**c**
900°C	4.94	4.52	5.81	4.53	4.81	4.75	4.05	3.09	4.44
20,000 hours	5.02	4.98	6.09	4.53	4.83	4.87	4.18	4.23	5.74
	5.28	5.08	6.15	4.63	5.02	5.27	4.76	4.31	5.91
	5.73	5.21	6.3	4.64	5.21	5.92	5.28	4.4	5.99
	5.85	5.32	6.75	5.49	5.23	6.12	5.3	4.63	6.37
	5.99	5.85	6.82	5.79	5.62	6.52	5.86	4.73	7.12
	6.1	5.94	6.92	6.2	5.91	6.87	6	6.4	7.27
	7.96	6.04	7.38	6.45	6.75	7.02	6.43	6.77	7.35
	8.3	6.16	8.2	6.75	7.1	7.27	6.75	7.2	7.97
	9.72	6.48	8.37	6.97	9.74	8.13	8.39	8.75	8.88

Sample ID	Thickness at location (µm)								
81-BSYA-6	**A**	**B**	**C**	**D**	**E**	**F**	**a**	**b**	**c**
900°C	2.71	2.41	3.26	2.49	2.07	3.19	na	na	na
4000 hours	3.02	3.06	3.38	2.75	2.7	3.21	na	na	na
	3.13	3.26	3.48	2.86	2.71	3.34	na	na	na
	3.25	3.32	3.7	2.95	2.78	3.42	na	na	na
	3.36	3.45	3.88	2.99	2.88	3.58	na	na	na
	3.42	3.49	3.98	3.04	2.94	3.59	na	na	na
	3.44	3.52	4.12	3.45	2.99	3.77	na	na	na
	3.55	3.69	4.13	3.64	3.05	3.8	na	na	na
	3.77	3.74	4.3	3.67	3.52	3.84	na	na	na
	3.88	3.81	5.2	4.01	3.68	4.02	na	na	na

Sample ID	Thickness at location (µm)								
81-BSYA-7	**A**	**B**	**C**	**D**	**E**	**F**	**a**	**b**	**c**
900°C	3.55	4.15	3.34	3.28	3.04	3.18	3.38	4.01	3.71
7000 hours	3.79	4.22	3.39	3.66	3.65	3.19	3.88	4.02	3.81
	3.98	4.25	3.64	3.68	4.29	3.59	4.18	4.24	3.84
	4.29	4.41	3.66	3.8	4.31	3.95	4.53	4.59	3.93
	4.31	4.48	3.89	4.48	4.39	4	4.74	4.71	4.25
	4.41	4.98	3.96	4.77	4.49	4.16	4.87	4.92	4.44
	4.58	5.07	4.08	4.89	4.5	4.29	4.96	4.93	4.53
	4.63	5.14	4.28	5	4.56	4.7	5.18	5.01	5.41
	4.9	5.79	4.31	5.09	4.83	5.21	5.68	5.44	5.44
	5.39	5.92	4.66	5.63	4.94	5.22	6.08	5.82	6.14

Sample ID	Thickness at location (µm)								
81-BSYA-8	**A**	**B**	**C**	**D**	**E**	**F**	**a**	**b**	**c**
900°C	4.18	3.11	4.52	3.09	3.52	3.98	3.49	3.68	4.44
15,000 hours	4.28	3.5	4.56	4.44	3.67	4.3	3.64	4.25	4.66
	4.66	4.07	4.73	4.45	4.22	4.63	4.71	4.41	4.75
	5.14	4.47	5.22	4.53	4.56	4.65	4.73	4.66	5.02
	5.15	4.47	5.43	4.98	4.82	5.34	4.79	4.84	5.23
	5.56	4.52	5.5	5.13	4.84	5.75	4.89	4.84	5.35
	5.58	4.71	5.92	5.41	5.02	5.79	5.72	5.39	5.38
	6.04	5.21	6.48	5.75	5.44	6.28	6.17	5.54	5.57
	6.34	6.17	6.76	5.98	5.5	6.7	6.65	5.81	5.61
	6.41	6.56	7.48	6.29	6.18	6.71	7.33	7.38	5.95

Sample ID	Thickness at location (µm)								
81-BSYA-9	**A**	**B**	**C**	**D**	**E**	**F**	**a**	**b**	**c**
950°C	4.14	3.99	3.64	3.98	3.42	3.65	na	na	na
4000 hours	4.21	4.06	3.81	4.39	4.13	3.76	na	na	na
	4.38	4.13	3.87	4.46	4.26	4.14	na	na	na
	4.64	4.24	3.9	4.54	4.77	4.22	na	na	na
	4.66	4.26	4.06	4.54	4.8	4.34	na	na	na
	4.72	4.31	4.12	4.72	4.83	4.78	na	na	na
	4.93	4.41	4.27	4.81	4.9	4.85	na	na	na
	4.97	4.46	4.5	5.26	4.92	4.87	na	na	na
	5.07	4.71	5	5.37	5.15	5.17	na	na	na
	5.14	4.72	5.17	5.77	5.36	5.76	na	na	na

Sample ID	Thickness at location (µm)								
81-BSYA-11	**A**	**B**	**C**	**D**	**E**	**F**	**a**	**b**	**c**
950°C	4.37	4.12	4.38	4.26	4.78	4.46	na	na	na
5000 hours	5.41	4.16	4.56	4.29	4.84	4.51	na	na	na
	5.42	4.34	4.67	4.75	4.86	4.7	na	na	na
	5.72	4.74	5.05	5.48	5.01	5.02	na	na	na
	5.84	4.78	5.27	5.99	5.06	5.05	na	na	na
	6.53	5.75	5.28	6.25	5.14	5.17	na	na	na
	6.67	5.91	5.55	6.42	5.26	5.38	na	na	na
	6.72	5.92	5.76	6.44	5.33	5.39	na	na	na
	6.87	6.35	5.79	6.46	5.37	5.76	na	na	na
	6.89	6.65	5.84	6.64	5.81	5.99	na	na	na

Sample ID	Thickness at location (µm)								
81-BSYA-12	**A**	**B**	**C**	**D**	**E**	**F**	**a**	**b**	**c**
950°C	4.02	3.8	3.98	4.23	4.06	3.86	4.65	4.02	4.44
2780 hours	4.42	4.04	4.63	4.27	4.59	3.88	4.69	4.52	4.77
	4.69	4.11	4.76	4.91	4.73	4.26	4.69	4.78	4.84
	4.88	4.16	4.78	4.92	5.46	4.41	4.89	4.87	4.92
	4.95	4.17	4.95	5.09	5.58	4.55	4.99	4.88	5.49
	4.97	4.24	5.01	5.09	5.72	4.99	5.31	5.13	5.8
	4.98	4.28	5.01	5.45	5.76	5.16	5.47	5.34	5.98
	5.06	4.37	5.08	5.56	5.79	5.19	5.71	5.4	6.17
	5.51	4.76	5.2	5.76	5.81	5.43	5.8	6.03	6.18
	5.8	4.84	5.86	5.97	6.28	5.44	6.43	6.27	7

Sample ID	Thickness at location (µm)								
81-BSYA-13	**A**	**B**	**C**	**D**	**E**	**F**	**a**	**b**	**c**
950°C	4.21	4.28	4.25	4.9	5.05	4.28	3.93	4.69	4.28
4000 hours	4.26	4.82	4.31	4.95	5.05	4.35	4.01	4.78	4.29
	4.55	4.97	4.32	5.16	5.11	4.38	4.75	4.82	4.46
	4.84	5.01	4.65	5.37	5.32	4.45	4.76	5.2	4.48
	5.25	5.22	4.95	5.42	5.4	4.63	4.92	5.31	5.01
	5.29	5.26	5.13	5.46	5.82	5.24	5.02	5.38	5.08
	5.34	5.41	5.23	5.84	5.85	5.74	5.12	5.7	5.22
	5.35	5.66	5.27	5.87	6.07	5.76	5.41	5.72	5.79
	5.51	5.73	5.34	5.99	6.3	6.4	6.28	6.03	6.09
	5.68	5.97	5.81	6.29	6.57	6.81	6.34	6.29	6.97

Sample ID	Thickness at location (µm)								
81-BSYA-14	**A**	**B**	**C**	**D**	**E**	**F**	**a**	**b**	**c**
950°C	4.75	3.83	3.87	4.06	3.49	3.74	na	na	na
2780 hours	4.91	3.86	4.16	4.07	3.88	4.01	na	na	na
	4.92	4.23	4.22	4.14	4.06	4.23	na	na	na
	4.96	4.31	4.29	4.55	4.23	4.38	na	na	na
	5.01	4.53	4.34	4.73	4.58	4.39	na	na	na
	5.16	4.75	4.42	4.91	4.67	4.41	na	na	na
	5.18	4.83	4.53	4.96	4.68	4.63	na	na	na
	5.64	4.9	4.62	5.8	5.04	4.74	na	na	na
	5.66	4.92	5.09	5.86	5.35	4.83	na	na	na
	5.76	5.18	5.33	5.95	5.36	6.04	na	na	na

Sample ID	Thickness at location (µm)								
81-BSYA-16	**A**	**B**	**C**	**D**	**E**	**F**	**a**	**b**	**c**
950°C	4.12	4.89	4.4	4.87	3.28	4.4	4.09	4.66	4.51
5000 hours	4.59	4.9	4.6	4.9	3.83	4.73	4.45	4.75	4.92
	4.8	4.93	4.98	5.28	3.93	5.14	4.81	4.87	5.22
	4.83	5.04	5.36	5.57	4.05	5.46	5.04	5.15	5.42
	4.86	5.23	5.38	5.69	4.52	5.6	5.18	5.45	5.53
	4.89	5.32	5.43	5.94	4.58	5.66	5.35	5.49	5.65
	4.93	5.42	5.87	5.98	4.79	5.86	5.59	6.18	6.25
	5.19	5.49	6.18	6.04	4.83	6.04	5.79	6.75	6.68
	5.22	5.65	6.4	6.37	4.94	6.74	6.29	6.76	6.96
	5.89	6.42	7.64	6.7	5.63	6.87	6.39	7.53	6.98

Sample ID	Thickness at location (µm)								
81-BSYA-17	**A**	**B**	**C**	**D**	**E**	**F**	**a**	**b**	**c**
1000°C	4.34	3.02	3.92	4.59	3.79	3.21	na	na	na
1500 hours	4.75	3.92	4.61	4.9	3.85	3.49	na	na	na
	4.78	4.1	4.61	5.19	3.91	3.95	na	na	na
	4.86	4.16	4.83	5.23	4.22	4.26	na	na	na
	4.88	4.25	4.84	5.31	4.55	4.61	na	na	na
	5.09	4.47	5.03	5.35	4.68	4.75	na	na	na
	5.48	4.58	5.11	5.41	4.83	4.81	na	na	na
	5.75	4.87	5.38	5.69	4.95	5	na	na	na
	5.93	4.95	5.65	5.79	5.06	5.12	na	na	na
	6.04	4.96	5.7	6.09	5.17	5.15	na	na	na

Sample ID	Thickness at location (µm)								
81-BSYA-18	**A**	**B**	**C**	**D**	**E**	**F**	**a**	**b**	**c**
1000°C	3.57	4.2	3.29	3.9	3.28	4.51	3.07	3.41	3.74
1050 hours	3.81	4.36	3.93	3.99	4.01	4.64	3.39	3.81	4.25
	3.99	4.43	3.98	4.03	4.13	4.67	3.49	4.44	4.49
	4.01	4.52	4.06	4.67	4.2	4.86	3.82	4.82	4.83
	4.43	4.98	4.16	4.76	4.48	4.99	4.63	4.82	5.08
	4.43	4.99	4.61	4.82	4.51	5.03	4.99	4.98	5.16
	4.65	5.07	4.76	4.9	4.53	5.04	5.07	5.17	5.37
	5.19	5.24	4.86	4.94	4.58	5.89	5.19	5.31	5.64
	5.49	5.5	4.88	5.01	4.6	6.05	5.59	5.45	5.73
	5.59	5.51	5.27	5.13	4.6	6.39	6.41	5.79	5.88

Sample ID	Thickness at location (µm)								
81-BSYA-19	**A**	**B**	**C**	**D**	**E**	**F**	**a**	**b**	**c**
1000°C	3.86	3.98	4.55	4.09	4.06	4.39	4.25	4.69	4.03
1500 hours	4.19	4.04	5.04	4.77	4.28	4.49	4.47	4.75	4.9
	4.43	4.09	5.05	4.92	4.31	4.67	5.04	4.78	4.91
	4.5	4.09	5.24	5.01	4.34	4.91	5.4	4.9	5.52
	4.74	4.55	5.63	5.06	4.37	5.13	5.49	4.9	5.58
	5.17	4.63	5.66	5.16	4.56	5.2	5.64	5.02	5.65
	5.44	4.72	5.77	5.21	4.85	5.55	5.81	5.22	6.23
	6.16	4.79	5.91	5.23	4.87	5.57	6.2	5.49	6.53
	6.28	5.24	6.33	5.36	4.94	5.63	6.26	5.92	6.54
	6.42	5.43	6.4	5.43	5.19	6.16	6.36	5.94	6.78

Sample ID	Thickness at location (µm)								
81-BSYA-20	**A**	**B**	**C**	**D**	**E**	**F**	**a**	**b**	**c**
1000°C	4.07	3.35	4.05	4.12	3.67	3.91	na	na	na
1050 hours	4.19	3.51	4.17	4.2	3.71	4.07	na	na	na
	4.53	3.74	4.18	4.23	3.91	4.13	na	na	na
	4.71	3.88	4.24	4.69	4.01	4.23	na	na	na
	4.81	4.39	4.31	4.73	4.12	4.49	na	na	na
	4.94	4.51	4.81	4.81	4.15	4.57	na	na	na
	4.99	4.6	4.83	5.07	4.31	4.75	na	na	na
	5.21	4.67	4.91	5.11	4.42	4.85	na	na	na
	5.66	4.69	5.03	5.18	4.49	4.88	na	na	na
	5.86	4.78	5.17	5.49	5.49	5.07	na	na	na

Sample ID	Thickness at location (µm)								
81-BSYA-22	**A**	**B**	**C**	**D**	**E**	**F**	**a**	**b**	**c**
1000°C	3.58	3.22	3.94	4.03	4.52	3.48	na	na	na
1050 hours	3.66	3.87	4.42	4.93	4.54	3.93	na	na	na
	3.87	4.2	4.53	5.02	4.62	4.18	na	na	na
	4.17	4.38	4.6	5.07	4.78	4.4	na	na	na
	4.18	4.6	4.69	5.12	4.98	4.89	na	na	na
	4.38	4.72	4.83	5.24	5.04	4.94	na	na	na
	4.75	4.73	4.86	5.29	5.21	4.95	na	na	na
	5.27	4.76	4.9	5.57	5.55	5.25	na	na	na
	5.38	4.91	4.97	5.58	5.61	5.52	na	na	na
	5.71	5.03	5.25	6.98	5.69	5.68	na	na	na

Sample ID	Thickness at location (µm)								
81-BSYA-23	**A**	**B**	**C**	**D**	**E**	**F**	**a**	**b**	**c**
1000°C	5.11	4.44	4.3	4.15	4.75	4.29	na	na	na
1500 hours	5.13	4.8	4.51	4.93	4.83	5.18	na	na	na
	5.32	4.83	4.71	4.96	4.97	5.38	na	na	na
	5.39	5.74	4.92	5.41	4.99	5.95	na	na	na
	5.77	5.95	5.05	5.6	5.4	6.42	na	na	na
	5.88	5.98	5.08	5.61	5.45	6.44	na	na	na
	5.91	6.28	5.43	5.7	5.59	6.75	na	na	na
	5.92	6.29	5.51	5.81	5.8	6.84	na	na	na
	5.93	6.42	5.77	6.46	5.82	7.42	na	na	na
	6.37	6.9	6.18	6.67	6.1	8.01	na	na	na

Sample ID	Thickness at location (µm)								
81-BSYA-24	**A**	**B**	**C**	**D**	**E**	**F**	**a**	**b**	**c**
1000°C	4.14	4.02	3.83	4.04	3.77	3.88	na	na	na
1050 hours	4.4	4.19	4.15	4.07	3.9	4.13	na	na	na
	4.58	4.3	4.34	4.12	4.04	4.41	na	na	na
	4.84	4.39	4.41	4.18	4.2	4.48	na	na	na
	5.03	4.41	4.43	4.3	4.27	4.59	na	na	na
	5.26	4.58	5	4.31	4.8	4.9	na	na	na
	5.61	4.76	5.09	4.69	4.9	4.93	na	na	na
	5.65	4.9	5.35	5.3	5.14	4.96	na	na	na
	5.67	5.39	5.8	6.08	5.16	5.53	na	na	na
	5.95	5.4	6.53	6.09	5.52	5.62	na	na	na

Sample ID	Thickness at location (µm)								
81-BSYA-25	**A**	**B**	**C**	**D**	**E**	**F**	**a**	**b**	**c**
925°C	3.54	2.64	3.32	3.11	3.28	3.99	2.84	3.56	3.96
10,000 hours	3.81	4.06	3.77	3.77	3.32	4.16	4.1	3.86	4.77
	4.14	4.1	3.77	4.06	3.99	4.18	4.64	4.1	5.21
	4.47	4.77	3.77	4.28	4.1	4.28	4.71	4.5	5.37
	4.71	5.22	3.81	4.37	4.71	4.47	4.87	4.59	5.43
	4.84	5.24	4.06	4.64	5.3	4.64	5.23	5.01	5.6
	4.95	5.26	4.06	4.65	5.99	4.65	5.4	5.12	5.6
	4.97	5.57	4.47	4.71	6.17	4.81	5.58	5.15	5.79
	5.95	5.97	4.95	5.15	6.52	4.89	6.23	6.18	6.1
	6.42	6.14	5.08	5.26	7.46	6.1	6.58	7.1	6.6

Sample ID	Thickness at location (µm)								
81-BSYA-26	**A**	**B**	**C**	**D**	**E**	**F**	**a**	**b**	**c**
925°C	0.71	1.43	0.9	1.93	0.9	1.29	0.9	1.55	0.8
100 hours	1.01	1.47	1.3	2.06	1.66	1.43	1.77	1.77	1.18
	1.55	1.51	1.35	2.09	1.8	1.53	1.77	1.95	1.48
	1.64	1.58	1.53	2.19	1.82	1.55	1.82	1.98	1.61
	1.82	1.69	1.55	2.44	1.91	1.57	1.93	2.14	1.77
	1.88	1.84	1.66	2.58	2.14	1.83	2.25	2.17	1.8
	2.08	1.89	1.74	2.59	2.32	1.84	2.37	2.68	2.26
	2.23	1.89	1.96	2.59	2.6	1.86	2.64	2.74	2.42
	2.39	2.03	1.97	2.94	2.89	2.17	2.77	2.75	2.58
	2.96	2.38	2.66	3.5	3.12	2.3	3.23	3.13	2.7

Sample ID	Thickness at location (µm)								
81-BSYA-27	**A**	**B**	**C**	**D**	**E**	**F**	**a**	**b**	**c**
925°C	3.36	3	3.11	2.53	2.89	3.04	3.26	4.05	4.25
4000 hours	3.42	3.24	3.12	3.12	3.18	3.34	3.5	4.35	2.91
	3.69	3.34	3.14	3.4	3.7	3.53	4.19	4.71	3.11
	4.11	3.35	3.31	3.6	3.73	3.98	4.23	4.84	3.45
	4.41	3.38	3.98	3.71	3.77	3.99	4.65	4.84	4.17
	4.61	3.65	4.02	4.1	3.77	3.99	4.95	5.02	4.44
	4.83	3.86	4.18	4.14	4.36	3.99	4.97	5.08	4.79
	4.88	4.46	4.23	5.14	5.47	4.42	5.79	5.21	4.9
	5.21	4.91	4.3	5.58	5.53	4.44	6.04	5.22	4.94
	5.31	5.43	4.41	5.66	5.96	4.58	6.18	5.92	4.94

Sample ID	Thickness at location (µm)								
81-BSYA-29	**A**	**B**	**C**	**D**	**E**	**F**	**a**	**b**	**c**
925°C	2.94	3.34	2.65	2.93	3.7	2.64	3.02	3.73	2.44
2740 hours	3.32	3.47	2.72	3.08	3.81	2.66	3.27	3.86	3.49
	3.46	3.56	3.38	3.18	3.91	2.77	3.43	4.06	3.53
	3.55	3.6	3.6	3.25	3.95	2.84	3.47	4.19	3.77
	3.55	3.8	3.74	3.87	4.01	2.93	3.56	4.21	3.8
	3.78	4.07	3.81	3.89	4.04	2.98	3.6	4.28	3.97
	3.8	4.44	4.25	3.96	4.1	3.35	3.86	4.29	4.07
	3.99	4.56	4.55	4.08	4.22	3.44	3.86	4.52	4.77
	4.06	4.68	5.04	4.3	4.55	3.76	4.36	4.87	4.77
	5.36	4.92	5.06	4.51	5	4.68	4.49	5	4.98

Sample ID	Thickness at location (µm)								
81-BSYA-31	**A**	**B**	**C**	**D**	**E**	**F**	**a**	**b**	**c**
925°C	4.84	4.07	5.55	4.94	3.25	2.84	3.94	3.94	4.51
7000 hours	5.21	4.41	5.83	5.06	4.48	4.11	3.96	4.39	2.72
	5.33	4.85	5.79	5.44	4.73	4.72	4.07	4.55	4.43
	5.41	4.94	6.04	5.54	4.81	5.48	4.54	4.73	4.53
	5.41	5.15	5.35	5.59	5.02	5.64	4.61	4.78	4.59
	5.8	5.26	5.49	5.98	5.4	5.69	4.85	4.99	4.72
	5.91	5.6	5	6.08	5.41	5.83	5.24	5.25	5.68
	6.32	5.62	4.92	6.52	5.41	5.87	5.49	6.05	6.48
	6.53	6.01	4.36	7.94	6.39	6.24	5.51	6.07	6.78
	7.21	7.73	4.83	8.59	6.95	6.68	6.08	6.78	7.25

Sample ID	Thickness at location (µm)								
81-BSYA-35	**A**	**B**	**C**	**D**	**E**	**F**	**a**	**b**	**c**
975°C	2.41	1.95	1.73	2.01	2.62	2.5	1.97	2.72	1.45
300 hours	2.65	2.13	1.79	2.21	2.77	2.59	2.24	2.75	2.07
	2.78	2.44	2.27	2.31	2.97	2.61	2.37	2.79	2.37
	3.05	2.63	2.54	2.48	2.99	2.65	2.79	3.02	2.6
	3.08	2.79	2.76	2.51	3.01	2.87	2.89	3.16	2.62
	3.11	2.92	2.86	2.81	3.03	3.1	2.97	3.21	2.72
	3.15	2.93	2.89	2.89	3.17	3.15	2.98	3.28	2.74
	3.25	2.98	3.07	3.1	3.19	3.32	3.21	3.57	3.54
	3.33	3.08	3.18	3.15	3.24	3.43	3.37	3.58	3.73
	3.88	3.64	3.38	4.04	3.26	3.64	3.62	4.06	3.77

Sample ID	Thickness at location (µm)								
81-BSYA-36	**A**	**B**	**C**	**D**	**E**	**F**	**a**	**b**	**c**
975°C	5.24	5.17	4.52	4.81	4.86	na	na	na	3.63
3000 hours	5.38	5.59	4.56	5.26	5.06	na	na	na	4.24
	5.78	5.77	5.02	5.63	5.66	na	na	na	4.46
	6.68	5.85	5.26	5.85	5.71	na	na	na	4.59
	6.69	5.99	5.41	5.98	5.84	na	na	na	5
	7.69	6.03	5.73	6.02	5.89	na	na	na	5.13
	7.84	6.32	5.91	6.38	6.2	na	na	na	5.36
	9.4	6.85	6.18	6.83	6.61	na	na	na	5.58
	10.2	6.88	6.28	7.04	7.43	na	na	na	5.79
	10.87	7.47	6.95	8.86	7.48	na	na	na	6.13

Sample ID	Thickness at location (µm)								
81-BSYA-37	**A**	**B**	**C**	**D**	**E**	**F**	**a**	**b**	**c**
975°C	4.65	4.4	4.38	3.88	4.17	3.81	4.58	4.59	4.15
3000 hours	4.79	4.52	4.68	4.83	4.95	4.81	4.84	4.69	4.49
	4.87	5.12	4.83	4.86	5.9	4.99	4.98	4.88	4.8
	4.94	5.68	5.11	4.89	5.95	5.45	5.11	4.97	5.06
	5.08	6.07	5.23	5.18	5.98	5.5	5.32	5.06	5.21
	5.91	6.09	5.31	5.33	6.59	5.52	5.56	5.19	5.34
	6.36	6.34	5.36	5.45	6.84	5.65	5.74	5.43	5.41
	6.76	7.05	5.98	5.83	6.9	5.8	6.17	5.45	5.66
	6.85	7.37	6.17	6.2	7.05	7.59	6.84	5.52	5.79
	7.23	7.63	6.27	7.07	7.46	8.61	6.86	6.51	6.84

APPENDIX E – MEASURED OUTWARD AND INWARD β-DEPLETION ZONES THICKNESSES ON MODIFIED AEROFOIL-SHAPED SAMPLES (µm)

na: data non available

in red: BC was completely depleted by depletion zone could be measured thanks to γ'-Ni_3Al phase

no β: BC was completely depleted of β-NiAl

OUTWARD β-DEPLETION ZONE:

Sample (81-BSYA)	**1**	**2**	**3**	**4**	**5**	**6**	**7**	**8**
Temperature (°C)	900	900	900	900	900	900	900	900
Exposure time (hours)	4000	10,000	2780	2780	20,000	4000	7000	15,000
A	26.6	26.6	26.6	27.3	34.7	29.6	no β	36.2
B	23.3	23.3	23.3	24.9	29.9	26.0	no β	no β
C	26.9	26.9	26.9	19.8	42.1	29.6	30.5	34.9
D	23.7	23.7	23.7	22.7	32.9	26.4	27.3	29.3
E	27.8	27.8	27.8	41.8	41.1	36.9	39.9	30.5
F	24.1	24.1	24.1	24.6	31.3	no β	27.9	no β
a	29.4	29.4	na	31.3	63.9	na	47.6	36.7
b	24.9	24.9	na	24.1	47.1	na	35.6	28.7
c	36.9	36.9	na	46.7	61.5	na	54.1	45.6

Sample (81-BSYA)	**12**	**13**	**14**	**16**	**18**	**19**
Temperature (°C)	950	950	950	950	1000	1000
Exposure time (hours)	2780	4000.0	2780.0	5000	1050	1500
A	53.0	58.0	48.4	no β	no β	no β
B	no β	no β	no β	no β	no β	no β
C	50.4	44.5	50.6	no β	70.5	no β
D	37.6	52.0	42.5	no β	59.3	no β
E	no β	59.9	no β	no β	no β	no β
F	no β	45.9	46.8	no β	no β	no β
a	86.1	56.8	na	no β	108.3	no β
b	38.3	62.9	na	no β	55.4	90.0
c	61.6	45.0	na	no β	97.6	no β

Sample (81-BSYA)	**25**	**26**	**27**	**29**	**31**	**35**	**36**	**37**
Temperature (°C)	925	925	925	925	925	975	975	975
Exposure time (hours)	10,000	100	4000	2740	7000	300	3000	2700
A	45.5	14.2	30.2	30.9	no β	34.3	no β	no β
B	11.0	no β	23.9	no β	no β	42.3	no β	no β
C	36.6	13.3	34.2	33.9	38.6	28.8	no β	61.5
D	35.1	14.8	30.1	27.7	41.4	35.0	no β	59.1
E	34.4	18.8	30.6	36.2	40.3	29.9	no β	no β
F	20.9	4.9	29.3	32.5	37.7	46.0	no β	no β
a	25.6	16.0	32.5	37.7	46.3	25.0	83.4	68.2
b	28.0	14.8	41.8	30.6	55.4	30.0	69.3	75.7
c	11.8	19.2	36.6	40.8	58.0	35.0	no β	78.7

INWARD β-DEPLETION ZONE:

Sample (81-BSYA)	**1**	**2**	**3**	**4**	**5**	**6**	**7**	**8**
Temperature (°C)	900	900	900	900	900	900	900	900
Exposure time (hours)	4000	10,000	2780	2780	20,000	4000	7000	15,000
A	21.0	45.0	9.1	14.0	57.4	15.4	no β	42.4
B	27.3	25.4	10.5	12.0	28.8	29.7	no β	no β
C	19.0	29.8	7.8	11.9	58.1	15.5	43.6	61.9
D	13.2	50.1	16.4	13.9	58.9	18.9	29.4	47.4
E	23.9	38.2	6.4	26.2	16.5	29.9	29.9	38.6
F	17.7	29.9	32.8	19.3	42.5	no β	25.2	no β
a	12.8	52.8	na	10.5	65.9	na	12.8	65.0
b	8.1	15.6	na	6.6	38.4	na	18.3	78.2
c	13.1	56.8	na	20.5	47.3	na	14.9	39.0

Sample (81-BSYA)	**12**	**13**	**14**	**16**	**18**	**19**
Temperature (°C)	950	950	950	950	1000	1000
Exposure time (hours)	2780	4000.0	2780.0	5000	1050	1500
A	46.2	28.3	36.5	no β	no β	no β
B	no β	no β	no β	no β	no β	no β
C	49.5	54.7	48.8	no β	15.4	no β
D	55.4	33.5	56.0	no β	17.5	no β
E	no β	47.9	no β	no β	no β	no β
F	no β	26.0	30.0	no β	no β	no β
a	24.7	42.9	na	no β	14.9	no β
b	30.6	36.4	na	no β	18.6	24.8
c	66.2	19.7	na	no β	17.5	no β

Sample (81-BSYA)	**25**	**26**	**27**	**29**	**31**	**35**	**36**	**37**
Temperature (°C)	925	925	925	925	925	975	975	975
Exposure time (hours)	10,000	100	4000	2740	7000	300	3000	2700
A	45.5	3.4	29.2	27.6	no β	0.0	no β	no β
B	11.0	no β	23.8	no β	no β	8.3	no β	no β
C	36.6	2.5	22.4	15.6	38.6	13.7	no β	43.8
D	35.1	2.6	34.6	15.7	41.4	5.0	no β	35.3
E	34.4	2.6	11.0	32.6	40.3	4.9	no β	no β
F	20.9	19.3	16.7	30.1	37.7	7.0	no β	no β
a	25.6	3.0	51.6	17.9	46.3	5.0	28.3	27.2
b	28.0	3.1	27.3	15.2	55.4	5.0	19.4	51.1
c	11.8	4.1	9.9	15.4	58.0	0.0	no β	33.3

APPENDIX F – REMAINING β-PHASE MEASUREMENTS ON MODIFIED AEROFOIL-SHAPE SAMPLE

Sample (81-BSYA-)	**ref 1**	**ref 2**
Temperature (°C)	0	0
Exposure time (hours)	0	0
A	51.66	58.01
B	34.71	37.36
C	41.29	53.53
D	61.33	24.65
E	49.99	53.19
F	38.63	44.14
a	38.66	na
b	49.95	na
c	52.87	na

Sample (81-BSYA-)	**1**	**2**	**4**	**5**	**7**	**8**
Temperature (°C)	900	900	900	900	900	900
Exposure time (hours)	4000	10,000	2780	20,000	7000	15,000
A	8.98	0.77	9.52	0.00	0.00	0.00
B	0.00	0.00	0.00	0.00	0.00	0.00
C	13.34	9.81	12.04	0.00	4.22	0.00
D	12.09	3.46	13.15	0.00	4.93	0.00
E	0.00	0.00	0.00	0.00	0.72	0.00
F	0.00	0.00	0.00	0.00	0.00	0.00
a	13.35	0.00	10.48	0.00	13.45	0.00
b	17.64	13.42	25.51	3.90	7.28	0.00
c	7.94	0.00	1.29	0.00	15.38	0.00

Sample (81-BSYA-)	**9**	**12**	**13**	**14**	**16**
Temperature (°C)	950	950	950	950	950
Ox. Time (h)	4000	2780	4000	2780	5000
A	0.73	0.00	0.00	0.00	0.00
B	0.00	0.00	0.00	0.00	0.00
C	9.48	0.28	0.00	0.21	0.00
D	6.20	0.41	0.00	0.00	0.00
E	4.64	0.00	0.00	0.00	0.00
F	0.00	0.00	0.00	0.00	0.00
a	na	0.00	1.97	na	1.71
b	na	8.85	0.00	na	0.00
c	na	1.49	7.58	na	0.00

Sample (81-BSYA-)	**17**	**18**	**19**	**20**	**22**	**23**	**24**
Temperature (°C)	1000	1000	1000	1000	1000	1000	1000
Ox. Time (h)	1500	1050	1500	1050	1050	1500	1500
A	0.00	0.00	0.00	0.00	0.00	0.00	0.00
B	0.00	0.00	0.00	0.00	0.00	0.00	0.00
C	0.21	4.33	0.00	2.63	4.00	0.00	0.00
D	0.00	2.54	0.00	1.11	2.65	0.00	0.00
E	0.00	0.00	0.00	0.00	0.00	0.00	0.00
F	0.00	0.00	0.00	0.00	0.00	0.00	0.00
a	na	1.19	0.00	na	na	na	na
b	na	9.93	1.49	na	na	na	na
c	na	1.51	0.00	na	na	na	na

Sample (81-BSYA-)	**25**	**26**	**27**	**29**	**31**
Temperature (°C)	925	925	925	925	925
Ox. Time (h)	10,000	100	4000	2740	7000
A	1.03	33.35	3.72	4.78	0.00
B	0.00	0.00	0.00	0.00	0.00
C	5.55	24.26	6.85	7.10	0.00
D	7.24	22.69	4.73	10.89	0.00
E	2.57	15.68	9.09	3.17	0.00
F	0.00	0.00	0.00	0.00	0.00
a	9.04	18.78	12.00	13.65	7.79
b	9.36	24.21	6.04	11.85	0.00
c	7.62	29.99	5.89	14.26	5.53

Sample (81-BSYA-)	**35**	**36**	**37**
Temperature (°C)	975	975	975
Ox. Time (h)	300	3000	2700
A	8.98	0.00	0.00
B	1.78	0.00	0.00
C	13.96	0.00	0.00
D	9.11	0.00	0.00
E	8.54	0.00	0.00
F	4.16	0.00	0.00
a	0.00	3.17	0.00
b	0.00	6.53	2.24
c	0.00	0.00	0.00

APPENDIX G – FRACTION OF SPINELS/MIXED OXIDES IN TGO ON MODIFIED AEROFOIL-SHAPE SAMPLE

Sample (81-BSYA)	**1**	**2**	**4**	**5**	**7**	**8**
Temperature (°C)	900	900	900	900	900	900
Exposure time (hours)	4000	10,000	2780	20,000	7000	15,000
A	0.15	0.10	na	0.02	0.11	0.02
B	0.17	0.38	0.45	0.12	0.27	0.12
C	0.12	0.26	0.19	0.19	0.31	0.13
D	0.18	0.23	0.20	0.27	0.21	0.08
E	0.38	0.44	0.29	0.29	0.24	0.20
F	0.08	0.10	0.27	0.04	0.17	0.23
a	0.20	0.36	0.14	0.28	0.34	0.15
b	0.16	0.25	0.11	0.22	0.28	0.05
c	0.19	0.49	0.38	0.40	0.31	0.26

Sample (81-BSYA)	**9**	**12**	**13**	**14**	**16**
Temperature (°C)	950	950	950	950	950
Exposure time (hours)	4000	2780	4000	2780	5000
A	0.06	0.16	0.11	0.15	0.02
B	0.23	0.29	0.25	0.18	0.19
C	0.04	0.48	0.16	0.29	0.21
D	0.02	0.04	0.03	0.09	0.12
E	0.28	0.26	0.19	0.35	0.45
F	0.17	0.06	0.30	0.12	0.18
a	na	0.35	0.41	na	0.20
b	na	0.26	0.23	na	0.32
c	na	0.27	0.32	na	0.28

Sample (81-BSYA)	**17**	**18**	**19**	**20**	**22**	**23**	**24**
Temperature (°C)	1000	1000	1000	1000	1000	1000	1000
Exposure time (hours)	1500	1050	1500	1050	1050	1500	1500
A	0.02	0.04	0.14	0.02	0.18	0.11	0.03
B	0.09	0.14	0.10	0.13	0.06	0.17	0.11
C	0.25	0.23	0.23	0.09	0.07	0.38	0.29
D	0.26	0.04	0.09	0.14	0.06	0.18	0.02
E	0.40	0.19	0.46	0.43	0.38	0.27	0.35
F	0.26	0.04	0.13	0.37	na	0.22	0.02
a	na	0.24	0.27	na	na	na	na
b	na	0.35	0.34	na	na	na	na
c	na	0.29	0.39	na	na	na	na

Sample (81-BSYA)	**25**	**26**	**27**	**29**	**31**
Temperature (°C)	925	925	925	925	925
Exposure time (hours)	10,000	100	4000	2740	7000
A	0.06	0.13	0.03	0.16	0.04
B	0.09	0.17	0.08	0.11	0.18
C	0.20	0.28	0.25	0.19	0.30
D	0.19	0.12	0.17	0.05	0.14
E	0.25	0.14	0.18	0.28	0.40
F	0.21	0.25	0.22	0.22	0.34
a	0.20	0.08	0.25	0.26	0.26
b	0.27	0.04	0.43	0.19	0.21
c	0.30	0.11	0.31	0.37	0.41

Sample (81-BSYA)	**35**	**36**	**37**
Temperature (°C)	975	975	975
Exposure time (hours)	300	3000	2700
A	0.25	0.02	0.07
B	0.04	0.14	0.08
C	0.26	0.16	0.12
D	0.05	0.04	0.14
E	0.23	0.12	0.18
F	0.14	0.16	0.02
a	0.33	0.27	0.20
b	0.23	0.18	0.00
c	0.43	0.40	0.09

APPENDIX H – MEASURED SECONDARY REACTION ZONE THICKNESSES ON MODIFIED AEROFOIL-SHAPED SAMPLES (µm)

na: data non available

Sample (81-BSYA)	**1**	**2**	**4**	**5**	**6**	**7**	**8**
Temperature (°C)	900	900	900	900	900	900	900
Exposure time (hours)	4000	10,000	2780	20,000	4000	7000	15,000
A	53.2	64.2	50.7	97.5	63.8	67.3	87.7
B	50.8	67.9	43.4	61.9	44.4	44.5	72.5
C	58.1	69.1	50.7	97.5	57.6	57.1	81.4
D	57.1	83.1	46.5	100.3	62.4	36.8	83.1
E	50.7	43.0	42.0	61.6	42.3	62.6	83.6
F	44.7	44.4	34.5	53.5	49.4	65.0	61.1
a	64.4	na	57.0	72.8	na	67.9	61.9
b	47.3	66.8	34.2	67.6	na	48.4	80.7
c	57.3	66.1	47.0	76.3	na	70.9	85.2

Sample (81-BSYA)	**9**	**12**	**13**	**14**	**16**	**18**	**19**
Temperature (°C)	950	950	950	950	950	1000	1000
Exposure time (hours)	4000	2780	4000.0	2780.0	5000	1050	1500
A	68.7	71.6	82.7	67.7	80.0	54.0	87.3
B	38.4	242.8	51.1	51.7	75.0	52.6	25.7
C	81.5	78.6	84.4	71.6	90.0	51.3	84.8
D	76.1	82.9	78.8	71.6	90.0	62.5	80.0
E	74.1	49.8	76.7	54.6	60.0	34.7	79.4
F	58.6	51.7	84.7	68.9	65.0	43.4	75.6
a	na	74.8	77.2	na	75.0	59.6	91.6
b	na	77.0	65.8	na	90.0	67.1	79.4
c	na	89.3	67.2	na	80.0	49.5	89.7

Sample (81-BSYA)	**25**	**26**	**27**	**29**	**31**	**35**	**36**	**37**
Temperature (°C)	925	925	925	925	925	975	975	975
Exposure time (hours)	10,000	100	4000	2740	7000	300	3000	2700
A	75.9	34.4	54.4	56.9	85.2	45.2	103.0	98.5
B	47.7	29.2	69.1	45.3	52.4	34.7	46.3	32.4
C	71.5	15.0	68.5	67.5	94.6	43.1	116.5	92.6
D	74.8	31.5	69.2	46.5	101.0	65.0	112.7	78.0
E	50.0	10.1	39.1	49.6	75.1	47.8	80.8	82.2
F	38.2	20.8	55.7	53.2	60.8	50.0	61.4	57.1
a	75.3	11.5	62.5	65.8	74.0	59.3	82.5	80.4
b	77.1	16.0	65.8	63.7	95.1	48.3	89.3	87.0
c	66.2	26.2	83.1	52.9	69.4	48.3	83.7	79.7

APPENDIX I – MODIFIED AEROFOIL-SHAPED SAMPLES (REFERENCE SHEET)

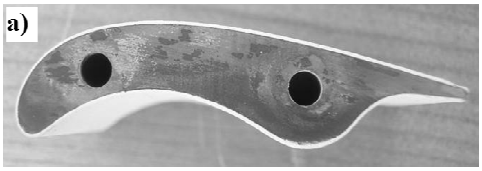

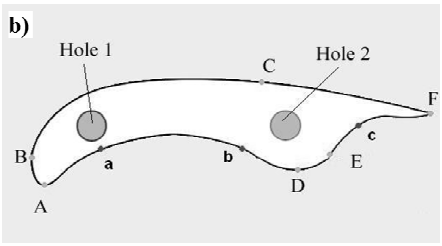

Location	Curvature (mm^{-1})
A	0.85
B	0.14
C	0.01
D	0.18
E	Theoretical 0
F	2.86
a	-0.06
b	-0.05
c	-0.20

shaped
entation.
convex

erent positions around
ample

81-BSYA-	Oxidation Temperature (°C)	Total exposure time (hours)	81-BSYA-	Oxidation Temperature (°C)	Total exposure time (hours)
1	900	4000	20	1000	1050
2	900	10,000	21	1000	1050
3	900	2780	22	1000	1050
4	900	2780	23	1000	1500
5	900	20,000	24	1000	1050
6	900	4000	25	925	10,000
7	900	7000	26	925	100
8	900	15,000	27	925	4000
9	950	4000	28	925	>10,000
10	950	5000	29	925	2740
11	950	5000	30	925	2740
12	950	2780	31	925	7000
13	950	4000	32	925	>10,000
14	950	2780	33	975	4000
15	950	5000	34	975	3000
16	950	5000	35	975	300
17	1000	1500	36	975	3000
18	1000	1050	37	975	2700
19	1000	1500			

Modified aerofoil-shaped samples denomination, oxidation temperatures and total exposure times